THÈSE

Pour obtenir le grade de

DOCTEUR DE L'UNIVERSITÉ GRENOBLE ALPES
et de l'UNIVERSITÉ DE TSUKUBA

École doctorale : PHYS - Physique
Spécialité : Physique Subatomique et Astroparticules
Unité de recherche : Laboratoire de Physique Subatomique et Cosmologie

Challenges en astrophysique et en cosmologie avec des caméras KID

Challenges in astrophysics and cosmology with KID-based cameras

Présentée par :

Damien CHEROUVRIER

Direction de thèse :

Juan-Francisco MACIAS-PEREZ DIRECTEUR DE RECHERCHE, CNRS DELEGATION ALPES	Directeur de thèse
Nario KUNO FULL PROFESSOR, UNIVERSITY OF TSUKUBA	Co-directeur de thèse

Rapporteurs :

DOUSPIS MARIAN
ASTRONOME, UNIVERSITE PARIS- SACLAY
BARBARA SARTORIS
DOCTEURE EN SCIENCES HDR, LUDWIG-MAXIMILIANS-UNIVERSITÄT MÜNCHEN

Thèse soutenue publiquement le **7 novembre 2025**, devant le jury composé de :

GILLES HENRI, PROFESSEUR DES UNIVERSITES, UNIVERSITE GRENOBLE ALPES	Président
DOUSPIS MARIAN, ASTRONOME, UNIVERSITE PARIS- SACLAY	Rapporteur
BARBARA SARTORIS, DOCTEURE EN SCIENCES HDR, LUDWIG-MAXIMILIANS-UNIVERSITÄT MÜNCHEN	Rapporteure
LAURA SALVATI, CHARGEE DE RECHERCHE, CNRS DELEGATION ILE-DE-FRANCE SUD	Examinatrice
STEPHANIE ESCOFFIER, DIRECTRICE DE RECHERCHE, CNRS DELEGATION PROVENCE ET CORSE	Examinatrice
TAKUYA HASHIMOTO, ASSISTANT PROFESSOR, UNIVERSITY OF TSUKUBA	Examinateur
KEN OHSUGA, FULL PROFESSOR, UNIVERSITY OF TSUKUBA	Examinateur
TETSU KITAYAMA, FULL PROFESSOR, TOHO UNIVERSITY	Examinateur

Acknowledgments

I would first like to express my gratitude to the members of my thesis committee. In particular, I would like to thank Barbara Sartoris and Marian Douspis for reviewing my thesis and providing thoughtful comments. I also thank Gilles Henri, Stéphanie Escoffier, Prof. Ken Ohsuga, Prof. Tetsu Kitayama, and Prof. Takuya Hashimoto for their kindness through the stressful ordeal that is the PhD defense.

I am deeply grateful to my co-supervisor, Prof. Nario Kuno, for his continuous support during my time in the University of Tsukuba. Thank you very much for helping me get settled in Japan, and making me feel at home.

Un grand merci à Juan d'avoir cru en moi lorsque, sorti de nulle part, je suis venu discuter d'une thèse en cotutelle, et d'avoir soumis une demande de financement en quelques jours top chrono ! Plus de 4 ans après notre première rencontre, je dois avouer avoir fait semblant de comprendre les 3/4 des concepts dont tu m'as parlé ce jour-là. Malgré toutes les difficultés qu'une cotutelle représentait, tu as toujours été à l'écoute et disponible pour m'aider, pour me soutenir. Je m'excuse auprès des personnes qui te trouvent surbooké, tu devais sûrement être coincé dans un appel Skype de 4h avec moi !
Je me souviendrai longtemps des bons moments passés au Nobeyama et de tes escapades dans les montagnes japonaises sans téléphone ni GPS. Je suis très heureux d'avoir pu réaliser cette thèse sous ta supervision, et je te remercie encore pour toute ton aide et tes conseils qui ont façonné le scientifique (et la personne) que je suis aujourd'hui.

I would like to thank everyone in the *MKID* group at the University of Tsukuba for their warm welcome and for putting up with me despite my lack of Japanese skills. みなさん、ありがとう！またね！

Merci du fond du cœur à toute l'équipe COSMO-ML/DARK/Cosmologie Observationnelle du LPSC et collaborateurs proches, en commençant par les membres honorifiques, Nico et Xavier. Merci pour votre aide précieuse pour mon intégration dans la collaboration NIKA2 et pour les nombreuses discussions qui m'ont permis de progresser dans mes recherches. Merci Alessandro pour toute ton aide avec la caméra Grenoble-Tsukuba, notamment lorsque j'étais perdu dans les tests en labo. Même si ce n'était pas gagné d'avance, je suis très heureux d'avoir pu ajouter ma pierre à l'édifice et d'avoir vu la caméra aboutir. J'attends avec impatience les prochaines itérations !
Merci à tous les permanents de l'équipe pour leur gentillesse tout au long de ces trois années et pour tous ces moments de teambuilding. Merci Andrea pour nos discussions sur l'instrumentation et les KIDs. Merci Fred et Laurence de m'avoir intégré au LPSZ et de ne pas avoir perdu patience en réunion face aux 2^{16} plots de sources radio aux flux négligeables.

Cette thèse n'aurait pas vu le jour sans l'aide de tous les doctorant·es et postdocs du *gang du 3ème*, celles·eux déjà partis et les nouvelles·aux : Constantin, Eduardo, Miren, Carolina, Corentin, Alice, Marina, Sofia, Louise, Matthieu, Loux, Mateo, Juan, Gaël, Antoine, Aparajita, Benedetta, Samuel. Impossible de faire une liste complète de tous les bons moments passés ensemble, au labo et en dehors. La briscola, le H2, les soirées chez Corentin, Montpellier, l'école Euclid, le *bitchage*. Que de bons souvenirs qui m'ont permis de tenir bon dans les moments de solitude à l'autre bout du monde. Encore merci pour tout.

Merci aux *Zamis* Paul, Alex, Lulu, Juju, Matyas, Jerem pour tous les bons moments depuis le collège/lycée. Je sais que je peux toujours compter sur vous, et que même dans 20 ans on se retrouvera toujours à Clamart autour d'un bon sushi. Le Régal à jamais dans nos cœurs.

Je voudrais également remercier tous·tes mes ami·es que j'ai pu rencontrer au cours de mes études à Paris-Sud puis Paris-Saclay, et que j'ai malheureusement perdus de vue depuis. Je garde de très bons souvenirs grâce à vous et j'espère que nos chemins se recroiseront un jour.

Merci à toute ma famille de me soutenir depuis 26 ans maintenant. Merci Maman et Papa d'avoir toujours été là pour moi, pour tous nos voyages, pour le saxo, pour le tennis, pour tout. Même si mes passages à la maison s'espacent au fil du temps, je suis toujours heureux de revenir comme si je n'étais jamais vraiment parti. Merci Mamie Kaija et Papy Daniel pour toutes nos vacances à Radon depuis tout petit, pour les chansons, le vélo sur la digue, Port Dienville, pour Elliott et Sirius. Merci aux cousins Victor et Selma, Anna et Andreas sans qui ces vacances n'auraient pas été les mêmes ! Nous sommes maintenant un peu grands pour y rentrer, mais la cabane des cousins restera toujours là pour attester de tous ces bons moments. Merci Mamue et Grand-Père pour tous les moments passés au Perreux puis à Antony, et sans oublier Houlgate. Merci pour tous les bons plats spécialement préparés pour la personne difficile que je suis, pour les châteaux et les pièges sur la plage, les balades au Tremblay, Intervilles. Mathilde, ma petite sœur, je suis désolé de parler aussi peu et d'être obligé de l'écrire plutôt que de le dire à voix haute : je suis extrêmement fier de toi depuis toujours. J'attends avec impatience de lire ta thèse, même si je n'y comprendrai pas grand-chose.

Manon (Manon de Nîmes pour les intimes), merci d'être toujours là pour moi même au fil des mois passés à distance, je n'aurais pas pu y arriver sans toi. Tu as réussi à me faire sortir de ma carapace, ce que personne n'avait réussi à faire. J'ai appris à profiter au maximum de chaque moment, même ceux passés loin de toi, afin de mieux te les partager. Nos prochaines aventures aux quatre coins du monde ne seront que le début d'une longue histoire que j'ai hâte de partager avec toi. Je t'aime.

Abstract

Clusters of galaxies are formed at the latest stages of structure formation and are unique cosmological probes to study structure formation and its evolution. With the advent of large CMB surveys like those from the Planck satellite, the ACT and SPT telescopes, we now have access to a large catalog of galaxy clusters detected at millimeter wavelengths via the tSZ effect. Nevertheless, it is necessary to complement them with high angular resolution (tens of arcseconds) observations to target the lowest mass and highest redshift clusters. In this context, the NIKA2 camera, installed at the IRAM 30-m telescope provides a powerful tool for studying distant galaxy clusters with exquisite precision, thanks to its large field of view and high angular resolution. Equipped with 2900 Lumped Element Kinetic Inductance Detectors (LEKIDs), the camera has demonstrated great sensitivity, enabling a wealth of astrophysical studies across a wide range of fields, from cosmology to galactic and extra-galactic science. KIDs have thus emerged as promising alternatives to bolometers for the development of astrophysical instruments operating across millimeter to terahertz wavelengths.

This thesis makes use of two cameras equipped with LEKIDs. The first part is dedicated to the Tsukuba-Grenoble 100 GHz camera, currently installed at the Nobeyama Radio Observatory (NRO) in Japan. We present results from laboratory measurement campaigns and changes to the experimental setups leading up to the installation and observations at NRO. We then describe the data reduction pipeline used to characterize the camera's on-sky performance, as well as the scientific results obtained.

The second part focuses on the NIKA2 camera and work done within two Guaranteed Time Large Programs: the SZ Large Program (LPSZ) and the NIKA2 Cosmological Legacy Survey (N2CLS). We discuss the identification, matching, and comparison of point sources in the LPSZ cluster fields, with a particular emphasis on radio sources, showing that their accurate characterization is crucial to limit bias on pressure profile estimation. We also discuss the methodology used to compare LPSZ cluster masses to those in the literature. Finally, we present results from the blind detection of clusters in the N2CLS COSMOS field, covering data reduction to cluster candidate characterization, as well as the cluster detection algorithm. We discuss the unique sample of high-redshift, low-mass clusters obtained.

Contents

Introduction **17**

I Cosmology with galaxy clusters **20**

1 Cosmology Standard Model and large-scale structures **22**
1.1 The standard model of cosmology . . . 22
1.2 The Cosmic Microwave Background . . . 23
1.3 Origin and evolution of large-scale structures . . . 24
1.3.1 Limitations of the standard model . . . 25
1.3.2 Linear growth of density perturbations . . . 26
1.3.3 The Press-Schechter formalism and halo mass function . . . 27
1.4 Conclusion . . . 28

2 Clusters of galaxies **29**
2.1 Clusters and groups of galaxies . . . 30
2.2 Observation of galaxy clusters . . . 30
2.2.1 Optical and infrared . . . 31
2.2.2 Radio . . . 31
2.2.3 X-ray . . . 31
2.2.4 Millimeter: Sunyaev-Zel'dovich effect . . . 31
2.3 Galaxy clusters detection in large surveys . . . 34
2.3.1 History of cluster detection . . . 34
2.3.2 The first galaxy cluster catalogs . . . 36
2.3.3 Optical large surveys and catalogs . . . 37
2.3.4 X-ray large surveys and catalogs . . . 38
2.3.5 SZ large surveys and catalogs . . . 40
2.4 Cosmology with galaxy clusters . . . 43
2.4.1 Universal pressure profile and scaling relations . . . 43
2.4.2 Number counts . . . 44
2.4.3 Gas mass fraction . . . 45
2.4.4 tSZ angular power spectrum . . . 45
2.4.5 X-ray/SZ distances . . . 45

2.5 Conclusion . . . 47

II Towards a LEKIDs camera at 100 GHz **48**

3 A 100 GHz LEKIDs camera for the Nobeyama telescope **50**
3.1 Lumped Element Kinetic Inductance Detectors (LEKIDs) . . . 51
3.1.1 Principle of operation . . . 51
3.1.2 Comparison of readout and calibration techniques . . . 53
3.2 The Grenoble-Tsukuba (GT) 100 GHz LEKIDs camera . . . 58
3.2.1 Detector design . . . 59
3.2.2 The cryostat . . . 60
3.3 Laboratory characterization and validation: 2021 lab campaign . . . 60
3.3.1 Data reduction pipeline . . . 61
3.3.2 Noise measurements . . . 62
3.3.3 Beam shape measurements . . . 62
3.4 2024 laboratory campaign . . . 66
3.4.1 $\mathbf{S_{21}}$ spectrum . . . 66
3.4.2 Quality factors . . . 67
3.4.3 Beam measurements . . . 68
3.5 Summary and conclusion . . . 69

4 Observations with the Nobeyama telescope **70**
4.1 The Nobeyama 45-m telescope . . . 70
4.2 SZ observations at the Nobeyama telescope . . . 71
4.3 GT camera installation and setup . . . 73
4.3.1 New GT camera readout system . . . 73
4.3.2 Installation at the telescope . . . 73
4.3.3 Final noise measurements before observations . . . 73
4.4 Observations . . . 74
4.4.1 Target selection . . . 74
4.4.2 Weather conditions . . . 77
4.4.3 Finding and tuning KIDs before observations . . . 77
4.4.4 Scanning strategy . . . 79
4.4.5 Online processing . . . 80
4.4.6 Focus . . . 80
4.4.7 Skydip . . . 81

5 Development of the GT camera data reduction pipeline **84**
5.1 Frequency shift reconstruction . . . 85
5.1.1 RANSAC calibration technique . . . 85
5.1.2 Caveats of the RANSAC method . . . 86
5.2 Description of the time-ordered data components . . . 87

5.2.1 Atmospheric noise . . . 88
5.2.2 Electronic noise . . . 88
5.2.3 Anomalous correlated noise . . . 89
5.2.4 Intrinsic noise . . . 90
5.3 Data selection . . . 90
5.3.1 Selection of valid detectors . . . 90
5.3.2 Samples selection . . . 91
5.4 Correlated noise substraction . . . 91
5.5 Map-making . . . 94
5.5.1 Individual maps per detector . . . 94
5.5.2 Combined map . . . 95
5.6 Commissioning results . . . 96
5.6.1 Beam size estimation and focal plane reconstruction . . . 96
5.6.2 Absolute calibration . . . 98
5.6.3 Sensitivity . . . 100
5.7 Conclusion and perspectives . . . 101

III Detection and study of clusters with NIKA2 **103**

6 NIKA2 and its Guaranteed Time Large Programs **105**
6.1 NIKA2 . . . 105
6.1.1 The IRAM 30-m telescope . . . 105
6.1.2 The NIKA2 camera . . . 106
6.2 The NIKA2 SZ Large Program . . . 109
6.2.1 LPSZ cluster sample . . . 109
6.2.2 Scientific goals . . . 110
6.2.3 Up-to-date results . . . 111
6.2.4 Study of the hydrostatic mass bias with the LPSZ . . . 113
6.3 The N2CLS Large Program . . . 114
6.3.1 GOODS-North . . . 114
6.3.2 COSMOS . . . 116
6.3.3 Scientific goals . . . 118
6.3.4 Up-to-date results . . . 119
6.4 NIKA2: a powerful instrument to study the tSZ effect . . . 121
6.4.1 Very high resolution . . . 121
6.4.2 High sensitivity . . . 121
6.4.3 Dual-band capabilities . . . 122
6.5 Conclusion . . . 122

7 LPSZ clusters: Impact of point sources on pressure profiles **123**
7.1 Point sources in the LPSZ fields . . . 124
7.1.1 Sub-millimeter sources . . . 124

7.1.2 Radio sources . . . 124
7.2 LPSZ point source catalogs . . . 125
7.2.1 MB catalog constructed from the final LPSZ cluster maps . . . 125
7.2.2 FPS catalog built from point source optimized LPSZ maps . . . 127
7.2.3 Cross-validation of the two catalogs . . . 128
7.2.4 Validation with external catalogs . . . 132
7.3 Undetected sources in the LPSZ fields . . . 133
7.3.1 Undetected DSFGs . . . 134
7.3.2 Finding radio sources in astrophysical databases . . . 135
7.3.3 Problematic radio sources in the LPSZ sample . . . 137
7.3.4 Pressure profile reconstruction . . . 138
7.3.5 Impact of undetected radio sources on the pressure profile reconstruction . . . 139
7.4 Validation of cluster masses . . . 139
7.4.1 Literature search . . . 140
7.4.2 The mass of PSZ2G080 . . . 140
7.4.3 Mass estimates for the full LPSZ sample . . . 142
7.5 Conclusion . . . 143

8 Blind detection of galaxy clusters in the COSMOS field 146
8.1 Galaxy clusters in the COSMOS field . . . 147
8.2 Revisiting N2CLS maps . . . 147
8.2.1 Data reduction pipeline . . . 147
8.2.2 Final sky maps . . . 149
8.3 Cluster detection methodology . . . 149
8.3.1 tSZ signal modelling . . . 149
8.3.2 Matched-filtering . . . 151
8.3.3 Identification of cluster candidates . . . 151
8.3.4 Serendipitous detection rate . . . 152
8.4 Cluster detection characterization via simulations . . . 152
8.4.1 Cluster detection on simulations . . . 152
8.4.2 Completeness . . . 154
8.4.3 Purity . . . 155
8.5 Cluster candidates validation . . . 156
8.5.1 Cross-matching in NED, SIMBAD and VizieR databases . . . 156
8.5.2 Spectroscopic and photometric redshift catalogs . . . 158
8.5.3 Known bright clusters in the field . . . 158
8.6 Properties of cluster candidates . . . 161
8.6.1 Integrated tSZ emission . . . 161
8.6.2 Cluster candidate mass estimates . . . 163
8.7 Conclusion and perspectives . . . 164

Conclusions and perspectives 168

Appendix **172**

Cluster catalogs in the literature 172

Clusters in the LPSZ sample 179

Catalog of radio sources in the LPSZ fields 180

Mass estimates of LPSZ clusters in the literature 185

Cluster candidate cutouts 193

Bibliography **195**

List of Figures

1.1 Map of the CMB as seen by COBE, WMAP, and *Planck* . . . 25

2.1 (Left): CMB spectrum undistorted and distorted by the tSZ effect. (Right): Spectra of the tSZ and kSZ effects at different ICM temperatures . . . 33

2.2 Abell2319 as seen by *Planck* . . . 33

2.3 Illustration of William Herschel's 40-foot telescope built in 1789 . . . 34

2.4 Distribution of extragalactic nebulae in Shapley and Ames (1932) . . . 35

2.5 (Left): Photographic plate of a section of the sky around the Coma cluster. (Right): Coma cluster as sketched by Zwicky in 1963 . . . 36

2.6 Maps of the first four clusters detected in the SPT SZ survey at 150 GHz and their associated match-filtered maps . . . 41

2.7 Distribution in the mass-redshift plane of clusters in the latest tSZ cluster catalogs . . 42

2.8 Current constraints on the cosmological parameters Ω_m, σ_8, and the S_8 parameter from different cluster related probes . . . 46

3.1 Schematic representation of the amplitude (left) and phase (right) of the S_{21} parameter for one KID . . . 52

3.2 (Left): Schematic representation of the NIKA2 readout setup used to monitor a KID array. (Right): Same for a FFT-based readout setup . . . 54

3.3 Reconstruction of the resonance frequency shift in the complex I-Q plane . . . 55

3.4 Simulation of the modulation as a function of the sample number within one CONCERTO data block . . . 56

3.5 Resonance circle in the (I, Q) plane . . . 57

3.6 $|S_{21}|$ spectrum acquired by the Tsukuba FFTS readout and best-fit results . . . 58

3.7 (Left): Comparison of the techniques for a point source. (Right): ξ_{amp} as a function of δf_0^{exp} for the different readout techniques . . . 59

3.8 ξ_{amp} in the $v_s - \delta f_0^{exp}$ plane for different readout techniques: *RfdIdQ* (top-left), *cftoi* (top-right), 3-points (bottom-left), and FFTS (bottom-right) . . . 59

3.9 Picture of a prototype LEKIDs array . . . 60

3.10 (Top): Cross-sectional view of the GT camera cryostat showing the cold optics and the four temperature stages. (Bottom): Cold optical layout inside the cryostat . . . 61

3.11 Noise PSD measurement performed in Grenoble in 2019. . . . 62

3.12 Noise PSD measurement for each detector performed at NAOJ in 2021 63
3.13 (Left): Picture of the knife-edge setup used to measure the beam shape of the LEKIDs array. (Top-Right): Illustration of the knife-edge method. (Bottom-Right): Example of the frequency shift of one resonance during a knife-edge measurement 64
3.14 (Top-left): Model of the shift in resonance frequency δf_0 as a function of the knife-edge position for one detector. (Top-right): Derivative of the δf_0 model as a function of the knife-edge position for one detector. (Bottom-left): Measurements of the δf_0 shift for all detectors in the array. (Bottom-right): Derivative of δf_0 for a subsample of 20 KIDs. 65
3.15 Focal plane geometry of the array 65
3.16 Comparison of the noise PSD measured using the *RfdIdQ* and the FFTS techniques . 66
3.17 VNA scan of the GT LEKIDs array, showing the $|S_{21}|$ parameter as a function of the frequency 67
3.18 (Left): VNA scan data of four resonances and the best-fit. (Right): Quality factors Q_i, Q_c, and Q_{tot} of each LEKID 68
3.19 (Left): Beam size distribution along the X and Y axes. (Right): Focal plane geometry of the array 69

4.1 (Left): Picture of the Nobeyama 45-meter telescope. (Right): Schematic representation of the optical path from the main reflector to the receiver cabin 71
4.2 150 GHz map of RX J1347-1145, where the central radio source has been subtracted, from Komatsu et al. (1999) 72
4.3 Schematic representation of the NIKEL readout system 74
4.4 (Left): Picture of the inside of the receiver cabin. (Right): Picture of the rack where the readout electronics are installed on the upper level 75
4.5 (Left): Noise PSD measurement performed at NRO on October 16th, 2024. (Right): Noise PSD distribution 76
4.6 Elevation of the sources during one observation night, October 22nd 76
4.7 PWV and relative humidity measured during the observation period 78
4.8 Tones before and after the `tuning` procedure 78
4.9 Scan path of the telescope in the alt-azimuthal plane during a typical scan of Mars . . 79
4.10 Maps of Saturn (left) and Jupiter (right) for one detector obtained during the online processing 80
4.11 Results from 5 focus scans performed on Saturn on October 21st. (Top): Combined maps obtained for increasing focus values. (Bottom): Measured FWHM and amplitude as a function of the sub-reflector position 81
4.12 Results of a `skydip` performed on October 23rd 82

5.1 Comparison of the raw TOIs obtained for one detector with three different calibration methods 85
5.2 Comparison of the circle fit obtained with the RANSAC algorithm and the individual 3-points fits for one detector 86
5.3 Distribution of the circle parameters obtained from 2000 runs of the RANSAC algorithm for one detector 87

5.4 (Left): Common mode of the TOIs, i.e., the correlated noise between all detectors in the array. (Right): Power spectrum of the common mode. The power law fit is shown in red . . . 89
5.5 Projected maps of Mars for half of the detectors in the array. The maps framed by a blue line show detectors saturated by noise. In pink, we indentify detectors in diaphony or two KIDs tuned to the same resonance frequency. Maps framed by an orange line show detectors out of resonance . . . 91
5.6 Telescope's path in the alt-azimuthal plane during a scan of Mars . . . 92
5.7 Combined map of Mars obtained by stacking the maps from each detector without any decorrelation . . . 92
5.8 (Left): Raw TOIs of 32 working detectors during a Mars scan. (Right): Cleaned TOIs after common mode subtraction of three detectors . . . 93
5.9 Correlation matrix of the TOIs for working detectors in the GT array during an observation of Mars. (Left): Raw TOIs correlations. (Right): Correlations after subtraction of a common mode . . . 94
5.10 Projected map of Mars for each working detector. . . . 95
5.11 (Top) Combined Mars map obtained with 32 detectors. (Bottom left): Map of the integration time per pixel. (Bottom right): Standard deviation map from the same analysis . . . 97
5.12 3C84 map per detector used to reconstruct the focal plane geometry of the array . . . 98
5.13 (Left): Beam FWHM distribution (Right): Focal plane geometry of the array reconstructed from a *beammap* of 3C84 . . . 98
5.14 Results of the fit of a 2D Gaussian to the combined map of Mars . . . 99
5.15 Sensitivity map obtained during the analysis of a Mars scan . . . 101

6.1 NIKA2 bandpasses at 150 GHz and 260 GHz, plotted with the atmospheric transmission and tSZ spectral distortion . . . 106
6.2 IRAM 30-m telescope sky coverage in galactic coordinates . . . 107
6.3 Picture of the IRAM 30-m telescope . . . 107
6.4 Cross-section of the NIKA2 camera illustrating the optical chain and the main elements 108
6.5 Distribution of the LPSZ cluster sample in the five bins in integrated Compton parameter and two in redshift . . . 110
6.6 First tSZ maps of a cluster with NIKA and NIKA2 . . . 112
6.7 150 GHz maps of the 38 clusters part of the final NIKA-LPSZ sample . . . 115
6.8 Selection of existing surveys in GOODS-N . . . 116
6.9 Selection of existing surveys in COSMOS . . . 117
6.10 Comparison between the N2CLS cumulative source number counts at 260 GHz (left) and 150 GHz (right) with results from the literature . . . 119
6.11 Angular size $2\theta_{500}$ of a cluster as a function of redshift for different masses . . . 121

7.1 Overview of the MB catalog with a total of 301 sources . . . 126
7.2 $9' \times 9'$ NIKA2 maps of PSZ2G155 at 150 GHz (left columns) and 260 GHz (right columns) 127

7.3 Overview of the FPS catalog with a total of 261 sources . . . 128
7.4 Comparison of the detection properties of common point sources in the MB and FPS catalogs, at 260 GHz (left) and 150 GHz (right) . . . 130
7.5 (Top): Distribution of the SNR at 150 GHz (left) and 260 GHz (right) of unmatched sources for both catalogs. (Bottom): Distribution of the distance to the cluster center of unmatched sources . . . 131
7.6 $6.5' \times 6.5'$ SZ maps of the ACTJ0022 cluster at 150 GHz (left), 260 GHz (middle), and residuals (right) . . . 131
7.7 $6.5' \times 6.5'$ maps of the PSZ2G126 cluster at 150 GHz (left) and 260 GHz (right) . . . 132
7.8 150 GHz flux as a function of the 260 GHz flux for the sources with a radio counterpart detected in the FPS, MB, or both catalogs . . . 135
7.9 Spatial distribution of the radio sources averaged over all LPSZ fields . . . 136
7.10 $6.5' \times 6.5'$ NIKA2 150 GHz map of PSZ2G201 . . . 137
7.11 $6.5' \times 6.5'$ NIKA2 150 GHz (left) and residuals (right) map of PSZ2G212 . . . 138
7.12 (Left): From left to right, NIKA2 150 GHz map, best-fit model, and residuals maps of PSZ2G212 with the radio source PSZ2G212_1 not included in the model (top) and included (bottom). (Right): Pressure profiles with and without the radio source included in the model . . . 139
7.13 M_{500} estimates for PSZ2G111 in the literature . . . 141
7.14 Preliminary comparison of the NIKA2-LPSZ M_{500} with lensing (top-left), X-ray only (top-right), X-ray+SZ (bottom-left) and dynamical (bottom-right) mass estimates from the literature . . . 143
7.15 Median value of M_{500} per estimate type (lensing, X-ray only, X-ray+SZ and dynamical masses) for every cluster in the LPSZ sample . . . 144

8.1 Transfer function for the pipeline used to construct the NIKA2 150 GHz COSMOS maps 149
8.2 NIKA2 COSMOS maps at 150 GHz (top) and 260 GHz (bottom) . . . 150
8.3 SNR map of the matched-filtered 150 GHz COSMOS map . . . 152
8.4 Pixel negative SNR distribution in the match-filtered N2CLS 150 GHz signal map and null map . . . 153
8.5 (Left): Distribution of all simulated clusters as a function of redshift and mass. (Right): Example of a simulated NIKA2 150 GHz map . . . 155
8.6 Distribution of the number of detections with SNR > 4 per simulated map . . . 156
8.7 Color coded completeness defined as the probability for a cluster of mass M_{500} and redshift z to be detected . . . 157
8.8 (Left): Completeness as a function of the mass, M_{500}, for different redshift ranges. (Right) Purity as a function of SNR for different redshift ranges . . . 157
8.9 Hyper Suprime-Cam (HSC) combined three color image of NK2-CL J100004.4+021148.4 158
8.10 Normalized spectroscopic and photometric redshift counts within a 1 arcmin radius around each cluster candidate . . . 159
8.11 NIKA2 150 GHz map of the COSMOS field with our NIKA2 cluster candidates and XMM-COSMOS clusters . . . 161

8.12 (Left): θ_{500}- Y_{500} range of possible values based on the redshift and mass priors used. (Right): θ_{500}- Y_{500} 68% confidence values, for each cluster candidate in the NIKA2 sample 162

8.13 Results of the fit of $200'' \times 200''$ cutouts of the NIKA2 COSMOS 150 GHz map centered on two cluster candidates: NK2-CL J100004.4+021148.4 (top) and NK2-CL J100045.8+020514.3 (bottom) 163

8.14 Corner plot of the $\theta_{500} - Y_{500}$ posterior maximum likelihood distribution for each of the cluster candidates 164

8.15 NIKA2 matched cluster sample in the mass-redshift plane. Cluster samples from other blind tSZ surveys such as PSZ2, ACT DR5, SPT-ECS, SPTpol, SPT-SZ, and SPT-Deep are shown for comparison 166

8.16 Cluster surface density as a function of cluster mass 166

17 Comparison of M_{500} estimates in the literature for a subsample of six LPSZ clusters. From top to bottom and left to right: ACTJ0022, ACTJ0119, ACTJ0215, ACTJ0223, ACTJ0240, and ACTJ2130 186

18 Comparison of M_{500} estimates in the literature for: ACTJ2302, PLCKG079, PLCKG227, PSZ1G080, PSZ1G226, and PSZ2G045 187

19 Comparison of M_{500} estimates in the literature for: PSZ2G046, PSZ2G080, PSZ2G081, PSZ2G084, PSZ2G085, and PSZ2G086 188

20 Comparison of M_{500} estimates in the literature for: PSZ2G087, PSZ2G091, PSZ2G094, PSZ2G099, PSZ2G104, and PSZ2G108 189

21 Comparison of M_{500} estimates in the literature for: PSZ2G111, PSZ2G126, PSZ2G133, PSZ2G141, PSZ2G144, and PSZ2G155 190

22 Comparison of M_{500} estimates in the literature for: PSZ2G160, PSZ2G183, PSZ2G193, PSZ2G201, PSZ2G209, and PSZ2G211 191

23 Comparison of M_{500} estimates in the literature for PSZ2G212 (left) and PSZ2G228 (right) 192

24 $200'' \times 200''$ cutouts of the NIKA2 COSMOS 150 GHz map around each cluster candidate 193

List of Tables

1.1 Latest constraints on cosmological parameters 24

4.1 Summary of the number of scans and total time on source for each target 77

6.1 Summary of the main characteristics of the NIKA2 instrument 109
6.2 Summary of single dish (sub)mm continuum observations in GOODS-N and COSMOS 117

7.1 Catalog of NIKA2 point sources associated with a radio point source 134

8.1 Summary of available cluster/group catalogs in the COSMOS field 147
8.2 Galaxy cluster candidates, sorted by decreasing SNR, with SNR > 4 154
3 Summary of available optical cluster catalogs in the literature 172
4 Summary of available X-ray cluster catalogs in the literature 176
5 Summary of available SZ cluster catalogs in the literature 178
6 Overview of the LPSZ cluster sample 179
7 Complete catalog of radio sources in the LPSZ fields 181

Introduction

Thanks to the observational progress made in recent years, modern cosmology has entered a precision era. The standard model of cosmology, ΛCDM, has been quite successful in explaining a wide range of observations, from the cosmic microwave background (CMB, Penzias and Wilson (1965)) to the large-scale structure of the Universe. Despite this apparent consistency, the origin and nature of the two main components of the Universe, dark matter and dark energy, remain unknown.

In this context, galaxy clusters, formed in the latest stages of structure formation, are unique cosmological probes to study structure formation and its evolution [Voit, 2005; Allen et al., 2011]. Their detection is a major field of research in modern cosmology, with a need to observe large samples of clusters to further reduce uncertainties on cosmological parameters. Large cluster catalogs have been built over the last decades at different wavelengths, from optical surveys to X-ray observations. Since the first detection of a cluster through the Sunyaev-Zel'dovich effect (SZ, Sunyaev and Zeldovich (1972)) in the 1970s [Pariiskii, 1973; Gull and Northover, 1976], observations at millimeter wavelengths have emerged as a great tool for the detection and study of galaxy clusters. The *Planck* satellite [Tauber et al., 2010], the South Pole Telescope (SPT, Ruhl et al. (2004)) and the Atacama Cosmology Telescope (ACT, Kosowsky (2003)) have detected hundreds to thousands of clusters over large fractions of the sky. However, these surveys are limited by their angular resolution, which makes the detection of high-redshift low-mass clusters very challenging. As a consequence, there is a need for high angular resolution instruments (tens of arcseconds) in order to map the SZ signal for high redshift and/or low-mass clusters of galaxies. Clusters in this mass-redshift regime are expected to be of great cosmological interest [Tinker et al., 2008], especially to verify our current understanding of structure formation.

To detect and study these low-mass, high-redshift clusters, we need two complementary ingredients: large millimeter cameras equipped with very sensitive detectors and large telescopes (diameter of 15-m or larger) that provide the required angular resolution. In the work presented in this thesis, we used two different instruments that meet these requirements. The first one is the Grenoble-Tsukuba (GT) camera, developed in a collaboration between the Grenoble-Alpes University and the University of Tsukuba, and installed at the Nobeyama 45-m telescope. The second one is the NIKA2 camera installed at the IRAM 30-m telescope. Both instruments are equipped with kinetic inductance detectors (KIDs, Day et al. (2003)), a technology that has emerged in the last two decades and proved to be very promising for millimeter observations.

This thesis is dedicated to the scientific exploitation of these two instruments to detect and study galaxy clusters via the SZ effect. As the GT camera was actively developed during this thesis, part of this work was also devoted to the laboratory characterization of the camera and its installation at the Nobeyama 45-m telescope. On the other hand, as the NIKA2 camera has been fully operational since 2015 and several large programs have already been conducted, the work developed with NIKA2 is part of two of these large programs: the NIKA2 SZ (LPSZ, Mayet et al. (2020)) and NIKA2 Cosmological Legacy Survey (N2CLS, Bing et al. (2023)) large programs.

This thesis is organized in three parts. The first part contextualises the work carried out by presenting the theoretical and observational background associated with the study of galaxy clusters:

– Chapter 1 presents the standard model of cosmology, describing the fundamental equations that govern the evolution of the Universe. We discuss how large-scale structures form and evolve, from initial density fluctuations to the complex structures we observe today.

– Chapter 2 is dedicated to galaxy clusters. We describe their main properties and their observations at different wavelengths, with a focus on the Sunyaev-Zel'dovich effect. A review of the history of galaxy cluster detections is also presented, from the first optical detections to the future of cluster surveys. We conclude the chapter with a description of how galaxy clusters can be used as cosmological probes.

The second part presents the work carried out with the Grenoble-Tsukuba camera, from its laboratory characterization to the commissioning observations at the Nobeyama 45-m telescope:

– In Chapter 3, the working principle of kinetic inductance detectors is described, along with a brief introduction to their readout electronics and signal reconstruction methods. We then describe the Grenoble-Tsukuba (GT) LEKIDs camera, one of the two instruments used during this thesis. A crucial step in the development of an instrument, the characterization of its performance, is presented. The results from two laboratory characterization campaigns are shown.

– Chapter 4 presents the Nobeyama 45-m telescope, as well as its history observing the SZ effect, where the GT camera was installed. A review of the final camera setup is given, along with the observation strategy. We finish by providing an overview of the different operations conducted at the telescope during the observation campaign.

– Building on the previous chapters, Chapter 5 gives a detailed description of the data reduction pipeline developed for the GT camera. We present the various fundamental steps in the analysis of the raw data, leading to the final maps. The on-sky performance of the camera is then assessed, with a focus on the absolute flux calibration, sensitivity and angular resolution.

The third and final part details the analyses conducted in the context of two NIKA2 large programs, the LPSZ and N2CLS programs. The former is dedicated to the high-angular resolution follow-up of a sample of 38 clusters, while the latter is a deep survey of two extragalactic fields in which clusters can be detected:

– In Chapter 6, we present the NIKA2 camera installed on the IRAM 30-m telescope, and describe its main characteristics. Then, for both the LPSZ and N2CLS large programs, we present their observation targets and their main scientific objectives, as well as the results obtained by both so far. We also explain why NIKA2 is a well-suited instrument for these programs and the study of the SZ effect in general.

– In Chapter 7, we investigate the impact of point sources, mainly sub-millimeter and radio galaxies, on the thermodynamical characterization of galaxy clusters in the LPSZ sample. The two methods used to detect point sources in the LPSZ cluster maps are detailed, along with the cross-validation of the two catalogs of point sources obtained. We then seek to identify all radio sources that are undetected in the field of view of the LPSZ clusters, and assess their impact on the reconstruction of their pressure profiles. In the same chapter, we present the comparison of the masses obtained by different works in the literature for the LPSZ clusters.

– Chapter 8 presents the first blind detection of galaxy clusters at millimeter wavelength at high angular resolution (18.5″) using the NIKA2 camera. We use the N2CLS observations of the COSMOS field to detect cluster candidates with a match-filter approach. We characterize the selection function of the survey using realistic simulations, which contain the contribution of both

the SZ signal and all the relevant astrophysical contaminants. The cluster sample we obtain is validated using ancillary cluster catalogs in the COSMOS field. We reconstruct the mass and integrated quantities of each cluster candidate by modelling their SZ signal and compare the results to previous works in the literature.

Part I

Cosmology with galaxy clusters

CHAPTER 1

Cosmology Standard Model and large-scale structures

1.1 The standard model of cosmology . . . 22
1.2 The Cosmic Microwave Background . . . 23
1.3 Origin and evolution of large-scale structures . . . 24
1.3.1 Limitations of the standard model . . . 25
1.3.2 Linear growth of density perturbations . . . 26
1.3.3 The Press-Schechter formalism and halo mass function . . . 27
1.4 Conclusion . . . 28

In this introductory chapter, we define the theoretical framework of this thesis. We first briefly describe the ΛCDM model, which is the current standard model of cosmology. Then, we present the thermal history of the Universe, from its early stages to the Cosmic Microwave Background (CMB). Finally, we discuss the formation of large-scale structures, from the initial density perturbations to the collapse of matter into virialized halos.

1.1 The standard model of cosmology

The standard model of cosmology is based on the laws of general relativity, and on the cosmological principle (see Abdalla et al. (2022) for a review). The latter states that the Universe is isotropic and homogeneous on the largest scales, i.e., our position in the Universe is not special and another observer somewhere else would on average see the same. Enforcing these conditions on the space-time metric yields the Friedmann-Lemaître-Robertson-Walker (FLRW) metric, which can be written as:

$$\mathrm{d}s^2 = c^2\mathrm{d}t^2 - a^2(t)\left[\frac{1}{1-Kr^2}\mathrm{d}r^2 + r^2\mathrm{d}\theta^2 + r^2\sin^2\theta\,\mathrm{d}\phi^2\right], \tag{1.1}$$

where (t, r, θ, ϕ) are the four-dimensional spherical coordinates, c the speed of light in vacuum, $a(t)$ the scale factor which describes how distances in the Universe expand or contract over time, and K the spatial curvature. The scale factor $a(t)$ evolves over time according to the dynamics of the Universe, which are governed by the Einstein field equations. These equations relate the geometry of space-time, encoded in the metric tensor, to the distribution of matter and energy in the Universe:

$$G_{\mu\nu} - \Lambda g_{\mu\nu} = \frac{8\pi G}{c^4}T_{\mu\nu}\,, \tag{1.2}$$

with $G_{\mu\nu}$ and $g_{\mu\nu}$ the Einstein tensor and metric, respectively. Together with the cosmological constant Λ, they describe the geometry of space-time. On the right side of the equation, $T_{\mu\nu}$, the stress-energy tensor, describes the matter and energy content of the Universe. G is the gravitational constant. Then, by combining the FLRW metric (Eq. 1.1) with the Einstein field equations (Eq. 1.2) and assuming that the Universe is filled with a perfect fluid with equation of state $p = w\rho c^2$, we obtain the Friedmann equations [Friedmann, 1924]:

$$H^2(t) \equiv \left(\frac{\dot{a}}{a}\right)^2 = \frac{8\pi G}{3}\rho + \frac{\Lambda c^2}{3} - \frac{kc^2}{a^2}\,, \tag{1.3}$$

$$\frac{\ddot{a}}{a} = -\frac{4\pi G}{3}\left(\rho + \frac{3}{c^2}p\right) + \frac{\Lambda c^2}{3}\,, \tag{1.4}$$

where $H(t)$ is the Hubble parameter, ρ the energy density of the fluid, p its pressure, w a constant between -1 and 1, and $\dot{a}$ and $\ddot{a}$ the first and second time derivatives of the scale factor, respectively. The first Friedmann equation (1.3), is usually written in terms of the density parameter Ω of each component of the Universe, defined as:

$$\Omega_i \equiv \frac{8\pi G}{3H^2}\rho_i = \frac{\rho_i}{\rho_{\rm crit}}\,, \tag{1.5}$$

with $\rho_{crit} = \frac{3H^2}{8\pi G}$ the critical density of a flat ($K = 0$) Universe. With the curvature density and dark energy density parameters defined as $\Omega_K \equiv -\frac{Kc^2}{a^2H^2}$ and $\Omega_\Lambda \equiv \frac{\Lambda c^2}{3H^2}$, the first Friedmann equation (Eq. 1.3) becomes:

$$H^2(t) = H_0^2\left[\Omega_{\rm r}\, a^{-4} + \Omega_{\rm m}\, a^{-3} + \Omega_k\, a^{-2} + \Omega_\Lambda\right]\,, \tag{1.6}$$

where $\Omega_{\rm m}$ is the total matter density (including both baryonic and dark matter) and $\Omega_{\rm r}$ the radiation term. The scale factor is usually normalized to $a(t_0) = 1$ at the present time t_0, and the Hubble parameter at the present time is called the Hubble constant H_0. Since all components evolve differently as a function of a, in general the Universe will not be dominated by the same component during its evolution. In an expanding Universe, radiation dominates first, followed by matter, then curvature, and finally dark energy. The expansion of the Universe induces a shift of the wavelength λ of photons similar to the Doppler effect. A photon emitted at time t_1 with wavelength λ_1 will see its wavelength increase (towards the red) as the Universe expands, so that at time t_0 it will be observed with a wavelength λ_0. The redshift z quantifies this effect as

$$1 + z = \frac{\lambda_0}{\lambda_1} = \frac{a(t_0)}{a(t_1)}\,. \tag{1.7}$$

From the most recent constraints on the different density parameters obtained by the *Planck* collaboration [Planck Collaboration et al., 2020b] shown in Table 1.1, it seems that our Universe is flat, expanding, and currently dominated by dark energy. Non-relativistic matter (dark matter + baryons) is the second most important component, mainly in the form of cold dark matter (CDM). This description of the Universe forms the basis of the standard model of cosmology, also known as the ΛCDM model.

1.2 The Cosmic Microwave Background

As we have seen previously, since all components evolve differently as a function of the scale factor a, in general the Universe will not be dominated by the same component during its whole evolution.

Component	*Planck*-ACT
Ω_m	0.3003 ± 0.0035
Ω_r	$\sim 10^{-5}$
Ω_Λ	0.6997 ± 0.0035
Ω_K	-0.010 ± 0.009

Table 1.1: Latest constraints on the cosmological parameters describing the energy content of the Universe obtained by the ACT collaboration [Louis et al., 2025]. We present the results obtained from the combination of ACT, *Planck* [Planck Collaboration et al., 2020b], and DESI DR2 [DESI Collaboration et al., 2025] data.

The early stages of the Universe were dominated by radiation ($\rho_r \propto a^{-4}$), and are well described by a hot, dense plasma (primordial plasma) in thermal equilibrium. Particles were in constant interaction, but as the Universe expanded and cooled down, it reached a temperature where protons and neutrons could combine to form the first atomic nuclei. This process is known as Big Bang Nucleosynthesis (BBN).

As the Universe continued to cool down and matter started to dominate over radiation ($\rho_m \propto a^{-3}$), it reached a temperature of about 3000 K (at a redshift of $z \sim 1100$), where electrons and protons combined into neutral hydrogen atoms. This event is known as recombination. The mean free path of photons, which is the average distance a photon can travel between interactions with charged particles, increased rapidly and eventually reached the scale of the Universe. Photons are now able to travel freely through space and form what we call the Cosmic Microwave Background (CMB). The CMB is the oldest light we can observe, when primordial photons interacted for the last time with matter. The emission from the CMB was first detected in 1965 by Arno Penzias and Robert Wilson at a frequency of 4.08 GHz [Penzias and Wilson, 1965]. At the time, the Big Bang theory was not fully accepted, but this discovery left little doubt that the Universe began in a hot, dense state.

Penzias and Wilson only measured a single frequency, but much stronger evidence for the Big Bang can be found in the CMB spectrum. If the primordial plasma was in thermal equilibrium at the time of recombination, then the CMB should have a characteristic blackbody spectrum. Nearly 30 years later, the Far Infrared Absolute Spectrometer (FIRAS) instrument on board the Cosmic Background Explorer (COBE) satellite measured the CMB spectrum over a wide range of frequencies [Fixsen et al., 1996]. The resulting spectrum is a near perfect match to a blackbody at a temperature of 2.7255 ± 0.002 K [Mather et al., 1999]. The CMB is extremely uniform at large scales, with small temperature variations of the order of 10^{-4} K. Figure 1.1 illustrates the improvement in the measurements of these temperature anisotropies over the years. They were first detected by the Differential Microwave Radiometer (DMR) instrument on board the COBE satellite [Smoot et al., 1992], followed by refined measurements from the Wilkinson Microwave Anisotropy Probe (WMAP) [Bennett et al., 2003], and finally the *Planck* satellite [Planck Collaboration et al., 2020a]. These fluctuations, due to small density variations in the primordial plasma, are at the origin of the structures present in the Universe today. However, as we will see in the next section, the standard model of cosmology does not provide an explanation for the origin of these fluctuations.

1.3 Origin and evolution of large-scale structures

In this section, we discuss some limitations of the standard model of cosmology, and how the theory of inflation can address them. We then describe how small density perturbations in the early Universe evolved into the large-scale structures we observe today.

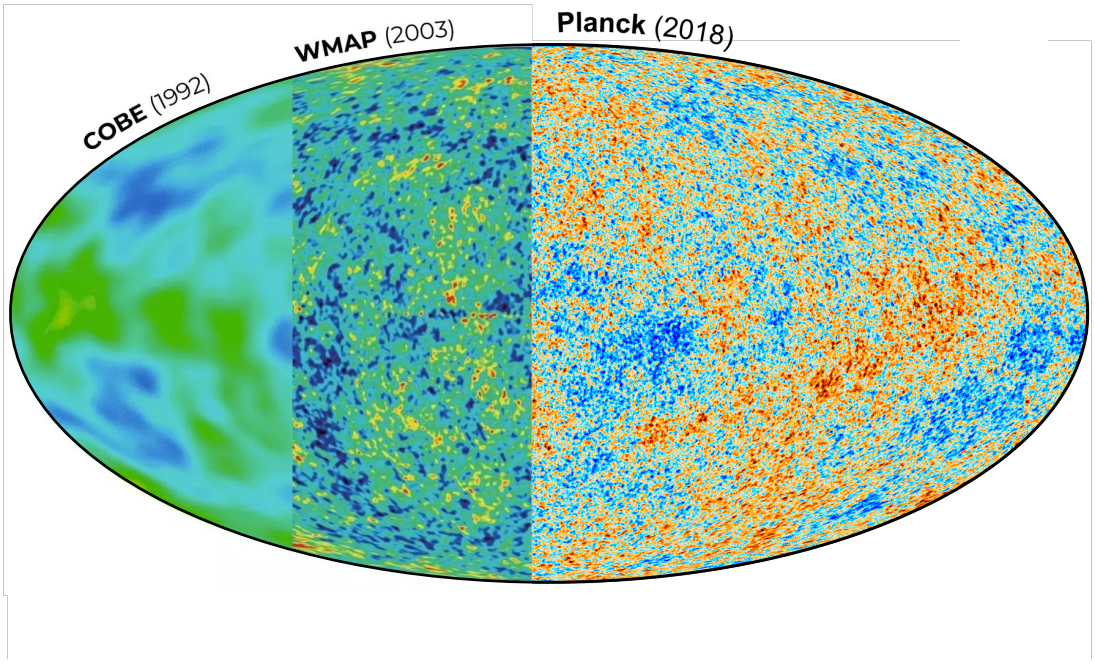

Figure 1.1: Progressive improvement in measurements of the CMB temperature anisotropies. From left to right: COBE [Smoot et al., 1992], WMAP [Bennett et al., 2003], and *Planck* [Planck Collaboration et al., 2020a] satellite data. Each map shows the temperature fluctuations across the sky, with increasing resolution and sensitivity. Figure inspired from Vazquez et al. (2018), updated with the latest Planck map.

1.3.1 Limitations of the standard model

Horizon problem

The particle horizon d_H is defined as the current physical distance to the farthest objects theoretically observable. Any objects further away are and have been fundamentally unobservable and are causally disconnected from us (but they might be observable in the future). Going back to the Friedmann equations, and considering a flat Universe ($K = 0$), the scale factor evolves as $a(t) = a_0 t^{\frac{2}{3(w+1)}}$, with w the equation of state parameter. In the case of a radiation-dominated Universe ($w = 1/3$), $a(t) \propto t^{1/2}$, while in a matter-dominated Universe ($w = 0$), $a(t) \propto t^{2/3}$. As the particle horizon $d_H \propto t$, we see that during these two epochs, d_H grows faster than the physical size of the Universe. This implies that regions we observe today were not in causal contact in the past, yet the Universe is highly homogeneous and isotropic as seen at large scales in the CMB.

Flatness problem

In standard cosmology, the Universe's total density must match the critical density $\rho_{\rm crit}$, i.e., $\Omega_{tot} = \Omega_m + \Omega_r + \Omega_\Lambda = 1$, to result in a flat geometry ($K = 0$). As mentioned in Section 1.1, observations show that Ω_{tot} is indeed compatible with 1. However, deviations from flatness grow during matter/radiation domination ($\rho_m, \rho_r \propto a^{-3}, a^{-4}$), which would imply that the early Universe had to be extremely close to flat (with $|\Omega_{tot} - 1| < 10^{-60}$ at the Planck time) to result in the near-flatness we observe today. This is a fine-tuning issue called the flatness problem.

Initial conditions for the fluctuations observed today

Even though the Universe is homogeneous and isotropic on large scales, we observe structures such as galaxies and clusters at smaller scales. The standard model does not explain how these structures

formed from the nearly uniform early Universe observed in the CMB.

Inflation as a solution

To address these problems, the theory of inflation was proposed by Guth (1981); Linde (1982); Starobinsky (1982). According to this model, inflation would be a period of extremely rapid expansion in the early Universe. This theory is able to solve the horizon problem, as it suggests that regions now far apart were once close enough to be in causal contact. Inflation also addresses the flatness problem by driving the Universe towards flatness, as any initial curvature would be stretched out during this rapid expansion. Finally, the inhomogeneity problem is resolved by quantum fluctuations in the scalar field driving inflation, which evolve into density perturbations at the origin of the large-scale structures we observe today.

1.3.2 Linear growth of density perturbations

Quantum fluctuations during inflation lead to small perturbations in the density of matter and energy in the early Universe. We can model these inhomogeneities as random fluctuations of a density field around a mean density $\bar{\rho}_m(t)$, defining the density contrast $\delta(\vec{x}, t)$ at position $\vec{x}$ and time t as

$$\delta(\vec{x}, t) = \frac{\rho(\vec{x}, t) - \bar{\rho}_m(t)}{\bar{\rho}_m(t)} \,. \tag{1.8}$$

Modelling the Universe as a fluid (see Section 1.1), it thus needs to satisfy the continuity, Euler, and Poisson equations. Assuming that the perturbations are small, the linear evolution of the density contrast δ is given by

$$\ddot{\delta} + 2H(t)\dot{\delta} = \left[4\pi G\bar{\rho}_m(t) + \frac{c_s^2}{a^2}\nabla^2\right]\delta(\vec{x}, t) \,, \tag{1.9}$$

where c_s is the speed of sound in a fluid. For fluctuations that are relatively small compared to the mean density of the Universe, applying a Taylor expansion to the equation gives a simple solution $\delta(t) = \delta_0 D(t)$, where δ_0 is the initial density contrast and $D(t)$ is the linear growth factor. In general, solving the exact linear growth equation numerically gives a solution with two modes, a growing mode $D_+(t)$ and a decaying mode $D_-(t)$:

$$\delta(\vec{x}, t) = D_+(t)\delta_+(\vec{x}, t_i) + D_-(t)\delta_-(\vec{x}, t_i) \,. \tag{1.10}$$

During the matter-dominated era, the growing mode $D_+(t)$ dominates and fluctuations grow exponentially to form large-scale structures, while the decaying mode $D_-(t)$ becomes negligible over time. At later times, when dark energy starts to dominate, perturbations are stable and the growth of structures slows down.

We can define the two-point correlation function of $\delta(\vec{x})$ as

$$\xi(\vec{r}) = \langle\delta(\vec{r})\delta(\vec{x} + \vec{r})\rangle \,, \tag{1.11}$$

where $\langle ... \rangle$ indicate that the average is taken over all positions $\vec{x}$. The two-point correlation function measures the excess probability of finding pairs of points separated by a distance R compared to a random distribution. The Fourier transform of the correlation function is the power spectrum $P(k)$, which can be written as

$$P(k) = \int \xi(\vec{r}) e^{-i\vec{k}\cdot\vec{r}} \mathrm{d}^3 r \,, \tag{1.12}$$

where k is the wavenumber. As perturbations grow over time, their initial distribution, described by the primordial power spectrum $P_{\mathrm{prim}}(k)$, is modified by a transfer function $T(k)$. The transfer function, which depends on the redshift, contains all the physical processes that impact the linear growth of perturbations. The power spectrum can thus be rewritten as

$$P(k, z) = P_{\mathrm{prim}}(k) \times T^2(z, k) \,. \tag{1.13}$$

An important summary statistic derived from the matter power spectrum is σ_8, which quantifies the amplitude of density fluctuations on scales of $8\,h^{-1}$ Mpc at $z = 0$:

$$\sigma_8 = \sqrt{\sigma^2(z = 0, R = 8h^{-1}\ \mathrm{Mpc})} \,, \tag{1.14}$$

where

$$\sigma^2(z, r) = \frac{1}{(2\pi)^3} \int W(kR) P(z, k) \mathrm{d}^3 k \,, \tag{1.15}$$

and $W(kR)$ is the Fourier transform of a spherical top-hat window function (see Cui et al. (2008) for more details).

The growth of the aforementioned perturbations remains valid in the linear regime, i.e., when $\delta(\vec{x}, t) \ll 1$. However, this hypothesis breaks down once certain regions of the Universe become significantly denser than the average. This is the case for galaxy clusters, where the density can reach up to 10^4 times the mean density of the Universe. Complex non-linear processes appear in these regions and require to go beyond the linear regime to understand them.

1.3.3 The Press-Schechter formalism and halo mass function

To study the non-linear evolution of structures, a widely used approach is the Press-Schechter formalism [Press and Schechter, 1974]. This theory is based on the idea that all matter present in the Universe today ($z = 0$) is contained in spherical dark matter halos, which are virialized and in hydrostatic equilibrium. According to the Press-Schechter theory, regions in which linear density perturbations smoothed at a certain scale R exceed a critical threshold δ_c will collapse and form virialized halos. Assuming that the density fluctuations are Gaussian, the probability for a point to be in a region satisfying the condition $\delta > \delta_c$ is

$$P(\delta > \delta_c) = \frac{1}{\sqrt{2\pi\sigma^2(z, R)}} \int_{\delta_c}^{\infty} \exp\left(\frac{-\delta^2}{2\sigma^2(R)}\right) \mathrm{d}\delta = \frac{1}{2} \mathrm{erfc}\left(\frac{\delta_c}{\sqrt{2\sigma^2(R)}}\right) , \tag{1.16}$$

where $\sigma^2(R)$ is defined in Equation 1.15, and $\mathrm{erfc} = 1 - \mathrm{erf(x)}$ is the complementary error function. Then, it is common to use the mass $M = 4\pi\bar{\rho}_m R^3/3$ instead of the scale R.

A known problem with this approach is that, if we take $M \longrightarrow 0$, then $P(\delta > \delta_c) = 1/2$, which indicates that only half of the total mass in the Universe is contained in collapsed objects of any mass. An argument can be made that, in a Gaussian field, half of the remaining mass is contained in underdense regions that will not collapse according to linear theory, and thus $P(\delta < \delta_c) = 1/2$. However, these underdense regions can be embedded within larger overdense regions and still end up in collapsed objects of larger mass. This is known as the cloud-in-cloud problem [Bond et al., 1991;

Jedamzik, 1995]. To account for this, Press and Schechter (1974) simply multiplied the probability $P(\delta > \delta_c)$ by a factor 2, without a proper demonstration. If we accept (for now) this solution, we can express the fraction of the total mass in the Universe contained in halos of mass greater than M as

$$F(> M) = 2\,P(\delta > \delta_c) = \mathrm{erfc}\left(\frac{\delta_c}{\sqrt{2\sigma^2(M)}}\right). \tag{1.17}$$

The number of virialized objects with masses between M and $M + \mathrm{d}M$ is therefore given by:

$$\frac{dn}{dM}dM = \frac{\bar{\rho}_m}{M}\left|\frac{dF(> M)}{dM}\right|dM = \sqrt{\frac{2}{\pi}}\frac{\bar{\rho}_m}{M}\frac{\delta_c}{\sigma}\left|\frac{d\ln\sigma}{dM}\right|\exp\left(-\frac{\delta_c^2}{2\sigma^2}\right)dM\,, \tag{1.18}$$

with dn/dM the halo mass function (HMF). As discussed above, the Press-Schechter formalism does not account for important effects such as the cloud-in-cloud problem. Modern cosmological analyses based on the study of the statistical properties of halos rely on halo mass functions calibrated on numerical N-body simulations. The HMF can be expressed as [Tinker et al., 2008]:

$$\frac{\mathrm{d}n}{\mathrm{d}M} = f(\sigma)\frac{\bar{\rho}_m}{M}\left|\frac{\mathrm{d}\ln\sigma^{-1}}{\mathrm{d}M}\right|, \tag{1.19}$$

with

$$f(\sigma) = A\left[1 + \left(\frac{\sigma}{b}\right)^{-a}\right]\exp\left(-\frac{c}{\sigma^2}\right), \tag{1.20}$$

where $f(\sigma)$ is the halo multiplicity function which depends on the amplitude of matter fluctuations σ. The coefficients A, a, b, and c are calibrated from a variety of simulations (see, for example, Tinker et al. (2008); Bocquet et al. (2016); Euclid Collaboration et al. (2023)). As we will see in the next chapter, the HMF is a key ingredient of cosmological analyses based on galaxy clusters, as it depends on the matter distribution in the Universe and therefore on the cosmological parameters.

1.4 Conclusion

The standard model of cosmology describes remarkably well our current observations of the Universe. In this chapter, we have seen that this model, based on general relativity and Friedmann's equations, describes a homogeneous and isotropic expanding Universe currently dominated by dark energy and dark matter. However, some open questions still remain, such as the nature of dark matter and dark energy. The model also suffers from some limitations, that can be explained by the theory of inflation, even though it remains to be confirmed observationally. The answer to these questions lies in the use of cosmological probes, such as galaxy clusters, which we will discuss in more detail in Chapter 2.

CHAPTER 2

Clusters of galaxies

2.1 Clusters and groups of galaxies . . . 30
2.2 Observation of galaxy clusters . . . 30
2.2.1 Optical and infrared . . . 31
2.2.2 Radio . . . 31
2.2.3 X-ray . . . 31
2.2.4 Millimeter: Sunyaev-Zel'dovich effect . . . 31
2.3 Galaxy clusters detection in large surveys . . . 34
2.3.1 History of cluster detection . . . 34
2.3.2 The first galaxy cluster catalogs . . . 36
2.3.3 Optical large surveys and catalogs . . . 37
2.3.4 X-ray large surveys and catalogs . . . 38
2.3.5 SZ large surveys and catalogs . . . 40
2.4 Cosmology with galaxy clusters . . . 43
2.4.1 Universal pressure profile and scaling relations . . . 43
2.4.2 Number counts . . . 44
2.4.3 Gas mass fraction . . . 45
2.4.4 tSZ angular power spectrum . . . 45
2.4.5 X-ray/SZ distances . . . 45
2.5 Conclusion . . . 47

Clusters of galaxies are formed in the latest stages of structure formation and are unique cosmological probes to study structure formation and its evolution. In particular, cluster number counts as a function of mass and redshift are sensitive to the universe matter content and density fluctuations via the Ω_m and σ_8 cosmological parameters defined in the previous Chapter.

In this Chapter, we first define what are galaxy clusters and groups of galaxies, and present the different observables used to study them. We will focus on the Sunyaev-Zel'dovich effect, which is the main observable used in this thesis. Then, we will review the history of cluster detection, from the first optical detection to the latest large surveys. We will finish by presenting the different methods used to constrain cosmological parameters with galaxy clusters.

2.1 Clusters and groups of galaxies

Galaxy clusters are the largest gravitationally bound structures in the Universe and form around density peaks in the matter field through accretion of their surrounding environment. This process, called hierarchical growth, describes how galaxy clusters form by gradually accreting smaller and less massive structures [Voit, 2005; Allen et al., 2011]. Clusters thus form at low redshifts, $z \lesssim 3$ and structures at higher redshifts, composed of only a few galaxies, are called protoclusters. Galaxy clusters are extremely massive objects, of the order $10^{13} - 10^{15} M_{\odot}$, and are composed primarily of dark matter, about $\sim 85\%$ of their total mass. The baryonic content is dominated by the hot ionized gas forming the intracluster medium (ICM) which constitutes about $\sim 12\%$ of the mass content [White et al., 1993]. Even though clusters can host thousands of galaxies, they only amount to a negligible fraction of the total mass, about $\sim 3\%$.

Depending on the number of gravitationally bound galaxies, clusters can also be referred to as groups. Galaxy groups occupy an intermediate halo-mass range between massive galaxies and galaxy clusters, with distinct properties and different evolution processes compared to clusters [McGee et al., 2009; Lovisari et al., 2021]. However, there is no universal definition of what differentiates a group from a cluster, and the distinction is often merely based on the mass of the system or the galaxy number. In the literature, groups are typically defined as having a mass below $10^{14} M_{\odot}$, or structures with less than 50 galaxy members [Paul et al., 2017]. Studies have shown that a distinction could be made based on the study of the brightest galaxies in the system. Indeed, the brightest galaxies in clusters have higher stellar masses as well as higher velocity dispersions than the brightest galaxies in groups [Jõeveer et al., 1978; Sohn et al., 2020; Chu et al., 2021; Einasto et al., 2022].

We have seen in Section 1.3.3 that the mass of galaxy clusters is a crucial parameter for their use in cosmological analyses. Since clusters are diffuse objects whose physical boundaries are not clearly determined, it is important to establish a definition of their size in order to constrain their mass within a given radius. The virial radius, which describes the extent of a spherical halo in equilibrium, is often used as a reference to estimate the mass. However, the morphology of clusters can show large deviations from spherical symmetry due to different physical processes, such as merger events [Lacey and Cole, 1994]. The virial radius is thus not always easily estimated. Instead, it is common to define a characteristic radius R_{Δ} by the average of the density contrast Δ it contains:

$$\Delta \equiv \frac{\langle \rho(< R_{\Delta}) \rangle}{\rho_{\rm crit}(z)} \,, \tag{2.1}$$

with $\langle \rho(< R_{\Delta}) \rangle$ the mean density contained within a sphere of radius R_{Δ}, and $\rho_{\rm crit}(z)$ the critical density of the Universe at the redshift z of the object. Commonly used values for the contrast are $\Delta = 2500$, 500 or 200, corresponding to looking at the core, up to intermediate regions, and up to the outskirts of clusters, respectively. The mass enclosed in this characteristic radius R_{Δ} is thus

$$M_{\Delta} = \frac{4\pi}{3} \Delta \rho_{\rm crit}(z) R_{\Delta}^3 \,. \tag{2.2}$$

In this thesis, we will mostly use M_{500} and R_{500}, values adapted for the study of intermediate regions of galaxy clusters.

2.2 Observation of galaxy clusters

Galaxy clusters are complex objects that can be observed and studied through various physical effects, each tracing different components of the cluster. In this section, we will review the main observables which allow us to study galaxy clusters.

2.2.1 Optical and infrared

Galaxy clusters were observed for the first time about 200 years ago by Charles Messier and William Herschel [Biviano, 2000] in the optical, as observations in other wavelengths at that time were simply unavailable. Optical and infrared observations trace the stellar content of galaxy clusters, revealing the distribution and properties of member galaxies. The brightest galaxies in the cluster, called Brightest Cluster Galaxy (BCG), are also the most massive, and are usually found at the center of the cluster. The number of member galaxies in a cluster is called the richness, and is directly linked to its mass. These member galaxies lie at the same redshift and evolve together, which allows to detect clusters via the study of the member galaxies position in the color-magnitude diagram. Galaxies in clusters are located in a specific region of the diagram called the red sequence [Gladders and Yee, 2000] and can thus be singled out from foreground or background galaxies. Clusters can also be observed in the optical/infrared via spectroscopic observations, to study their dynamical state and determine their redshift by identifying known spectral lines in the galaxies spectrum. These observations enable the measurement of the velocity dispersion of the different galaxies in a cluster, which can then be used to infer its total mass assuming dynamical equilibrium [Sifón et al., 2016; Aguado-Barahona et al., 2022]. Finally, optical data can be used to estimate the mass of clusters via an effect called gravitational lensing. As the light travels towards us, it can be deflected by massive structures along the line of sight, such as galaxy clusters. This gravitational lensing effect distorts and magnifies the images of background galaxies.

2.2.2 Radio

Galaxy clusters form through collisions and by accreting material from their surroundings. The radio emission observed at frequencies below 1 GHz traces the synchrotron emission of relativistic electrons produced by these events, revealing the presence of magnetic fields and other processes. There are two types of radio emission in clusters: radio halos and radio relics. Radio halos follow the distribution of the ICM in clusters, and are correlated to the X-ray luminosity and the mass [Cassano et al., 2013; Cuciti et al., 2021]. Radio relics, on the other hand, are found at the outskirts of clusters and are associated with shock waves produced by cluster mergers. For a complete review of the radio emission in clusters, we refer the reader to van Weeren et al. (2019). Radio observations of clusters are also very important to detect possible contaminants, such as radio galaxies, as we will see in more details in Chapter 7.

2.2.3 X-ray

As discussed earlier, a majority of the cluster baryonic content is in the form of hot ionized gas. At such temperatures, the free electrons in the gas emit X-ray radiation, primarily via thermal bremsstrahlung with contributions from spectral line emission. For more details, we refer the reader to the complete review of Böhringer and Werner (2010). This emission provides information on the distribution of hydrogen gas, which makes up the dominant fraction of the baryonic matter in a cluster. Assuming the gas is in thermal equilibrium, it is possible to infer the cluster's total mass.

2.2.4 Millimeter: Sunyaev-Zel'dovich effect

The Sunyaev-Zel'dovich effect (SZ, Sunyaev and Zeldovich (1970a); b; 1972; 1980) is a distortion of the cosmic microwave background (CMB) radiation caused by the inverse Compton scattering between high-energy electrons in the hot ICM and the CMB photons. During the interaction, CMB photons will gain energy which will shift the CMB blackbody spectrum. Since the observable is the CMB rather than the cluster itself, the SZ signal depends on the cluster's distance only through its angular size. Thus, the SZ effect, unlike other probes, is not affected by cosmological dimming and

is only limited by the angular resolution and sensitivity of the instrument. The SZ effect is a very powerful observable to detect high-redshift clusters, as we will see in detail throughout this thesis and especially in Chapter 8. Several types of SZ effects can be distinguished: the thermal (tSZ), kinetic (kSZ), relativistic (rSZ), and polarised (pSZ) SZ effects. In this section, we will present the tSZ and kSZ effect. Complete reviews of the different effects can be found in Birkinshaw (1999); Carlstrom et al. (2002); Mroczkowski et al. (2019).

Thermal SZ effect

The tSZ effect is the most prominent out of the effects listed above, and is caused by the thermal motion of electrons in the ICM. As CMB photons gain energy, they will be shifted towards higher frequencies. The spectral dependence of the tSZ effect is given by the Kompaneets equation [Kompaneets, 1957], which describes how the photon density changes with energy during scattering events. The spectral dependence of the tSZ effect is expressed as:

$$f(x, T_e) = \frac{x^4 e^x}{(e^x - 1)^2} \left(x \coth\left(\frac{x}{2}\right) - 4 \right) (1 + \delta_{tSZ}(x, T_e)) \,, \tag{2.3}$$

where $x \equiv \frac{h\nu}{k_b T_{\rm CMB}}$ is the reduced dimensionless frequency with ν the photon frequency and $T_{\rm CMB}$ the CMB temperature. δ_{tSZ} is the relativistic correction of the tSZ spectrum which depends on the ICM temperature (see Challinor and Lasenby (1998) for more details). The relative change in the CMB specific intensity I_0 due to the tSZ effect is then given by:

$$\frac{\Delta I_{tSZ}}{I_0} = y \, f(x, T_e) \,. \tag{2.4}$$

The amplitude of the distortion is given by the Compton parameter y defined as:

$$y = \frac{\sigma_T}{m_e c^2} \int P_e \, dl \,, \tag{2.5}$$

with σ_T the Thomson cross section, $m_e c^2$ the electron rest mass energy, and P_e the ICM electronic pressure.

The left panel of Figure 2.1 highlights the CMB spectrum distortion due to the tSZ effect, where the spectrum is shifted towards higher frequencies. As noted at the top of the figure, the Compton parameter $y = 0.15$ is a very large value chosen to clearly illustrate the effect. The right panel of Figure 2.1 shows the tSZ spectrum for $y = 10^{-4}$ and different ICM temperatures. We see that at 217 GHz, the amplitude of the tSZ effect is null, negative below this frequency and positive above. The detection of galaxy clusters at millimeter wavelengths is based on this very distinct shape of the tSZ spectrum, where multi-frequency observations can detect the tSZ increment and decrement, as shown in Figure 2.2. The Figure presents observations of the Abell2319 cluster at 7 frequencies between 44 and 545 GHz with the *Planck* satellite. As we expect, the tSZ effect is detected at all frequencies with the exception of 217 GHz, where the tSZ effect is null. Below 217 GHz, the tSZ effect at the center of the cluster is negative (blue), and positive above (red).

Furthermore, observations of the tSZ effect enable the measurement of the integrated Compton parameter Y_Δ up to a radius R_Δ as

$$Y_\Delta = 4\pi \frac{\sigma_T}{m_e c^2} \int_0^{R_\Delta} P_e(r) r^2 dr \,. \tag{2.6}$$

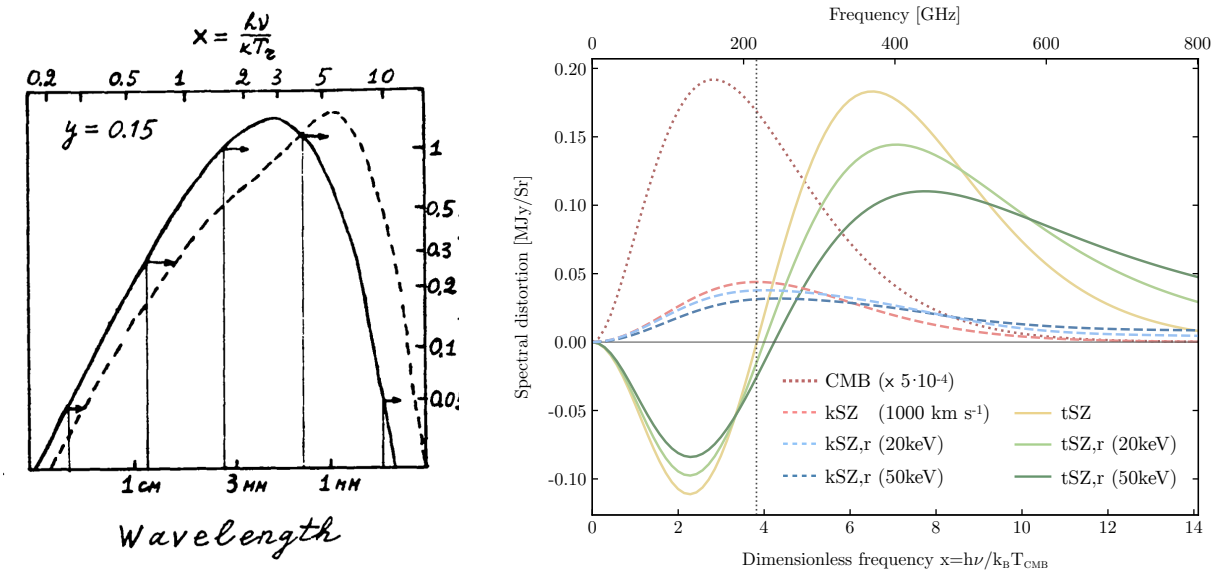

Figure 2.1: (Left): The CMB spectrum, undistorted (solid line) and distorted by the tSZ effect (dashed line). Figure extracted from Sunyaev and Zeldovich (1980). (Right): Spectra of the tSZ (solid) and kSZ (dashed) effects at different ICM temperatures, both with or without relativistic corrections. Figure taken from Mroczkowski et al. (2019).

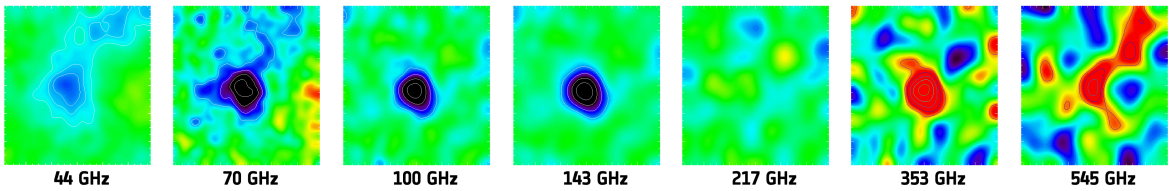

Figure 2.2: Observations of the Abell2319 cluster by *Planck* at 7 frequencies between 44 and 545 GHz. The colorbar highlights negative (blue) and positive (red) distortions. Figure taken from the *Planck* database `https://sci.esa.int/s/WvJQxgW`

It provides a direct measurement of the total pressure content within the ICM and thus of the thermal energy of the cluster. This integrated parameter is a good tracer of the hydrostatic mass of the cluster and is used as a mass proxy in scaling relations (see Section 2.4.1).

Kinetic SZ effect

The kSZ effect is caused by the motion of the cluster's electrons relative to the CMB reference frame. This motion will induce a Doppler shift of the CMB spectrum and thus a change in the CMB intensity as [Birkinshaw, 1999]:

$$\frac{\Delta I_{kSZ}}{I_0} = y_{kSZ} \frac{x^4 e^x}{(e^x - 1)^2} (1 + \delta_{kSZ}(x, v_z, T_e)) \,, \tag{2.7}$$

where the relativistic correction δ_{kSZ} depends on the radial velocity v_z of the cluster along the line of sight [Itoh et al., 1998]. The amplitude y_{kSZ} also depends on v_z as:

$$y_{kSZ} = -\frac{\sigma_T v_z}{c} \int n_e \, dl \,. \tag{2.8}$$

The line of sight velocity of the cluster can either be negative or positive, depending on whether the gas is moving towards or away from us. As seen in the right panel of Figure 2.1, the kSZ spectrum (red

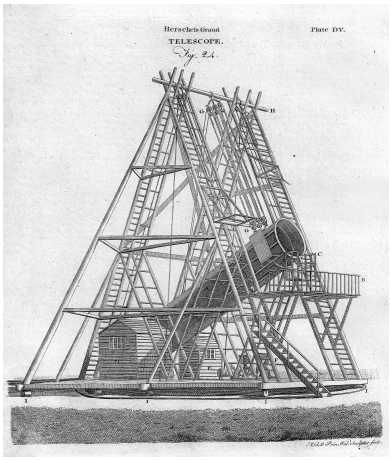

Figure 2.3: Illustration of William Herschel's 40-foot telescope built in 1789, the largest telescope of its time. Credit: Andrew Bell and Colin Macfarquhar, 1797

dashed line) has a similar shape to that of the CMB spectrum if we neglect relativistic corrections. Even though the CMB anisotropies and the kSZ signal have the same spectrum, we can still separate them based on the spatial distribution of the signal, as CMB fluctuations dominate at large scales, whereas the cluster signal is much more compact. However, the kSZ effect is largely subdominant compared to the tSZ effect, about a factor 10 for typical velocities [Mroczkowski et al., 2019], and requires very sensitive observations to be detected. The study of the kSZ effect usually involves stacking the signal from several clusters [Hand et al., 2012; Tanimura et al., 2021] or using very deep observations of a cluster at very high angular resolution [Adam et al., 2017b]. We will briefly discuss the latter in Chapter 6.

2.3 Galaxy clusters detection in large surveys

Formed in the latest stages of structure formation, galaxy clusters are unique cosmological probes to study structure formation and its evolution. However, as we will see in Section 2.4, catalogs of thousands of clusters are required to constrain cosmological parameters. In this section, we will review the history of cluster detection, from the first detections in the optical to the latest advancements in the field. The following discussion takes inspiration from Biviano (2000); Gioia (2000); Yee and Gladders (2002).

2.3.1 History of cluster detection

The first reference to a galaxy cluster dates back to 1784, when Charles Messier reported his observations of nebulae (galaxies) while hunting for comets [Messier, 1781]. It was later found that he unknowingly observed the Virgo cluster, making him the first to record the existence of a galaxy cluster. At the same time period, William Herschel was also interested in the study of nebulae, and he had access to the largest telescope of his time, illustrated in Figure 2.3. In 1785, Herschel published his findings, with notable observations of a structure formed of hundreds of nebulae, which he called the *nebulous stratum of Coma Berenices* from the name of the constellation where he observed it [Herschel, 1785]. This object is now known as the Coma cluster, one of the most massive and best-studied clusters.

The nature of these nebulae was not known until 1864, when William Huggins performed spectroscopic observations of some known nebulae such as M57 and M31. In Huggins and Miller (1864b), when talking about M57 and some other nebulae, he noted that they *"can no longer be regarded as aggregations of suns"* and that *"we must probably regard these objects, or at least their photo-surfaces,*

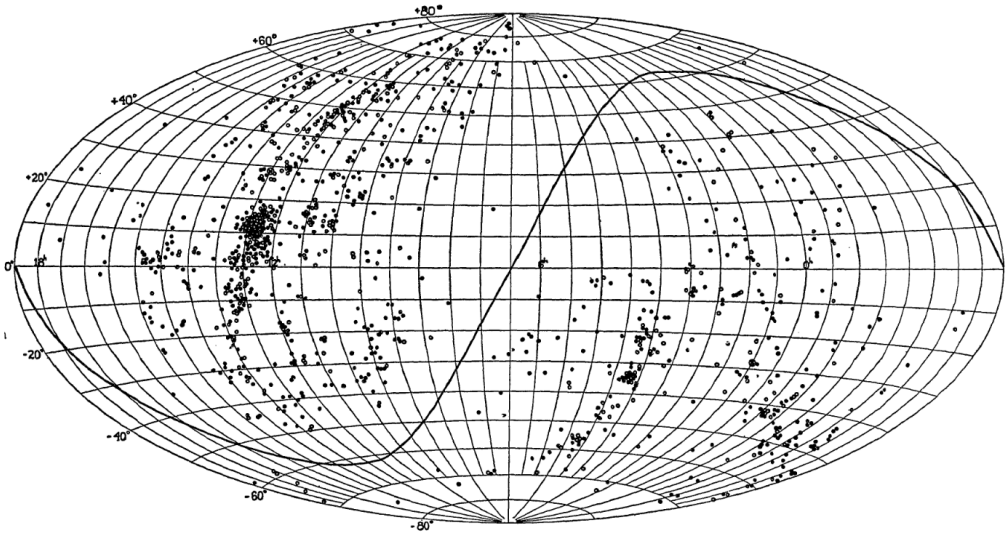

Figure 2.4: Distribution of extragalactic nebulae brighter than 13th magnitude. The dots represent the nebulae, 734 in total. Figure extracted from Shapley and Ames (1932)

as enormous masses of luminous gas or vapour". Indeed, he had just discovered that the spectra of these objects contained emission lines characteristic of gas, while others, e.g., M31, had spectra similar to those of stars he had observed earlier in the year [Huggins and Miller, 1864a]. The distinction between nebulae, which are bright parts of the interstellar medium, and galaxies, was thus made even though they were not called galaxies at the time.

However, proof of the extragalactic nature of such objects was not found until the early XXth century, first through the work of Henrietta Leavitt on Cepheid variable stars in the Small Magellanic Cloud. She found that their luminosity was related to their period, and thus their distance from Earth [Leavitt and Pickering, 1912]. In the following years, two astronomers, Vesto Slipher and Heber Curtis, independently observed M31 (Andromeda galaxy) with the former measuring its velocity (~ -300 km.s^{-1}, Slipher (1913)) and the latter estimating its distance [Curtis, 1917]. Both measures indicated that M31 was far outside our stellar system and reinforced the *"island universe"* theory, which was the name given to galaxies at the time.

Nevertheless, not all astronomers were convinced, which sparked the famous Great Debate[1] in 1920 between Harlow Shapley and Heber Curtis. Shapley argued that the Milky Way was the whole Universe and that the nebulae were simply on the outer edges of our galaxy. Meanwhile, Curtis drew on his discovery of Andromeda's distance to argue that the Milky Way was much smaller than what his opponent suggested, and that "island universes" were indeed far outside of the Milky Way. Three years later, Curtis was proven right when Edwin Hubble found Cepheids in Andromeda, confirming its distance and thus the existence of extragalactic nebulae [Hubble, 1929]. Andromeda was the first of many island universes to be discovered, and their clustering tendency was quickly noted, as seen in Figure 2.4. The dots show the position of bright extragalactic nebulae, and we can clearly see overdensities around (R.A., Dec.) $\sim$ (12h50m, +12d00m), which is the position of the Virgo cluster, and (3h30m, -35d00m), where the Fornax cluster is located.

In 1956, Humason et al. (1956) published a compilation of redshifts for more than 900 extragalactic nebulae, which was the first large catalog enabling the study of galaxy distribution and clustering. They also included the redshift of 26 clusters of nebulae, or galaxy clusters.

[1] Transcripts of the debate can be found at https://apod.nasa.gov/htmltest/gifcity/cs_nrc.html

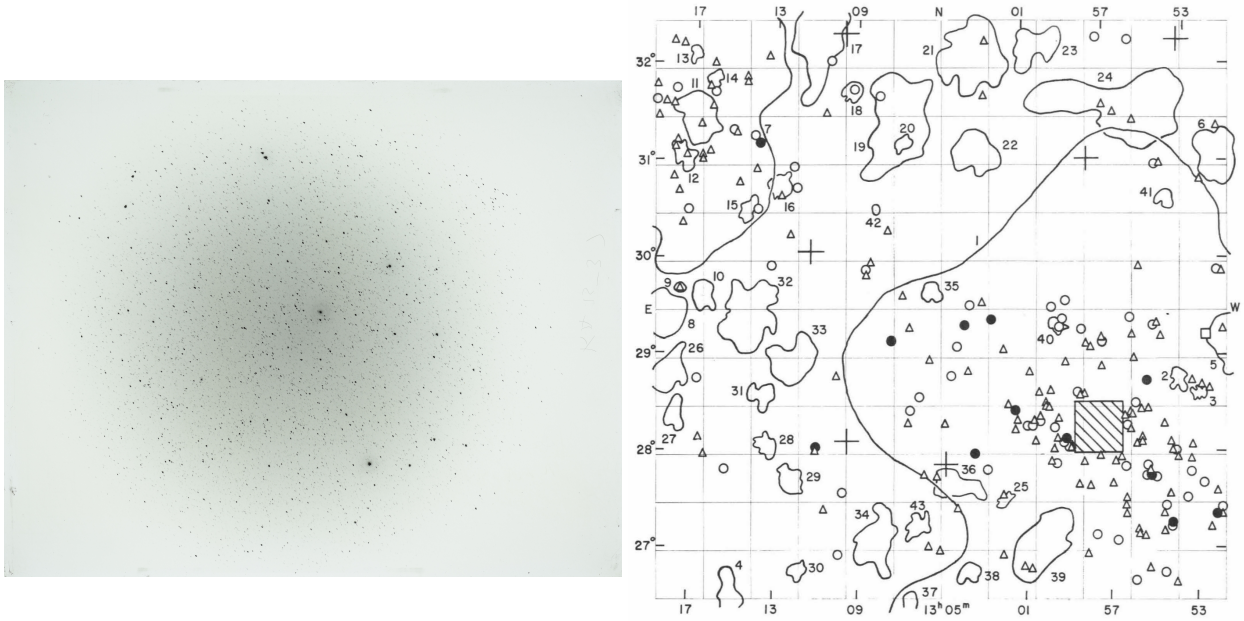

Figure 2.5: (Left): Photographic plate of a section of the sky around the Coma cluster. The observation was conducted on January 23rd, 1950 in Soledad, New Mexico. Credit: StarGlass, https://starglass.cfa.harvard.edu/ (Right): Coma cluster, n°1 on the chart (largest contour), as sketched by Zwicky in 1963. Figure taken from Zwicky et al. (1963a).

2.3.2 The first galaxy cluster catalogs

After it became evident that galaxies were not uniformly distributed in the Universe, the study of clusters of galaxies became a major field of research. The first catalog of clusters was published in 1958 by George Abell [Abell, 1958], with a total of 2712 entries at $z \leqslant 0.2$. He used photographic plates from the Palomar Observatory Sky Survey (POSS), covering about 66% of the sky. We show in the left panel of Figure 2.5 an example of how clusters were identified at the time, with a picture of a plate used to observe the region around the Coma cluster. From 1961 to 1968, Zwicky, Herzog, and Wild published a catalog of around 10000 clusters, the Catalog of Galaxies and Clusters of Galaxies [Zwicky et al., 1963a; b; 1966; 1968; Zwicky et al., 1965; Zwicky and Kowal, 1968]. Each volume contains sketches of clusters, such as Coma shown in the right panel of Figure 2.5. The solid lines are the contours of different clusters, with the Coma cluster being the largest one, n°1 on the chart. The Abell catalog was later updated to include observations of the Southern sky, with a total of 4073 clusters [Abell et al., 1989].

In the following years, several catalogs such as Klemola (1969); Snow (1970); Rose (1976); Duus and Newell (1977) were published, targeting the southern sky which was not observed in the POSS. As mentioned in Section 2.1, a distinction can be made between clusters and groups of galaxies. In the 1970s, de Vaucouleurs (1975) first published a catalog of groups of galaxies, which he defines as a small number of bound galaxies, e.g, $n \backsimeq 10$. Other studies also targeted groups specifically, such as Rose (1977) and Turner and Gott (1976). The search for groups or clusters was still done by eye on photographic plates, which was a very time-consuming process. The first automated search for clusters was conducted by MacGillivray et al. (1976). They built a computer called COSMOS (Co-Ordinates, Sizes, Magnitudes, Orientations and Shapes Pratt et al. (1975)) to analyze images of stars and galaxies and automatically distinguish between the two.

The 1960-70s were also the first years of X-ray astronomy, with the first observations in X-ray in 1966 [Byram et al., 1966]. As one of the brightest known clusters at the time, Coma was observed by the Uhuru satellite in 1971 [Gursky et al., 1971], which revealed extended X-ray emission (see Section 2.2.3). In addition to optical surveys which were previously the only way to detect clusters,

X-ray observations were now also used in this regard, with the first blind X-ray detection of 13 clusters in 1978 [Lugger, 1978].

As mentioned previously, clusters are found in optical data using various visual techniques, resulting in subjective catalogs. The first cluster catalog built from a blind search of galaxy density peaks in a galaxy catalog was published in 1985 [Shectman, 1985]. From this development, and using automated techniques as the COSMOS computer, a few other catalogs were automatically built using Abell-like criteria, such as Lumsden et al. (1992); Dalton et al. (1997). In 1977, the first spectroscopic survey of galaxies, the CfA redshift survey, started in 1977 and led to the development of new techniques to detect clusters directly in redshift space [Huchra and Geller, 1982; Geller and Huchra, 1983].

With the construction of larger telescopes and satellites, the future of cluster detection grew brighter at all wavelengths. In the following, we will separate the catalogs and surveys based on their wavelength. A summary of all published catalogs in the literature can be found in Tables 3, 4, and 5 in the appendix.

2.3.3 Optical large surveys and catalogs

As we have seen, the traditional wavelength to build cluster catalogs is the optical. The first large optical survey was the Palomar Optical Sky Survey (POSS) used for the construction of the Abell catalog [Abell, 1958]. However, such surveys based on photographic plates, even when digitized and using automated techniques (e.g., Lumsden et al. (1992); Dalton et al. (1997)), were strongly limited by projection effects (i.e. line of sight contamination, Dekel et al. (1989)). Several catalogs were still built using digitized POSS and POSS-II plates, such as the Edinburgh/Durham Cluster Catalog-II (EDCCII, Bramel et al. (2000)), or the Northern Sky Optical Survey (NoSOCS, Gal et al. (2000); 2003; Lopes et al. (2004)). The first large survey to use CCDs was the Palomar Deep Cluster Survey (PDCS, Postman et al. (1996)), with the construction of a cluster catalog of 79 candidates in a 5deg^2 field. In this paper, the authors also introduced a new method to detect clusters, called the matched-filter technique. The technique uses known properties of clusters, such as their luminosity function and their radial profile, to detect them in slices of redshift space. Unfortunately, CCD cameras were still limited in terms of field of view, and thus their cluster detection capabilities were also affected.

In 2000, the Sloan Digital Sky Survey (SDSS, York et al. (2000)) was launched, with the goal of mapping thousands of degrees with both a photometric and spectroscopic survey. Complementing the matched-filter technique, other methods were also developed, like the cut-and-enhance (CE) method [Goto et al., 2002], which uses simple color cuts, the Voronoi tessellation method [Kim et al., 2002], or the maxBCG method [Annis et al., 1999]. In 2007, Koester et al. (2007) published a catalog of 13 823 clusters detected in the SDSS DR5 with accurate redshift estimates, using the maxBCG method. At the same time, the Red Sequence Cluster Survey (RCS, Gladders and Yee (2001)), designed to detect clusters up to $z \sim 1.4$, used another technique based on the red sequence of galaxies in the color-magnitude diagram (see Section 2.2.1).

With subsequent data releases of the SDSS, new cluster catalogs were published, such as Wen et al. (2009); Szabo et al. (2011) for DR6. For the 7th data release, Hao et al. (2010) used a new Gaussian Mixture Brightest Cluster Galaxy (GMBCG) algorithm to detect over 55 000 clusters. For the 8th data release, or the first data release of the SDSS-III, with new instrumentation and more area covered [Aihara et al., 2011], a few major catalogs were published. Wen et al. (2012) identified 132 684 clusters, the largest catalog at the time, with redshifts up to $z \sim 0.8$. Then, Rykoff et al. (2014) introduced the Red-sequence Matched-filter Probabilistic Percolation (redMaPPer) algorithm, which is based on identifying overdensities of red-sequence galaxies. The algorithm is also able to assign a photometric redshift and a richness estimate to each cluster. The catalog built from SDSS DR8 contains 26 311 clusters with $0.08 < z < 0.55$. The redMaPPer algorithm was also used to build a catalog of 6643 clusters from the Dark Energy Survey (DES, The Dark Energy Survey Collaboration

(2005)) Science Verification data [Rykoff et al., 2016], and to refine the SDSS DR8 catalog.

Since then, several other optical surveys have been conducted, such as the Kilo-Degree Survey (KiDS, de Jong et al. (2013)), the Hyper Suprime-Cam Subaru Strategic Program (HSC-SSP, Aihara et al. (2018a)), the Dark Energy Survey (DES, The Dark Energy Survey Collaboration (2005)), the DESI Legacy Imaging Surveys [Dey et al., 2019], and many others [Benitez et al., 2014; Ansarinejad et al., 2023]. Notable results include the KiDS ESO-DR2 cluster catalog of 1858 clusters up to $z = 0.7$ [Radovich et al., 2017], built using a new technique called the Adaptive Matched Identifier of Clustered Objects (AMICO, Bellagamba et al. (2018)), based on the optimal matched-filter technique introduced in Postman et al. (1996). There is also the HSC-SSP catalog of 1921 clusters up to $z = 1.1$ [Oguri et al., 2018], and the DES Y1 catalog of more than 76 000 clusters up to $z = 0.8$ [McClintock et al., 2019]. One of the largest published optical catalogs to date is the DESI Legacy catalog presented in Wen and Han (2024), with more than 1.58 million clusters up to $z = 1.5$.

Looking ahead, the Vera C. Rubin Observatory has now started its Legacy Survey of Space and Time (LSST, Ivezić et al. (2019)), which will map half of the sky in six optical bands over a period of 10 years. The survey is expected to detect more than 300 000 clusters up to $z \sim 1.2$ [LSST Science Collaboration et al., 2009]. Similarly, the *Euclid* satellite [Laureijs et al., 2011] is expected to detect more than 200 000 clusters up to $z \sim 2$ [Sartoris et al., 2016; Euclid Collaboration et al., 2019]. The first *Euclid* Quick Release (Q1) data has already been released [Euclid Collaboration et al., 2025a], with the first validated galaxy clusters detected via the mission's cluster-finding pipeline [Euclid Collaboration et al., 2025b]. The two official algorithms used for the cluster detection are AMICO [Bellagamba et al., 2018] and PZWav [Gonzalez, 2014; Euclid Collaboration et al., 2019], which is based on a wavelet transform of the 3D galaxy distribution. A total of 426 clusters were detected in the Q1 data, up to $z = 1.5$. With the upcoming *Euclid* DR1 data release[1], we can expect a significant increase in the number of detected clusters.

2.3.4 X-ray large surveys and catalogs

As we have seen in Section 2.3.2, X-ray surveys of clusters started in the early 1970s with the Uhuru satellite [Gursky et al., 1971], which showed that bright X-ray sources are associated with rich galaxy clusters. The first X-ray selected catalogs of clusters were published in 1978, with both the Uhuru satellite [Lugger, 1978; Forman et al., 1978] and the *Ariel V* satellite [McHardy, 1978; Cooke et al., 1978]. The number of clusters were around a few tens at the time, and were only considered as clusters if they were previously known from optical catalogs such as the Abell catalog [Abell, 1958]. The next year, the HEAO-1 satellite [Rothschild et al., 1979] conducted an all-sky survey and provided the first flux-limited sample of clusters, with 30 detections at low redshift [Piccinotti et al., 1982]. However, the large beamsizes of these early X-ray satellites (e.g., $> 1°$ for HEAO-1) limited the number of detected clusters, as confusion with other nearby sources was common. With the launch of the *Einstein Observatory* [Giacconi et al., 1979], and thanks to its relatively high angular resolution, the previous catalogs were expanded to include 55 known clusters [Edge et al., 1990]. In addition to this low-redshift sample, the *Einstein Observatory* Extended Medium Sensitivity Survey (EMSS, Gioia et al. (1990)) produced a catalog of 93 clusters extending to $z = 0.58$. Follow-up programs of the EMSS clusters such as the Canadian Network for Observational Cosmology (CNOC, Yee et al. (1996)) were also conducted to study the cluster evolution at $z > 0.2$. These early catalogs used a detection technique called the sliding cell method, where a square cell is moved across the image, and sources are detected as positive fluctuations above a local background. However, this method is not well suited for extended sources such as clusters, and more advanced techniques were later developed, such as wavelet-based algorithms [Rosati et al., 1995; Vikhlinin et al., 1998].

The next major advancement in X-ray astronomy came with the launch of the ROentgen SATel-

[1] Planned for October 21, 2026, see https://euclid.caltech.edu/page/data-release-timeline

lite (*ROSAT*, Truemper (1982)). One of the instruments installed onboard, the Position Sensitive Proportional Counter (PSPC, Pfeffermann et al. (1987)), together with the 84 cm mirror system [Aschenbach, 1988], was particularly well suited for detecting extended sources such as galaxy clusters. The ROSAT All-Sky Survey (RASS, [Truemper, 1993; Voges et al., 1999]) thus provided the first all-sky X-ray survey with good angular resolution ($\sim 30''$) and sensitivity. Pointed observations were also conducted, covering a much smaller fraction of the sky, but with a much higher sensitivity. These two modes of observation led to the construction of several cluster catalogs. The complete list of catalogs, together with their coverage, redshift range (if available), and the number of clusters is given in Table 4. The main catalogs built from ROSAT data are:

- The ROSAT Brightest Cluster Sample (BCS, Ebeling et al. (1998)) and its extension (eBCS, Ebeling et al. (2000)), which comprises 313 clusters in the northern hemisphere up to $z \sim 0.3$.
- The Northern ROSAT All-Sky galaxy cluster survey (NORAS, Böhringer et al. (2000b)), which contains 378 clusters in the southern hemisphere up to $z \sim 0.36$.
- The ROSAT-ESO Flux Limited X-ray Galaxy Cluster Survey (REFLEX, Böhringer et al. (2004)) catalog, which is the southern counterpart of NORAS, with 447 clusters in a similar redshift range.
- The South Galactic Pole survey (SGP, Cruddace et al. (2002)), with 186 clusters up to $z \sim 0.3$.
- The Massive CLuster Survey (MACS, Ebeling et al. (2001)), based on the BCS catalog, which targets very luminous clusters at $z > 0.3$. A final catalog has yet to be published, but several papers have provided subsamples of the survey, such as Ebeling et al. (2007); 2010; Mann and Ebeling (2012); Repp and Ebeling (2018).
- The Clusters in the Zone of Avoidance catalog (CIZA, Ebeling et al. (2002); Kocevski et al. (2007)), which focuses on detecting X-ray clusters in the Galactic plane, where optical observations are hindered by dust extinction. The final catalog contains 130 clusters.
- The North Ecliptic Pole survey (NEP, Henry et al. (2006)), a 81 $\deg^2$ region where ROSAT data is the deepest. 64 sources are identified as clusters, with the most distant one at $z = 0.81$.
- Other serendipitous catalogs built from pointed observations, such as the 160 Square Degree Survey (160SD, Mullis et al. (2003)), the Wide Angle ROSAT Pointed Survey I and II (WARPS/WARPS-II, Perlman et al. (2002); Horner et al. (2008)), the SHARC survey (SHARC Bright and Southern, Romer et al. (2000); Burke et al. (2003)), the 400 Square Degree Survey (400SD, Burenin et al. (2007)), and many others [Pierre et al., 1994a; Castander et al., 1995; Rosati et al., 1998; Campana et al., 1999; Donahue et al., 2002].

The ROSAT satellite was decommissioned in 1999, but the data is still widely used today. For example, the Meta-Catalog of X-ray detected Clusters of galaxies (MCXC, Piffaretti et al. (2011)) compiled almost all ROSAT-based catalogs mentioned above, for a total of 1743 clusters. They have also been used to study the properties of clusters in X-rays, in particular their thermodynamic properties and the scaling relations linking the X-ray surface brightness to the cluster mass [Arnaud et al., 2010; Pratt et al., 2009; 2010]. However, as said in Clerc and Finoguenov (2023), the cluster density in the RASS is about ~ 0.3 $\deg^{-2}$, compared to ~ 15 $\deg^{-2}$ in wide-field surveys performed by its successors, *XMM-Newton* [Jansen et al., 2001] and *Chandra* [Weisskopf et al., 2000]. Both satellites were launched the same year as *ROSAT* was decommissioned, and have much better angular resolution ($\sim 0.5''$ and $\sim 5''$ for *Chandra* and *XMM-Newton*, respectively) and sensitivity. Unlike their predecessor, both satellites have mostly been used for very deep observations of small fields, rather than all-sky surveys. This has led to the construction of much deeper catalogs at higher redshift, such

as the XXL survey [Pacaud et al., 2016; Adami et al., 2018], which covers 50 deg^2 and contains 365 clusters up to $z \sim 1$.

The latest X-ray satellite, the extended ROentgen Survey with an Imaging Telescope Array (*eROSITA*, Merloni et al. (2012)), launched in 2019, was designed to detect very large samples of clusters ($\sim 10^5$) up to redshifts above 1. The first all-sky survey (eRASS1, Merloni et al. (2024)), was completed in June 2020 and led to the publication of the first eROSITA catalog of galaxy clusters [Bulbul et al., 2024], with more than 11 000 clusters detected in a $\sim$ 13 000 deg^2 field. Unfortunately, the German-Russian *eROSITA* satellite has been in safe mode[1], i.e. not taking any data, since February 2022 due to the ongoing invasion of Ukraine. The current last completed all-sky survey is eRASS4. In the future, the New Advanced Telescope for High-ENergy Astrophysics (*NewAthena*, Cruise et al. (2025)), planned for launch in 2037, could be the next milestone for X-ray cluster detection. Its Wide Field Imager will be able to conduct large surveys and map the properties of low-mass galaxy groups even above $z = 2$ [Zhang et al., 2020].

2.3.5 SZ large surveys and catalogs

Detection method

Before talking about the history of cluster detection at millimeter wavelength, it is important to introduce the method used to detect them in the maps.

In millimeter large surveys, clusters are identified using matched-filter techniques [Herranz et al., 2002; Melin et al., 2006; 2012], based on the same principles as its optical counterpart. The match-filter relies on the expected spatial distribution of a typical galaxy cluster signal, as well as the spectral characteristics of the tSZ effect to build a filter that will maximize the cluster signal after filtering. If we consider a survey conducted at several frequencies in the millimeter range ν_i, $i \in [1\,..\,N]$, such as the survey from the South Pole Telescope (SPT, Ruhl et al. (2004); Carlstrom et al. (2011)), the obtained maps can be described as

$$\mathbf{M}(\vec{x}) = y_0\, \mathbf{S}(\vec{x}, \theta_c) + \mathbf{N}(\vec{x})\,, \tag{2.9}$$

where the maps at different frequencies have been arranged in a column vector $\mathbf{M}(\vec{x})$, $\vec{x}$ is the position on the sky, y_0 is the Compton parameter at the cluster center, $S(\vec{x}, \theta_c)$ is the spatial distribution of the SZ signal for a cluster of angular size θ_c, and $N(\vec{x})$ contains the noise maps. These maps contain both the instrumental noise, as well as all other astrophysical signals (e.g., CMB, point sources, unresolved SZ background) that will act as contaminants for the cluster detection. A filter is then built in Fourier space as

$$\mathbf{\Psi}(\vec{k}, \theta_c) = \sigma^2(\theta_c)\, \mathbf{P}^{-1}(\vec{k})\, \mathbf{S}(\vec{k}, \theta_c)\,, \tag{2.10}$$

where $\sigma^2(\theta_c)$ is the total noise variance through the filter, and $\mathbf{P}(\vec{k})$ is the power spectrum of the noise maps. To accurately detect clusters, the key is to choose the best possible model for the cluster signal spatial distribution S. There are a few different models, all based on the expected 3D pressure profile of clusters. For example, Staniszewski et al. (2009) compared the performance of three models, the generalized Navarro-Frenk-White (gNFW, Nagai et al. (2007)), a β model [Cavaliere and Fusco-Femiano, 1976], and a simple Gaussian model. The first two models are 3D pressure profiles, which need to be integrated to obtain the 2D spatial distribution. They finally opted for the β model, and the SPT collaboration has since continued to use this model for their cluster detection. On the other hand, the Atacama Cosmology Telescope (ACT, Kosowsky (2003)) uses, in its most recent release, a gNFW model for the pressure.

[1] Announcement available at https://www.mpe.mpg.de/7856215/news20220303

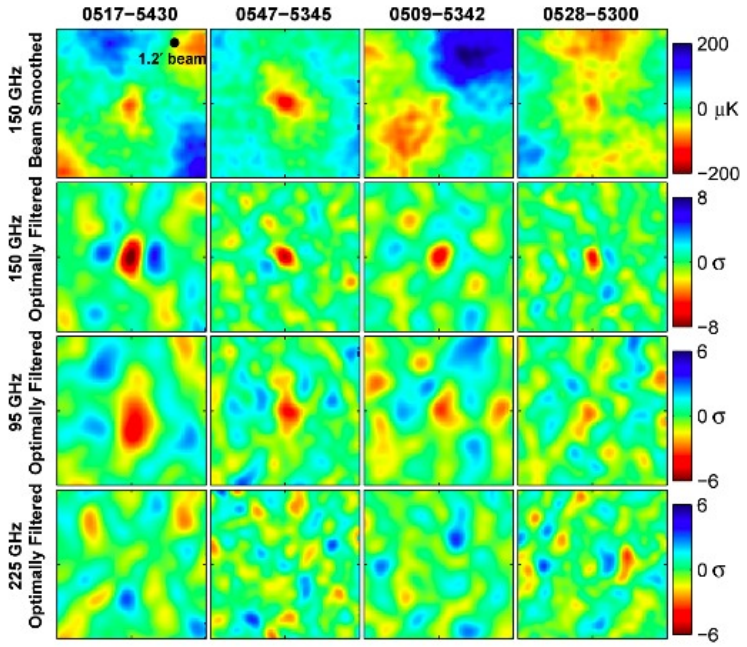

Figure 2.6: From left to right: Maps of the first four clusters detected in the SPT SZ survey at 150 GHz (top row), and filtered maps at 150, 95, and 225 GHz (bottom three rows). The colorbar shows the significance of the detection, with negative values in red. Figure taken from Staniszewski et al. (2009).

The match-filter described above is referred to as a multi-frequency matched-filter (MMF), as it is applied simultaneously to several frequency maps. This technique can also be used on single-frequency maps, as we will see in more detail in Chapter 8.

History of SZ surveys

As we have discussed in Section 2.2.4, the SZ effect was formulated by Sunyaev and Zel'dovich in the early 1970s [Sunyaev and Zeldovich, 1970a; 1972]. The SZ effect was first detected by Pariiskii (1973) while observing the Coma cluster, followed by Gull and Northover (1976) and Birkinshaw et al. (1984). Telescopes and cameras built for millimeter observations were scarce at the time, with one of the first mm telescopes being a repurposed 3.7m telescope at the Green Bank observatory in 1962. In the following decades several others were built, such as the Owens Valley Radio Observatory (OVRO) 40m telescope in 1968, the Nobeyama 45m telescope in 1982 [Akabane, 1983], and the Institute for Radio Astronomy in the Millimeter Range (IRAM) 30m telescope in 1984 [Baars et al., 1987]. However, the observations were still limited to a few clusters and no SZ selected catalogs of clusters could be built.

After the early targeted SZ observations, a shift toward broad, survey-based approaches was made in parallel with advances in cosmic microwave background (CMB) observations. The COBE satellite [Mather, 1982] (not designed for SZ science with its 7° angular resolution) measured the CMB temperature fluctuations with high precision, and thus showed that high resolution measurements would be of particular interest to complement this discovery. In 1992, two separate CMB instruments were proposed to ESA, the Cosmic Background Radiation Anisotropy Satellite (COBRAS) and the Satellite for Measurement of Background Anisotropies (SAMBA) [Bersanelli et al., 1996]. The two projects were then merged a few years later into one, the *Planck* satellite [The Planck Collaboration, 2006], with one of its main goals being to map thousands of galaxy clusters via the tSZ effect. Meanwhile, on the ground, the South Pole Telescope Ruhl et al. (2004); Carlstrom et al. (2011) and the Atacama Cosmology Telescope Kosowsky (2003) were also being built to map the sky at even higher resolu-

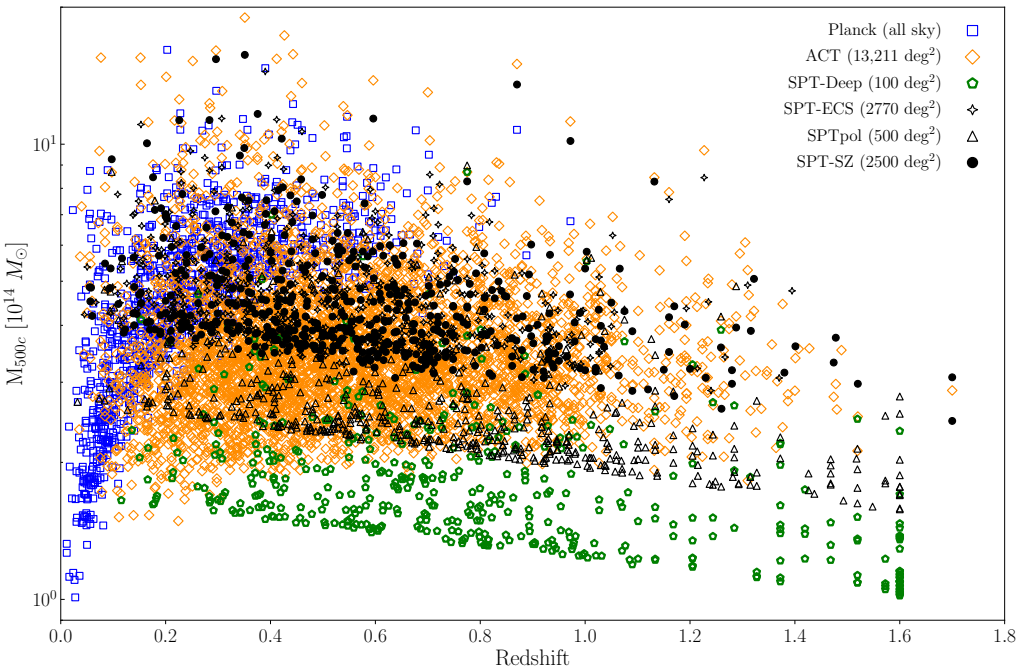

Figure 2.7: Distribution in the mass-redshift plane of clusters published in the *Planck* (blue, Planck Collaboration et al. (2016c)), ACT (orange, Hilton et al. (2021)), SPT-Deep (green, Kornoelje et al. (2025)), SPT-ECS (black diamonds, Bleem et al. (2020)), SPTpol (black triangles, Bleem et al. (2024)), and SPT-SZ (black circles, Bleem et al. (2015b)) catalogs. The $z = 1.6$ limit for some catalogs is due to the fact that the method they used to obtain redshifts flattens out above this redshift threshold.

tion ($\sim 1'$). The first blind detection of a galaxy cluster via the tSZ effect occurred in 2008, when Staniszewski et al. (2009) reported four significant SZ decrements at 150 GHz in a 40 deg^2 field, of which three were previously unknown.

We show in Figure 2.6 the first four clusters found in the SPT SZ survey. The first row shows the maps at 150 GHz, and the second to last row the filtered maps at 150, 95 and 225 GHz, respectively. The colorbar shows the significance, with negative values in red. From the filtered maps at the three different frequencies, we can recognize the spectral dependence of the tSZ effect, with a strong negative decrement (red) at 150 GHz, a weaker decrement at 95 GHz, and most importantly, no SZ signal at 225 GHz, where we expect the tSZ effect to be null. These results show the power of the match-filter to detect clusters, even when the signal is weak compared to other contaminants.

Building on this first success, SZ selected cluster catalogs grew bigger and bigger, from ~ 20 in the following year [Menanteau et al., 2010b; Vanderlinde et al., 2010], to a few hundreds [Hasselfield et al., 2013; Bleem et al., 2015b], and finally to thousands of clusters in the (almost) latest catalogs [Hilton et al., 2021; Bleem et al., 2020]. The *Planck* satellite also published its early SZ cluster catalog in 2011 [Planck Collaboration et al., 2011a], with 189 candidates, followed by the PSZ1 and PSZ2 catalogs in 2013 and 2016, with 1227 and 1653 clusters, respectively [Planck Collaboration et al., 2014b; 2016c]. At the time of writing, the latest ACT DR6 catalog [ACTDESHSC Collaboration et al., 2025] contains almost 10000 clusters, making it the largest SZ selected cluster catalog to date. The complete list of published SZ cluster catalogs is presented in Table 5, and we show in Figure 2.7 the distribution in the mass-redshift plane of clusters from the main SZ catalogs (the latest ACT catalog is not available yet). We see that the majority of clusters are found at redshift below 1, and with masses above 2×10^{14} $M_\odot$. We also distinguish the mass-redshift space probed by each survey. The *Planck* satellite, with its low angular resolution ($\sim 5'$), is sensitive to low-redshift clusters (high and low mass) and to massive high-redshift ones. On the other hand, ACT and SPT, with their higher angular resolution ($\sim 1'$), are sensitive to smaller angular scales, and thus lower mass and higher redshift clusters.

The latest SPT-Deep sample, which uses very deep observations of a smaller 100 deg^2 field, is able to probe clusters in a low-mass high-redshift regime previously unexplored [Kornoelje et al., 2025]. The median mass of the sample is $M_{500} = 1.7 \times 10^{14}\ M_\odot$, which is about a factor of two lower than previous SPT catalogs. We will see in Chapter 8 that this regime can also be probed by telescopes with higher angular resolution, such as the NIKA2 camera [Adam et al., 2018b] on the IRAM 30m telescope.

These results are extremely promising and demonstrate what will be possible with upcoming stage IV CMB experiments, such as the Simons Observatory [Ade et al., 2019] and ~~CMB-S4~~[2] [Abazajian et al., 2019], which will map the sky with unprecedented sensitivity. With the current Large Aperture Telescope (LAT) of the Simons Observatory, forecasts predict the detection of $\sim$ 16000 clusters, with a few dozen at $z > 2$ [Ade et al., 2019]. The most recent forecast, based on future upgrades of the SO LAT [Abitbol et al., 2025], predicts that the upgrade will enable the detection of $\sim$ 33000 clusters, with ≈ 200 at $z > 2$.

Together with the LSST, *Euclid*, *eROSITA*, and other upcoming surveys, cosmological analysis with clusters will enter a new era, with large multi-wavelength datasets enabling better control of systematics and thus tighter cosmological constraints.

2.4 Cosmology with galaxy clusters

Galaxy clusters can be used as cosmological probes in several ways. These different methods rely on distinct physical principles, and their combination can greatly improve the cosmological constraints we obtain. This section will provide a brief overview of methods that use clusters as a probe to test cosmological models. A complete review of the subject can be found in Allen et al. (2011). Before we discuss the different cluster related methods to constrain cosmology, it is important to introduce two key ingredients of cosmological analyses with SZ clusters: the universal pressure profile (UPP), and the scaling relations between cluster observables and their mass.

2.4.1 Universal pressure profile and scaling relations

In a self-similar growth scenario, galaxy clusters are considered to be spherical structures formed through a hierarchical process governed by gravity [Kaiser, 1986]. Under this hypothesis, the radial distribution of thermodynamic properties of the ICM should be well described by a universal profile, scaled according to their characteristic mass and size [Navarro et al., 1996]. Deviations from self-similarity can occur due to baryonic processes that will modify the energy content of the cluster. However, comparison between simulations and observations of the impact of these processes on the thermodynamical properties of clusters [Nagai et al., 2007] have shown that pressure profiles exhibit a behavior close to self-similarity.

The most commonly used universal pressure profile was obtained by Arnaud et al. (2010), who measured the pressure profile of 33 local ($z < 0.2$) clusters using XMM-*Newton* data. The scaled profile is defined as $p(x) = \frac{P_e(r)}{P_{500}}$, which gives [Arnaud et al., 2010]:

$$P_e(r) = P_{500} \left[\frac{M_{500}}{3 \times 10^{14}\, h_{70}^{-1}\, M_\odot} \right]^{0.12} p(x) \tag{2.11}$$

$$= 1.65 \times 10^{-3}\, h(z)^{8/3} \left[\frac{M_{500}}{3 \times 10^{14}\, h_{70}^{-1}\, M_\odot} \right]^{2/3+0.12} p(x)\ \ h_{70}^2\, \mathrm{keV\,cm^{-3}}\,, \tag{2.12}$$

[2] On July 9, 2025, the project was stopped in its original form, but the community is actively working on a successor

where $h_{70} = \frac{H_0}{70 \text{ km s}^{-1} \text{ Mpc}^{-1}}$, $h(z)$ the dimensionless Hubble parameter, and $p(x)$ the generalized Navarro-Frenk-White (gNFW) model proposed by Nagai et al. (2007):

$$p(x) = \frac{P_0}{(c_{500}x)^\gamma \, [1 + (c_{500}x)^\alpha]^{(\beta-\gamma)/\alpha}} , \tag{2.13}$$

with P_0 a normalization constant, γ and β the inner and outer slopes of the profile, respectively, $c_{500} = \frac{R_{500}}{r_s}$ the concentration where r_s is the transition radius between the inner and outer regimes of the profile, α the slope of the transition, and $x = \frac{r}{R_{500}}$ a normalized radius. The best-fit model parameters obtained by Arnaud et al. (2010) are given by

$$[P_0, c_{500}, \gamma, \alpha, \beta] = [8.403 \, h_{70}^{-3/2}, 1.177, 0.3081, 1.0510, 5.4905] \tag{2.14}$$

As we have seen in Section 2.3.5, a good knowledge of the universal pressure profile is crucial for the detection of clusters, as well as for cosmological analyses using the tSZ power spectrum (see Section 2.4.4).

Another constraint in using clusters to constrain cosmological parameters is the accurate estimation of the cluster masses. As the mass of clusters is not directly measured, we need to rely on scaling relations between the observables and the cluster mass. The observable is different depending on the wavelength at which the clusters were detected. For optical surveys, the observable is usually the richness, broadly defined as the number of galaxies in a cluster above a certain luminosity threshold (see, for example, Euclid Collaboration et al. (2025b)). For X-ray surveys, the luminosity L_X or the temperature T_X of the intra-cluster medium are commonly used as mass proxies (e.g., Pacaud et al. (2018)). Finally, for SZ surveys, the integrated Compton parameter Y_Δ (see Equation 2.6) is the observable. Such scaling relations have to be calibrated on representative samples of clusters, i.e., a sample that accurately reflects the overall cluster population, in order not to be biased towards specific clusters.

Providing an accurate scaling relation, as well as an estimate of the mean pressure profile for SZ clusters are two of the main goals of the SZ Large Program (LPSZ, Mayet et al. (2020)), as we will discuss in Chapter 6.

2.4.2 Number counts

The cluster samples we have described in the previous section can be used to constrain cosmological parameters by comparing the observed number of objects per mass and redshift bin with the predictions from a given cosmological model as a function of its parameters:

$$\frac{\mathrm{d}n}{\mathrm{d}z} = \int \mathrm{d}\Omega \int \hat{\chi}(z, M, l, b) \, \frac{\mathrm{d}n}{\mathrm{d}z \mathrm{d}M \mathrm{d}\Omega} \mathrm{d}M \, , \tag{2.15}$$

where N is the number of clusters, Ω the survey area, $\hat{\chi}(z, M, l, b)$ is the survey selection function which depends on the mass M, redshift z, and the position on the sky (l, b), and $\frac{dn}{dM}$ is the halo mass function defined in Section 1.3.3 and Equation 1.19. Clusters are, by nature, very sensitive to the matter distribution in the Universe, and thus to the cosmological parameters that govern structure formation. In particular, they are sensitive to two parameters that we defined in the previous chapter: Ω_m and σ_8 (see Equation 1.14). The number counts are also sensitive to dark energy parameters, such as w, as they form in the late Universe when dark energy starts to dominate.

We show in Figure 2.8 a summary of the current constraints on the cosmological parameters Ω_m, σ_8, and the parameter $S_8 = \sigma_8(\Omega_m/0.3)^{0.5}$, which quantifies the level of structure formation. The *Planck* results from primary CMB measurement [Planck Collaboration et al., 2020b] is shown at the

very top of the figure. The rest of the figure is divided in blocks, with the first three blocks showing results from cluster number counts with clusters from X-ray, SZ, and optical surveys, respectively. We can recognize from Section 2.3 the names of catalogs from which clusters were taken for the different cosmological analyses. The last three blocks show results from probes not related to clusters, such as cosmic shear measurements, 3x2pt analyses (combination of cosmic shear, galaxy-galaxy clustering, and galaxy-galaxy lensing), and galaxy clustering. The main takeaway from this figure is that there is a tension at the 2-3σ level between the results from early Universe probes, such as primary CMB measurements, and low-redshift probes (cluster number counts, weak lensing, and galaxy clustering), with the latter preferring lower values of S_8. To explain this tension, Madhavacheril et al. (2024) suggest that it reflects a discrepancy between measurements at low redshifts and non-linear scales, and those at intermediate z and linear scales, with each regime giving different cosmological constraints. Other authors try to modify the matter power spectrum on non-linear scales to reconcile cosmic shear and *Planck* constraints [Amon and Efstathiou, 2022]. Still, further investigations are needed to understand its origin and whether or not it is due to new physics beyond the ΛCDM model.

2.4.3 Gas mass fraction

Another way to use clusters as cosmological probes is through their gas mass fraction, measured through the total baryon fraction $f_b = f_{gas} + f_{stars}$, where f_{stars} is the baryonic mass in stars. The underlying assumption is that clusters are representative of the matter content of the Universe, and thus their baryon fraction is $f_b = \Omega_b/\Omega_m$. Wicker et al. (2023) have recently measured the gas mass fraction in *Planck* clusters to constrain Ω_m, as well as another parameter which is the hydrostatic mass bias.

2.4.4 tSZ angular power spectrum

The tSZ angular power spectrum is another probe that is sensitive to the cosmological parameters Ω_m and σ_8. It is complementary to the number counts, as it probes the overall cluster population, including low-mass clusters that are not detected individually. The advantage of using the tSZ power spectrum is that it does not require individual cluster mass estimates, and is not sensitive to selection effects. Several measurements of the tSZ power spectrum have been published (e.g., Planck Collaboration et al. (2016a)) and combinations of these measurements have also been performed (*Planck*+SPT, Douspis et al. (2022)). With *Planck*'s low angular resolution, probing low multipoles ($\ell \leqslant 2000$) and SPT high-ℓ measurements, the combination of the two shows improved constraints on cosmological parameters.

2.4.5 X-ray/SZ distances

The combination of X-ray and SZ observations of clusters can be used to estimate their angular diameter distance D_A and thus measure the Hubble constant H_0, based on their different dependence on the electronic density n_e. Briefly, the X-ray emission S_X and the SZ decrement ΔT_{SZ} both depend on n_e as [Silk and White, 1978; Reese et al., 2002]:

$$S_X \propto \int n_e^2 \Lambda_{ee} dl\,, \tag{2.16}$$

$$\Delta T_{SZ} \propto \int n_e T_e dl\,, \tag{2.17}$$

where Λ_{ee} the X-ray cooling function and T_e the electron temperature. Substituting $dl = D_A d\theta$, and eliminating n_e from the two equations, we obtain:

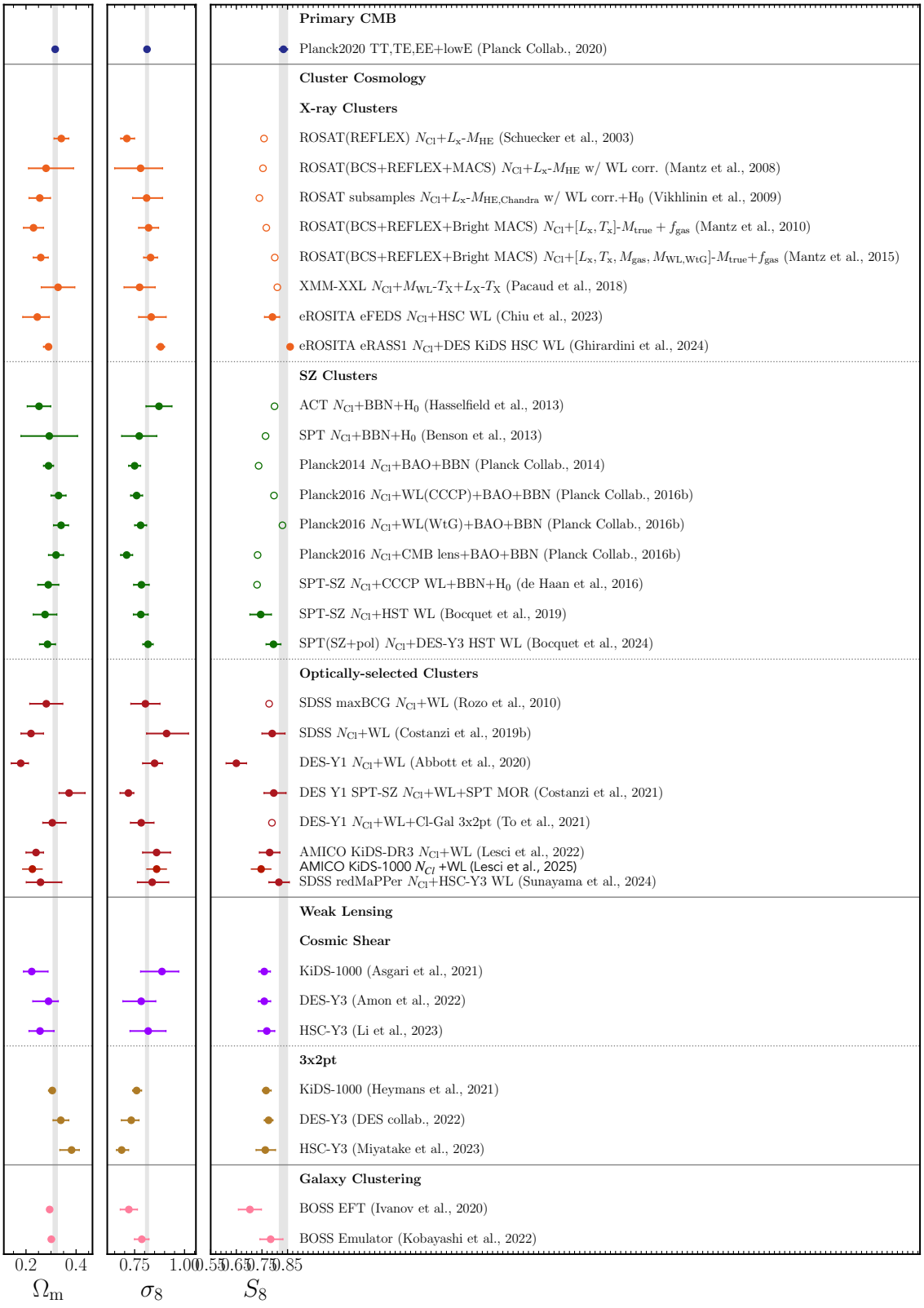

Figure 2.8: Current constraints on the cosmological parameters Ω_m, σ_8, and the parameter S_8 from different cluster related probes. The *Planck* results from primary CMB measurement is shown at the top, and as the grey contour in the rest of the figure. Figure taken from Miyatake (2025). The latest results from KiDS-1000 [Lesci et al., 2025] have been added manually in the optically-selected clusters block.

$$D_A \propto \frac{(\Delta T_{SZ})^2 \Lambda_{ee}}{S_X T_e^2} \frac{1}{\theta_c} \propto \frac{cz}{H_0}\,, \tag{2.18}$$

with θ_c the angular size of the cluster. Wan et al. (2021) have recently used this method to measure H_0, and found $H_0 = 67.3^{+21.3}_{-13.3}$ km s^{-1} Mpc^{-1}. The large errors are due to the X-ray temperature estimation, which should be improved in the near future to provide constraints with per cent level precision.

2.5 Conclusion

Galaxy clusters are a powerful probe for cosmology, provided that their observables can be accurately linked to their mass. The physics of clusters is complex and significantly influences observables in the various wavelengths at which they are detected. As we have seen, the constraints on cosmological parameters derived from cluster related probes are in tension with those from the CMB. Thus, further investigations of the physical processes in clusters are required, especially in the low-mass and high-redshift regime. Detecting and studying clusters in this regime via the tSZ effect would be key to verifying our current knowledge of structure formation, as well as the self-similar hypothesis. In this context, sensitive and very high angular resolution SZ observations seem very promising to better characterize low-mass high-redshift clusters, and provide new insights on the impact of this new population of clusters on cosmology.

Part II

Towards a LEKIDs camera at 100 GHz

CHAPTER 3

A 100 GHz LEKIDs camera for the Nobeyama telescope

3.1 Lumped Element Kinetic Inductance Detectors (LEKIDs) . . . 51
3.1.1 Principle of operation . . . 51
3.1.2 Comparison of readout and calibration techniques . . . 53
3.2 The Grenoble-Tsukuba (GT) 100 GHz LEKIDs camera . . . 58
3.2.1 Detector design . . . 59
3.2.2 The cryostat . . . 60
3.3 Laboratory characterization and validation: 2021 lab campaign . . . 60
3.3.1 Data reduction pipeline . . . 61
3.3.2 Noise measurements . . . 62
3.3.3 Beam shape measurements . . . 62
3.4 2024 laboratory campaign . . . 66
3.4.1 S_{21} spectrum . . . 66
3.4.2 Quality factors . . . 67
3.4.3 Beam measurements . . . 68
3.5 Summary and conclusion . . . 69

In the previous chapter, we have seen that galaxy clusters, the largest gravitationally bound structures in the Universe, are a unique tracer of the matter distribution. They are thus a powerful tool to constrain cosmological parameters and structure formation. To detect and study clusters in the low-mass high-redshift regime, which is currently poorly explored, we need two complementary ingredients: large millimeter cameras with very sensitive detectors, and large telescopes with high angular resolution. Developing and testing such cameras through laboratory measurements is as crucial as the observations themselves. The work presented in this thesis will rely on both aspects.

In this chapter, we will first introduce the operating principle of Kinetic Inductance Detectors (KIDs), which are the type of detectors used throughout this thesis. We also present the different readout techniques used to reconstruct the signal of interest from the raw KID data. Then, we will describe the design and the laboratory characterization of a 100 GHz Lumped Element KIDs (LEKIDs) camera, the Grenoble-Tsukuba (GT) camera, designed for the Nobeyama 45-m telescope.

3.1 Lumped Element Kinetic Inductance Detectors (LEKIDs)

To date, millimeter-wave observations have mostly used bolometric detectors. As the need for higher sensitivity and faster mapping has grown, modern instruments now use larger arrays, often with thousands of pixels [Sobrin et al., 2022; Abitbol et al., 2025]. The readout electronics needed for these large arrays are complex and require too many wires to read all the detectors. To solve this problem, multiplexing methods have been developed that allow several detectors to share the same readout line.

However, bolometers are not intrinsically suited for multiplexing. In this context, Kinetic Inductance Detectors (KIDs), invented in 2003 at Caltech and JPL [Day et al., 2003], have in recent years emerged as an alternative to bolometers as they are naturally suited for multiplexing.

3.1.1 Principle of operation

KIDs are superconducting resonators with high quality factors. Below a critical temperature T_c, superconductors are populated by quasiparticles, which are free electrons, and bound pairs of electrons called Cooper pairs, with binding energy

$$2\Delta \approx 3.52\, k_b\, T_c\,. \tag{3.1}$$

Typically, for a thin film of aluminum ($\approx 18\,\mathrm{nm}$), $T_c = 1.19\,\mathrm{K}$ and $2\Delta \approx 0.36\,\mathrm{meV}$.

The Cooper pair density n_s depends on the temperature T as:

$$\frac{n_s}{n} = 1 - \left(\frac{T}{T_c}\right)^4\,, \tag{3.2}$$

where n is the total number density, quasiparticles and Cooper pairs included. We see that, when $T \ll T_c$, the Cooper pair density is very close to the total density. An incident photon with energy $h\nu > 2\Delta$ can then break Cooper pairs, generating two quasiparticles. In a KID resonator, which is composed of an inductor (L), a capacitor (C) and a resistance (R), changing n_s will in turn change the resonant frequency f_0 which depends on L and C:

$$f_0 = \frac{1}{2\pi\sqrt{LC}} = \frac{1}{2\pi\sqrt{(L_g + L_k)C}}\,, \tag{3.3}$$

where L_g and L_k are the geometric and kinetic inductance, respectively. L_k is inversely proportional to the Cooper pair density (see d'Addabbo (2014)) as:

$$\delta L_k \propto -\delta n_s\,. \tag{3.4}$$

From Equations 3.3 and 3.4, we can see that the absorption of an incident photon will lead to a shift in the resonance frequency of the KID. Differentiating Equation 3.3 with respect to L_k gives:

$$\delta f_0 = \delta L_k \frac{\delta f_0}{\delta L_k} = -2\pi^2 C f_0^3 \delta L_k \propto -\delta P_{\mathrm{opt}}\,, \tag{3.5}$$

where δP_{opt} is the change in optical power.

To absorb the incident radiation, several KID designs have been proposed, and the two most commonly used are the antenna-coupled KIDs and Lumped Element KIDs (LEKIDs). In this thesis we will concentrate on LEKIDs, which have been used for both the Grenoble-Tsukuba (GT, see

Section 3.2) and NIKA2 (see Chapter 5) cameras. The particularity of LEKIDs compared to other types of KIDs is that they are designed to act both as the absorber and the sensing element [Doyle, 2008]. An advantage of such a design is that the resonator has a uniform current distribution, which means that the shift in resonance frequency will be the same regardless of where the photon was absorbed. There is thus no need to redirect the incoming radiations to a specific part of the detector, as is the case for antenna-coupled KIDs.

As mentioned earlier, KIDs are a good alternative to bolometers, as their fabrication process is easier and faster. The main advantage of KIDs is their multiplexable nature. Each KID's resonance frequency can be tuned by changing the capacitance C of the resonator (see Equation 3.3), such that hundreds of detectors can be coupled and read with a single transmission feedline. The feedline probes the response of each KID as a function of frequency. The transmission is usually expressed by the S_{21} parameter, which is the ratio between the transmitted signal and the input signal. S_{21} can be expressed as:

$$S_{21}(f) = 1 - \frac{\frac{Q_{tot}}{Q_c}}{1 + 2jQ_{tot}(\frac{f-f_0}{f})}, \tag{3.6}$$

where Q_{tot} is the total quality factor of the resonator and Q_c the coupling quality factor [Zmuidzinas, 2012]. For the detectors of NIKA2 (see Chapter 5) and the GT camera (see Section 3.2), Q_{tot} is of the order of $\sim 10^4 - 10^5$. As shown in Equation 3.6, the transfer function changes significantly even if the shift in f_0 is small with respect to the readout frequency f. The S_{21} parameter can generally be expressed as:

$$S_{21}(f) = I + jQ, \tag{3.7}$$

with I and Q the real (*in-phase*) and imaginary (*quadrature*) part, respectively. Figure 3.1 shows the amplitude $A = \sqrt{I^2 + Q^2}$ and phase $\phi = \arctan\left(\frac{Q}{I}\right)$ of the S_{21} parameter for a typical KID as a function of the excitation frequency, for two different optical loads. We clearly see the expected shift toward lower values of the resonance frequency when the optical load increases (red curves).

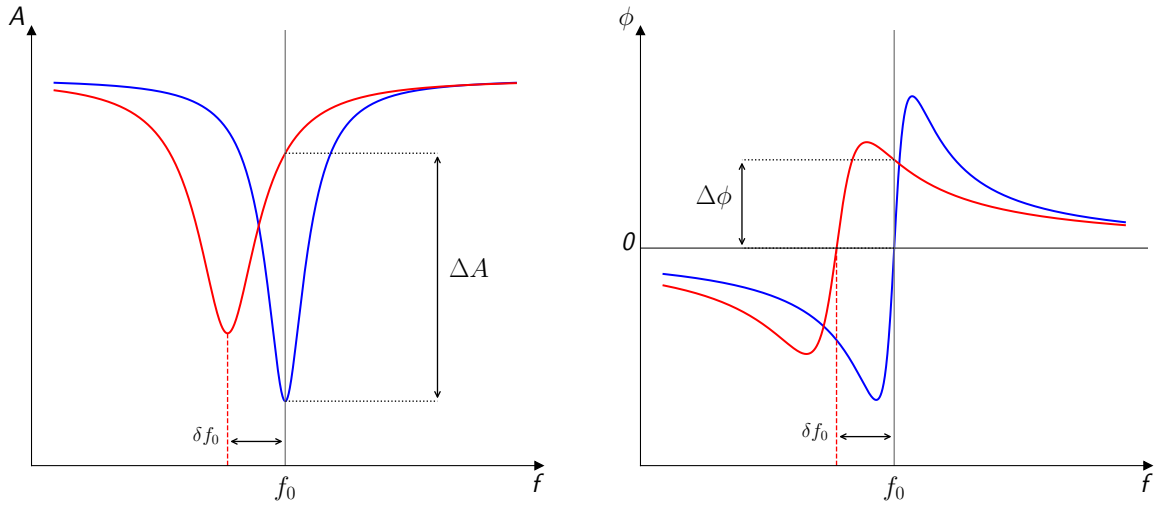

Figure 3.1: Schematic representation of the amplitude (left) and phase (right) of the S_{21} parameter (see Equation 3.6) for a KID, as a function of the excited tone injected in the transmission feedline. The optical load absorbed by the detector is low for the blue curves and increases for the red curves. Figure adapted from Ruppin (2018).

3.1.2 Comparison of readout and calibration techniques

Depending on the scientific requirements, the characteristics of the instrument, and the readout electronics, there are several techniques to reconstruct the shift in resonance frequency of the KIDs. In the prospect of developing a joint Grenoble-Tsukuba (GT) camera, I performed a comparison of the different signal calibration techniques used to go from raw data (mainly variations of the KID transfer function with time) to the resonance frequency shift, which is proportional to the sky power.

Readout electronics

As said in Section 3.1.1, KIDs have high multiplexing factors, which means that hundreds of detectors can be coupled to a single transmission feedline and read out with a dedicated readout board. There are two major readout electronics types for KIDs: single tone monitoring readout and Fast Fourier Transform (FFT) based readout. We show in Figure 3.2 a schematic representation of both readout setups, with the NIKA2 readout on the left and the FFT-based readout on the right. As we can see, they are quite similar, and the core principle is the same. The board (electronics) generates a frequency comb with up to 400 probe tones over a 500 MHz bandwidth, each usually tuned to a KID resonance frequency. These tones can also be tuned *off-resonance*, which is useful when reducing the data (see Section 8.2). As KIDs have, in general, resonance frequencies higher than 1 GHz, the frequency comb is first generated at a lower frequency band, and then mixed with the signal of a local oscillator (LO) to be up-converted to the desired frequency band. The signal is then passed through the cryostat and the KIDs array before being mixed with the same LO signal and down-converted to the baseband. Finally, the signal is sent to the Data AcQuisition (DAQ) system at a certain sampling rate. This signal is composed of the real and imaginary parts of the S_{21} parameter (see Equation 3.7). Let us now describe the differences between the two readout techniques.

1) Single tone monitoring per KID: Single tone readouts only measure S_{21} at one or a few frequencies around the resonance frequency of each KID, as we will discuss in the next sections. This approach is used for example by the NIKA [Catalano et al., 2014a], NIKA2 [Monfardini et al., 2014; Adam et al., 2018b; Calvo et al., 2016a], and CONCERTO [CONCERTO Collaboration et al., 2020] instruments.

2) FFT-based readout: A complex FFT is performed on the signal before it is sent to the DAQ. The FFT splits the continuous time-domain signal into several narrow frequency bins, enabling the acquisition of the full S_{21} spectrum of each KID (more than a hundred samples) instead of just one measurement of S_{21} at a fixed probe tone. A Fast Fourier Transform Spectrometer (FFTS) [Kiuchi et al., 2015] called the FSP4000 is used for this purpose. This technique is used for example by the Japanese team for the MKID camera [Honda et al., 2023b] and the GT camera described in Section 3.2.

In this thesis, we have worked with both kinds of electronics: a single tone NIKEL (New Iram KID ELectronics, Bourrion et al. (2011); 2012; 2013; 2016) CONCERTO-like electronic [Bourrion et al., 2022] and the FSP4000 from Tsukuba [Kiuchi et al., 2015]. We primarily worked with the former, used for observations with the GT camera (see Chapters 4 and 5). We will present the NIKEL electronics in more detail in the next chapter.

In the following, we will see that the sampling rate varies between the different readout electronics, depending on the scientific goal and the reconstruction technique used.

NIKA2 2-point technique: RfdIdQ

To accurately measure the optical load absorbed by a KID during an observation, the change in resonance frequency needs to be monitored continuously and simultaneously for all KIDs on the same feedline. To achieve this, Calvo et al. (2016a) developed a readout method using a fast electronic 2-points modulation of the excited tone.

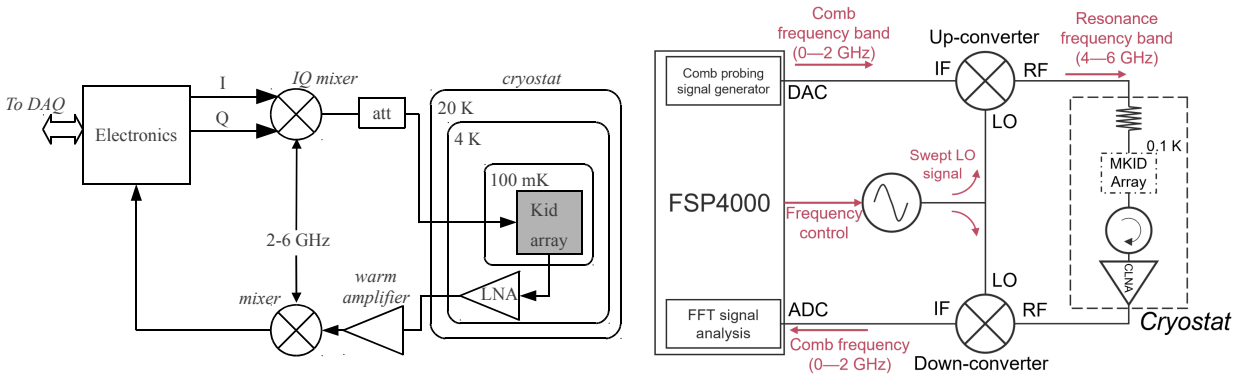

Figure 3.2: (Left): Schematic representation of the NIKA2 readout setup used to monitor a KID array. The main difference between each experiment (NIKA, CONCERTO, etc) is the type of electronics used. (Right): GT camera initial readout system. The difference with the other readout setup comes from the FSP4000 [Kiuchi et al., 2015], which performs a FFT once the signal has passed through the KID array. Figures taken from Bourrion et al. (2011) and Murayama, Yosuke (2022), respectively.

When starting the measurements, the resonance frequency of each detector is obtained for the existing background via a resonance sweep. Then, the transfer function is monitored for each detector k at its initial resonance frequency at high rate, 954 Hz. From this, we can derive the real and imaginary components $i_k(t)$ and $q_k(t)$ of the signal along the excitation frequency as a function of time. The excitation frequency or probe tone, generated by the LO, aligns with the resonance frequency of KID k and is modulated to alternate between $f^k_\pm = f^k_{\text{tone}} \pm \frac{\delta f_{\text{tone}}}{2}$, where $\delta f_{\text{tone}} = 2\,\text{kHz}$. The latter is much smaller than the typical width of a resonance, which is of the order of $\sim$ 200kHz. These 954 Hz samples are then averaged over $N_m = 40$ points, reducing the rate to 23.84 Hz, to compute $I(t)$ and $Q(t)$, along with the averaged differences $\delta I(t)$ and $\delta Q(t)$ between samples measured at f^- and f^+. Thus, $I(t)$, $Q(t)$, $\delta I(t)$, and $\delta Q(t)$ are obtained such that:

$$\begin{cases} I = \sum_{p=1}^{N_m} i_p \\ Q = \sum_{p=1}^{N_m} q_p \\ \delta I = \sum_{p=1}^{N_m/2} i_{2p} - i_{2p-1} \\ \delta Q = \sum_{p=1}^{N_m/2} q_{2p} - q_{2p-1}\,. \end{cases} \tag{3.8}$$

Figure 3.3 shows a resonance in the complex plane where the red points are the I and Q values once averaged. When a detector array is illuminated by incident radiation, the quantities (I, Q) change by $\vec{V} = (\Delta I, \Delta Q)$. To measure the shift in the resonance frequency between two samples, one can compare $\vec{V}$ with the reference values $d\vec{V} = (dI, dQ)$ caused by the known modulation δf_{tone}. The change in resonance frequency between two samples is then proportional to the projection of $\vec{V}$ onto $d\vec{V}$ [Catalano et al., 2014b]:

$$\Delta(\delta f_0) = \delta f_{\text{tone}} \frac{d\vec{V} \cdot \vec{V}}{\left|d\vec{V}\right|^2} = \delta f_{LO} \frac{\Delta I \langle \delta I \rangle_{50} + \Delta Q \langle \delta Q \rangle_{50}}{\langle \delta I \rangle^2_{50} + \langle \delta Q \rangle^2_{50}}\,, \tag{3.9}$$

where $\langle \cdot \rangle_{50}$ means that we average the δI and δQ over 50 points before and after the considered value. The shift in resonance frequency as a function of time is then given by the cumulative sum of the differences between consecutive samples:

$$\delta f_0(t) = \sum_{t'=0}^{t} \Delta(\delta f_0)(t')\,. \tag{3.10}$$

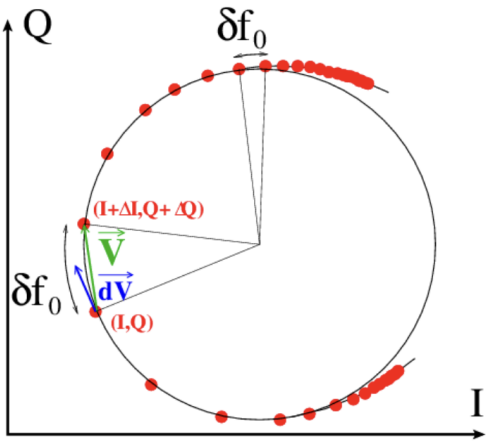

Figure 3.3: Schematic representation of the reconstruction of the resonance frequency shift in the complex I-Q plane. The vectors $\vec{V} = (\Delta I, \Delta Q)$ and $d\vec{V} = (dI, dQ)$ are shown in green and blue, respectively. The change in resonance frequency is constant between each red point, but the distance between them is not constant in the complex plane. The resonance frequency is reconstructed from the modulation, which is known and serves as a local reference in the complex plane. Figure taken from [Adam, 2015].

This estimate of δf_0 is referred to as *RfdIdQ* [Catalano et al., 2014b]. More recently, an alternative method was proposed based on the 2 points modulation [Ponthieu et al., 2025]. The main idea is to project I, Q, dI, and dQ onto an axis so that they maintain an almost linear relationship with frequency, which itself is directly related to the optical power. To do that, the first step is to fit the resonance circle in the complex plane to find its center and radius. The circle is then scaled, translated, rotated, and reversed before being inverted using the Möbius transform. The data points now lie along the imaginary axis $I = 1$. This calibration method is more robust against quick variations of the signal, making it more linear than the *RfdIdQ* method. This updated method, referred to as *cftoi* hereafter, is now used in the NIKA2 data reduction pipeline.

CONCERTO/KISS 3-points technique

The CONCERTO instrument [CONCERTO Collaboration et al., 2020] and its pathfinder KISS [Fasano et al., 2021] are wide-field spectrometers, capable of both photometry and spectroscopy. They are equipped with a Martin-Puplett interferometer (MPI), which is designed to sample four interferograms per pixel per second. This requires a very high sampling rate ($\sim 4\,\mathrm{kHz}$) to properly sample the interferograms and avoid being limited by atmospheric fluctuations. The 3-points technique was thus developed for this purpose, as the continuous frequency modulation of the *RfdIdQ* technique was no longer viable at this sampling rate. In the following, we will describe the 3-points technique in the case of CONCERTO [Bounmy et al., 2022].

As done for NIKA2, the excitation frequency generated by the LO is modulated as $f^k_\pm = f^k_{\mathrm{tone}} \pm \frac{\delta f_{\mathrm{tone}}}{2}$, where $\delta f_{\mathrm{tone}} = 10\,\mathrm{kHz}$. However, a third unmodulated point ($f^k = f^k_{\mathrm{tone}}$) is added to enable the reconstruction of the resonance circle in the complex plane. These three modulation points, that we will refer to as p_1, p_2, and p_3 form a data block as shown in Figure 3.4. This data block $M(j)$ is composed of 1536 samples and can be described as:

$$M(j) = \begin{cases} p_1(I_1, Q_1) = f_+ = f_{LO} + \frac{\delta f_{\mathrm{tone}}}{2} & 0 \leq j < 32 \\ p_2(I_2, Q_2) = f_- = f_{LO} - \frac{\delta f_{\mathrm{tone}}}{2} & 32 \leq j < 64 \\ p3(I_3, Q_3) = f_{LO} & 64 \leq j < 1536\,, \end{cases} \tag{3.11}$$

with j the sample number. The unmodulated (*science*) part represents approximately 96% of the data acquisition, with the rest dedicated to calibration purposes. The S_{21} transfer function is thus sampled

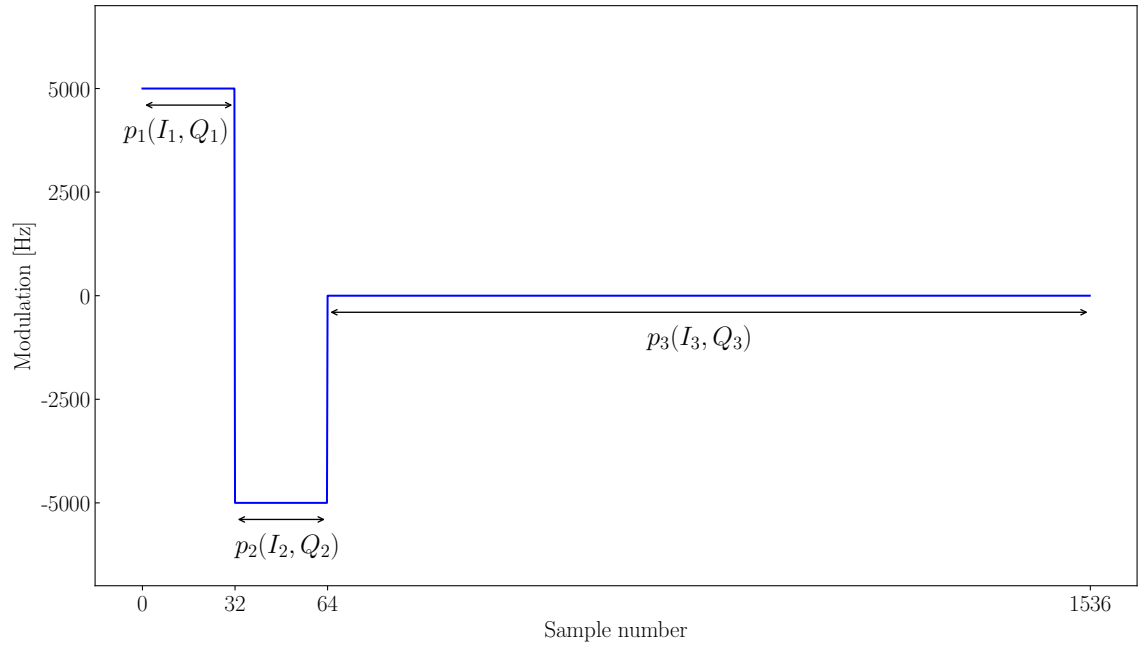

Figure 3.4: Simulation of the modulation as a function of the sample number within one CONCERTO data block. The sampling rate is 3.816 kHz, which gives a 2.48 Hz data block rate. The modulated points only represent ~4% of the block. The modulated part has been rescaled for visualization purposes. Adapted from Bounmy et al. (2022)

following the modulation described above, giving (I, Q) values (see Equation 3.7). We now need to derive a quantity that is linear with the shift in resonance frequency. For each block, we perform a circular fit with the median values of p_1, p_2, and p_3, to find the center of the circle in the I-Q plane, $p_0(I_0, Q_0)$. This process is illustrated in Figure 3.5. Using the center coordinates, we can compute the modulation angles θ_1 and θ_2 as:

$$\theta_{1(2)} = \arctan\left(\frac{I_0 - I_{1(2)}}{Q_0 - Q_{1(2)}}\right). \tag{3.12}$$

Finally, the conversion factor C can be estimated as:

$$C = \frac{\delta f_{\text{tone}}}{\Delta\theta}, \tag{3.13}$$

where $\Delta\theta = \theta_2 - \theta_1$. We can now convert the scientific data into the resonance frequency shift δf_0:

$$\delta f_0 = (\theta_3 - \theta_0) \times C, \tag{3.14}$$

where $\theta_3 = \arctan\left(\frac{I_0 - I_3}{Q_0 - Q_3}\right)$ and $\theta_0 = \arctan\left(\frac{I_0}{Q_0}\right)$. For each data block, we obtain a measure of δf_0 at a rate of approximately 2.48 Hz in the case of CONCERTO, which corresponds to the signal integrated over the full bandwidth of the instrument. This technique can also be used in photometric mode, when no interferograms are acquired. In this case, we follow the same procedure to reconstruct the change in resonance frequency, but δf_0 can be sampled at a much higher rate. For the observations with the Grenoble-Tsukuba camera (see Section 5.1), we sampled δf_0 at a rate of 240 Hz.

Tsukuba FFTS technique

For the Tsukuba MKIDs camera commissioned in 2021 [Honda et al., 2023], the readout modulates the excitation tone using a fast Fourier transform spectrometer (FFTS) [Kiuchi et al., 2015]. Here,

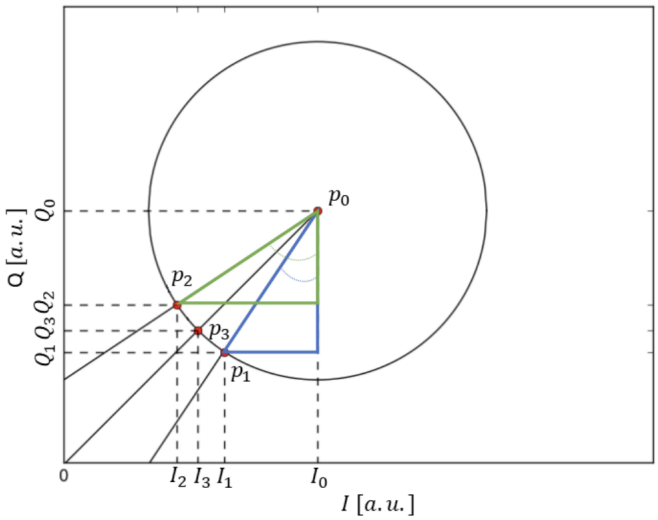

Figure 3.5: Resonance circle in the (I, Q) plane, with p_1, p_2 the modulation points, p_3 the measurement points and p_0 the center of the fitted circle. Adapted from Fasano et al. (2021)

instead of measuring S_{21} at 2 or 3 frequencies around the resonance frequency of each KID, the FFTS enables the acquisition of more than a hundred measurements of S_{21} at a high sampling rate. The acquisition of the signal from probe tones is controlled by two main parameters called the divide number N_d and the window number N_w, both expressed as powers of 2. The divide number N_d sets how many times per second the system collects a full S_{21} resonance spectrum. In the case of LEKIDs, 2^7 or 128 spectra are acquired per second which means that $N_d = 8$ [Nagai et al., 2022]. Each divide is further split into many short windows of size $\Delta t = 4\ \mu s$, which are used for the FFT calculation. N_w determines the number of FFT windows in one divide, and this directly sets the number of frequency points in each measured spectrum. Spectra acquired for LEKIDs by the FFTS readout have 128 frequency points ($N_w = 7$) over a sweep range $\Delta f_{sweep} = 700$ kHz, which amounts to a bin width of ±5.47 kHz. We can notice that according to the divide number one spectrum is acquired every 1/128 Hz or 7.81 ms. However, the actual spectrum sampling rate is given by $2^{N_w} \cdot \Delta t = 0.51$ ms, which means that there is a dead time of 7.30 ms between two consecutive spectra. This dead time is intentionally introduced because the FFT outputs a large volume of data, and the data generation rate may exceed the writing speed of the disk where the data are stored. This sets an upper limit on N_d and N_w values which need to satisfy $N_d + N_w <= 15$. An eighth-order polynomial is then fitted to each spectra (see Figure 3.6) to estimate the resonance frequency f_0 and measure the frequency shift δf_0 over time.

Readout techniques comparison

The three techniques presented above are all based on a frequency-sweeping scheme, although they differ in how they reconstruct the shift in resonance frequency. In the following, to compare their performances, we will assume that they are used for observations at the Nobeyama 45-m telescope. We assume a FWHM of 18″ which is expected for the telescope at 100 GHz. For the sampling, we use the values described in the previous sections unless otherwise stated. We simulate a small portion of a TOI, mimicking the observation of a point source with known flux.

To assess the validity of the techniques, we simulated observations of point sources with varying fluxes and different scan speeds, v_s, to test the robustness of the methods against fast flux variations. The comparison between the reconstructed resonance frequency shift, $\delta f_0^{meas}(t)$, and the expected one, $\delta f_0^{exp}(t)$, is done using the following quantity:

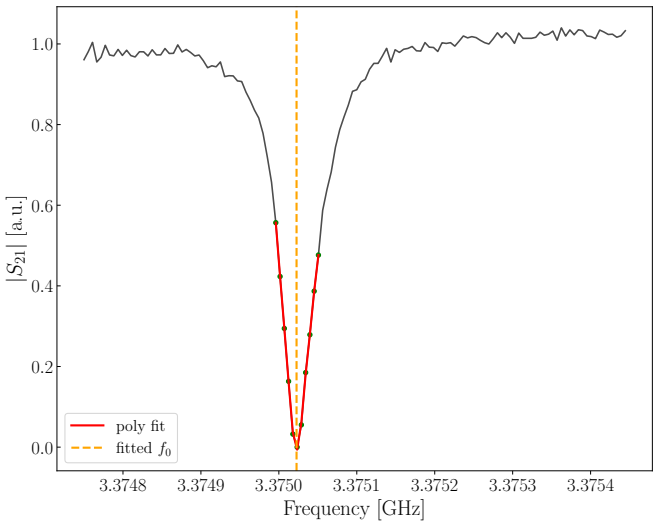

Figure 3.6: $|S_{21}|$ spectrum acquired by the Tsukuba FFTS readout. The red and orange lines show the polynomial fit used to estimate the resonance frequency f_0 and the fit result, respectively.

$$\xi_{amp} = \frac{\max(\delta f_0^{meas}(t))}{\max(\delta f_0^{exp}(t))}\,, \tag{3.15}$$

where ξ_{amp} allows us to estimate the photometric accuracy at the peak of emission of the source. We expect this quantity to be close to unity in the case of a good reconstruction of the flux. We show in the left panel of Figure 3.7 an example of a point source simulation with $\delta f_0^{exp} = 5$ kHz, which is a typical value for a bright source. A comparison of all techniques is also shown in the right panel of Figure 3.7, where we plot ξ_{amp} as a function of δf_0^{exp} for a given scan speed of 16 arcsec/s, a typical value for the Nobeyama telescope. We see that even when δf_0^{exp} is very large, the *cftoi* technique is still able to reconstruct the signal within 1% accuracy. The FFTS technique is also very robust and only limited by its sweeping range. Indeed, as discussed in Section 3.1.2, the frequency sweep spans a range of 700 kHz or ±350 kHz around the resonance frequency. As the FFTS reconstruction is based on a direct fit of the resonance spectrum, if the expected frequency shift is larger than the sweep range, the photometric accuracy will drop significantly. The 3-points technique is less accurate than the others, but it has other advantages, such as the ability to sample the signal at a much higher rate, which is useful for fast sky scanning and spectroscopy. Figure 3.8 shows the results for the four techniques considered, this time with v_s varying from 10 to 100 arcsec/s. The δf_0^{exp} values are intentionally unrealistic to test the robustness of the methods.

3.2 The Grenoble-Tsukuba (GT) 100 GHz LEKIDs camera

The prototype for the GT camera was a 109-pixel MKID camera, also operating at 100 GHz [Honda et al., 2023], developed at the University of Tsukuba. The MKID camera was commissioned at the Nobeyama 45-m telescope in 2018 and 2021 and showed very promising results [Honda et al., 2023a]. However, MKID detectors are based on complex technology, which makes replication and scaling to large focal planes very difficult. A LEKIDs array was thus considered as a suitable alternative. The GT camera uses the same cryostat and readout electronics as its predecessor and will be discussed in the following.

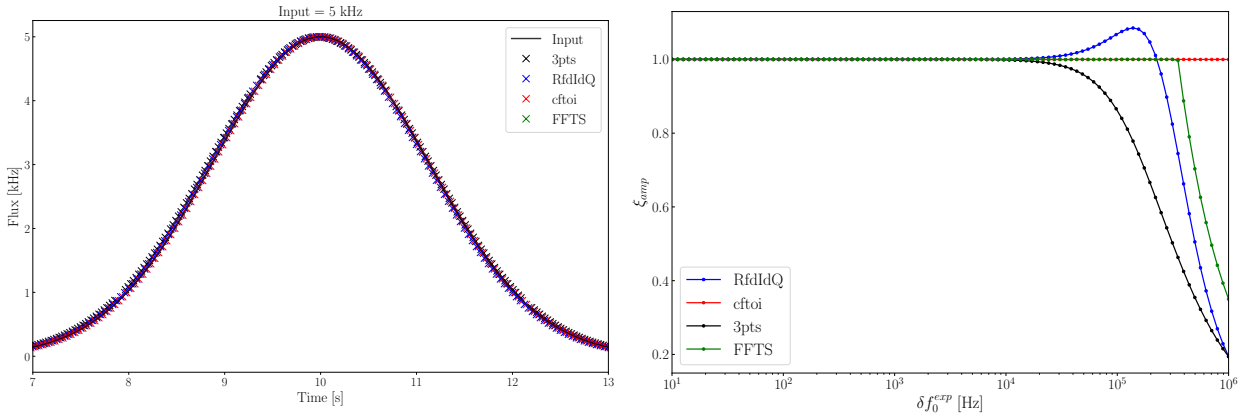

Figure 3.7: (Left): Comparison of the techniques for a point source with $\delta f_0^{exp} = 5$ kHz. (Right): ξ_{amp} as a function of δf_0^{exp} for the different readout techniques. The scan speed is fixed at 16 arcsec/s.

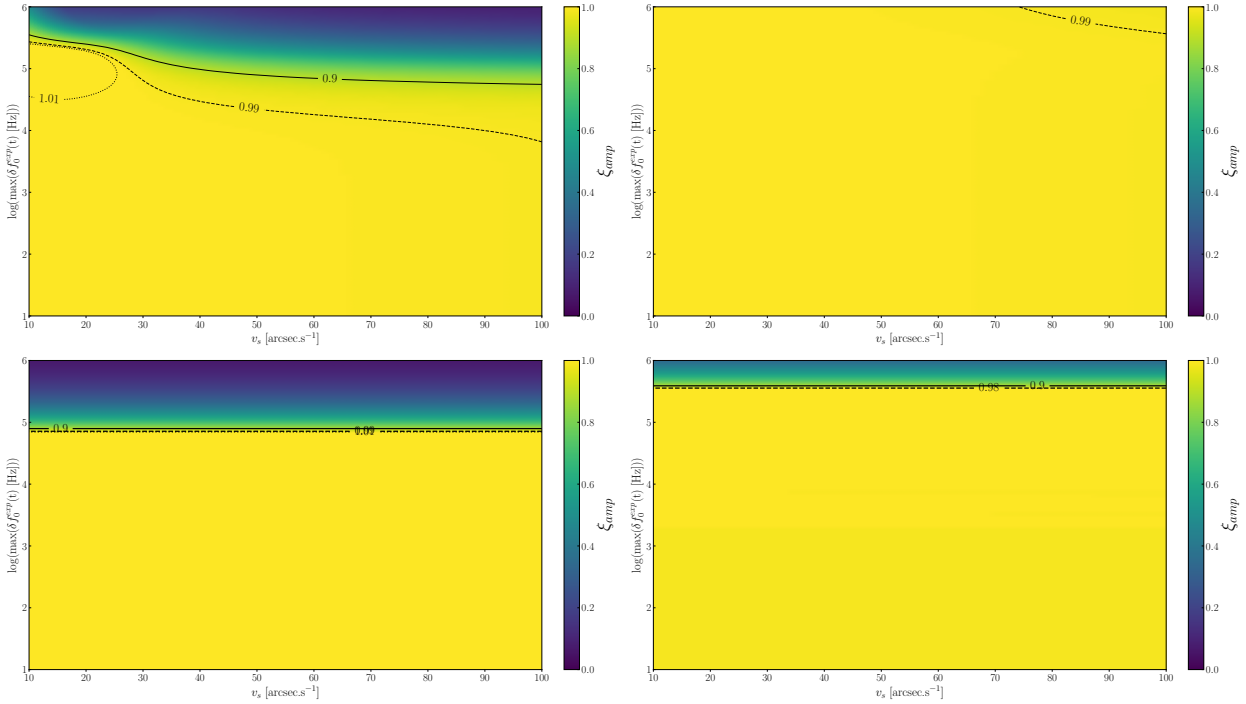

Figure 3.8: ξ_{amp} in the $v_s - \delta f_0^{exp}$ plane for the different readout techniques. (Top-left): *RfdIdQ* technique. (Top-right): *cftoi* technique. (Bottom-left): 3-points technique. (Bottom-right): FFTS readout technique. The dashed lines show ξ_{amp} contours, with the contour value shown on the line. All methods are very robust up to $\delta f_0^{exp} \sim 10^5$ Hz. We stress that such high values of δf_0^{exp} are not expected during observations.

3.2.1 Detector design

The LEKIDs array used for the GT camera was designed and fabricated at Institut Néel, Grenoble. The detector design takes advantage of the knowledge acquired with the NIKA/NIKA2 instruments [Monfardini et al., 2011; Adam et al., 2018b]. The array is composed of 144 detectors of 4.86×4.86 mm^2 operating at 100 GHz, with resonance frequency in the range 650-900 MHz. They are made of a ∼ 10-25 nm Titanium-Aluminium bi-layer film with $T_c = 0.9$ K. The energy gap is $2\Delta \approx 0.27$meV, which corresponds to the energy of ∼ 70 GHz photons. The coupling factors Q_c were optimized to be in the range $Q_c \approx 5 \times 10^4 - 10^5$, which is comparable to the values for the detector arrays in NIKA2 (see Section 6.1.2). The LEKIDs array mounted in its holder is shown in Figure 3.9. We can see in the array (center of the image) black squares corresponding to the KIDs in the feedline. The latter is

matched to the input and output connectors, which are visible on the top of the figure. It is important to note that the array we use is a spare, as the original one was damaged during transportation to Japan. The spare array is not optimal, especially in terms of cosmetics, i.e, the resonances are not homogeneously distributed on the feedline (see Section 3.4.1).

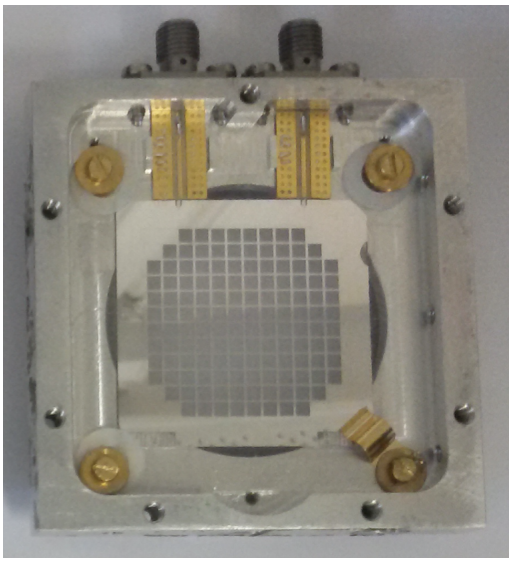

Figure 3.9: Picture of a prototype LEKIDs array, used to design the final array for the GT camera

3.2.2 The cryostat

The LEKIDs array is installed in a cryostat that cools the detectors down to 100 mK, which is about an order of magnitude below the critical temperature of the Titanium-Aluminium film (T_c = 0.9K; see Section 3.1.1). The interior of the cryostat is shown in Figure 3.10. The cryostat has five different temperature stages at 300 K, 40 K, 4 K, 1 K, and 0.1 K, where the detectors are placed. The cooling process of the array down to 100 mK is achieved first using a Gifford-McMahon (GM) refrigerator down to 4 K. Further cooling from 4 K to 0.1 K is done using a ^{3}He/^{4}He dilution refrigerator. As shown in the bottom of Figure 3.10, the light enters the cryostat through a vacuum window and is focused on the detectors by two silicon lenses.

3.3 Laboratory characterization and validation: 2021 lab campaign

After its fabrication, the LEKIDs array was first characterized at Institut Néel in 2019. Figure 3.11 shows the main result, which is the measurement of the power spectral density (PSD) of the noise per detector. The average noise for detectors in the array was found to be $\sim 1.5\ \frac{\mathrm{Hz}}{\sqrt{Hz}}$ at f = 10 Hz. In the figure, the noise level seems slightly lower than this value, because only a third of the detectors are shown.

The array was then shipped to Japan in 2020 and characterized several times at NAOJ since then. In the following sections, I will present the results from two lab campaigns. The first one took place in April 2021, before I joined the project. Since I did not actively participate in this campaign, I later used the specific data reduction pipeline developed by the team for the Tsukuba MKID camera [Honda et al., 2023] to re-analyze the data and reproduce their results. The second campaign took place in February 2024, where I actively participated in the measurements and analysis.

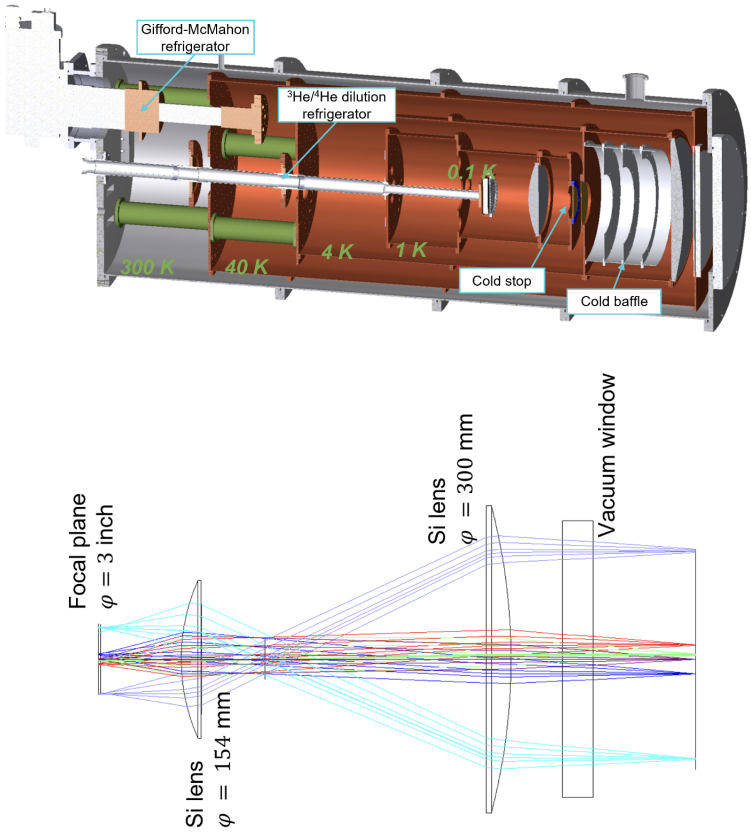

Figure 3.10: (Top): Cross-sectional view of the GT camera cryostat showing the cold optics and the four temperature stages. The LEKIDs array is installed in the 0.1 K stage. (Bottom): Cold optical layout inside the cryostat. Figures taken from Murayama, Yosuke (2022).

3.3.1 Data reduction pipeline

During the 2021 lab campaign, a thorough characterization of the LEKID array properties was performed. I was able to get familiar with the data reduction pipeline developed by Makoto Nagai and reproduce the results obtained by the previous team [Suzuki, Ryuji, 2020]. At the beginning of the campaign, the resonance frequencies of each detector were measured using a vector network analyzer (VNA) and stored in a file which was used as input in the data reduction pipeline. Out of the 144 detectors, 137 were identified in the VNA scan, and 114 were successfully read out by the FSP electronics. The probe tones (usually one per resonance) that will be used to read out the detectors were then generated using the resonance frequencies measured by the VNA. Each probe tone is given an ID which is used to identify its associated detector during the data reduction. The probe tones and their ID, as well as information on the frequency sweep, the LO frequency, and other FFTS parameters like N_d and N_w (see Section 3.1.2), are stored in a main configuration file called `BAR0`.

Once the previously mentioned input files are ready, the data reduction can start. The data acquired by the FSP are stored in a single binary file per measurement. There are several steps before we can obtain the resonance frequency shift δf_0 as a function of time:

1. Based on the number of probe tones in the frequency comb, the original data file is split into several sub-files, each containing the data for one probe tone. If two resonances are too close to each other, e.g. less than 250 kHz apart, the same probe tone is assigned to both and the data are stored in the same sub-file. This explains why only 114 of the 137 identified resonances were

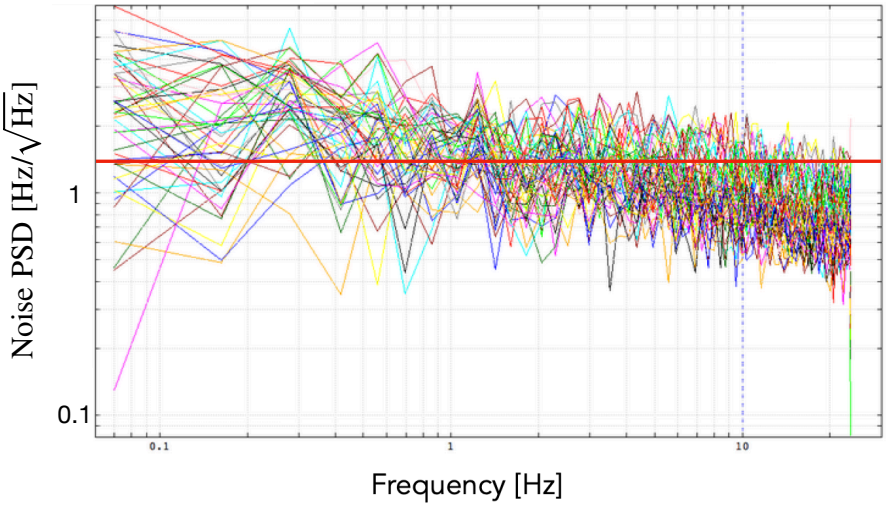

Figure 3.11: Noise PSD measurement performed in Grenoble in 2019. Each colored line corresponds to one detector, for a total of 50 detectors out of 144 in the array. The red line shows the average noise level ~ 1.5 $\frac{\text{Hz}}{\sqrt{Hz}}$. Credit: Alessandro Monfardini.

successfully read out by the FSP.

2. The raw (I, Q) data are extracted from each sub-file and divided into spectra of size 2^{N_w} points.
3. As each tone probes the same frequency range during the whole measurement, the frequency points for each tone can be easily computed knowing the frequency sweep range Δf_{sweep} as:

$$f_i = f_{\text{tone}} + i \cdot \frac{\Delta f_{\text{sweep}}}{2^{N_w}}, \quad i = 0, 1, 2, \ldots, 2^{N_w} - 1\,, \tag{3.16}$$

4. As discussed in Section 3.1.2, each spectrum is fitted with an eighth-order polynomial to estimate the resonance frequency f_0.

We thus have a total of 114 KIDs with their associated f_0 time-ordered information (TOI) that we can use to characterize the properties of the array.

3.3.2 Noise measurements

To characterize the noise properties of the array, we first place an object with a known optical load in front of the cryostat window. In the following, we will present the results obtained with a mirror placed in front of the cryostat, with a temperature $T \sim 30$ K. We then acquire about 20 seconds of data, which is enough with the high acquisition rate of the FFTS readout (see Section 3.1.2). To compute the noise power spectral density (PSD), we use the f_0 TOI that is produced by the data reduction pipeline described above, without any additional processing (no filtering or noise decorrelation). Taking the Fourier transform of the TOI, we can obtain the noise PSD for each detector. We show the results in Figure 3.12 as solid color lines. We find an average noise (blue dashed line) of 36.9 ± 7.9 $\frac{\text{Hz}}{\sqrt{Hz}}$, which is an order of magnitude higher than expected from measurements in Grenoble (red dashed line), as shown in Figure 3.11 and Section 3.3.

3.3.3 Beam shape measurements

Knife-edge technique

The knife-edge technique is a simple method to measure the beam shape of a detector. The measurement principle is illustrated in Figure 3.13. The experimental setup consists of a cold load

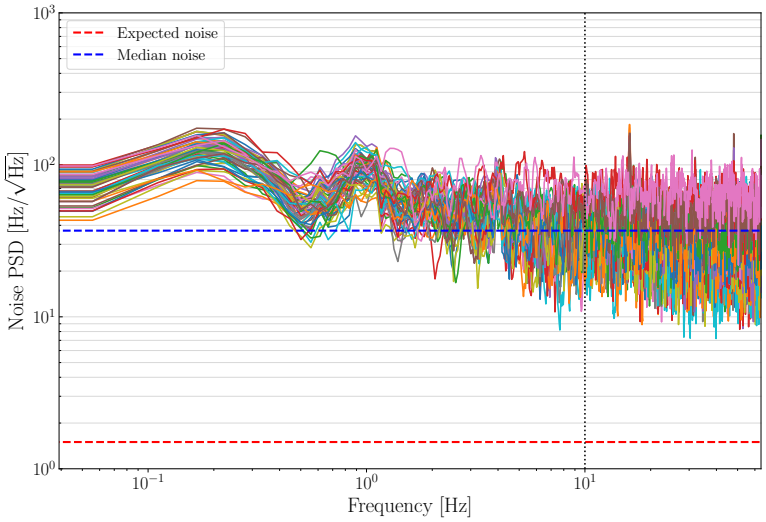

Figure 3.12: Noise PSD measurement for each detector (solid lines) performed at NAOJ in 2021, with a black-body temperature of 30 K. The red and blue dashed lines correspond to the median noise measured in Grenoble, 1.5 $\frac{\text{Hz}}{\sqrt{Hz}}$, and NAOJ, 36.9 $\frac{\text{Hz}}{\sqrt{Hz}}$, respectively.

(77 K) placed in front of the cryostat window, and a hot load (300 K). The hot load, which is positioned perpendicular to the optical axis of the beam, is first placed far from the array, such that the detectors are not illuminated. Once the data acquisition starts, the hot load is moved by a platform along one axis (X or Y) toward the detectors, at a speed of 2.5 mm/s. The measurements are performed along both the X and Y directions to determine the 2D beam shape and the position of each detector on the focal plane. In the bottom-right panel of Figure 3.13, we show the measurement of the resonance shift of one detector. As expected, its resonance frequency f_0 shifts to lower values as the hot load approaches the detector.

As the hot load approaches the detectors, their resonance frequency will shift, as shown in the left panels of Figure 3.14. In the top panel, we represent a model of the expected frequency shift δf_0 as a function of the knife-edge displacement for one detector. In the bottom panel, we show the actual measurements of δf_0 for all detectors along the X axis. We clearly see that the shift does not happen at the same time for all detectors, giving us information about their position in the array. The beam shape can then be inferred by differentiating the measured resonance frequency shift δf_0 with respect to the knife-edge displacement, as illustrated in the right panels of Figure 3.14. Similarly to the left panels, the top panel shows the derivative of the δf_0 model for one detector, while we plot the derivative of the δf_0 measurements for a subsample of 20 detectors in the bottom one. By fitting a Gaussian to this derivative, we can estimate the FWHM of the beam as well as the position (along the X or Y axis) of the detector in the focal plane. Combining the results from the X and Y scans, we can find the (x, y) position of each detector and its 2D beam FWHM.

The detectors average beam FWHM was found to be $\theta_{FWHM} = 33.0 \pm 3.4$ mm, which is larger than the average beam size of 20 mm found for the MKID array [Suzuki, Ryuji, 2020]. We show in Figure 3.15 the focal plane geometry of the array, where each point and number corresponds to one detector. The beam shape of each detector is represented by a cyan ellipse. The x and y axes are the offsets with respect to the reference detector, n°126, chosen because it was the closest to the center of the array.

We highlighted two main issues with the results obtained during this 2021 lab campaign. First, the noise level is an order of magnitude higher than what was measured in Grenoble (see Figure 3.12). Second, the beam size of the LEKIDs array is larger than expected. These discrepancies indicated a problem with either the readout electronics used at NAOJ (see Section 3.1.2), the optical coupling of the array, or the experimental setup.

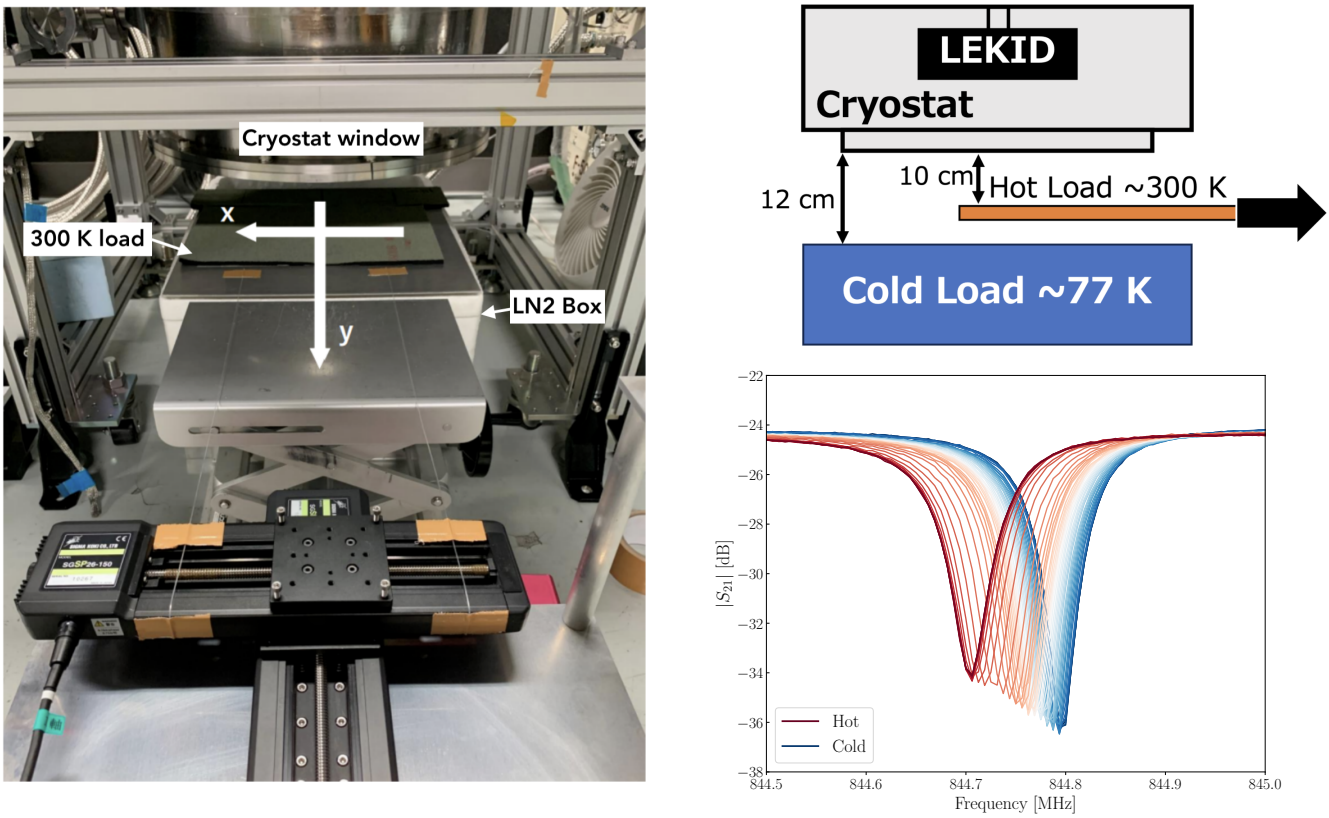

Figure 3.13: (Left): Picture of the knife-edge setup used to measure the beam shape of the LEKIDs array, extracted from Suzuki, Ryuji (2020). The cold load (LN2 Box) is placed in front of the cryostat window, and the hot load is moved along the X and Y axes. (Top-Right): Illustration of the knife-edge method extracted from Ishizaki, Yuji (2025). (Bottom-Right): Example of the frequency shift of one resonance during a knife-edge measurement. From blue to red, the hot load is moved closer to the detectors in steps of 5 mm.

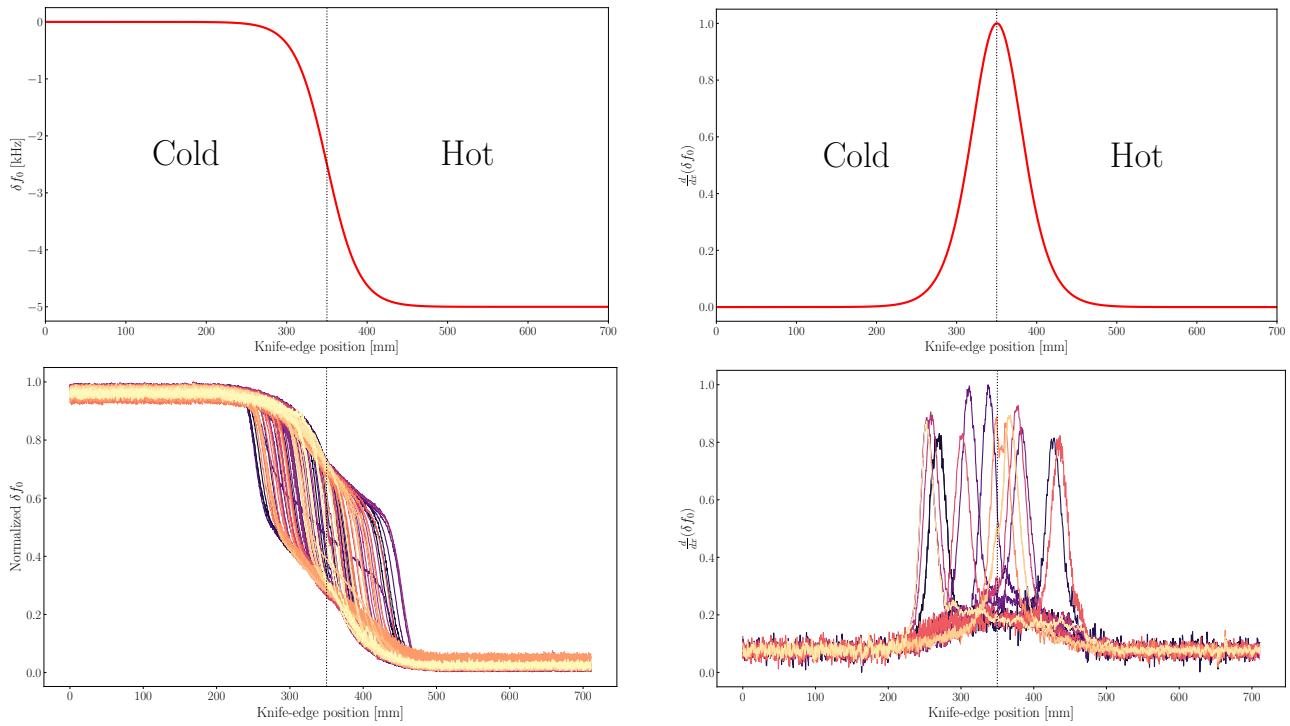

Figure 3.14: (Top-left): Model of the shift in resonance frequency δf_0 as a function of the knife-edge position for one detector. f_0 shifts to lower values as the hot load moves closer. (Top-right): Derivative of the δf_0 model as a function of the knife-edge position for one detector. (Bottom-left): Measurements of the δf_0 shift for all detectors in the array along the X axis, shown as solid curves. Compared to the model in the upper panel, δf_0 is normalized, so that we can plot all detectors at once. (Bottom-right): Derivative of δf_0 for a subsample of 20 KIDs. As expected, they peak at different times depending on their position in the array. The dashed black line in the four panels shows the position where the hot load and the central detector are aligned.

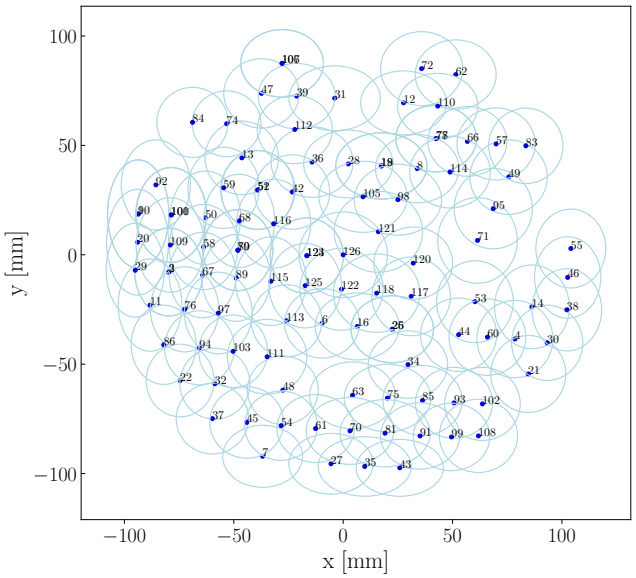

Figure 3.15: Focal plane geometry of the array. Each detector is shown as a blue dot, with its associated number. The cyan ellipses show the beam shape of each detector. The central pixel, n°126, was chosen by the team in 2021 as the reference detector.

Validation of the reconstruction technique

To test the validity of the FFTS reconstruction technique on LEKIDs data, we decided to try and calibrate the raw (I, Q) data using the *RfdIdQ* technique used for the NIKA2 camera (see Section 3.1.2). As a reminder, a NIKA2-like electronic readout samples the transfer function S_{21} continuously at 2 points around the tone frequency $f_{\rm tone}$, $f_{\pm} = f_{\rm tone} \pm \frac{\delta f_{\rm tone}}{2}$, where $\delta f_{\rm tone} = 2\,$kHz. As the bin width is ±5.47 kHz in the FFTS data, we interpolate the data to obtain the two desired points at ±1 kHz around $f_{\rm tone}$ to mimic the NIKA2 readout. With 128 spectra per second, the $RfdIdQ$ sampling is thus 256 Hz which is a factor ∼ 4 slower than the NIKA2 sampling. Thus, instead of averaging over 20 consecutive spectra we only average over five spectra to match the δf_0 sampling rate of NIKA2. The results of the $RfdIdQ$ calibration on the noise PSD estimation per detector are shown in Figure 3.16. We obtain identical results with both techniques, showing that the FFTS technique is accurately measuring δf_0. However, this also indicates that the high detector noise may be due to the FSP4000 readout system itself and its high dead time in between two consecutive spectra.

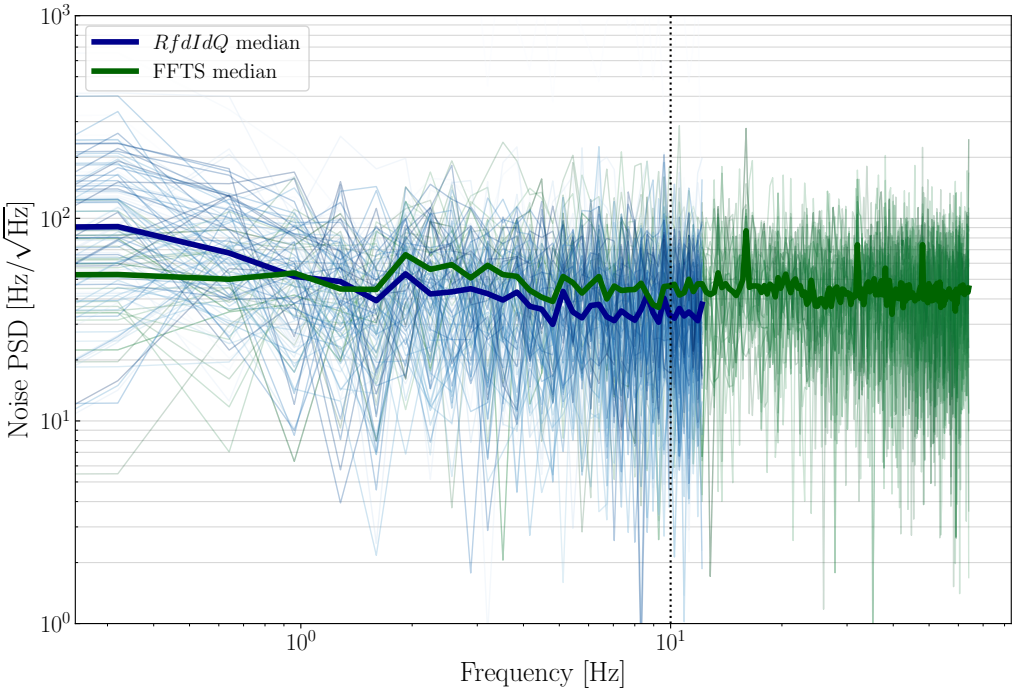

Figure 3.16: Comparison of the noise PSD measured using the *RfdIdQ* (blue) and the FFTS (green) techniques. The faint and bold lines show the individual measurements and the median, respectively. We obtain similar results with the two methods.

3.4 2024 laboratory campaign

Based on the results of the 2021 array characterization, we decided to conduct a new lab campaign in February 2024 at NAOJ, using the exact same setup to see if we could reproduce the same results. Unfortunately, we were unable to use the FSP4000 readout system as it was not functioning properly. We were limited to VNA scans, which meant that we were not able to characterize the noise PSD.

3.4.1 S_{21} spectrum

As discussed before, the first step in the characterization of the LEKIDs array is to perform a frequency sweep using a vector network analyzer (VNA) to measure the transmission parameter S_{21} (see Section 3.1.1) and identify the resonances. Figure 3.17 shows the S_{21} parameter as a function of the frequency in the 650-900 MHz range, where the resonance frequencies of the detectors are expected.

We can see several dips in the spectrum, which correspond to the resonances of the detectors. They are usually spaced by at least 1 MHz to avoid cross-talk between them, but it might not always be the case. Using the `find_peaks` routine from the `scipy` Python package, we identify working detectors. Of the 144 expected resonances, 138 were identified, giving a yield of 97%.

We also checked the spacing between resonances, and found 57 resonance pairs spaced by less than 1 MHz. In total, 95 (66%) resonances are affected by this short-spacing problem. This will lead to cross-talk between detectors and will affect the performance of the array. As we mentioned in Section 3.2.1, the array is a spare, which explains the non-homogeneous distribution of the resonances on the feedline. In Chapter 5, we will show in detail how this problem impacts the observations.

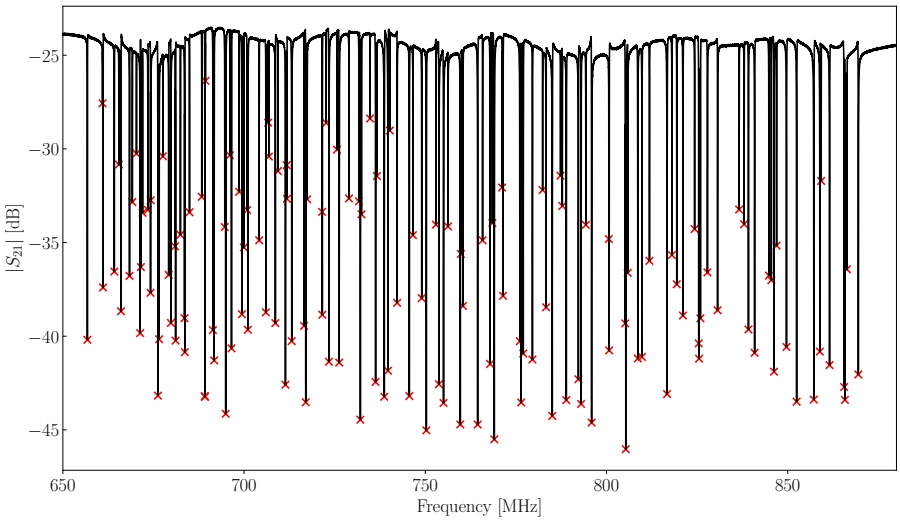

Figure 3.17: VNA scan of the GT LEKIDs array, showing the $|S_{21}|$ parameter as a function of the frequency for a 77 K black-body background. Resonances appear as dips in the spectrum, and each red cross corresponds to one resonance.

3.4.2 Quality factors

Now that we have identified our resonances, we can fit the VNA scan data using Equation 3.6 to estimate the quality factors Q_{tot}, Q_c, and Q_i of each detector. The coupling factor Q_c represents how well the detector is coupled to the readout line, and is designed to have similar values as the internal quality factor Q_i. Q_i quantifies the energy loss within the resonator, which mostly depends on the quality of the superconducting film. Q_i is defined as:

$$\frac{1}{Q_i} = \left(\frac{1}{Q_{tot}} - \frac{1}{Q_c}\right)^{-1} . \tag{3.17}$$

We present in the left panel of Figure 3.18 an example of a simultaneous fit for several resonances, using a code developed by Shunsuke Honda. Because some resonances are very close to each other, the code groups nearby detectors into fitting regions instead of trying to fit each resonance individually. To do that, we define a frequency range around each resonance, typically ±500 kHz. If two resonances or more are separated by less than two times this threshold, they form a group and are fitted simultaneously. Then, assuming a constant baseline which is a good approximation for small frequency ranges, the code fits the n resonances using a multi-resonator model based on Equation 3.6:

$$S_{21}(f) = \prod_{n=1}^{N} \left[1 - \frac{\frac{Q_{tot,n}}{Q_{c,n}}}{1 + 2jQ_{tot,n}(\frac{f-f_{0,n}}{f})}\right] . \tag{3.18}$$

We show in the right panel of Figure 3.18 the quality factor values obtained for the 138 identified detectors. The median values are $Q_i = 6.28 \times 10^4$, $Q_c = 1.44 \times 10^4$, and $Q_{tot} = 1.15 \times 10^4$. These values are consistent with the expected quality factor for LEKIDs (see Section 3.1.1), as well as with the values found in 2021 [Suzuki, Ryuji, 2020].

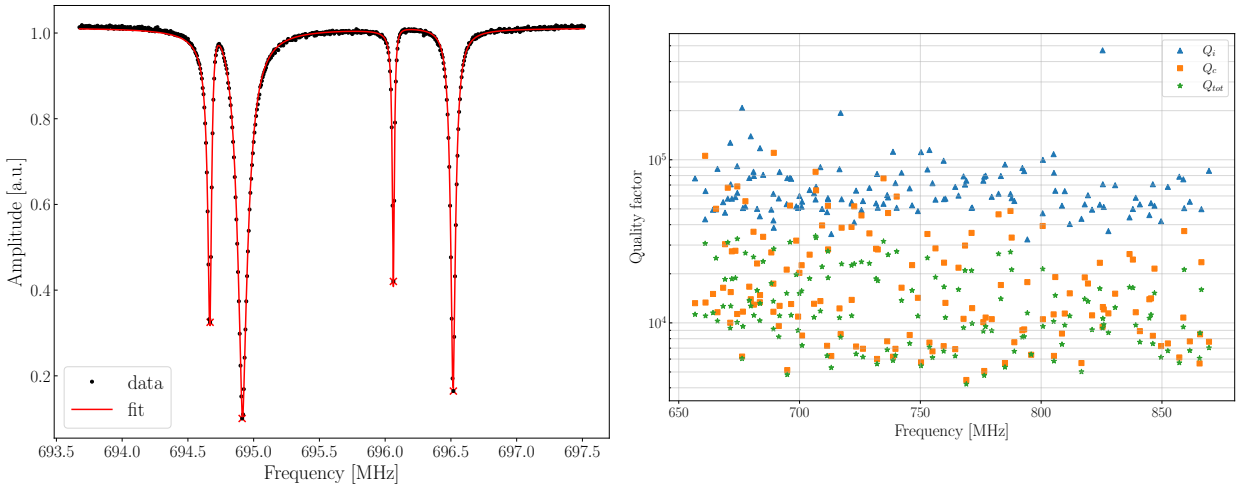

Figure 3.18: (Left): VNA scan data of four resonances and the best-fit (red) using the procedure described in Section 3.4.2. (Right): Quality factors Q_i (blue), Q_c (orange), and Q_{tot} (green) of each LEKID as a function of their resonance frequency, with a 77 K blackbody background.

3.4.3 Beam measurements

To measure the beam shape of the detectors and the focal plane geometry, we used the same knife-edge technique as in 2021 (see Section 3.3.3 and Figure 3.13). However, since the FSP4000 readout system was not working, we could not continuously monitor the resonance frequency shift while the hot load was moving. Instead, we manually moved the hot load toward the detectors in 5 mm steps, and we performed a frequency sweep using a VNA at each position.

During the measurements, we noticed two small drift components at the beginning and end of the measurement, and the Gaussian fitting presented in Section 3.3.3 was not accurate. We thus opted for a better fitting model [Ishizaki, Yuji, 2025]:

$$f(x) = [1 - \mathrm{CDF}_{\mathrm{norm}}(x, \sigma)]\,(a_1 x + c_1) + \mathrm{CDF}_{\mathrm{norm}}(x, \sigma)(a_2 x + c_2)\,, \tag{3.19}$$

$$\text{where} \quad \mathrm{CDF}_{\mathrm{norm}}(x, \sigma) = \frac{1}{2}\left[1 + \mathrm{erf}\left(\frac{x - x_0}{\sqrt{2}\sigma}\right)\right].$$

The cumulative distribution function (CDF) is used to model the transition between the two linear components, which allows for a better fit to the data. The parameters a_1, c_1, a_2, and c_2 are the slopes and intercepts of the two linear components, respectively, and x_0 is the position of the transition between them. With this model, we fit δf_0 directly instead of its derivative (see Figure 3.14).

We show in Figure 3.19 the obtained beam size distribution obtained, as well as the reconstructed focal plane geometry of the array. We find median beam sizes of 32.3 ± 3.2 mm and 33.7 ± 6.8 mm along the X and Y axes, respectively. These values are consistent with the results obtained in 2021 (see Figure 3.15). We also observe that the beam shapes of detectors far from the center of the array are more elliptical than those near the center. This is likely due to the liquid nitrogen container (cold load, see Figure 3.13) not being large enough, such that detectors on the edges were not fully illuminated.

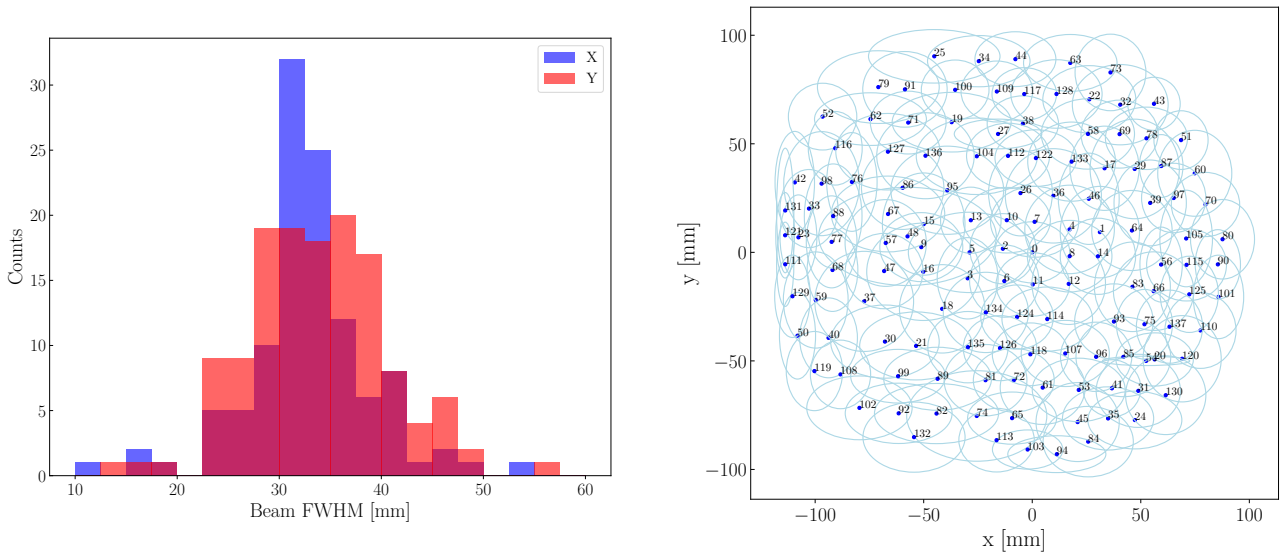

Figure 3.19: (Left): Beam size distribution along the X (blue) and Y (red) axes. (Right): Focal plane geometry of the array. The ellipses show the beam shape of each detector.

3.5 Summary and conclusion

In this chapter, we first presented the working principle of KID detectors and the different readout techniques used to reconstruct the shift in resonance frequency. We compared the performances of the different techniques, and showed that they all provide robust results in terms of photometric accuracy. We then presented the GT LEKIDs camera, its design, the cryostat, and the readout system. Finally, we described the laboratory characterizations of the LEKIDs array. A first campaign at NAOJ in 2021 showed that the noise was an order of magnitude higher than expected, and the beam size larger than that found for a MKID array using the same experimental setup. We performed a new lab campaign in February 2024, where we were able to reproduce the beam size results, but not the noise measurements as the readout system was not working properly.

After a careful study of Zemax simulations for the LEKIDs array performed by Andrea Catalano, we found that the expected beam size was around 30 mm, which is consistent with the values we obtained during both lab campaigns. The optical coupling of the array was thus not the issue. Since the FSP4000 readout system did not work anymore, and it was most probably the source of the high noise measured in 2021, we decided to change the readout electronics to a CONCERTO-like setup (see Section 3.1.2), which is more suitable for LEKIDs arrays.

CHAPTER 4

Observations with the Nobeyama telescope

4.1 The Nobeyama 45-m telescope . . . 70
4.2 SZ observations at the Nobeyama telescope . . . 71
4.3 GT camera installation and setup . . . 73
4.3.1 New GT camera readout system . . . 73
4.3.2 Installation at the telescope . . . 73
4.3.3 Final noise measurements before observations . . . 73
4.4 Observations . . . 74
4.4.1 Target selection . . . 74
4.4.2 Weather conditions . . . 77
4.4.3 Finding and tuning KIDs before observations . . . 77
4.4.4 Scanning strategy . . . 79
4.4.5 Online processing . . . 80
4.4.6 Focus . . . 80
4.4.7 Skydip . . . 81

In the previous chapter, we have presented the GT 100 GHz camera, which was designed to be used at the Nobeyama 45-m telescope. In this chapter, we describe the installation of the instrument at the telescope and the operations performed during the commissioning campaign. We will first introduce the Nobeyama telescope where the camera is installed, and review the previous SZ observations performed with this facility. We will then see how we planned the commissioning observations with the GT camera and the scanning strategy we adopted. We will also present the different operations carried out at the telescope, such as focus measurements to optimize the coupling between the camera and the telescope, and skydips to measure the atmospheric opacity.

4.1 The Nobeyama 45-m telescope

The Nobeyama Radio Telescope (NRO, Figure 4.1) is a 45-meter radio telescope located on the Nobeyama plateau in Nagano Prefecture, Japan, at an altitude of 1350 meters above sea level. The telescope is equipped with several receivers operating at frequencies between 1-150 GHz, such as the FOREST receiver at 100 GHz [Minamidani et al., 2016]. The telescope is also open to visitor instruments developed by the scientific community and has been used for various scientific projects, including the GT camera predecessor [Honda et al., 2023].

The GT camera will be installed in the NOBA receiver cabin, named after the NObeyama Bolometer Array [NOBA, Kuno et al., 1993]. This cabin is located above the M4 mirror as shown in the right panel of Figure 4.1. The light collected by the primary mirror of the telescope is transmitted by a series of mirrors to the receiver cabin, where the light enters the cryostat through the vacuum window at the bottom.

The angular response of the telescope, referred to as the instrumental beam, is primarily determined by the diffraction associated with the 45-meter aperture. For monochromatic radiation from a point source, this angular response is represented by the Airy pattern of the primary mirror aperture. The angular resolution, determined by the full width at half maximum (FWHM) of the Airy pattern's main peak, is given by $\theta = \arcsin\left(\frac{1.029\lambda}{D}\right)$. This corresponds to 16.8 arcseconds for monochromatic signals at frequencies of 100 GHz. In practice, the incident radiation is polychromatic, and its multiple reflections result in a broadening of the beam. Therefore, the angular resolution achieved by the various receiver instruments in the telescope cabin is somewhat lower than these ideal values.

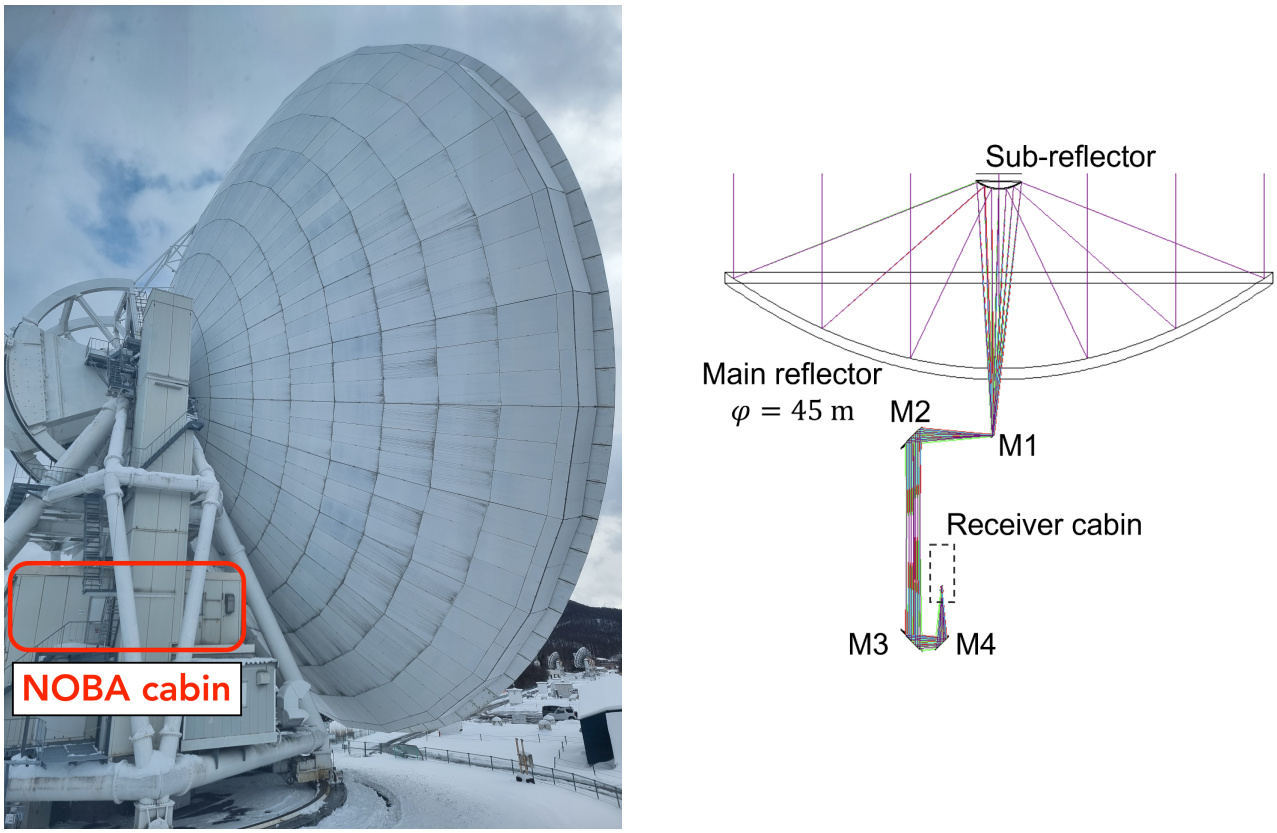

Figure 4.1: (Left): Picture I took of the Nobeyama 45-meter telescope. (Right): Schematic representation of the optical path from the main reflector to the receiver cabin. Figure extracted from Murayama, Yosuke (2022)

4.2 SZ observations at the Nobeyama telescope

With its very large aperture and thus high angular resolution, the Nobeyama telescope is well suited for SZ observations. The earliest announcement of a SZ observation project at Nobeyama dates back to 1998, when Tsuboi et al. (1998a) reported the development of a new superconductor insulator superconductor (SIS) receiver centered at 40 GHz that was designed for observations of the SZ effect. The first results were very promising, with the detection and estimation of the central SZ decrement in the Abell 2218 cluster [Tsuboi et al., 1998b]. A total of eight X-ray bright clusters were observed over the years with this receiver and its upgrades [Tsuboi et al., 2000], with redshifts between 0.18 and 0.55. From these observations, Tsuboi et al. (2004) was able to constrain the Hubble constant

$H_0 = 64 \pm 17$ km.s^{-1}.Mpc^{-1}, which was in good agreement with the H_0 value derived from type Ia supernova observations [Riess et al., 1998].

In 1999, Komatsu et al. (1999) reported the successful detection of the SZ effect toward the extremely luminous RX J1347-1145 X-ray cluster at $z = 0.45$. Observations at 21 and 43 GHz with the Nobeyama telescope combined with James Clerk Maxwell Telescope (JCMT) 350 GHz observations were used to estimate the first resolved SZ profile of a cluster in the millimeter band. The 21 GHz instrument, with a beam size $\theta_{\rm FWHM} \sim 80''$, was also used to map the SZ decrement around the RX J2228+2037 cluster [Pointecouteau et al., 2002]. Combined with X-ray data, the gas profile as well as the hydrostatic mass of the cluster was derived, highlighting the power of X-ray/SZ data combination to study the properties of galaxy clusters.

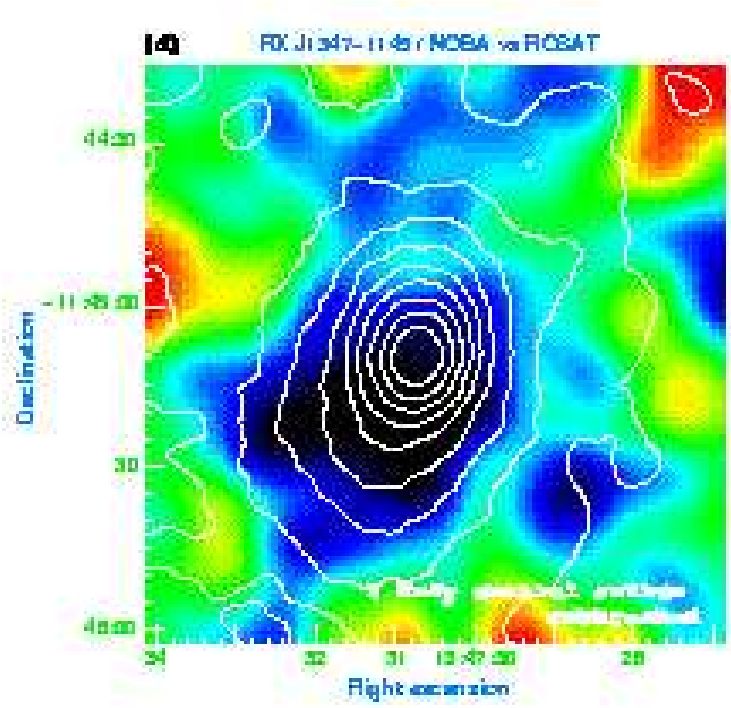

Figure 4.2: 150 GHz map of RX J1347-1145 where the central radio source has been subtracted. The white lines show the ROSAT X-ray contours [Schindler et al., 1997]. Figure extracted from Komatsu et al. (1999). Unfortunately the quality could not be improved.

At that time, the NOBA array [Kuno et al., 1993] was already installed at the Nobeyama telescope but had not yet been used for SZ observations. This instrument was composed of 7 bolometric detectors operating at 150 GHz, with a beam size $\theta_{\rm FWHM} = 12.5''$. To build on their previous results, Komatsu et al. (2001) used the NOBA array and its very high angular resolution to map RX J1347-1145 down to a 1σ noise level of 1.6 mJy/beam. We show in Figure 4.2 the 150 GHz map of RX J1347-1145 obtained by Komatsu et al. (2001) after the central radio source was subtracted. The study revealed complex substructures in the cluster which could not be resolved with low-resolution instruments. This first map of the SZ effect with the Nobeyama telescope was a major step forward and highlighted the importance of high angular resolution observations to better characterize the properties of clusters.

In a follow-up study, Kitayama et al. (2004) used the exact same 150 GHz data, combined with 350 GHz observations with the Sub-millimeter Common User Bolometer Array (SCUBA, Holland et al. (1999)) and Chandra X-ray data to present a prototype multiwalength analysis of the SZ effect. Compared to Pointecouteau et al. (2002), the use of very high angular resolution data allowed for a more precise measurement of the cluster properties, once again showing the power of high angular resolution SZ observations.

For the past two decades, except for a pilot study of the SZ effect in a radio galaxy [Yamada et al., 2010], there have been no published SZ observations with the Nobeyama telescope. However, the facility remains one of the most powerful for this type of study, and, together with the GT camera, it will be possible to perform high angular resolution SZ observations of clusters.

4.3 GT camera installation and setup

4.3.1 New GT camera readout system

As discussed in the previous chapter, the readout system of the GT camera was changed to a new CONCERTO-like setup as shown in Figure 4.3. This electronic system was specifically constructed for this project and designed to be portable. There are three main components in the readout system: the NIKEL board, the GPS, and the HSM2001B RF synthesizer. The NIKEL board is located in the frame in the bottom left, and it is connected to the cryostat via the *cryo in* and *cryo out* cables. The board sends and receives the signal to/from the array via these cables. The board used here is identical to what was used for the CONCERTO instrument [Bourrion et al., 2022] and can readout all 144 detectors at the same time. The GPS is essential to track the time and synchronize the data acquisition. The use of a GPS is very important in this setup but it can sometime be difficult to get a good satellite signal if the cabin has thick walls. Fortunately, this was not the case for the NOBA receiver cabin. The HSM2001B is a RF synthesizer used to generate the local oscillator (LO) signal and up-convert the baseband frequency comb to the detectors resonance frequency and vice versa (see Section 3.1.2). HCM3 is a simple ethernet communications module for the synthesizer. These components are all (except the GPS) connected to a network switch (D-LINK), itself connected to the DAQ computer responsible for setting up the instrument at startup and recording the data during observations.

The new readout system was tested together with the array at NAOJ in September 2024 before installation at the telescope. Unfortunately, we found that the electronics, designed for the CONCERTO array, limit to 50 the number of tones it can generate in a 100 MHz band. However, for the GT LEKIDs array, we have a total of 144 detectors and an equivalent number of tones distributed across ~ 200 MHz. As a result, we were able to read 97 out of the 144 detectors of the array. During the observations, we thus used only the 97 detectors that were successfully read.

4.3.2 Installation at the telescope

The instrument was installed at the Nobeyama telescope from October 1st to 3rd, 2024. As mentioned earlier, the instrument was installed in the NOBA receiver cabin using a crane to lift all the components. Inside the cabin, there are two levels: the lower level where the DAQ PC and the GPS are placed, and the upper level which houses the cryostat, readout electronics, and the gas handling system used to cool down the cryostat. We show in Figure 4.4 a picture of the inside of the receiver cabin.

Once the cryostat was positioned between the two levels, as shown in the picture, its alignment was adjusted to be perfectly parallel with respect to the ground and the incoming light from the M4 mirror. Once the cryostat was aligned and all the components were installed (cooling system, readout electronics, etc.), the cooling process was started. It then took about a week to cool down the cryostat to mK temperatures. We reached a minimum temperature of 103 mK for the observations.

4.3.3 Final noise measurements before observations

Once the cryostat was cooled down, we performed a final noise measurement to check the performance of the array as well as the acquisition system. We covered the horn where the incident light

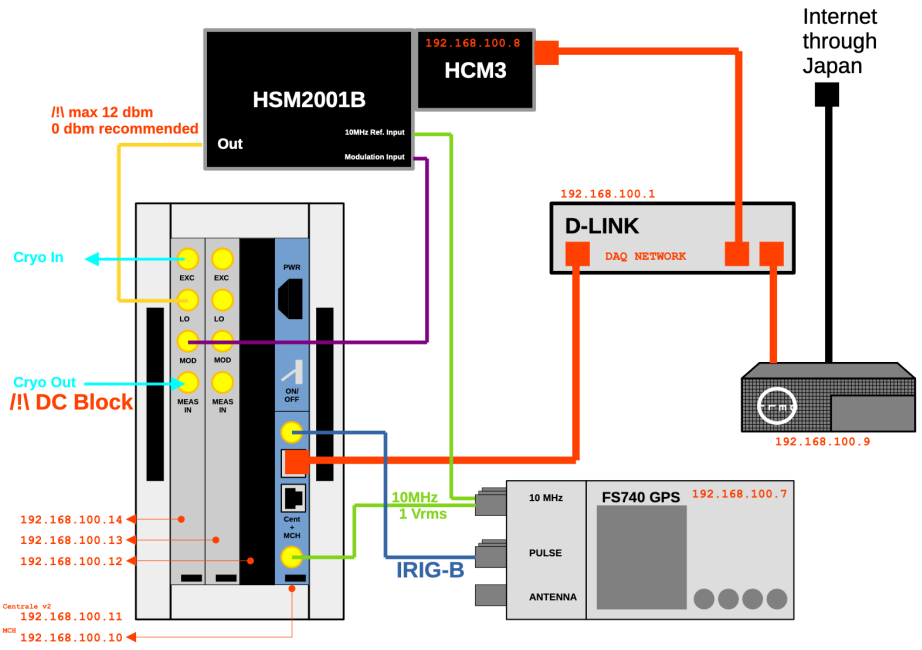

Figure 4.3: Schematic representation of the NIKEL readout system. The camera is read out by one NIKEL board. The signal from the board is sent to the cryostat through the *cryo in* cable, and the output signal from the array is sent back to the board through the *cryo out* cable. The GPS is essential to track the time and synchronize the data acquisition. Its 10 MHz frequency output is used to synchronize all electronics, and the IRIG-B signal is a standard time code format that ensures that all data are timestamped accurately. The HSM2001B is a RF synthesizer used to generate the LO signal. Credit: Julien Bounmy

enters the cabin (see Figure 4.4) with a 30 K mirror and acquired data for a few minutes. As we used NIKEL electronics, we used the method detailed in Section 3.1.2 to convert the raw (I, Q) data to TOIs. We then Fourier transformed the TOI to obtain the PSD of the noise. Figure 4.5 shows the distribution of the noise PSD measured for all detectors in the array. We found an average noise of $1.66 \pm 0.38 \ \frac{\text{Hz}}{\sqrt{Hz}}$, which is in perfect agreement with the values found at Institut Néel, in Grenoble, and an order of magnitude lower than the values found at NAOJ in 2021 (see Section 3.3.2). We can also distinguish two unwanted peaks in the noise PSD at 45 and 100 Hz approximately. At the time of writing, their origin is not yet known.

4.4 Observations

For the GT camera commissioning, we asked for and were granted a total of 50 hours of observing time at the Nobeyama telescope, spread over 7 nights from October 17th to 24th, 2024. We detail our observation strategy in the following sections.

4.4.1 Target selection

Our observation strategy involved selecting three types of targets serving different purposes:

- **Planets**: perform the absolute calibration of the array as well as evaluate the beam pattern for each detector and its position in the focal plane
- **Quasars**: validate the stability of the detectors response and calibration
- **Faint sources**: evaluate the detectors sensitivity

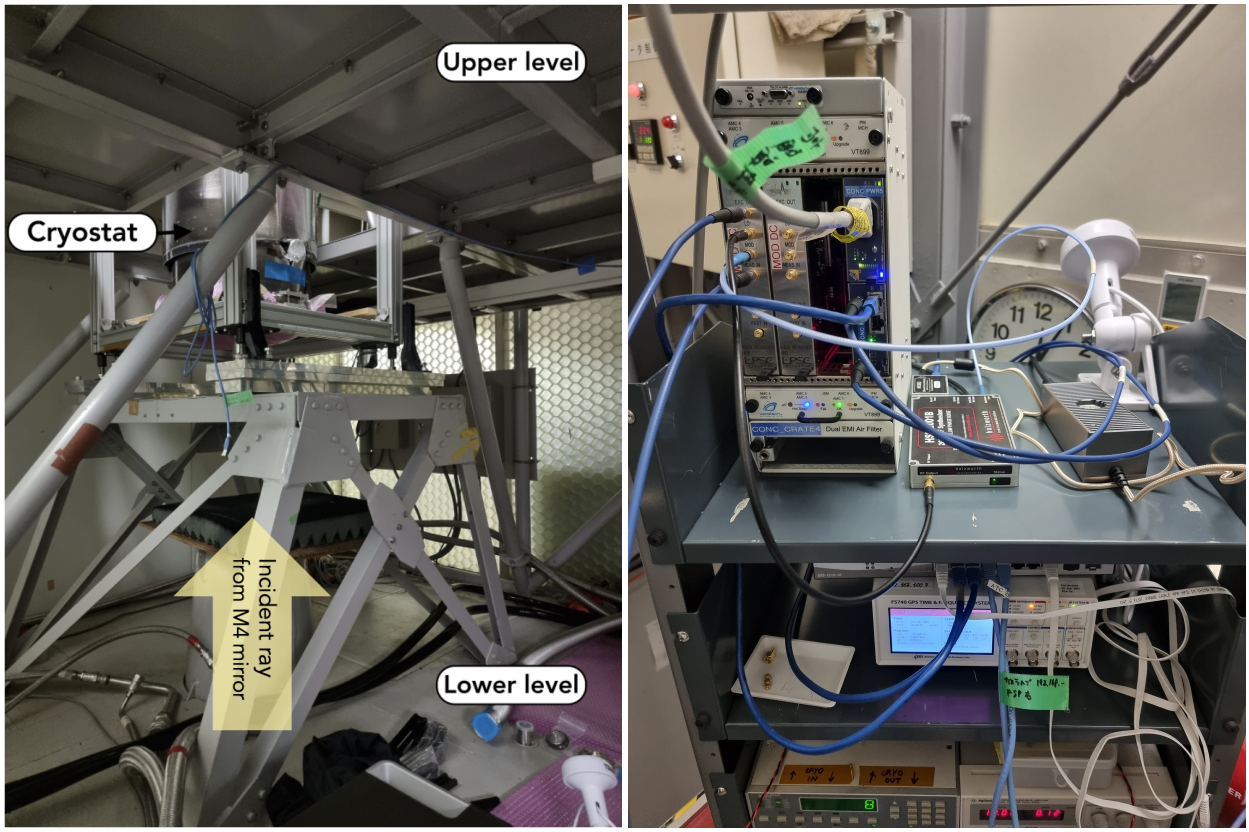

Figure 4.4: (Left): Picture I took of the inside of the receiver cabin. The incident light is blocked with an ecosorb during the installation. (Right): Picture of the rack where the readout electronics are installed on the upper level. We can recognize the frame housing the NIKEL board (top-left), the HSM2001B synthesizer next to it, and the GPS just below.

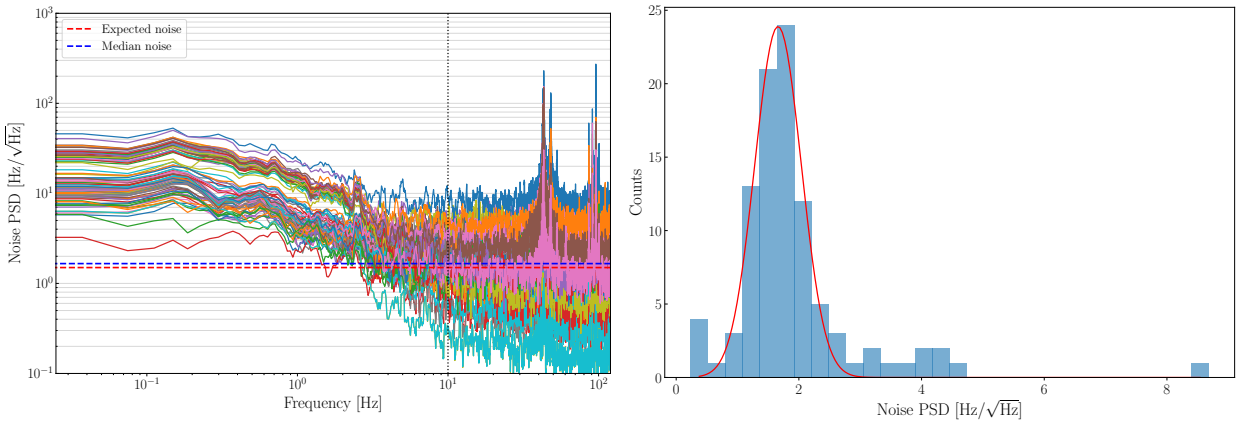

Figure 4.5: (Left): Noise PSD measurement performed at NRO on October 16th, 2024. The average noise and expected noise are shown as blue and red dashed lines, respectively. (Right): Noise PSD distribution. By fitting the distribution, we found an average noise of 1.66 ± 0.38 $\frac{\text{Hz}}{\sqrt{Hz}}$.

Besides the planets (Mars, Jupiter, Saturn, and Uranus), the other targets were selected based on their flux and their visibility during the observation period. We show in Figure 4.6 the elevation of the planets and targets during one night of observation. We only observe sources when they are above 20-30 degrees in elevation to minimize the effects of atmospheric attenuation and ground pickup (i.e, contributions from surrounding buildings and trees). Indeed, at low elevations, the airmass ($\propto 1/\sin(\text{elevation})$, see Section 4.4.7) increases rapidly, causing the atmospheric opacity to rise and the sensitivity to decrease exponentially. This is why, for example, we prefer to observe Mars later during the night, when it is sufficiently high in the sky. Apart from the four planets mentioned above, the other targets were two quasars, 3C84 and 3C454.3, and one faint source, the M82 galaxy. During the last observation night, we dedicated a few scans to the Cygnus A galaxy as it was visible at high elevation in the early hours of the night.

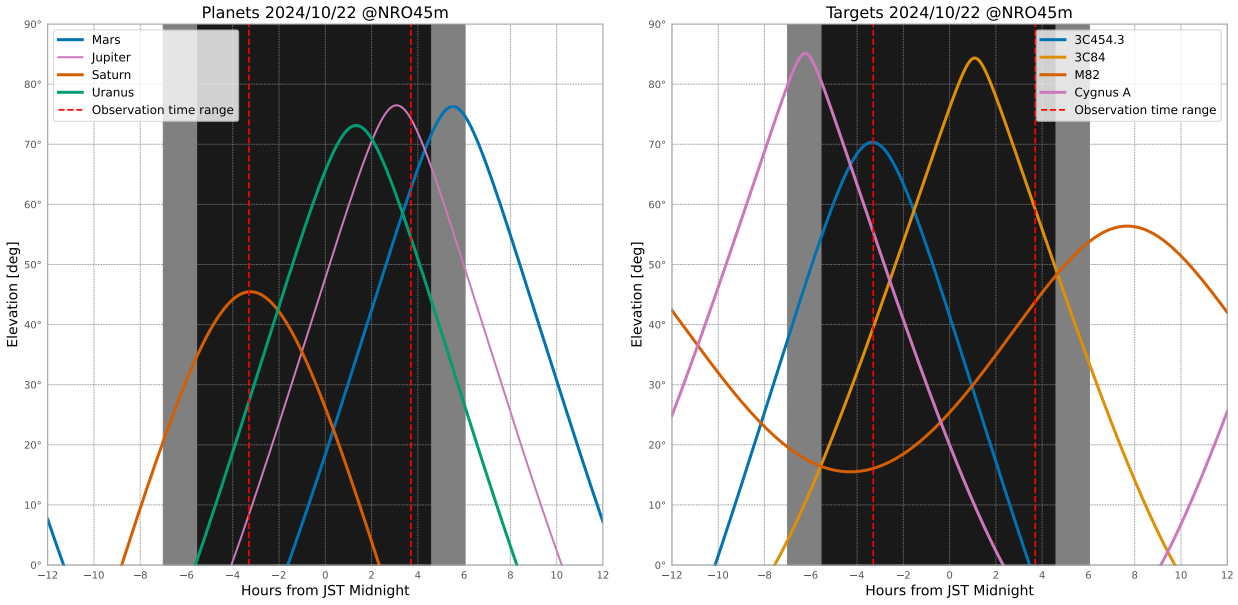

Figure 4.6: Elevation of the sources during one observation night, October 22nd. The grey and black regions show the times when the Sun is below 0 deg and -18 deg in elevation, respectively. The two red dashed lines show the start and end of our observation shift. (Left): The four observed planets, Mars, Jupiter, Saturn, and Uranus. (Right): The two quasars 3C84 and 3C454.3, and the two faint sources M82 and Cygnus A.

We summarize the observations in Table 4.1. We see that most of the observations targeted planets

as they are bright and easy to observe, even under bad weather conditions. The total time on source is 26.3 hours, with 9.6 hours during the two "good" nights, when the weather conditions were more stable (see Section 4.4.2).

Targets	Nbr of scans	Total time on source (hours)
Mars	14 (6)	4.4 (1.4)
Jupiter	17 (3)	5.8 (1.0)
Saturn	19 (14)	4.8 (2.9)
Uranus	13 (7)	4.4 (2.3)
3C84	9 (2)	3.0 (0.7)
3C454.3	3 (1)	1.0 (0.3)
M82	3 (3)	1.0 (1.0)
Cygnus A	4 (0)	1.3 (0.0)
Total	84 (36)	26.3 (9.6)

Table 4.1: Summary of the number of scans and total time on source for each target. Numbers in red parentheses indicate scans/time during "good" observation nights, when the weather conditions were better (see Section 4.4.2).

4.4.2 Weather conditions

The weather conditions during the observations were very unstable, with very high humidity throughout. We show in Figure 4.7 the precipitable water vapor (PWV) measured during the observation period. We see that, for five out of seven observation nights, the PWV was above 15 mm, which is very high and usually means very cloudy conditions or even rain. We had to stop observing on two nights due to rain. These weather conditions lead to very high atmospheric noise in the data, which makes the subsequent data reduction and analysis very difficult. We thus decided to focus our analysis on the data acquired during the two "good" nights, October 21st and 22nd, when the PWV was below 10 mm. We show in red parentheses in Table 4.1 the number of scans and total time on source for these two nights.

4.4.3 Finding and tuning KIDs before observations

As we have seen in Section 3.4.1, we can identify detectors and their resonance frequency for a fixed background temperature. This knowledge is then used to build the frequency comb used to read out the detectors (see Section 3.1.2). However, during observations, the optical signal varies due to changes in the sky background or changes in elevation. The KIDs resonance frequencies will thus change as a function of these background variations, which means that we need to adjust the frequency comb tones to the new resonance frequencies before each observation scan. To mitigate the effect of these variations on the data, Bounmy et al. (2022) developed several techniques to find and tune the KIDs before each observation. The first step is to perform a frequency sweep to determine the KIDs resonance frequencies and the associated frequency comb at the start of the observation campaign. This initial frequency comb will be used as a starting point for subsequent operations during the campaign. Then, at the beginning of each observation night, we use the `locate` procedure to measure the global shift of the resonance frequencies compared to the initial sweep. This difference is then averaged over all detectors to deduce the global frequency shift to apply to the frequency comb.

Before each observation scan, we use two techniques, `follow` and `tuning`, to fine-tune the frequency comb. When the telescope moves between scans, the background signal can change and again shift

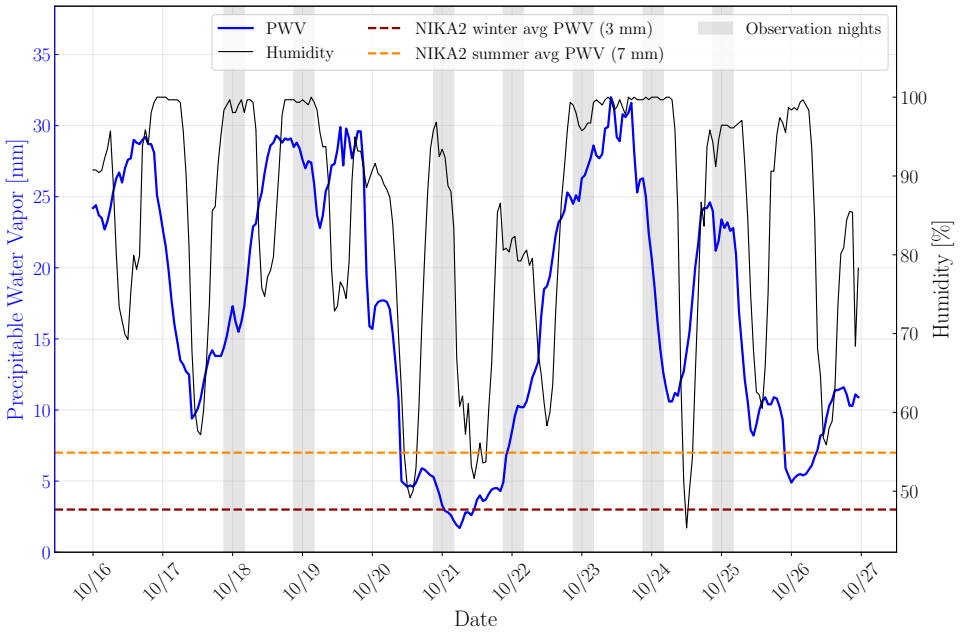

Figure 4.7: PWV (blue) and relative humidity (black) measured during the observation period. Observation nights are shown as grey bands. The red and orange dashed lines indicate the average PWV at the IRAM 30-m telescope in winter and summer, respectively. Data taken from the open-weather database.

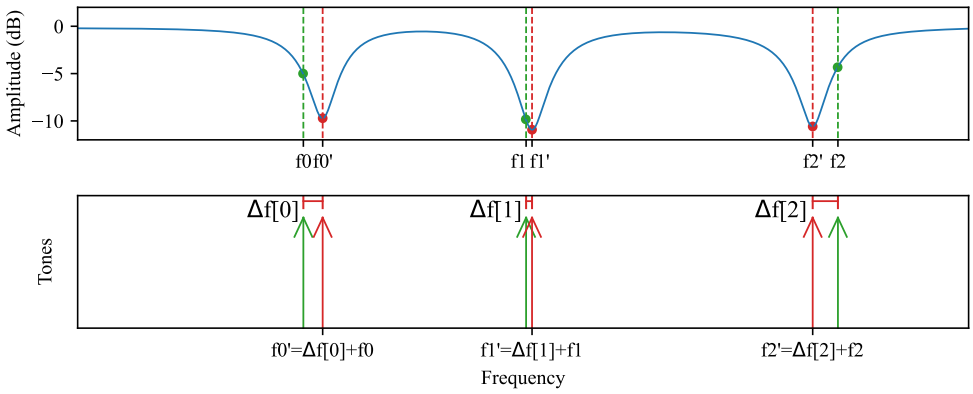

Figure 4.8: Tones before (green) and after (red) the `tuning` procedure. The tones are individually corrected and now better match their resonance frequency. This step is essential to ensure that the KIDs are well tuned before starting the observation scan. Figure taken from Bounmy et al. (2022).

the resonance frequencies. During the travel time of the telescope to the starting position of the next scan, the `follow` procedure, which works the same way as `locate`, will adjust the frequency comb a few times per second to follow the KIDs resonance frequencies. This procedure is especially important under unstable weather conditions, when the background signal can change drastically and rapidly. In this case, if `follow` is not used, the KIDs can be out of resonance at the beginning of the next scan, which can lead to their loss for the duration of the scan. Finally, when the telescope has stopped moving just before starting a scan, we use the `tuning` procedure to precisely adjust the tones to each KIDs frequencies, as shown in Figure 4.8. The procedure uses the 3-points calibration method presented in Section 3.1.2 to measure the frequency shift between the expected resonance frequency and the actual resonance frequency of each KID. The procedure then adjusts the tones to the new resonance frequencies in about 30 seconds.

4.4.4 Scanning strategy

Once the tones have been successfully tuned, we can start the observations. To measure an astrophysical signal with the GT camera or KID-based instruments in general, it is necessary to modulate the observed signal as a function of time. Indeed, KIDs are not well adapted to the measurement of a constant signal, as they are sensitive to the resonance frequency shift induced by variations in the background signal. We thus use raster scans, where the telescope follows a path made of a succession of parallel, evenly-spaced straight lines (also called subscans) in either equatorial (Right-ascension, Declination) or alt-azimuthal (azimuth, elevation) coordinates. An example of a raster scan performed on Mars during the campaign is shown in Figure 4.9. With the GT camera, a typical scan covers a $4' \times 4'$ region centered on the source, with a spacing of $4''$ between subscans. The scan speed is 17 arcsec/s, which amounts to a total scan time of 17 minutes. For compact and/or faint sources, this scan speed is preferred to have a better sampling of the source. For more extended or brighter sources, like Saturn or Mars, we would switch between this nominal scan speed and a faster one of 34 arcsec/s, which would reduce the total scan time to 8.5 minutes.

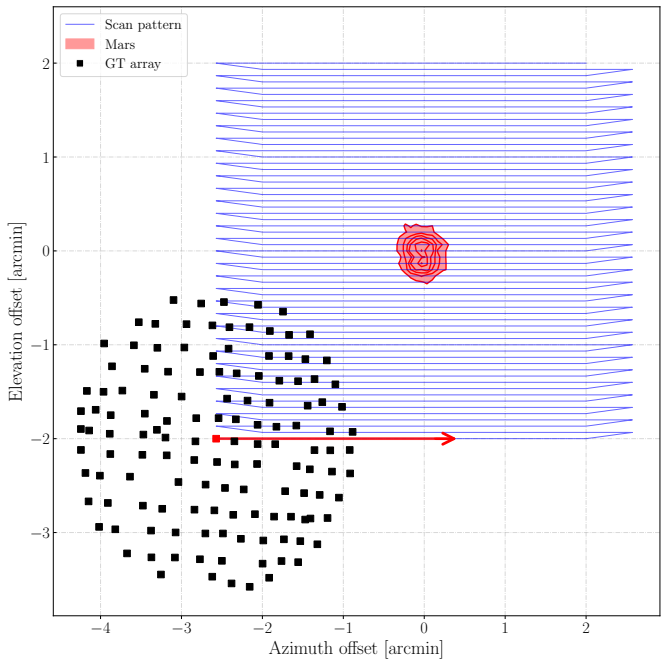

Figure 4.9: Scan path of the telescope in the alt-azimuthal plane during a typical scan of Mars (red region). The GT array footprint on the sky is shown as black squares, with the reference detector in red. The red arrow indicates the direction of the scan.

4.4.5 Online processing

During the observations, we processed the data in real-time to monitor the instrument performance and the quality of the data. The online processing is done using a simpler and faster frequency shift reconstruction method than the CONCERTO 3-point method described in Section 3.1.2. In the following, we will call it the phase calibration method. As we have seen in Section 3.1.1, we can compute the phase ϕ of the signal from the raw (I, Q) data acquired by the instrument. As the signal is modulated at a fixed frequency Δf, we can estimate the detector's response to a known modulation by computing the phase difference between the two $\pm\Delta f$ modulated samples as:

$$C = \frac{\Delta f}{\phi_{+\Delta f} - \phi_{-\Delta f}}. \tag{4.1}$$

We then obtain the raw TOIs by multiplying the unmodulated phase data by the calibration factor C. Using a median filter, we can remove some of the noise in the TOI and obtain a first map of the source. This method is very fast and works well for very bright sources such as Jupiter or Saturn. We show in Figure 4.10 maps obtained during the online processing. We can see that the maps are still quite noisy, especially the Jupiter map (right panel) as it was taken under poor weather conditions. We will see in Section 5.6 that after a more thorough removal of the noise, the maps obtained using this phase calibration method are comparable to the ones obtained using the CONCERTO 3-point method.

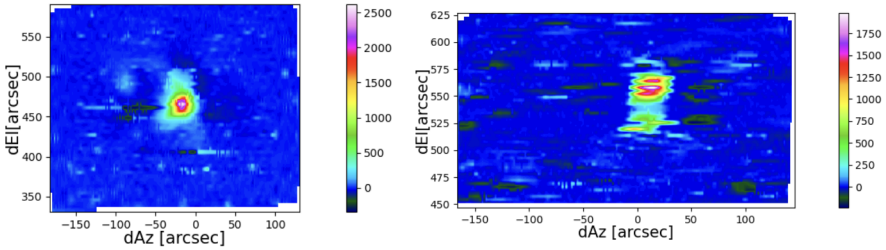

Figure 4.10: Maps of Saturn (left) and Jupiter (right) for one detector. These maps were obtained during the online processing using the phase calibration method described in Section 4.4.5. The Jupiter map was obtained under very unstable weather conditions, as shown by the high noise components distorting the map.

4.4.6 Focus

To successfully couple the detectors to the telescope, the array must be accurately positioned at the focal plane. This alignment can be controlled and optimized by adjusting the position of the sub-reflector (see right panel of Figure 4.1) along the optical axis. To determine the optimal focus setting, we perform a series of consecutive scans of a bright point source, such as Mars, with different sub-reflector positions. A preliminary focus was performed on the first observation night using the online processing method presented in Section 4.4.5. A sub-reflector position of $\Delta_{subref} = 0.0$ mm was chosen based on the online maps and kept for all subsequent scans of the campaign (except for focus scans).

The focus assessment was done again after the observations, using the data reduction pipeline described in Chapter 5. The TOIs measured during these scans are cleaned and projected into maps following the method described in Chapter 5. The resulting maps of a focus performed on Saturn during the night of October 21st are shown in the upper panel of Figure 4.11. They were obtained for sub-reflector positions $\Delta_{subref} = -1.0,\ -0.5,\ 0.5,\ 1.0,$ and 1.5 mm (from left to right). A 2D Gaussian is fitted to each map to extract both the FWHM and the measured flux. A parabolic fit is then applied to the FWHM and flux values to determine the optimal focus position. The optimal focus is identified

by the position that yields the smallest FWHM and the highest flux, indicating the most concentrated beam. It is also important to note that under poor atmospheric conditions, beam broadening may occur, distorting the final maps and impacting focus determination. The results of the fit are shown in the bottom panel of Figure 4.11. We see that the fitting results for both the FWHM and the amplitude are consistent, with an expected optimal focus position of Δ_{subref} = 0.21 mm and 0.13 mm, respectively. The focus position adopted during the campaign is thus not far from the optimal position. In future observation campaigns, a more precise focus adjustment should be performed on each observation night to correct any beam broadening.

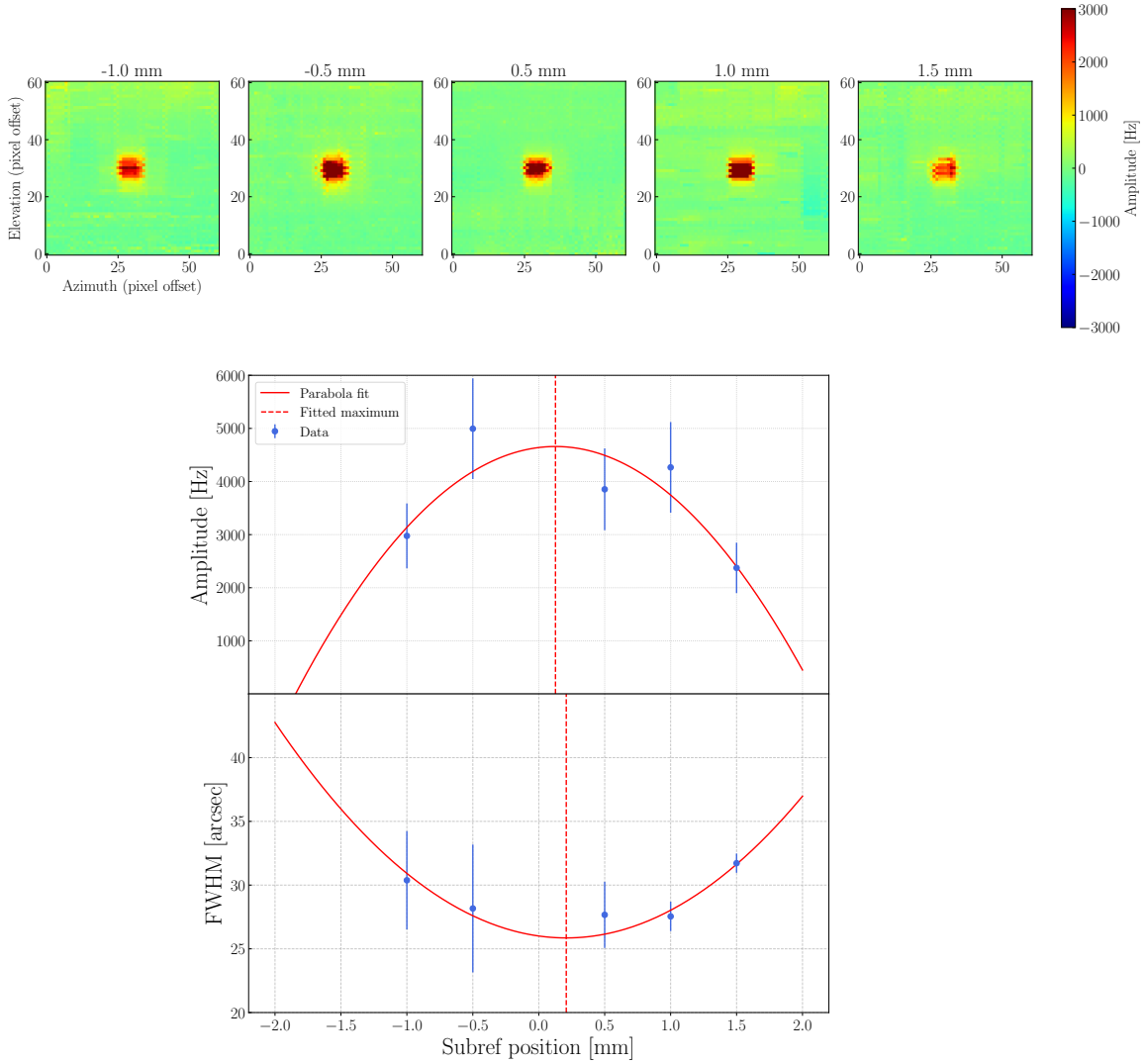

Figure 4.11: Results from 5 focus scans performed on Saturn on October 21st. (Top): Combined maps obtained for increasing focus values from left to right. (Bottom): Measured FWHM and amplitude as a function of the sub-reflector position are shown as blue dots with their associated error bars. The red plain lines show the parabolic fit results and the vertical dashed line indicates the optimal focus position.

4.4.7 Skydip

As we have seen in Section 6.1, observations at millimeter wavelength are very sensitive to the water vapour in the atmosphere, as the atmospheric absorption increases with the amount of PWV present. The atmosphere's opacity will attenuate the signal from the observed source by a factor $e^{-\tau_\nu / sin(\delta)}$, where τ_ν is the opacity at the observed frequency and δ the elevation of the source. The latter is known at all times from the telescope pointing data. We thus need to estimate the opacity τ_ν

to correct the TOIs for the atmospheric attenuation. The atmosphere is also responsible for a thermal emission, which increases with both τ_ν and the airmass x such that the resonance frequency of each detector at frequency ν is given by [Catalano et al., 2014b]:

$$f_{0,k} = C_k^0 - C_k^1 \times T_{atm}\left[1 - e^{-\tau_\nu x}\right], \tag{4.2}$$

where C_k^0 is the resonance frequency of the detector k at zero opacity, C_k^1 is a calibration conversion factor in Hz/K linking the atmospheric optical power variations to changes in the resonance frequency, and T_{atm} is the blackbody temperature of the atmosphere, assumed to be constant at 270 K. The airmass is defined as $x = 1/sin(\delta)$, assuming that the atmosphere is plane-parallel and homogeneous. Since the NRO does not have a dedicated tau-meter to measure the opacity during the observations, we use a different type of scanning strategy than the typical raster scan (see Section 4.4.4), called `skydip`, to estimate the opacity and the C_k^0 and C_k^1 parameters. During a `skydip`, the telescope scans the sky from 20 to 80 degrees in elevation at a constant azimuth. The telescope moves continuously in elevation and the resonance frequency $f_{0,k}$ of each detector is measured at each elevation. We can then fit Equation 4.2 to the data to constrain C_k^0, C_k^1, and τ_ν. We show in Figure 4.12 the results of a `skydip` performed on October 23rd under unstable weather conditions. The median opacity is $\tau = 0.679 \pm 0.184$ estimated with 44 detectors, which is quite high as expected.

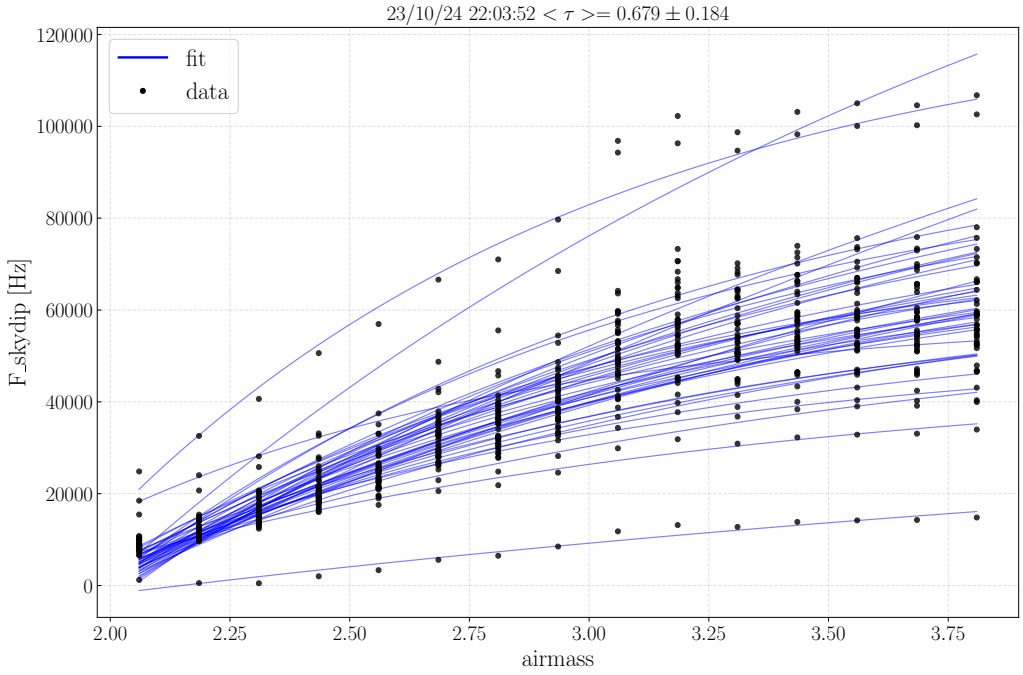

Figure 4.12: Results of a `skydip` performed on October 23rd. The black dots show the measured binned absolute resonance frequency shift of each working detector as a function of airmass x. The blue lines show the best fit for each detector using Equation 4.2.

As the C_k^0 and C_k^1 parameters are intrinsic properties of the detectors, they should not vary significantly during an observation campaign. Therefore, these coefficients can in principle be used for the whole campaign, and, as $f_{0,k}$ is known, we can invert Equation 4.2 to retrieve τ_ν for each scan as:

$$\tau_\nu = -\frac{1}{x} \ln\left[\frac{f_{0,k} - C_k^0}{C_k^1 \times T_{atm}} + 1\right]. \tag{4.3}$$

In practice, several `skydips` performed under stable weather conditions are needed to accurately estimate C_k^0 and C_k^1 for each detector. At high humidity and high PWV, the atmosphere can be very unstable, which can lead to large variations in the response of each detector between `skydips`. In

this case, the above equation cannot be used to accurately measure the opacity of each scan during the observation campaign. Since we still require a measure of the opacity to correct the absolute flux calibration on planets (see Section 5.6.2), we can try to estimate it from the precipitable water vapor values. As the opacity increases linearly with the PWV [Chamberlin and Bally, 1995], and we have measured the opacity above at a certain PWV value, we can estimate it for other PWV values using a simple linear scaling. We have two estimates of the PWV: one provided by the Nobeyama telescope in units of hPa, which is not easily convertible to mm, and another from the open-weather database given directly in mm (see Figure 4.7). From the previous measurement, we thus obtain $\tau = 0.679$ for PWV = 16.8 hPa and PWV $\sim$ 25 mm. In the next chapter, we will use a Mars scan performed on October 22nd as an illustration of the data reduction pipeline. The PWV during this scan was equal to 7.5 hPa and 10 mm, respectively. Scaling the opacity linearly with the PWV, we obtain $\tau = 0.303$ and $\tau = 0.272$. The two estimations are in good agreement, which is reassuring.

A better estimate of the opacity could also be obtained by using an accurate atmospheric model, such as the ATM model [Pardo et al., 2001]. Unfortunately, we do not have the required atmospheric data for the Nobeyama telescope site to run the model. We instead used the ATM model of the Sardinia radio telescope to estimate an upper limit on the opacity at 100 GHz for a PWV of 10 mm. Indeed, as this telescope is located at an altitude of 600 m, lower than the Nobeyama telescope (1350 m), we expect the opacity to be higher in similar weather conditions. We find an upper limit on the opacity $\tau = 0.37$ for a PWV of 10 mm at 100 GHz.

In the following, as the PWV measurements from the Nobeyama telescope are more accurate than the open-weather data, we will use $\tau = 0.303 \pm 0.082$ for our calculations.

CHAPTER 5

Development of the GT camera data reduction pipeline

5.1 Frequency shift reconstruction . . . 85
5.1.1 RANSAC calibration technique . . . 85
5.1.2 Caveats of the RANSAC method . . . 86
5.2 Description of the time-ordered data components . . . 87
5.2.1 Atmospheric noise . . . 88
5.2.2 Electronic noise . . . 88
5.2.3 Anomalous correlated noise . . . 89
5.2.4 Intrinsic noise . . . 90
5.3 Data selection . . . 90
5.3.1 Selection of valid detectors . . . 90
5.3.2 Samples selection . . . 91
5.4 Correlated noise substraction . . . 91
5.5 Map-making . . . 94
5.5.1 Individual maps per detector . . . 94
5.5.2 Combined map . . . 95
5.6 Commissioning results . . . 96
5.6.1 Beam size estimation and focal plane reconstruction . . . 96
5.6.2 Absolute calibration . . . 98
5.6.3 Sensitivity . . . 100
5.7 Conclusion and perspectives . . . 101

After the observations, we built a data reduction pipeline based on the KISS pipeline [Fasano et al., 2021; Macías-Pérez et al., 2024] to process the data and obtain maps of the observed sources. In this chapter, we will explain how the pipeline works. The first section describes the different techniques we have tried to accurately reconstruct the frequency shift δf_0 from the raw (I, Q) data. Secondly, the main noise components contained in the time-ordered data (TOIs) are explained. The third section details how we select valid detectors and samples for further analysis. In the following two sections, the method to subtract the correlated noise components from the TOIs is described, as well as the map-making procedure. Finally, the characterization of the camera's on-sky performance is presented. We also give some perspectives to improve both the camera and the pipeline for future observations. Throughout this chapter, we will consider the raw data from an observation scan of Mars performed on October 22nd in order to present the different data reduction steps.

5.1 Frequency shift reconstruction

As we have seen in Section 3.1.2, the raw data acquired by the instrument during the observations are the (I, Q) parts of the S_{21} transmission parameter. We have also seen that this transfer function is sampled at different rates depending on the instruments and the readout electronic used. For the GT instrument, with NIKEL electronics, we decide to opt for a slightly different approach than the one used for CONCERTO and described in Section 3.1.2. Since we work in photometric mode, we are not limited by any interferometric constraints and can sample the signal at a much higher rate. As a reminder, CONCERTO acquires samples at a rate of 3.8 kHz to form data blocks of 1536 samples, with one measure of δf_0 per data block which means at a rate of 2.48 Hz. We chose here to use a lower acquisition rate of 240 Hz, with data blocks of 512 samples to have modulated points for calibration more frequently. Then, instead of measuring δf_0 once per block, we measure it at each unmodulated sample which means that we do not downsample the signal and keep the 240 Hz sampling rate.

5.1.1 RANSAC calibration technique

Even if we process data blocks differently, we still use the same 3-points technique and compute calibration factor C (see Equation 3.13) for each block. However, due to the unstable weather, the method was not effective in reconstructing the signal for most of the detectors.

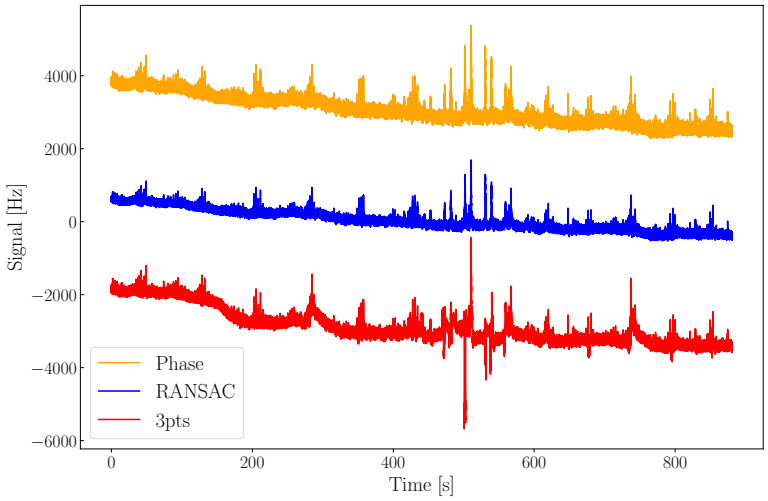

Figure 5.1: Comparison of the raw TOIs obtained for one detector with three different calibration methods: phase (orange), RANSAC (blue), and 3-points (red). The TOIs have been shifted for visualization purposes. The source signal clearly seen in the first two TOIs is alternatingly positive and negative in the last one, showing the issue with the 3-points calibration method.

We show in Figure 5.1 the raw TOI obtained for one detector for three different calibration methods (the TOIs have been shifted for visualization purposes). Notice that the TOIs have periodic strong, large, and unwanted spikes. This noise may be due to vibrations of the GM refrigerator (see Section 3.2.2). The likely origin of this noise is explained in Section 5.2.3 and dealt with in Section 5.4. For all three TOIs, we clearly see emission peaks when the detector goes through the planet, but the 3-points TOI (red) has an issue with the estimation of the calibration factor, which leads to a wrong reconstruction of the source signal. The TOI obtained with the phase calibration (orange), described in Section 4.4.5, is much more stable and reconstructs the signal well. However, the technique shows some increase in the overall noise level. We thus tried to implement a new calibration method based on the 3-points technique. Here, instead of fitting a circle to each block, we use a more robust RANdom SAmple Consensus (RANSAC, Fischler and Bolles (1981)) algorithm to find the circle model that best fits the whole data. The RANSAC algorithm works well in the presence of outliers, i.e., when the (I, Q) data are noisy and do not follow the expected circle model in the complex plane. To find the circle

center $p_0(I_0, Q_0)$, we implement the algorithm as follows:

1. We randomly select three points from the whole (I, Q) dataset, with one point for each modulation frequency $(-\Delta f,\ 0,\ +\Delta f)$.
2. We fit a circle to these three points to find the center coordinates (I_0, Q_0) and the radius r_0.
3. We evaluate the quality of the circle fit by computing the sum of absolute deviations d_{min} of all data points from the circle.
4. We repeat the process for a large number of iterations and the model with the smallest total deviation d_{min} is chosen.

Once we have found the best circle model, we compute the calibration factor C and reconstruct the frequency shift δf_0 following Equations 3.13 and 3.14, in the same way as for the 3-points method. Do note that we only have one measure of the calibration factor per detector, instead of one per data block.

In Figure 5.2, we show the results of the circle fit of one detector, with the RANSAC circle in red and the individual 3-points circles in black. We see that the RANSAC circle is a good fit to the whole data, whereas most of the individual circles are failing to accurately find the true center $p_0(I_0, Q_0)$ and radius r_0.

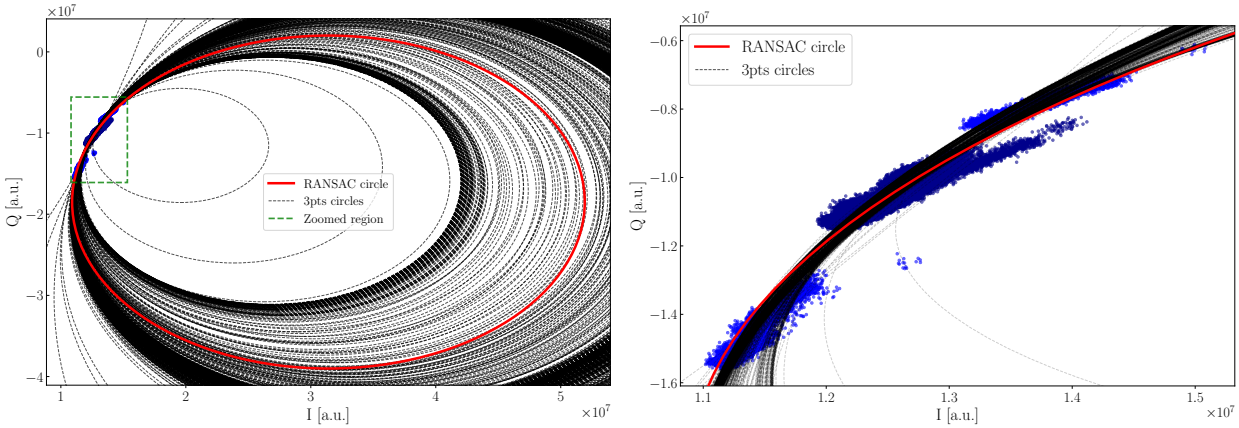

Figure 5.2: Comparison of the circle fit obtained with the RANSAC algorithm (red) and the individual 3-points fits (black) for one detector. (Left): Region centered on the RANSAC circle. (Right): Zoom on the data, with modulated and unmodulated points in blue and darkblue, respectively. Some individual circles are clearly not fitting the data well, leading to wrong calibration factors.

5.1.2 Caveats of the RANSAC method

A problem that we found early on with the RANSAC method is that the amplitude of the reconstructed signal varies significantly each time we run the algorithm. Even though the resulting circles are similar at the percent level, the small differences in the center coordinates (I_0, Q_0) and radius r_0 lead to large variations in the C calibration factor. We tried to change the algorithm, such as greatly increasing the number of iterations, and removing calibration points that are on-source, but the results were still unstable.

Then, instead of running the algorithm once with tens of thousands of iterations, we tried to run it multiple times with a lower number of iterations, and take the median of the results as our final estimation of the circle parameters. In practice, we compute the median of the calibration factor C distribution, we extract the circle that corresponds to this value, and we continue the signal

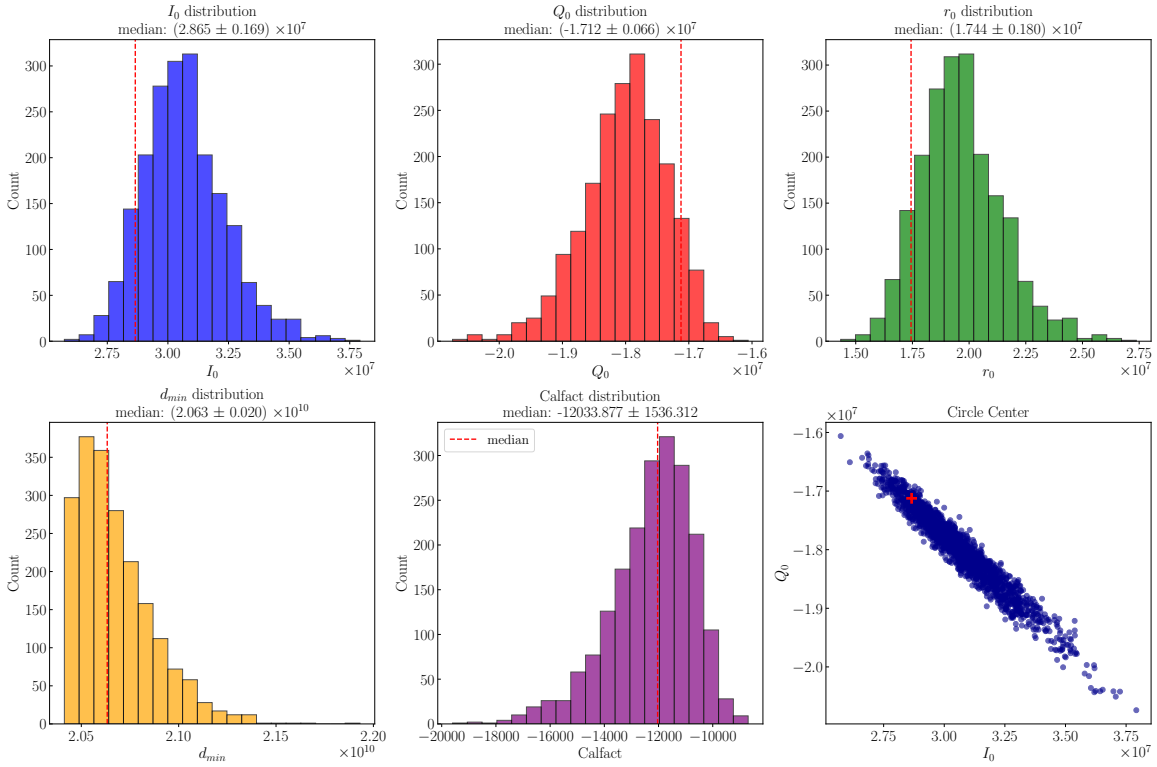

Figure 5.3: Distribution of the circle parameters obtained from 2000 runs of the RANSAC algorithm for one detector. (Top): Distribution of the circle parameters I_0, Q_0, and r_0. (Bottom): Distribution of the minimum distance parameter d_{min}, calibration factor C, and center coordinates (I_0, Q_0). The red cross shows the (I_0, Q_0) coordinates of the final circle.
The red dashed lines indicate the final adopted values, which correspond to the median of the calibration factor C distribution.

reconstruction from there. We found that running the algorithm 2000 times with 100 iterations was a good compromise between computation time and stability of the results.

We show in Figure 5.3 the results of this process for one detector. In the top panels, we plot the distribution of the center coordinates I_0, Q_0, and radius r_0 obtained from the 2000 runs of the algorithm and the final adopted values as red dashed lines. We see that the distributions have a distinctive peak, but the final values do not correspond at all to the peak position. If instead of taking the median of C to find the best circle we take the median of I_0, Q_0, and r_0, we end up with the same problem as before, i.e. the amplitude is unstable. In the bottom panels, we show the distribution of the d_{min} parameter, C (Calfact), and the (I_0, Q_0) center values. The main conclusion is that taking the median calibration factor C does fix our problem with the varying signal amplitude, as expected. But the uncertainty on the calibration factor is very high, around 13% for this detector. On average, this error is around 14% for all detectors.

For the few detectors where all three methods work well, we found that the amplitude of the reconstructed signal was very consistent between the phase and 3-points calibration methods, whereas this new iteration of the RANSAC method systematically outputed a lower amplitude, around a 20% difference. The results are not satisfactory and several improvements are still needed to make the RANSAC method more stable and accurate. For the rest of the analysis presented in this chapter, we thus decided to use the phase calibration method.

5.2 Description of the time-ordered data components

Following the reconstruction of the frequency shift δf_0, we obtain raw time-ordered data measured for each KID k, where the modulated points have been flagged and removed (see Section 5.3.2) and

only "science" points remain. These TOIs can be expressed as the sum of several components:

$$\mathrm{TOI}_k(t) = P_k(t,x,y)\cdot S_k(t,x,y) + \alpha_k(t)\cdot A_{\bar{k}}(t) + \epsilon_k(t)\cdot E_{\bar{k}}(t) + \zeta_k\cdot C_{\bar{k}}(t) + N_k(t)\,, \tag{5.1}$$

where $S_k(t,x,y)$ is the astrophysical signal of interest and $P_k(t,x,y)$ the pointing matrix characterizing the position of detector k on the sky at a time t. $P_k(t,x,y)$ is determined from the telescope pointing data and, at each time t, is equal to 1 if the detector k is observing the sky position (x,y), and 0 otherwise. The $\bar{k}$ notation indicates that the contribution is the average over all, or a subset, of detectors.

Terms $A_{\bar{k}}(t)$ and $E_{\bar{k}}(t)$ are the atmospheric and electronic contributions, respectively. For a large telescope like the NRO, with its 45-m diameter, the atmospheric contamination can be assumed to be common to all detectors, with α_k the response of each detector to this contaminant. The electronic noise is also correlated between all detectors, as the whole array is read out by the same electronic board as seen in Section 4.3.1. Each detector has a different response to this noise, which is taken into account through term $\epsilon_k(t)$. Term $C_{\bar{k}}(t)$ is due to vibrations from the cryostat, likely at the origin of the anomalous correlated noise spikes that we will discuss in Section 5.2.3. Coefficients $\alpha_k(t)$, $\epsilon_k(t)$, and $\zeta_k(t)$ are slowly varying over time, due to the drift in the resonance frequency of detector k relative to the readout frequency during a scan (see Section 4.4.3). Finally, $N_k(t)$ is the intrinsic noise of each detector, which regroups all noise components uncorrelated between detectors.

5.2.1 Atmospheric noise

During observations, except for very bright planets like Jupiter, the thermal emission from the atmosphere is the main background component in the TOIs. This emission can be modeled as a grey body whose emission is given by:

$$I_{atm} \propto \nu^2 T_{atm}\,(1 - e^{-\tau x})\,, \tag{5.2}$$

where τ is the zenith opacity and $x = 1/sin(\delta)$ the airmass. We see that the amplitude of the atmospheric emission is fainter as the elevation increases and τ decreases. Disregarding the anomalous noise due to the cryostat vibration described in a following subsection, the noise induced by atmospheric turbulences dominates, even under the best observing conditions. There are three main reasons for this: atmospheric absorption that will attenuate the signal (see Section 4.4.7), thermal emission of the atmosphere that will increase the photon noise, and atmospheric temporal and spatial fluctuations due to clouds or variations in water vapor content. The latter can be described by a $1/f$ spectrum, with an amplitude that evolves over time depending on the weather conditions. We show in Figure 5.4 the common mode, which is the correlated noise between all detectors as described in Section 5.4 as well as its power spectrum. The power spectrum is well fitted by a power law model $\hat{P(f)} = w + A\times f^{\beta}$ where w is the white noise level, A the amplitude of the $1/f$ noise, and β the slope of the power law. The amplitude of the noise hints at the weather conditions during the observations, with a high amplitude indicating poor weather conditions.

5.2.2 Electronic noise

Fluctuations in the position of the readout frequency comb around each KID's resonance frequency induce an electronic contamination that is correlated between detectors read out by the same electronic board. Even if the atmospheric and anomalous noise dominate, this contamination is still non negligible and must be taken into account. For experiments like NIKA2 (see Chapter 6), where detectors in a large array are read out by several boards, the electronic noise is more easily identifiable by analyzing the correlation matrix of the detectors once the atmospheric noise has been removed.

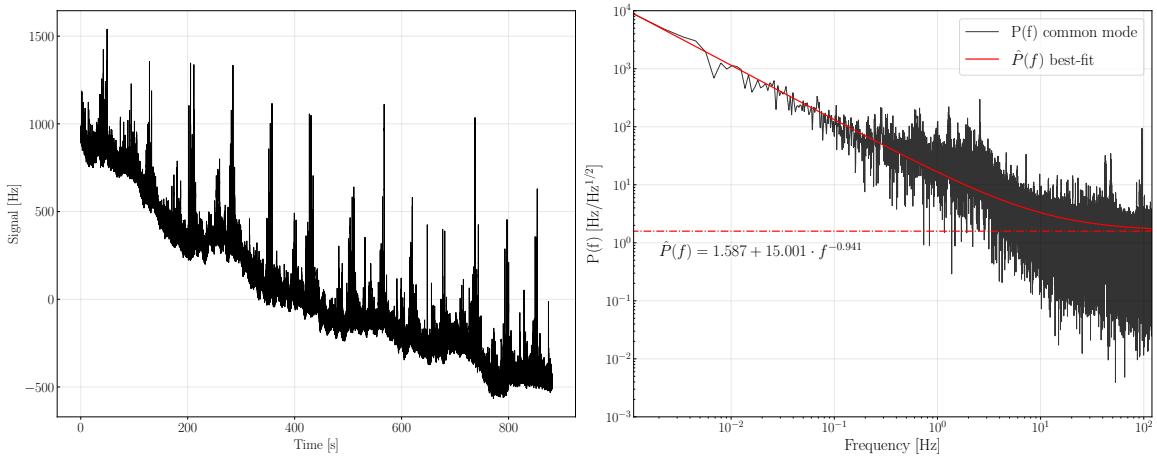

Figure 5.4: (Left): Common mode of the TOIs, i.e., the correlated noise between all detectors in the array. Despite the large spikes due to the anomalous correlated noise, the atmospheric noise dominates at large scales. (Right): Power spectrum of the common mode. The power law fit is shown in red, with the white noise level w in dashed red. The equation of the power law is shown below the dashed red line. The anomalous noise spikes in the common mode appear as peaks in the power spectrum.

In our case, since the detectors are all read out by the same board, the electronic noise is efficiently subtracted during the correlated noise subtraction procedure described in Section 5.4.

5.2.3 Anomalous correlated noise

As we can see in Figure 5.4, the common mode (see Section 5.4) of the TOIs shows strong spikes of unknown origin added to the other noise contributions. Our first hypothesis was that these spikes could be due to magnetic coupling between the KIDs and an external magnetic field. Indeed, during observation scans, the telescope moves following a pattern of successive straight lines at constant elevation (see Figure 4.9). During the transition between two lines, the telescope accelerates to reach the new elevation, and decelerates to change the direction of the scan. Throughout these acceleration and deceleration phases, the motors of the telescope induce a magnetic field that can couple with the KIDs. If the cryostat is not equipped with magnetic shields [Calvo et al., 2016b], this magnetic coupling can affect the KID's resonance frequencies and manifest as periodic spikes in the TOIs. To try and confirm this hypothesis, we looked at data we had taken while the telescope was static, and found that these noise spikes were still present in the TOIs. They are thus not related to the telescope's movements.

After discussion with the Japanese team, we found that the GM refrigerator used to cool down the cryostat (see Section 3.2.2) is likely the source of this unwanted noise. It is known that the GM refrigerator periodically vibrates, due to the pistons moving inside it to create the cooling cycle. The sound produced by these vibrations is clearly recognizable when standing next to the cryostat. However, an additional irregular vibration is also heard from the refrigerator. The origin of this irregular vibration is being investigated by the Japanese team. Nevertheless, it is likely that these vibrations are the source of the anomalous correlated noise.

This noise is thus included in term $C_{\tilde{k}}(t)$ in Equation 5.1. Similarly to the atmospheric and electronic noise, each detector has a different response $\zeta_k(t)$ to this contaminant. Fortunately, these spikes are correlated between all detectors in the array and are safely removed during the correlated noise subtraction procedure.

5.2.4 Intrinsic noise

In addition to the correlated noise affecting all detectors in the array, KIDs are also subject to an ultimate noise component, $N_k(t)$, which cannot be substracted since it is intrinsic to each detector and indepedent from the others. This noise is dominated by contributions from the photon noise and spontaneous fluctuations in the Cooper pair population. $N_k(t)$ is well approximated by white noise and is thus the limiting factor of the GT camera sensitivity. We will see how it is estimated in Section 5.6.3

5.3 Data selection

Before subtracting the correlated noise components from the data, we first need to discard detectors and samples that would degrade the quality of the analysis. In this section, we describe the factors that can affect the quality of the analysis, and how we select the data to keep for the analysis.

5.3.1 Selection of valid detectors

Even if we have identified and successfully monitored 97 detectors during laboratory measurements (see Section 4.3.1), some of them may malfunction or be affected by systematics during specific observation scans and must be excluded from the analysis. This selection of good detectors is done only once, using the target that we will use as our primary flux calibrator. As only the selected detectors are intercalibrated (see Section 5.5.2), we will use the exact same detector list for constructing the maps of all the other sources. Of course, an additional selection may be done for each different scan if any detectors present systematics affecting the quality of its map. Since we have less than a hundred detectors, we can select good detectors by eye by looking at the individual detector maps of Mars. There are several reasons why a detector may be flagged during a scan as illustrated in Figure 5.5:

- The detector is out of resonance, i.e., the resonance frequency is too far away from its assigned tone. For example, detectors KB045 and KB055, framed by the orange line in the Figure, are not responsive at all to the signal of Mars.
- Two detectors may have resonance frequencies that are too close to each other and may overlap during the observations. These detectors can be identified by looking for maps where the target signal can be seen two or more times at different coordinates, as for example KB022 and KB025. These detectors are framed in pink in the Figure.
- It is also possible that during the `tuning` procedure, two tones may be tuned to the same frequency, which means that two detectors will be read out as the same detector. Their maps will then be identical, as we can see for KB075 and KB076 in the second to last row of the Figure. These kinds of detectors are also framed in pink.

After identifying the detectors belonging to the different categories described above, the remaining are used for further analysis. In practice, we first make individual maps for all detectors in the array as described in Section 5.5.1, select the valid KIDs, and then start the analysis again from the beginning with the selected detectors. This is done to avoid any bias when cleaning the data from the correlated noise (see Section 5.4), as noisy detectors may affect the common mode estimation.

At this stage, we also select a reference detector that will be used as a reference in both the decorrelation and map-making process. As we have only analyzed data acquired from one observation night due to the poor conditions during the others, the best choice as a reference is the detector that is the most stable during the whole night, i.e, not affected by any systematics and valid throughout. In the following, we will use detector `KB057` as our reference.

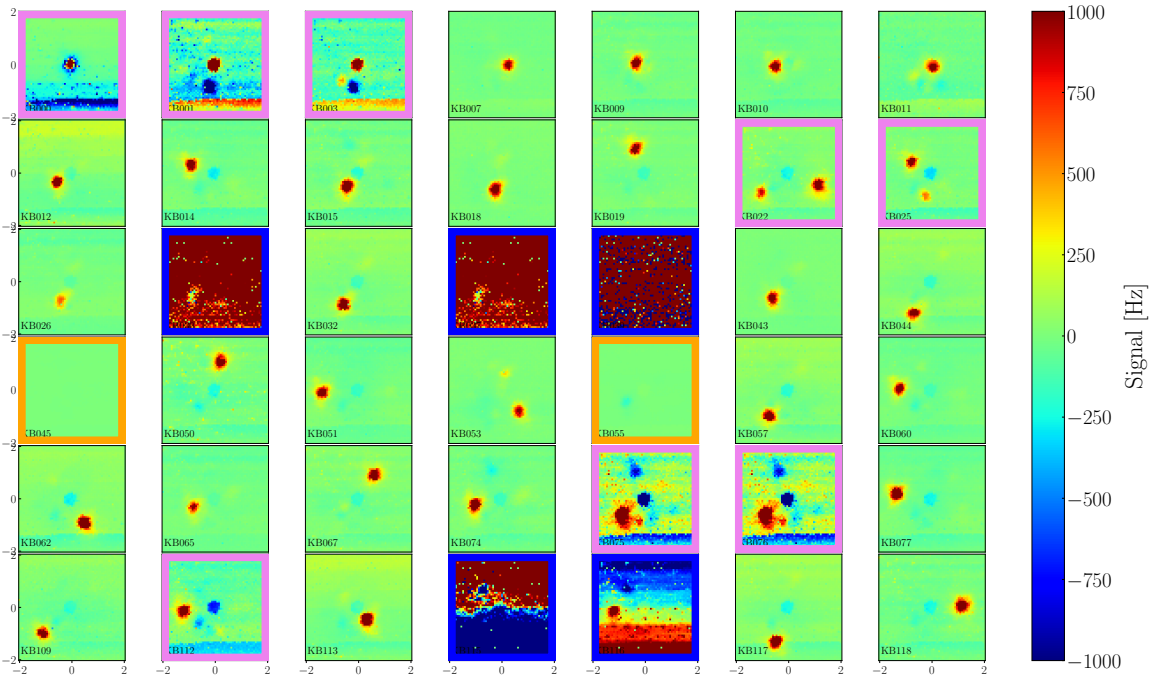

Figure 5.5: Projected maps of Mars for half of the detectors in the array. The detectors are ordered by their number, from left to right and top to bottom. The majority of KIDs show a clear signal from Mars. The maps framed by a blue line show detectors saturated by noise. In pink, we identify detectors in diaphony or two KIDs tuned to the same resonance frequency. Maps framed by an orange line show detectors out of resonance and thus not sensitive to the point source signal. The other detectors are kept for the map-making. The negative signal we can distinguish in some maps of working detectors is because we have used all detectors, even bad ones, to compute the common mode (see Section 5.4). This negative signal is gone after removing these bad detectors from the analysis.

5.3.2 Samples selection

As we have seen in Section 4.4.4, the telescope scans the sky in straight lines at constant elevation with a constant speed. However, between each elevation step, the telescope accelerates to reach the new elevation and change the direction of the scan. The samples acquired during this acceleration phase have larger uncertainty in their pointing position which may impact the quality of the projected maps. We show in Figure 5.6 the path of the telescope during a typical $4' \times 4'$ raster scan. The samples where the telescope accelerates are shown as red dots and are masked before projection. The red dots along the diagonal are samples acquired while the telescope was moving back to its initial position after finishing the scan and are masked as well. The green dots correspond to times when modulated samples are acquired for calibration purposes, as described in Section 5.1. These samples are also masked out in the TOIs as we only work with the unmodulated or "science" samples. In total, the masked data amount to $\sim 5\%$ of the scan.

5.4 Correlated noise substraction

As previously mentioned, it is essential to subtract all the correlated contaminants in the TOIs before projecting them as they dominate over the astrophysical signal of interest. This is especially true for faint sources such as M82 where the signal is at least an order of magnitude fainter than the noise. Figure 5.7 shows the combined map of Mars made from raw TOIs without any decorrelation. The map is dominated by the atmospheric noise inducing a large noise gradient across the field of view. We can still distinguish Mars in the center of the map as it is a bright planet, but any analysis of fainter sources would be impossible. Our aim is thus to minimise the noise in the TOIs to be as close as possible to the intrinsic noise of the detectors. There are several decorelation techniques to do so, but we will focus here on the method that we used for the GT camera data reduction pipeline.

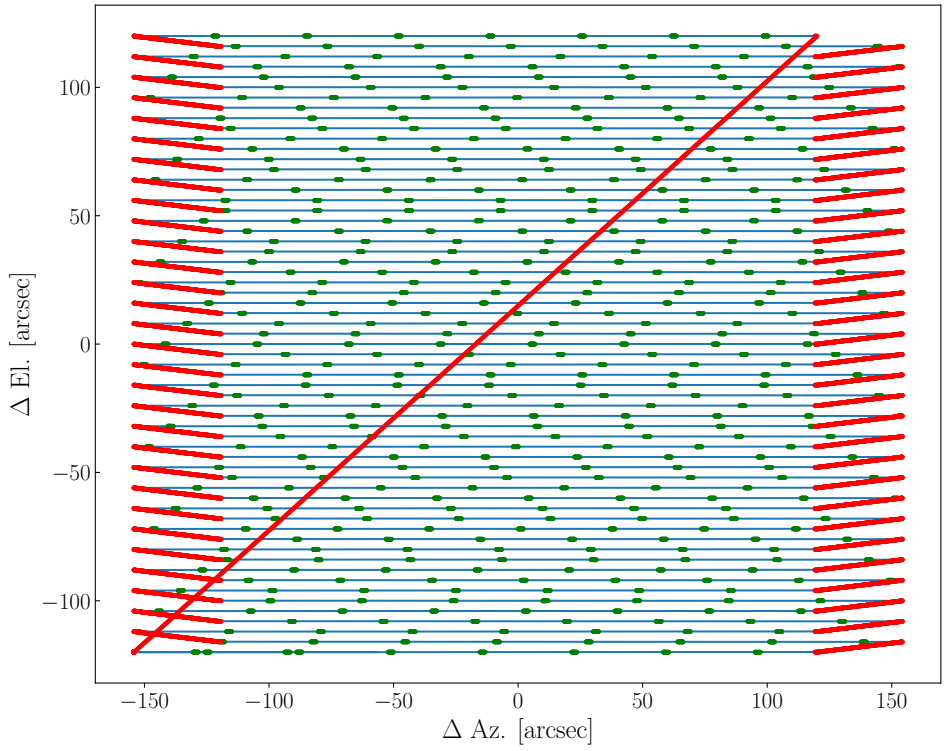

Figure 5.6: Telescope's path in the alt-azimuthal plane during a scan of Mars. Transitions between subscans at constant elevation are shown as red dots and are masked in the following analyses. Green dots correspond to modulated samples used for calibration and are also masked.

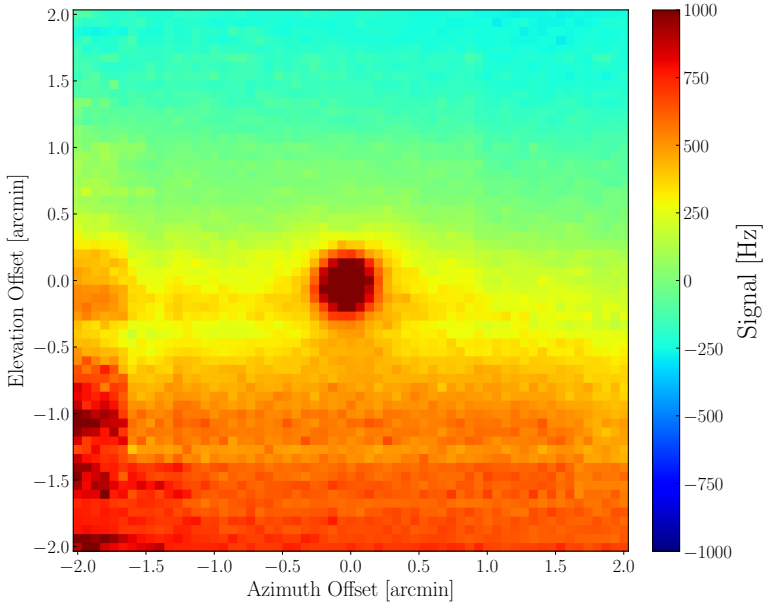

Figure 5.7: Combined map of Mars obtained by stacking the maps from each detector without any decorrelation. The map is dominated by the atmospheric noise but we can still see Mars in the center as it is a very bright source.

During a scan, at a fixed time t, the detectors see the same correlated noise (atmospheric, electronic, magnetic) with different amplitudes, but a different astrophyiscal signal $S_k(t, x, y)$ depending on their position (x, y) on the sky. It is thus possible to estimate a common mode $CM(t)$ from the TOIs of all working detectors in the array to efficiently subtract the correlated components. To compute this common mode, even though we have selected only the working detectors for further analysis as described in Section 5.3.1, we make an additional selection of the best detectors based on their median absolute deviation. This step usually keeps all the initial detectors, but it is important to make sure we do not introduce any bias in the common mode estimation. We then choose a reference detector k_0 as described in Section 5.3.1. The correlation coefficients r_k between all detectors and the reference detector are then computed to normalize their TOIs before estimating the common mode as:

$$\mathrm{CM(t)} = \mathrm{Med}\left[\frac{\mathrm{TOI}_k(t)}{r_k}\right], \tag{5.3}$$

where Med is the median. The source is masked to make sure that the common mode does not include any astrophysical signal. As different detectors have different responses to the correlated noise, the common mode is adjusted to each KID by performing a linear regression and then removed from the TOIs:

$$\mathrm{TOI}_k^{clean}(t) = \mathrm{TOI}_k(t) - (a_k \cdot \mathrm{CM}(t) + b_k), \tag{5.4}$$

Whe show in Figure 5.8 the TOIs of all working detectors during a scan of Mars (blue lines). The different peaks in the TOIs are due to the signal from Mars seen at different times by the detectors. The red curves shows the common mode, which fits well the atmospheric noise at large scales and the large spikes due to the magnetic coupling noise. The right panel shows the cleaned TOIs after common mode subtraction. We see that the large-scale behavior of the noise is suppressed, leaving only the astrophysical signal and a minor noise component, which is mostly uncorrelated between detectors. This is also illustrated in Figure 5.9, where we show the correlation matrix of the TOIs before and after common mode subtraction. In the left panel, we see that the raw TOIs are highly correlated, with correlation coefficients exceeding 90% on average. On the right, we see that the correlations are greatly reduced after common mode subtraction, with values below 10% for most of the detectors. The remaining small correlations are due to the Mars signal overlapping between detectors, which is expected as the planet is large enough to be seen by several detectors at the same time.

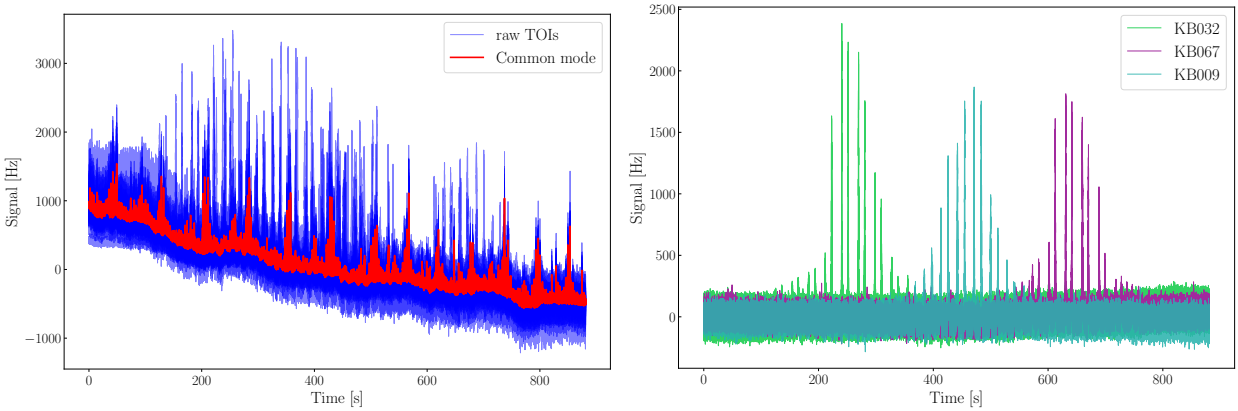

Figure 5.8: (Left): Raw TOIs of 32 working detectors during a Mars scan. The common mode is shown as a red curve. (Right): Cleaned TOIs after common mode subtraction of three detectors. The noise level is constant and the signal from Mars is clearly visible. We only show the timelines of three detectors to clearly see the signal from Mars, but all 32 detectors show similar patterns after decorrelation.

For future observation campaigns, improvements can be made to the described decorrelation method. For example, estimating a common mode for each subscan at constant elevation instead of the whole scan could provide better results. Using a principal component analysis (PCA) method could also be more efficient for very faint sources. An alternative pipeline using a PCA approach is currently being built by the Japanese team.

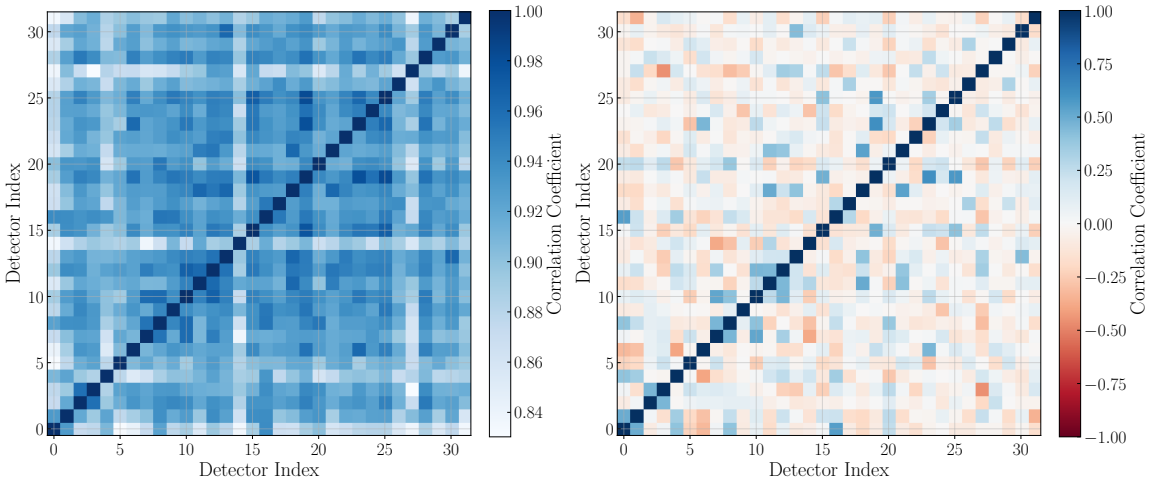

Figure 5.9: Correlation matrix of the TOIs for working detectors in the GT array during an observation of Mars. (Left): Raw TOIs correlations. (Right): Correlations after subtraction of a common mode computed from all working detectors in the array.

5.5 Map-making

5.5.1 Individual maps per detector

Once we have cleaned the TOIs from the correlated noise components and masked the bad samples, we can project the TOIs onto a grid of pixels to obtain a map of the observed source per detector. We estimate the size of the map based on the scan size and the telescope pointing data. As seen in Section 5.3.2 and Figure 5.6, we mask samples outside of the original scan size, where the telescope accelerates and decelerates, before projection. The pixel size was chosen as ~5 pixels across the beam to satisfy the Nyquist-Shannon sampling theorem, which is about 4″. The beam size estimation is described in details in Section 5.6.1.

The projection we use is based on the nearest grid point method, where a sample at a time t is projected on the closest pixel to the detector's position on the sky at t. The first product of the projection are `hits` maps, which quantify the number of samples projected on each pixel as

$$N_{\mathrm{hits},k}(x,y) = \sum_t P_k(t,x,y)\,, \tag{5.5}$$

where $P_k(t,x,y)$ is the pointing matrix defined in Section 5.2. A high hit count per pixel is always prefered, as combining many samples lowers the statistical uncertainty by a factor $\sqrt{N_{hits}(x,y)}$ in pixel (x,y). The signal map, which is at first simply the sum of the signals of all samples projected on each pixel, is then normalized by the `hits` map to yield the average signal per pixel:

$$M_k(x,y) = \frac{\sum_t P_k(t,x,y) \times \mathrm{TOI}_k^{clean}(t)}{N_{\mathrm{hits},k}}\,. \tag{5.6}$$

We thus obtain individual maps of the source for each detector in frequency shift δf_0 units. We show in Figure 5.10 the projected maps of Mars for each good detector in the array. In each of them

we clearly see the bright point-source like Mars signal. As previously mentioned, each detector sees Mars at a different time as shown by the changing position of the signal in the maps. There are faint noise residuals in some maps (e.g., KB012, KB053), but overall the correlated noise has been accurately subtracted. These individual maps are used to reconstruct the geometry of the focal plane and estimate the beam size of the camera, as described in Section 5.6.1.

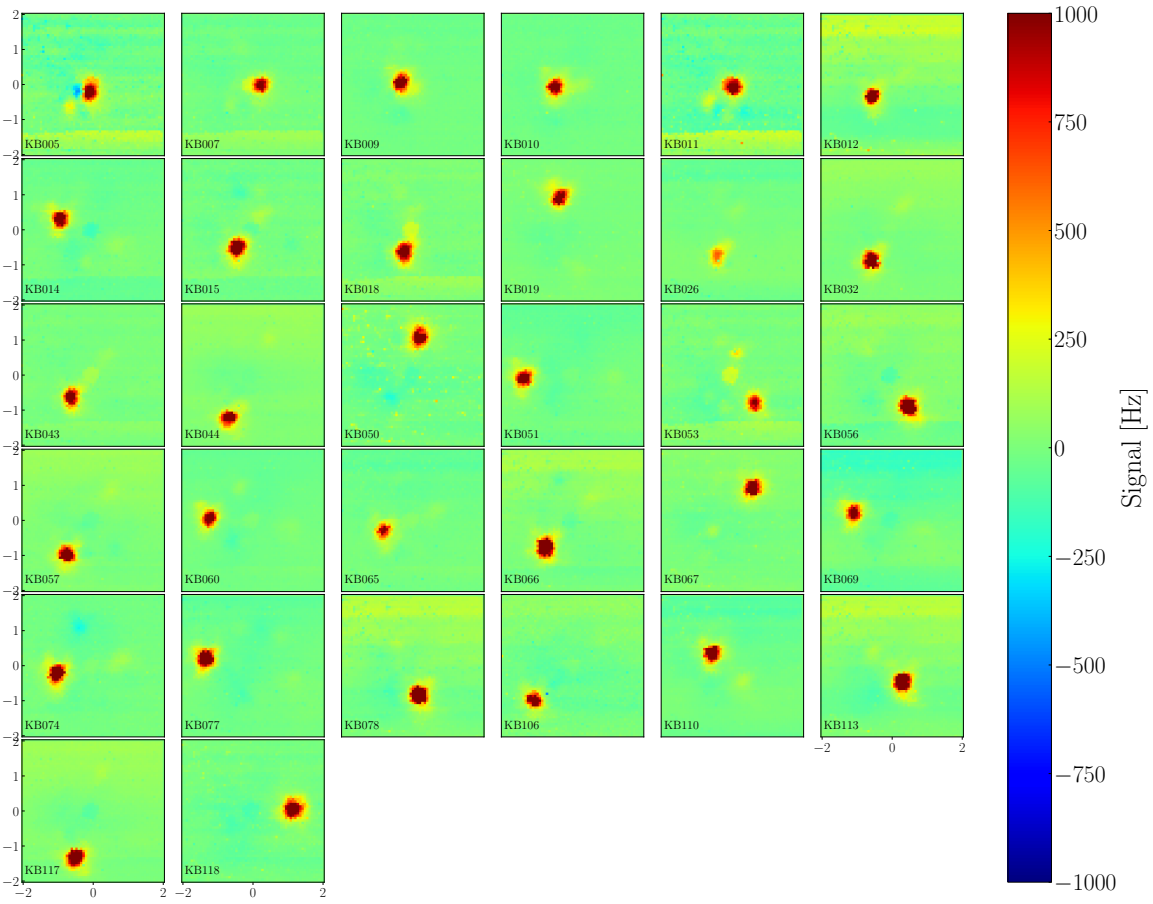

Figure 5.10: Projected map of Mars for each working detector. Before projection, the TOIs were cleaned from the common mode shown in Figure 5.8.

5.5.2 Combined map

Even if the source can already be seen in individual maps, we can further improve the signal-to-noise ratio and decrease uncertainties by combining the individual maps of all good detectors. As the signal from the source is not centered on the same pixel for each detector, we first need to correct the pointing to align them. We thus fit a 2D Gaussian to each map as:

$$M_k(x, y) = \delta f_{0,k} \ \exp\left(-\frac{(x - x_0)^2 + (y - y_0)^2}{2\sigma_k^2}\right), \tag{5.7}$$

to find the center coordinates (x_0, y_0) of the source signal as well as its amplitude $\delta f_{0,k}$. We use the fitted coordinates to correct the individual pointing of each KID, such that the source now lies in the center of the map. A very important step in the map-making is to intercalibrate the response of all detectors with respect to a reference detector that is the same as the one used for the common mode subtraction (see Section 5.4). The intercalibration factors, simply defined as $\frac{\delta f_{0,k}}{\delta f_{0,k_0}}$, are only computed once for all detectors using an observation of the target chosen as the primary flux calibrator, which is

Mars in our case (see Section 5.6.2). These intercalibration factors are then stored and used as is for all other observations, by simply multiplying the TOIs of each detector by its respective intercalibration factor before projection. Finally, the combined signal map is computed as

$$M_{tot}(x,y) = \frac{\sum_{k,t} P_k(t,x,y) \times w_k \times \mathrm{TOI}_k^{clean}(t)}{\sum_{k,t} P_k(t,x,y) \times w_k(t)}\,, \tag{5.8}$$

where w_k are the weights for detector k computed as the inverse of the variance of the cleaned TOI (only considering samples outside the source region):

$$w_k = \frac{1}{\mathrm{Var}_{\text{off-source}}[\mathrm{TOI}_k^{clean}(t)]}\,. \tag{5.9}$$

The weights w_k also allow us to estimate the standard deviation map, which is the square root of the variance map. The combined `hits` map is simply the sum of the `hits` maps of all detectors $N_{\mathrm{hits}}(x,y) = \sum_k N_{\mathrm{hits},k}(x,y)$. By dividing $N_{\mathrm{hits}}(x,y)$ by the sampling frequency of the TOIs, we can estimate the integration time per pixel. We show in Figure 5.11 the combined map of Mars obtained from the detector maps shown in Figure 5.10, as well as the associated standard deviation and integration time maps. As expected, the noise is lower at the center of the map, as this region is seen by all detectors, while the edges of the map are only seen by a few detectors. The low noise region does however seem a bit shifted from the center of the map, where we would expect the integration time to be the highest. This is likely due to to the non-uniform coverage of the field of view by the detectors, as we only have 32 working detectors in the array.

5.6 Commissioning results

The majority of the observation campaign was dedicated to the *commissioning* of the GT camera. Our goal was to characterize the on-sky performance of the camera in terms of responsivity, sensitivity and angular resolution. In this section, we describe the methods used to derive these parameters, as well as the results obtained.

5.6.1 Beam size estimation and focal plane reconstruction

As we have seen in Section 4.4.3, the exact position of each resonance on the transmission line is not known before each observation. Indeed, as resonances may shift inbetween observations, it becomes difficult to correctly associate each resonance to its corresponding detector. Similarly, the link between the position of the resonances in frequency space and the position of the detectors in the focal plane is not known a priori before the observations. It is thus important to reconstruct the focal plane geometry of the camera and associate each detector with a precise position on the sky. This operation is performed by observing a bright point-like source, for example a quasar such as 3C84, and producing maps for each detector. These maps, called *beammaps*, enable us to both estimate the beam size of each KID and to determine its position in the array. A 2D Gaussian is fitted to each *beammaps* as in Equation 5.7 to estimate the position of each KID (x_k, y_k), as well as the beam FWHM θ_k.

The per-detector maps obtained on 3C84 can be seen in Figure 5.12. These maps yield the position of each KID on the sky, as illustrated in Figure 5.13, as well as the beam FWHM distribution across the array. We find that the beam FWHM is $\theta_{FWHM} = 22.4 \pm 2.5$ arcsec, which is larger than the value found for the MKID camera in 2021 (16.7″, Honda et al. (2023)), as expected (see Section 3.5). We note that only 43 working detectors are used for this analysis, which is less than half of the total number of KIDs we monitor. The main reason for this low number of detectors, beside the weather,

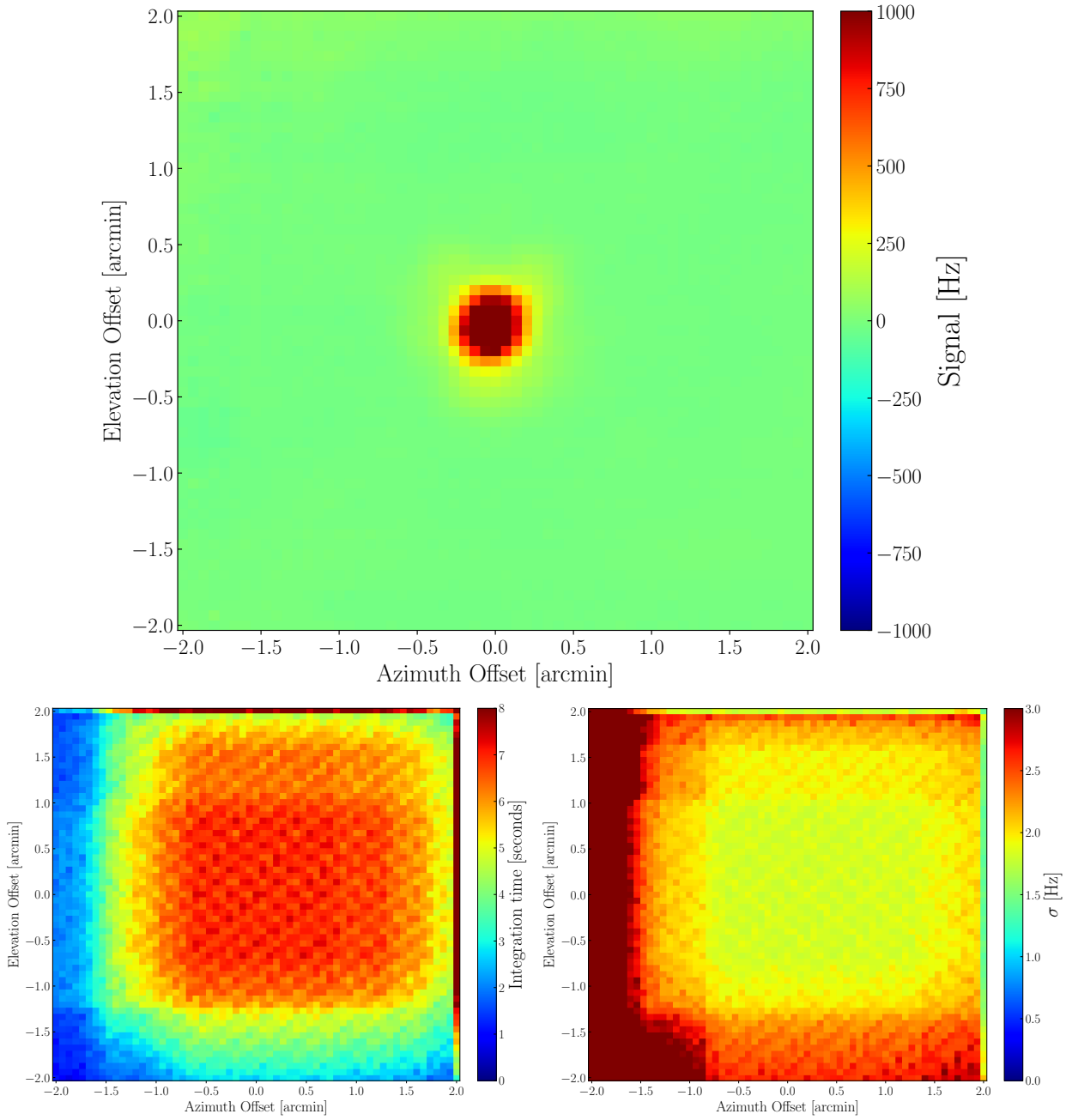

Figure 5.11: (Top) Mars map obtained with 32 detectors. (Bottom left): Map of the integration time per pixel after combining the individual maps. (Bottom right): Standard deviation map from the same analysis. A region with high noise can be seen in the left part of the map, where the integration time is the lowest. This might be due to the fact that detectors do not uniformly cover the field of view.

is that several pairs of detectors have resonance frequencies that are too close to each other. As a consequence, the `tuning` procedure (see Section 4.4.3) assigns them the same resonance frequency and only one is effectively read out. We note that this kind of issue was expected from the results of the array lab characterization (see Section 3.4.1). A new LEKIDs array, with a better spacing between resonances, would greatly help to minimize this issue in future observations.

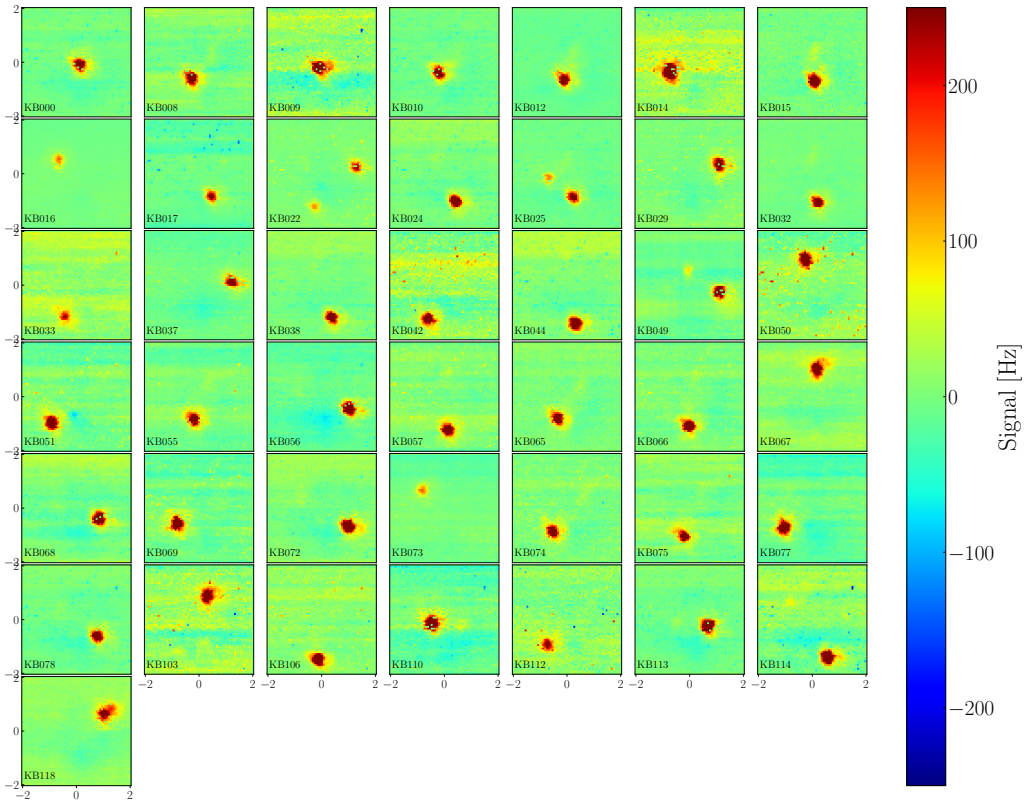

Figure 5.12: 3C84 map per detector used to reconstruct the focal plane geometry of the array. Working KIDs are selected following the procedure described in Section 5.3.1.

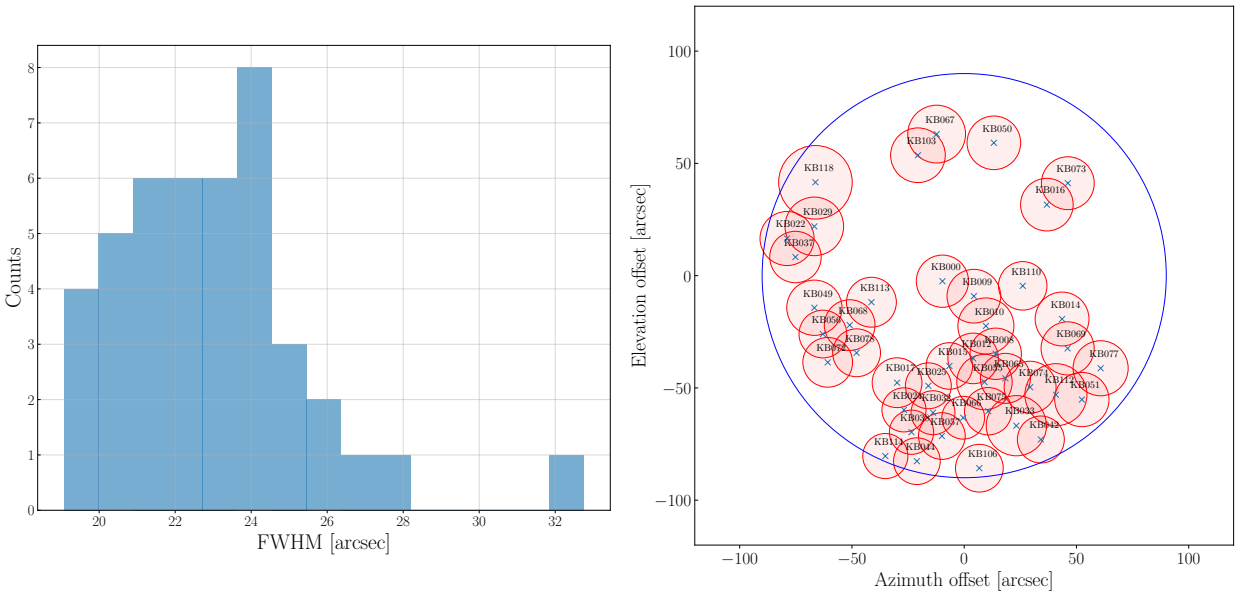

Figure 5.13: (Left): Beam FWHM distribution (Right): Focal plane geometry of the array reconstructed from a *beammap* of 3C84. The red circles show the beam size of each detector and the blue circle indicates a 3 arcmin region.

5.6.2 Absolute calibration

The responsivity of a KID camera describes how much the resonance frequencies of detectors in the array will shift with respect to a change in the source flux, and is expressed in Hz/K units. Responsivity is usually measured by observing bright sources, such as planets, whose brightness temperature is well

known. We chose here Mars as our primary calibrator, as it is bright and visible even under unstable weather conditions. Its brightness temperature was also accurately modeled by the Planck satellite [Planck Collaboration et al., 2017], equal to $T_B = 194.3 \pm 1.3$ K at 100 GHz. As mentioned previously, Mars and this scan in particular are used as a reference for the other analysis. Most importantly, the selection of working detectors and the intercalibration procedure are done for this scan only and then applied to all other scans. For the noise decorrelation and the map-making, we use detector `KB057` as our reference detector, as it is the most stable and can be used as reference throughout the whole observation night. Once we obtain our combined map shown in the upper panel of Figure 5.11, we need to estimate the peak amplitude of the source signal by fitting a 2D Gaussian as in Equation 5.7. As we know the beam FWHM from the beam size estimation procedure described in Section 5.6.1, we can fix the width σ of the Gaussian to better estimate the amplitude $\delta f_0^{\max}$.

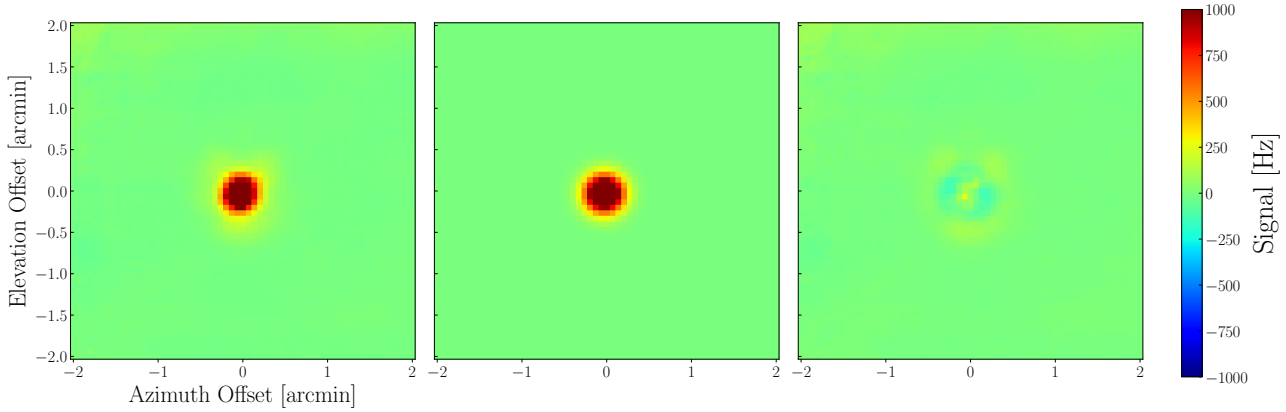

Figure 5.14: Results of the fit of a 2D Gaussian to the combined map of Mars. The left map corresponds to the Mars signal map. Then, we show the model of the Gaussian best-fit and the residuals, respectively. The residuals do show some leftover signal in a few pixels, but overall the fit is good. The color scale is the same for all maps.

In Figure 5.14, we show the results of the fitting procedure with, from left to right, the combined map of Mars, the best-fit Gaussian model and the residuals. The model is a good fit to the data. We find $\delta f_0^{\max} = 1718.1 \pm 2.3$ Hz. Before we can estimate the responsivity, there are several factors to take into account. First, we need to correct the temperature of Mars by a dilution factor η, which describes how much the signal is diluted inside the beam as

$$\eta = \frac{\Omega_p}{\Omega_b} = \frac{\theta_p^2}{8\theta_b^2}, \tag{5.10}$$

where Ω_p and Ω_b are the planet and beam solid angles, respectively, and θ_p and θ_b are the planet and beam FWHM. In our case, Mars's angular diameter during the observation was $\theta_p \sim 8.6''$, yielding a small dilution factor $\eta \sim 0.1$. Then, we also need to account for the atmospheric opacity τ at the time of observation and the elevation. We adopt here an opacity of $\tau = 0.303 \pm 0.082$ (see Section 4.4.7), determined from a skydip measurement. The temperature of Mars is then corrected as

$$T_B^{\text{corr}} = T_B \cdot \eta \cdot e^{-\tau x}. \tag{5.11}$$

We thus estimate the responsivity and flux calibration factor of the camera to be equal to 141.2 ± 33.5 Hz/K. The large uncertainty comes from the estimation of the opacity which was hard to accurately measure, as well as the uncertainty on the beam FWHM (see Section 5.6.1). Before we began the observations, we estimated a responsivity of ~ 300 Hz/K, based on the response of the detectors to a change in the background load. Our on-sky result is lower than expected, but considering the

weather conditions, and the fact that the LEKID array is only a spare (see Section 3.2.1), this result is promising.

5.6.3 Sensitivity

The sensitivity of the camera is an extremely important parameter for estimating the observation time required to measure a source at a given signal-to-noise ratio. It is defined as the standard deviation of the residual noise in the signal maps reached in one second of observation for a point source, and is usually expressed in terms of noise equivalent flux density (NEFD) in $\mathrm{mJy.s^{1/2}}$ units. From the map-making procedure described in Section 5.5.2, we have access to the standard deviation map in δf_0 units. As we have estimated the flux calibration factor from Hz to Kelvin in Section 5.6.2, we can convert the uncertainty map first to Kelvin and then to mJy/beam, using the Rayleigh-Jeans approximation:

$$\sigma_{\mathrm{mJy/beam}} = \frac{2k_b\nu^2}{c^2} \times \sigma_K \times \Omega\,, \tag{5.12}$$

where k_b is the Boltzmann constant, ν the frequency of observation, σ_K the standard deviation in Kelvin and Ω the beam solid angle. Now that we have our point-source uncertainty in flux units, we need to estimate the integration time spent in the source region t_{source} to normalize $\sigma_{\mathrm{mJy/beam}}$ to one second of observation. As discussed in Section 5.5.2, we have access to the integration time map, and we can estimate t_{source} as the average integration time per pixel within one FWHM round the source. We thus find $t_{\mathrm{source}} \sim 6.92$ seconds. The NEFD is then computed using the previous quantities:

$$\mathrm{NEFD} = \sigma_{\mathrm{mJy/beam}} \times \sqrt{t_{\mathrm{source}}}\,. \tag{5.13}$$

We show in Figure 5.15 the obtained sensitivity map. The center region is masked in order not to bias the NEFD estimation. On average, we find a sensitivity of $\mathrm{NEFD} \sim 150.81 \pm 44.29$ $\mathrm{mJy.s^{1/2}/beam}$. The uncertainty is driven by the error on the responsivity. We do stress that we expect NEFD estimations on bright point sources to be over-estimated. Also, looking at the power spectrum of the combined map, some residual noise is still present, which could dominate the NEFD estimate. Overall, we expect this sensitivity value to be an upper limit.

We also estimated the sensitivity from the white-noise level in the map, as done in Macías-Pérez et al. (2024). We find that the noise level in the map is ~ 2.3 $\mathrm{Hz\,s^{1/2}}$, compatible with the value obtained during the final noise measurements before the observations (see Section 4.3.3). From the responsivity estimated in Section 5.6.2, and converting to mJy/beam, we find $\mathrm{NEFD} \sim 66.1$ $\mathrm{mJy.s^{1/2}/beam}$. This estimate is in good agreement with our expectations at the time of writing the proposal, where we expected a sensitivity of ~ 60 $\mathrm{mJy.s^{1/2}/beam}$.

Compared to other KID-based cameras, our sensitivity is comparable to the one from CONCERTO (~ 70 $\mathrm{mJy.s^{1/2}}$, Hu et al. (2024)), but lower than NIKA2 (~ 9 $\mathrm{mJy.s^{1/2}}$ at 150 GHz, Perotto et al. (2020)), as expected. We can compare the result to what the GT camera predecessor, the MKID camera [Honda et al., 2023a], achieved in a 2021 commissioning run. The sensitivity of the MKID camera was estimated to be ~ 500 $\mathrm{mJy.s^{1/2}}$. The GT camera thus has a sensitivity about an order of magnitude better. This result shows that the LEKID array, together with the new readout system, are a great improvement and future optimisations of the camera will help improve the measurements even further.

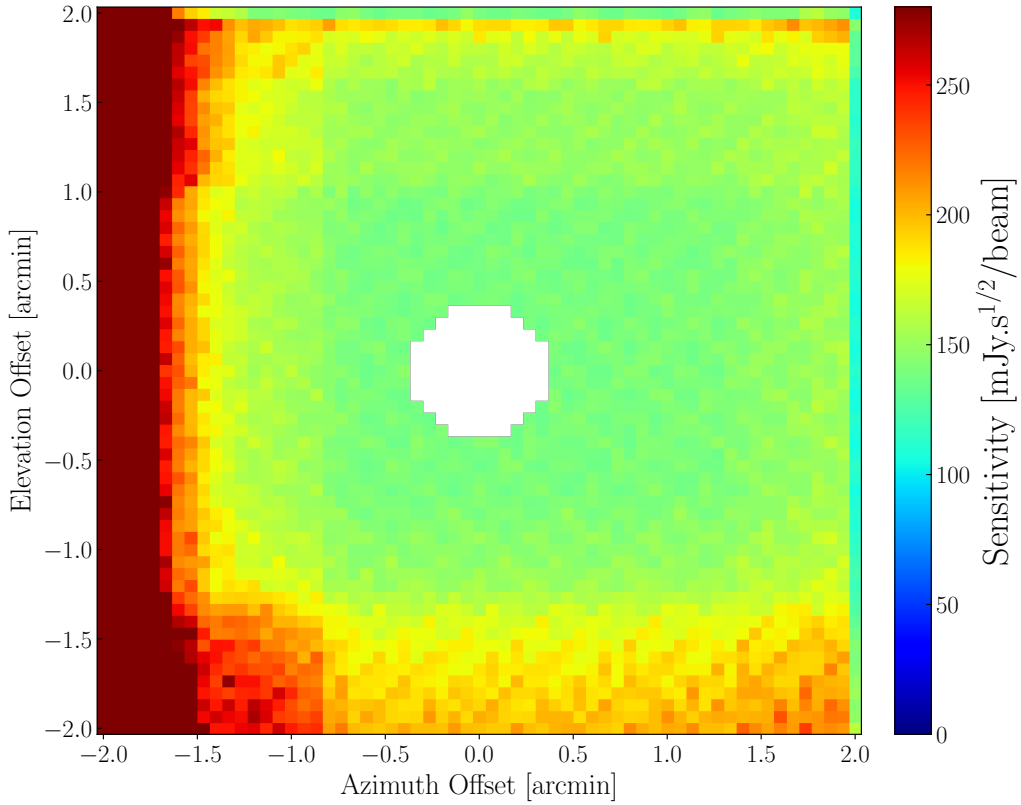

Figure 5.15: Sensitivity map obtained during the analysis of a Mars scan. The center region is masked to avoid biasing the NEFD estimation. We see that the sensitivity decreases on the edges of the map due to the lower integration time in these regions.

5.7 Conclusion and perspectives

The commissioning phase of a camera is crucial to characterize the performance of the instrument for future scientific observations. The GT camera commissioning, spanning seven nights and 50 hours of observations, was successful despite the challenging weather conditions. In this chapter, we have described the data reduction pipeline developed for the GT camera, which converts raw data into astrophysical maps. Its construction is necessary in order to exploit the observations scientifically. We have first compared the performance of three different calibration methods to convert the raw (I, Q) data to TOIs, showing that the phase calibration method is currently the most accurate.

These TOIs are dominated by atmospheric noise correlated between detectors, as well as an anomalous noise likely due to vibrations in the cryostat. After removing bad samples and bad detectors, we subtract a common mode estimated from the information of all working detectors to clean the TOIs from these correlated noise components. The cleaned TOIs are then projected onto a pixel grid to obtain individual maps per detector, which are then combined to yield a final combined map of the source.

The maps obtained following this procedure are then used to characterize the on-sky performance of the camera. We find a beam FWHM of 22.4 ± 2.5 arcsec, larger than the previous MKID camera as expected from simulations (see Section 3.5). From observations of Mars, we estimate a responsivity of 141.2 ± 33.5 Hz/K, which is lower than our expectations, but considering the weather conditions, the result is still promising. Finally, we measure the camera's sensitivity using two different methods, finding NEFD $\sim 150.81 \pm 44.29$ mJy.s$^{1/2}$/beam from the standard deviation map and NEFD ~ 66.1 mJy.s$^{1/2}$/beam from the white noise level. As the former is not very reliable when computed from bright point sources, we expect the latter to be a better estimate. Compared to the previous MKID camera [Honda et al.,

2023a], we improve the sensitivity by about an order of magnitude. These results are very promising, especially for observations of galaxy clusters which require high resolution and good sensitivity.

In Chapter 4, we reviewed the SZ observations that were conducted with the Nobeyama telescope. To estimate the potential of the GT camera for SZ science, we can compare its sensitivity to that of the previous observations. In Komatsu et al. (1999) and Kitayama et al. (2004), a 1σ noise level of ~ 1.6 mJy/beam was achieved after ~ 22.56 hours of integration time at 150 GHz. With the GT camera, we would require only about 28 minutes of integration time to reach the same noise level which is a great improvement.

Compared to the NIKA2 camera [Adam et al., 2016], which has been very successful for SZ cluster science, the GT camera is much less sensitive and requires more integration time. For example, for a galaxy cluster of mass $M_{500} = 6 \times 10^{14} M_{\odot}$ at redshift $z = 0.5$, NIKA2 can reach a 0.1 mJy noise level in 2.4 hours. With the GT camera's sensitivity, we would need 127 hours which is not feasible. With the current characteristics of the GT camera, we would thus only be able to observe the most massive clusters. However, cluster observations at 100 GHz are very valuable to detect radio sources in the field of view, which can contaminate SZ measurements at higher frequencies. Combined with the two bands of NIKA2 at 150 and 260 GHz, the GT camera would thus be a great complement to accurately measure the SZ effect in clusters.

To conclude, there are several improvements we can make to the GT camera to enhance its performance. First, a new LEKIDs array with a more homogeneous spacing between resonances would greatly help reduce the cross-talk and increase the number of working detectors per scan. Similarly, increasing the number of tones per 100 MHz the readout electronics can monitor (see Section 4.3.1) is a priority. Currently, about 50 out of 144 detectors cannot be monitored due to this limitation. We do note that increasing the frequency spacing between resonances would also mitigate this issue. The anomalous noise we discussed in Section 5.2.3 is also impacting our results and needs to be fully understood and removed before future observations. Finally, as shown in Section 4.4.2, the weather conditions during the observation campaign were terrible. A new campaign under better conditions, with the aforementioned improvements, would certainly yield much better results and show the capabilities of the GT camera for SZ science.

Part III

Detection and study of clusters with NIKA2

CHAPTER 6

NIKA2 and its Guaranteed Time Large Programs

6.1 NIKA2 . . . 105
6.1.1 The IRAM 30-m telescope . . . 105
6.1.2 The NIKA2 camera . . . 106
6.2 The NIKA2 SZ Large Program . . . 109
6.2.1 LPSZ cluster sample . . . 109
6.2.2 Scientific goals . . . 110
6.2.3 Up-to-date results . . . 111
6.2.4 Study of the hydrostatic mass bias with the LPSZ . . . 113
6.3 The N2CLS Large Program . . . 114
6.3.1 GOODS-North . . . 114
6.3.2 COSMOS . . . 116
6.3.3 Scientific goals . . . 118
6.3.4 Up-to-date results . . . 119
6.4 NIKA2: a powerful instrument to study the tSZ effect . . . 121
6.4.1 Very high resolution . . . 121
6.4.2 High sensitivity . . . 121
6.4.3 Dual-band capabilities . . . 122
6.5 Conclusion . . . 122

In this chapter, we present the NIKA2 instrument, installed at the IRAM 30-m telescope, and two of its Guaranteed Time Large Programs: the SZ Large Program (LPSZ), a follow-up of 45 galaxy clusters, and the NIKA2 Cosmological Legacy Survey (N2CLS), a deep and wide survey in the COSMOS and GOODS-N fields. The chapter begins with a description of the IRAM 30-m telescope and the technical characteristics of the NIKA2 camera. We then detail the scientific motivations, survey strategies, and sample selection for both the LPSZ and N2CLS programs.

6.1 NIKA2

6.1.1 The IRAM 30-m telescope

The NIKA2 camera is installed at the Institut de Radioastronomie Millimétrique (IRAM) 30-meter telescope, located in the Sierra Nevada, near Granada in southern Spain, at an altitude of nearly 2900 meters above sea level.

The telescope features a 30-meter diameter parabolic primary mirror constructed from aluminum and polyurethane panels. To mitigate temperature variations caused by sunrise and sunset, which induce deformations in the primary mirror, it is actively thermally stabilized and coated to reflect infrared radiation. A secondary mirror, 2 meters in diameter, is positioned at a distance of 10.5 meters from the primary mirror, corresponding to the focal length of the latter. The assembly is coupled to a Nasmyth cabin and installed on an alt-azimuth mount.

As discussed for the Nobeyama telescope in Chapter 4, the angular resolution of the IRAM telescope is primarily determined by the diffraction associated with the 30-meter aperture. This corresponds to 14.1 and 8.2 arcseconds for monochromatic signals at frequencies of 150 and 260 GHz, respectively. In practice, as the light is polychromatic, the angular resolution is lower during observations.

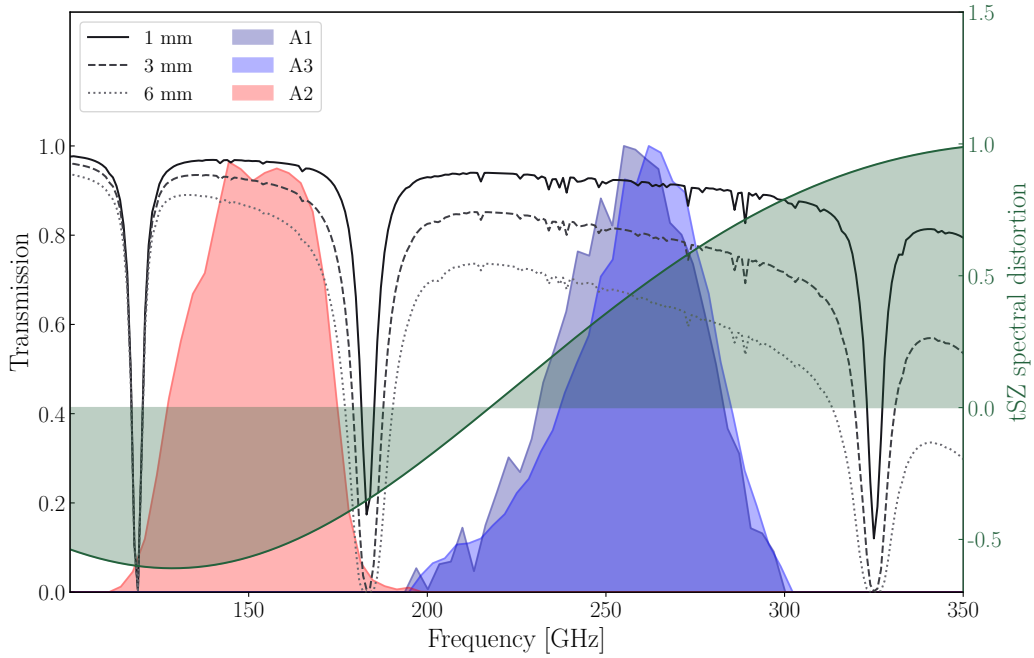

Figure 6.1: NIKA2 bandpasses at 150 GHz (red) and 260 GHz (blue). The atmospheric transmission for different PWV values is shown as grey lines. In green we present the spectral distortion due to the tSZ effect. Figure adapted from Kéruzoré (2021)

The Pico Veleta site was selected for its high altitude and relatively low humidity, as water vapor is the primary source of atmospheric noise in millimeter-wave observations. Figure 6.1 shows the variation in atmospheric transmission for different precipitable water vapor (PWV) values, from the model of Pardo et al. (2001). When temperatures rise, the atmosphere can hold more water vapor, meaning that optimal observation conditions are primarily found during winter. On average, the PWV at zenith is approximately 3 mm in winter, compared to 7 mm in summer. The commonly measured opacity (see Section 4.4.7), τ_{225}, at 225 GHz, has average values of 0.3 in winter and 0.5 in summer at this site.

The telescope's observable sky is limited to the northern celestial hemisphere. Objects with declinations below $-20°$ in equatorial coordinates never reach elevations greater than 30°. At such low elevations, the atmosphere traversed by incoming photons becomes excessively thick, leading to significant attenuation.

6.1.2 The NIKA2 camera

The New IRAM KID Array (NIKA2, Monfardini et al. (2014); Bourrion et al. (2016); Calvo et al. (2016a); Adam et al. (2018b)) is a dual-band millimeter camera composed of three arrays of KIDs

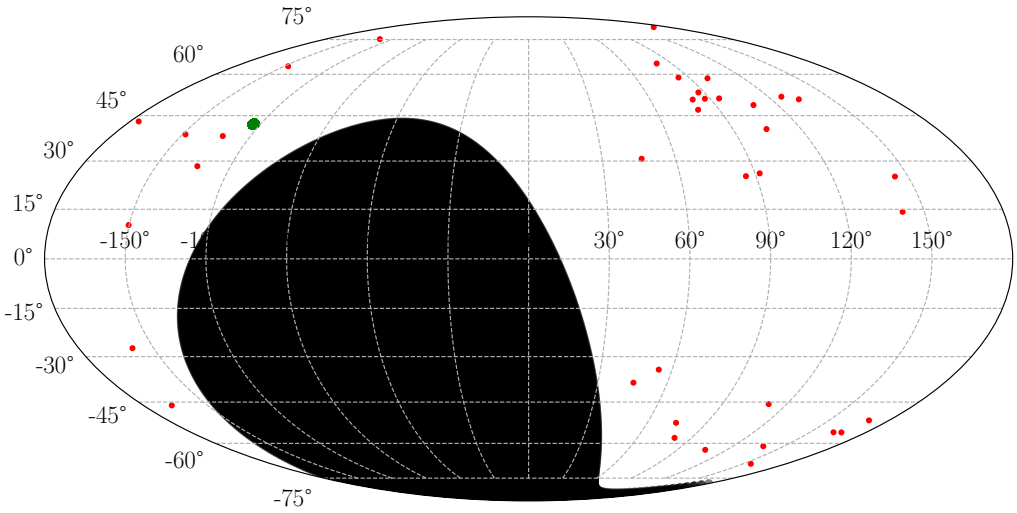

Figure 6.2: IRAM 30-m telescope sky coverage in galactic coordinates. The unaccessible region is shown in black, assuming a minimum declination of -20 degrees. The green region shows the COSMOS field, and the red dots the LPSZ clusters. The red dots are larger than the expected cluster sizes for visualization purposes.



Figure 6.3: Picture I took of the IRAM 30-m telescope in January 2023.

installed at the IRAM 30-m telescope. Compared to the Ti-Al KIDs of the GT camera presented in Chapter 3, NIKA2 KIDs are made of an aluminum layer only, with a critical temperature of $T_c = 1.19$K and gap energy $2\Delta = 0.36$ meV. Please refer to Chapter 3 for an in-depth description of KIDs and their working principle. Array A2 operates at 150 GHz (2 mm), while arrays A1 and A3 operate at 260 GHz (1.2 mm). A2 contains 616 KIDs of 2.8×2.8 mm^2, connected to four separate NIKEL_AMC electronic boxes [Bourrion et al., 2016]. A1 and A3 each contain 1140 KIDs of 2×2 mm^2, connected to eight NIKEL_AMC electronic boxes. Figure 6.1 shows the bandpasses for the three arrays, with A2 in red and A1/A3 in blue/dark blue, as well as the atmospheric transmission in shades of grey and the tSZ spectral distortion in green. The observing frequencies were defined to avoid atmospheric absorption lines (oxygen at 118 GHz and water vapor at 183 and 325 GHz). They are also particularly well adapted for studying the tSZ effect, enabling measurements both at its maximum decrement and in its positive part (near zero).

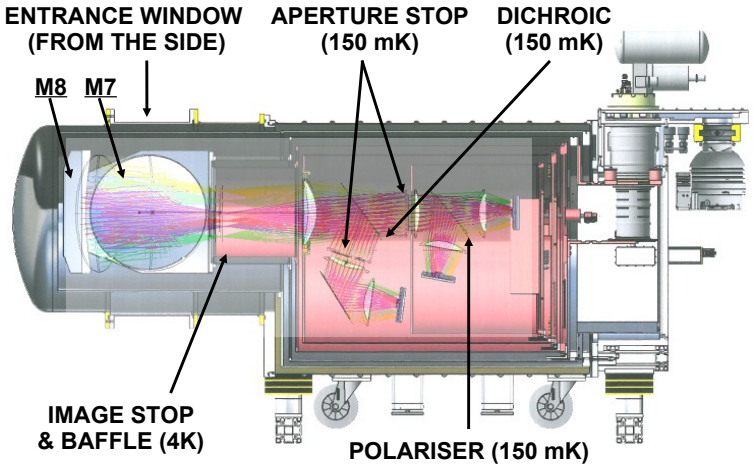

Figure 6.4: Cross-section of the NIKA2 camera illustrating the optical chain and the main elements. The dichroic and polariser, used for polarization measurements with the two 260 GHz arrays, are shown. The pulse tubes (top right of the cryostat) cool down the stages down to 4 K. Further cooling to 150 mK is performed using a dilution refrigerator (see Section 3.2.2). Figure taken from Adam et al. (2018b).

The optical system of NIKA2 and the IRAM telescope are quite similar to those of the GT array and the Nobeyama telescope described in Chapter 4. The main differences lie in the use of multiple arrays at different frequencies, and the polarization capabilities of NIKA2. A dichroic element (see Figure 6.4) splits the incoming light in two, with one part going to the 150 GHz array and the other passing through a polarizer before reaching the two 260 GHz arrays. In this thesis, data from the two 260 GHz arrays are combined, and the polarization capabilities of NIKA2 are not exploited.

We present the main characteristics of the NIKA2 camera in Table 6.1. These measurements were performed during the commissioning phase of the instrument [Perotto et al., 2020]. The commissioning observations were similar to those presented in Chapters 4 and 5. The angular resolution of NIKA2 is 17.6 and 11.1 arcseconds at 150 and 260 GHz, respectively, slightly larger than the theoretical values (see Section 6.1.1). The camera is very sensisitive, with a NEFD of 9 and 30 mJy.s$^{1/2}$ at 150 and 260 GHz, respectively. We will see in more details in Section 6.4 why NIKA2 is a particularity well suited instrument for the work presented in this thesis.

	A2 (150 GHz)	A1 and A3 (260 GHz)
Reference wavelength [mm]	2.0	1.15
Bandwidth [GHz]	40.7	49.2 and 48.0
Number of designed detectors	616	1140
Fraction of valid detectors [%]	90	84
FWHM [arcsec]	17.6 ± 0.1	11.1 ± 0.2
Reference FWHM [arcsec]	18.5	12.5
Field of view [arcmin]	6.5	6.5
rms pointing error [arcsec]	< 3	< 3
Absolute calibration uncertainty [%]	5	5
NEFD [mJy $s^{1/2}$]	9 ± 1	30 ± 3
Mapping speed [$arcmin^2$ mJy^{-2} h^{-1}]	1388 ± 174	111 ± 11
Conversion factor y-Jy $beam^{-1}$	-11.9 ± 0.9	3.7 ± 0.4

Table 6.1: Summary of the main characteristics of the NIKA2 instrument. We give the values found in Perotto et al. (2020) and Ruppin et al. (2018).

6.2 The NIKA2 SZ Large Program

The NIKA2 Sunyaev Zel'dovich Large Program (LPSZ) is one of the five large programs of the NIKA2 collaboration. Out of the 1300 hours awarded to the collaboration, 300 hours were allocated to the LPSZ.

6.2.1 LPSZ cluster sample

The observing time allocated to the LPSZ was distributed among a sample of 45 galaxy clusters. The sample spans a wide range of masses ($M_{500} \in [3, 11] \times 10^{14}\, M_\odot$) at high redshifts ($z \in [0.5, 0.9]$), with clusters selected from the *Planck* [Planck Collaboration et al., 2016c] and ACT [Hasselfield et al., 2013] catalogs. To ensure a uniform coverage of the mass-redshift plane, it was divided into ten bins, with two redshift intervals and five mass intervals. Five clusters were randomly selected from each bin, using the ACT catalog for low-mass bins and the *Planck* catalog for the others. The mass estimates used for this distribution were based on the integrated SZ signal measured by the surveys, and calibrated with the scaling relation from Arnaud et al. (2010) (nicknamed A10 in the following). Figure 6.5 shows the distribution in the $z - Y_{500}$ plane of the LPSZ sample, with the initial selection of 10 ACT and 35 *Planck* clusters. We see that the highest mass, highest redshift bin is only filled with one cluster, as there were no other suitable clusters at the time. The stars indicate clusters not included in the final analysis, either because they were a false detection or because they were too close to the declination limit of the telescope. Three additional clusters were later selected to replace false detections. A priority was given to clusters with associated X-rays observations, either with the XMM-*Newton* or *Chandra* satellite. Figure 6.2 shows the IRAM telescope's coverage, with the final 38 LPSZ clusters shown as red dots.

As mentioned before, 300 observation hours were awarded to the LPSZ program. The time allocated to each cluster was calculated to achieve a S/N = 3 for the SZ surface brightness profile at the characteristic radius R_{500}, using the following assumptions:

- The pressure profile of each cluster follows the UPP from A10
- The masses M_{500} are those provided in the *Planck* and ACT catalogs, derived using the scaling relation from A10
- The NIKA2 expected performance at the time of building the sample

Deviations from these assumptions could affect the expected signal quality. As a result, the overall quality of NIKA2 observations of the sample might be lower than expected. The 300 hours of observations have been completed, with the last observations in February 2023. As discussed before, the final LPSZ sample consists of 38 clusters, observed homogeneously to ensure that the analysis is not biased towards clusters with higher S/N.

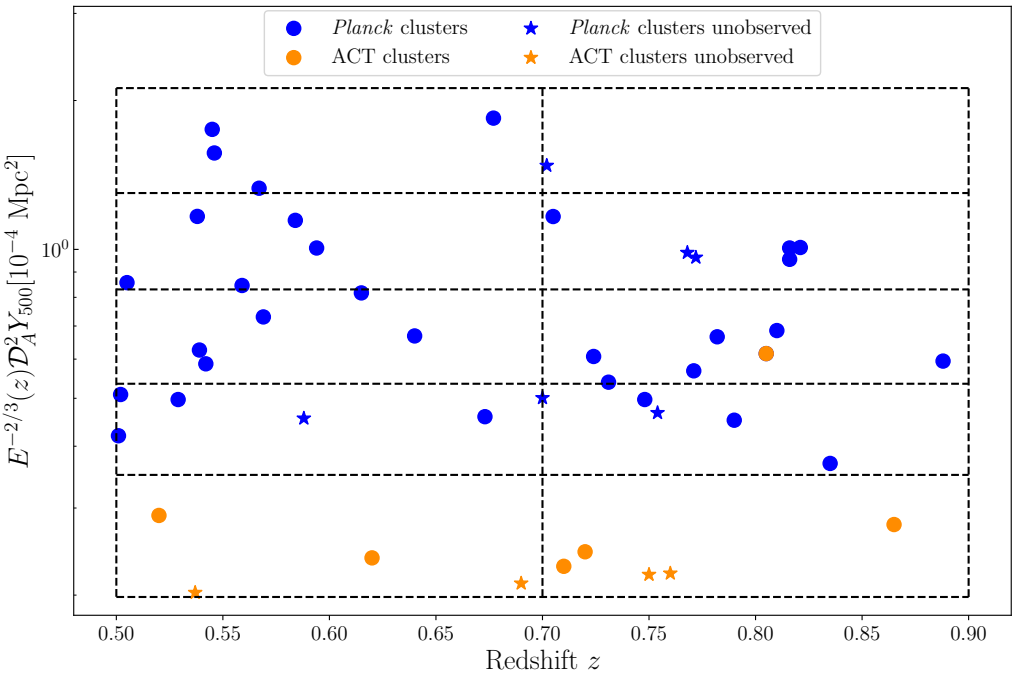

Figure 6.5: Distribution of the LPSZ cluster sample in the five bins in integrated Compton parameter and two in redshift. The blue and orange points represent clusters from the *Planck* and ACT catalogs, respectively. Stars of the same color indicate clusters which are not in the final analysis. Figure adapted from Hanser (2025)

6.2.2 Scientific goals

Mean pressure profile

One of the primary objectives of the LPSZ program is to measure the mean pressure profile of high-redshift galaxy clusters. The universal profile derived by Arnaud et al. [Arnaud et al., 2010], based on the analysis of the REXCESS X-ray sample at $z < 0.2$, has been widely used in constructing several SZ cluster catalogs, notably by the ACT [Hilton et al., 2021] and *Planck* [Planck Collaboration et al., 2016c] collaborations. However, these catalogs include clusters at redshifts significantly higher than 0.2, the maximum redshift of the REXCESS sample. If pressure profiles evolve with redshift, the UPP may not be representative of the mean pressure profile at higher redshifts. This redshift dependecy has yet to be confirmed.

The LPSZ aims to provide an estimate of the mean pressure profile at higher redshift ($0.5 < z < 0.9$) and thus better adapted for other tSZ based surveys and their cosmological analyses. Indeed, as shown in Ruppin et al. (2019b), a 15% difference in the amplitude of the pressure profile can significantly alter the final cosmological constraints.

Thermodynamical analysis

The LPSZ will not only study the pressure of clusters, but also their temperature and entropy which are essential to unveil cluster thermodynamic history. The shape of the entropy profile can be used

to distinguish between different populations: relaxed (or *cool-core*) and disturbed clusters. Traditionally, deep spectroscopic X-ray observations are used to derive thermodynamical properties. However, combining resolved SZ and X-ray observations will aleviate the need for spectroscopic measurements, which in turn will greatly shorten the time needed to derive these properties.

$Y - M$ scaling relation

Another key objective of the LPSZ is to refine the scaling relation between the tSZ observable, the integrated Compton parameter Y, and cluster mass. Accurate estimates of the parameters of this relation are vital for cosmological studies using large surveys. Existing scaling relations, often based on low-redshift ($z < 0.5$) cluster samples and X-ray-derived masses [Arnaud et al., 2010; Planck Collaboration et al., 2011b], may not fully represent the tSZ cluster samples currently available.

To study potential evolutions in the scaling relation using the LPSZ sample, it is essential to determine the hydrostatic masses of the clusters. As discussed previously in Chapter 2, the SZ effect alone does not allow for direct measurement of cluster mass. However, it can be estimated through the combination of SZ and X-ray data, which is why clusters with complementary XMM-*Newton* and *Chandra* observations were given priority.

Point sources in the LPSZ cluster fields

As we will see in Chapter 6, the LPSZ enables the detection of point sources in the cluster fields, which can be used to study the properties of galaxies within a cluster, as well as the impact of gravitational lensing on background galaxies. An important product of the LPSZ will be a catalog of point sources detected at 150 and 260 GHz, essential both for the study of the galaxy population around clusters and the estimation of the clusters' thermodynamical properties.

6.2.3 Up-to-date results

Since the beginning of the LPSZ observations in October 2017, several analyses of individual clusters part of the sample have been published.

Pilot study with NIKA

A pilot study was conducted using the NIKA camera, NIKA2's prototype installed from 2012 to 2015 at the IRAM 30-m telescope. A total of six clusters were observed as part of this study[1]. The first observation of the tSZ effect with NIKA was of the RX J1347.5-1145 cluster [Adam et al., 2014], which had also been observed with the Nobeyama 45-m telescope (see Chapter 4). This first map is shown in the left panel of Figure 6.6. These observations demonstrated NIKA's capabilities for high-resolution tSZ mapping. The pressure distribution of the CL J1226.9+3332 cluster was also studied [Adam et al., 2015; Romero et al., 2018], and its mass derived from a combination of SZ and X-ray data. The result, $M_{500} = 5.96^{+1.02}_{-0.79} \times 10^{14}\ M_{\odot}$, is in good agreement with other estimates in the literature. A similar analysis was conducted for the PSZ1 G045.85+57.71 cluster [Ruppin et al., 2017], which showed that it was a cool-core cluster.

The impact of point source (sub-millimeter and/or radio sources) contamination was the focus of the analysis of the MACS J1423.8+2404 cluster [Adam et al., 2016]. This study highlighted the importance of identifying and characterizing point sources in order to set strong constraints on the pressure profile of clusters. A major part of Chapter 7 will be dedicated to this topic.

Additional studies of the tentative mapping of the kinetic SZ effect (see Chapter 2) and of the hot gas temperature in MACS J0717.5+3745 were also conducted [Adam et al., 2017b; a]. The

[1] Public release available at https://lpsc.in2p3.fr/NIKA2LPSZ/nika2sz.release.php

former revealed the challenges of measuring the kSZ effect, which can only be detected in clusters or substructures with extreme velocities along the line-of-sight. The latter showed that the hot gas temperature can be derived from a combination of tSZ and X-ray imaging data, without relying on X-ray spectroscopy. Finally, Adam et al. (2018a) presented the detection of substructures and mergers in clusters observed with NIKA, and demonstrated that high-resolution tSZ observations can be used to study the dynamical state of clusters.

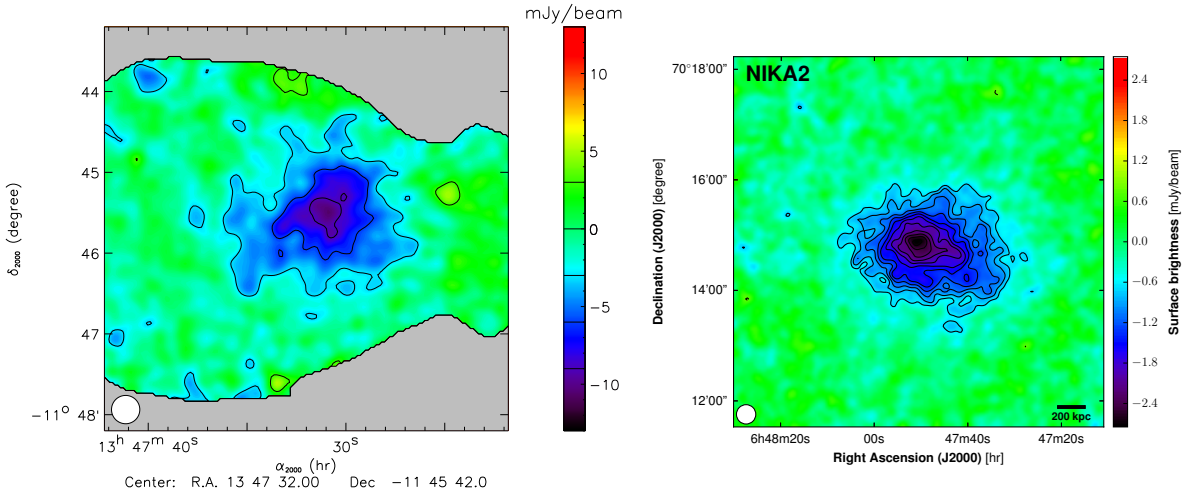

Figure 6.6: First tSZ maps of a cluster with NIKA and NIKA2. (Left): NIKA 140 GHz map of RX J1347.5-1145 extracted from [Adam et al., 2014], where the central radio source has been subtracted. This map can be compared to the map obtained by Komatsu et al. (1999) (see Figure 4.2, in Chapter 4). (Right): NIKA2 150 GHz map of PSZ2 G144.83+25.11 taken from [Ruppin et al., 2018]. The black contours show the significance of the signal, starting at $3\,\sigma$ with steps of $1\,\sigma$. For visualization purposes, both maps have been smoothed with a Gaussian 2D kernel of 10″.

First tSZ mapping of a LPSZ cluster with NIKA2

The first cluster of the LPSZ sample to be observed with NIKA2 was PSZ2 G144.83+25.11 at $z = 0.58$. The 150 GHz map is shown in the right panel of Figure 6.6. One of the main features of this cluster is a thermal pressure excess in its south-west region discovered in the NIKA2 data. A complete characterization of the pressure distribution of the cluster was performed, combining NIKA2, BOLOCAM, MUSTANG, and *Planck* data. The analysis showed that the identified over-pressure region significantly impacts the pressure profile and other derived quantities, such as the mass M_{500} and the integrated Compton parameter Y_{500}. After masking the disturbed region, the M_{500} and Y_{500} values were found to deviate from the unmasked values by 65% and 79%, respectively. This first analysis of a LPSZ cluster showed the importance of high-resolution tSZ observations to assess the impact of morphology of clusters on the $Y_{500} - M_{500}$ scaling relation (see Section 6.2.2).

A challenging case: ACT-CL J0215.4+0030

The second cluster of the LPSZ sample to have been analyzed was ACT-CL J0215.4+0030 [Kéruzoré et al., 2020]. It is a low-mass, $M_{500}^{\rm ACT} = 3.5 \times 10^{14}\ M_\odot$, and high-redshift, $z = 0.865$, cluster, one of the most distant in the sample. The analysis of this cluster was challenging because of its low mass and thus faint signal ($8.5\,\sigma$ detection of the SZ peak) and the contamination by point sources. Indeed, observations showed that the cluster is very compact and faint, and a point source located near its center could greatly impact the analysis if not properly accounted for. Similarly to previous studies, the NIKA2 data were combined with ACT and XMM-*Newton* data to derive the cluster's thermodynamical properties. The results on the mass and integrated Compton parameter, $M_{500} = 3.79 \pm 0.58 \times 10^{14}\ M_\odot$ and $Y_{500} = 3.76 \pm 0.39 \times 10^{-5}$ Mpc^2, were found to be in good agreement with the values provided by ACT

and XMM-*Newton*, and with smaller uncertainties. This analysis demonstrated that the techniques developed for the LPSZ are effective even for low-mass, high-redshift clusters in the sample, and also led to the development of the panco2 software [Kéruzoré et al., 2023]. panco2 is designed to estimate the pressure profile of clusters from SZ maps, which we will discuss in the next chapter.

Disturbed clusters

In Artis et al. (2022), the authors presented the study of a massive highly disturbed cluster, PSZ2 G091.83+26.11. This cluster shows a morphology characteristic of a merger event, with two main substructures in the NIKA2 150 GHz map. The Mach number of the potential merger shock was computed, and found to be consistent with what is expected for such an event. To derive the pressure profile of the cluster, two models were considered: one assuming a single spherical cluster, and another considering two sub-halos. The resulting profiles were found to be compatible, and the complete thermodynamical analysis should soon be published [Artis, in prep.].

Another disturbed cluster in the sample is ACT-CL J0240.0+0116, presented in Paliwal et al. (2025). This cluster is not an extreme case like PSZ2 G091.83+26.11, but still shows signs of disturbance, such as the misalignement of the Brightest Cluster Galaxy (BCG) and the center of the halo, and tail-like features in the X-ray data. In addition to the usual thermodynamical study, the authors also investigated for the first time the dynamical state of the cluster using different morphological parameters. The asymmetry, centroid shift, offset of the BCGs, and others were computed from both NIKA2 and XMM-*Newton* data, and compared to simulations to determine the probability of the cluster being disturbed $P_{\rm dis}$. It was shown that $P_{\rm dis} > 90\%$, confirming its disturbed nature. The mass estimation thus suffers from larger uncertainties which will need to be accounted for when calibrating the LPSZ $Y_{500} - M_{500}$ scaling relation.

LPSZ twin samples in simulations

In order to assess how the dynamical state of clusters and other physical processes could impact the final results of the LPSZ, the collaboration created twin samples in hydrodynamical simulations. A twin sample consists of simulated clusters, with known true profiles, in a similar redshift and mass range as the LPSZ sample, and with similar morphological properties. A first twin sample was created using the simulation MUltidark SImulations of galaxy Clusters (MUSIC, see Sembolini et al. (2013) for details). Ruppin et al. (2019a) used this sample to study how ICM disturbances could impact the mean pressure profile (see Section 6.2.2) and the scaling relation. The simulated sample contains an almost equal number of relaxed and disturbed clusters to compare the two types and better understand their impact. It was shown that the scatter on Y_{500} for disturbed clusters is seven times as large than that of the relaxed subsample. The NIKA2 tSZ pipeline run on the mock clusters was able to reconstruct the mean pressure profile with great accuracy, and highlights a $> 2\,\sigma$ difference in the profile between the two populations.

A series of twin samples were also obtained from the `The Three Hundred` project [Cui et al., 2018]. They were used to study the impact of projection effects on integrated quantities Y and M, as well as to build 3D $Y - M$ scaling relations [Paliwal et al., 2024].

6.2.4 Study of the hydrostatic mass bias with the LPSZ

The cluster masses we have discussed so far are hydrostatic masses, $M_{\rm HSE}$, based on the assumption that clusters are in hydrostatic equilibrium (HSE). However, it has been shown that masses reconstructed under this hypothesis are biased low compared to the true mass of clusters. This hydostratic mass bias, denoted b or $b_{\rm HSE}$, could be a key element to explain the tension on cosmological parameters derived from cluster number count (which rely on the HSE mass) and primary CMB anisotropies.

The LPSZ sample and its twin samples have been used to study this bias. In Gianfagna et al. (2021), the authors first estimated b by comparing the X-ray/SZ HSE mass and the true dynamical mass for a set of 260 clusters. The same analysis was done for the LPSZ twin sample of 32 clusters, and the results were found to be compatible, with a bias of about 20%.

In Ferragamo et al. (2022), a comparison between the HSE and lensing masses of the PSZ2 G144.83+25.11 cluster was done to estimate the HSE-to-lensing mass bias. Under the assumption that lensing masses are unbiased estimates of the true mass, then the HSE-to-lensing bias is a good approximation of the HSE bias. Lensing data from the CLASH survey [Postman et al., 2012] were used to derive the lensing mass profile. Different estimates of the HSE masses were obtained using different assumptions, such as masking or not the over-pressure region (see Section 6.2.3). The HSE-to-lensing bias was found to be between ~ 0.6 to ~ 1, i.e., $b_{\rm HSE/lens} \sim 0$ to ~ 0.4, from the different estimates. Putting aside the discrepancy between the different mass values due to the cluster's nature, the results show that HSE masses are overall smaller than the lensing mass.

Muñoz-Echeverría et al. (2023) performed a similar study fo the CL J1226.9+3332 cluster. The authors first show that the uncertainties on the NIKA2 HSE mass estimate are dominated by assumptions on the model, and not by data processing or instrumental effects. The comparison with lensing data shows that the X-ray only HSE mass is much smaller, with $1 - b_{\rm HSE/lens} = 0.66 \pm 0.14$, whereas the SZ+X-ray mass is in better agreement, with $1 - b_{\rm HSE/lens} = 0.86 \pm 0.20$. Further investigations on the HSE bias with the final LPSZ sample will be conducted for the final LPSZ results.

Final LPSZ results

The LPSZ observations were completed in January 2023, and, at the time of writing this thesis, the final results are expected to be published in the following months. A first overview of the results was presented by Corentin Hanser [Hanser, 2025]. He optimized the standard LPSZ data reduction pipeline used in previous analyses to produce the (almost) final maps shown in Figure 6.7. Several studies are currently being finalized, including the LPSZ mean pressure profile [Hanser, in prep.(b)], the $Y - M$ scaling relation [Moyer-Anin, in prep.], and the thermodynamical analysis [Hanser, in prep.(a)] of the full sample. As we will see in details in the next chapter, the study of point sources in the cluster fields is also being prepared [Désert, in prep.]. Following the publication of the final results, the LPSZ data products (maps, profiles, etc.) will be made public.

6.3 The N2CLS Large Program

The NIKA2 Cosmological Legacy Survey (N2CLS) large program acquired 300 hours of observations distributed between the GOODS-N and COSMOS fields. The main goal of the survey is to study dust-obscured galaxies up to very high redshift, but we will see in Chapter 7 that the detection of galaxy clusters via the tSZ effect is also possible. The observations started in October 2017 and ended in January 2023, under project ID 192-16.

6.3.1 GOODS-North

The GOODS-North field (GOODS-N hereafter) is one of the most studied regions in the sky for extragalactic astronomy. It was chosen because it has very little foreground emission from our galaxy and already has extensive multiwavelength data. GOODS-N has been observed in a wide range of wavelengths, from X-rays to radio, with both space and ground-based experiments such as JWST, HST [Williams et al., 1996; Giavalisco et al., 2004; Grogin et al., 2011], Chandra, Spitzer, Herschel [Elbaz et al., 2011], Keck, Subaru, CFHTLS, VLA [Morrison et al., 2010], ALMA, and many others. Figure 6.8 shows the coverage of the GOODS-N field at different wavelengths, along with the NIKA2 coverage.

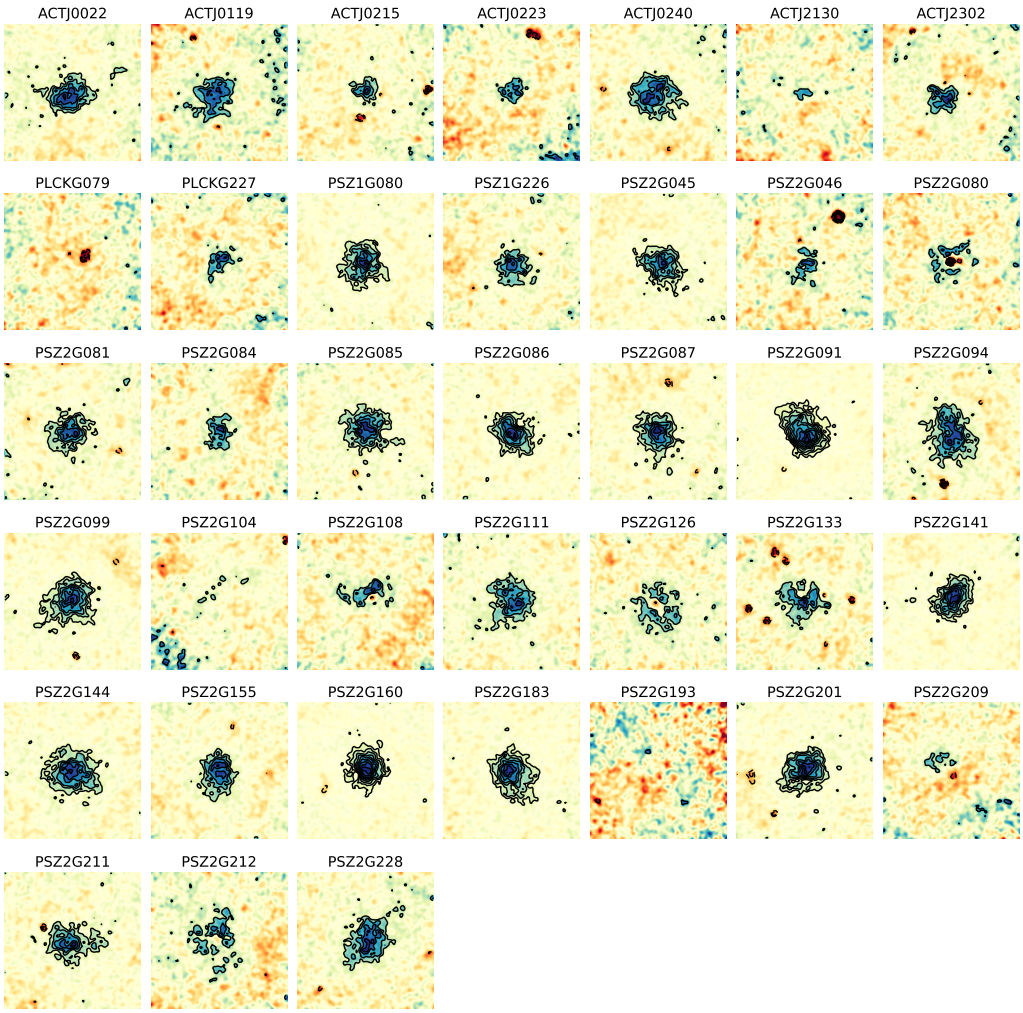

Figure 6.7: 150 GHz maps of the 38 clusters part of the final NIKA-LPSZ sample. The black contours show SNR levels, starting at $\pm 3\,\sigma$ with steps of $\pm 2\,\sigma$. Some clusters show no sign of any SZ decrement at the center, which could indicate that they were false detections to begin with. Figure adapted from Hanser (2025).

The N2CLS observations of the GOODS-N field covered an area of ~160 arcmin^2, designed as a narrow and deep survey. Two groups of $12.0' \times 6.3'$ and $6.5' \times 12.3'$ scans were performed, centered on (R.A., Dec.)$_{J2000}$ = (12h36m55.03s, +62d14m37.59s). The two groups of scans were executed at speeds of 40 and 35 $''$ /s, at position angles of -40 and -130 degrees in the RA-DEC coordinate system of the telescope [Bing et al., 2023]. A total of 86.15 hours of observations were dedicated to this field, between October 2017 and May 2021. The final GOODS-N maps reach noise levels of 0.047 mJy/beam and 0.17 mJy/beam at 150 and 260 GHz, respectively. This is within a factor 2 of the source confusion limit at 260 GHz [Ponthieu et al., 2025]. A comparison of the N2CLS depth with other submm surveys is given in Table 6.2. The GOODS-N data are not used in this thesis.

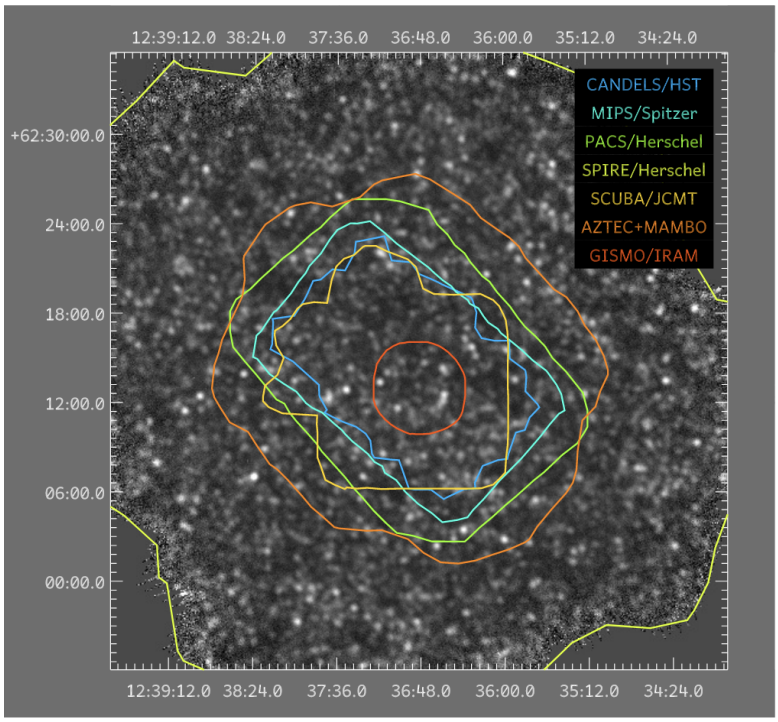

Figure 6.8: Selection of existing surveys in GOODS-N. The NIKA2 deep field covers the same area as the CANDELS survey in blue. Credit: D. Liu.

6.3.2 COSMOS

The COSMOS field is particularly well adapted to study high-redshift galaxies as it is widely visible, and also uncontaminated by bright X-ray, UV and radio sources as well as massive tSZ clusters. The field has been thoroughly observed by both space and ground-based experiments such as the JWST, XMM-Newton [Finoguenov et al., 2007], HST [Koekemoer et al., 2007; Grogin et al., 2011; Skelton et al., 2014], Chandra [Civano et al., 2016], Spitzer [Sanders et al., 2007], GALEX [Zamojski et al., 2007], Herschel [Oliver et al., 2012; Lutz et al., 2011], Keck, Subaru, ESO-VLT, CFHTLS telescopes and others [see Scoville et al., 2007]. This wealth of data enabled the assembly of cluster catalogs in COSMOS, which will be described in Chapter 7.

The N2CLS data set of the COSMOS field corresponds to a total of 195 hours of observations carried out from October 2017 to January 2023. Two groups of $27.0' \times 34.7'$ and $35.0' \times 28.0'$ raster scans, centered on (R.A., Dec.)$_{J2000}$ = (10h00m28.81s, +02d17m30.44s), were executed for a total area of ~ 1400 arcmin^2. The two groups of scans were performed with a speed of 60 $''$ /s at position angles of 0 and 90 degrees [Bing et al., 2023]. We reach a 1σ depth of 0.09 mJy/beam and 0.3 mJy/beam at 150 and 260 GHz, respectively (see Table 6.2 for a comparison with other surveys).

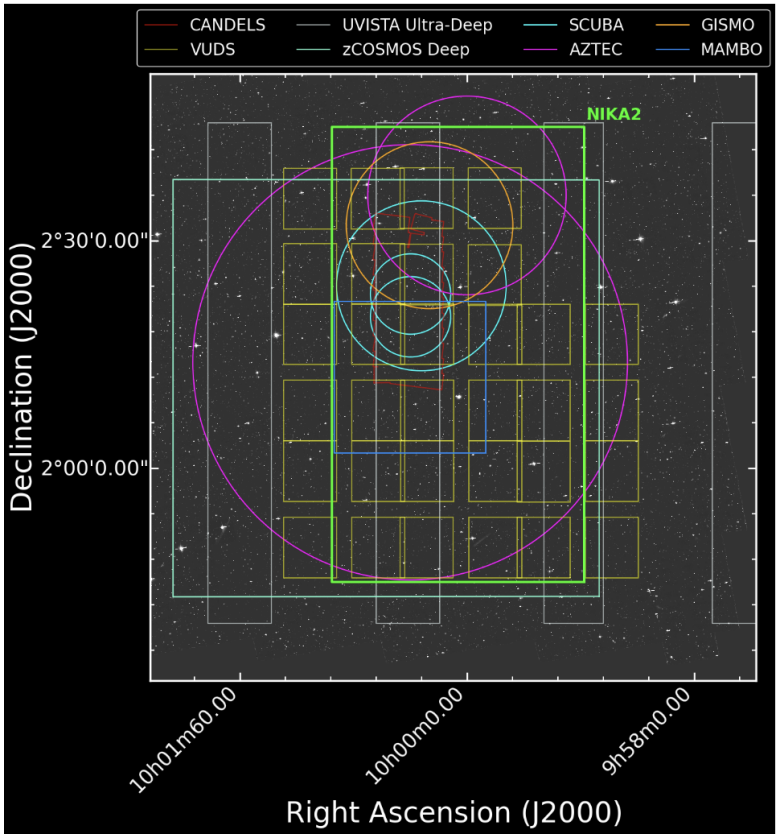

Figure 6.9: Selection of existing surveys in COSMOS. The N2CLS footprint is shown in green. Credit: B. Ribeiro.

Field	Survey	ν_{obs} GHz	Area arcmin^2	rms mJy/beam	References
GOODS-N	AzTEC/JCMT	273	245	0.84	Perera et al. (2008)
	SCUBA2/JCMT	353	140	0.16	Cowie et al. (2017)
	GISMO/30m	150	31	0.14	Staguhn et al. (2014)
	N2CLS	150	159	0.047	Béthermin et al. (2025)
	N2CLS	255	159	0.17	Béthermin et al. (2025)
COSMOS	AzTEC/ASTE	273	2592	1.00	Aretxaga et al. (2011)
	MAMBO/30m	255	400	1.00	Bertoldi et al. (2007)
	S2COSMOS/JCMT	353	5760	0.47	Simpson et al. (2019)
	GISMO/30m	150	250	0.23	Magnelli et al. (2019)
	N2CLS	150	1100	0.09	Béthermin et al. (2025)
	N2CLS	255	1100	0.3	Béthermin et al. (2025)

Table 6.2: Summary of single dish (sub)mm continuum observations in GOODS-N and COSMOS. The first column indicates the field, the second the instrument/telescope names, the third the observing frequency, the fourth the area covered by the survey, the fifth the rms noise level and the last column gives references for each survey. We give the values found in Bing et al. (2023) and Béthermin et al. (2025).

6.3.3 Scientific goals

The N2CLS program was optimized to answer some of the open questions of dusty star formation at high redshift.

Probe dusty star-forming galaxies at high redshift (z $\gtrsim$ 3)

NIKA2 is a powerful instrument that can measure the star formation rate (SFR) of normal galaxies at high redshift ($z > 2.5$), a key period for understanding how galaxies grow. With its sensitivity, NIKA2 can detect galaxies with high infrared luminosity at $z \sim 1.5$ and above, which make up most of the star formation at these times. It is also able to study galaxies with lower masses and SFRs than previous surveys. By observing many galaxies, N2CLS helps to find out if most galaxies at high redshift formed stars in the same way as those in the nearby universe, or if starbursts were more important.

SFR density at high redshift

Most current studies of star formation in the early Universe at $z > 3.5$ use galaxies found in UV light. However, this approach misses many massive galaxies that are hidden by dust, since dust blocks UV light. As a result, these studies do not give a complete view of star formation at high redshift. Observing at (sub-)millimetre wavelengths is needed to find these dusty galaxies. The N2CLS survey is important because it can detect normal galaxies at $z > 3$, which are still not well known. For galaxies that are too faint to detect individually, stacking methods using UV-selected samples or Lyman-break galaxies (LBGs) can help measure how much dust is present and whether these galaxies are the main source of star formation at $z > 3$.

Clustering of dusty star-forming galaxies

The large number of sources expected to be detected by N2CLS in the COSMOS field at 260 GHz (over 1100 at $z > 2$) will allow measurement of the 2-point auto-correlation function, which is used to study how galaxies are clustered. These measurements will help to understand how the properties of galaxies relate to the properties of the dark matter halos they live in, and will provide information about the mass scale where star formation is most efficient. By having a large sample of millimeter galaxies in one field, it will also be possible to study how clustering changes with redshift. These results will provide important constraints for theoretical models of galaxy evolution in the Universe.

Confusion noise limit

The confusion noise, defined as the background surface brightness fluctuations below which sources cannot be detected individually, is a key parameter of the performance of extragalactic deep fields [Ponthieu et al., 2025]. N2CLS has provided the first measurement of the confusion noise limit at the IRAM-30m telescope.

Blind detection of galaxy clusters

The N2CLS program has conducted the first wide survey at sub 20 arcsec angular resolution in the (sub)mm domain. The sensitivity and resolution of NIKA2 allow for the detection of galaxy clusters via the tSZ effect, especially at low mass and high redshift. This prospect is an important part of the work presented in this thesis, as we will see in Chapter 6.

6.3.4 Up-to-date results

Preliminary study using NIKA2 science verification data

As part of the NIKA2 science verification phase, Bing et al. (2024) observed a small area of 185 arcmin^2 for about 3.5 hours, centered on a lensed galaxy at very high redshift, $z = 5.24$. Four dusty star-forming galaxies (DSFGs) identified in this initial survey with high SNR were selected for follow-up observations with the NOEMA interferometer. From these observations, the millimeter spectra of each source were extracted and their redshift estimated via different methods. All sources were found to be at $z > 3$, with two very close sources both at $z = 5.2$. This could hint at a possible overdensity of DSFGs at $z = 5.2$, which was later investigated (see Section 6.3.4). This first study showed the potential of the developed method to accurately estimate the redshift of sources detected in the N2CLS maps.

Galaxy number counts

The first results of the N2CLS survey were presented in Bing et al. (2023), with the data acquired up to May 2021. At that time, the GOODS-N observations were completed, but only ~ 50% of the COSMOS data had been acquired. Still, the survey was already the deepest and largest ever made at both 150 and 260 GHz. Taking into account the effects of flux boosting, as well as the completeness and purity of the N2CLS sample computed from simulations, the authors found a total of 120 and 195 sources at 260 GHz and 67 and 76 sources at 150 GHz in the GOODS-N and COSMOS fields, respectively. The sample is pure at the 80% level. From these detections and their accurate photometry, they derived the source number counts for both frequencies as shown in Figure 6.10. The galaxy number counts (red and orange solid lines for COSMOS and GOODS-N, respectively) are lower than the source counts because of the blending effect of sources inside the NIKA2 beam [Béthermin et al., 2017]. The results are in good agreement with previous measurements from single-dish and interferometric surveys.

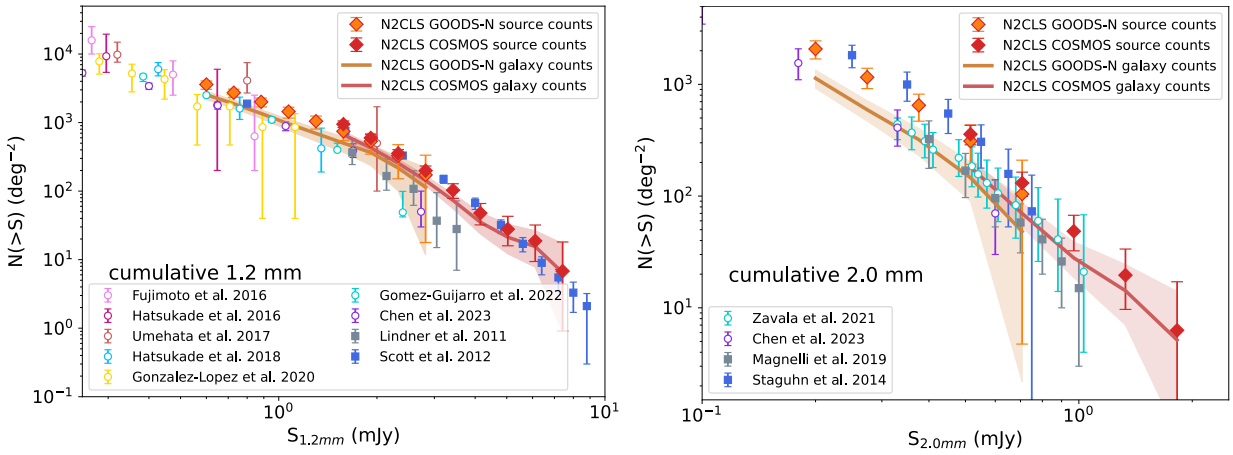

Figure 6.10: Comparison between the N2CLS cumulative source number counts at 260 GHz (left) and 150 GHz (right) with results from the literature. The COSMOS and GOODS-N number counts are shown separately as red and orange diamonds, respectively. The galaxy number counts is shown as a solid line and a shaded region following the same color code. Figure extracted from Bing et al. (2023).

High-redshift galaxies in GOODS-N

A thorough study of the sources in the GOODS-N field was performed in Berta et al. (2025). The catalog, called N2GN, consists of 71 sources, with 65 extracted from the Bing et al. (2023) catalog, using a 95% purity threshold (S/N >4.2), and 6 others from NOEMA observations performed

by other teams. To fully characterize the N2GN sample, we obtained multi-wavelength data, from radio observations (VLA), X-ray (*Chandra*), other (sub)mm instruments (SCUBA2, NOEMA, JCMT, SMA), infrared (*Spitzer*, *Herschel*), and finally optical surveys (*Hubble*, *JWST*, and others). The N2GN sources were then cross-matched with these catalogs, and their redshift obtained from the literature. The median redshift of the catalog is $z = 2.819$, with a clear overdensity at $z = 5.2$, as already hinted at in Bing et al. (2024).

The spectral energy distribution (SED) of each source was fitted using eight different methods, to derive a robust estimate of the dust mass, the infrared luminosity, and the stellar mass. An important result was the discovery of several high-z galaxies with very high stellar masses, $M_* > 10^{11}\ M_\odot$, at $z > 4$, which would contradict current galaxy formation models. However, only future observations with JWST can confirm these results. The dust mass function obtained from the N2GN sample was found to be consistent with previous studies. Finally, the dust mass density was computed up to $z \sim 7$ for the first time. The comparison with other literature estimates, as well as model predictions, shows that there is no consensus on the cosmic evolution of dust. Deeper and larger surveys will be needed in order to better understand what is truly going on.

Using the N2GN catalog, Lagache et al. (2025) further investigated the $z = 5.2$ overdensity in GOODS-N. Using NOEMA observations, a new massive DSFG is identified in this region for a total of 10 DSFGs at $z = 5.2$. Only three of these sources had been previously identified [Sun et al., 2024; Herard-Demanche et al., 2025; Xiao et al., 2024], while the other seven are reported for the first time. Five of these sources have spectroscopic redshifts, while the other five have previously reported photometric redshifts. For the latter, new photometric z estimates were derived to validate the results. Using the SEDs computed in Berta et al. (2025), the star formation rate (SFR) of the 10 DSFGs was estimated and found to be much higher than the predictions for the star-forming main sequence at this redshift [Popesso et al., 2023]. This discovery, enabled by the N2CLS survey, suggests that the accelerated evolution of the stellar and dust mass assembly in overdense regions is not correctly reproduced by current galaxy formation models and simulations.

Confusion noise in GOODS-N

The confusion noise (see Section 6.3.3) results have already been published in Ponthieu et al. (2025). Using GOODS-N data, and masking all sources detected above a SNR of 4.6, the confusion noise is found to be $139.1^{+15.9}_{-19.2} \pm 11.9\,\mu$Jy/beam at 260 GHz and $38.6^{+9.6}_{-13.1} \pm 3.7\,\mu$Jy/beam at 150 GHz, which corresponds to half the instrumental noise.

Final source catalogs at 150 GHz

The final source catalogs at 150 GHz in both GOODS-N and COSMOS fields have been published in Béthermin et al. (2025), and are available on the dedicated N2CLS website[1]. A complete description of the data reduction, source extraction, and simulations used to characterize the catalogs will be given in a subsequent paper [Carvajal-Bohorquez, in prep.]. With a 95% purity threshold, the 150 GHz catalog contains 25 and 90 sources in GOODS-N and COSMOS, respectively. The median redshift are $z = 3.6 \pm 0.3$ and $z = 3.0 \pm 0.2$ in GOODS-N and COSMOS, with the former being higher than predictions from simulations. This is due to the overdensity at $z = 5.2$ discussed in Berta et al. (2025) and Lagache et al. (2025). The paper shows that the N2CLS single dish survey is more efficient at finding high-z galaxies than interferometric surveys. Together with the results from Berta et al. (2025), 260 GHz (1.2 mm) appears as the most effective frequency to build large samples of high-z DSFGs, and should be a priority for future surveys.

[1] https://data.lam.fr/n2cls/

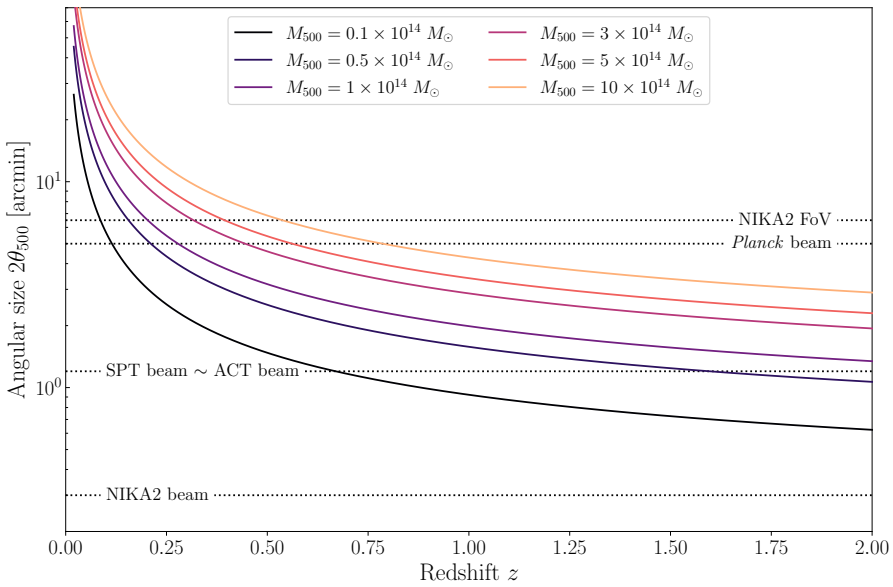

Figure 6.11: Angular size $2\theta_{500}$ of a cluster as a function of redshift for different masses. The NIKA2, SPT, ACT and *Planck* angular resolutions are shown as dotted lines. We consider the NIKA2 resolution at 150 GHz. Figure adapted from Kéruzoré (2021).

6.4 NIKA2: a powerful instrument to study the tSZ effect

During this thesis, the study of galaxy clusters via the tSZ effect was a major focus. To this effect, the NIKA2 camera is a very powerful instrument thanks to its high angular resolution, sensitivity and dual-band capabilities.

6.4.1 Very high resolution

As discussed in Chapter 2, the amplitude of the tSZ effect is not affected by cosmological dimming. This implies that if we want to detect and study clusters at high redshift, the cluster's angular size will be the only limiting factor. Galaxy clusters typically have masses between 10^{13} and 10^{15} $M_\odot$, which translates to angular sizes $2\theta_{500}$ of about 1.5-6.9 and 0.9-4.3 arcmin at redshifts of 0.5 and 1, respectively. Large CMB surveys, like *Planck*, SPT and ACT have relatively poor angular resolutions, with 5 arcmin for *Planck*, and about 1 arcmin for SPT and ACT which will limit their capabilities in the detection and resolution of high redshift clusters. Indeed, for the detailed study of clusters, the beam size of the instrument should be much smaller (about an order of magnitude smaller) than the angular size of the cluster, to be able to resolve substructures. As shown in Figure 6.11, *Planck* is only sensitive to low redshift and/or very high mass clusters, whereas SPT and ACT can detect clusters with masses $M_{500} > 10^{14}$ $M_\odot$ up to high redshift, but not fully resolve them. For the LPSZ sample, with redshifts between 0.5 and 0.9, NIKA2's resolution is an order of magnitude smaller than their angular size, enabling the precise estimation of their physical properties which is not possible with most other mm instruments.

Additionally, we can see that a blind survey with the NIKA2 camera would be able to detect clusters at low mass and/or high redshift, a regime where we currently have a handful of detections from other large surveys. Even if it was not the original goal, the N2CLS program allows to test this blind detection as we will see in Chapter 8.

6.4.2 High sensitivity

As we have seen in Chapter 5, when we observe faint sources, the noise induced by atmospheric fluctuations largely dominates over the astrophysical signal of interest. This is especially true for

clusters, as they have low surface brightness, of the order of a few mJy/beam at most. With a mapping speed of 1388 arcmin^2 at 150 GHz, which is the region the instrument can map in an hour with a noise level of 1 mJy, NIKA2 is able to map a cluster and its surroundings with sufficient S/N in only a few hours. The low noise level in the final N2CLS COSMOS map (see Section 6.3.2) at 150 GHz is also due to the great sensitivity of the camera. Without this sensitivity, and mapping speed, the N2CLS observations would have taken much longer and would simply not have been possible.

6.4.3 Dual-band capabilities

The two bands of the camera are designed to map the surface brightness decrement of the tSZ effect at 150 GHz and the slightly positive signal at 260 GHz, as seen in Figure 6.1. However, as we will see in more details in Chapters 7 and 8, we do not actually detect the SZ effect at 260 GHz. If we look at Table 6.1, we see that the sensitivity at 260 GHz is about 3 times lower than at 150 GHz. We would then need to integrate longer to reach the same S/N at 260 GHz as at 150 GHz. Furthermore, as shown again in Figure 6.1, the atmospheric transmission is worse at 260 GHz, especially as the PWV increases. Together with the fact that the SZ effect amplitude at 260 GHz is smaller by a factor ~ 3 than at 150 GHz [Ruppin et al., 2018], it's extremely difficult to detect the tSZ effect with sufficient S/N at 260 GHz. Despite these limitations, the 260 GHz band is still useful for other reasons, mainly for the detection of point sources in the cluster fields. These point sources are the main topic of the next chapter, where we will see how they can contaminate the tSZ signal and bias the derived cluster properties.

Considering the several advantages of the NIKA2 camera, it is safe to say that the instrument is currently one of the best suited to study the tSZ effect in galaxy clusters.

6.5 Conclusion

The NIKA2 camera is a powerful instrument installed at the IRAM 30-m telescope, capable of observing the sky at very high angular resolution and with great sensitivity. The NIKA2 collaboration has been awarded a total of 1300 hours of guaranteed time divided in five large programs. The SZ Large Program aims at measuring the mean pressure profile of clusters at high redshift and refining the scaling relation between the tSZ observable and cluster mass. The N2CLS large program, on the other hand, aims to study dusty star-forming galaxies at high redshift in the COSMOS and GOODS-N fields, with a focus on measuring the galaxy number counts, and clustering properties.

CHAPTER 7

LPSZ clusters: Impact of point sources on pressure profiles

7.1 Point sources in the LPSZ fields . . . 124
7.1.1 Sub-millimeter sources . . . 124
7.1.2 Radio sources . . . 124
7.2 LPSZ point source catalogs . . . 125
7.2.1 MB catalog constructed from the final LPSZ cluster maps . . . 125
7.2.2 FPS catalog built from point source optimized LPSZ maps . . . 127
7.2.3 Cross-validation of the two catalogs . . . 128
7.2.4 Validation with external catalogs . . . 132
7.3 Undetected sources in the LPSZ fields . . . 133
7.3.1 Undetected DSFGs . . . 134
7.3.2 Finding radio sources in astrophysical databases . . . 135
7.3.3 Problematic radio sources in the LPSZ sample . . . 137
7.3.4 Pressure profile reconstruction . . . 138
7.3.5 Impact of undetected radio sources on the pressure profile reconstruction . . . 139
7.4 Validation of cluster masses . . . 139
7.4.1 Literature search . . . 140
7.4.2 The mass of PSZ2G080 . . . 140
7.4.3 Mass estimates for the full LPSZ sample . . . 142
7.5 Conclusion . . . 143

As discussed in the previous Chapter, the LPSZ aims to provide the community with very high angular resolution maps of a sample of galaxy clusters, together with the precise estimation of their properties. One of the main goals is to accurately reconstruct the thermal pressure profile of individual clusters, from the inner to the outer regions, and derive a universal pressure profile to be used in cosmological analyses. However, the SZ signal can be affected by the presence of point sources in the maps, which can bias the pressure profile reconstruction. These point sources are classified in two categories: sub-millimetre (submm) sources, which are mainly dusty star-forming galaxies (DSFGs), and radio sources. As we will see in this Chapter, sub-millimeter point sources are well detected at 260 GHz, and their contribution is correctly taken into account during the SZ effect modelling. However, radio sources, which are mainly detected at 150 GHz, may be hidden by the SZ decrement and thus not properly taken into account in the analysis.

In this Chapter, I first present the validation work I performed on the point-source catalogs used by the collaboration in the pressure profile reconstruction. Then, I focus on my identification and characterization of radio sources around LPSZ clusters, especially those I found to be associated with residuals in the SZ maps after modelling. Finally, I present the validation of the cluster masses derived from the LPSZ maps, by comparing them to other mass estimates that I compiled from the literature. In the following, we will refer to the LPSZ clusters by their short name. Their corresponding full name is given in Table 6.

7.1 Point sources in the LPSZ fields

In Chapter 2, we have seen that the amplitude of the SZ effect is positive above a frequency of 217 GHz, and negative below. In the LPSZ maps, the SZ effect is thus seen as a surface brightness decrement in the 150 GHz maps, and not detected in the 260 GHz maps (see Section 6.4.3). The negative SZ signal can be contaminated by point sources with positive fluxes, which can then impact the modelling of the SZ effect. These sources can be classified in two main categories: sub-millimeter sources, and radio sources.

7.1.1 Sub-millimeter sources

Sub-millimeter sources are primarily dusty star-forming galaxies (DSFGs or simply SMGs), where the dust absorbs and re-emits radiation at wavelengths below the millimeter domain. These SMGs were first observed in the 1990s [Smail et al., 1997] with the Submillimeter Common-User Bolometer Array (SCUBA, Holland et al. (1999)) installed on the James Clerk Maxwell Telescope (JCMT), and subsequent surveys followed quickly to build catalogs of these sources [Hughes et al., 1998; Barger et al., 1998; Eales et al., 2000; Cowie et al., 2002]. In the last decade, several other surveys were conducted with even better sensitivity and resolution, such as the SCUBA-2 Cosmology Legacy Survey (S2CLS, Geach et al. (2017)) and the N2CLS survey as we have seen in Chapter 5. These surveys have led to the detection of thousands of SMGs, with a large fraction of them at high redshift ($z > 2$). However, in the context of the LPSZ, these catalogs are not helpful as they only cover limited areas of the sky and cannot be used to validate sources found in the LPSZ maps. Indeed, as we will discuss in more details in Section 7.3.4, ancillary catalogs of SMG fluxes at frequencies below 260 GHz are extremely useful to constrain the flux of SMGs contaminating the SZ signal. In that regard, catalogs of SMGs built by CMB large surveys like *Planck* [Planck Collaboration et al., 2016b], SPT [Everett et al., 2020], and ACT [Gralla et al., 2020] cover a substantial fraction of the sky and could be used by the LPSZ. In practice, NIKA2 cannot observe the SPT fields due to its declination, and *Planck* and ACT do not have sufficient resolution to detect sources at the same level as NIKA2. The *Herschel* Space Observatory [Pilbratt et al., 2010] and its instruments, the Photoconductor Array Camera and Spectrometer (PACS, Poglitsch et al. (2010)) and the Photometric Imaging Receiver (SPIRE, Eales et al. (2010)), provide the most comprehensive wide-field high resolution survey of DSFGs at six frequencies between 600 and 4283 GHz, which are complementary to the NIKA2 observations. The survey covers 20 out of the 38 LPSZ clusters (i.e., 18 clusters with no *Herschel* detections within 15′ from the cluster center), enabling the cross-matching of NIKA2 sources with *Herschel* sources to accurately fit their spectral energy distribution (SED).

7.1.2 Radio sources

On the other hand, sources with a flat or decreasing spectrum with frequency are radio galaxies (RGs), which are mainly detected at 150 GHz. These sources are usually associated with active galactic nuclei (AGN), where the radio emission comes from synchrotron radiation of relativistic electrons in the magnetic field of the AGN [Hogan et al., 2015]. These sources are often not detected at 260 GHz,

making them harder to identify as the 150 GHz map is dominated by the SZ effect. However, their contribution is not negligeable as they can correspond to the brightest cluster galaxy (BCG) found close to the center of clusters, and thus impact the signal even if the RG is faint. We thus rely on radio surveys to identify and characterize these sources. The most complete surveys to complement the LPSZ are the NRAO VLA Sky Survey (NVSS, Condon et al. (1998)) and the Faint Images of the Radio Sky at Twenty-Centimeters (FIRST, Becker et al. (1995)), with a coverage of 82% and 25% of the sky, respectively. They include $N \approx 10^6$ sources with flux densities above 2.5 mJy at 1.4 GHz, or about 0.1 mJy at 150 GHz. Apart from these two surveys, the LOFAR Two-metre Sky Survey at 144 MHz (LOTSS, Shimwell et al. (2022)), the Very Large Array Sky Survey at 3-6 GHz (VLASS, Lacy et al. (2020)), the Green Bank survey at 4.85 GHz (GB6, Gregory et al. (1996)), and others [Rengelink et al., 1997; Hurley-Walker et al., 2017] provide complementary information at different frequencies. We will go into more details about the cross-matching of NIKA2 sources with radio sources in Section 7.1.2.

7.2 LPSZ point source catalogs

The LPSZ collaboration has developed a dedicated data reduction pipeline to produce maps optimized for the characterization of the SZ effect. These maps are also used to detect and recover the fluxes of radio and submm sources, that will then be taken into account for the pressure profile reconstruction. As these sources are also important for other prospects such as the number counts of DSFGs and RGs, the pipeline was adapted to produce "SZ-free" maps optimized for point sources and thus more suitable for their detection. Both types of maps have a dedicated method to detect point sources. In practice, both detection methods were applied to both maps, resulting in four independent point source catalogs. In the following, we only describe and compare the two catalogs constructed by applying each detection method to its corresponding optimized map, as they are the most reliable. We present here the main steps of the two data processing pipelines and point source detection methods before discussing the resulting catalogs and their validation.

7.2.1 MB catalog constructed from the final LPSZ cluster maps

Method

The data reduction pipeline used to produce the LPSZ maps is based on the *baseline* method described in Perotto et al. (2020). A complete review of the LPSZ pipeline is available in Hanser (2025), and we here summarize its main steps. Similarly to the GT camera reduction pipeline presented in Chapter 5, the estimation of a common mode is needed to remove the correlated noise from the TOIs. However, even if clusters are drowned in the noise due to their low surface brightness, estimating a common mode without masking could filter some of the cluster's signal. To account for this, a circular mask of size based on the cluster's size in the *Planck* or ACT catalogs is applied to the TOIs before estimating the common mode. Point sources also need to be masked at this step in order not to remove some of their signal as well. A first map is then produced to detect point sources and create a mask that will then be used together with the cluster mask in the decorrelation process. The mask radius is defined based on the source's SNR as [Hanser, 2025]:

$$r_\nu = \begin{cases} 1.2 \log(\mathrm{SNR} \times 0.54) \times \mathrm{FWHM}_\nu & \text{if } \nu = 150 \text{ GHz} \\ 2 \log(\mathrm{SNR} \times 0.68) \times \mathrm{FWHM}_\nu & \text{if } \nu = 260 \text{ GHz}\,. \end{cases} \tag{7.1}$$

Once the common mode has been subtracted, the map-making process follows the same guidelines as in the GT camera pipeline, from the projection to the weighting scheme. The main difference comes from the fact that maps from multiple scans are co-added to reach a better sensitivity in the final map. In that case, the signal map is simply:

$$M(x,y) = \frac{\sum_s w_s(x,y) M_s(x,y)}{\sum_s w_s(x,y)}, \tag{7.2}$$

with $M_s(x,y)$ the signal map of scan s, and $w_s(x,y)$ the weight map in pixel (x,y) of scan s:

$$w_s(x,y) = \frac{N_{\mathrm{hits},s}(x,y)}{\mathrm{Var}_{\text{off-source}}\left[M_s(x,y) \times \sqrt{N_{\mathrm{hits},s}(x,y)}\right]}. \tag{7.3}$$

From the final LPSZ maps at 150 and 260 GHz, point sources are blindly detected by using a match-filter approach, where the signal maps are convolved with a Gaussian kernel of size equal to the beam FWHM. The resulting SNR maps are then used to detect peaks above a given SNR. Finally, the photometry of point sources in each map is recovered by fitting all of them at the same time. This allows us to correct for biases on the estimated point-source fluxes, which could be induced by the overlapping of point sources. This source finding method is nicknamed "MB" for Mathieu Béthermin who developed it. The final point source catalog contains all sources detected at 150 and/or 260 GHz, with their fluxes at both frequencies.

Results

The final MB catalog contains a total of 301 sources above a SNR threshold of 4 in the 38 LPSZ fields around clusters. From these 301 sources 193 are detected at 260 GHz only, 48 at 150 GHz only and 56 at both frequencies, as shown in the first panel of Figure 7.1. The second panel shows the distribution of the sources distance to the cluster center. We note that SMGs (260 GHZ only sources) are uniformely distributed in the field of view. This is expected as they are the only significant signal in the 260 GHz map. On the contrary, there are very few detected RGs (150 GHz only sources) close to the cluster center, as expected. Most of them are found at a distance greater than 2 arcmin. The SNR distributions of sources at 260 GHz and 150 GHz are also shown. The main takeaway is that, except for a few very high SNR detections, the majority of sources have a SNR below 6-7, especially at 150 GHz. We also see that sources detected in both maps have higher SNR at 260 GHz than at 150 GHz, where they are close to the 4σ detection limit.

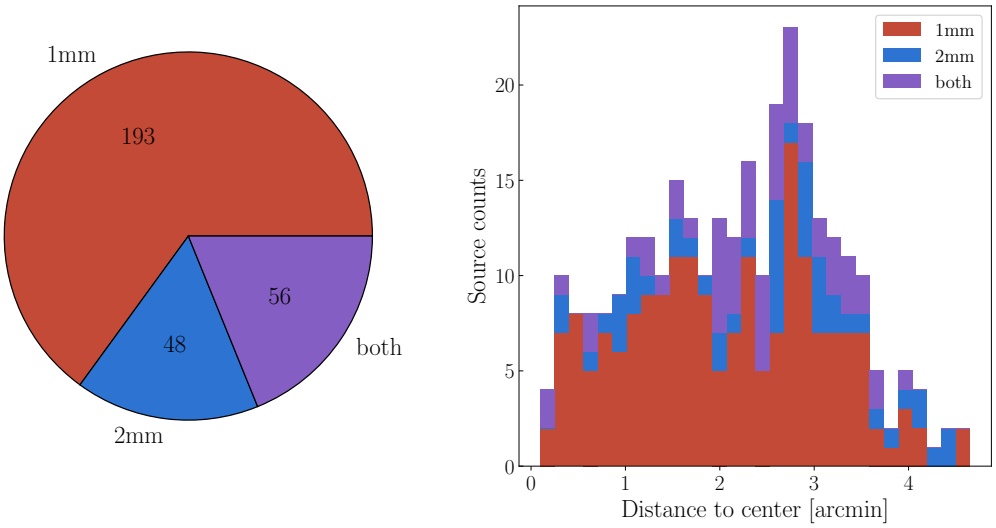

Figure 7.1: Overview of the MB catalog with a total of 301 sources. (Left): Number of sources detected at 260 GHz (1 mm) only, 150 GHz (2 mm) only and at both frequencies. (Right): Distribution of the sources distance to the cluster center.

7.2.2 FPS catalog built from point source optimized LPSZ maps

Method

The FPS method, described in details in Désert (in prep.), follows the same principles as the MB method, but instead of detecting point sources in maps optimized for the study of the SZ effect, it uses maps optimized for point-source detection and on which the tSZ effect clusters has been removed. At 260 GHz, the SZ effect is well below the noise level and does not affect the detection of point sources, but at 150 GHz, the SZ effect is significant and can hide faint sources. Once the SZ optimized maps are obtained for each cluster, a beta model [Cavaliere and Fusco-Femiano, 1976] is fitted to each as:

$$S_{2mm} \propto (1 + \theta^2/\theta_c^2)^{-\frac{3}{2}\beta+\frac{1}{2}} , \tag{7.4}$$

where θ_c is the core radius and β is the slope of the beta model. For the blind detection of clusters, β is usually fixed to 1 [Kornoelje et al., 2025], but here it is only constrained to be less than 1. The model is then subtracted from the 150 GHz map. In the first row of Figure 7.2, we show the 150 GHz maps obtained with both methods, where we can clearly see that the SZ decrement has been accurately subtracted in the bottom map. In the final maps, pixels where the number of hits is less than 20 percent of the central hits number are masked before further analysis.

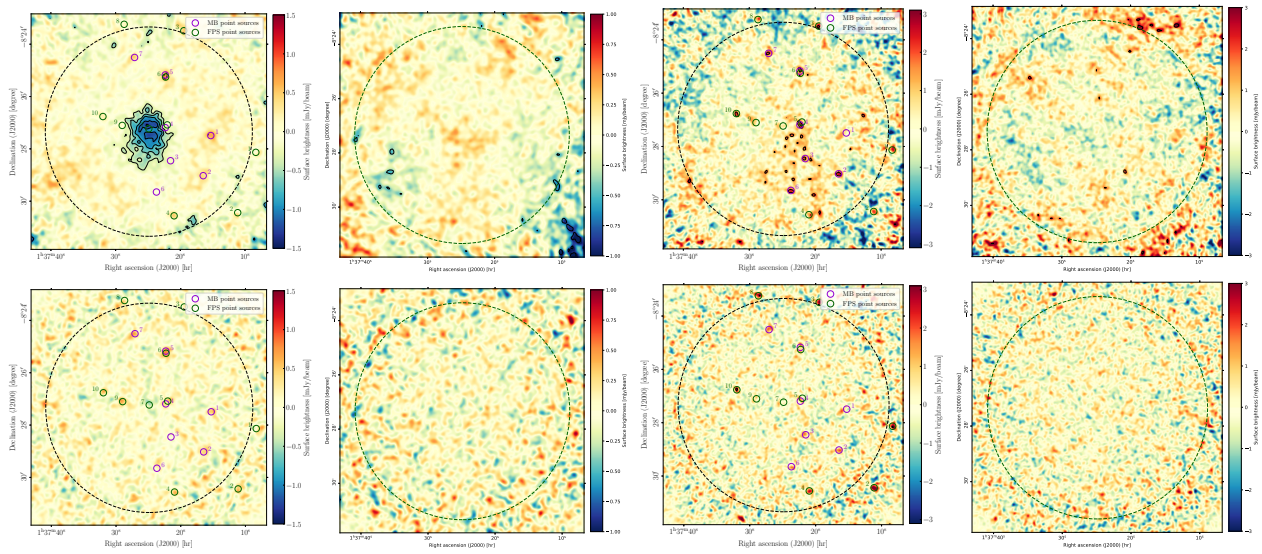

Figure 7.2: $9' \times 9'$ NIKA2 maps of PSZ2G155 at 150 GHz (left columns) and 260 GHz (right columns). The first row shows the SZ optimized maps (see Section 7.2.1), and the second row the point source optimized maps where the SZ decrement has been subtracted. For each frequency, its corresponding jackknife (JK) map used for noise estimation is shown alongside it. Point sources detected in the MB and FPS catalogs are marked by violet and green circles, respectively. The black contours show SNR levels, starting at $\pm 3\,\sigma$ with steps of $\pm 2\,\sigma$. The dashed black circle indicate a 8 arcmin diameter region.

The detection of point sources is similar to what is done in the MB method, with the identification of peaks above a SNR threshold of 4 in the 150 and 260 GHz convolved maps and a final simultaneous fit to estimate their flux. The final point source catalog contains all sources detected at 150 and/or 260 GHz, with their fluxes at both frequencies.

Results

The final FPS catalog contains a total of 261 sources detected at 150 GHz and/or 260 GHz above a SNR threshold of 4. From these 261 sources, 175 are detected at 260 GHz only, 34 at 150 GHz only and 52 at both frequencies. In this catalog, sources are classified in three categories: DSFGs, radio

galaxies, and SZ fluctuations (SZFs). As the name suggests, the latter are likely to be residuals of the beta-model subtraction, and are not real point sources. DSFGs and RGs are classified based on their fluxes at 150 and 260 GHz, with DSFGs having a higher flux at 260 GHz and RGs at 150 GHz. SZFs are identified as the faint and central sources at 150 GHz that are not detected at 260 GHz. We show the distribution of the sources in Figure 7.3. 229 sources are classified as DSFGs, 18 as RGs, and 14 as SZFs. As expected, SZFs are within $\sim 1.5'$ of the cluster center with $\mathrm{SNR}_{2mm} < 6$. All RGs have SNR_{1mm} well below 4 except one source, which has a flat spectrum.

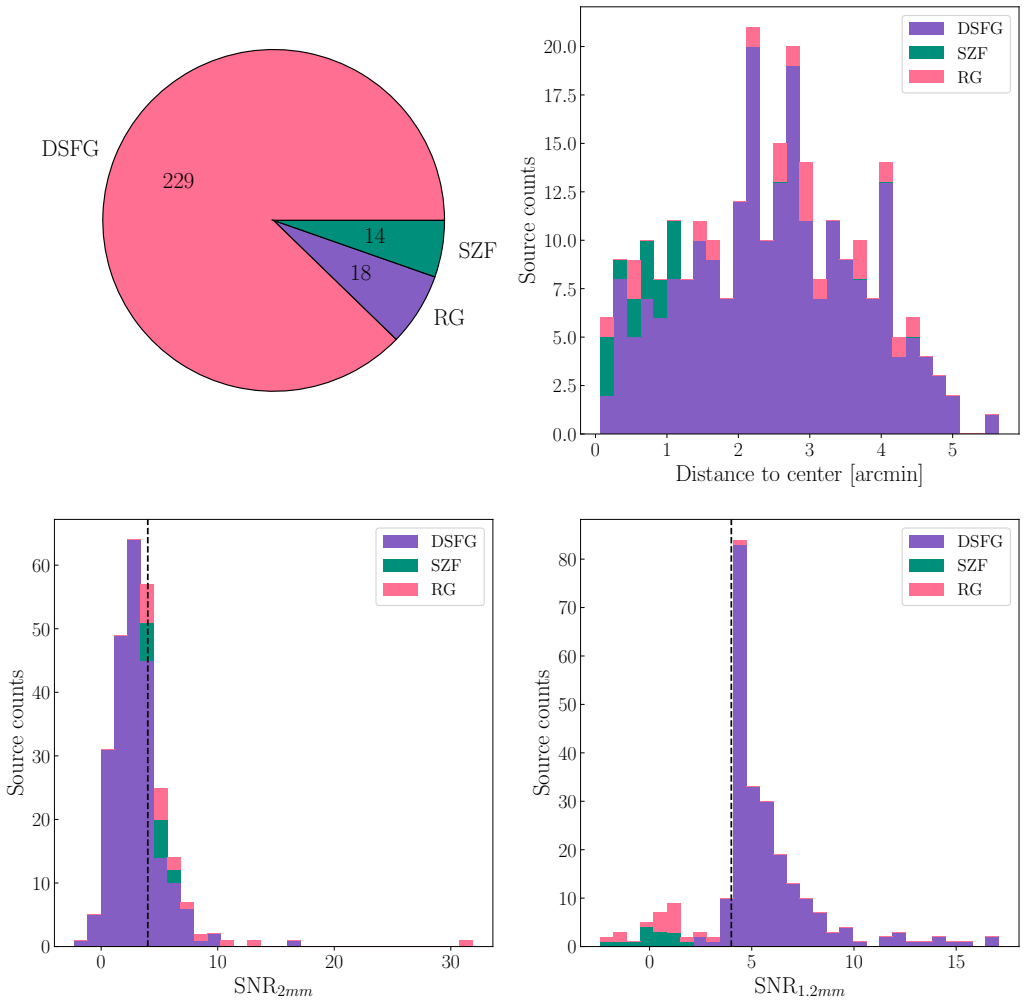

Figure 7.3: Overview of the FPS catalog with a total of 261 sources. (Top-left): Number of sources classified as DSFGs, RGs, or SZFs. (Top-right): Distribution of the sources distance to the cluster center. (Bottom): Distribution of the sources SNR at 150 GHz (left) and 260 GHz (right).

7.2.3 Cross-validation of the two catalogs

We match the sources from both catalogs within a radius of 8.5 arcseconds, which is obtained from

$$r = \frac{1}{2}\sqrt{\mathrm{FWHM}_1^2 + \mathrm{FWHM}_2^2}, \tag{7.5}$$

where FWHM_1 and FWHM_2 are the FWHM of the instruments used to produce the catalogs to match, respectively. Of course here we are matching two NIKA2 catalogs, so we have $\mathrm{FWHM}_1 = \mathrm{FWHM}_2 = 11.5''$ at 260 GHz, which gives $r \approx 8.5''$. If we use $\mathrm{FWHM} = 18.5''$ to match sources at 150 GHz, we only find four more sources in common. All four have SNR below 4 at 150 GHz, and we thus do not

consider them. We find that 155 sources are common to both catalogs, which means that $\sim 52\%$ and $\sim 60\%$ of the MB and FPS sources are matched, respectively.

Common detections

The results of the cross-matching are shown in Figure 7.4. We see in the top panels that the fluxes of the common sources are in good agreement at both 150 GHz and 260 GHz, with a small scatter around the 1:1 line in orange. The error on the estimated fluxes is systematicaly higher in the FPS catalog, which is expected from the different data reduction steps chosen (see Section 7.2), as well as the additional step of the SZ decrement subtraction leading to a higher noise level in the 150 GHz SZ-free maps. The noise properties of the two maps are shown in Figure 7.2, where we see that the noise is slightly higher but more uniform across the SZ-free map. This higher noise then translates into higher uncertainties on the point source fluxes. As a result, the SNR of the common sources is slightly lower in the FPS catalog, as shown in the bottom panels of Figure 7.4. Of course the comparison of common detections is important to check that the results are consistent in the two catalogs before further analysis. However, the crucial point is to understand why more than 40% of sources in both catalogs are not cross-matched and what would be the impact of unmatched sources on both the pressure profile reconstruction and the number counts of point sources.

Unique detections in the catalogs

In the MB and FPS catalogs, 142 and 106 sources have no counterpart in the other catalog, respectively. This discrepancy can be explained by several factors. The first is that the two types of maps have different transfer functions, i.e, they filter the astrophysical signal differently (see Section 8.2.1). In the SZ-free maps used for the FPS catalog, large scales are mostly filtered out to optimize the detection of point-like sources, whereas in the SZ optimized maps used for the MB catalog, large scales are preserved to keep the extended SZ signal. Secondly, as we can see in the SNR distributions shown in Figure 7.5, 79% of the unmatched sources have a SNR below 5. With a SNR threshold of 4, it is expected that sources close to the detection limit may be slightly below the limit in the other catalog. As we have seen just before, the noise is higher in the SZ-free maps which further explains why some low SNR sources are not detected. Thirdly, the distance from the cluster center up to which sources are detected is larger in the FPS catalog. Indeed, as shown in the bottom panel of Figure 7.5, about a third of unmatched FPS detections are further than 4 arcmin, whereas there are very few MB sources at such distances. This is because, as we have mentioned in the previous section, the different maps used for the two catalogs have different noise properties. In Figure 7.2, we show both types of maps, at 150 GHz and 260 GHz, together with their associated noise maps. The green circle indicates the 4 arcmin radius from the cluster center. Comparing the noise maps, we see that the noise increases significantly beyond 4 arcmin in the SZ optimized maps, whereas it is more uniform in the SZ-free maps. Point sources are thus more likely to be detected at large distances in the latter. The last factor comes from false sources classified as SZFs in the FPS catalog. As we have seen, these sources are likely to be residuals of the SZ model subtraction and we thus do not expect any counterpart in the MB catalog.

In total, 84% of unmatched sources fall into the three categories described above. The remaining 16% however need to be investigated further as they may have an impact on the future analyses we conduct. The unmatched sources that could have an impact on the SZ analysis are those detected in the FPS catalog with SNR above 5, not classified as SZ fluctuations, and close to the cluster center. For each cluster, we choose a distance threshold equal to 1.5 times the cluster size θ_{500}, which is taken from the *Planck* or ACT catalogs. Sources above this threshold will only have an impact if they are extremely bright, which is not the case for any of the unmatched sources here. They can safely be neglected. We find that 7 sources fill this criterion, which requires an additional check to understand if

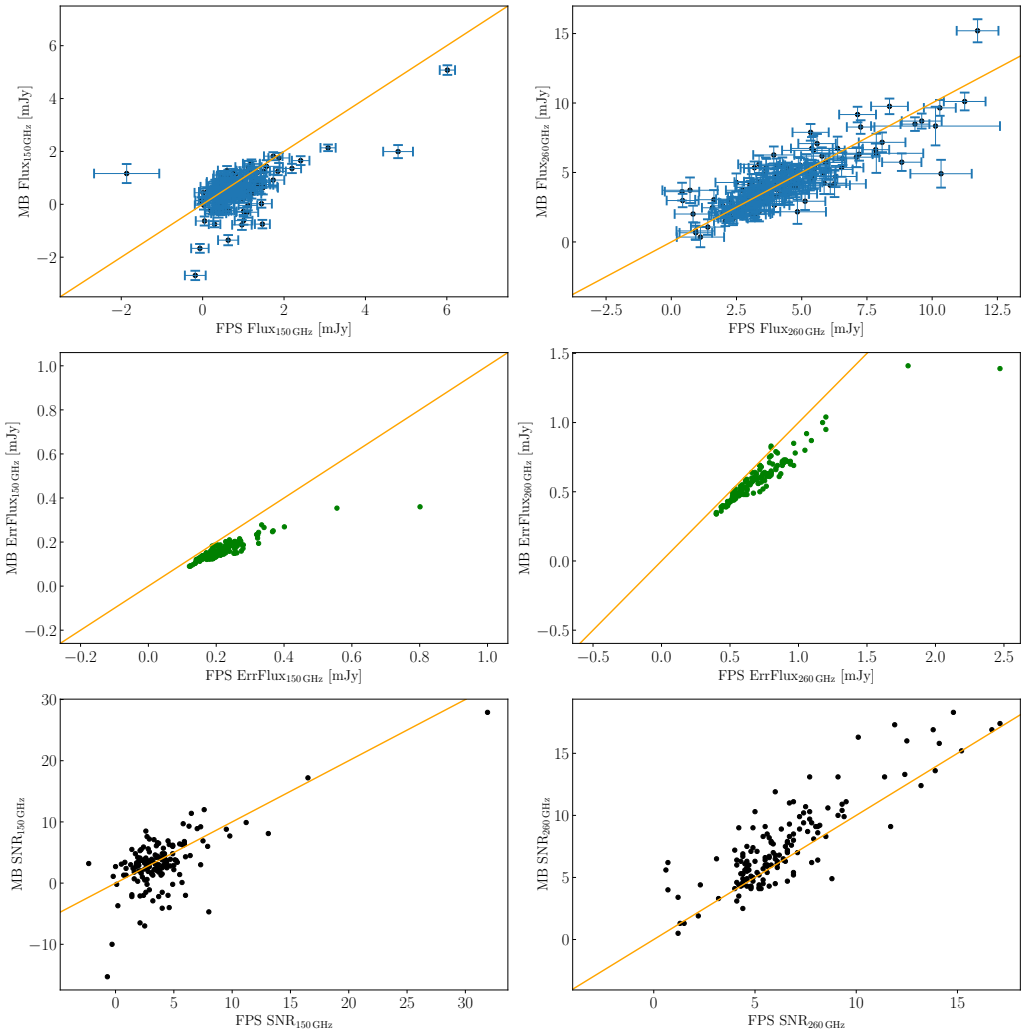

Figure 7.4: Comparison of the detection properties of common point sources in the MB and FPS catalogs, at 260 GHz (left) and 150 GHz (right). (Top): Comparison of the recovered fluxes. (Center): Uncertainty on the recovered flux. (Bottom): SNR. The orange line in all plots shows the 1:1 relation.

they truly have an impact on the SZ signal. The highest SNR unmatched source in the FPS catalog is detected around the ACTJ0022 cluster at 150 GHz only, with SNR = 8.5 and only 28 arcseconds away from the cluster center. This source is classified as a radio galaxy with a flux of 2.0 mJy at 150 GHz which is absolutely not negligible. We show in Figure 7.6 the 150 GHz, 260 GHz and residuals maps of ACTJ0022, where the source position is indicated by a red circle. In the 150 GHz map, the source is not visible as it could be hidden by the SZ decrement. The residuals map, which is the difference between the 150 GHz data and best-fit SZ model (see Section 7.3.4 for details), shows no sign of leftover positive signal at the source position, meaning that the source is not contaminating the SZ signal and the model fits the data well even without accounting for this source. We thus concluded that there was no need to include this particular source in further analysis. A similar check was performed for all 7 sources and only one was found to have an impact on the SZ signal modelling. We will discuss this source in more details in Section 7.3.

Similarly, we checked the 46 unmatched sources in the MB catalog with SNR above 5 and no constraint on the distance. It is important to understand why they are not detected in the FPS catalog as it could affect the validity of the number counts derived from the FPS catalog, especially bright sources as they are rare and often associated to lensing effects. Thus, even one missing source can have an impact on the number counts results. The highest SNR source, with $\mathrm{SNR}_{260\ \mathrm{GHz}} = 8.0$, has

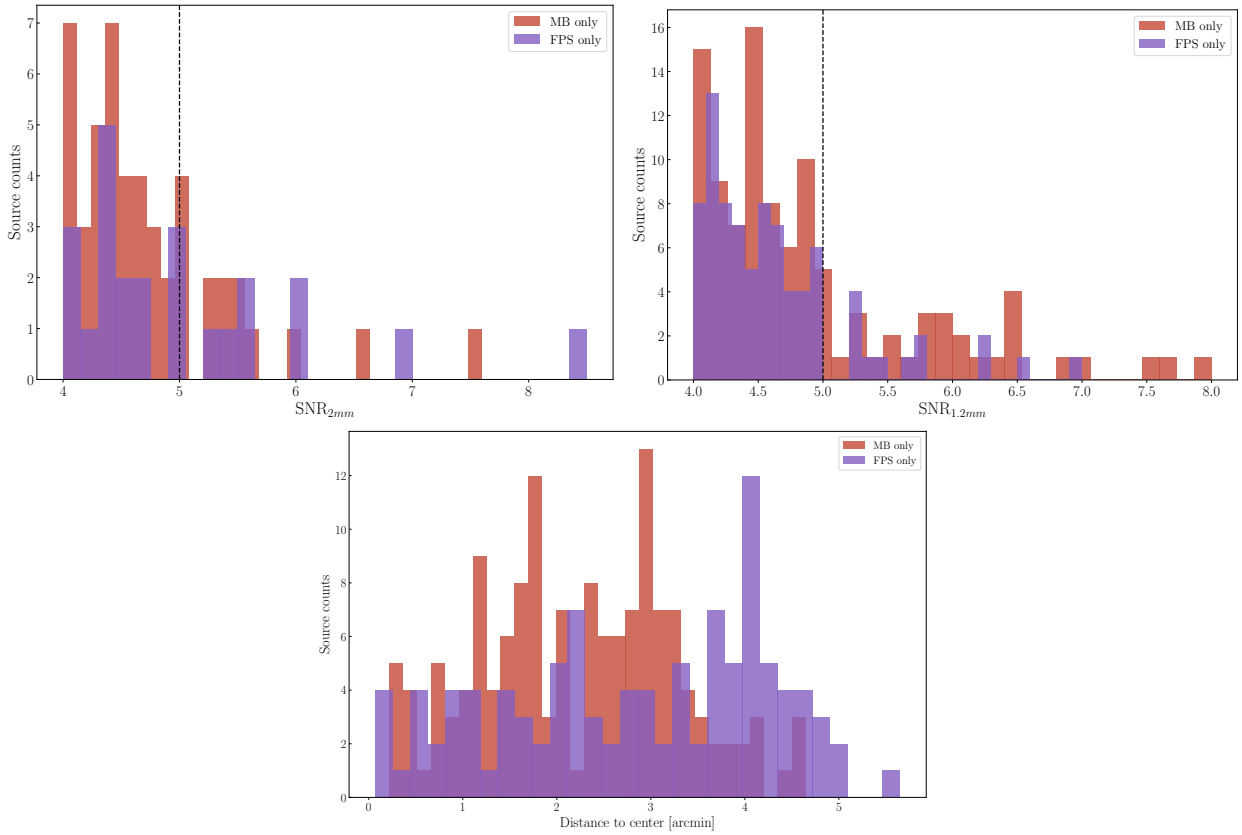

Figure 7.5: (Top): Distribution of the SNR at 150 GHz (left) and 260 GHz (right) of unmatched sources for both catalogs. The majority of sources have SNR below 5 illustrated by the dashed black line. (Bottom): Distribution of the distance to the cluster center of unmatched sources.

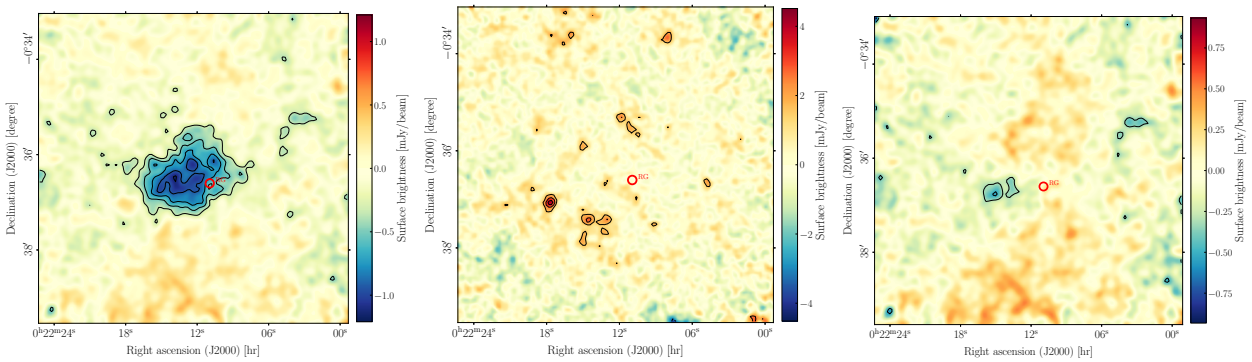

Figure 7.6: 6.5′ × 6.5′ SZ maps of the ACTJ0022 cluster at 150 GHz (left) and 260 GHz (middle), centered on the SZ position. The residuals map after the SZ model subtraction (see Section 7.3.4) is shown on the right. The high SNR RG source is marked by a red circle close to the cluster center. The maps have been smoothed with a Gaussian kernel of 10″ and 6″ for the 150 and 260 GHz maps, respectively. The black contours have similar scaling as in Figure 7.2.

a flux of 6.73 mJy at 260 GHz and is only 11 arcseconds away from the center of PSZ2G126, as seen in Figure 7.7. This cluster is a bit particular as it has a central extremely bright BCG which completely compensates the SZ negative signal. The unmatched source is only a few arcseconds north-west of the BCG, but no signal can be seen at that position in the SZ-free maps. We note that the BCG is much more compact and less bright by a few mJy in the SZ-free 260 GHz map than in the SZ optimized map. The two matched sources in PSZ2G126 are also fainter in the SZ-free map, which could indicate that the different signal filtering in the two maps is causing this difference. After checking all these unmatched sources, we concluded that most of them can be explained by the different signal filtering

and noise properties of the two types of maps. However, some specific cases, such as the PSZ2G183 cluster where no source is detected in the FPS catalog, need to be investigated further and the maps re-analyzed to understand the origin of these discrepancies.

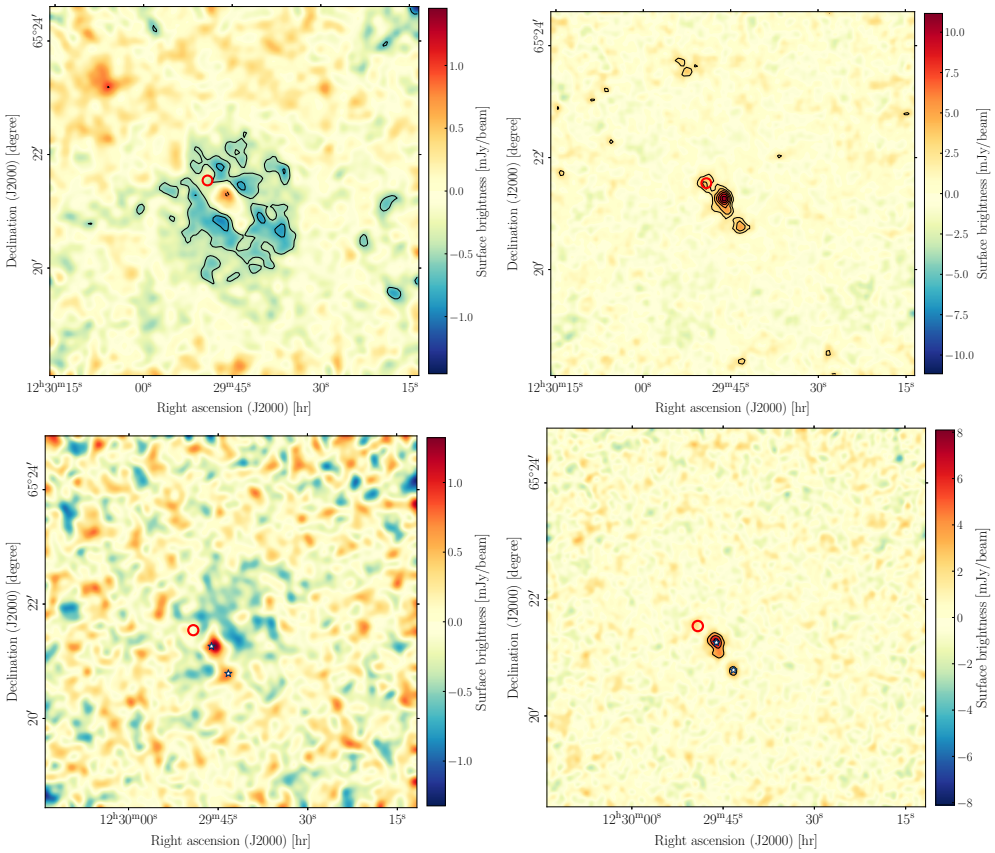

Figure 7.7: 6.5′ × 6.5′ maps of the PSZ2G126 cluster at 150 GHz (left) and 260 GHz (right), centered on the SZ position. The problematic high SNR source is marked by a red circle close to the cluster center. (Top): SZ optimized maps where the source is detected. (Bottom): SZ-free maps where the source is not detected. White stars indicate the position of other point sources. The maps have been smoothed with a Gaussian kernel of 10″ and 6″ for the 150 and 260 GHz maps, respectively. Black contours have similar scaling as in Figure 7.2.

7.2.4 Validation with external catalogs

Now that we have cross-validated the two catalogs, a last step is the comparison with external catalogs found in the literature.

Sub-millimeter catalogs

As we have seen in Section 7.1.1, the most complete catalogs of sub-millimeter sources are those from the *Herschel* satellite [Pilbratt et al., 2010] and its PACS and SPIRE instruments. This cross-match is essential for both the SZ signal modelling and the source number counts, as it will enable the fitting of the SED of sources with *Herschel* counterparts. The SED fits are then used in the cluster pressure profile reconstruction pipeline (see Section 7.3.4) as well as for the estimation of the dust mass and mean dust temperature of the sample. There are a total of 6 *Herschel* point source catalogs: SPIRE at 600, 856, and 1200 GHz and PACS at 1873, 3000, and 4283 GHz. The cross-matching radius for each frequency is determined using Equation 7.5, where $\mathrm{FWHM}_1 = 11.5''$ is the NIKA2 beam at 260 GHz and FWHM_2 the SPIRE/PACS beam. The radius thus varies between 6.4″ and 18.5″ with increasing frequency. As mentioned in Section 7.1.1, the *Herschel* catalogs cover 20 out of the 38

LPSZ clusters. We thus do not consider sources from the 18 clusters without *Herschel* coverage in the following analysis. We find that ~ 32% of the NIKA2 sources (MB and FPS catalogs combined) have a counterpart in at least one *Herschel* band. From these, four have $\mathrm{SNR}_{260\,\mathrm{GHz}} < 4$ indicating that they are chance associations. However, 39 sources with $\mathrm{SNR}_{260\,\mathrm{GHz}} > 5$ in either of the two catalogs are not matched to any *Herschel* source. This makes the *Herschel* unmatched sources harder to deal with in the SZ modelling as the flux estimation will be less accurate.

Radio sources catalog at 1.4 GHz

As radio sources are harder to detect in the LPSZ maps, we rely on external catalogs to estimate their fluxes. For the cross-matching, we will only use the NVSS and FIRST catalogs at 1.4 GHz, as more than 80% of radio sources around LPSZ clusters only have measurements at this frequency (see Section 7.3). We adopt a search radius of ~ 9″ based on the FWHM = 5″ of the two radio surveys.

First, in the FPS catalog, we find that 19 sources have a radio counterpart. We give the results in Table 7.1, with the name of the counterpart, its coordinates, the distance to the NIKA2 source, and its flux at 1.4 GHz.

We find that, among the 19 associations, only 8 NIKA2 sources are classified as RG, with a 1.4 GHz flux ranging from 4 to 100 mJy. Among the 11 others, which are DSFGs, 3 may be chance associations (within a 7 arcsecond distance), one has a nearly flat spectrum (PSZ2G155_5), and 6 are in PSZ2G201 with a sub-mJy 1.4 GHz flux. There are 10 RG NIKA2 sources without a clear radio counterpart, of which one is within one arcminute of the cluster centre: ACT0022_1 that could be qualified as radio BCG. In a second step, we searched the VizieR[1] database for any possible radio counterparts within 9 arcseconds of these sources. We found that only one of them (PSZ2G133_14) may have a radio counterpart. This source has a completely flat spectrum across the whole radio spectrum, from 144 MHz to 260 GHz.

In the MB catalog, we also find 19 sources with a radio counterpart, of which 7 have a higher flux at 150 GHz than at 260 GHz as expected for a radio source. For the unmatched sources, we double checked those close to the cluster center, as they are more problematic, with $F_{150\,\mathrm{GHz}} \gtrsim F_{260\,\mathrm{GHz}}$. Of the 21 sources fitting the criteria, only 1 has a counterpart in Vizier, PSZ2G094_1, but it has a flux of 0.815 mJy at ~ 4 GHz, which is negligible once extrapolated to 150 GHz.

We show in Figure 7.8 the 150 GHz flux as a function of the 260 GHz flux for the sources with a radio counterpart at 1.4 GHz in both LPSZ catalogs. The dotted line shows the distinction between RGs (left of the line) and DSFGs (right of the line). We see that most of the matched sources behave like DSFGs and are likely chance associations. On the left of the line, we see that 4 sources are not common to both catalogs and could thus be important to take into account in the respective analyses. On closer inspection, the two MB only sources (green) are both faint ($\mathrm{SNR}_{150\,\mathrm{GHz}} < 5$) with a flux just below the SNR threshold in the FPS catalog (see Section 7.2.3). Similarly, one of the FPS only sources (black) is faint with $\mathrm{SNR}_{150\,\mathrm{GHz}} = 4.3$. The last source, located at the very center of the PSZ2G212 cluster, is a perfect example of why this work is important and will be discussed in the next section.

7.3 Undetected sources in the LPSZ fields

We now consider sources that are not detected by NIKA2, but are known in external catalogs. As these sources could have an impact on the SZ signal modelling and the source number counts, it is important to identify them and quantify their effect. In this section, we will present the analysis of undetected sources, mostly RGs, in the LPSZ fields and the method to identify the most prob-

[1] https://vizier.cds.unistra.fr/

Cluster	id/Class	RadioName	ra °	dec °	d2d ″	$F_{1.4}$ mJy	$\sigma_{1.4}$ mJy
PSZ2G155	5 DSFG	NVSS J013722-082513	24.34208	-8.42039	3	33.9	1.1
ACTJ0215	1 RG	NVSS J021516+003037	33.81862	0.51033	2	114.0	4.1
ACTJ0215	8 DSFG	NVSS J021540+003208	33.92198	0.53522	7	7.2	0.5
ACTJ0223	2 RG	NVSS J022306-005422	35.77739	-0.90736	1	4.0	0.6
PSZ2G201	1 DSFG	MM J045407.14-030033.9	73.52885	-3.00966	1	0.061	0.017
PSZ2G201	2 DSFG	MS 0451.6-0305:[BKG2010] E3	73.54563	-3.02356	2	0.063	0.015
PSZ2G201	3 DSFG	MM J045411.57-030307.5	73.54858	-3.05222	2	0.051	0.017
PSZ2G201	5 DSFG	MM J045412.72-030043.7	73.55375	-3.01300	7	0.058	0.017
PSZ2G201	7 DSFG	MM J045417.49-030306.6	73.57196	-3.05089	2	0.189	0.017
PSZ2G201	9 DSFG	MM J045421.55-030109.9	73.59025	-3.01903	1	0.084	0.017
PSZ2G212	2 RG	NVSS J105252+241530	163.21846	24.25844	4	26.9	0.9
PSZ2G212	3 DSFG	NVSS J105254+241912	163.22871	24.32014	6	8.6	0.5
PSZ2G228	0 RG	NVSS J114922+222330	177.34296	22.39065	0	16.7	1.1
PSZ2G160	5 RG	NVSS J122718+333206	186.82775	33.53502	5	23.20	1.16
PSZ2G099	4 RG	NVSS J141445+544426	213.69051	54.74045	1	14.6	1.0
PSZ2G099	9 RG	NVSS J141513+544921	213.80662	54.82269	3	133.0	4.0
PSZ2G108	2 DSFG	NVSS J142703+653925	216.76608	65.65379	7	3.9	0.6
PSZ2G080	4 DSFG	NVSS J142716+440732	216.81725	44.12558	6	48.6	1.9
PSZ2G046	2 RG	NVSS J171658+240634	259.24483	24.10953	1	104.0	3.1

Table 7.1: Catalog of NIKA2 point sources associated with a radio point source. The catalog gives the cluster short name, the id of the NIKA2 source and its class, the name of the radio point source, its position, its angular distance (d2d) to the NIKA2 source, and the measured flux at 1.4 GHz.

lematic sources. Then, we will show how these sources are taken into account in the pressure profile reconstruction, taking as an example the source in PSZ2G212.

7.3.1 Undetected DSFGs

Undetected DSFGs in the LPSZ fields are not a major problem as they should be very faint at 150 GHz. However, it is important to check that the brightest DSFGs are all detected. We thus first look for every Herschel source within a 3.25′ radius of the cluster center, which corresponds to half the FOV of NIKA2. Then, we can choose an approximate flux threshold to determine which sources would be problematic if not detected. Assuming a modified black-body spectrum, we can broadly infer the flux at 150 GHz from the *Herschel* flux as:

$$F_{150} \propto F_\nu \left(\frac{150}{\nu}\right)^\beta \frac{B_{150}(T)}{B_\nu(T_d)}\,, \tag{7.6}$$

where ν is the frequency of the *Herschel* source, β the emissivity index, B_ν is the Planck function at frequency ν, and T_d is the dust temperature. We fix $\beta = 1.8$ and $T_d = 39$ K, which are the mean values found in Désert (in prep.) for the LPSZ sample. Note that, as the sources' redshifts are unknown, a redshift of $z = 3$ is chosen in order to obtain this median effective temperature estimate. For $\nu = 600$ GHz, we set a threshold of 47 mJy, which is ~ 1 mJy at 150 GHz. We find that all *Herschel* sources above this flux threshold are detected in the NIKA2 maps. Similarly, all bright *Herschel* sources at $\nu = 856$ GHz are detected except one which is at the very edge of the NIKA2 FOV.

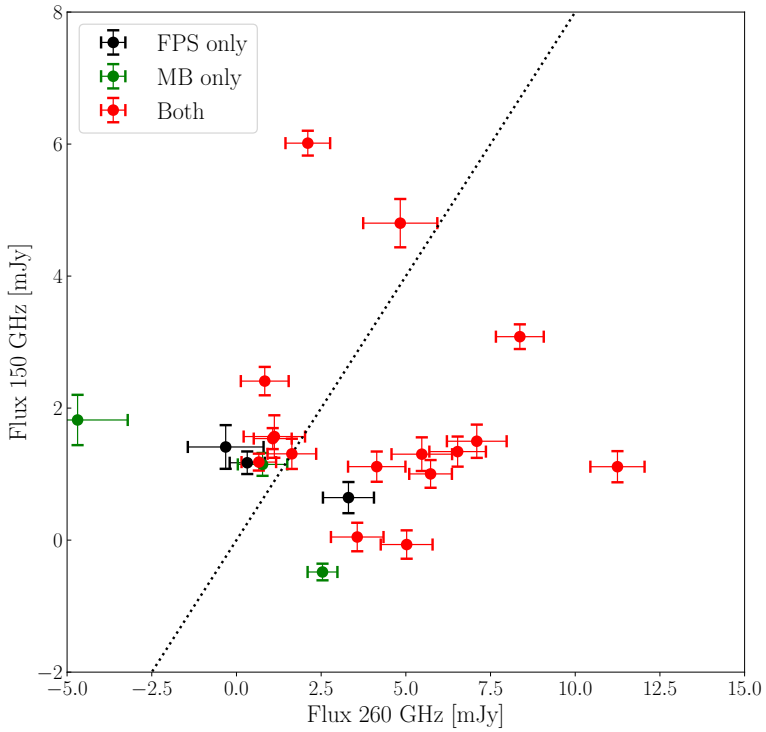

Figure 7.8: 150 GHz flux as a function of the 260 GHz flux for the sources with a radio counterpart detected in the FPS (black), MB (green), or both (red) catalogs. The dashed line has a slope of 0.8 to help visualise the separation between RGs (left of the line) and DSFGs (right of the line).

7.3.2 Finding radio sources in astrophysical databases

To search for all the undetected radio sources around the 38 LPSZ clusters, we make use of the NASA/IPAC Extragalactic Database[1] (NED). This database contains a majority of the published radio sources catalogs as well as the fluxes for each source, which is what we are interested in, as we will discuss shortly. We could also use the SIMBAD[2] database, but the sources fluxes are only available in the optical/NIR bands, which is not what we are looking for.

Similarly to the *Herschel* sources, we search for radio sources within a 3.25′ radius of the cluster center. We query NED using the `astroquery` Python package. This search in NED is not straightforward, as querying sources identified as 'RadioS' does not return all sources with radio flux measurements. Indeed, some radio sources have counterparts at other wavelengths, mainly optical, and are thus identified as their counterpart type, e.g. 'G' for galaxy or 'IrS' for infrared sources. As a result, we consider the following steps:

1. We query NED for all sources (not only radio sources) within a 3.25′ radius of the cluster center.
2. For each source, we query its associated photometry table, where all flux measurements are stored.
3. We extract the flux density and uncertainty from all measurements below 1000 GHz. In practice, the highest measurement frequency we found was 273 GHz, down to 38 MHz.
4. We remove duplicate sources, i.e. if two or more radio sources are within 5 arcseconds of each other, we merge them if they have measurements at different frequencies. If they only have flux density measurements at 1.4 GHz, we keep the one with the highest flux density.

[1] https://ned.ipac.caltech.edu/
[2] https://simbad.u-strasbg.fr/simbad/

In a second step, we completed the NED catalog by querying the RADIO Master catalog[1], which is a compilation of all radio catalogs on the HEASARC database[2], and finally the Vizier database. In practice, querying only Vizier would return all radio sources without the need to query any other database, but it is extremely tedious to parse the results. The full catalog of radio sources in the LPSZ fields is given in Table 7.

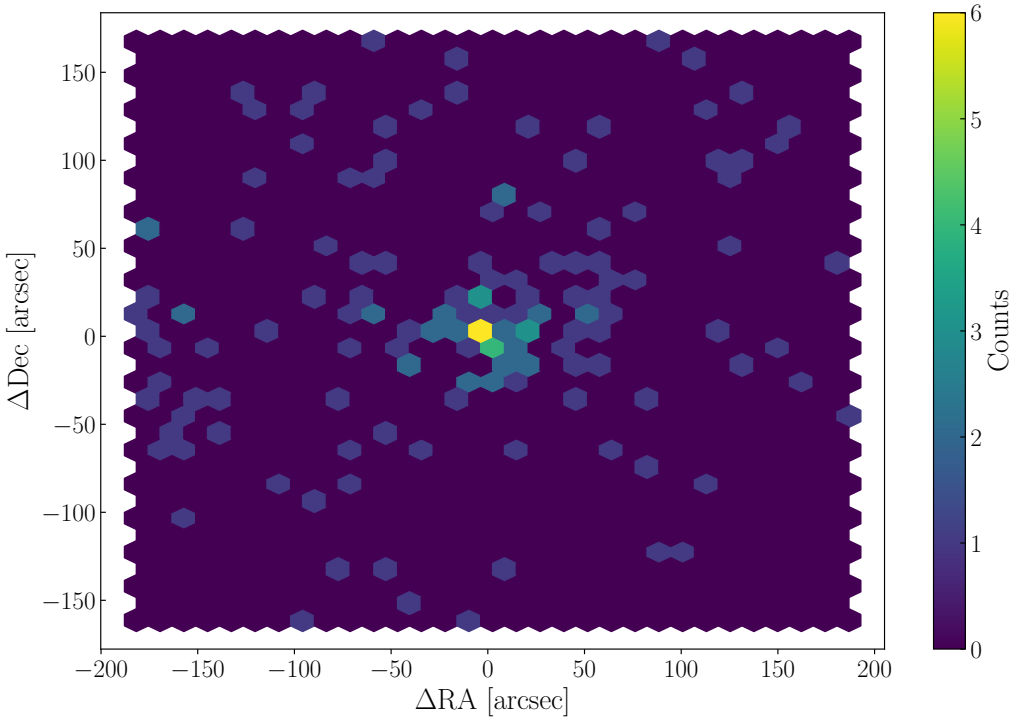

Figure 7.9: Spatial distribution of the radio sources averaged over all LPSZ fields.

We find a total of 158 radio sources around 37 of the 38 LPSZ clusters. The only cluster for which we did not find any radio source is PSZ2G141. Of those, ~ 66% have a flux measurement in the FIRST [Becker et al., 1995] or NVSS [Condon et al., 1998] catalogs at 1.4 GHz. We show in Figure 7.9 the radio sources spatial distribution around the cluster centers. We see that the majority are close to the center, within 50 arcseconds.

Then, we need to estimate the expected flux at 150 GHz of each source to determine which ones could contaminate the SZ signal. As done in previous works [Adam et al., 2016; Ruppin et al., 2017], we model the source SED as a power law:

$$F_\nu = F_{1\mathrm{GHz}} \left(\frac{\nu}{\nu_0} \right)^\alpha . \tag{7.7}$$

In the case where we have multiple flux measurements for the same source at different frequencies, we can constrain both the amplitude $F_{1\mathrm{GHz}}$ and the spectral index α. We can then infer the flux at 150 GHz using the equation above and the fitting results. If we have only a single flux measurement, we assume a spectral index of $\alpha = -0.7 \pm 0.2$ [Planck Collaboration et al., 2013] and infer the flux at 150 GHz as done previously. The flux estimates are also given in Table 7.

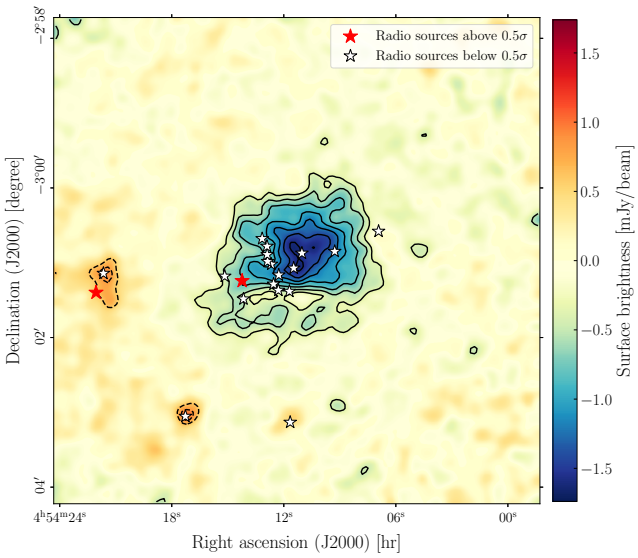

Figure 7.10: $6.5' \times 6.5'$ NIKA2 150 GHz map of PSZ2G201, centered on the cluster position. White and red stars indicate the position of radio sources with a flux below $0.5\,\sigma$ and above, respectively. Countours show SNR levels starting at $\pm 3\,\sigma$ and spaced by $\pm 2\,\sigma$. The map has been smoothed with a Gaussian kernel of $10''$.

7.3.3 Problematic radio sources in the LPSZ sample

Now that we have a complete catalog of radio sources around each cluster as well as their estimated flux at 150 GHz, we need to determine which sources may be problematic if not included in the SZ modelling. Our first approach was to select sources within $60''$ of the center and with a flux above a given threshold, based on the noise level in the 150 GHz map of each cluster. As the integration time and thus the noise level may vary between different clusters, we computed the flux threshold based on the noise level, σ, in the null maps (see Section 8.2.2). For each cluster, we compute σ as the standard deviation in the null map in a $6.5' \times 6.5'$ region centered on the cluster position and keep only sources above a threshold of $1\,\sigma$. We show in Figure 7.10 the NIKA2 150 GHz map of PSZ2G201, which is the cluster with the highest number of radio sources (20). From the 20 sources, only 2 (red star) have a flux above $1\,\sigma$, with one very far from the cluster center while the other is only detected at 150 MHz with a very large uncertainty. After this selection, 14 sources are left as potentially problematic sources. We then decided to compare the position of these sources with possible leftover positive signals in the residuals map after the SZ model subtraction (see Section 7.3.4). Residual positive signal close to the cluster center indicates that the SZ model is underestimating the SZ decrement and thus the cluster properties derived from the SZ modelling. If a source matches a positive leftover signal, it would be a clear indication that the source needs to be included in the modelling.

Looking at the residuals, we found that only 3 central radio sources match a positive signal. The first source, PSZ2G080_1, has an estimated flux of 3.89 mJy at 150 GHz and is already included in the SZ modelling. However, it seems that the upper limit on the flux is not high enough and must be increased. The second source, PSZ2G099_1, is fainter (F_{150} = 0.34 mJy) and farther away from the center, but is still detected in the residuals map. The last source, PSZ2G212_1, is the source with the most visible impact as shown in Figure 7.11. The source completely compensates the SZ decrement at the cluster center, leaving a high positive signal in the residuals. This source was not detected in the MB catalog (see Section 7.2.4), but was found in the FPS catalog. Thanks to the work done in this thesis, these three sources are now included in the pressure profile reconstruction pipeline [Hanser, in prep.(b)].

[1] https://heasarc.gsfc.nasa.gov/w3browse/master-catalog/radio.html
[2] https://heasarc.gsfc.nasa.gov/

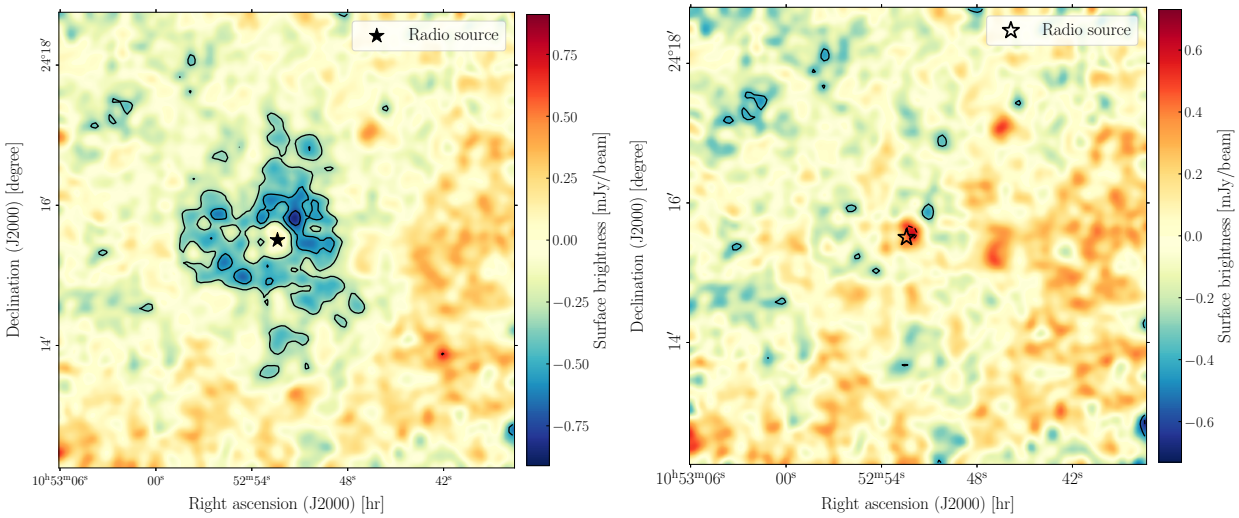

Figure 7.11: $6.5' \times 6.5'$ NIKA2 150 GHz (left) and residuals (right) map of PSZ2G212. The black star shows the position of the bright radio source hiding the SZ decrement in the 150 GHz map, and matched to leftover positive signal in the residual map. Contours have the same scaling as in Figure 7.10. The map has been smoothed with a Gaussian kernel of $10''$.

7.3.4 Pressure profile reconstruction

Now that we have a complete catalog of both submm and radio point sources in the LPSZ fields, we can proceed with the modelling of the SZ effect. The latest version of the pipeline is described in Hanser (2025), and we will here only give a brief overview of the steps involved, most importantly how the point sources are dealt with.

Point source contamination

The first step is to infer the source's flux at 150 GHz. If the source is not matched to any external catalog, its flux is estimated from the information at 260 GHz. If the source is matched to either *Herschel* or radio catalogs, the 150 GHz flux is estimated using a model depending on the source type. For both detected and undetected radio sources, we use the model presented in Section 7.3.3 and Equation 7.7 to infer their flux. For submm sources, the flux estimation is done using the `PSTools` software developed by Kéruzoré (2021) and based on previous work from Adam et al. (2016) and Ruppin et al. (2017). The software uses information from the *Herschel*-SPIRE catalogs at 600, 856, and 1200 GHz to fit the SED of each source as a modified black-body spectrum:

$$F(\nu) = F_0 \left(\frac{\nu}{\nu_0}\right)^{\beta} B_\nu(T)\,, \tag{7.8}$$

where F_ν is the source's flux at frequency ν, F_0 is the amplitude of the SED at a reference frequency $\nu_0 = 500$ GHz, β is the dust spectral index, and $B_\nu(T)$ is the blackbody spectrum of temperature T. It is also possible to incorporate measurements from the PACS catalogs at higher frequency as seen in Chapter 3 of Echeverria (2023). The SED fitting is performed via a Monte Carlo Markov Chain (MCMC) method, using a Gaussian likelihood together with a normal prior on the blackbody temperature T and a Gaussian prior on β as in the literature [Magnelli et al., 2012]. Finally, if the source is faint and far from the cluster center, its flux can be directly subtracted from the NIKA2 map before the next step. In the case of bright sources, their contribution is incorporated in the SZ model as we will see in the next section.

tSZ modelling

The main assumption for the tSZ modelling is that the cluster is spherically symmetric. Thus, its pressure distribution can be described by the radial profile of the electron pressure $P_e(r)$ within the ICM. As we have seen in Chapter 2, the most commonly used model is the Generalized Navarro-Frenk-White (gNFW, Nagai et al. (2007)) model defined in Equation 2.13. By integrating the pressure model along the line of sight, we obtain a 2D map of the Compton y parameter. The contribution of point sources is then added to this model, where they are modelled as 2D Gaussians with a prior based on their flux at 150 GHz. The SZ model is then fitted to the NIKA2 map using the `panco2` pipeline [Kéruzoré et al., 2023], with the latest version described in Hanser (2025). The pipeline uses MCMC sampling to fit the parameters of the gNFW profile, the point sources fluxes, and the zero level in the map. Finally, the cluster pressure profile is reconstructed from the best-fit parameters of the gNFW model.

7.3.5 Impact of undetected radio sources on the pressure profile reconstruction

As we have seen in Section 7.3.3, three radio sources were identified as problematic and included in the pressure profile reconstruction. For the first two sources, PSZ2G080_1 and PSZ2G099_1, the pressure profiles with and without taking the sources into account overlap, and the best-fit flux of the source is compatible with zero. However, for the last source, PSZ2G212_1, the radio source is very bright and completely compensates the SZ decrement at the cluster center, as we saw in the left panel of Figure 7.11 and impacts the pressure profile reconstruction. We show in Figure 7.12 the results on the reconstruction of the pressure profile of PSZ2G212 with and without the radio source included in the model. The left panel highlights the difference in the model and residuals maps when we include the radio source in the model. We see that central positive leftover signal is effectively removed in the lower panel as expected. The right panel shows the pressure profiles obtained for the two analyses. The profile with the source included in the modelling is in better agreement with the XMM-*Newton* data, which is shown as black dots. The pressure is now much better reconstructed especially close to the cluster center, where the previous profile was completely flat.

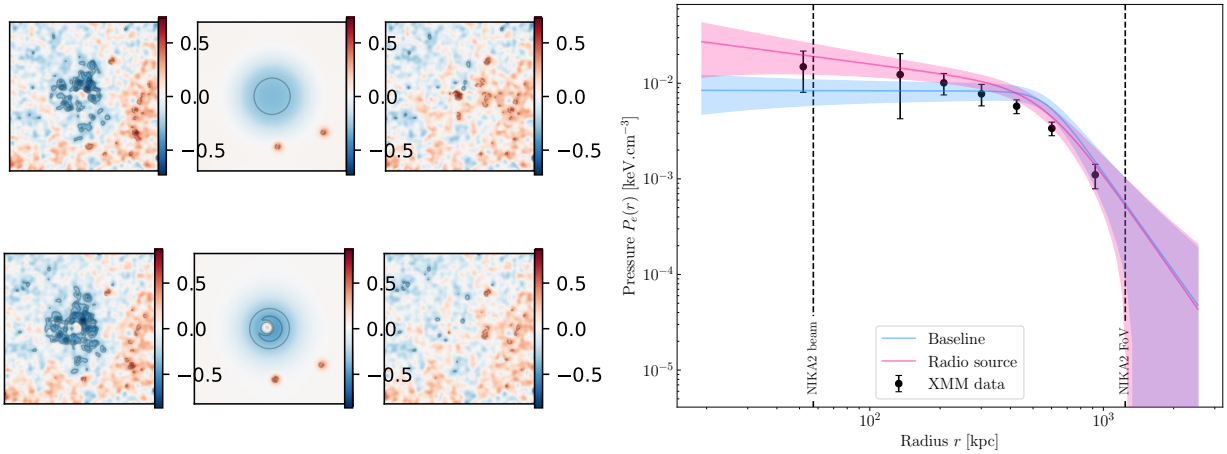

Figure 7.12: (Left): From left to right, NIKA2 150 GHz map, best-fit model, and residual maps of PSZ2G212 with the radio source PSZ2G212_1 not included in the model (top) and included (bottom). (Right): Pressure profiles with (pink) and without (blue) the radio source included in the model. The black dots are XMM-*Newton* data. Figure adapted from Hanser (2025).

7.4 Validation of cluster masses

The pressure profile is not the only important product delivered by the LPSZ collaboration. Assuming that the cluster is in hydrostatic equilibrium, the pressure profile, together with the electron

density can be used to derive the cluster mass at R_{500}, M_{500} (see Chapter 2). We can then use these mass estimates to validate the NIKA2 results by comparing them with other estimates in the literature at all wavelengths. We present here the method used to find the literature mass estimates, and then show the results for the PSZ2G080 cluster as an example. We note that the masses are not homogenised and may be derived using different cosmological parameters.

7.4.1 Literature search

The method to find the literature mass estimates is very straightforward. We first query the Vizier database, which is the only database where mass estimates can be found for some clusters. Unfortunately, expect for the *Planck* [Planck Collaboration et al., 2016c], ACT [Hilton et al., 2021], and ComaLit [Sereno, 2015; Sereno and Ettori, 2017] catalogs, a vast majority of results are not stored in Vizier or anywhere easily accessible. Hence, we have to compile, for each cluster, a list of articles where the cluster is mentioned and then search for mass estimates within the text. There are two ways to build this list: either through the Astrophysics Data System[1] (ADS) or through Simbad. Simbad is more convenient as they have already compiled a list of articles for each cluster and it is quite easy to query. Using ADS is way more tedious and isn't recommended. At the time of writing this thesis, some large language models (LLMs) are somewhat good at parsing PDFs and extracting text/tables, but there is still a long way to go before they can be efficiently used for this task. Instead, we extract the mass estimates by checking the articles. Figure 7.13 illustrates the results for the PSZ2G080 cluster, for which several mass estimates exist based on different analyses. Similar plots are available for all clusters in the LPSZ sample in Appendix 8.7.

7.4.2 The mass of PSZ2G080

PSZ2G080, also known as MACS J1427.2+4407, was first discovered in the RASS survey and included in the MACS catalog [Mann and Ebeling, 2012]. The first published mass estimate for this cluster is reported in Ehlert et al. (2013), $M_{500} = 6.35 \times 10^{14}\ M_\odot$. This mass was estimated using the luminosity-mass scaling relation from Mantz et al. (2010). Similarly, Rossetti et al. (2017) used the $L-M$ scaling relation from Pratt et al. (2009) to estimate the mass, and found $M_{500} = 6.92 \times 10^{14}\ M_\odot$. No uncertainties are given in both articles. Liu et al. (2020) used a different approach, and performed their own reduction of *Chandra* data to estimate the global temperature of the cluster. Then, they used the $M-T$ scaling relation from Vikhlinin et al. (2006) to obtain $M_{500} = (7.36 \pm 0.95) \times 10^{14}\ M_\odot$.

The first SZ mass analysis was done by Planck Collaboration et al. (2016c), where they used the SZ-mass scaling relation from Equation 7 in Planck Collaboration et al. (2014a) to obtain the hydrostatic mass, $M_{500} = 5.17^{+0.57}_{-0.60} \times 10^{14}\ M_\odot$. Following a joint X-ray and SZ detection using *Chandra* and *Planck* data, Tarrío et al. (2019) re-estimated PSZ2G080's mass using the same scaling relation from Planck Collaboration et al. (2014a), but a different method to extract the integrated Compton parameter Y_{500}. They found $M_{500} = 6.30^{+0.81}_{-0.87} \times 10^{14}\ M_\odot$, in agreement with the *Planck* estimate.

The first weak-lensing analysis for this cluster, Applegate et al. (2014), used data from the Weighing the Giants project [von der Linden et al., 2014]. The authors used a color-cut method [Hoekstra, 2007] to estimate the lensing mass at a radius $R = 1500\,\mathrm{kpc}$, and found $M(< R) = 5.9^{+2.4}_{-2.5} \times 10^{14}\ M_\odot$. Then, based on the weak and strong lensing analysis from Sereno and Covone (2013), Sereno (2015) applied the same procedure to the full CoMaLit[2] catalog and obtained $M_{500} = (3.3 \pm 2.1) \times 10^{14}\ M_\odot$. The authors also estimated the mass within $R = 1500\,\mathrm{kpc}$, and found $M(< R) = (5.2 \pm 2.4) \times 10^{14}\ M_\odot$, in good agreement with Applegate et al. (2014).

In addition, Sereno and Ettori (2017) re-calibrated *Planck*, SDSS RedMaPPer [Rykoff et al., 2016], and MCXC [Piffaretti et al., 2011] cluster masses using weak-lensing measurements. The *Planck*

[1] https://ui.adsabs.harvard.edu/

[2] COmparing MAsses in the LITerature. Catalog available at http://pico.oabo.inaf.it/~sereno/CoMaLit/

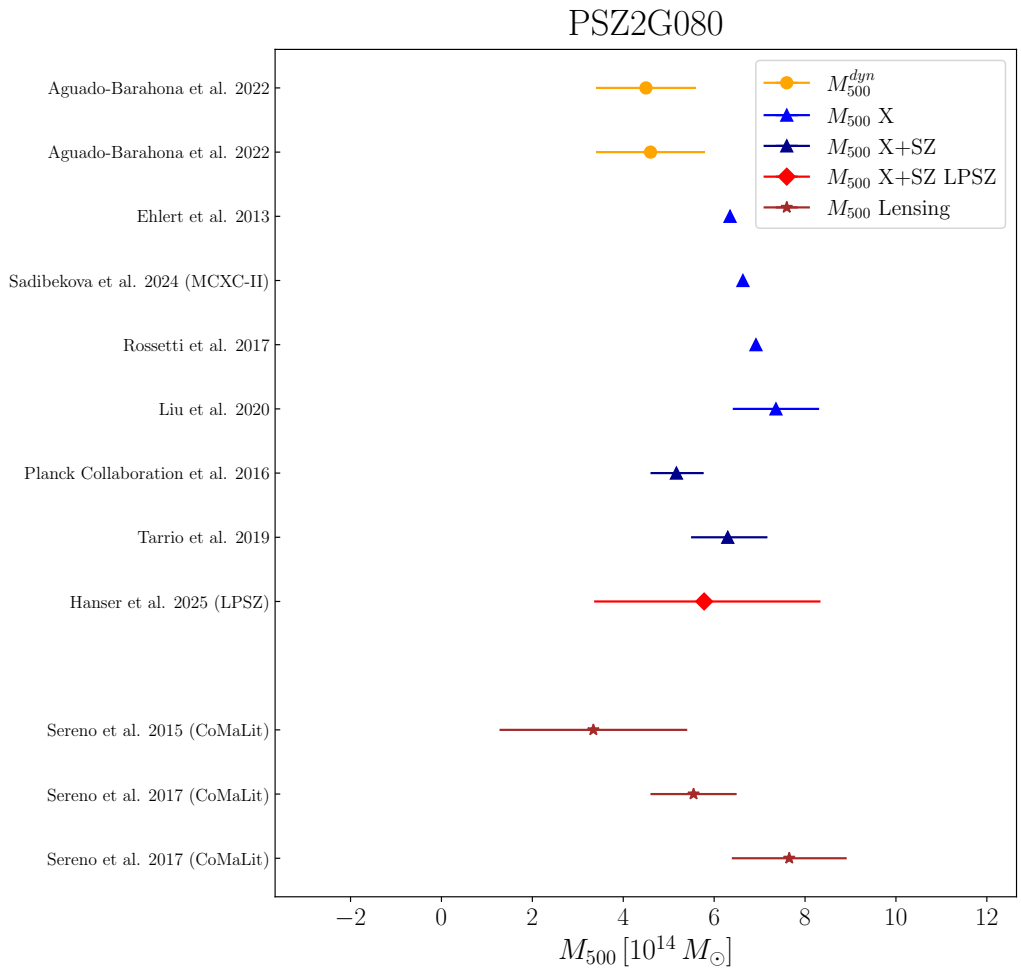

Figure 7.13: M_{500} estimates for PSZ2G111 in the literature. Brown stars correspond to lensing mass estimates. Blue and dark blue triangles represent X-ray only and the combination of SZ and X-ray data results, respectively. The red diamond is the NIKA2 X-ray+SZ mass estimate.

WL-calibrated mass is $M_{500} = (7.65 \pm 1.26) \times 10^{14}\ M_{\odot}$. The authors use the richness given in the RedMaPPer catalog to find $M_{200} = (5.55 \pm 0.95) \times 10^{14}\ M_{\odot}$. As the cluster was not yet in the MCXC catalog, no WL mass estimate was given. Recently, an updated version of the MCXC catalog (MCXC-II, Sadibekova et al. (2024)) was published, with PSZ2G080 now included. In this new release, the authors re-calculated the luminosity L_{500} of each cluster and used a $L_{500} - M_{500}$ relation (Equation 6 in Sadibekova et al. (2024)) to estimate the mass. The authors obtained $M_{500} = 6.63 \times 10^{14}\ M_{\odot}$ with no uncertainties given.

Another study based on the velocity dispersion of galaxy members presented in Aguado-Barahona et al. (2022) obtained two estimates of the dynamical mass: $M_{500} = (4.5 \pm 1.1) \times 10^{14}\ M_{\odot}$ and $M_{500} = (4.6 \pm 1.2) \times 10^{14}\ M_{\odot}$, from the velocities of 40 and 37 galaxies, respectively.

In Figure 7.13, we show the M_{500} estimates from the literature discussed above. The estimates are ordered by type of analysis: dynamical (orange circles), X-ray only (blue triangles), SZ+X-ray (dark blue triangles), and lensing (brown stars). Finally, the NIKA2-LPSZ estimate from Hanser (2025) is shown as a red diamond. We see that the NIKA2 estimate has large uncertainties, which is due to a very bright radio source at the cluster center (see Section 7.3.5). The estimate is in good agreement with the two other SZ+X-ray estimates, and compatible with the X-ray only estimates despite a slightly lower value.

Interestingly, the lensing estimate from Sereno (2015) is lower than all other masses, which is not expected as lensing masses are usually higher due to the hydrostatic mass bias [Muñoz-Echeverría et al., 2023]. We still note that the lensing mass is compatible within errors with the NIKA2 estimate, and that the other WL-lensing calibrated masses are in better agreement.

7.4.3 Mass estimates for the full LPSZ sample

We show in Figure 7.14 the comparison of the NIKA2-LPSZ M_{500} estimates with other types of estimates. As some clusters have several M_{500} estimates of the same type, we compute the median value per type of analysis and its associated uncertainties for each cluster. In the top-left panel, we see that the lensing mass estimates are systematically higher, as expected due to the hydrostatic-to-lensing mass bias [Muñoz-Echeverría et al., 2023]. If we try to compute a preliminary value of the bias $1 - b_{\rm HSE/lens} = M_{500}^{\rm HSE}/M_{500}^{\rm lens}$ without discarding any clusters, we find a median value of $1 - b_{\rm HSE/lens} \sim 0.66$. This value is in agreement with previous studies [Ferragamo et al., 2022; Muñoz-Echeverría et al., 2023]. We note that this is merely a preliminary estimate, and a more detailed study of the HSE-to-lensing bias will be done for the full sample by Miren Muñoz-Echeverría.

In the top-right and bottom-left panels of Figure 7.14, we notice that the NIKA2 estimates are overall compatible with both X-ray only and X-ray+SZ estimates, at least within errors. We can recognize some outliers, such as PSZ2G144, which has the highest M_{500} in the sample. Finally, the LPSZ vs dynamical masses comparison shows a discrepancy at low dynamical masses, where the NIKA2 estimates are higher by a large margin. This may be explained by a low number of galaxy members used to estimate the dynamical mass. Unlike lensing masses, dynamical masses are expected to be lower than SZ masses. For the 18 clusters with both LPSZ and dynamical mass estimates, we find a SZ-to-dynamical mass ratio of $1 - b_{\rm Dyn/SZ} \sim 0.78$, which is in very good agreement with other estimates from past studies [Ferragamo et al., 2021; Aguado-Barahona et al., 2022].

In 7.15, we present the median value of M_{500} per type of analysis (lensing, X-ray only, X-ray+SZ and dynamical masses) for every cluster in the LPSZ sample. The colors and symbols follow the same rules as in Figure 7.13. In total, the LPSZ did not estimate the mass for 8 clusters, either because no SZ signal was detected, indicating that the cluster was probably a false detection in the *Planck* or ACT catalog, or because the cluster was too contaminated by point sources.

As discussed above, PSZ2G144 stands out as the most massive cluster in the LPSZ sample, $M_{500}^{\rm LPSZ} =$

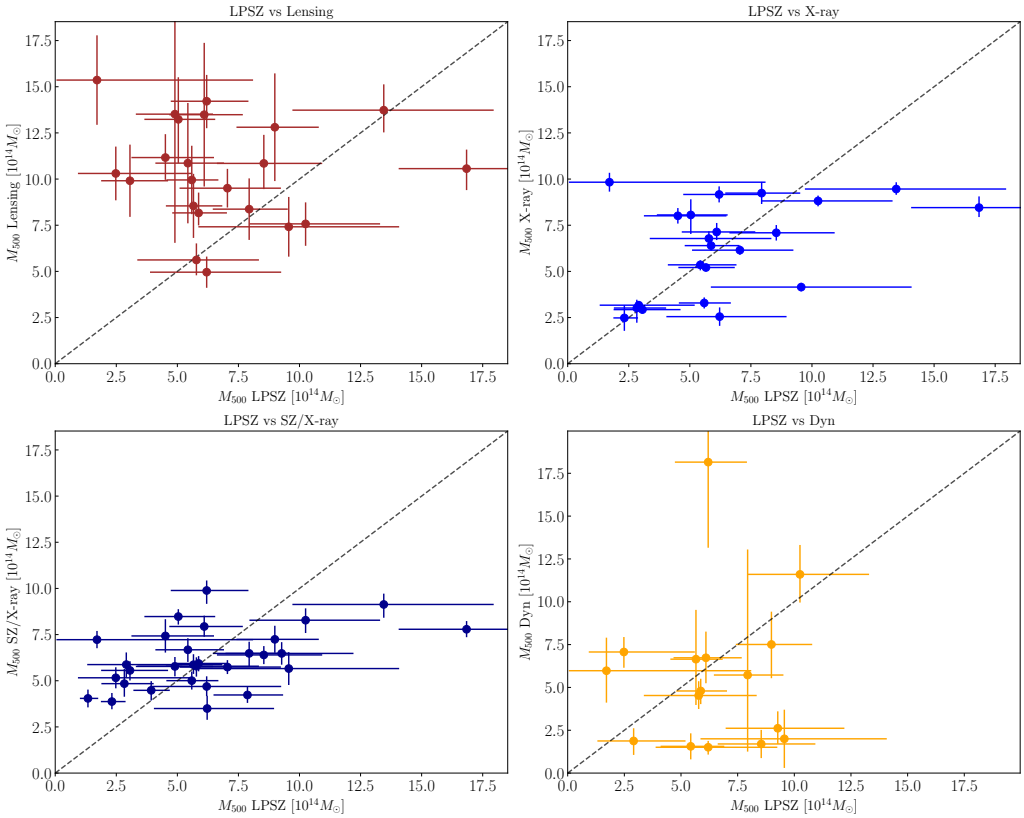

Figure 7.14: Preliminary comparison of the NIKA2-LPSZ M_{500} with lensing (top-left), X-ray only (top-right), X-ray+SZ (bottom-left) and dynamical (bottom-right) mass estimates from the literature. The dashed black line shows the 1:1 relation.

$16.84^{+2.78}_{-3.31} \times 10^{14}\ M_\odot$. This is because, as we have seen previously in Chapter 6, this cluster has an overdense region that greatly impacts the mass estimate which is not masked here. In Ruppin et al. (2018), this overdensity was masked to obtain a mass estimate of $M_{500} = 6.95^{+0.56}_{-0.56} \times 10^{14}\ M_\odot$, which is in much better agreement with other masses in the literature.

7.5 Conclusion

In this chapter, we have studied the impact of point sources, mainly radio sources, on the pressure profile reconstruction of clusters in the LPSZ sample. We carefully cross-validated two point source catalogs produced by the LPSZ collaboration. The two catalogs were built from two types of maps: one (MB catalog) optimized for SZ science, and the other (FPS catalog) for point source detection where the SZ effect was subtracted. We found that 52% and 60% of the sources in the MB and FPS catalogs are common to both, respectively. After investigating the sources that are not matched, we concluded that most of them can be explained by the different data reduction steps taken to produce the two types of maps, which induce different noise properties and signal filtering. However, we found that some of the 'SZ-free' maps used to produce the FPS catalog may need to be refined to improve the detection of point sources.

To characterize the impact on the SZ signal of bright submm sources that were undetected in the NIKA2 maps, we used the *Herschel*-SPIRE/PACS catalogs [Eales et al., 2010; Poglitsch et al., 2010] and found that all bright submm sources were in fact detected. We then compiled a catalog of all radio sources in the NIKA2 FoV from several databases. After estimating their flux at 150 GHz, we found that three central radio sources undetected in the NIKA2 maps were problematic for the SZ modelling. We then presented the method used to reconstruct the pressure profile of clusters in the

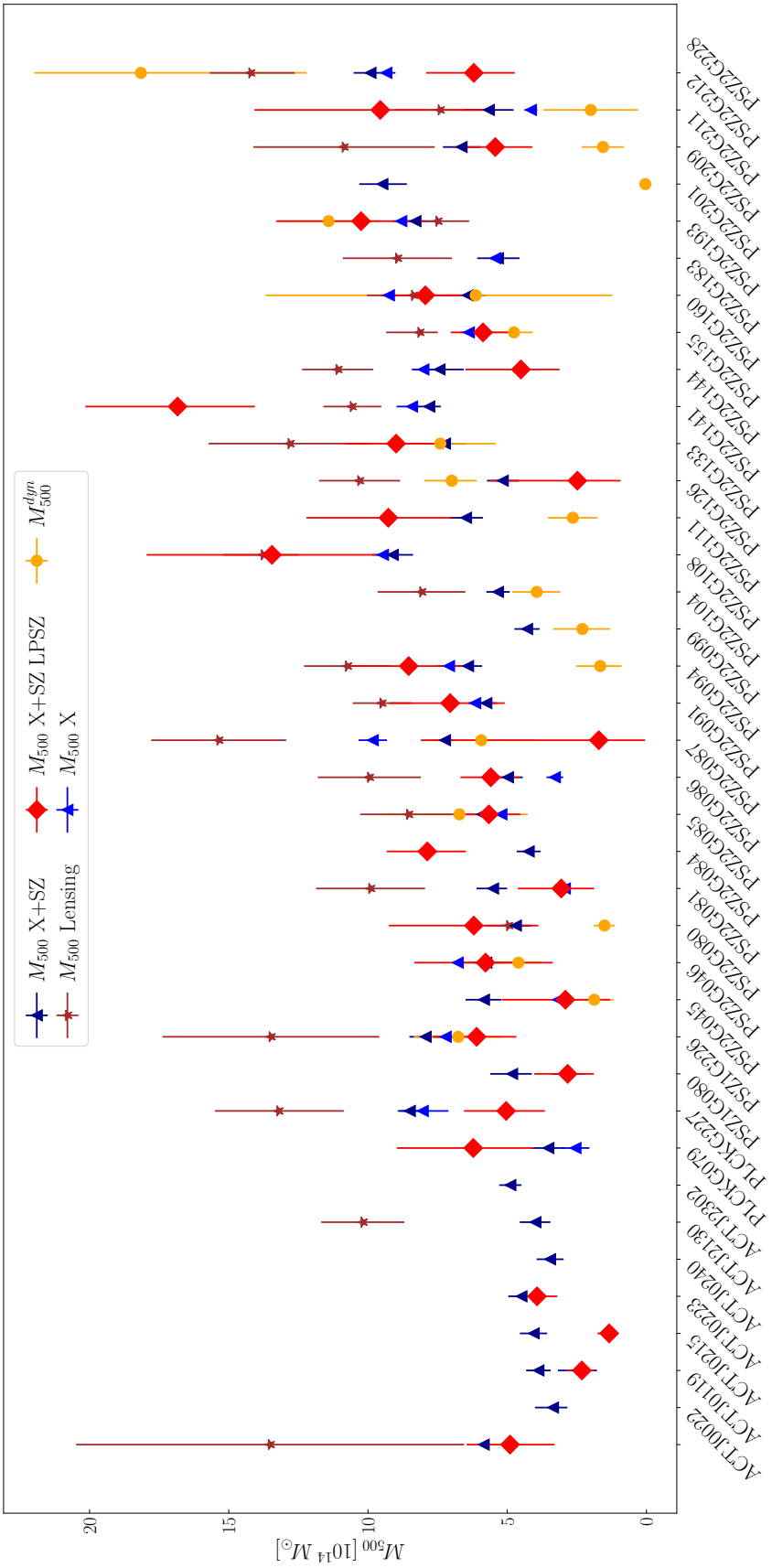

Figure 7.15: Median value of M_{500} per estimate type (lensing, X-ray only, X-ray+SZ and dynamical masses) for every cluster in the LPSZ sample. The NIKA2 mass estimates are shown as red diamonds. We see that the NIKA2 estimates are consistent with X-ray derived masses, as expected. Dynamical masses are overall below the tSZ masses. The difference with the lensing masses is expected and due to the HSE-to-lensing mass bias.

LPSZ sample, taking into account the point sources. We showed that one of the three problematic radio sources had a strong impact on the pressure profile reconstruction of PSZ2G212, completely changing the shape of the profile close to the cluster center.

Finally, we also compared the LPSZ clusters hydrostatic mass estimates with other estimates in the literature. We found that overall, the NIKA2 masses are in good agreement with both X-ray only and X-ray+SZ estimates, as expected.

Radio sources are thus a non negligible contaminant for the SZ signal at 150 GHz. Dedicated follow-up observations of LPSZ clusters at lower frequencies would be very useful to better detect and characterize radio sources. In that regard, the GT camera presented in Part II would be a good complement to NIKA2, as it would allow us to observe the clusters at 100 GHz with a similar angular resolution.

CHAPTER 8

Blind detection of galaxy clusters in the COSMOS field

8.1 Galaxy clusters in the COSMOS field . . . 147
8.2 Revisiting N2CLS maps . . . 147
8.2.1 Data reduction pipeline . . . 147
8.2.2 Final sky maps . . . 149
8.3 Cluster detection methodology . . . 149
8.3.1 tSZ signal modelling . . . 149
8.3.2 Matched-filtering . . . 151
8.3.3 Identification of cluster candidates . . . 151
8.3.4 Serendipitous detection rate . . . 152
8.4 Cluster detection characterization via simulations . . . 152
8.4.1 Cluster detection on simulations . . . 152
8.4.2 Completeness . . . 154
8.4.3 Purity . . . 155
8.5 Cluster candidates validation . . . 156
8.5.1 Cross-matching in NED, SIMBAD and VizieR databases . . . 156
8.5.2 Spectroscopic and photometric redshift catalogs . . . 158
8.5.3 Known bright clusters in the field . . . 158
8.6 Properties of cluster candidates . . . 161
8.6.1 Integrated tSZ emission . . . 161
8.6.2 Cluster candidate mass estimates . . . 163
8.7 Conclusion and perspectives . . . 164

In Chapter 6, we have presented the N2CLS large program, which aims to study high-redshift dusty galaxies in the GOODS-N and COSMOS fields. Thanks to the deep and very high resolution observations, detecting the tSZ effect is also possible. In this chapter, we describe the blind detection methodology, the data reduction pipeline, and the cluster candidate sample detected. An important part of the work presented in this chapter has been published in Chérouvrier et al. (2025).

8.1 Galaxy clusters in the COSMOS field

As we have seen in Section 6.3.2, the COSMOS field has been extensively observed at many wavelengths, from X-ray to radio. This wealth of data enabled the assembly of a large number of cluster catalogs. A summary of currently available catalogs specific to the COSMOS field is given in Table 8.1. Clusters have also been detected in this region by larger surveys like the SDSS [Wen et al., 2012], DESI [Zou et al., 2021], XMM [Mehrtens et al., 2012], KiDS [Lesci et al., 2022] and Subaru Weak-Lensing [Miyazaki et al., 2007] surveys. These catalogs will be essential to validate our blind detections, as we will be able to match any cluster candidate with the aforementioned catalogs and identify optical or X-ray counterparts.

	Survey/Instrument	$N_{clusters}$	z_{range}	Reference
Optical/IR	HIROCS	12	1.2–1.6	Zatloukal et al. (2007)
	zCOSMOS 10k	800	0.08–0.73	Knobel et al. (2009)
	CFHTLS Deep Field	187	0.2–1.6	Olsen et al. (2007); Wen and Han (2011)
	BMH2011	147	0.12–0.80	Bellagamba et al. (2011)
	zCOSMOS 20k	1498	0.08–0.83	Knobel et al. (2012)
	SCC2012	1780	0.2–3.0	Söchting et al. (2012)
	GEEC2	11	0.8–1	Balogh et al. (2014)
	ALHAMBRA	348	0.2–1.2	Ascaso et al. (2015)
	COSMOS Wall	26	~0.73	Iovino et al. (2016)
	AMICO-COSMOS	1269	0.1–2.0	Toni et al. (2024)
	MAGIC	143	0.18–0.67	Epinat et al. (2024)
	COSMOS-Web	1678	0.08–3.70	Toni et al. (2025)
X-ray	XMM-*Newton*	72	0.1–1.5	Finoguenov et al. (2007)
	XMM-*Newton*/*Chandra*	247	0.08–1.3	Gozaliasl et al. (2019)

Table 8.1: Summary of available cluster/group catalogs in the COSMOS field, sorted by increasing publication date. The first column indicates the type of survey. The second column lists the name of the survey or instrument. The third and fourth columns give the number of clusters and the redshift range of the catalog, respectively. The last column gives the associated reference.

The ACT and *Planck* large surveys also observed the COSMOS field. However, at the time of writing, there are no detections of SZ clusters in the area covered by the N2CLS survey. We do note that there is one tSZ cluster candidate in the HAD catalog [Hurier et al., 2021] within the NIKA2 COSMOS footprint, but without any mass or redshift information.

8.2 Revisiting N2CLS maps

The N2CLS collaboration uses the Pointing and Imaging In Continuum (PIIC, Zylka (2013)) software to reduce the raw NIKA2 data. The data reduction process is described in Bing et al. (2023), and is optimized for the detection of positive point sources, mainly high-redshift dusty galaxies. Negative signal from the tSZ effect is filtered out in this pipeline. Furthermore, we extensively used simulations (see Section 8.4) that require full access to the code, which was more difficult to achieve with the PIIC software. Thus, we decided to re-process the raw NIKA2 data using a different procedure.

8.2.1 Data reduction pipeline

The raw NIKA2 data per detector array were reduced using the data reduction pipeline described in [Ponthieu et al., 2025], which is optimized for the detection of faint and small angular size objects. It is an evolution of that of [Perotto et al., 2020], which is the pipeline used to produce the LPSZ

maps described in Chapter 7. As we already presented in detail the data reduction process of the GT camera in Chapter 3, we will refer the reader to this chapter for more details. We will here focus on the steps that are different between the two pipelines.

First, the NIKA2 raw data are transformed into KID resonance frequency shift δf_0 (see Chapter 3) using the 2-points calibration technique [Calvo et al., 2016a] described in Section 3.1.2. Then, Uranus is used as a primary calibrator to estimate the absolute flux calibration factor and convert the KID frequency shift to mJy/beam units. Skydips (see Section 4.4.7) are used to measure the atmospheric opacity and correct the TOIs. The noise decorrelation procedure used here is different from the one used in the GT pipeline (see Section 5.4). For each 45s sub-scan, we fit the TOI of each detector, k, to the following model:

$$\begin{aligned} \mathrm{TOI}_k(t) = S_k^{sky}(t) + a_k \cdot S^{atm}(t) + b_k \cdot S^{atm'}(t) + d_k \cdot (S^{atm}(t))^2 + \sum_i e_{k,i} \cdot T_i^{elec}(t) \\ + \sum_{h=0}^{N_{harms}} (A_{h,k} \cos(w_h t) + B_{h,k} \sin(w_h t)) + c_k + c'_k \cdot t \,, \end{aligned} \tag{8.1}$$

where S_k^{sky} is the astronomical signal at the position observed by detector k. S^{atm} is a template of the atmospheric signal built from all detectors of a given array, and $S^{atm'}$ its time derivative to account for gradients across the array. The square of the atmospheric model is also added to account for possible non-linearities of a given KID. To account for electronic noise we use off-resonance measurements [Catalano et al., 2014b]. Off-resonance measurements are sampled as the detector signal and come from reading tone frequencies set apart from any KID resonance. As the electronic noise is strongly correlated between detectors and the off-resonance measurements, the electronic noise templates, T_i^{elec}, are constructed by coadding all off-resonance that belong to the same electronic box i. The harmonic term consists of a series of cosine and sine terms with $N_{harms} = 8$, equivalent to a high pass filtering above 1/3 Hz. The final terms $c_k + c'_k \cdot t$ allow a linear baseline, where t is the time. For each KID k, a single linear regression is performed per sub-scan, to determine the coefficients a_k, b_k, c_k, c'_k, d_k, $e_{k,i}$, $A_{h,k}$ and $B_{h,k}$, once the templates S^{atm}, $S^{atm'}$, and T_i^{elec}, have been computed. We observe some residuals in maps which are projected in Nasmyth coordinates, with striping corresponding to the electronic box orientation at 260 GHz. We decided to correct for this pattern with one template per array.

The cleaned TOIs are then projected on a grid and coadded with weights depending on their noise level, using an inverse variance weighting scheme (see Section 5.5), to produce the final maps per array. The decorrelation method needs to be performed iteratively because the sky signal can impact the procedure. By subtracting from S_k^{sky} the high SNR point source signal from the previous iteration, we can improve the quality of the final maps. We have found that only a few iterations are needed for this process to converge. The processing parameters (basically the high pass filtering) have been tuned to optimize the detection of point and compact sources, but the filtering is mild enough to allow slightly extended sources to be detected, in particular the SZ effect of compact clusters or groups. We found that the decorrelation procedure induces a filtering at large scales on the final maps (due to the final harmonic term) that we need to take into account in our analysis.

To characterize this filtering, we run a white noise simulation through the pipeline and compute the transfer function as the ratio between the power spectra of the input white noise map and of the pipeline output. The transfer function is shown in Figure 8.1 as a function of the inverse of the angular scale, k. We observe significant filtering for $k < 0.5$ arcmin^{-1}.

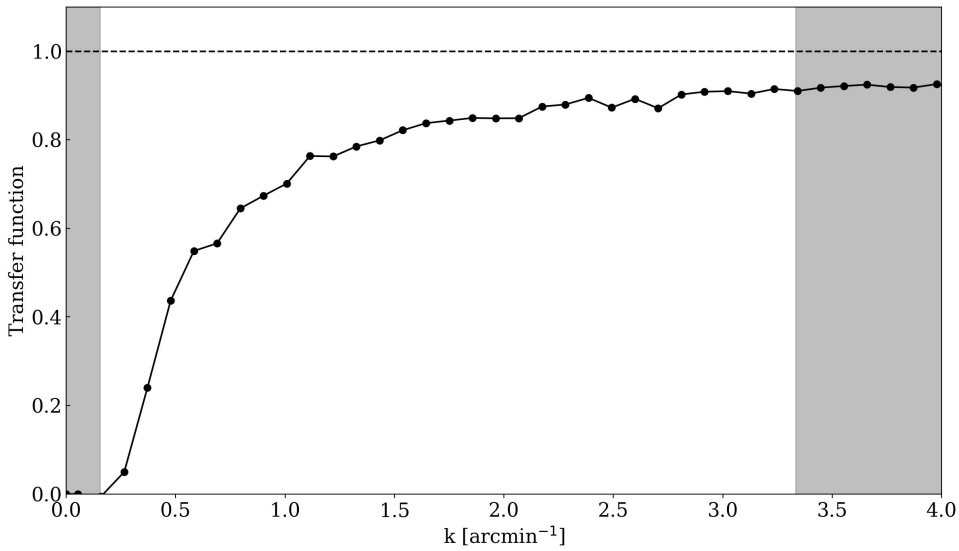

Figure 8.1: Transfer function as a function of angular scale for the pipeline used to construct the NIKA2 150 GHz COSMOS maps discussed in this chapter. The shaded gray regions represent the NIKA2 FoV (left) and instrumental beam (right).

8.2.2 Final sky maps

The final 150 and 260 GHz maps, constructed combining the signal from all available observation scans for the final iteration step of the pipeline, are shown in Figure 8.2. We can see that on the edges, the noise increases significantly. We thus decided to limit our analysis to the central region of the map, shown inside the black contour in Figure 8.2. We chose a region of 877 arcmin^2 (~ 0.25 deg^2) where the noise is below 1.2 times the median noise value over the full map.

In addition, null maps, or JK McIntosh (2016) maps, are constructed by alternately multiplying scan pairs by +1, -1 and co-adding them. This effectively subtracts the astrophysical signal to obtain realistic noise maps. These noise maps are used in our cluster detection algorithm presented in Section 8.3.

8.3 Cluster detection methodology

8.3.1 tSZ signal modelling

The tSZ cluster contribution to the NIKA2 150 GHz maps can be modeled as

$$S^{\rm tSZ}_{150\ \rm GHz}(x) = C^{\rm tSZ}_{150\ \rm GHz}\ y(x)\,, \tag{8.2}$$

where x is the spatial dependency and $C^{\rm tSZ}_{150\ \rm GHz}$ accounts for the tSZ spectrum in Jy/beam units for the 150 GHz NIKA2 band [see, Ruppin et al., 2018; Kéruzoré et al., 2020; Muñoz-Echeverría et al., 2023].

As a reminder, the Compton parameter y, defined in Equation 2.5, is given by the integration along the line of sight of the electronic pressure P_e of the ICM. In the following, we assume that clusters are spherically symmetric, and that their pressure profile is well described by the universal pressure profile (UPP) model defined in Arnaud et al. (2010) (see Chapter 2 and Section 2.4.1). In this model, we only considered as free parameters the cluster redshift, z, and the mass M_{500}. The rest of the parameters were fixed to the values derived in Arnaud et al. (2010) and shown in Equation 2.14.

In the same paper, the authors also provide a scaling relation between the integrated cluster mass and the integrated Compton parameter at R_{500}:

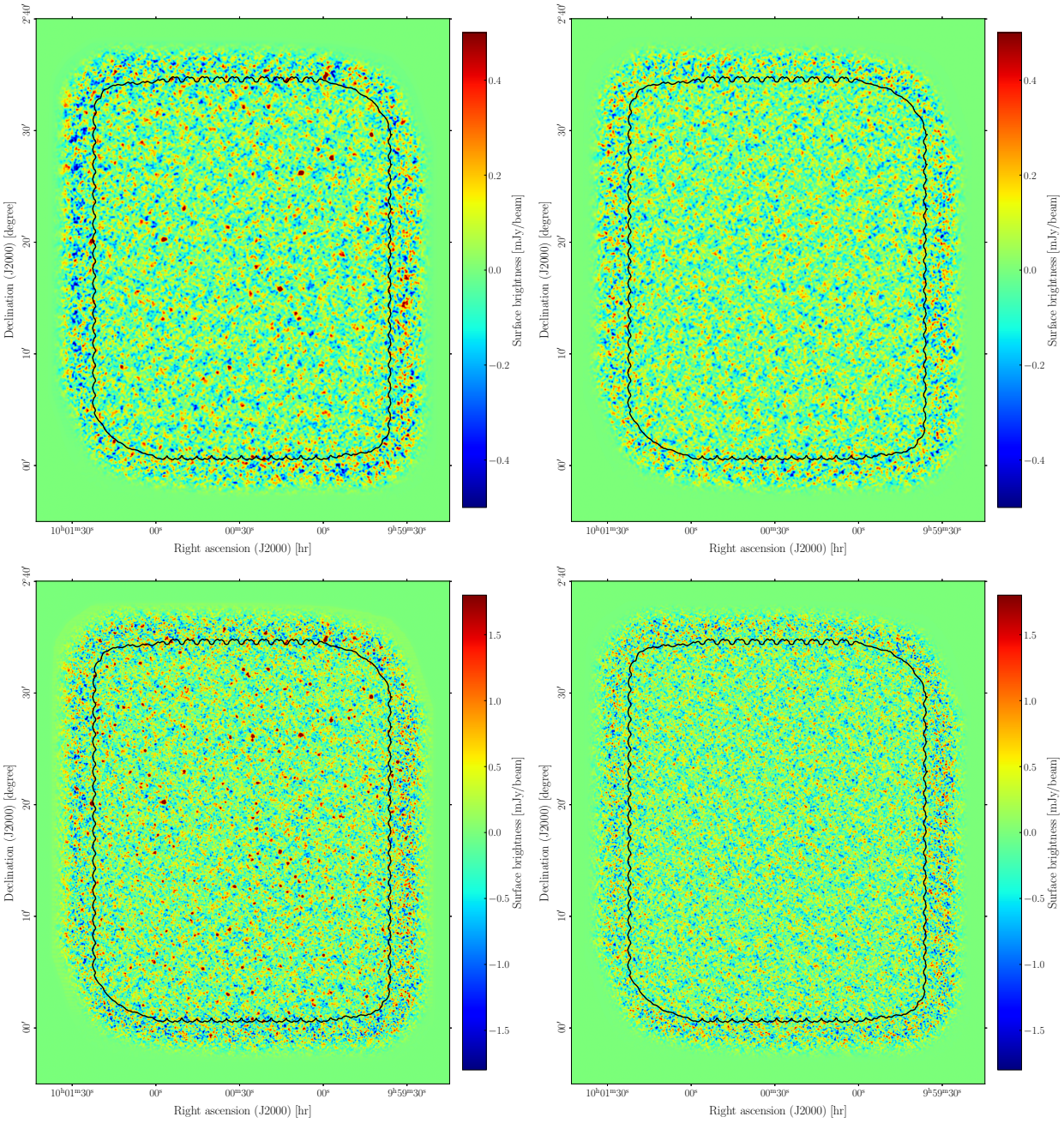

Figure 8.2: NIKA2 COSMOS maps at 150 GHz (top) and 260 GHz (bottom), and their associated JK maps. The black contour shows the high quality region defined in Section 8.2.2. Outside this region, the noise increases significantly. We can see some very bright positive point-like sources in both maps, corresponding to either dusty galaxies or radio sources. If we look carefully, we can also see some negative compact signal in the 150 GHz map, which could be due to the tSZ effect of galaxy clusters.

$$Y_{500} = 2.925 \times 10^{-5} I(1)\, h(z)^{2/3} \left[\frac{M_{500}}{3 \times 10^{14} h_{70}^{-1} M_{\odot}} \right]^{5/3+0.12} h_{70}^{-1}\ \mathrm{Mpc}^2\,, \tag{8.3}$$

where $I(1) = 0.6145$. The angular size of a cluster θ_{500} is defined as

$$\theta_{500} = \arctan\left(\frac{R_{500}}{\mathcal{D}_A} \right). \tag{8.4}$$

The pressure model was integrated along the line of sight and projected on a 2D grid to obtain a Compton parameter map, $y(\theta)$. We converted it to surface brightness (see Equation 8.2) using the $C^{\rm tSZ}_{150\,\rm GHz}$ value discussed in Ruppin et al. (2018). We convolved the model map with the NIKA2 150 GHz beam and corrected by the transfer function computed in Section 8.2.1 to account for the filtering at large angular scales.

8.3.2 Matched-filtering

We search for galaxy cluster candidates in the N2CLS data using a matched filter technique [Herranz et al., 2002; Melin et al., 2006], to optimally extract the tSZ signal from the map. As discussed in Section 2.3.5, this method has been used by previous large SZ surveys to blindly detect galaxy clusters, without prior knowledge of their positions. In this analysis, we only use the 150 GHz data, as the tSZ signal is expected to be well below the noise in the 260 GHz map, and the contamination due to point sources, mainly dusty galaxies, is too high. As an example, the expected peak tSZ signal at 260 GHz of an intermediate redshift ($z = 0.5$) and high mass ($M_{500} = 5 \times 10^{14} M_{\odot}$) cluster is 0.28 mJy/beam, which is approximately two times smaller than the rms noise in the map (0.48 mJy/beam).

We use the *PyMF* Python package described in [Erler et al., 2019] as our matched-filter algorithm. As our spatial template of the tSZ signal S (see Equation 2.9), we use the tSZ model presented in the previous section and given by Equation 8.2. To cover a wide range of possible cluster angular sizes, we produce a set of 15 cluster templates, with typical angular sizes $\theta_{500} \in [18.5\,'', 185\,'']$. For simplicity, we keep the redshift constant and vary the cluster's mass to obtain different cluster sizes. The SZ cluster templates are obtained using the *minot* Python package [Adam et al., 2020].

8.3.3 Identification of cluster candidates

Using the method detailed in Section 8.3, we obtain a set of match-filtered maps where the tSZ signal is enhanced. Using the *find_peak* routine in the *photutils* package [Bradley et al., 2023], we identify cluster candidates as peaks above a SNR threshold of 4 in the match-filtered maps. The extraction box size is set to 9 pixels, to only extract 1 candidate per beam. When a candidate is detected in multiple filtered maps, its center position and SNR are taken from the map where the detection has the highest SNR value. During the match-filtering process, we also carefully mask bright positive point sources in the map. Indeed, the filtering of these sources can produce ringing artifacts with negative signal, and thus impact cluster detection.

Figure 8.3 shows, as an example, one of the SNR maps, filtered to optimally extract objects with $\theta_{500} = 30.4''$. The cluster's SNR will be positive, as the negative sign of the tSZ signal at 150 GHz has already been accounted for in the filter. Positive peaks in this map, highlighted in black, can be identified as cluster candidates. To validate the significance of the SNR estimates, we also applied the matched filtering technique to the null maps (see Section 8.3.4). Figure 8.4 shows the pixel SNR distribution for both the match-filtered data and null maps. For the null map (red), we obtain a Gaussian-like distribution consistent with the noise distribution in the data. For the filtered data (blue), we clearly observe a large negative SNR tail corresponding to point sources in the original map. We also observe a positive tail, which corresponds to the cluster candidates.

As presented in Table 8.2, we detect 16 cluster candidates in the low noise area defined in Section 8.2.2. The mean SNR of our candidate sample is SNR $\sim$ 4.51, with detections spanning from a SNR of 4 to 5.31. Figure 24 shows a cutout of the 150 GHz signal map around each of the cluster candidates. In this case, they appear as compact negative objects in the map, due to the filtering of the signal at large angular scales.

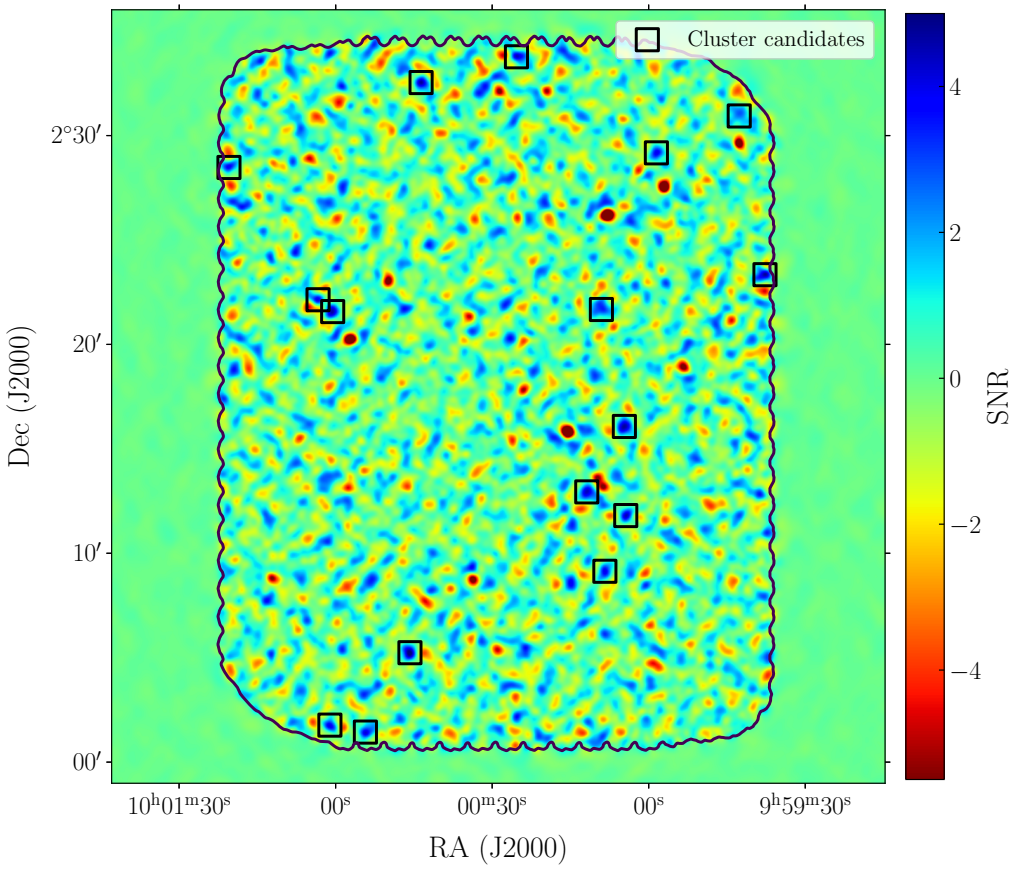

Figure 8.3: SNR map of the matched-filtered 150 GHz COSMOS map. Positive SNR values corresponding to cluster candidates are shown in blue, matching the colors in Figures 8.13 and 24, as expected for tSZ emission. The angular size of the applied matched filter is equal to 30.4″. The black contour shows the high quality region discussed in Section 8.2.2. Cluster candidates are highlighted in black squares. 16 candidates have been detected above a SNR threshold of 4 (see Section 8.3.3).

8.3.4 Serendipitous detection rate

To estimate the expected number of random detections in the survey area, we generate 1000 noise-only maps without any tSZ signal, and run the detection algorithm. We find an average of 2.36 serendipitous detections above a SNR of 4 per null map. We thus expect an overall purity of 85% for our sample, excluding point source effect. The overall purity increases to 93% above a SNR of 4.2, where we only expect ~ 1 random detection. A more detailed assessment of the purity using tSZ simulations is given in Section 8.4.

8.4 Cluster detection characterization via simulations

8.4.1 Cluster detection on simulations

To characterize our cluster detection algorithm, we use a set of realistic simulations of the COSMOS field. We have first produced 1000 large mock cluster catalogs. We estimate the expected number of clusters in the area considered in our analysis (877 arcmin^2), by integrating the Tinker et al. (2008) mass function in bins of redshift ($0 < z < 3$) and mass ($2 \times 10^{13} M_\odot < M_{500} < 3 \times 10^{15} M_\odot$). For each catalog, we draw the number of clusters from a Poisson distribution, assign to each cluster a mass and redshift drawn from the mass function, and a random position in the survey area. The distribution of simulated clusters in the mass-redshift plane is shown in the left panel of Figure 8.5. To model the cluster signal, we use the model presented in Section 8.3.1. To these thermal SZ maps we add residual

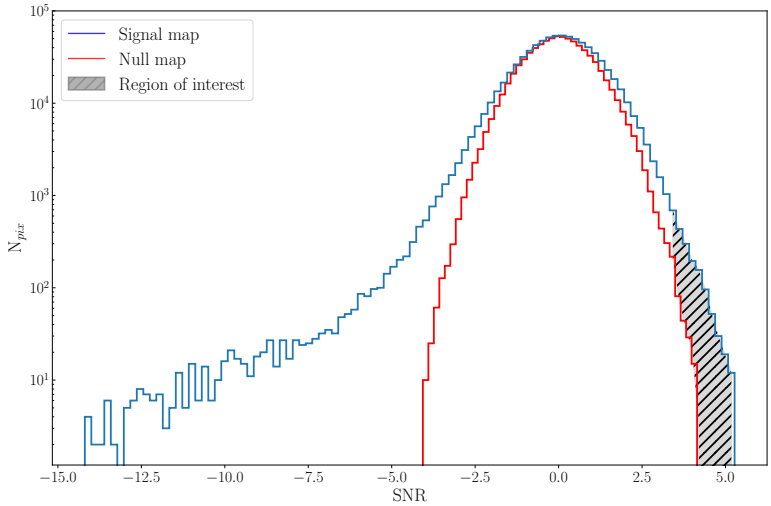

Figure 8.4: Pixel negative SNR distribution in the match-filtered N2CLS 150 GHz signal map (blue) and null map (red). The high negative SNR tail is due to point sources. The hatched grey area shows a small positive SNR tail up to SNR ~ 5, indicating strong negative signal in the 150 GHz signal map, as expected for the SZ sources.

atmospheric and instrumental noise by using the null maps described in Section 8.2.2.

We also need to investigate the contribution of CMB anisotropies to the NIKA2 150 GHz map. Note that measurements of the CMB power spectrum, $C_\ell^{\rm CMB}$, at the very high ℓ multipoles sampled by NIKA2 ($\ell > 10^4$) are not available. Furthermore, theoretical models become inaccurate at such small angular scales. Thus, we fit a power law to the current *Planck* best-fit CMB power spectrum and extrapolate it to very large ℓ multipoles. Finally, we compute the expected CMB rms signal as

$$\sigma^2_{\rm CMB} = \langle T_1 T_2 \rangle = \frac{1}{4\pi} \sum_\ell (2\ell + 1) C_\ell^{\rm CMB} P_\ell(\cos(0)) \,, \tag{8.5}$$

where P_ℓ are the Legendre polynomials. We find that, accounting for the pipeline transfer function, the CMB induced noise is negligible at the scales probed in this analysis. Thus, it will not be accounted for in the following.

Finally, we use the Simulated Infrared Dusty Extragalactic Sky model (SIDES, Béthermin et al. (2017); Béthermin et al. (2022)) to account for the signal expected from other sky components (e.g., point sources). SIDES includes galaxy clustering, and produces a catalog of galaxies with a large set of physical parameters. We use the SIDES light cone from the Uchuu simulation [Ishiyama et al., 2021; Gkogkou et al., 2023]. Contributions from radio sources and the spatial correlation between simulated components are not taken into account. For each simulated cluster catalog, we produce 104 simulated maps using independent tiles from the SIDES sky model. This will prevent any overlapping of bright point sources and massive clusters from impacting the completeness and purity of the sample (see Section 8.4.2 and 8.4.3). We show in Figure 8.5 an example of a simulated map, including the tSZ signal from clusters and all other contributions.

We first run the detection algorithm presented in Section 8.3 on the full set of simulated maps, using a 2D Gaussian as template, to detect very bright positive sources in the maps (above SNR = 10). The filtering of these bright sources could produce ringing artifacts with negative signal, and thus impact cluster detection. The detected bright sources are fitted with a 2D Gaussian and subtracted from the simulations. We then convolve these simulated maps with the NIKA2 beam and correct by the pipeline's transfer function shown in Figure 8.1. The bright sources are added back after filtering. This method was also used in the data reduction pipeline described in Section 8.2.1. Using the transfer function directly is a good compromise, as processing all simulated maps through the pipeline is very

Candidate Name	RA °	DEC °	SNR	z	θ_{500} arcmin	Y_{500} 10^{-5} arcmin^2	M_{500} 10^{14} $M_\odot$	Matching cluster name (distance [″])	Reference(s)
NK2-CL J100045.8+020514.3	150.1907	2.0873	5.31	–	$0.74^{+0.40}_{-0.20}$	$1.60^{+1.45}_{-0.56}$	–	–	–
NK2-CL J095937.7+022320.4	149.9071	2.3890	5.00	0.74±0.03 (p)	$1.38^{+0.12}_{-0.13}$	$3.35^{+1.77}_{-1.34}$	$1.51^{+0.40}_{-0.38}$	ALH J0959.38+0223.03 (17.8″)	(1)
NK2-CL J100004.7+021604.4	150.0194	2.2679	4.97	–	$0.92^{+0.62}_{-0.29}$	$1.95^{+2.65}_{-0.88}$	–	–	–
NK2-CL J100043.6+023232.4	150.1818	2.5423	4.87	–	$0.65^{+0.31}_{-0.13}$	$1.11^{+0.75}_{-0.30}$	–	–	–
NK2-CL J100025.3+023346.4	150.1056	2.5629	4.67	0.72±0.02 (p)	$1.37^{+0.12}_{-0.14}$	$2.90^{+1.57}_{-1.24}$	$1.38^{+0.38}_{-0.37}$	[BMH2011] 124 (11.5″)	(2), (3), (4)
NK2-CL J100100.6+022134.4	150.2524	2.3596	4.67	0.77±0.01 (p)	$1.36^{+0.09}_{-0.11}$	$3.47^{+1.42}_{-1.25}$	$1.56^{+0.33}_{-0.34}$	[SCC2012] 0788 (9.1″)	(5)
NK2-CL J100004.4+021148.4	150.0183	2.1968	4.60	0.94±0.05 (s)	$1.10^{+0.09}_{-0.10}$	$2.10^{+0.91}_{-0.78}$	$1.21^{+0.27}_{-0.27}$	[KLI2009] 146* (8.7″)	(3)
NK2-CL J100103.4+022208.4	150.2641	2.3690	4.54	–	$0.59^{+0.23}_{-0.09}$	$0.85^{+0.35}_{-0.20}$	–	–	–
NK2-CL J100011.9+021256.5	150.0494	2.2157	4.48	0.24±0.08** (p)	$3.79^{+2.11}_{-1.01}$	$28.20^{+69.45}_{-16.79}$	$2.83^{+1.55}_{-0.88}$	XMMXCS J100012.3+021246.7 (11.7″)	(6)
NK2-CL J100101.1+020146.6	150.2546	2.0296	4.30	–	$0.71^{+0.44}_{-0.16}$	$0.96^{+0.83}_{-0.29}$	–	–	–
NK2-CL J100054.3+020126.4	150.2262	2.0240	4.28	1.42±0.01 (p)	$0.81^{+0.05}_{-0.06}$	$1.56^{+0.62}_{-0.53}$	$1.00^{+0.21}_{-0.21}$	[SCC2012] 1517 (16.0″)	(5)
NK2-CL J100009.1+022140.3	150.0378	2.3612	4.27	–	$2.56^{+2.96}_{-1.16}$	$14.30^{+81.99}_{-10.55}$	–	–	–
NK2-CL J095942.6+023056.5	149.9277	2.5157	4.08	0.73±0.02 (s)	$1.45^{+0.11}_{-0.13}$	$4.10^{+1.83}_{-1.55}$	$1.69^{+0.39}_{-0.39}$	DESI 2353000051 (12.0″)	(7)
NK2-CL J100120.5+022828.2	150.3353	2.4745	4.07	–	$0.71^{+0.44}_{-0.15}$	$0.93^{+0.75}_{-0.28}$	–	–	–
NK2-CL J100008.4+020908.3	150.0350	2.1523	4.04	–	$0.77^{+0.65}_{-0.21}$	$1.20^{+1.72}_{-0.44}$	–	–	–
NK2-CL J095958.5+022910.4	149.9938	2.4862	4.01	0.40±0.01 (p)	$2.52^{+0.22}_{-0.23}$	$12.24^{+6.22}_{-4.77}$	$2.38^{+0.61}_{-0.57}$	[SCC2012] 0270 (14,8″)	(5)

Table 8.2: Galaxy cluster candidates, sorted by decreasing SNR, with SNR > 4. The first column gives the name of the candidate. The right ascension (J2000) and declination (J2000) are presented in the second and third columns, respectively. The SNR of each candidate is given in the fourth column. The fifth column lists the candidates' estimated redshift, z, associated uncertainties and redshift type (photometric (p) or spectroscopic (s)). In the sixth and seventh columns we present the cluster angular size θ_{500} and tSZ flux, Y_{500} (see Section 8.6). For candidates with known redshift, we list their estimated mass M_{500} and uncertainties in the eighth column (see Section 8.6.2). The last column gives the name of the matched counterpart in external catalogs with its distance to the NIKA2 cluster candidate center in arcsec and the reference. A * indicates that the object is a group of galaxies. A ** indicates a possible superposition of a low and a high-redshift cluster (see Section 8.5.2). References: (1) Ascaso et al. (2015); (2) Bellagamba et al. (2011); (3) Knobel et al. (2009); (4) Iovino et al. (2016); (5) Söchting et al. (2012); (6) Mehrtens et al. (2012); (7) Zou et al. (2021).

long and computationally expensive. There are no big differences between the two processes, as bright sources have been subtracted before filtering.

We then run the detection algorithm on the simulated maps using the cluster template presented in Section 8.3.1. We identify SNR peaks with SNR > 4 in the resulting match-filtered maps. The position and SNR of each cluster candidate is stored in an output catalog. We define the matching radius to 20″ – the size of the NIKA2 beam slightly extended for uncertainties as in previous studies [see e.g. Planck Collaboration et al., 2016c]. We first match each input cluster with the closest detection in the output catalog using the *astropy* function *match_to_catalog_sky*. Then, we match the output catalog with the input catalog. Note that we will always require two-way matches for the following studies. If there are multiple associated input clusters with a single output cluster in a radius the size of the NIKA2 beam around the detection, we choose the best matching cluster based on 2 criteria: the Y_{500} value and the cluster-detection separation. This will prevent detections from being matched with very faint clusters, which can introduce biases on the sample's completeness (see Section 8.4.2). From the results we can compute the average number of detections in the simulations and compare it to what we find in the data. We show in Figure 8.6 the distribution of the number of detections with SNR > 4 in our simulations. Taking the median (black line) we find an average of 26 ± 5 detections for SNR > 4. In the COSMOS data, we found 16 detections (red line) with SNR > 4, which is lower but still compatible within 2σ with the simulations.

8.4.2 Completeness

The completeness of a survey is a crucial information to characterize the sample and the performance of the detection algorithm. We define it as the fraction of true cluster detected with respect to the clusters in the input mock catalog:

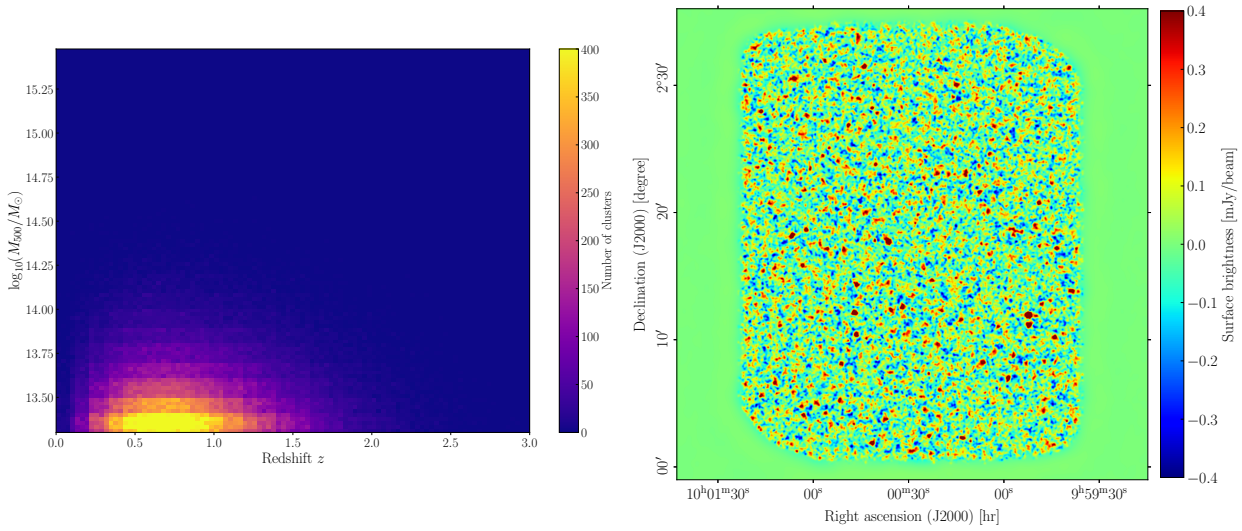

Figure 8.5: (Left): Distribution of all simulated clusters as a function of redshift and mass. (Right): Example of a simulated NIKA2 150 GHz map including the tSZ signal from clusters, realistic noise, and contributions from point sources using the SIDES sky model.

$$C = \frac{N_{\rm det}^{\rm true}}{N_{\rm input}} \,. \tag{8.6}$$

In Figure 8.7 we present, color coded, the completeness in bins of mass and redshift for the NIKA2 sample as derived from the simulations described above. We observe, as expected, that the detection algorithm performance is limited at low mass and low redshift, for which clusters are faint and extended and thus filtered out by the pipeline transfer function (see Section 8.2.1). However, at higher redshift, $z > 1$, we reach a completeness above 80% for $M_{500} > \ 2 \times 10^{14} M_\odot$. As the redshift increases, we can effectively detect clusters with lower and lower masses, down to $M_{500} \sim 1 \times 10^{14} M_\odot$ at $z \sim 1.5$. This is also what we observe in the left panel of Figure 8.8, which shows the completeness as a function of M_{500} for different redshift ranges. The whole sample is complete, $C > 80\%$, for $M_{500} > 1.7 \times 10^{14} M_\odot$ in all redshift ranges. We expect to detect most clusters above this mass threshold in the survey area. These results highlight the interest of high resolution instruments to target the detection via the tSZ effect of high redshift and low mass clusters, which are not accessible with more traditional CMB experiments. We stress also that the limit in cluster mass is mainly imposed by the depth of the survey, which in the case of the COSMOS field was not optimized for cluster detection.

8.4.3 Purity

Another key information that we can draw from the simulations is the purity of the extracted cluster sample, which we define as the percentage of true detections in the sample:

$$P = \frac{N_{\rm det}^{\rm true}}{N_{\rm det}} \,. \tag{8.7}$$

We show in the right panel of Figure 8.8 the purity of the sample as a function of the SNR for different redshift ranges. We find that the purity increases significantly with redshift. For high-redshift clusters, $z > 1$, the purity is above 65% (90 %) for SNR > 4 (> 5). From the simulations and the results presented in Section 8.3.4, we have observed that the purity of the sample is much better if point sources are not included in the simulations. In Section 8.3.4, where we describe a best case scenario where the detection is noise limited, we found that the purity is 85% for SNR > 4. This is because adding point sources shifts the map's overall and local zero-level and introduces ringing

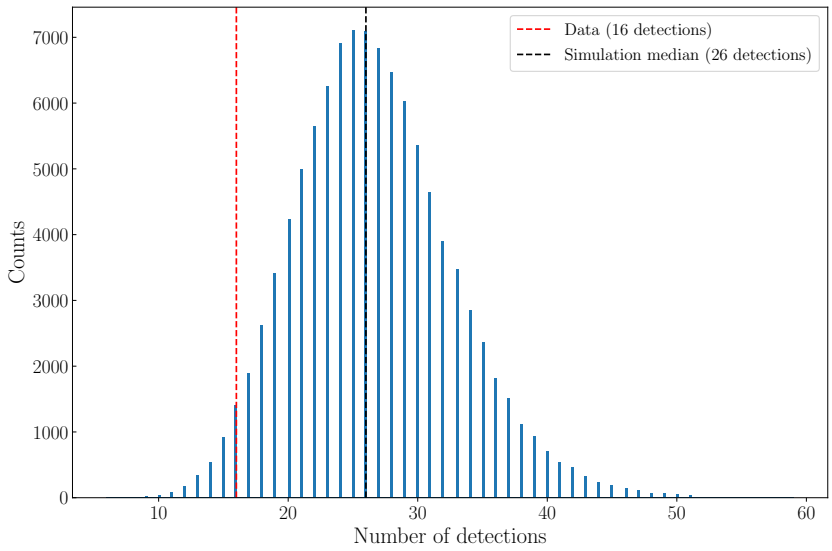

Figure 8.6: Distribution of the number of detections with SNR > 4 per simulated map. The median value is 26 ± 5 detections. The red and black dashed lines show the number of detections found in the NIKA2 COSMOS 150 GHz map and the median of the simulations, respectively.

artifacts from processing and also extra local variance. From these results, we can effectively validate the SNR threshold of 4 we have chosen to build our cluster candidate sample.

8.5 Cluster candidates validation

We have performed an extensive validation of the cluster candidates presented in Section 8.3.3 using existing datasets and archives.

8.5.1 Cross-matching in NED, SIMBAD and VizieR databases

We search for known clusters around our candidates in the NED[1] and SIMBAD[2] databases, where most of the detected clusters are cataloged. We adopt a search radius of 20 arcsecond around each candidate for both databases. In SIMBAD, we only query objects listed as galaxy clusters or group of galaxies. For NED, after querying all objects in the vicinity of the candidates, we only consider objects listed as a cluster or group of galaxies for the matching. We also perform a systematic query in the VizieR[3] database to avoid missing any association with recent cluster catalogs (e.g., DESI, Wen and Han (2024)). Our candidates are matched with VizieR catalogs classified as 'Clusters of galaxies'.

We find that, from our sample of 16 cluster candidates, 8 are matched with a known cluster. From those, 7 were identified in the SIMBAD and NED databases, and 1 in VizieR. For each cluster candidate, the name of the closest counterpart, the distance to it, and its redshift are given in Table 8.2. The median redshift of the sample is $z \sim 0.74$, with 2 candidates at high redshift, $z > 0.9$. We have no match with already detected tSZ clusters from traditional large CMB surveys when querying the SZMC database [4]. We have 7 matches in optical and NIR cluster catalogs like the ALHAMBRA [Ascaso et al., 2015], BMH [Bellagamba et al., 2011], DESI [Wen and Han, 2024], COSMOS 10k [Scoville et al., 2007], COSMOS Wall [Iovino et al., 2016] and SCC [Söchting et al., 2012] catalogs. One candidate matches with an X-ray detected cluster in the XMMXCS catalog [Finoguenov et al.,

[1] https://ned.ipac.caltech.edu/
[2] https://simbad.u-strasbg.fr/simbad/
[3] https://vizier.cds.unistra.fr/
[4] http://szcluster-db.ias.u-psud.fr/

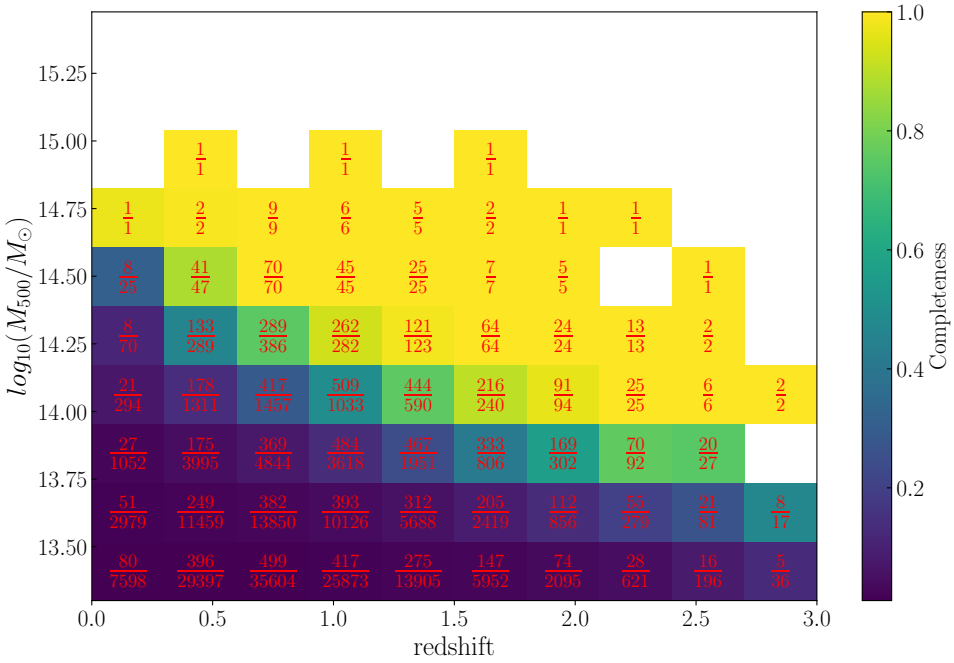

Figure 8.7: Color coded completeness defined as the probability for a cluster of mass M_{500} and redshift z to be detected. The number of true clusters detected with respect to the total number of simulated clusters is given for each bin in mass and redshift.

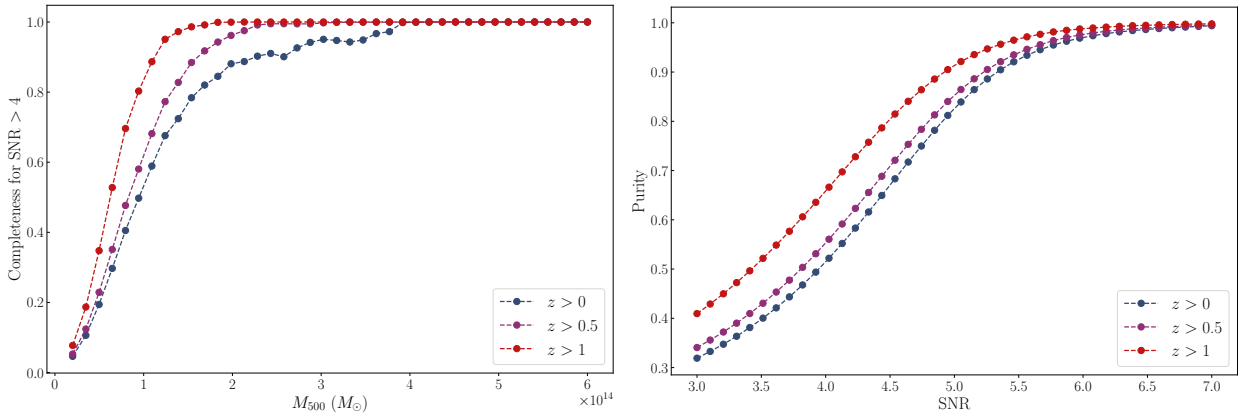

Figure 8.8: (Left): Completeness as a function of the mass, M_{500}, for different redshift ranges. We reach 80% completeness at all redshifts for $M_{500} > 1.7 \times 10^{14} M_\odot$. (Right): Purity as a function of SNR for different redshift ranges. The purity rises quickly with SNR, reaching 50% and 80% at SNR $\sim$ 4 and $\sim$ 5 at all redshifts, respectively.

2007]. We notice that the highest SNR cluster candidate, NK2-CL J100045.8+020514.3, does not match any known cluster, making it an interesting candidate for follow up observations. Figure 8.9 shows an example optical image of the NK2-CL J100004.4+021148.4 candidate, which has an optical counterpart at $z = 0.94$.

To quantify the impact of random association between our cluster candidates and clusters in the literature, we use our cross-matching procedure described in Section 8.5.1 on our detected simulated clusters from Section 8.4. We found that 24.6% of them are matched with a cluster in the literature, compared to 50% in our observed sample. We found that $\sim$ 0.28% are randomly matched with an X-ray cluster, compared to 6.5% for our sample. There is a non negligible 6.9% chance for a simulated cluster to match at random with a detection from the SCC catalog [Söchting et al., 2012]. In our observed sample, 19% are matched with a cluster in the SCC catalog. We have tested other matching radii, but found that this one (20″) gives the best ratio between true and random associations.

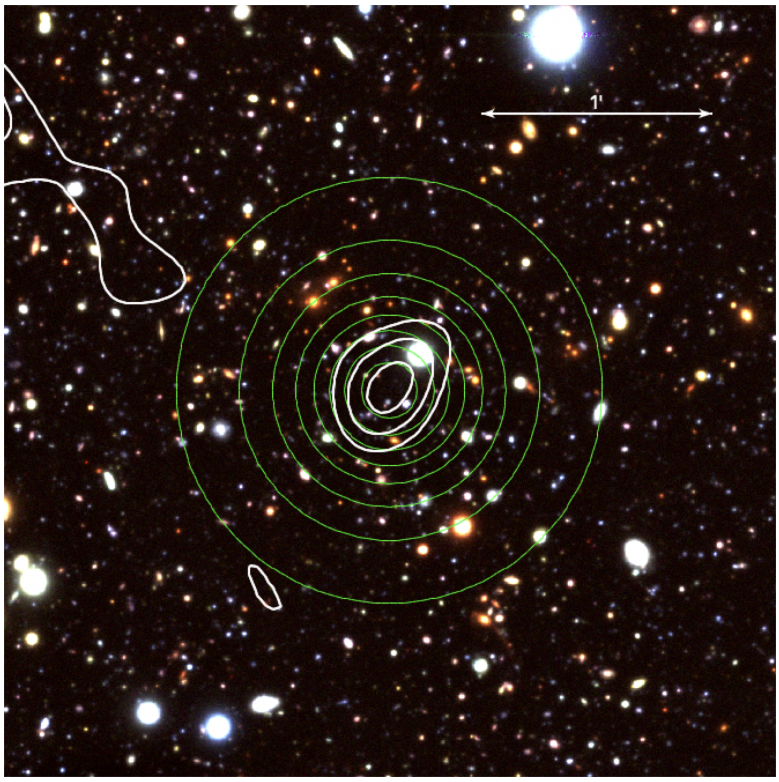

Figure 8.9: Hyper Suprime-Cam (HSC, Aihara et al. (2018b)) combined three color image of NK2-CL J100004.4+021148.4, using the g, r, and i filters. The image is 200″ on a side, with north at the top and east at the left. The contours in white show SNR levels in the match-filtered map from Figure 8.3, starting at 2σ and spaced by 1σ. The green contours show the unfiltered tSZ cluster model, as seen in the third panel of Figure 8.13.

8.5.2 Spectroscopic and photometric redshift catalogs

To completement the validation process, we also had access to a spectroscopic [Khostovan et al., 2025] and a photometric redshift catalog [Weaver et al., 2022]. For both catalogs, we searched for all objects labeled as galaxies, with an available redshift measurement, within a radius of 1 arcmin around each cluster candidate. This search radius is consistent with the average θ_{500} value we have found for the NIKA2 candidates (see Section 8.6.1 and Table 8.2). For each of the NIKA2 cluster candidates we show histograms of spectroscopic (blue) and photometric (red) galaxy redshifts in Figure 8.10. When available, redshift estimates of the cluster candidates are shown as a black dashed line. We observe that in some cases, for example in panels (b), (g), (m) and (p), the expected redshift for the identified NIKA2 candidates lies in the peak of the redshift distribution of galaxies. We note that we expect to have both cluster member galaxies as well as fore/background galaxies. Furthermore, we observe that for some of the unmatched NIKA2 cluster candidates, such as in panels (l) and (o), well-defined redshift peaks are found at relatively high redshifts. In some cases, for example NK2-CL J100011.9+021256.5 (panel (i)) with a known counterpart at $z = 0.24$, we find multiple well-defined peaks, suggesting a superposition of a low and a high-redshift cluster. A more detailed analysis of optical data was not possible at the time of writing this thesis.

8.5.3 Known bright clusters in the field

As presented in Section 8.1, there are several cluster catalogs in the COSMOS field. Our final validation step was to check in these catalogs if any bright clusters were not detected in the NIKA2 COSMOS map. We first checked the Finoguenov et al. (2007) catalog, with 21 clusters in the NIKA2 COSMOS footprint. We show in Figure 8.11 the NIKA2 150 GHz map with our NIKA2 cluster

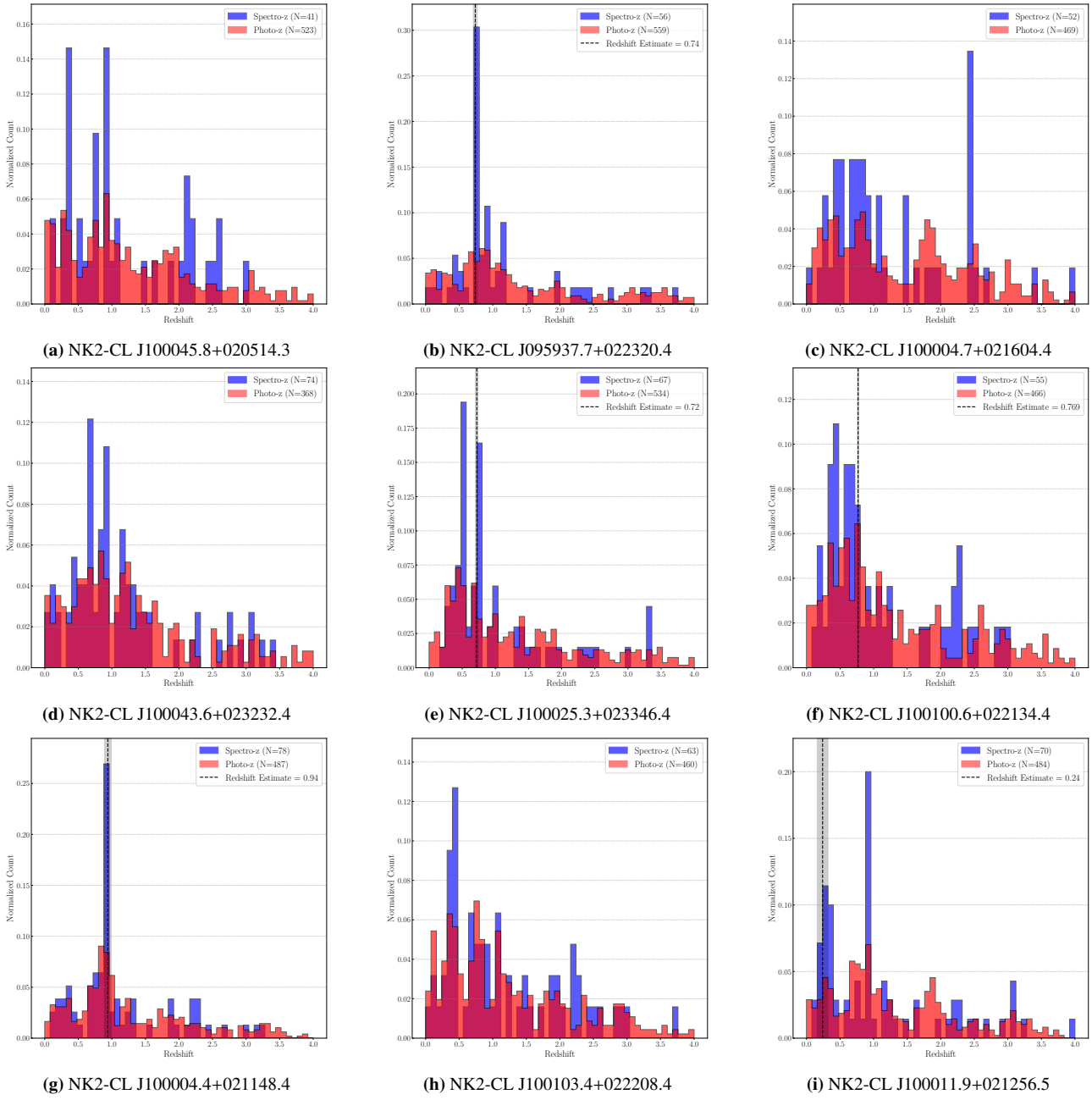

(a) NK2-CL J100045.8+020514.3 **(b)** NK2-CL J095937.7+022320.4 **(c)** NK2-CL J100004.7+021604.4

(d) NK2-CL J100043.6+023232.4 **(e)** NK2-CL J100025.3+023346.4 **(f)** NK2-CL J100100.6+022134.4

(g) NK2-CL J100004.4+021148.4 **(h)** NK2-CL J100103.4+022208.4 **(i)** NK2-CL J100011.9+021256.5

Figure 8.10: Normalized spectroscopic (blue) and photometric (red) redshift counts within a 1 arcmin radius around each cluster candidate. The total number of galaxies, N, within this radius is indicated in the legend of the figure for each redshift type. The number of galaxies per redshift bin is obtained by multiplying N by the normalized counts. If the NIKA2 cluster candidate has a redshift estimate (see Table 8.2), its redshift is represented by a black dashed line.

candidates (red circles) and the XMM-COSMOS clusters (black circles). The size of the black circles depends on the cluster mass, with larger circles for more massive clusters. In the top right region, we see that the most massive X-ray cluster at $M_{500} = 1.89 \times 10^{14} M_{\odot}$ and $z = 0.73$ is matched with one of our candidates (NK2-CL J095942.6+023056.5). All other XMM-COSMOS clusters have masses below $M_{500} < 5 \times 10^{13} M_{\odot}$, where our completeness is lower than 20% (see Section 8.4.2). Thus, we do not expect to detect them in the NIKA2 map. We also performed a similar check in the following catalogs:

– The X-Class catalog [Koulouridis et al., 2021], which contains four clusters in the NIKA2 COSMOS footprint. No masses are available, but the cluster with the highest number of counts is

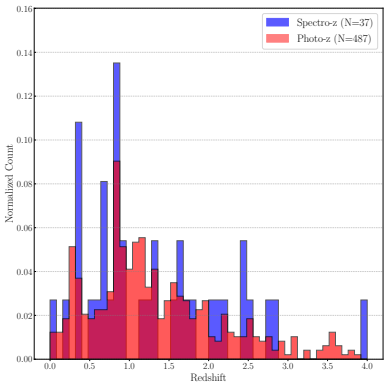

(j) NK2-CL J100101.1+020146.6

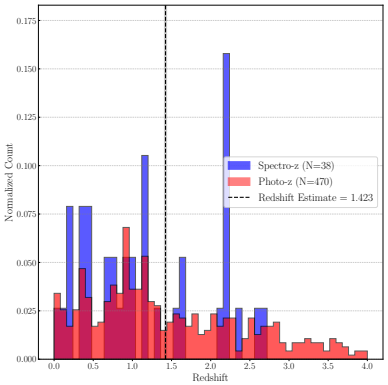

(k) NK2-CL J100054.3+020126.4

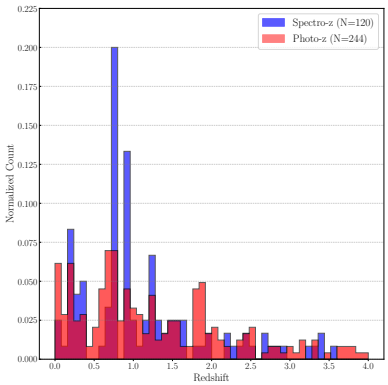

(l) NK2-CL J100009.1+022140.3

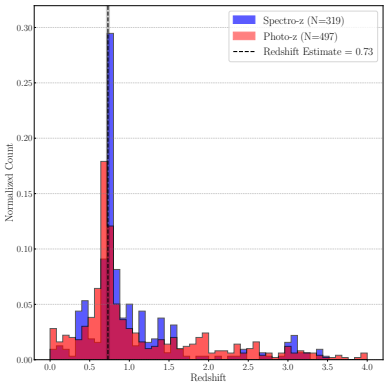

(m) NK2-CL J095942.6+023056.5

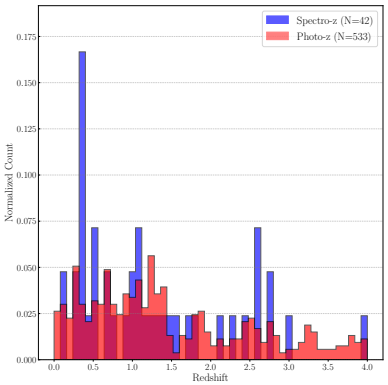

(n) NK2-CL J100120.5+022828.2

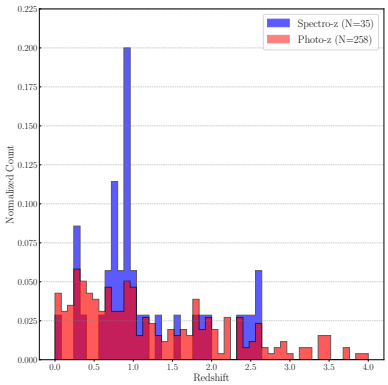

(o) NK2-CL J100008.4+020908.3

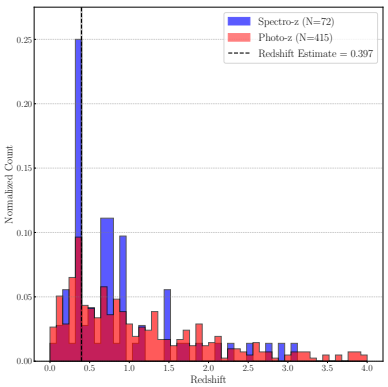

(p) NK2-CL J095958.5+022910.4

Figure 8.10: Continued.

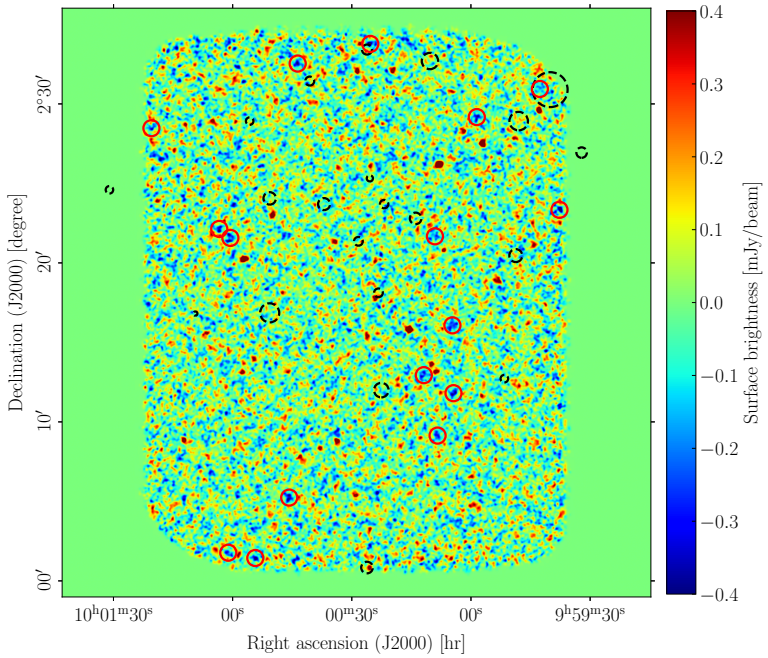

Figure 8.11: NIKA2 150 GHz map of the COSMOS field with our NIKA2 cluster candidates and XMM-COSMOS clusters [Finoguenov et al., 2007] shown as red and black circles, respectively. The size of the black circles depends on the cluster mass. Only the data inside the high quality region shown in Figure 8.2 are shown. Figure inspired by Figure 1 of Finoguenov et al. (2007).

matched to our candidate NK2-CL J095942.6+023056.5. The others are much fainter and not detected.

– The XMM-XCS catalog [Mehrtens et al., 2012]: Only five clusters are in the NIKA2 field, with two of them matched to our candidates. The three others have both very low luminosity and low redshift.

– In the newest DESI catalog [Wen and Han, 2024], we find 47 clusters in the region, with four at masses $M_{500} > 1.7 \times 10^{14} M_{\odot}$, where our completeness is above 80% (see Section 8.4.2). Two of them are within 30″ of a NIKA2 candidate. The other two are not detected. One is at a low redshift of $z = 0.22$ and thus too extended. For the last undetected cluster at redshift $z = 0.89$, we note that, despite its high mass in the DESI catalog, its X-ray counterpart [Gozaliasl et al., 2019] has a low estimated mass of $M_{200} = 3.4 \pm 0.7 \times 10^{13} M_{\odot}$.

– At millimeter wavelengths, there is only one cluster candidate in COSMOS, HAD-0924 from Hurier et al. (2021). We find that it is at a 33″ distance to one of our candidate, NK2-CL J100004.4+021148.4.

From this analysis, we conclude that the brightest clusters in the N2CLS COSMOS field are detected in the NIKA2 map. The other known clusters in the field have either low mass and/or low redshift, where our completeness falls below 20%.

8.6 Properties of cluster candidates

8.6.1 Integrated tSZ emission

In order to characterize the tSZ contribution in each cluster candidate, we perform an MCMC analysis by fitting the millimeter emission in the cluster candidate cutout maps (see Appendix 8.7) to

the spherical model of the tSZ emission presented in Section 8.4.1. We consider a Gaussian likelihood function as in Muñoz-Echeverría et al. (2023), with the cluster redshift, z, and mass M_{500} as free parameters. We use flat priors on the mass and redshift, with $0.1 < z < 3$ and $5 \times 10^{13} M_\odot < M_{500} < 8 \times 10^{14} M_\odot$. We illustrate the range of possible values in the θ_{500}-Y_{500} plane based on these priors in the left panel of Figure 8.12. The lower limit in redshift is motivated by the fact that detecting clusters at redshift $z < 0.1$ is not possible with NIKA2, as they would be completely filtered out in the data processing (see Section 8.2.1). Similarly, the lower and upper limits in mass are chosen based on the completeness of the sample presented in Section 8.4.2.

For the cluster candidates with known counterparts, we consider a Gaussian prior on the redshift $z \sim \mathcal{N}(z_{\rm lit}, \sigma_z)$, based on the values and uncertainties from the literature. We use the *emcee* package [Foreman-Mackey et al., 2013] to run the MCMC analysis. The sampling is performed using 50 walkers and 10^4 steps, with a burn-in of 10^3 samples. The convergence of the chains is checked using the $\hat{R}$ test of Gelman and Rubin (1992) and shows that the sampling we chose is sufficient to converge. The mass and redshift posterior distributions are then converted to relevant cluster quantities, the integrated tSZ flux Y_{500} and the cluster's angular size θ_{500}, using Equations 8.3 and 8.4.

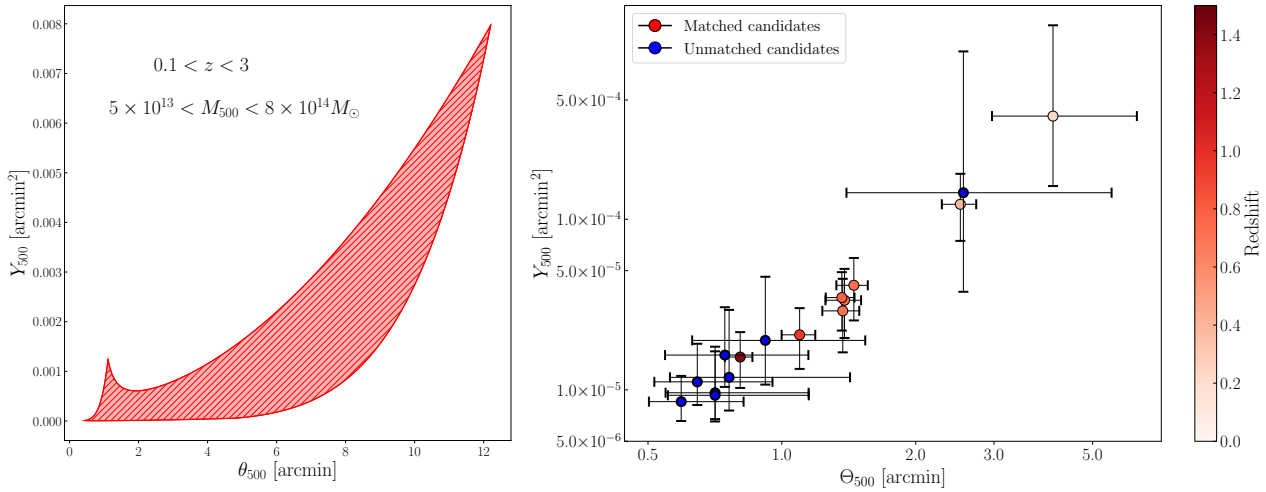

Figure 8.12: (Left): θ_{500}- Y_{500} range of possible values based on the redshift ($0.1 < z < 3$) and mass ($5 \times 10^{13} M_\odot < M_{500} < 8 \times 10^{14} M_\odot$) priors used is shown in hatched red. (Right): θ_{500}- Y_{500} 68% confidence values, for each cluster candidate in the NIKA2 sample. Matched and unmatched candidates (see Section 8.5) are depicted in red and blue, respectively. The redshift of matched counterparts is illustrated with the red colorbar.

As an illustration, we present in Figure 8.13 examples of the results of the fitting procedure at the map level for two cluster candidates. NK2-CL J100004.4+021148.4 (top) has a known redshift $z = 0.94$, that is used in the MCMC analysis via a Gaussian prior as discussed before. By contrast, for NK2-CL J100045.8+020514.3 (bottom) we found no counterpart. On the left, we present the 260 GHz map centered on the cluster candidates, which is dominated by dusty point sources and has negligible tSZ contribution. Then, from left to right we present the NIKA2 150 GHz cutout maps, the best-fit model, and residuals. We observe that the model is a good fit to the data, and the residuals maps are consistent with the local noise level, including point sources. We also notice that the latter are much fainter at 150 GHz (as expected for dusty sources), and do not significantly affect the fit.

We show in the right panel of Figure 8.12 the estimated tSZ signal and angular size of each cluster candidate in the $Y_{500} - \theta_{500}$ plane. The 68% confidence values for Y_{500} and θ_{500} and uncertainties can be found in Table 8.2. Posterior likelihood distributions in the $Y_{500} - \theta_{500}$ plane are shown in Figure 8.14. We observe that cluster candidates for which a cluster counterpart has been identified, and thus a redshift estimate obtained, present much smaller scatter than unmatched candidates. A tighter redshift prior provides better constraints, as seen from the uncertainties given in Table 8.2.

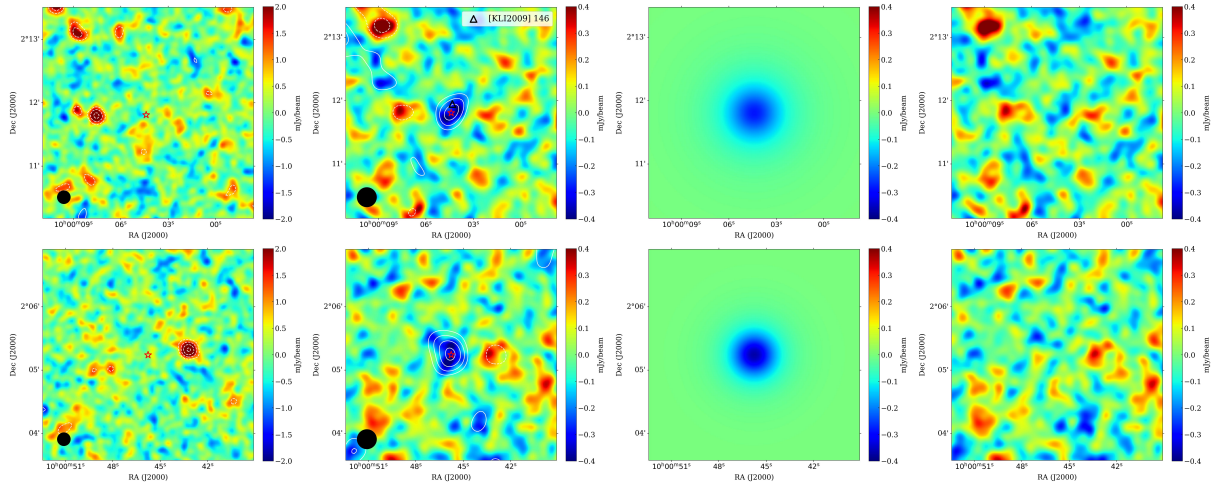

Figure 8.13: Results of the fit of 200″ × 200″ cutouts of the NIKA2 COSMOS 150 GHz map centered on two cluster candidates. NK2-CL J100004.4+021148.4 (top) has a counterpart at $z = 0.94 \pm 0.05$. In contrast, for NK2-CL J100045.8+020514.3 (bottom) we found no counterpart. The left map corresponds to the 260 GHz map centered on the cluster candidate. Then, from left to right, we show the 150 GHz cutout map for the cluster candidate, the best-fit tSZ model and residuals. For visualization purposes, the maps have been smoothed with a Gaussian 2D kernel of 6″ and 10″ for the 260 GHz and 150 GHz maps, respectively. The effective FWHM for the 260 GHz and 150 GHz maps is represented as a black disk in the bottom left corner. The white contours have the same scaling as in Figure 8.9. We observe that the tSZ effect at the cluster position is negative in the 150 GHz band, and not observed at the 260 GHz band, as expected.

However, at low redshift, where candidates are expected to have a large angular size, constraining their tSZ flux, mass, and size becomes challenging because much of the signal is filtered out (e.g. candidate NK2-CL J100011.9+021256.5 which has a counterpart at $z = 0.24$).

8.6.2 Cluster candidate mass estimates

As discussed above, for matched cluster candidates we can use strong priors on the cluster redshift and then obtain reliable mass estimates from the MCMC analysis presented in Section 8.6.1. We stress that these mass estimates are only valid within the context of the assumed model (see Section 8.3.1), but are still very useful to understand the detection performance and capabilities of NIKA2. Figure 8.15 shows the mass-redshift distribution for our matched sample and several other large SZ surveys. The mass 68% confidence values and uncertainties are also presented in Table 8.2. We show the 20%, 50% and 80% completeness contours of our NIKA2 survey (see Section 8.4) as solid, dashed and dotted red lines. These contours are computed directly from the completeness in mass-redshift bins presented in Figure 8.7 by interpolating the values to finer bins. Computing the completeness in smaller bins directly, without interpolation, also yields similar contours, but with larger scatter due to the limited number of clusters per bin. We see that our completeness contours are steeper at high redshifts compared to other surveys, as expected from NIKA2's compact beam. This is because the tSZ flux of distant (and compact) clusters is less affected by beam dilution, making it more sensitive to fainter, lower-mass clusters.

In Figure 8.16, we show the cluster surface density as a function of mass for the same surveys as in Figure 8.15. We see that a dedicated NIKA2 survey would complement the currently available tSZ cluster catalogs quite well, especially at low mass. The median mass of the NIKA2 cluster candidate sample is $M_{500} = 1.54^{+0.76}_{-0.30} \times 10^{14} M_{\odot}$. Overall, confirmed NIKA2 detections correspond to intermediate and high redshift, low-mass clusters, probing a similar region in the mass-redshift plane as the newest SPT-Deep catalog [Kornoelje et al., 2025], which is currently the deepest tSZ cluster survey.

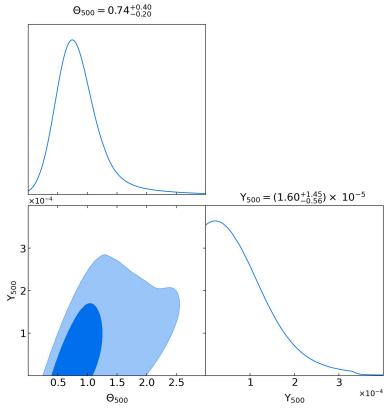

(a) NK2-CL J100045.8+020514.3

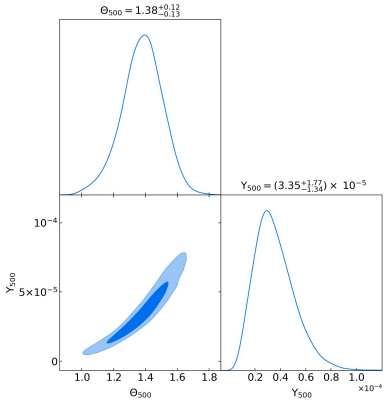

(b) NK2-CL J095937.7+022320.4

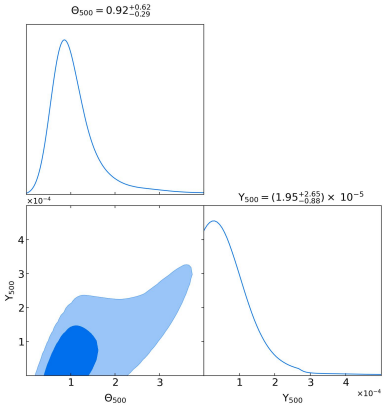

(c) NK2-CL J100004.7+021604.4

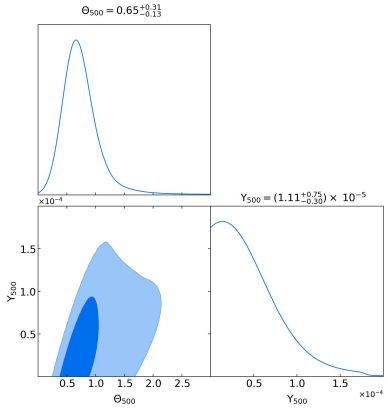

(d) NK2-CL J100043.6+023232.4

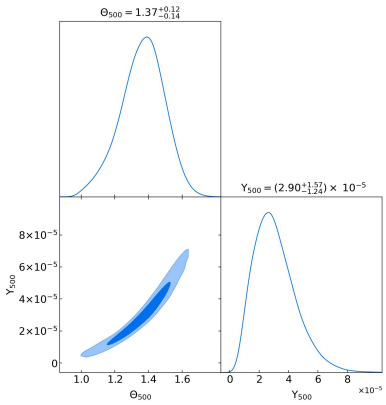

(e) NK2-CL J100025.3+023346.4

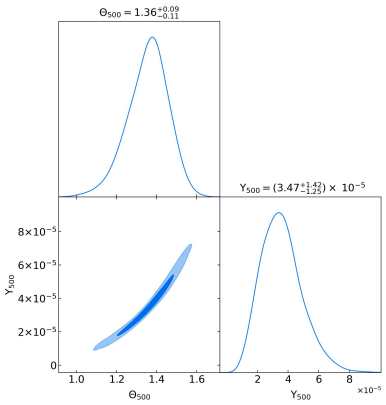

(f) NK2-CL J100100.6+022134.4

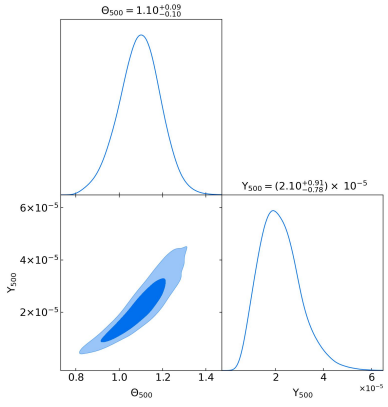

(g) NK2-CL J100004.4+021148.4

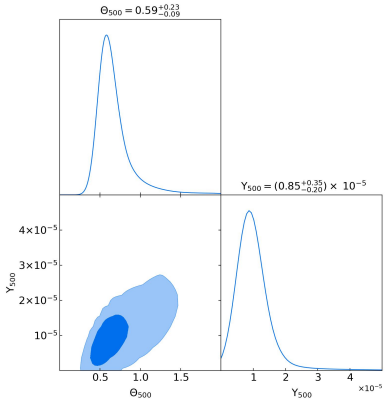

(h) NK2-CL J100103.4+022208.4

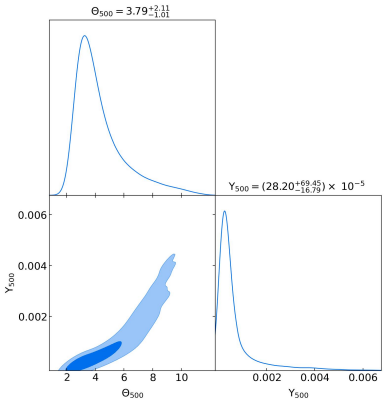

(i) NK2-CL J100011.9+021256.5

Figure 8.14: Corner plot of the $\theta_{500} - Y_{500}$ posterior maximum likelihood distribution for each of the cluster candidates. A more detailed description of the fitting procedure can be found in Section 8.6.1. The 68% confidence values and uncertainties are given in the figure. We see that the posterior distributions are much better constrained for cluster candidates with a redshift estimate, as expected from the tighter redshift prior.

8.7 Conclusion and perspectives

In this chapter, we have presented the blind detection of galaxy cluster candidates in the NIKA2 COSMOS field at 150 GHz. We used a matched-filtering approach to extract the tSZ signal from the NIKA2 map, and chose a detection threshold of SNR > 4 to build our cluster candidate sample. This threshold was later validated on simulations. Our cluster sample consists of 16 cluster candidates, with a median SNR of ~ 4.51.

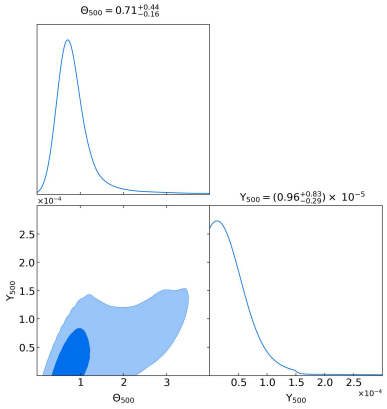

(j) NK2-CL J100101.1+020146.6

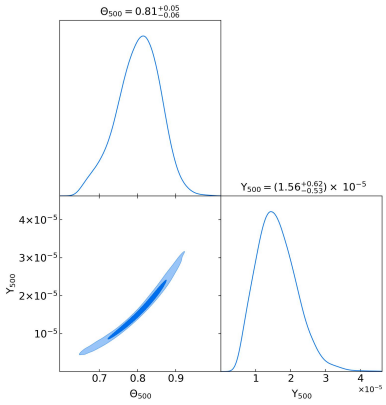

(k) NK2-CL J100054.3+020126.4

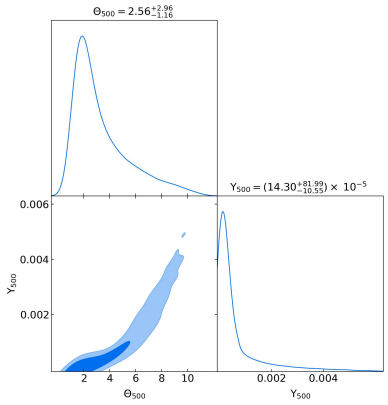

(l) NK2-CL J100009.1+022140.3

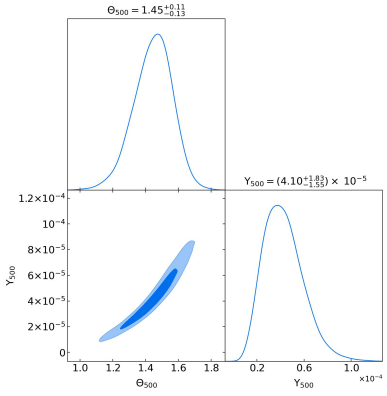

(m) NK2-CL J095942.6+023056.5

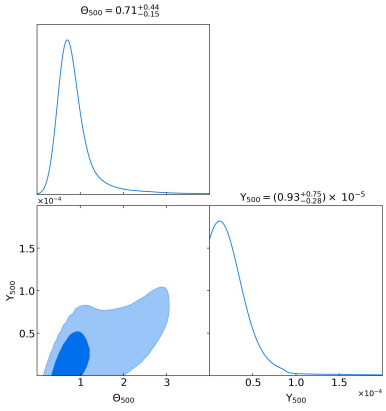

(n) NK2-CL J100120.5+022828.2

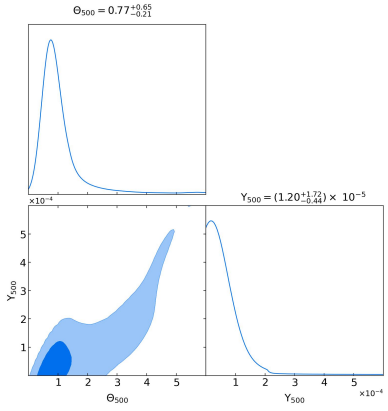

(o) NK2-CL J100008.4+020908.3

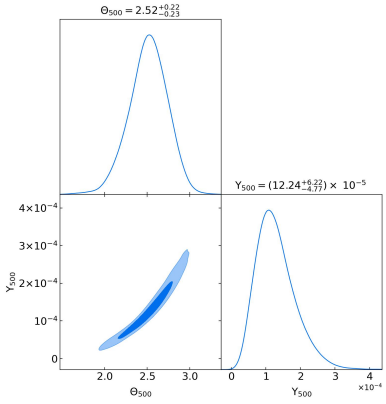

(p) NK2-CL J095958.5+022910.4

Figure 8.14: Continued.

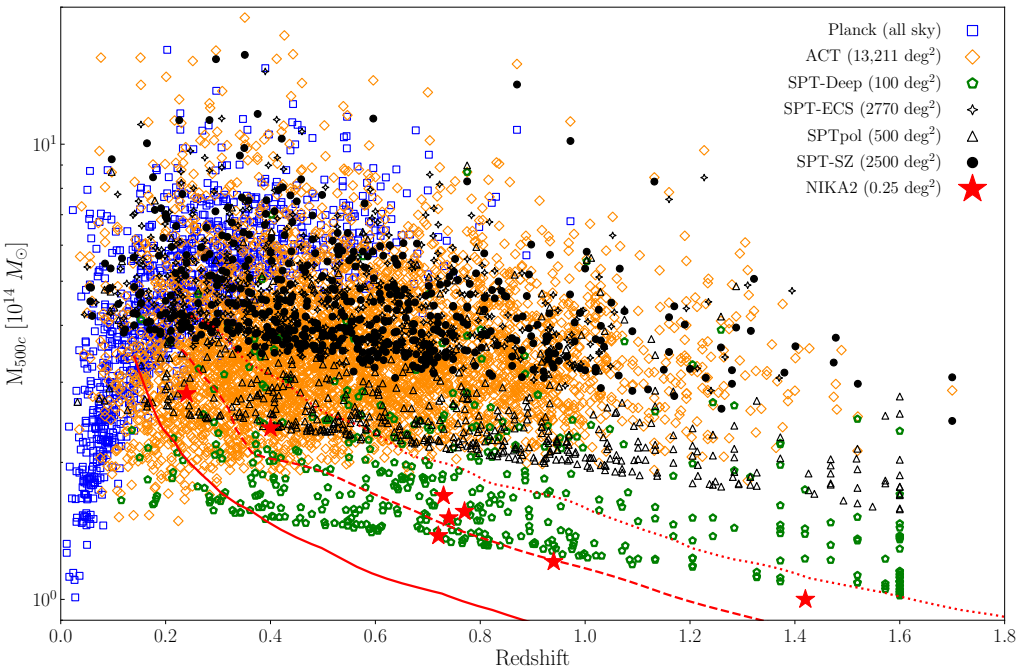

Figure 8.15: NIKA2 matched cluster sample in the mass-redshift plane. Cluster samples from other blind tSZ surveys such as PSZ2 [Planck Collaboration et al., 2016c], ACT DR5 [Hilton et al., 2021], SPT-ECS [Bleem et al., 2020], SPTpol [Huang et al., 2020], SPT-SZ [Bleem et al., 2015b], and SPT-Deep Kornoelje et al. (2025) are shown for comparison. The 20%, 50% and 80% completeness contours are shown as solid, dashed and dotted red lines, respectively.

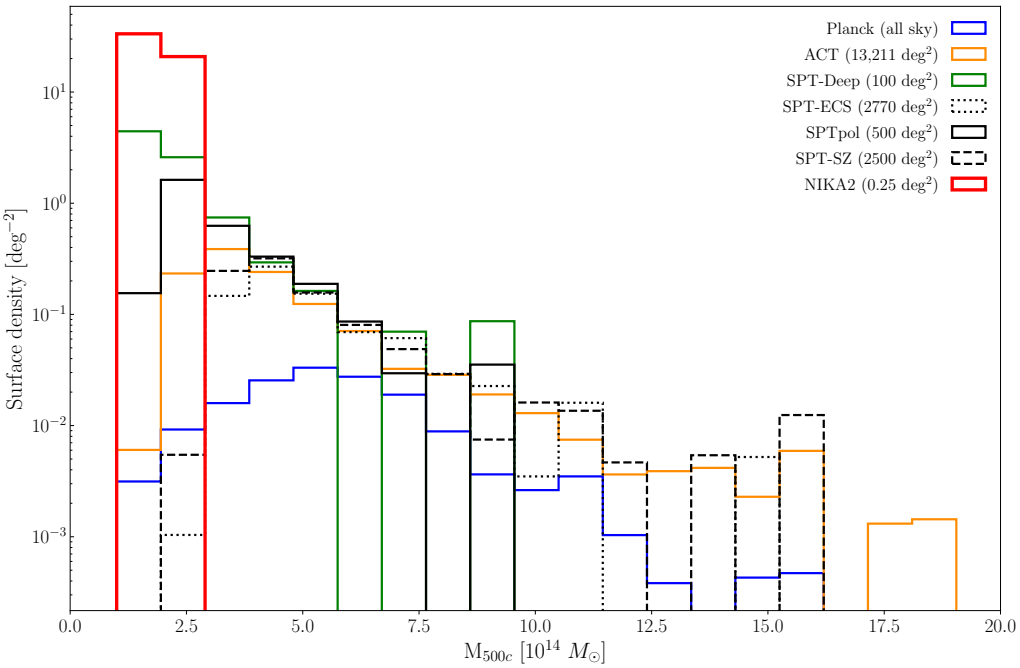

Figure 8.16: Cluster surface density as a function of cluster mass. The plotted surveys are similar to those in Figure 8.15.

We then produced realistic simulations of the NIKA2 COSMOS dataset, including instrumental and atmospheric noise, tSZ signal, and point sources. We used these simulations to validate our detection algorithm and to estimate the completeness and purity of the sample. At our selected SNR threshold of 4, the purity is about 50%. On the other hand, the completeness is above 80% for cluster masses $M_{500} > 1.7 \times 10^{14} M_\odot$. For eight of the cluster candidates, we have found a counterpart by searching

the SIMBAD, NED or VizieR databases. Out of these eight clusters, seven have been matched with optical and infrared clusters, and one with an X-ray cluster. The median redshift of the sample is $z \sim 0.74$, with values ranging from $0.24 < z < 1.42$, and two detections at high redshift $z > 0.9$.

We used available photometric and spectroscopic redshift catalogs to complete the previous search. For most of the matched candidates, their redshift estimates match with a peak in the galaxies redshift distribution. Some unmatched candidates also show a well-defined peak at intermediate or high redshift. For the 8 cluster candidates with redshift estimates, we were able to derive reliable mass estimates.The median mass of the sample is $M_{500} = 1.54 \times 10^{14} M_{\odot}$, spanning from 1.0 to $3.1 \times 10^{14} M_{\odot}$ at intermediate to high redshift.

In this study, we showed that the NIKA2 camera is a very powerful instrument to blindly detect low-mass high-redshift galaxy clusters via the SZ effect. As the N2CLS survey was not optimized for this prospect, we expect that a dedicated NIKA2 cluster survey would greatly improve the number of detections. Looking ahead, future upgrades of the NIKA2 camera are being planned to enhance its sensitivity and mapping speed by scaling up the number of detectors, as well as adding two new frequency bands at 90 and 230 GHz [Fernández-Torreiro et al., 2025]. Together with the 150 GHz band, these additional frequencies will enable the use of multi-matched filtering techniques as discussed in Section 2.3.5, further improving the detection performance. Forecasts of the capabilities of such an upgraded NIKA3 camera for cluster detection are currently being conducted by Mateo Fernández-Torreiro with very promising results. A realistic dedicated SZ survey with NIKA3 would cover 100 deg^2 in about 4000 hours. This is a factor of ten improvement in mapping speed compared to NIKA2, which required about 200 hours for the N2CLS COSMOS survey of 0.4 deg^2. With these upgrades, the NIKA3 survey would match the depth achieved by NIKA2, but over a much larger area, allowing for the detection of a significantly larger sample of clusters.

In addition, a new instrument that would be placed on a 13-m telescope is currently being studied. The main goal of this new camera would be to cover a large fraction of the northern sky with a FoV of 1 deg and an angular resolution of 1 arcmin at 90 GHz. The planned survey strategy includes two components: a wide survey covering 6000 deg^2, which is slightly larger than the area covered by SPT [Ruhl et al., 2004], and a deep survey covering 300 deg^2. This instrument would complement quite well the current southern hemisphere surveys conducted by SPT [Bleem et al., 2024; Kornoelje et al., 2025].

Finally, follow-up observations of the most distant cluster candidates presented in this chapter, NK2-CL J100054.3+020126.4 at $z = 1.42$, are being carried out with the NOEMA interferometer [Guilloteau, 1994]. With an angular resolution of about 5″ at 82 GHz, NOEMA is well suited to confirm the tSZ nature of this candidate and obtain a very high resolution tSZ map. If the observations are successful, the synergies between NIKA2 and NOEMA could open a unique window towards the study of SZ-selected high-redshift low-mass clusters.

Conclusions and perspectives

During my PhD thesis, I had the chance to work on very different aspects of millimeter wavelengths instrumentation and observations. An important part of my work was dedicated to the Grenoble-Tsukuba (GT) camera, a new instrument that I helped develop and install at the Nobeyama 45-m telescope. As PI, I also led the commissioning observations of the camera and the development of a dedicated data reduction pipeline. The other part of my thesis was focused on the scientific exploitation of the NIKA2 camera installed at the IRAM 30-m telescope, in the context of two large programs: the NIKA2 SZ and NIKA2 Cosmological Legacy Survey programs. As a member of the NIKA2 collaboration, I participated in two observation campaigns, both on-site and remotely. As a result of my contributions, I became a full member of the NIKA2 Core Team.

One of my first contributions to both instruments was the comprehensive comparison of four different techniques used to reconstruct the KID signal in the NIKA2, CONCERTO, and GT cameras data reduction pipelines. I demonstrated that all techniques are very robust even against very bright sources. This study highlights the different strengths and weaknesses of each method and is valuable to choose the most appropriate one for future KID-based instruments.

My involvement in the GT camera project included active participation in the laboratory characterization campaigns at the National Astronomical Observatory of Japan (NAOJ) in Tokyo. Although I was not yet part of the project during the 2021 campaign, I later reproduced and validated the team's results. This work revealed that the measured noise level was much higher than expected. To investigate this discrepancy, I reduced the data using a different KID reconstruction method and showed that the results were consistent. This result indicated that the high noise was likely due to the readout system. During the 2024 laboratory campaign, I actively participated in the setup and execution of the measurements and contributed to the analysis of the data. Even if we were not able to measure the noise at that time, the results from both campaigns showed that a new readout electronic system was needed for the camera to reach its expected performances. As the new electronics were built in Grenoble, I was in charge of their implementation in Japan during the 2024 observation campaign and learned how to operate them. With the new readout electronics, I was able to measure the noise level of the camera and showed that it was now in perfect agreement with the expected performance. At the same time, I also discovered a significant issue with the new electronic setup: only 97 out of 144 detectors could be read simultaneously.

Following these laboratory campaigns, I participated in the installation of the GT camera at the Nobeyama 45-m telescope. As PI of the GT camera commissioning observations, I was in charge of selecting the observation targets and adapting our observation scripts to our scientific needs. Despite the terrible weather conditions, the campaign was still successful, achieving the first light of a LEKIDs array at 100 GHz, with a total of 26.3 hours of on-source observations.

After the observation campaign, I led the development of a dedicated data reduction pipeline for the GT camera, based on the pipeline built for the KISS instrument. An important part of my work was dedicated to implementing and comparing different calibration techniques to achieve the best possible photometric accuracy. In this context, I implemented a new method based on a RANSAC algorithm.

I tested multiple iterations of this method and showed that the results are promising compared to the original 3-points method. However, it still has some limitations that need to be adressed before being used in the final pipeline.

Once the pipeline was fully operational, I assessed the on-sky performance of the GT camera. Using observations of the 3C84 quasar and Mars, I estimated the beam size of the instrument to be $\theta_{FWHM} = 22.4 \pm 2.5''$, and the responsivity to be about 141.2 ± 33.5 Hz/K, which is lower than expected but still reasonable given the weather conditions. Most importantly, I estimated the sensitivity (NEFD) of the camera based on the white noise level in the maps, and found NEFD ~ 66.1 mJy.s$^{1/2}$/beam. I demonstrated that the GT camera achieves roughly an order of magnitude improvement in sensitivity compared to its predecessor, thanks to the new KID array and readout system. The results I obtained show that, while the camera's current sensitivity limits it to observation of only the most massive clusters, it would greatly complement higher-frequency cluster observations with NIKA2 for example, enabling a better characterization of radio sources and contaminants in the SZ signal.

The second part of my work consisted of several contributions to the NIKA2 SZ large program. One of the main challenges in the analysis of the SZ signal is the contamination by point sources, mainly radio galaxies. Two catalogs of point sources detected in two types of LPSZ cluster maps, SZ optimized and point source optimized, were produced. I performed a detailed cross-validation of the two catalogs and showed that more than half of the sources are detected by both methods with good agreement on their fluxes. For the remaining $\sim 40\%$ of the sources that are unique to each catalog, I demonstrated that the differences arise from the different data reduction approaches, noise properties, and signal filtering of the two map types. However, I identified that some of the point source optimized maps require refinement to improve the accuracy of the source's detection. An important part of my work was then to characterize the impact of point sources which are undetected in the LPSZ maps. For sub-millimeter (submm) sources, I used *Herschel* catalogs covering 20 out of the 38 clusters, finding that a third of NIKA2 sources have counterparts in *Herschel*. Most importantly, I confirmed that all bright submm sources expected to contaminate the SZ signal were detected in the NIKA2 maps.

To address the contamination from radio sources, I developed a methodology to identify all radio sources in the LPSZ fields, combining multiple astronomical databases. For each source, I compiled all available radio flux measurements from the literature, and implemented a robust flux estimation procedure based on previous work within the LPSZ collaboration. My analysis identified three central radio sources that significantly impact the SZ modelling despite being undetected in the NIKA2 maps. These three sources were added to the SZ modelling of their respective clusters. The most significant impact was found for the PSZ2G212 cluster, with a substantial change in the reconstructed pressure profile after taking the central radio source into account. This work directly contributed to the improvement of individual cluster pressure profiles, which will be used to estimate a mean pressure profile for the LPSZ sample. Finally, I conducted a preliminary validation of the masses obtained by the LPSZ with masses in the literature. I found that the LPSZ masses are overall in agreement with previous measurements obtained from SZ and/or X-ray observations. Future analyses, performed by other members of the LPSZ collaboration, will include a more detailed comparison with weak lensing masses to measure the hydrostatic-to-lensing mass bias.

The last part of my work focused on the blind detection of galaxy clusters in the NIKA2 Cosmological Legacy Survey (NCLS) large program. Based on existing cluster detection algorithms, I applied a match-filter approach to the NIKA2 map of the COSMOS field, and identified 16 cluster candidates above a SNR threshold of 4. To characterize the purity and completeness of the sample, I developed a simulation pipeline to generate realistic NIKA2 observations of the COSMOS field, including the main astrophysical components (tSZ signal, point sources, and noise). Using these simulations, I demonstrated that the survey achieves $> 80\%$ completeness for clusters with $M_{500} > 1.7 \times 10^{14} M_{\odot}$, a mass threshold lower than that of other SZ surveys. I showed that the purity of the sample is about 50% at SNR> 4, rising to $\sim 80\%$ at SNR> 5. To validate the cluster candidates, I cross-matched them with

existing multi-wavelength cluster catalogs and found counterparts for 8 of the 16 candidates. With a median redshift of $z = 0.74$ and two detections at $z > 0.9$, the NIKA2 sample is able to probe a higher redshift range than most other SZ surveys. Looking at the available galaxies redshift catalogs in the COSMOS field, the estimated redshifts of our candidates from the literature coincide with peaks in the local galaxy redshift distribution. Some unmatched candidates also show well-defined peaks, suggesting that they could be real clusters awaiting confirmation. For the candidates with confirmed redshifts, I estimated their masses by modelling their SZ signal and found that the median mass of the sample is $M_{500} = 1.54 \times 10^{14} M_{\odot}$. After comparing with other major SZ surveys, such as *Planck*, SPT, and ACT, I showed that the NIKA2 sample probes a low-mass and intermediate/high redshift region that is not well covered by these surveys. This work established that a dedicated NIKA2 cluster survey would complement well the existing cluster catalogs, especially at low mass. This work as been published in Chérouvrier et al. (2025).

To summarize, this thesis presents comprehensive work spanning the complete chain from millimeter instrument development to scientific exploitation for galaxy cluster studies. Through my contributions to both the GT camera at Nobeyama and the NIKA2 camera at the IRAM telescope, I have demonstrated the capabilities of KID-based instruments for the study of galaxy clusters.

Looking ahead, the GT camera has great potential for further development and scientific exploitation. The next step is to address the current limitations detailed in this thesis. Currently, a new LEKIDs array with much better cosmetics has been fabricated and could be installed in the camera to replace the spare array used during the commissioning observations. This first step would significantly improve the number of detectors we can use for our analyses. By adapting the readout electronics to read all 144 detectors simultaneously, we could also greatly increase the sensitivity of the camera. The origin of the anomalous noise seen in the commissioning data is being investigated by the Japanese team and could be addressed in future observation campaigns. Once these improvements are implemented, a new commissioning campaign conducted under better weather conditions would show the true capabilities of the GT camera. In the future, performing a dedicated cluster observation program with the GT camera would be very valuable, both on its own or in synergy with NIKA2. Targeting LPSZ clusters highly impacted by radio sources would be particularly interesting.

Following the blind detection of clusters with NIKA2 presented in the last chapter, I proposed a new open time project to observe the highest redshift cluster candidate in the sample with the NOEMA interferometer. With a resolution of about $5''$, NOEMA enables a detailed characterization of the SZ signal from distant clusters, as demonstrated by previous observations of the $z = 0.89$ cluster CL J1226.9+3332 [Echeverria, 2023]. The proposal was accepted by the IRAM programme committee and the observations are being carried out at the time of writing. If successful, these observations would provide the first confirmation of a cluster blindly detected by NIKA2, and demonstrate the synergy between NIKA2 and NOEMA for high-redshift cluster studies. Other NOEMA observations of NIKA2 cluster candidates could be proposed in the future to confirm more of them.

Moreover, future upgrades of the NIKA2 camera are already being considered by the collaboration to enhance its capabilities for cluster studies. With two extra frequency bands at 90 and 230 GHz, the NIKA3 camera project aims to improve even further the characterization of the SZ signal at very high angular resolution. In addition, the number of detectors would be scaled up to increase the mapping speed by a factor of 10. A large survey optimized for cluster detection with NIKA3 would be very valuable, as we have shown from our results with NIKA2. Building on the detection, simulation, and analysis pipelines I developed in this thesis, forecasts are being conducted by Mateo Fernández-Torreiro to optimize the survey design. I also plan to contribute to the preparation of this future survey. Currently, the proposed survey would cover 100 deg^2 in about 4000 hours of observation, matching the depth of the N2CLS survey in COSMOS. Using the information from the new frequency bands, the purity of the NIKA3 sample would also be greatly improved compared to NIKA2. The future of very high resolution SZ surveys looks very promising and I plan to continue contributing to

the project.

In addition, several 13-m telescopes will be built around the world as part of the next-generation Event Horizon Telescope (ngEHT, Doeleman et al. (2019)) project. In this context, an instrument similar to NIKA2 is being considered for installation on one of these telescopes. With a similar resolution as the SPT and ACT telescopes, such an instrument would be able to conduct a large SZ cluster survey in the northern sky with high angular resolution. The current survey strategy involves a wide survey covering 6000 deg^2, which is slightly larger than the area covered by SPT, and a deep survey covering 300 deg^2. The first forecasts show that, even with a smaller telescope, the high angular resolution and sensitivity of a NIKA2-like instrument would enable the detection of a large number of clusters, especially at high redshift.

Appendix

Appendix A: Cluster catalogs in the literature

In this appendix, we provide extensive tables of cluster catalogs available in the literature, classified by the wavelength at which they were detected: optical (Table 3), X-ray (Table 4), and millimeter (Table 5). The tables include the catalog name, reference, area covered, redshift range, and number of clusters in each catalog. We do not report here the catalogs built for follow-up observations, i.e., samples built from other catalogs.

Table 3: Extensive summary of available optical cluster catalogs in the literature. The first column indicates the catalog name, the second column the reference, the third column the area covered by the catalog, the fourth column the redshift range, and the last column the number of clusters in the catalog.

Catalog	Reference	Area deg^2	z	$N_{clusters}$
Abell	Abell (1958)	27 247	0-0.2	2 712
Zwicky (CGCG)	Zwicky et al. (1963a)	all-sky	–	10 000
Klemola69	Klemola (1969)	40	–	44
Snow70	Snow (1970)	–	–	34
Shakhbazian74 (POSS)	Shakhbazyan and Petrosyan (1974)	–	–	377
Sersic74	Sérsic (1974)	–	–	36
deVaucouleurs75	de Vaucouleurs (1975)	–	–	55
Holmberg75 (ESO-Uppsala)	Holmberg et al. (1975)	–	–	174
Morgan75 (POSS)	Morgan et al. (1975)	–	–	8
Gunn75	Gunn and Oke (1975)	–	0-0.47	28
Sandage76	Sandage et al. (1976)	–	0-0.45	16
MacGillivray76	MacGillivray et al. (1976)	–	–	6
Rose76	Rose (1976)	1 041	–	124
Turner76	Turner and Gott (1976)	–	–	103
Duus77 (ESO-SRC)	Duus and Newell (1977)	–	–	960
Rose77 (POSS)	Rose (1977)	–	–	203
Albert77	Albert et al. (1977)	–	–	7
Materne78	Materne (1978)	–	0.003-0.01	6
Braid78	Braid and MacGillivray (1978)	–	–	474
Hickson82 (POSS)	Hickson (1982)	–	0-0.02	100
Huchra82	Huchra and Geller (1982)	–	–	92
Geller83 (CfA)	Geller and Huchra (1983)	40	–	176
Schetman85	Shectman (1985)	–	0-0.14	646
Vennik86	Vennik (1986)	21 500	0-0.01	114
Gunn86	Gunn et al. (1986)	–	0.15-0.92	418
Tully87	Tully (1987)	all-sky	0-0.01	179
ACO	Abell et al. (1989)	all-sky	0-0.2	4 073
Ramella89 (CfA)	Ramella et al. (1989)	1 400	0-0.04	128

Table 3: Continued.

Catalog	Reference	Area deg^2	$z_{min} - z_{max}$	$N_{clusters}$
Maia89 (SSRS)	Maia et al. (1989)	5 745	0-0.02	87
Quintana90	Quintana and White (1990)	–	0-0.35	267
Plionis91	Plionis et al. (1991)	11 000	0-0.15	6 000
Couch91	Couch et al. (1991)	–	0-0.68	112
Abbott91	Abbott (1991)	–	0-0.35	38
EDCC	Lumsden et al. (1992)	1 640	0-0.17	737
Fouque92 (PGC)	Fouque et al. (1992)	–	0-0.02	264
Nolthenius93 (CfA1)	Nolthenius (1993)	–	–	173
LGG	Garcia (1993)	–	0-0.019	485
Prandoni94	Prandoni et al. (1994)	1 300	–	59
Postman96 (PDCS)	Postman et al. (1996)	5	0.2-1.2	79
RSCG	Barton et al. (1996)	3 709	0-0.05	89
Lidman	Lidman and Peterson (1996)	13	0-0.8	105
Dalton97 (APM)	Dalton et al. (1997)	4 300	0.03-0.18	957
Ramella97 (CfA2)	Ramella et al. (1997)	3 939	0-0.05	406
Zaritsky97	Zaritsky et al. (1997)	17.5	0.3-1.1	10
Kawasaki98	Kawasaki et al. (1998)	5.3	0.1-0.3	18
Ostrander98 (HST-MDS)	Ostrander et al. (1998)	0.4	0.2-0.9	92
PPS	Trasarti-Battistoni (1998)	2 495	0-0.04	188
Ramella99 (ESP)	Ramella et al. (1999)	23.2	0.02-0.22	231
White99 (CGCG)	White et al. (1999)	7 353	0-0.05	732
Scodeggio99 (EIS)	Scodeggio et al. (1999)	12	0.2-1.3	302
NOG	Giuricin et al. (2000)	all-sky	0-0.02	1 128
Kawasaki00 (APM)	Kawasaki (2000)	5 800	0-0.2	4 000
Lobo00 (EIS)	Lobo et al. (2000)	4.4	0.3-1.1	99
NSOCS	Gal et al. (2000)	60	0-0.3	85
LCCGs	Allam and Tucker (2000)	720	0.04-0.14	76
Tucker00 (LCRS)	Tucker et al. (2000)	720	0.03-0.15	1 495
Bramel00 (EDSGC)	Bramel et al. (2000)	1 067	0-0.15	2 109
LCDCS	Gonzalez et al. (2001)	130	0.3-1	1 073
Ramella01 (PDCS)	Ramella et al. (2001)	1	0.2-0.6	37
Willick01 (StaCS)	Willick et al. (2001)	60	0.3-0.9	20
CNOC2	Carlberg et al. (2001)	1.5	0.1-0.5	190
Goto02 (SDSS)	Goto et al. (2002)	350	0-0.6	363
Kim02 MF (SDSS)	Kim et al. (2002)	25	0-0.6	152
Kim02 VTT (SDSS)	Kim et al. (2002)	25	0-0.6	130
Postman02 (KPNO/DDCS)	Postman et al. (2002)	16	0.2-1.2	444
Caretta02	Caretta et al. (2002)	60	0.07-0.22	39
Donahue02 (KPNO)	Donahue et al. (2002)	5	0.2-1.2	155
UZC-SSRS2	Ramella et al. (2002)	4.69	0-0.038	1 168
Merchan02 (2dFGRS)	Merchán and Zandivarez (2002)	2 000	0-0.25	2 209
Adami02 (SSRS2)	Adami and Mazure (2002)	5 581	0-0.03	80
Gal03 (DPOSS)	Gal et al. (2003)	5 800	0.08-0.24	8 155
Bahcall03 (SDSS)	Bahcall et al. (2003)	400	0-0.3	799
Iovino03 (DPOSS)	Iovino et al. (2003)	2 000	0-0.2	84
Kochanek03 (2MASS)	Kochanek et al. (2003)	37 523	0-0.05	366
Einasto03 (SDSS)	Einasto et al. (2003)	330	0.003-0.22	5 155
NSOCS	Lopes et al. (2004)	2 700	0.1-0.5	9 956
Lee04 (SDSS)	Lee et al. (2004)	153	0-0.3	177
Balogh04 (SDSS+2dFGRS)	Balogh et al. (2004)	1 360	0.05-0.1	204
2PIGG	Eke et al. (2004)	2 000	0.002-0.01	29 000
Miller05 (SDSS DR2)	Miller et al. (2005)	2 600	0.02-0.17	748
Yang05 (2dFGRS)	Yang et al. (2005)	1 500	0-0.2	78 708

Table 3: Continued.

Catalog	Reference	Area deg^2	$z_{min} - z_{max}$	$N_{clusters}$
Gerke05 (DEEP2)	Gerke et al. (2005)	1	0-1	899
RCS	Gladders and Yee (2005)	10	0.2-1.4	429
Carvalho05 (DPOSS)	de Carvalho et al. (2005)	6 260	0-0.2	459
Merchan05 (SDSS DR3)	Merchán and Zandivarez (2005)	4 188	0.01-0.2	10 864
Weinmann06 (SDSS DR2)	Weinmann et al. (2006)	1 950	0-0.2	53 229
Tago06 (2dFGRS)	Tago et al. (2006)	2 000	0.01-0.2	25 215
Berlind06 (SDSS)	Berlind et al. (2006)	8 400	0.03-0.1	8 148
PF MRSS	Panko and Flin (2006)	5 000	–	6 188
FSVS	Söchting et al. (2006)	23	0.05-0.9	598
UKIDSS	van Breukelen et al. (2006)	0.5	0.6-1.4	13
Koester07 (SDSS)	Koester et al. (2007)	7 500	0.1-0.3	13 823
Yang07 (SDSS DR4)	Yang et al. (2007)	8 400	0.01-0.2	72 927
Deng07 (SDSS DR5)	Deng et al. (2007)	8 400	0.02-0.12	11 163
Olsen07 (CFHTLS)	Olsen et al. (2007)	4	0.2-1.1	169
2MASS	Crook et al. (2007)	all-sky	0-0.03	2 909
Miyazaki07 (Subaru)	Miyazaki et al. (2007)	21.82	0.14-0.85	101
Clewley07 (UKIDSS)	Clewley et al. (2007)	0.5	0.61-1.39	13
Gavazzi07 (CFHTLS)	Gavazzi and Soucail (2007)	4	0.1-0.7	9
HIROCS	Zatloukal et al. (2007)	0.66	1.23-1.55	12
BLOX	Dietrich et al. (2007)	2.8	0.1-0.9	116
Tago08 (SDSS DR5)	Tago et al. (2008)	8 400	0.01-0.1	50 362
Y08 (SDSS DR5)	Yoon et al. (2008)	8 400	0.05-0.1	924
Li08 (CNOC)	Li and Yee (2008)	1.5	0.1-0.5	192
AKARI NEP	Goto et al. (2008)	0.4	0.9-1.7	16
Spitzer-FLS	Muzzin et al. (2008)	3.8	0.1-1.3	99
Bergé08 (CFHTLS)	Bergé et al. (2008)	4	0.1-0.5	7
Eisenhardt08 (IRAC)	Eisenhardt et al. (2008)	7.25	0.1-1.4	335
G09 (CFHTLS)	Grove et al. (2009)	4	0.2-1.3	247
NSOCS	Gal et al. (2009)	11 411	0.02-0.27	15 502
McConnachie09 (SDSS DR6)	McConnachie et al. (2009)	9 583	0-1.6	77 085
zCOSMOS	Knobel et al. (2009)	1.7	0.08-0.73	800
CFHTLS-W	Thanjavur et al. (2009)	161	0-0.6	4 061
Wen09 (SDSS DR6)	Wen et al. (2009)	8 400	0.05-0.6	39 668
GMBCG (SDSS DR7)	Hao et al. (2010)	8 240	0.1-0.55	55 424
Adami10 (CFHTLS)	Adami et al. (2010)	175	0.15-1.42	1 200
3D-MF CFHTLS	Milkeraitis et al. (2010)	4	0.2-1	673
Tago10 (SDSS DR7)	Tago et al. (2010)	8 240	0.02-0.13	78 800
VVDS	Cucciati et al. (2010)	0.5	0.2-1	318
SCS	Menanteau et al. (2010a)	70	0.1-0.8	105
Wen11	Wen and Han (2011)	73.2	0.1-1.6	1 644
BMH11	Bellagamba et al. (2011)	2	0.12-0.8	27
SDSS S82	Geach et al. (2011)	270	0.16-0.52	4 098
Szabo11 (SDSS DR6)	Szabo et al. (2011)	8 240	0.05-0.78	69 173
George11 (COSMOS)	George et al. (2011)	1.64	0.1-1	183
Makarov11	Makarov and Karachentsev (2011)	all-sky	0-0.01	395
GAMA G^{3}Cv1	Robotham et al. (2011)	142	0-0.5	14 388
2SLAQ	Farrens et al. (2011)	–	0.45-0.7	313
Durret11 (CFHTLS)	Durret et al. (2011)	154	0.1-1.15	4 061
ORCA SDSS	Murphy et al. (2012)	7	0-0.6	97
Li12 (RCS1)	Li et al. (2012)	92	0.17-0.54	1 153
GTO2deg^2	Kurtz et al. (2012)	2.1	0.01-1.1	14
Blackburne12 (2MASS)	Blackburne and Kochanek (2012)	37 523	–	7 624
Tempel12 (SDSS DR8)	Tempel et al. (2012)	8 240	0.03-0.2	77 858

Table 3: Continued.

Catalog	Reference	Area deg^2	$z_{min} - z_{max}$	$N_{clusters}$
Gerke12 (DEEP2)	Gerke et al. (2012)	3	0.65-1.31	2 460
Smith12 (SDSS DR7)	Smith et al. (2012)	8 240	0.03-0.24	10 443
Scudder12 (SDSS DR7)	Scudder et al. (2012)	8 240	0.03-0.14	112
zCOSMOS12	Knobel et al. (2012)	1.7	0.1-1	1 498
Einasto12 (SDSS DR8)	Einasto et al. (2012)	14 000	0.01-0.2	109
WHL12 (SDSS DR8)	Wen et al. (2012)	14 000	0.05-0.8	132 684
CES	Söchting et al. (2012)	2	0.2-3	4 420
p2MCGs	Díaz-Giménez et al. (2012)	23 844	0-0.04	85
RedMaPPer (SDSS DR8)	Rykoff et al. (2014); 2016	10 000	0.08-0.6	26 311
Tempel14 (SDSS DR10)	Tempel et al. (2014)	7 221	0-0.2	82 458
Oguri14 (SDSS DR8)	Oguri (2014)	11 960	0.1-0.6	71 743
EVCC	Kim et al. (2014)	725	0-0.01	1 589
Castignani14 (COSMOS)	Castignani et al. (2014)	1.7	0.8-2.7	22
Tully15 (2MASS)	Tully (2015)	37 523	0.01-0.03	3 461
WHL15 (SDSS DR8)	Wen and Han (2015)	14 000	0.05-0.8	25 419
Bleem15 (BCS)	Bleem et al. (2015a)	80	0.1-0.8	764
ALHAMBRA	Ascaso et al. (2015)	2.78	0.2-1.2	348
Durret15 (SDSS Stripe 82)	Durret et al. (2015)	270	0.15-0.7	3 663
ECO	Moffett et al. (2015)	all-sky	0-0.02	9 443
RedGOLD	Licitra et al. (2016b)	60	0.1-1.1	652
NGVS	Licitra et al. (2016a)	104	0.08-0.9	1724
RedMaPPer (DES Y1)	Rykoff et al. (2016)	150	0.2-0.9	786
Tempel16 (2MRS)	Tempel et al. (2016)	37 523	0-0.07	6 282
Poudel16 (SDSS DR10+GAMA+WISE)	Poudel et al. (2016)	144	0-0.2	1 651
Toshikawa16 (CFHTLS)	Toshikawa et al. (2016)	4	3-6	8
CCPC	Franck and McGaugh (2016)	–	2-6.6	173
Wilson16 (KPNO)	Wilson et al. (2016)	–	0.02-0.8	210
Lu16 (2MRS)	Lu et al. (2016)	37 523	0-0.08	29 904
COSMOS-Wall	Iovino et al. (2016)	1.4	0.69-0.75	26
Saulder16 (SDSS DR12)	Saulder et al. (2016)	9 274	0-0.11	229 893
Saulder16 (2MRS)	Saulder et al. (2016)	37 523	0-0.16	31 506
Sohn16 (SDSS DR12)	Sohn et al. (2016)	9 274	0.01-0.19	1 588
Lim17 (2MRS+6dFGS+SDSS+2dFGRS)	Lim et al. (2017)	37 523	0-0.2	97 098
Paterno17 (Spitzer)	Paterno-Mahler et al. (2017)	–	0.1-1	190
KiDS ESO-DR2	Radovich et al. (2017)	114	0-0.7	1 858
Wen18 (2MASS+WISE+SCOSMOS)	Wen et al. (2018)	28 000	0.03-0.4	47 600
Wen18 (SDSS-DR14+WISE)	Wen et al. (2018)	14 000	0.7-1	1 959
Campusano18 (2dFGRS)	Campusano et al. (2018)	2 000	0.01-0.14	341
Tempel18 (2MRS)	Tempel et al. (2018)	37 523	0-0.07	7 755
Banerjee18 (SDSS DR9)	Banerjee et al. (2018)	11 500	0.05-0.64	46 479
Sarron18 (CFHTLS)	Sarron et al. (2018)	154	0.1-0.7	1 371
Gimenez18 (SDSS DR12)	Díaz-Giménez et al. (2018)	6 828	0-0.12	462
Socolovsky18 (UDS)	Socolovsky et al. (2018)	0.77	0.5-1	37
HSC-SSP	Oguri et al. (2018)	232	0.1-1.1	1 921
DES Y1	McClintock et al. (2019)	1 500	0.1-0.8	76 000
MaDCoWS	Gonzalez et al. (2019)	21 000	0.7-1.8	2 839
KiDS-DR3	Maturi et al. (2019)	438	0.1-0.8	7 988
GalWCat19 (SDSS DR13)	Abdullah et al. (2020)	14 555	0.01-0.2	1 800
Zheng20 (SDSS DR14)	Zheng and Shen (2020)	14 555	0.01-0.21	8 022
Lambert20 (2MRS)	Lambert et al. (2020)	37 523	0-0.08	3 022
Wang20 (zCOSMOS)	Wang et al. (2020)	1.7	0.1-1	12 002
Gao20 (SCUSS+SDSS+unWISE)	Gao et al. (2020)	3 700	0.05-0.65	19 610
WaZP (DES Y1)	Aguena et al. (2021)	1 511	0.05-0.9	60 547

Table 3: Continued.

Catalog	Reference	Area deg^2	$z_{min} - z_{max}$	$N_{clusters}$
WH21 (HSC-SSP+unWISE)	Wen and Han (2021)	800	0.1-2	21 661
REFINE	Sarron and Conselice (2021)	3	0.1-3.15	2 588
HectoMAP	Sohn et al. (2021)	55	0.05-0.55	346
SpARCS	Balogh et al. (2021)	3.8	0.1-1.3	99
Zou21 (DESI DR8)	Zou et al. (2021)	20 000	0.01-1	540 432
Yang21 (DESI DR8)	Yang et al. (2021)	18 253	0-1	5 171 997
WH22 (DES+unWISE)	Wen and Han (2022)	5 000	0.1-1.5	151 244
Zou22 (DESI DR9)	Zou et al. (2022)	20 000	0-1	532 810
Zou22 (DES DR2)	Zou et al. (2022)	5 000	0-1.2	86 963
Zou22 (HSC-SSP PDR3)	Zou et al. (2022)	700	0-1.6	36 566
Li22 (CFHT+HSC-SSP)	Li et al. (2022)	34.41	0-6	402 947
Werner23 (S-PLUS)	Werner et al. (2023)	273	0.1-0.4	4 499
Maturi23 (miniJPAS)	Maturi et al. (2023)	1	0.05-0.8	80
Brinch23 (COSMOS2020)	Brinch et al. (2023)	2	6-7.7	15
VST-ATLAS	Ansarinejad et al. (2023)	4 700	0-0.4	40 000
MaDCoWS2	Thongkham et al. (2024)	1 461	0.1-2	22 970
Yantovski24 (DESI DR9)	Yantovski-Barth et al. (2024)	19 700	0-1	298 487
WH24 (DESI DR9&10)	Wen and Han (2024)	24 000	0.01-1.5	1 581 179
AMICO-COSMOS	Toni et al. (2024)	1.69	0.12-2	1 269
Doubrawa24 (miniJPAS)	Doubrawa et al. (2024)	1	0.05-0.8	574
Zandivarez24 (GAMA)	Zandivarez et al. (2024)	180	0-0.42	4 632
Ma25 (SDSS DR13)	Ma et al. (2025)	14 555	0-0.2	421 797
COSMOS-Web	Toni et al. (2025)	0.45	0.08-3.7	1 678
EUCLID Q1	Euclid Collaboration et al. (2025b)	63	0.2-1.5	426

Table 4: Extensive summary of available X-ray cluster catalogs in the literature. The first column indicates the catalog name, the second column the reference, the third column the area covered by the catalog, the fourth column the redshift range, and the last column the number of clusters in the catalog.

Catalog	Reference	Area deg^2	$z_{min} - z_{max}$	$N_{clusters}$
Lugger78 (Uhuru)	Lugger (1978)	–	–	13
Forman78 (Uhuru)	Forman et al. (1978)	–	–	45
Ariel V 2A	Cooke et al. (1978)	–	–	13
McHardy78 (Ariel V)	McHardy (1978)	–	–	34
Ariel V 3A	McHardy et al. (1981)	–	–	41
Piccinotti82 (HEAO)	Piccinotti et al. (1982)	all-sky	0-0.1	30
Kowalski84 (HEAO)	Kowalski et al. (1984)	–	–	74
Gioia84 (EMSS)	Gioia et al. (1984)	40	–	10
Gioia90 (EMSS)	Gioia et al. (1990)	778	–	96
Stocke91 (EMSS)	Stocke et al. (1991)	–	0-0.6	101
Romer94	Romer et al. (1994)	–	–	345
Pierre94 (RASS)	Pierre et al. (1994b)	1 730	0-0.3	150
Henry95 (RASS NEP)	Henry et al. (1995)	84.7	0.025-0.04	23
RIXOS	Castander et al. (1995)	–	–	13
Scharf97 (WARPS)	Scharf et al. (1997)	17.2	0.1-0.7	58
Collins97 (ROSAT PSPC)	Collins et al. (1997)	17.2	0-0.7	35
Burke97 (SHARC)	Burke et al. (1997)	17.7	0.3-0.7	16
EXSS	Oppenheimer et al. (1997)	–	–	21
Vikhlinin98 (ROSAT PSPC)	Vikhlinin et al. (1998)	158	0-0.5	203

Table 4: Continued.

Catalog	Reference	Area deg^2	$z_{min} - z_{max}$	$N_{clusters}$
RDCS	Rosati et al. (1998)	–	0-0.8	70
Appenzeller98 (RASS)	Appenzeller et al. (1998)	–	–	73
BCS	Ebeling et al. (1998)	13 572	0-0.3	206
DeGrandi99 (SASS1)	De Grandi et al. (1999)	8 235	–	130
BMW ROSAT	Campana et al. (1999)	160	0.1-0.8	287
RASS-BSC	Voges et al. (1999)	all-sky	–	413
Guzzo99 (REFLEX)	Guzzo et al. (1999)	–	–	460
RASSCALS	Mahdavi et al. (2000)	–	0.01-0.04	260
Bohringer00 (RASS)	Böhringer et al. (2000a)	8 259	–	181
eBCS	Ebeling et al. (2000)	13 572	0.02-0.3	107
Romer00 (SHARC)	Romer et al. (2000)	178	0-0.8	37
NORAS	Böhringer et al. (2000b)	–	0.01-0.36	378
Ebeling (MACS)	Ebeling et al. (2001)	22 735	0.3-0.6	101
RASS-SGP	Cruddace et al. (2002)	3 325	0.03-0.3	186
WARPS	Perlman et al. (2002)	16.2	0.06-0.75	34
CIZA-I	Ebeling et al. (2002)	8 250	–	73
Boschin02 (Chandra)	Boschin (2002)	5.55	–	36
ROXS	Donahue et al. (2002)	5	0.06-1	57
EEMSS	Lewis et al. (2002)	780	–	3
160SD	Mullis et al. (2003)	160	–	201
SHARC	Burke et al. (2003)	17.7	0.05-0.7	32
REFLEX	Böhringer et al. (2004)	13 924	0-0.3	447
RASS-SDSS	Popesso et al. (2004)	–	0-0.8	114
BMW	Moretti et al. (2004)	160	0.1-0.9	154
GAVO	Schuecker et al. (2004)	140	0-0.5	75
Andreon05 (XMM)	Andreon et al. (2005)	2.9	0.8-1	19
ChaMP	Barkhouse et al. (2006)	13	0.01-0.76	49
SEXCLAS	Kolokotronis et al. (2006)	2.1	0.4-0.6	21
ROSAT NEP	Henry et al. (2006)	80.7	0.02-0.81	64
CIZA-II	Kocevski et al. (2007)	8.250	–	57
BLOX	Dietrich et al. (2007)	2.8	–	59
XMM-COSMOS	Finoguenov et al. (2007)	2.1	0.12-1.25	72
400d PSPC	Burenin et al. (2007)	397	0.01-0.83	242
WARPS-II	Horner et al. (2008)	56.7	0.04-0.8	125
2XMM	Watson et al. (2009)	500	–	422
SXDF	Finoguenov et al. (2010)	1.3	0.1-1.3	57
2XMMi-DR1	Takey et al. (2011)	504	0.11-0.59	175
XMM-XCS	Lloyd-Davies et al. (2011)	410	0-1.5	3 675
XDCP	Fassbender et al. (2011)	76.1	0.9-1.6	22
XMM-BCS	Šuhada et al. (2012)	6	0.1-1	46
XMM-XCS DR1	Mehrtens et al. (2012)	410	0.06-1.46	503
REFLEX-II	Böhringer et al. (2013)	13 924	0-0.3	915
AEGIS	Erfanianfar et al. (2013)	0.67	0.07-1.54	52
Hoon13 (XDCP)	de Hoon et al. (2013)	0.2	0.34-1.45	6
XMM-LSS	Clerc et al. (2014)	11.1	0.05-1.06	52
Gozaliasl14	Gozaliasl et al. (2014)	3	0.04-1.23	129
2XMMi-DR3	Takey et al. (2014)	210	0.06-0.78	145
SWXCS	Liu et al. (2015)	400	0.1-0.97	263
SACS	Dai et al. (2015)	125	–	442
ECDF-S	Finoguenov et al. (2015)	0.3	0.08-1.6	51
XXL BCS	Pacaud et al. (2016)	50	0.1-0.5	100
Takey16 (3XMM-DR5)	Takey et al. (2016)	11.25	0.05-1.1	94
Rabitz17 (XMM+SDSS)	Rabitz et al. (2017)	–	0.2-1.5	19

Table 4: Continued.

Catalog	Reference	Area deg^2	$z_{min} - z_{max}$	$N_{clusters}$
NORAS-II	Böhringer et al. (2017)	13 519	0-0.5	860
XXL	Adami et al. (2018)	50	0.05-1	365
Xu18	Xu et al. (2018)	all-sky	0.01-0.08	13
MARD-Y3	Klein et al. (2019)	5 000	0.02-1.1	1 086
CODEX	Finoguenov et al. (2020)	10 382	0.05-0.65	10 382
X-CLASS	Koulouridis et al. (2021)	269	0.05-1.5	1 646
CHiPS	Somboonpanyakul et al. (2021)	–	0.1-0.7	11
RXGCC	Xu et al. (2022)	26 722	0.01-0.55	944
eFEDS	Liu et al. (2022)	140	0.01-1.3	542
RASS-MCMF	Klein et al. (2023)	25 000	0.02-1	8 449
XVXGC	Xu et al. (2024)	13	0.11-0.91	141
SRG/eROSITA	Bulbul et al. (2024)	13 116	0-1.32	12 247

Table 5: Extensive summary of available millimeter (SZ) cluster catalogs in the literature. The columns are similar to the previous tables.

Catalog	Reference	Area deg^2	$z_{min} - z_{max}$	$N_{clusters}$
SPT09	Staniszewski et al. (2009)	40	0.4-0.8	4
ACT10	Menanteau et al. (2010b); Marriage et al. (2011)	455	0.1-1.1	23
SPT10	Vanderlinde et al. (2010)	178	0.15-1	21
SPT11	Williamson et al. (2011)	2 500	0.1-1.13	26
ESZ	Planck Collaboration et al. (2011a)	all-sky	0-0.44	189
SPT13	Reichardt et al. (2013)	720	0.08-1.5	224
ACT13	Hasselfield et al. (2013)	504	0.15-0.8	68
PSZ1	Planck Collaboration et al. (2014b)	all-sky	0.03-0.55	1 227
SPT-SZ	Bleem et al. (2015b)	2 500	0.15-1.1	677
PSZ2	Planck Collaboration et al. (2016c)	all-sky	0.03-0.55	1 653
Burenin17 (Planck)	Burenin (2017)	all-sky	0-0.88	2 964
ACTpol	Hilton et al. (2018)	987.5	0.1-1.4	182
ComPRASS (Planck+Rosat)	Tarrío et al. (2019)	all-sky	0.01-1.2	2 323
SPTpol	Huang et al. (2020)	100	0.15-1.38	89
SPT-ECS	Bleem et al. (2020)	2 770	0.1-1	470
PSZSPT	Melin et al. (2021)	2 500	0.02-1.7	419
HAD (Planck)	Hurier et al. (2021)	all-sky	–	3 969
ACT21	Hilton et al. (2021)	13 211	0.04-1.9	4 195
PSZ-MCMF	Hernández-Lang et al. (2023)	5 000	0-1.3	853
UPCluster-SZ (Planck)	Bahk and Hwang (2024)	all-sky	0.05-0.8	149
ComPACT (ACT+Planck)	Voskresenskaia et al. (2024)	18 000	0.2-1.5	2 962
SPTpol	Bleem et al. (2024)	500	0.03-1.6	689
SPT-SZ MCMF	Klein et al. (2024a)	2 500	0.1-1.7	811
ACT-DR5 MCMF	Klein et al. (2024b)	13 211	0.04-1.9	6 237
SPT-Euclid	Archipley et al. (2025)	10 000	0.07-1.6+	217
NIKA2-COSMOS	Chérouvrier et al. (2025)	0.3	0.2-1.4	16
SPT-Deep	Kornoelje et al. (2025)	100	0.12-1.8	500
Planck-SZiFi	Zubeldia et al. (2025)	all-sky	–	1 499
ACT25	ACTDESHSC Collaboration et al. (2025)	16 293	0-2	9 977

Appendix B: Clusters in the LPSZ sample

In this appendix we present the full list of clusters in the LPSZ sample, with their short name, full name and main properties. Their masses will be published in a future article [Hanser, in prep.(a)].

Full name	Short name	ra °	dec °	redshift
ACT-CL J0022.2-0036	ACTJ0022	5.5513	-0.6048	0.805
ACT-CL-J0119.9+0055	ACTJ0119	19.9971	0.9193	0.72
ACT-CL-J0215.4+0030	ACTJ0215	33.8682	0.5089	0.865
ACT-CL-J0223.1-0056	ACTJ0223	35.792	-0.9533	0.663
ACT-CL-J0240.0+0116	ACTJ0240	40.0141	1.2662	0.62
ACT-CL-J2130.1+0045	ACTJ2130	322.5361	0.7798	0.71
ACT-CL-J2302.5+0002	ACTJ2302	345.6436	0.0462	0.52
PLCK-G079.95+46.96	PLCKG079	240.5461	51.0615	0.79
PLCK-G227.99+38.11	PLCKG227	143.0891	5.69	0.81
PSZ1-G080.66-57.87	PSZ1G080	351.8654	-2.0771	0.705
PSZ1-G226.65+28.43	PSZ1G226	134.0858	1.7803	0.724
PSZ2-G045.32-38.46	PSZ2G045	322.3591	-7.6913	0.594
PSZ2-G046.13+30.72	PSZ2G046	259.2742	24.0737	0.569
PSZ2-G080.64+64.31	PSZ2G080	216.8172	44.1251	0.502
PSZ2-G081.02+50.57	PSZ2G081	234.779	50.613	0.501
PSZ2-G084.10+58.72	PSZ2G084	222.2535	48.5569	0.731
PSZ2 G085.95+25.23	PSZ2G085	277.6475	56.8947	0.782
PSZ2-G086.93+53.18	PSZ2G086	228.5022	52.8035	0.771
PSZ2-G087.39+50.92	PSZ2G087	231.6379	54.1523	0.748
PSZ2-G091.83+26.11	PSZ2G091	277.7925	62.2429	0.816
PSZ2-G094.56+51.03	PSZ2G094	227.0821	57.9164	0.539
PSZ2-G099.86+58.45	PSZ2G099	213.6952	54.784	0.615
PSZ2-G104.74+40.42	PSZ2G104	236.71	69.9441	0.835
PSZ2-G108.27+48.66	PSZ2G108	216.777	65.6528	0.673
PSZ2-G111.61-45.71	PSZ2G111	4.6399	16.4362	0.546
PSZ2-G126.57+51.61	PSZ2G126	187.436	65.356	0.816
PSZ2-G133.59+50.68	PSZ2G133	176.7103	65.0863	0.529
PSZ2-G141.77+14.19	PSZ2G141	70.2759	68.2202	0.821
PSZ2-G144.83+25.11	PSZ2G144	101.962	70.2573	0.584
PSZ2-G155.27-68.42	PSZ2G155	24.3536	-8.4557	0.567
PSZ2-G160.83+81.66	PSZ2G160	186.742	33.5463	0.888
PSZ2-G183.90+42.99	PSZ2G183	137.7032	38.8357	0.559
PSZ2-G193.31-46.13	PSZ2G193	53.9644	-6.9758	0.64
PSZ2-G201.50-27.31	PSZ2G201	73.5471	-3.0162	0.538
PSZ2-G209.79+10.23	PSZ2G209	110.5869	7.3993	0.677
PSZ2-G211.21+38.66	PSZ2G211	137.797	17.776	0.505
PSZ2-G212.44+63.19	PSZ2G212	163.2159	24.2584	0.542
PSZ2-G228.16+75.20	PSZ2G228	177.3976	22.4011	0.545

Table 6: Overview of the LPSZ cluster sample. The first two columns give the full name of the cluster and its associated short name that we use in this chapter. The last three columns give the coordinates of the cluster center and its redshift.

Appendix C: Catalog of radio sources in the LPSZ fields

We present here the full catalog of radio sources in the LPSZ fields, as described in Section 7.3.2. They were compiled from several databases and external catalogs.

Cluster	id	Source Name	ra °	dec °	Database	d2d arcsec	$F_{1.4\,GHz}$ mJy	$\sigma_{1.4\,GHz}$ mJy	$F_{150\,MHz}$ mJy	$\sigma_{150\,MHz}$ mJy	F_{other} mJy	σ_{other} mJy	ν_{other} GHz	$F_{150\,GHz}$ mJy	$\sigma_{150\,GHz}$ mJy
ACTJ0022	0	FIRST J002213.0-003633	5.5542	-0.6092	FIRST	19.14	19.03	0.137	67.8	9.1	–	–	–	0.722	0.005
	1	GLEAM J002208-003608	5.534	-0.6024	GLEAMEGCAT	63.06	–	–	278.14	112.731	–	–	–	2.209	0.895
	2	NVSS J002212-003504	5.5512	-0.5846	NVSS	72.9	2.4	0.5	–	–	–	–	–	0.091	0.019
	3	FIRST J002212.7-003457	5.5529	-0.5826	FIRST	80.22	1.49	0.135	–	–	–	–	–	0.057	0.005
	4	FIRST J002206.0-003555	5.525	-0.5988	FIRST	96.96	33.68	0.138	208.7	21.7	–	–	–	1.278	0.005
	5	TXS 0019-008	5.5092	-0.6219	TEXAS	163.68	–	–	–	–	405	71	0.365	5.995	1.051
	6	FIRST J002201.9-003800	5.5083	-0.6334	FIRST	186	0.99	0.138	–	–	–	–	–	0.038	0.005
ACTJ0119	0	FIRST J012003.3+005538	20.0141	0.9274	FIRST	67.56	3.8	0.5	–	–	–	–	–	0.144	0.019
ACTJ0215	0	WISEA J021528.03+003049.6	33.86683	0.51378	NED	18.24	0.787	0.191	–	–	–	–	–	0.03	0.007
	1	FIRST J021527.9+003009	33.8663	0.5025	FIRST	24	3.7	0.5	–	–	–	–	–	0.14	0.019
	2	[HBW2011] VLA J021533.18+003138.7	33.8883	0.5274	VLASS821P4	98.28	0.5	0.098	–	–	–	–	–	0.019	0.004
	3	VLSSr J021518.1+003048	33.8256	0.5134	VLSSR	154.14	–	–	–	–	733	99	0.074	3.551	0.48
	4	FIRST J021516.8+003028	33.8202	0.5081	FIRST	172.74	42.92	0.1	–	–	–	–	–	1.628	0.004
	5	NVSS J021516+003037	33.8189	0.5105	NVSS	177.54	113.4	4	550.2	55.3	585	88	0.365	4.302	0.152
	6	[HJB2016] J021516.4+003050	33.81826	0.51413	NED	180.78	1.1	0.188	–	–	–	–	–	0.042	0.007
	7	FIRST J021516.2+003043	33.8179	0.512	FIRST	181.38	67.34	0.101	–	–	–	–	–	2.554	0.004
ACTJ0223	0	FIRST J022310.0-005709	35.7919	-0.9526	FIRST	2.52	1.79	0.154	–	–	–	–	–	0.068	0.006
	1	NVSS J022309-005650	35.79	-0.9474	NVSS	22.5	3.1	0.6	–	–	–	–	–	0.118	0.023
	2	FIRST J022306.5-005426	35.7773	-0.9073	FIRST	173.76	3.8	0.154	–	–	–	–	–	0.144	0.006
	3	FIRST J022322.2-005631	35.8426	-0.9422	FIRST	186.36	1.89	0.149	–	–	–	–	–	0.072	0.006
ACTJ0240	0	FIRST J024001.8+011606	40.0075	1.2685	FIRST	25.2	6.5	0.5	–	–	–	–	–	0.247	0.019
ACTJ2130	0	FIRST J213008.8+004648	322.5369	0.7802	FIRST	3.3	7.09	0.133	–	–	–	–	–	0.269	0.005
	1	FIRST J213009.7+004540	322.5408	0.7611	FIRST	69.36	1.37	0.143	–	–	–	–	–	0.052	0.005
ACTJ2302	0	FIRST J230234.0+000220	345.6417	0.0391	FIRST	26.52	7.57	0.056	61.4	7.4	–	–	–	0.287	0.002
	1	NVSS J230233+000214	345.6387	0.0373	NVSS	36.72	11.4	1.3	–	–	–	–	–	0.432	0.049
	2	FIRST J230231.1+000147	345.6298	0.0299	FIRST	76.74	3.7	0.057	–	–	–	–	–	0.14	0.002
PLCKG079	0	FIRST J160219.5+510409	240.5815	51.0692	FIRST	84.78	2.46	0.135	–	–	–	–	–	0.093	0.005
PLCKG227	0	RACS-MID J093225.0+054319	143.1043	5.7219	Vizier	127.11	0.83	0.23	–	–	–	–	–	0.031	0.009
PSZ1G080	0	NVSS J232727-020355	351.866	-2.0654	NVSS	42	5.7	0.6	–	–	–	–	–	0.216	0.023
	1	MSH 23-011	351.9173	-2.0912	DIXON	193.56	–	–	–	–	1550	–	0.085	8.273	–
PSZ1G226	0	FIRST J085617.8+014638	134.0745	1.7774	FIRST	42.06	3.6	0.4	–	–	–	–	–	0.137	0.015
	1	FIRST J085617.8+014638	134.0745	1.7774	FIRST	42.06	3.09	0.151	–	–	9.3	3.5	0.325	0.117	0.006
	2	FIRST J085627.8+014526	134.116	1.7575	FIRST	136.14	1.95	0.145	–	–	–	–	–	0.074	0.006
PSZ2G045	0	WISEA J212930.21-074229.6	322.3759	-7.70817	NED	85.32	–	–	–	–	1.18	0.1	28.5	0.369	0.031
	1	FIRST J212919.1-074251	322.3298	-7.7143	FIRST	133.5	1.05	0.154	–	–	–	–	–	0.04	0.006
	2	NVSS J212915-074213	322.3141	-7.7038	NVSS	166.8	3.5	0.5	–	–	–	–	–	0.133	0.019
	3	FIRST J212915.2-074220	322.3134	-7.7058	FIRST	171.18	1.16	0.155	–	–	–	–	–	0.044	0.006
PSZ2G046	0	FIRST J171705.5+240423	259.2732	24.0733	FIRST	3.72	11.4	0.5	44.9	7.7	–	–	–	0.432	0.019
	1	FIRST J171705.1+240414	259.2714	24.0707	FIRST	14.28	1.52	0.14	–	–	–	–	–	0.058	0.005
	2	GLEAM J171659+240615	259.2467	24.1043	GLEAMEGCAT	142.26	–	–	355.133	–	–	–	–	2.821	–
	3	1714+2409	259.2359	24.0987	NORTH6CM	154.74	–	–	–	–	42	–	6	4.413	–
	4	FIRST J171658.6+240634	259.2446	24.1096	FIRST	161.7	103.1	3.1	396	40.3	286	53	0.365	3.911	0.118
	5	VLSSr J171658.9+240642	259.2457	24.1118	VLSSR	165.9	–	–	–	–	461	84	0.074	2.233	0.407
	6	GB6 J1716+2406	259.2367	24.1103	GB6	180.42	–	–	–	–	37	5	6	3.887	0.525

Table 7: Complete catalog of radio sources in the LPSZ fields. The columns are: (1) cluster name, (2) source id, (3) source name, (4) RA, (5) Dec, (6) database where the source is found, (7) distance to the cluster center, (8-9) flux at 1.4 GHz and associated uncertainty, (10-11) flux at 150 MHz and associated uncertainty, (12-13) flux and uncertainty at other frequencies, (14) frequency of the other fluxes, (15-16) estimated flux at 150 GHz and associated uncertainty. The sources are ordered by cluster name and id.

Cluster	id	Source Name	ra	dec	Database	d2d	$F_{1.4\,\mathrm{GHz}}$	$\sigma_{1.4\,\mathrm{GHz}}$	$F_{150\,\mathrm{MHz}}$	$\sigma_{150\,\mathrm{MHz}}$	F_{other}	σ_{other}	ν_{other}	$F_{150\,\mathrm{GHz}}$	$\sigma_{150\,\mathrm{GHz}}$
			°	°		arcsec	mJy	mJy	mJy	mJy	mJy	mJy	GHz	mJy	mJy
PSZ2G080	0	FIRST J142716.1+440730	216.8172	44.1252	FIRST	0.18	47.9	1.8	81.5	9.4	53	3.2	0.325	1.817	0.068
	1	ATATS J142717+440724	216.8221	44.1233	ATATS	14.16	47.9	4.4	–	–	–	–	–	1.817	0.167
	2	[VFK2015] J216.82133+44.12776	216.82133	44.12777	NED	14.34	48.8	–	–	–	–	–	–	1.851	–
	3	GB6 J1427+4407	216.8154	44.1297	GB6	17.28	–	–	–	–	44	5	6	4.623	0.525
	4	FIRST J142713.8+440729	216.8076	44.125	FIRST	24.84	1.11	0.143	–	–	–	–	–	0.042	0.005
	5	FIRST J142718.1+440749	216.8254	44.1304	FIRST	28.56	1.87	0.143	–	–	–	–	–	0.071	0.005
	6	1425+4421	216.8238	44.1329	NORTH6CM	32.82	–	–	–	–	41	–	6	4.308	–
	7	FIRST J142714.5+440945	216.8106	44.1625	FIRST	135.84	1.04	0.145	–	–	–	–	–	0.039	0.006
PSZ2G081	0	ILTJ153906.38+503645.3	234.7766	50.6126	Vizier	5.67	–	–	0.841	0.208	–	–	–	0.007	0.002
	1	ILTJ153911.15+503647.8	234.7965	50.6133	Vizier	39.99	–	–	1.119	0.216	–	–	–	0.009	0.002
	2	ILTJ153911.27+503706.5	234.797	50.6185	Vizier	45.64	–	–	3.035	0.765	–	–	–	0.024	0.006
	3	ILTJ153911.28+503731.1	234.797	50.6253	Vizier	60.42	–	–	5.695	0.261	–	–	–	0.045	0.002
	4	ILTJ153909.49+503754.8	234.7895	50.6319	Vizier	72.14	–	–	0.513	0.137	–	–	–	0.004	0.001
	5	ILTJ153915.06+503612.4	234.8127	50.6034	Vizier	84.39	–	–	1.087	0.204	–	–	–	0.009	0.002
	6	ILTJ153857.92+503734.7	234.7413	50.6263	Vizier	98.53	–	–	0.429	0.123	–	–	–	0.003	0.001
	7	ILTJ153859.05+503542.3	234.746	50.5951	Vizier	99.18	–	–	0.356	0.156	–	–	–	0.003	0.001
	8	ILTJ153915.24+503536.6	234.8135	50.5935	Vizier	105.56	–	–	1.081	0.193	–	–	–	0.009	0.002
	9	ILTJ153900.33+503816.4	234.7514	50.6379	Vizier	109.58	–	–	1.879	0.147	–	–	–	0.015	0.001
	10	ILTJ153854.52+503651.1	234.7272	50.6142	Vizier	118.41	–	–	0.465	0.122	–	–	–	0.004	0.001
	11	ILTJ153857.71+503510.0	234.7405	50.5861	Vizier	130.83	–	–	0.397	0.128	–	–	–	0.003	0.001
	12	ILTJ153919.81+503819.3	234.8326	50.6387	Vizier	153.44	–	–	0.88	0.133	–	–	–	0.007	0.001
	13	ILTJ153916.96+503445.1	234.8207	50.5792	Vizier	154.55	–	–	0.415	0.107	–	–	–	0.003	0.001
	14	ILTJ153859.12+503429.9	234.7463	50.575	Vizier	155.88	–	–	0.386	0.114	–	–	–	0.003	0.001
	15	ILTJ153905.63+503922.8	234.7734	50.6563	Vizier	156.4	–	–	0.672	0.133	–	–	–	0.005	0.001
	16	ILTJ153903.14+503412.6	234.7631	50.5702	Vizier	158.31	–	–	0.307	0.134	–	–	–	0.002	0.001
	17	ILTJ153917.58+503921.8	234.8233	50.6561	Vizier	185.22	–	–	1.032	0.119	–	–	–	0.008	0.001
PSZ2G084	0	ILTJ144901.32+483321.9	222.2555	48.5561	Vizier	5.57	–	–	6.019	0.361	–	–	–	0.048	0.003
	1	ILTJ144903.17+483307.5	222.2632	48.5521	Vizier	28.86	–	–	0.763	0.207	–	–	–	0.006	0.002
	2	ILTJ144857.22+483331.3	222.2384	48.5587	Vizier	36.56	–	–	0.522	0.145	–	–	–	0.004	0.001
	3	ILTJ144855.97+483317.0	222.2332	48.5547	Vizier	49.02	–	–	2.024	0.187	–	–	–	0.016	0.001
	4	ILTJ144854.06+483314.2	222.2253	48.554	Vizier	68	–	–	0.93	0.198	–	–	–	0.007	0.002
	5	ILTJ144853.32+483338.1	222.2222	48.5606	Vizier	75.76	–	–	2.237	0.262	–	–	–	0.018	0.002
	6	ILTJ144854.33+483410.8	222.2264	48.5697	Vizier	79.32	–	–	0.944	0.197	–	–	–	0.007	0.002
	7	ILTJ144845.05+483340.3	222.1877	48.5612	Vizier	157.54	–	–	0.794	0.285	–	–	–	0.006	0.002
	8	ILTJ144909.14+483612.2	222.2881	48.6034	Vizier	186.58	–	–	5.961	1.125	–	–	–	0.047	0.009
	9	ILTJ144848.44+483546.6	222.2018	48.5963	Vizier	187.84	–	–	1.374	0.221	–	–	–	0.011	0.002
PSZ2G085	0	NVSS J183035+565332	277.6474	56.8923	NVSS	8.52	24.4	1.1	149.5	16.2	102	4.3	0.325	0.926	0.042
	1	NVSS J183026+565304	277.6088	56.8845	NVSS	84.48	2.5	0.4	–	–	–	–	–	0.095	0.015
PSZ2G086	0	FIRST J151401.0+524840	228.5044	52.8112	FIRST	28.08	1.18	0.141	9.35	1.43	–	–	–	0.045	0.005
	1	FIRST J151342.0+524744	228.4251	52.7958	FIRST	170.04	2.51	0.136	6.93	1.36	–	–	–	0.095	0.005
PSZ2G087	0	FIRST J152633.1+540906	231.6383	54.1519	FIRST	1.62	1.49	0.152	–	–	–	–	–	0.057	0.006
	1	FIRST J152617.1+540808	231.5713	54.1356	FIRST	152.88	1.23	0.146	–	–	–	–	–	0.047	0.006

Table 8: Continued.

Cluster	id	Source Name	ra °	dec °	Database	d2d arcsec	$F_{1.4\,GHz}$ mJy	$\sigma_{1.4\,GHz}$ mJy	$F_{150\,MHz}$ mJy	$\sigma_{150\,MHz}$ mJy	F_{other} mJy	σ_{other} mJy	ν_{other} GHz	$F_{150\,GHz}$ mJy	$\sigma_{150\,GHz}$ mJy
PSZ2G091	0	VLSSr J183115.4+621431	277.8143	62.2422	VLSSR	36.6	–	–	–	–	536	69	0.074	2.596	0.334
	1	WN 1830.8+6212	277.8197	62.2472	WENSS	48.06	–	–	–	–	75	3.8	0.325	1.024	0.052
	2	NVSS J183117+621441	277.8229	62.2449	NVSS	51.42	15.8	1.5	211.1	21.6	–	–	–	0.599	0.057
	3	7C 183050.5+621229	277.8275	62.2457	UC7C151MHZ	59.52	–	–	678	–	–	–	–	5.386	–
	4	8C 1830+622	277.7626	62.2554	RRS8C38MHZ	67.32	–	–	–	–	3100	–	0.038	9.418	–
PSZ2G094	0	FIRST J150815.2+575355	227.0635	57.8987	FIRST	73.02	4.4	0.5	–	–	–	–	–	0.167	0.019
PSZ2G099	0	ILT J141440.0+544715.8	213.6668	54.7877	LOTSSPRCAT	60.48	–	–	43.1	5.94	–	–	–	0.342	0.047
	1	FIRST J141447.6+544827	213.6985	54.8077	FIRST	85.44	2.31	0.152	–	–	–	–	–	0.088	0.006
	2	FIRST J141445.7+544425	213.6905	54.7405	FIRST	157.08	13.98	0.154	–	–	–	–	–	0.53	0.006
PSZ2G104	0	NVSS J154637+695808	236.6573	69.969	NVSS	110.76	3.3	0.5	–	–	–	–	–	0.125	0.019
	1	NVSS J154625+695735	236.6082	69.9597	NVSS	137.7	12.1	0.5	69.6	9.5	40	4.8	0.325	0.459	0.019
PSZ2G108	0	WN 1425.9+6552	216.766	65.6538	WENSS	16.68	–	–	–	–	13	3.3	0.325	0.177	0.045
	1	NVSS J142703+653925	216.763	65.657	NVSS	25.74	3.3	0.5	26.7	4.6	–	–	–	0.125	0.019
PSZ2G111	0	GLEAM-X J001833.6+162611	4.634	16.4364	Vizier	0.65	–	–	38.945	7.26	–	–	–	0.309	0.058
PSZ2G126	0	TGSSADR J122945.7+652109	187.4406	65.3525	GMRTAS150M	14.34	–	–	31.3	4.1	–	–	–	0.249	0.033
	1	WN 1227.5+6538A	187.4272	65.3608	WENSS	21.78	–	–	–	–	25	3.6	0.325	0.341	0.049
	2	NVSS J122941+652147	187.4219	65.3631	NVSS	33.12	10.1	0.5	54.7	6.2	–	–	–	0.383	0.019
	3	WN 1227.5+6538	187.4587	65.3688	WENSS	57.36	–	–	–	–	32	3.6	0.325	0.437	0.049
	4	NVSS J122954+652158	187.4752	65.3663	NVSS	69.54	15.5	0.6	58.5	6.6	–	–	–	0.588	0.023
	5	WN 1227.5+6538B	187.4736	65.373	WENSS	83.16	–	–	–	–	32	3.6	0.325	0.437	0.049
	6	NVSS J122951+652258	187.4653	65.3828	NVSS	105.96	9.2	0.5	40.6	5	–	–	–	0.349	0.019
PSZ2G133	0	NVSS J114710+650603	176.792	65.1009	NVSS	134.64	3.2	0.5	–	–	–	–	–	0.121	0.019
PSZ2G144	0	NVSS J064815+701507	102.0663	70.252	NVSS	128.28	3.1	0.5	–	–	–	–	–	0.118	0.019
PSZ2G155	0	FIRST J013721.5-082517	24.3398	-8.4216	FIRST	132.42	9.88	0.139	–	–	–	–	–	0.375	0.005
	1	FIRST J013722.4-082510	24.3435	-8.4195	FIRST	135.18	33.3	1.1	252.5	25.9	–	–	–	1.263	0.042
	2	FIRST J013715.3-082727	24.3138	-8.4577	FIRST	141.84	4.31	0.141	–	–	–	–	–	0.163	0.005
	3	FIRST J013713.1-082624	24.3048	-8.4402	FIRST	182.64	1.02	0.142	–	–	–	–	–	0.039	0.005
PSZ2G160	0	FIRST J122658.1+333248	186.7425	33.5468	FIRST	2.4	4.3	0.5	–	–	–	–	–	0.163	0.019
	1	WN 1224.4+3349	186.7433	33.5489	WENSS	10.26	–	–	–	–	22	3	0.325	0.3	0.041
PSZ2G183	0	NVSS J091058+385008	137.744	38.8358	NVSS	114.54	3.9	0.5	–	–	–	–	–	0.148	0.019
	1	FIRST J091044.2+384750	137.6842	38.7974	FIRST	147.72	1.03	0.138	–	–	–	–	–	0.039	0.005
	2	NVSS J091036+384935	137.6516	38.8264	NVSS	148.62	15.9	1	78.6	9.9	27	4.2	0.325	0.603	0.038
	3	FIRST J091035.9+384931	137.6498	38.8254	FIRST	154.14	13.9	0.136	–	–	–	–	–	0.527	0.005
PSZ2G193	0	FIRST J033551.2-065900	53.9637	-6.9835	FIRST	27.66	2.35	0.14	–	–	–	–	–	0.089	0.005
	1	NVSS J033555-065829	53.9803	-6.9749	NVSS	56.88	2.9	0.4	–	–	–	–	–	0.11	0.015
	2	NVSS J033546-065957	53.9438	-6.9992	NVSS	112.08	4.7	0.6	–	–	–	–	–	0.178	0.023

Table 9: Continued.

Cluster	id	Source Name	ra °	dec °	Database	d2d arcsec	$F_{1.4\,\mathrm{GHz}}$ mJy	$\sigma_{1.4\,\mathrm{GHz}}$ mJy	$F_{150\,\mathrm{MHz}}$ mJy	$\sigma_{150\,\mathrm{MHz}}$ mJy	F_{other} mJy	σ_{other} mJy	ν_{other} GHz	$F_{150\,\mathrm{GHz}}$ mJy	$\sigma_{150\,\mathrm{GHz}}$ mJy
PSZ2G201	0	MS 0451.6-0305:[BGK2007] Fa	73.54779	-3.01787	NED	6.48	0.05	0.017	–	–	–	–	–	0.002	0.001
	1	MS 0451.6-0305:[BGK2007] Fb	73.54596	-3.01454	NED	7.26	0.07	0.02	–	–	–	–	–	0.003	0.001
	2	MS 0451.6-0305:[BGK2007] Rc1	73.55112	-3.01941	NED	18.48	0.055	0.016	–	–	–	–	–	0.002	0.001
	3	[TKN2003] A4	73.55279	-3.017	NED	20.64	0.0432	0.012	–	–	–	–	–	0.002	–
	4	MS 0451.6-0305:[BGK2007] Ra1	73.55362	-3.01639	NED	23.46	0.0438	0.012	–	–	–	–	–	0.002	–
	5	MS 0451.6-0305:[BKG2010] CR1	73.55371	-3.01486	NED	24.24	0.0366	0.012	–	–	–	–	–	0.001	–
	6	MS 0451.6-0305:[BGK2007] Rc2	73.54875	-3.02304	NED	25.32	0.058	0.018	–	–	–	–	–	0.002	0.001
	7	MS 0451.6-0305:[BGK2007] Rb1	73.55229	-3.02144	NED	26.52	0.168	0.022	–	–	–	–	–	0.006	0.001
	8	MM J045412.72-030043.7	73.55375	-3.013	NED	26.52	0.0583	0.017	–	–	–	–	–	0.002	0.001
	9	MS 0451.6-0305:[BGK2007] Rb2	73.55121	-3.02281	NED	27.96	0.1	0.022	–	–	–	–	–	0.004	0.001
	10	MS 0451.6-0305:[BGK2007] Fe	73.53864	-3.01414	NED	31.32	1.77	0.034	–	–	–	–	–	0.067	0.001
	11	MS 0451.6-0305:[BGK2007] Rc3	73.55483	-3.0113	NED	32.94	0.078	0.019	–	–	–	–	–	0.003	0.001
	12	GLEAM J045414-030114	73.5593	-3.0207	GLEAMEGCAT	46.68	–	–	92.693	122.398	–	–	–	0.736	0.972
	13	MS 0451.6-0305:[BGK2007] Fc	73.559	-3.02474	NED	52.68	0.044	0.009	–	–	–	–	–	0.002	–
	14	MS 0451.6-0305:[BGK2007] Fd	73.56318	-3.01967	NED	59.1	1.18	0.042	–	–	–	–	–	0.045	0.002
	15	SSTSL2 J045406.88-030034.4	73.52885	-3.00966	NED	69.72	0.0609	0.017	–	–	–	–	–	0.002	0.001
	16	SSTSL2 J045411.70-030305.3	73.54858	-3.05222	NED	129.78	0.051	0.017	–	–	–	–	–	0.002	0.001
	17	MM J045417.49-030306.6	73.57196	-3.05089	NED	153.54	0.189	0.017	–	–	–	–	–	0.007	0.001
	18	SSTSL2 J045421.65-030108.4	73.59025	-3.01903	NED	155.46	0.0843	0.017	–	–	–	–	–	0.003	0.001
	19	NVSS J045422-030123	73.5919	-3.0233	NVSS	162.96	14.4	0.6	–	–	–	–	–	0.546	0.023
PSZ2G209	0	GLEAM J072228+072535	110.6205	7.4266	GLEAMEGCAT	154.98	–	–	303.065	128.994	–	–	–	2.407	1.025
	1	NVSS J072229+072537	110.6241	7.4271	NVSS	166.32	17	1.7	226	22.8	–	–	–	0.645	0.064
	2	NVSS J072214+072116	110.5609	7.3545	NVSS	186.12	4	0.6	–	–	–	–	–	0.152	0.023
	3	VLSSr J072231.0+072550	110.6293	7.4306	VLSSR	188.82	–	–	–	–	429	84	0.074	2.078	0.407
PSZ2G211	0	FIRST J091107.6+174808	137.782	17.8024	FIRST	107.94	1.39	0.145	–	–	–	–	–	0.053	0.006
	1	FIRST J091059.4+174532	137.7478	17.7592	FIRST	179.1	3.1	0.5	–	–	–	–	–	0.118	0.019
	2	FIRST J091059.1+174735	137.7463	17.7932	FIRST	184.38	5.03	0.141	–	–	–	–	–	0.191	0.005
PSZ2G212	0	FIRST J105252.3+241530	163.2183	24.2584	FIRST	7.86	26.5	0.9	83.6	9.4	–	–	–	1.005	0.034
PSZ2G228	0	FIRST J114939.3+222431	177.414	22.4086	FIRST	60.9	2.8	0.5	–	–	–	–	–	0.106	0.019
	1	NVSS J114937+222603	177.4048	22.4343	NVSS	121.92	2.2	0.4	–	–	–	–	–	0.083	0.015
	2	FIRST J114943.4+222616	177.4312	22.4379	FIRST	173.58	6.41	0.151	–	–	–	–	–	0.243	0.006
	3	FIRST J114922.3+222326	177.343	22.3907	FIRST	185.64	15.8	1	–	–	–	–	–	0.599	0.038
	4	FIRST J114944.8+222617	177.4369	22.4381	FIRST	186.84	5.12	0.151	–	–	–	–	–	0.194	0.006
	5	FIRST J114946.3+222606	177.443	22.4352	FIRST	194.76	7.69	0.151	–	–	–	–	–	0.292	0.006

Table 10: Continued.

Appendix D: Mass estimates of LPSZ clusters in the literature

As discussed in Section 7.4, we present the mass estimates found in the literature for the 38 LPSZ clusters.

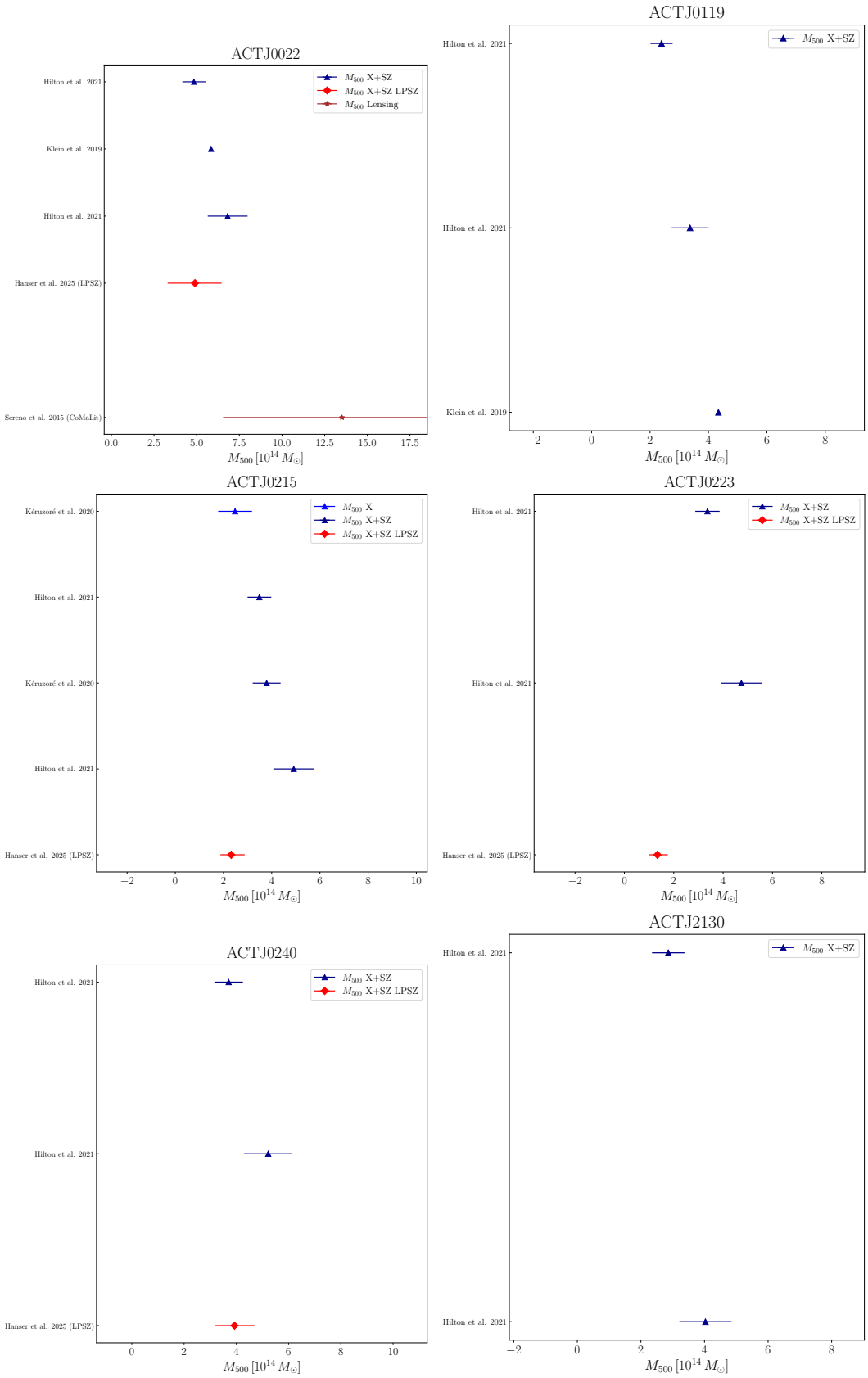

Figure 17: Comparison of M_{500} estimates in the literature for a subsample of six LPSZ clusters. Brown stars correspond to lensing mass estimates. Blue and dark blue triangles represent X-ray only and the combination of SZ and X-ray data results, respectively. The yellow circles are dynamical masses. The red diamond is the NIKA2-LPSZ X-ray+SZ mass estimate. From top to bottom and left to right: ACTJ0022, ACTJ0119, ACTJ0215, ACTJ0223, ACTJ0240, and ACTJ2130.

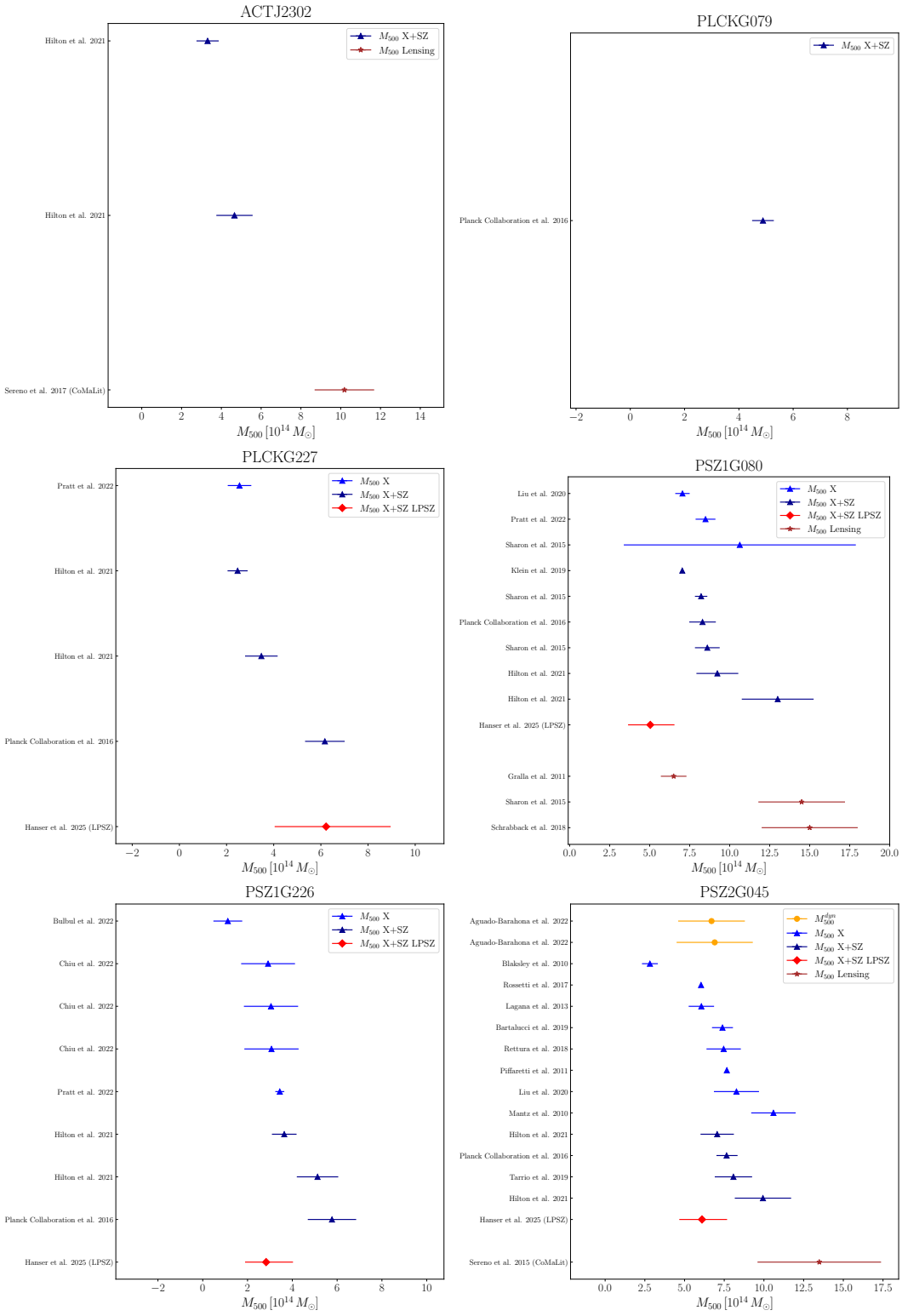

Figure 18: Comparison of M_{500} estimates in the literature for a subsample of six LPSZ clusters. From top to bottom and left to right: ACTJ2302, PLCKG079, PLCKG227, PSZ1G080, PSZ1G226, and PSZ2G045.

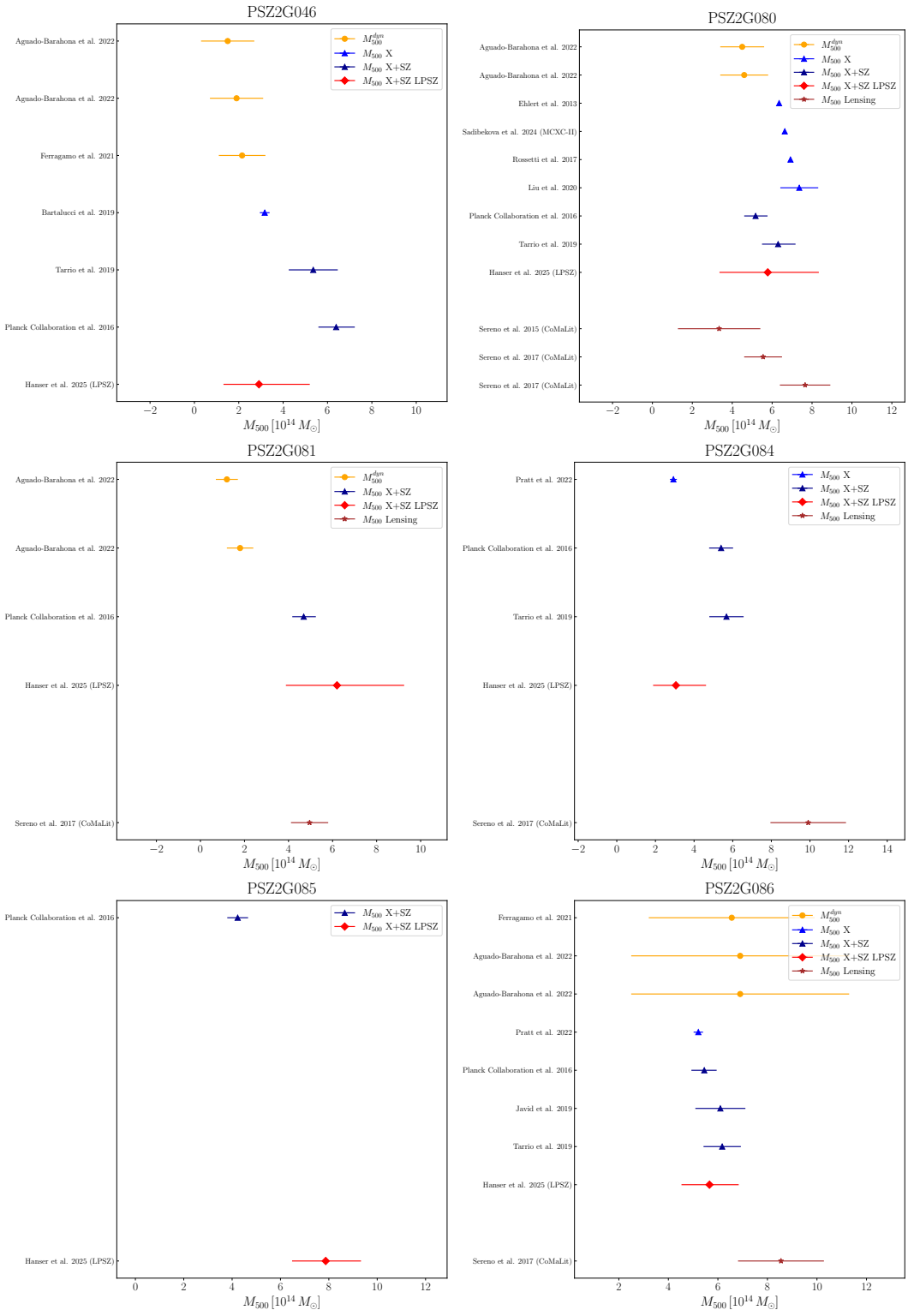

Figure 19: Comparison of M_{500} estimates in the literature for a subsample of six LPSZ clusters. From top to bottom and left to right: PSZ2G046, PSZ2G080, PSZ2G081, PSZ2G084, PSZ2G085, and PSZ2G086.

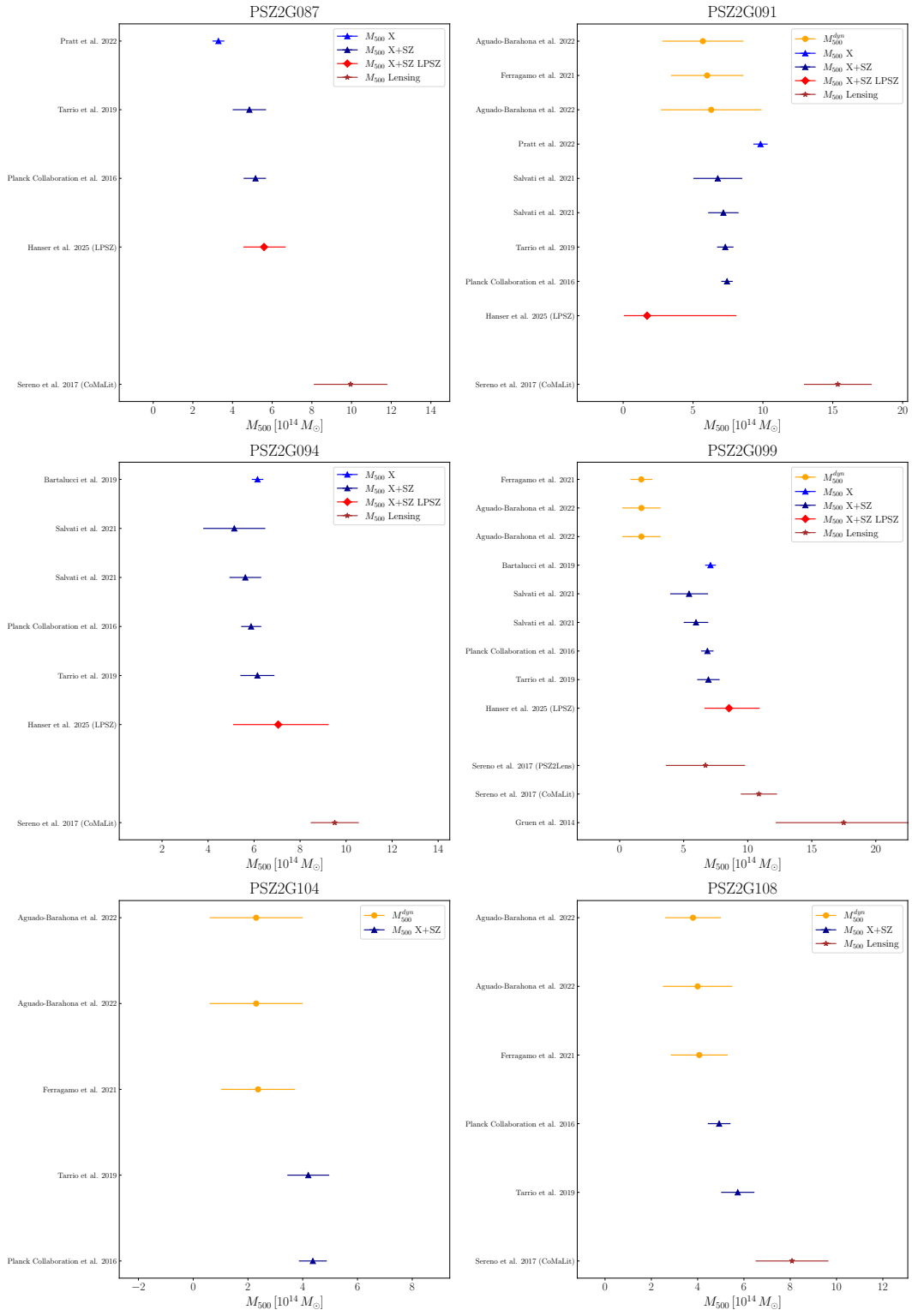

Figure 20: Comparison of M_{500} estimates in the literature for a subsample of six LPSZ clusters. From top to bottom and left to right: PSZ2G087, PSZ2G091, PSZ2G094, PSZ2G099, PSZ2G104, and PSZ2G108.

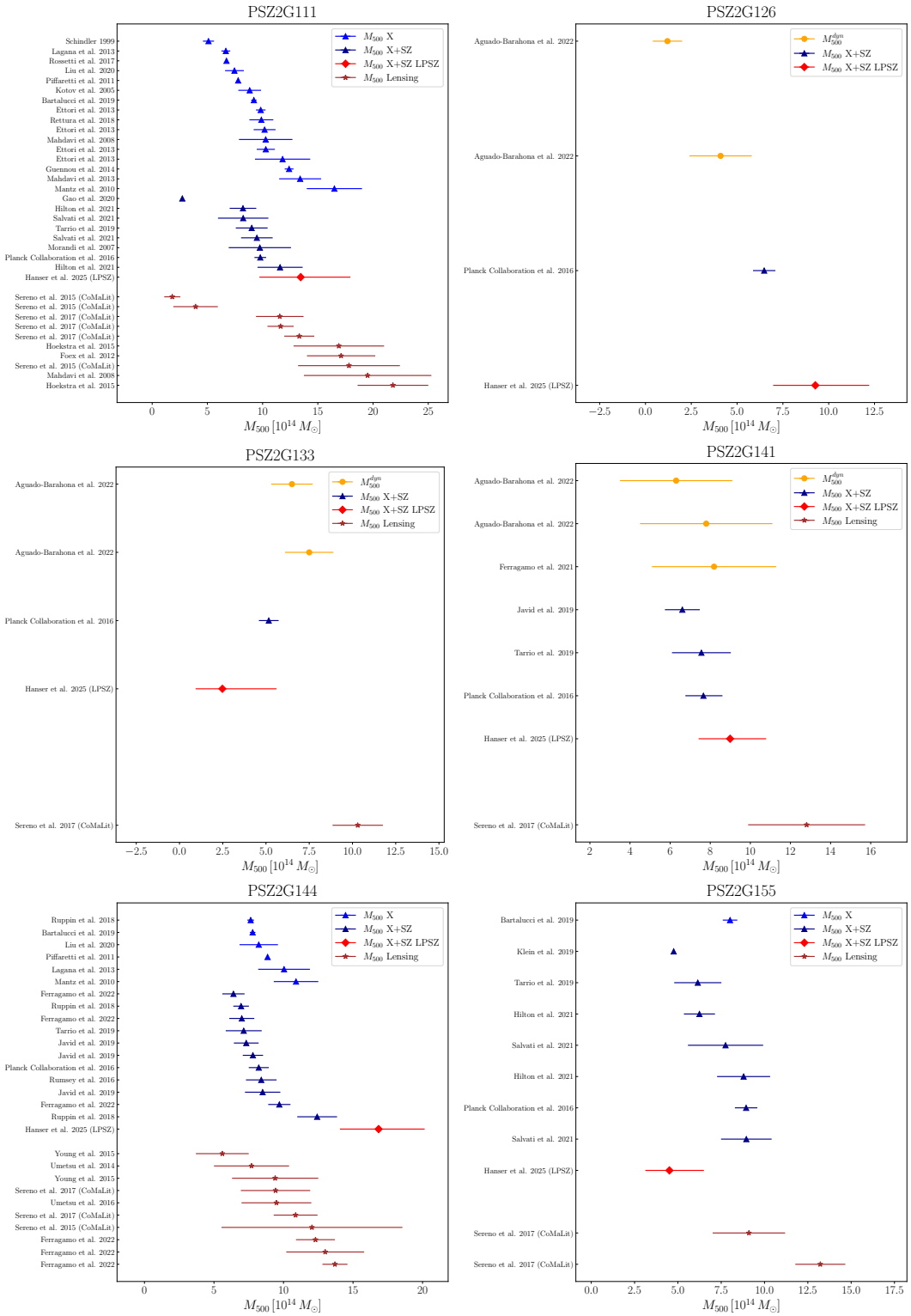

Figure 21: Comparison of M_{500} estimates in the literature for a subsample of six LPSZ clusters. From top to bottom and left to right: PSZ2G111, PSZ2G126, PSZ2G133, PSZ2G141, PSZ2G144, and PSZ2G155.

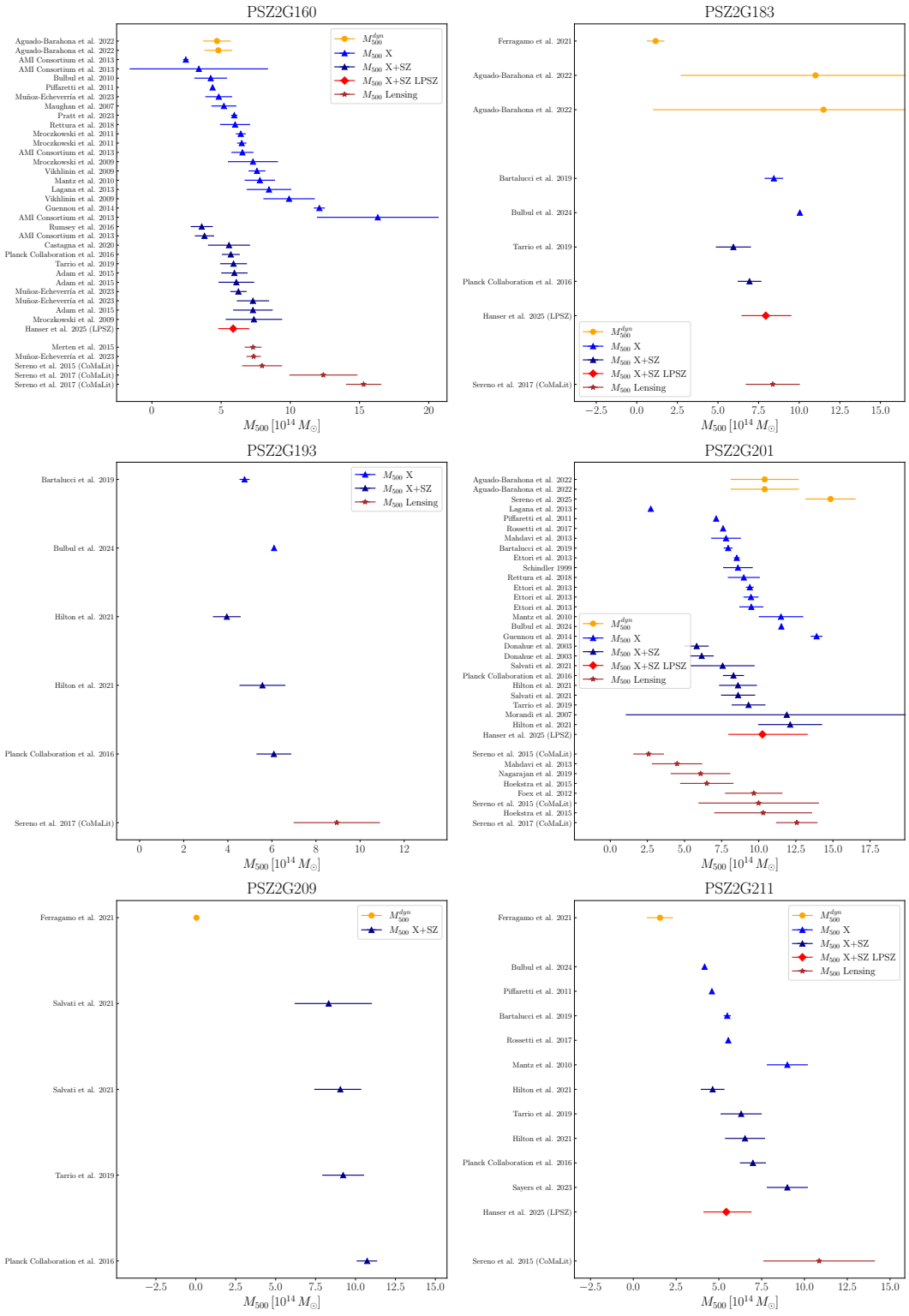

Figure 22: Comparison of M_{500} estimates in the literature for a subsample of six LPSZ clusters. From top to bottom and left to right: PSZ2G160, PSZ2G183, PSZ2G193, PSZ2G201, PSZ2G209, and PSZ2G211.

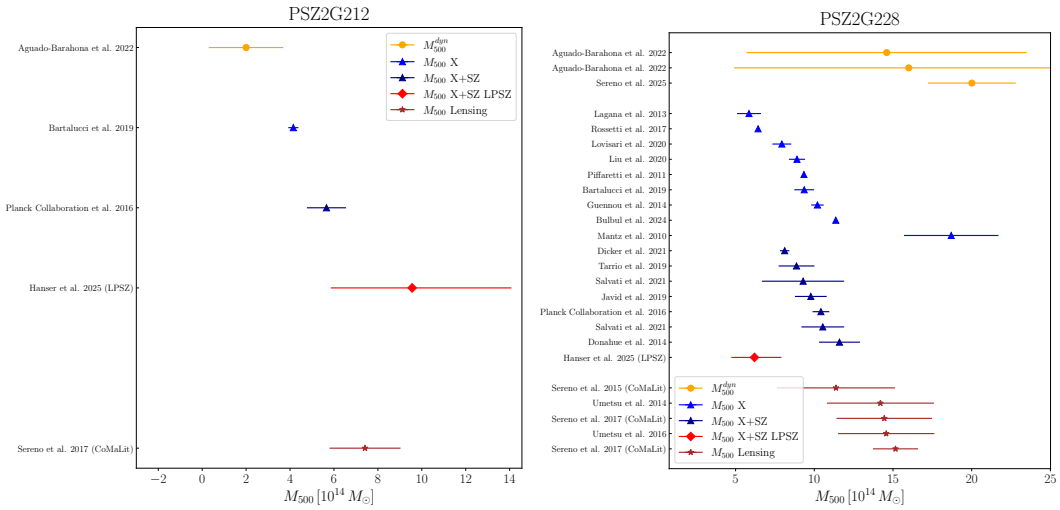

Figure 23: Comparison of M_{500} estimates in the literature for a subsample of the last two LPSZ clusters, PSZ2G212 (left) and PSZ2G228 (right).

Appendix E: Cluster candidate cutouts

We present in Figure 24 zoom-in views of the COSMOS NIKA2 150 GHz map centered at the location of each of the cluster candidates in Table 8.2. We can distinguish negative signal in the center of each of the maps, as expected for the tSZ effect in a cluster of galaxies. We can also observe some positive point sources corresponding to those discussed in detail in Bing et al. (2023).

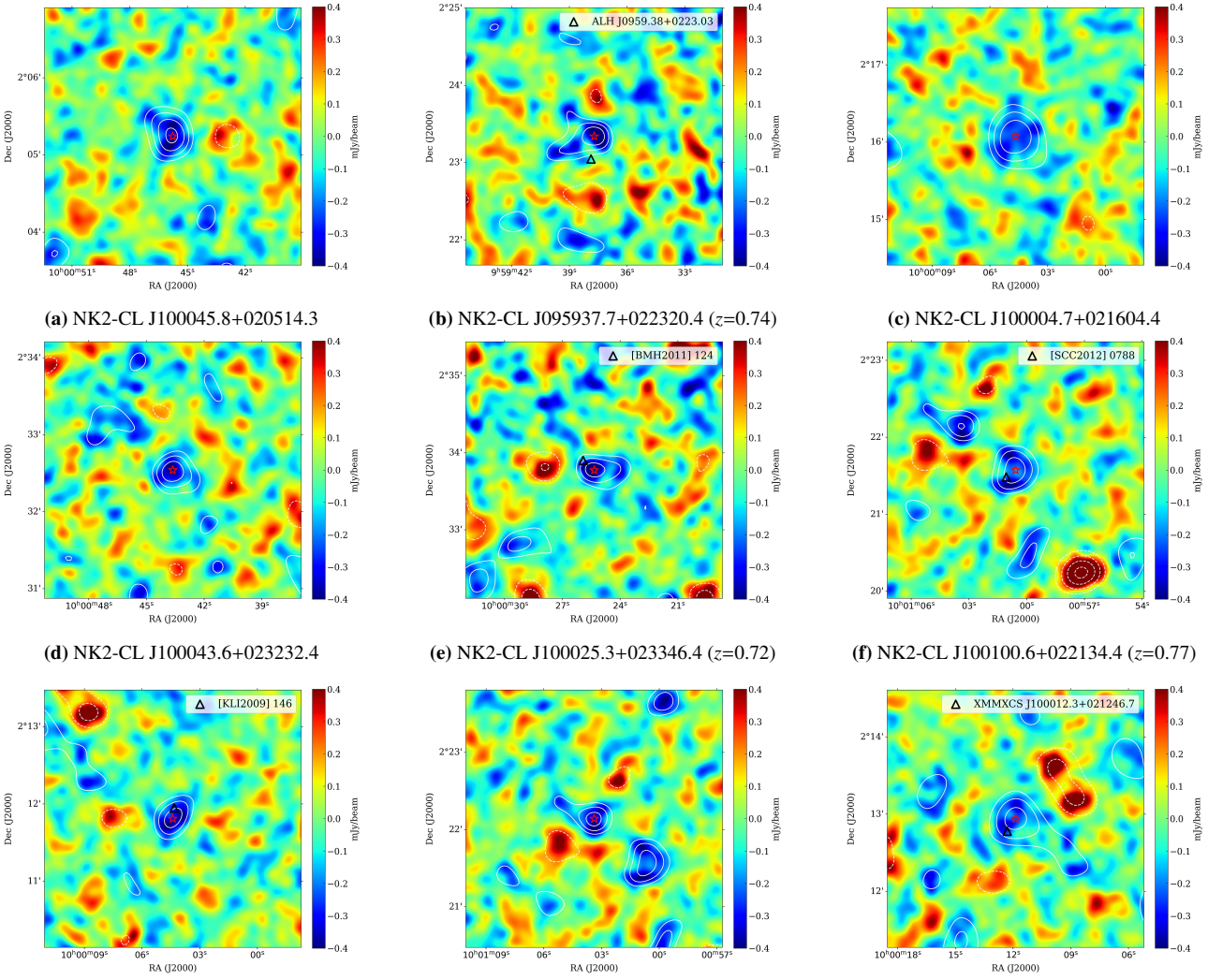

(a) NK2-CL J100045.8+020514.3 **(b)** NK2-CL J095937.7+022320.4 (z=0.74) **(c)** NK2-CL J100004.7+021604.4

(d) NK2-CL J100043.6+023232.4 **(e)** NK2-CL J100025.3+023346.4 (z=0.72) **(f)** NK2-CL J100100.6+022134.4 (z=0.77)

(g) NK2-CL J100004.4+021148.4 (z=0.94) **(h)** NK2-CL J100103.4+022208.4 **(i)** NK2-CL J100011.9+021256.5 (z=0.24)

Figure 24: 200″ × 200″ cutouts of the NIKA2 COSMOS 150 GHz map around each cluster candidate. The center of the candidate (red star) shows clear negative signal. Clusters found in the literature are shown as a black triangle. For each candidate, we show as white contours the SNR levels in the matched-filtered map where its detection SNR is maximum (see Section 8.3.3). The contours start at ±2σ and are spaced by ±1σ. The maps have been smoothed with a 10″ gaussian kernel for display purposes.

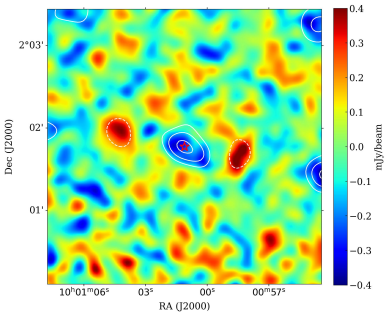

(j) NK2-CL J100101.1+020146.6

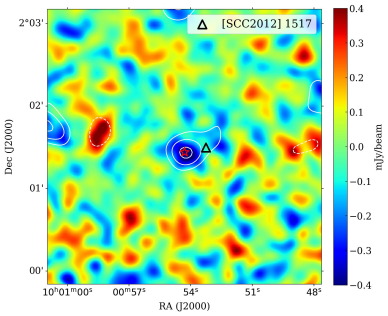

(k) NK2-CL J100054.3+020126.4 (z=1.42)

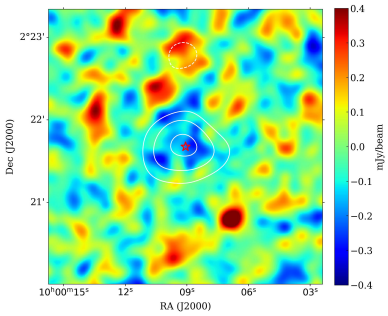

(l) NK2-CL J100009.1+022140.3

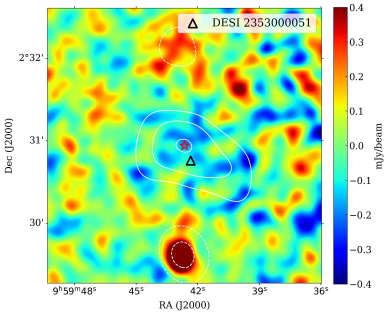

(m) NK2-CL J095942.6+023056.5(z=0.73)

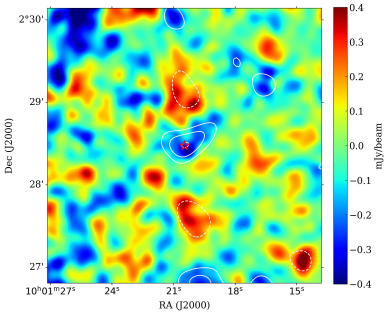

(n) NK2-CL J100120.5+022828.2

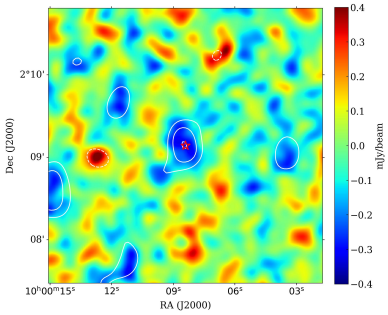

(o) NK2-CL J100008.4+020908.3

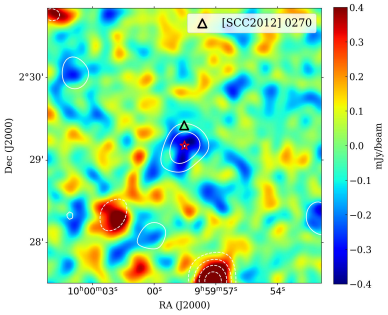

(p) NK2-CL J095958.5+022910.4 (z=0.40)

Figure 24: Continued.

Bibliography

ACTDESHSC Collaboration et al. (July 2025). "The Atacama Cosmology Telescope: DR6 Sunyaev-Zel'dovich Selected Galaxy Clusters Catalog". In: *arXiv e-prints*, arXiv:2507.21459, arXiv:2507.21459. DOI: 10.48550/arXiv.2507.21459. arXiv: 2507.21459 [astro-ph.CO].

Abazajian, Kevork et al. (July 2019). "CMB-S4 Science Case, Reference Design, and Project Plan". In: *arXiv e-prints*, arXiv:1907.04473, arXiv:1907.04473. DOI: 10.48550/arXiv.1907.04473. arXiv: 1907.04473 [astro-ph.IM].

Abbott, Mark Joseph (Jan. 1991). "A catalogue of moderately distant galaxy clusters". PhD thesis. University of Wisconsin, Madison.

Abdalla, Elcio et al. (June 2022). "Cosmology intertwined: A review of the particle physics, astrophysics, and cosmology associated with the cosmological tensions and anomalies". In: *Journal of High Energy Astrophysics* 34, pp. 49–211. DOI: 10.1016/j.jheap.2022.04.002. arXiv: 2203.06142 [astro-ph.CO].

Abdullah, Mohamed H. et al. (Jan. 2020). "GalWeight Application: A Publicly Available Catalog of Dynamical Parameters of 1800 Galaxy Clusters from SDSS-DR13, (GalWCat19)". In: *ApJS* 246.1, 2, p. 2. DOI: 10.3847/1538-4365/ab536e. arXiv: 1907.05061 [astro-ph.CO].

Abell, George O. (May 1958). "The Distribution of Rich Clusters of Galaxies." In: *ApJS* 3, p. 211. DOI: 10.1086/190036.

Abell, George O. et al. (May 1989). "A Catalog of Rich Clusters of Galaxies". In: *ApJS* 70, p. 1. DOI: 10.1086/191333.

Abitbol, M. et al. (Aug. 2025). "The Simons Observatory: science goals and forecasts for the enhanced Large Aperture Telescope". In: *J. Cosmology Astropart. Phys.* 2025.8, 034, p. 034. DOI: 10.1088/1475-7516/2025/08/034. arXiv: 2503.00636 [astro-ph.IM].

Adam, R. et al. (Sept. 2014). "First observation of the thermal Sunyaev-Zel'dovich effect with kinetic inductance detectors". In: *A&A* 569, A66, A66. DOI: 10.1051/0004-6361/201322902. arXiv: 1310.6237 [astro-ph.CO].

Adam, R. et al. (Apr. 2015). "Pressure distribution of the high-redshift cluster of galaxies CL J1226.9+3332 with NIKA". In: *A&A* 576, A12, A12. DOI: 10.1051/0004-6361/201425140. arXiv: 1410.2808 [astro-ph.CO].

Adam, R. et al. (Feb. 2016). "High angular resolution Sunyaev-Zel'dovich observations of MACS J1423.8+2404 with NIKA: Multiwavelength analysis". In: *A&A* 586, A122, A122. DOI: 10.1051/0004-6361/201527616. arXiv: 1510.06674 [astro-ph.CO].

Adam, R. et al. (Oct. 2017a). "Mapping the hot gas temperature in galaxy clusters using X-ray and Sunyaev-Zel'dovich imaging". In: *A&A* 606, A64, A64. DOI: 10.1051/0004-6361/201629810. arXiv: 1706.10230 [astro-ph.CO].

Adam, R. et al. (Feb. 2017b). "Mapping the kinetic Sunyaev-Zel'dovich effect toward MACS J0717.5+3745 with NIKA". In: *A&A* 598, A115, A115. DOI: 10.1051/0004-6361/201629182. arXiv: 1606.07721 [astro-ph.CO].

Adam, R. et al. (June 2018a). "Substructure and merger detection in resolved NIKA Sunyaev-Zel'dovich images of distant clusters". In: *A&A* 614, A118, A118. DOI: 10.1051/0004-6361/201731950. arXiv: 1712.01836 [astro-ph.CO].

Adam, R. et al. (Jan. 2018b). "The NIKA2 large-field-of-view millimetre continuum camera for the 30 m IRAM telescope". In: *A&A* 609, A115, A115. DOI: 10.1051/0004-6361/201731503. arXiv: 1707.00908 [astro-ph.IM].

Adam, R. et al. (Dec. 2020). "MINOT: Modeling the intracluster medium (non-)thermal content and observable prediction tools". In: *A&A* 644, A70, A70. DOI: 10.1051/0004-6361/202039091. arXiv: 2009.05373 [astro-ph.HE].

Adam, Rémi (Sept. 2015). "Observation des amas de galaxies par effet Sunyaev-Zel'dovich et de la polarisation du fond diffus cosmologique : de Planck à NIKA". Theses. Université Grenoble Alpes. URL: https://theses.hal.science/tel-01303736.

Adami, C. and A. Mazure (Jan. 2002). "Group analysis in the SSRS2 catalog". In: *A&A* 381, pp. 420–427. DOI: 10.1051/0004-6361:20011561. arXiv: astro-ph/0110696 [astro-ph].

Adami, C. et al. (Jan. 2010). "Galaxy structure searches by photometric redshifts in the CFHTLS". In: *A&A* 509, A81, A81. DOI: 10.1051/0004-6361/200913067. arXiv: 0910.3827 [astro-ph.CO].

Adami, C. et al. (Nov. 2018). "The XXL Survey. XX. The 365 cluster catalogue". In: *A&A* 620, A5, A5. DOI: 10.1051/0004-6361/201731606. arXiv: 1810.03849 [astro-ph.CO].

Ade, Peter et al. (Feb. 2019). "The Simons Observatory: science goals and forecasts". In: *J. Cosmology Astropart. Phys.* 2019.2, 056, p. 056. DOI: 10.1088/1475-7516/2019/02/056. arXiv: 1808.07445 [astro-ph.CO].

Aguado-Barahona, A. et al. (Mar. 2022). "Velocity dispersion and dynamical masses for 388 galaxy clusters and groups. Calibrating the $M_{SZ} - M_{dyn}$ scaling relation for the PSZ2 sample". In: *A&A* 659, A126, A126. DOI: 10.1051/0004-6361/202039980. arXiv: 2111.13071 [astro-ph.CO].

Aguena, M. et al. (Apr. 2021). "The WaZP galaxy cluster sample of the dark energy survey year 1". In: *MNRAS* 502.3, pp. 4435–4456. DOI: 10.1093/mnras/stab264. arXiv: 2008.08711 [astro-ph.CO].

Aihara, Hiroaki et al. (Apr. 2011). "The Eighth Data Release of the Sloan Digital Sky Survey: First Data from SDSS-III". In: *ApJS* 193.2, 29, p. 29. DOI: 10.1088/0067-0049/193/2/29. arXiv: 1101.1559 [astro-ph.IM].

Aihara, Hiroaki et al. (Jan. 2018a). "First data release of the Hyper Suprime-Cam Subaru Strategic Program". In: *PASJ* 70, S8, S8. DOI: 10.1093/pasj/psx081. arXiv: 1702.08449 [astro-ph.IM].

Aihara, Hiroaki et al. (Jan. 2018b). "The Hyper Suprime-Cam SSP Survey: Overview and survey design". In: *PASJ* 70, S4, S4. DOI: 10.1093/pasj/psx066. arXiv: 1704.05858 [astro-ph.IM].

Akabane, K. (Sept. 1983). "A large millimeter wave antenna". In: *International Journal of Infrared and Millimeter Waves* 4.5, pp. 793–808. DOI: 10.1007/BF01009698.

Albert, C. E. et al. (Jan. 1977). "cD galaxies in poor clusters. II." In: *ApJ* 211, pp. 309–310. DOI: 10.1086/154935.

Allam, S. S. and D. L. Tucker (Jan. 2000). "Compact Groups of Galaxies in the Las Campanas Redshift Survey". In: *Astronomische Nachrichten* 321.2, pp. 101–114. DOI: 10.1002/(SICI)1521-3994(200005)321:2<101::AID-ASNA101>3.0.CO;2-5. arXiv: astro-ph/0006155 [astro-ph].

Allen, S. W. et al. (Sept. 2011). "Cosmological Parameters from Observations of Galaxy Clusters". In: *ARA&A* 49, pp. 409–470. DOI: 10.1146/annurev-astro-081710-102514.

Amon, Alexandra and George Efstathiou (Nov. 2022). "A non-linear solution to the S_8 tension?" In: *MNRAS* 516.4, pp. 5355–5366. DOI: 10.1093/mnras/stac2429. arXiv: 2206.11794 [astro-ph.CO].

Andreon, S. et al. (June 2005). "Batch discovery of nine z~1 clusters using X-ray and K or R, z' images". In: *MNRAS* 359.4, pp. 1250–1260. DOI: 10.1111/j.1365-2966.2005.08998.x. arXiv: astro-ph/0503236 [astro-ph].

Annis, J. et al. (Dec. 1999). "The maxBCG technique for finding galaxy clusters in SDSS data". In: *American Astronomical Society Meeting Abstracts*. Vol. 195. American Astronomical Society Meeting Abstracts, 12.02, p. 12.02.

Ansarinejad, Behzad et al. (Mar. 2023). "VST ATLAS galaxy cluster catalogue I: cluster detection and mass calibration". In: *MNRAS* 520.1, pp. 1371–1389. DOI: 10.1093/mnras/stac3815. arXiv: 2207.03725 [astro-ph.CO].

Appenzeller, I. et al. (July 1998). "Identification of a Complete Sample of Northern ROSAT All-Sky Survey X-Ray Sources. III. The Catalog". In: *ApJS* 117.2, pp. 319–340. DOI: 10.1086/313125.

Applegate, Douglas E. et al. (Mar. 2014). "Weighing the Giants - III. Methods and measurements of accurate galaxy cluster weak-lensing masses". In: *MNRAS* 439.1, pp. 48–72. DOI: 10.1093/mnras/stt2129. arXiv: 1208.0605 [astro-ph.CO].

Archipley, M. et al. (May 2025). "Millimeter-wave observations of Euclid Deep Field South using the South Pole Telescope: A data release of temperature maps and catalogs". In: *arXiv e-prints*, arXiv:2506.00298, arXiv:2506.00298. DOI: 10.48550/arXiv.2506.00298. arXiv: 2506.00298 [astro-ph.GA].

Aretxaga, I. et al. (Aug. 2011). "AzTEC millimetre survey of the COSMOS field - III. Source catalogue over 0.72 deg^2 and plausible boosting by large-scale structure". In: *MNRAS* 415.4, pp. 3831–3850. DOI: 10.1111/j.1365-2966.2011.18989.x. arXiv: 1105.0890 [astro-ph.CO].

Arnaud, M. et al. (July 2010). "The universal galaxy cluster pressure profile from a representative sample of nearby systems (REXCESS) and the Y_{SZ} - M_{500} relation". In: *A&A* 517, A92, A92. DOI: 10.1051/0004-6361/200913416. arXiv: 0910.1234 [astro-ph.CO].

Artis, E. et al. (in prep.). "NIKA2 LPSZ: High resolution study of the complex massive and high redshift cluster PSZ2G091.83+26.11". In.

Artis, E. et al. (July 2022). "PSZ2 G091: A massive double cluster at z 0.822 observed by the NIKA2 camera". In: *mm Universe @ NIKA2 - Observing the mm Universe with the NIKA2 Camera*. Vol. 257. European Physical Journal Web of Conferences, 00003, p. 00003. DOI: 10.1051/epjconf/202225700003. arXiv: 2111.05082 [astro-ph.CO].

Ascaso, B. et al. (Sept. 2015). "Galaxy clusters and groups in the ALHAMBRA survey". In: *MNRAS* 452.1, pp. 549–565. DOI: 10.1093/\mnras/stv1317. arXiv: 1506.03823 [astro-ph.CO].

Aschenbach, Bernd (Apr. 1988). "Design, construction, and performance of the ROSAT high- resolution x-ray mirror assembly". In: *Appl. Opt.* 27.8, pp. 1404–1413. DOI: 10.1364/AO.27.001404.

Baars, J. W. M. et al. (Mar. 1987). "The IRAM 30-m millimeter radio telescope on Pico Veleta, Spain". In: *A&A* 175.1-2, pp. 319–326.

Bahcall, Neta A. et al. (Oct. 2003). "A Merged Catalog of Clusters of Galaxies from Early Sloan Digital Sky Survey Data". In: *ApJS* 148.2, pp. 243–274. DOI: 10.1086/377167. arXiv: astro-ph/0305202 [astro-ph].

Bahk, Hyeonguk and Ho Seong Hwang (May 2024). "UPCluster-SZ: The Updated Catalog of Galaxy Clusters from the List of Planck Sunyaev–Zel'dovich Sources". In: *ApJS* 272.1, 7, p. 7. DOI: 10.3847/1538-4365/ad323f. arXiv: 2403.03818 [astro-ph.CO].

Balogh, Michael L. et al. (Sept. 2014). "The GEEC2 spectroscopic survey of Galaxy groups at 0.8 < z < 1". In: *Monthly Notices of the Royal Astronomical Society* 443. Publisher: OUP ADS Bibcode: 2014MNRAS.443.2679B, pp. 2679–2694. ISSN: 0035-8711. DOI: 10.1093/mnras/stu1332. URL: https://ui.adsabs.harvard.edu/abs/2014MNRAS.443.2679B.

Balogh, Michael L. et al. (Jan. 2021). "The GOGREEN and GCLASS surveys: first data release". In: *MNRAS* 500.1, pp. 358–387. DOI: 10.1093/mnras/staa3008. arXiv: 2009.13345 [astro-ph.GA].

Balogh, Michael et al. (Mar. 2004). "Galaxy ecology: groups and low-density environments in the SDSS and 2dFGRS". In: *MNRAS* 348.4, pp. 1355–1372. DOI: 10.1111/j.1365-2966.2004.07453.x. arXiv: astro-ph/0311379 [astro-ph].

Banerjee, P. et al. (Jan. 2018). "An optical catalog of galaxy clusters obtained from an adaptive matched filter finder applied to SDSS DR9 data". In: *New A* 58, pp. 61–71. DOI: 10.1016/j.newast.2017.07.008. arXiv: 1704.03529 [astro-ph.CO].

Barger, A. J. et al. (July 1998). "Submillimetre-wavelength detection of dusty star-forming galaxies at high redshift". In: *Nature* 394.6690, pp. 248–251. DOI: 10.1038/28338. arXiv: astro-ph/9806317 [astro-ph].

Barkhouse, W. A. et al. (July 2006). "ChaMP Serendipitous Galaxy Cluster Survey". In: *ApJ* 645.2, pp. 955–976. DOI: 10.1086/504457. arXiv: astro-ph/0603521 [astro-ph].

Barton, Elizabeth et al. (Sept. 1996). "Compact Group selection From Redshift Surveys". In: *AJ* 112, p. 871. DOI: 10.1086/118060. arXiv: astro-ph/9608091 [astro-ph].

Becker, Robert H. et al. (Sept. 1995). "The FIRST Survey: Faint Images of the Radio Sky at Twenty Centimeters". In: *ApJ* 450, p. 559. DOI: 10.1086/176166.

Bellagamba, F. et al. (May 2011). "Optimal filtering of optical and weak lensing data to search for galaxy clusters: application to the COSMOS field". In: *MNRAS* 413.2, pp. 1145–1157. DOI: 10.1111/j.1365-2966.2011.18202.x. arXiv: 1006.0610 [astro-ph.CO].

Bellagamba, Fabio et al. (Feb. 2018). "AMICO: optimized detection of galaxy clusters in photometric surveys". In: *MNRAS* 473.4, pp. 5221–5236. DOI: 10.1093/mnras/stx2701. arXiv: 1705.03029 [astro-ph.CO].

Benitez, N. et al. (Mar. 2014). "J-PAS: The Javalambre-Physics of the Accelerated Universe Astrophysical Survey". In: *arXiv e-prints*, arXiv:1403.5237, arXiv:1403.5237. DOI: 10.48550/arXiv.1403.5237. arXiv: 1403.5237 [astro-ph.CO].

Bennett, C. L. et al. (Sept. 2003). "First-Year Wilkinson Microwave Anisotropy Probe (WMAP) Observations: Preliminary Maps and Basic Results". In: *ApJS* 148.1, pp. 1–27. DOI: 10.1086/377253. arXiv: astro-ph/0302207 [astro-ph].

Bergé, Joel et al. (Apr. 2008). "Combined analysis of weak lensing and X-ray blind surveys". In: *MNRAS* 385.2, pp. 695–707. DOI: 10.1111/j.1365-2966.2008.12902.x. arXiv: 0712.3293 [astro-ph].

Berlind, Andreas A. et al. (Nov. 2006). "Percolation Galaxy Groups and Clusters in the SDSS Redshift Survey: Identification, Catalogs, and the Multiplicity Function". In: *ApJS* 167.1, pp. 1–25. DOI: 10.1086/508170. arXiv: astro-ph/0601346 [astro-ph].

Bersanelli, M. et al. (1996). *COBRAS/SAMBA. A mission dedicated to imaging the anisotropies of the cosmic microwave background. Report on the phase A study.*

Berta, S. et al. (Apr. 2025). "A panchromatic view of N2CLS GOODS-N: The evolution of the dust cosmic density since z 7". In: *Astronomy and Astrophysics* 696. Publisher: EDP ADS Bibcode: 2025A&A...696A.193B, A193. ISSN: 0004-6361. DOI: 10.1051/0004-6361/202452894. URL: https://ui.adsabs.harvard.edu/abs/2025A&A...696A.193B.

Bertoldi, F. et al. (Sept. 2007). "COSBO: The MAMBO 1.2 Millimeter Imaging Survey of the COSMOS Field". In: *ApJS* 172.1, pp. 132–149. DOI: 10.1086/520511.

Béthermin, M. et al. (Nov. 2022). "CONCERTO: High-fidelity simulation of millimeter line emissions of galaxies and [CII] intensity mapping". In: *A&A* 667, A156, A156. DOI: 10.1051/0004-6361/202243888. arXiv: 2204.12827 [astro-ph.GA].

Béthermin, M. et al. (2025). "2mm map". In: *in prep.*

Béthermin, Matthieu et al. (Nov. 2017). "The impact of clustering and angular resolution on far-infrared and millimeter continuum observations". In: *A&A* 607, A89, A89. DOI: 10.1051/0004-6361/201730866. arXiv: 1703.08795 [astro-ph.GA].

Bing, L. J. et al. (Mar. 2024). "Faint mm NIKA2 dusty star-forming galaxies: Finding the high-redshift population". In: *A&A* 683, A232, A232. DOI: 10.1051/0004-6361/202243887. arXiv: 2403.00911 [astro-ph.GA].

Bing, L. et al. (Sept. 2023). "NIKA2 Cosmological Legacy Survey. Survey description and galaxy number counts". In: *A&A* 677, A66, A66. DOI: 10.1051/0004-6361/202346579. arXiv: 2305.07054 [astro-ph.GA].

Birkinshaw, M. (Mar. 1999). "The Sunyaev-Zel'dovich effect". In: *Phys. Rep.* 310.2-3, pp. 97–195. DOI: 10.1016/S0370-1573(98)00080-5. arXiv: astro-ph/9808050 [astro-ph].

Birkinshaw, M. et al. (May 1984). "The Sunyaev-Zeldovich effect towards three clusters of galaxies." In: *Nature* 309, pp. 34–35. DOI: 10.1038/309034a0.

Biviano, Andrea (Jan. 2000). "From Messier to Abell: 200 Years of Science with Galaxy Clusters". In: *Constructing the Universe with Clusters of Galaxies*. Ed. by Florence Durret and Daniel Gerbal, 1, p. 1. DOI: 10.48550/arXiv.astro-ph/0010409. arXiv: astro-ph/0010409 [astro-ph].

Blackburne, Jeffrey A. and Christopher S. Kochanek (Jan. 2012). "The Structure of 2MASS Galaxy Clusters". In: *ApJ* 744.1, 76, p. 76. DOI: 10.1088/0004-637X/744/1/76. arXiv: 1105.3944 [astro-ph.CO].

Bleem, L. E. et al. (Jan. 2015a). "A New Reduction of the Blanco Cosmology Survey: An Optically Selected Galaxy Cluster Catalog and a Public Release of Optical Data Products". In: *ApJS* 216.1, 20, p. 20. DOI: 10.1088/0067-0049/216/1/20. arXiv: 1403.7186 [astro-ph.GA].

Bleem, L. E. et al. (Feb. 2015b). "Galaxy Clusters Discovered via the Sunyaev-Zel'dovich Effect in the 2500-Square-Degree SPT-SZ Survey". In: *ApJS* 216.2, 27, p. 27. DOI: 10.1088/0067-0049/216/2/27. arXiv: 1409.0850 [astro-ph.CO].

Bleem, L. E. et al. (Mar. 2020). "The SPTpol Extended Cluster Survey". In: *ApJS* 247.1, 25, p. 25. DOI: 10.3847/1538-4365/ab6993. arXiv: 1910.04121 [astro-ph.CO].

Bleem, L. E. et al. (Feb. 2024). "Galaxy Clusters Discovered via the Thermal Sunyaev-Zel'dovich Effect in the 500-square-degree SPTpol Survey". In: *The Open Journal of Astrophysics* 7, 13, p. 13. DOI: 10.21105/astro.2311.07512. arXiv: 2311.07512 [astro-ph.CO].

Bocquet, Sebastian et al. (Mar. 2016). "Halo mass function: baryon impact, fitting formulae, and implications for cluster cosmology". In: *MNRAS* 456.3, pp. 2361–2373. DOI: 10.1093/mnras/stv2657. arXiv: 1502.07357 [astro-ph.CO].

Böhringer, H. et al. (Jan. 2000a). "Searching for X-Ray Galaxy Clusters in the Zone of Avoidance". In: *Mapping the Hidden Universe: The Universe behind the Mily Way - The Universe in HI*. Ed. by Renée C. Kraan-Korteweg et al. Vol. 218. Astronomical Society of the Pacific Conference Series, p. 93. DOI: 10.48550/arXiv.astro-ph/0011461. arXiv: astro-ph/0011461 [astro-ph].

Böhringer, H. et al. (Aug. 2000b). "The Northern ROSAT All-Sky (NORAS) Galaxy Cluster Survey. I. X-Ray Properties of Clusters Detected as Extended X-Ray Sources". In: *ApJS* 129.2, pp. 435–474. DOI: 10.1086/313427. arXiv: astro-ph/0003219 [astro-ph].

Böhringer, H. et al. (Oct. 2004). "The ROSAT-ESO Flux Limited X-ray (REFLEX) Galaxy cluster survey. V. The cluster catalogue". In: *A&A* 425, pp. 367–383. DOI: 10.1051/0004-6361:20034484. arXiv: astro-ph/0405546 [astro-ph].

Böhringer, H. et al. (July 2013). "The extended ROSAT-ESO flux limited X-ray galaxy cluster survey (REFLEX II) II. Construction and properties of the survey". In: *A&A* 555, A30, A30. DOI: 10.1051/0004-6361/201220722. arXiv: 1403.5886 [astro-ph.CO].

Böhringer, Hans and Norbert Werner (Feb. 2010). "X-ray spectroscopy of galaxy clusters: studying astrophysical processes in the largest celestial laboratories". In: *A&A Rev.* 18.1-2, pp. 127–196. DOI: 10.1007/s00159-009-0023-3.

Böhringer, Hans et al. (May 2017). "The Extended Northern ROSAT Galaxy Cluster Survey (NORAS II). I. Survey Construction and First Results". In: *AJ* 153.5, 220, p. 220. DOI: 10.3847/1538-3881/aa67ed. arXiv: 1704.06489 [astro-ph.CO].

Bond, J. R. et al. (Oct. 1991). "Excursion Set Mass Functions for Hierarchical Gaussian Fluctuations". In: *ApJ* 379, p. 440. DOI: 10.1086/170520.

Boschin, W. (Dec. 2002). "A deep cluster survey in Chandra archival data. First results". In: *A&A* 396, pp. 397–409. DOI: 10.1051/0004-6361:20021393. arXiv: astro-ph/0304324 [astro-ph].

Bounmy, Julien et al. (Aug. 2022). "CONCERTO: Digital processing for finding and tuning LEKIDs". In: *Journal of Instrumentation* 17. Publisher: IOP ADS Bibcode: 2022JInst..17P8037B, P08037. DOI: 10.1088/1748-0221/17/08/P08037. URL: https://ui.adsabs.harvard.edu/abs/2022JInst..17P8037B.

Bourrion, O. et al. (June 2011). "Electronics and data acquisition demonstrator for a kinetic inductance camera". In: *Journal of Instrumentation* 6. Publisher: IOP ADS Bibcode: 2011JInst...6.6012B, p. 6012. DOI: 10.1088/1748-0221/6/06/P06012. URL: https://ui.adsabs.harvard.edu/abs/2011JInst...6.6012B.

Bourrion, O. et al. (July 2012). "NIKEL: Electronics and data acquisition for kilopixels kinetic inductance camera". In: *Journal of Instrumentation* 7. Publisher: IOP ADS Bibcode: 2012JInst...7.7014B, p. 7014. DOI: 10.1088/1748-0221/7/07/P07014. URL: https://ui.adsabs.harvard.edu/abs/2012JInst...7.7014B.

Bourrion, O. et al. (Dec. 2013). "High speed readout electronics development for frequency-multiplexed kinetic inductance detector design optimization". In: *Journal of Instrumentation* 8. Publisher: IOP ADS Bibcode:

2013JInst...8C2006B, p. C12006. DOI: 10.1088/1748-0221/8/12/C12006. URL: https://ui.adsabs.harvard.edu/abs/2013JInst...8C2006B.

Bourrion, O. et al. (Nov. 2016). "NIKEL_AMC: readout electronics for the NIKA2 experiment". In: *Journal of Instrumentation* 11. 19 pages; 15 figures. arXiv admin note: text overlap with arXiv:1204.1415, P11001. DOI: 10.1088/1748-0221/11/11/P11001. URL: https://hal.in2p3.fr/in2p3-01267141.

Bourrion, O. et al. (Oct. 2022). "CONCERTO: readout and control electronics". In: *Journal of Instrumentation* 17. Publisher: IOP ADS Bibcode: 2022JInst..17P0047B, P10047. DOI: 10.1088/1748-0221/17/10/P10047. URL: https://ui.adsabs.harvard.edu/abs/2022JInst..17P0047B.

Bradley, Larry et al. (May 2023). *astropy/photutils: 1.8.0*. Version 1.8.0. DOI: 10.5281/zenodo.7946442. URL: https://doi.org/10.5281/zenodo.7946442.

Braid, M. K. and H. T. MacGillivray (Jan. 1978). "A finding list of southern clusters of galaxies - I." In: *MNRAS* 182, pp. 241–248. DOI: 10.1093/mnras/182.2.241.

Bramel, D. A. et al. (Apr. 2000). "The Local Space Density of Optically Selected Clusters of Galaxies". In: *ApJ* 533.2, pp. 601–610. DOI: 10.1086/308713. arXiv: astro-ph/9912275 [astro-ph].

Brinch, Malte et al. (Feb. 2023). "COSMOS2020: Identification of High-z Protocluster Candidates in COSMOS". In: *ApJ* 943.2, 153, p. 153. DOI: 10.3847/1538-4357/ac9d96. arXiv: 2210.17334 [astro-ph.GA].

Bulbul, E. et al. (May 2024). "The SRG/eROSITA All-Sky Survey. The first catalog of galaxy clusters and groups in the Western Galactic Hemisphere". In: *A&A* 685, A106, A106. DOI: 10.1051/0004-6361/202348264. arXiv: 2402.08452 [astro-ph.CO].

Burenin, R. A. (Aug. 2017). "An extension of the Planck galaxy cluster catalogue". In: *Astronomy Letters* 43.8, pp. 507–515. DOI: 10.1134/S1063773717080035. arXiv: 1703.05597 [astro-ph.CO].

Burenin, R. A. et al. (Oct. 2007). "The 400 Square Degree ROSAT PSPC Galaxy Cluster Survey: Catalog and Statistical Calibration". In: *ApJS* 172.2, pp. 561–582. DOI: 10.1086/519457. arXiv: astro-ph/0610739 [astro-ph].

Burke, D. J. et al. (Oct. 1997). "The Southern SHARC Survey: the Z = 0.3–0.7 Cluster X-Ray Luminosity Function 1". In: *ApJ* 488.2, pp. L83–L86. DOI: 10.1086/310943.

Burke, D. J. et al. (June 2003). "The Southern SHARC catalogue: a ROSAT survey for distant galaxy clusters". In: *MNRAS* 341.4, pp. 1093–1108. DOI: 10.1046/j.1365-8711.2003.06378.x.

Byram, E. T. et al. (Apr. 1966). "Cosmic X-ray Sources, Galactic and Extragalactic". In: *Science* 152.3718, pp. 66–71. DOI: 10.1126/science.152.3718.66.

CONCERTO Collaboration et al. (Oct. 2020). "A wide field-of-view low-resolution spectrometer at APEX: Instrument design and scientific forecast". In: *A&A* 642, A60, A60. DOI: 10.1051/0004-6361/202038456. arXiv: 2007.14246 [astro-ph.IM].

Calvo, M. et al. (Aug. 2016a). "The NIKA2 Instrument, A Dual-Band Kilopixel KID Array for Millimetric Astronomy". In: *Journal of Low Temperature Physics* 184.3-4, pp. 816–823. DOI: 10.1007/s10909-016-1582-0. arXiv: 1601.02774 [astro-ph.IM].

Calvo, M. et al. (Jan. 2016b). "The NIKA2 instrument, a dual-band kilopixel KID array for millimetric astronomy". In: *arXiv e-prints*, arXiv:1601.02774, arXiv:1601.02774. DOI: 10.48550/arXiv.1601.02774. arXiv: 1601.02774 [astro-ph.IM].

Campana, Sergio et al. (Oct. 1999). "The Brera Multiscale Wavelet ROSAT HRI Source Catalog. II. Application to the HRI and First Results". In: *ApJ* 524.1, pp. 423–433. DOI: 10.1086/307789. arXiv: astro-ph/9904375 [astro-ph].

Campusano, Luis E. et al. (Dec. 2018). "A 3D Voronoi+Gapper Galaxy Cluster Finder in Redshift Space to z ∼ 0.2. II. An Abundant Cluster Population Dominated by Late-type Galaxies Unveiled". In: *ApJ* 869.2, 145, p. 145. DOI: 10.3847/1538-4357/aaeff3.

Caretta, César A. et al. (Mar. 2002). "The Aquarius Superclusters. I. Identification of Clusters and Superclusters". In: *AJ* 123.3, pp. 1200–1215. DOI: 10.1086/338894. arXiv: astro-ph/0111541 [astro-ph].

Carlberg, R. G. et al. (May 2001). "Galaxy Groups at Intermediate Redshift". In: *ApJ* 552.2, pp. 427–444. DOI: 10.1086/320555. arXiv: astro-ph/0008201 [astro-ph].

Carlstrom, J. E. et al. (May 2011). "The 10 Meter South Pole Telescope". In: *PASP* 123.903, p. 568. DOI: 10.1086/659879. arXiv: 0907.4445 [astro-ph.IM].

Carlstrom, John E. et al. (Jan. 2002). "Cosmology with the Sunyaev-Zel'dovich Effect". In: *ARA&A* 40, pp. 643–680. DOI: 10.1146/annurev.astro.40.060401.093803. arXiv: astro-ph/0208192 [astro-ph].

Carvajal-Bohorquez, C. et al. (in prep.). "" In.

Cassano, R. et al. (Nov. 2013). "Revisiting Scaling Relations for Giant Radio Halos in Galaxy Clusters". In: *ApJ* 777.2, 141, p. 141. DOI: 10.1088/0004-637X/777/2/141. arXiv: 1306.4379 [astro-ph.CO].

Castander, Francisco J. et al. (Sept. 1995). "Deficit of distant X-ray-emitting galaxy clusters and implications for cluster evolution". In: *Nature* 377.6544, pp. 39–41. DOI: 10.1038/377039a0.

Castignani, G. et al. (Sept. 2014). "Cluster Candidates around Low-power Radio Galaxies at z ~1-2 in COSMOS". In: *ApJ* 792.2, 114, p. 114. DOI: 10.1088/0004-637X/792/2/114. arXiv: 1406.5255 [astro-ph.GA].

Catalano, A. et al. (Sept. 2014a). "Performance and calibration of the NIKA camera at the IRAM 30 m telescope". In: *A&A* 569, A9, A9. DOI: 10.1051/0004-6361/201423557. arXiv: 1402.0260 [astro-ph.IM].

— (Sept. 2014b). "Performance and calibration of the NIKA camera at the IRAM 30 m telescope". In: *A&A* 569, A9, A9. DOI: 10.1051/0004-6361/201423557. arXiv: 1402.0260 [astro-ph.IM].

Cavaliere, A. and R. Fusco-Femiano (May 1976). "X-rays from hot plasma in clusters of galaxies." In: *A&A* 49, pp. 137–144.

Challinor, Anthony and Anthony Lasenby (May 1998). "Relativistic Corrections to the Sunyaev-Zeldovich Effect". In: *ApJ* 499.1, pp. 1–6. DOI: 10.1086/305623. arXiv: astro-ph/9711161 [astro-ph].

Chamberlin, Richard A. and John Bally (May 1995). "The observed relationship between the south pole 225-GHz atmospheric opacity and the water vapor column density". In: *International Journal of Infrared and Millimeter Waves* 16.5, pp. 907–920. DOI: 10.1007/BF02066665.

Chérouvrier, D. et al. (June 2025). "NIKA2 Cosmological Legacy Survey: Blind detection of galaxy clusters in the COSMOS field via the Sunyaev-Zel'dovich effect". In: *arXiv e-prints*, arXiv:2506.18231, arXiv:2506.18231. DOI: 10.48550/arXiv.2506.18231. arXiv: 2506.18231 [astro-ph.CO].

Chu, A. et al. (May 2021). "Physical properties of brightest cluster galaxies up to redshift 1.80 based on HST data". In: *A&A* 649, A42, A42. DOI: 10.1051/0004-6361/202040245. arXiv: 2102.01557 [astro-ph.GA].

Civano, F. et al. (Mar. 2016). "The Chandra Cosmos Legacy Survey: Overview and Point Source Catalog". In: *ApJ* 819.1, 62, p. 62. DOI: 10.3847/0004-637X/819/1/62. arXiv: 1601.00941 [astro-ph.GA].

Clerc, N. et al. (Nov. 2014). "The XMM-LSS survey: the Class 1 cluster sample over the extended 11 deg^2 and its spatial distribution". In: *MNRAS* 444.3, pp. 2723–2753. DOI: 10.1093/mnras/stu1625. arXiv: 1408.6325 [astro-ph.CO].

Clerc, Nicolas and Alexis Finoguenov (2023). "X-Ray Cluster Cosmology". In: *Handbook of X-ray and Gamma-ray Astrophysics*, 123, p. 123. DOI: 10.1007/978-981-16-4544-0_117-1.

Clewley, L. et al. (Dec. 2007). "Detecting Galaxy Clusters at 0.1 ¡ z ¡ 2.0". In: *Deepest Astronomical Surveys*. Ed. by J. Afonso et al. Vol. 380. Astronomical Society of the Pacific Conference Series, p. 499. DOI: 10.48550/arXiv.astro-ph/0612118. arXiv: astro-ph/0612118 [astro-ph].

Collins, C. A. et al. (Apr. 1997). "On the Evolution of X-Ray Clusters at High Redshift". In: *ApJ* 479.2, pp. L117–L120. DOI: 10.1086/310593. arXiv: astro-ph/9701143 [astro-ph].

Condon, J. J. et al. (May 1998). "The NRAO VLA Sky Survey". In: *AJ* 115.5, pp. 1693–1716. DOI: 10.1086/300337.

Cooke, B. A. et al. (Feb. 1978). "The Ariel V (SSI) catalogue of high galactic latitude ". In: *MNRAS* 182, pp. 489–515. DOI: 10.1093/mnras/182.3.489.

Couch, J. J. et al. (Apr. 1991). "A uniformly selected catalogue of distant galaxy clusters." In: *MNRAS* 249, p. 606. DOI: 10.1093/mnras/249.4.606.

Cowie, L. L. et al. (May 2002). "Faint Submillimeter Counts from Deep 850 Micron Observations of the Lensing Clusters A370, A851, and A2390". In: *AJ* 123.5, pp. 2197–2205. DOI: 10.1086/339978. arXiv: astro-ph/0201426 [astro-ph].

Cowie, L. L. et al. (Mar. 2017). "A Submillimeter Perspective on the GOODS Fields (SUPER GOODS). I. An Ultradeep SCUBA-2 Survey of the GOODS-N". In: *ApJ* 837.2, 139, p. 139. DOI: 10.3847/1538-4357/aa60bb. arXiv: 1702.03002 [astro-ph.GA].

Crook, Aidan C. et al. (Feb. 2007). "Groups of Galaxies in the Two Micron All Sky Redshift Survey". In: *ApJ* 655.2, pp. 790–813. DOI: 10.1086/510201. arXiv: astro-ph/0610732 [astro-ph].

Cruddace, R. et al. (June 2002). "The ROSAT All-Sky Survey: a Catalog of Clusters of Galaxies in a Region of 1 steradian around the South Galactic Pole". In: *ApJS* 140.2, pp. 239–264. DOI: 10.1086/324519. arXiv: astro-ph/0201069 [astro-ph].

Cruise, Mike et al. (Jan. 2025). "The NewAthena mission concept in the context of the next decade of X-ray astronomy". In: *Nature Astronomy* 9, pp. 36–44. DOI: 10.1038/s41550-024-02416-3. arXiv: 2501.03100 [astro-ph.IM].

Cucciati, O. et al. (Sept. 2010). "The VIMOS-VLT deep survey: the group catalogue". In: *A&A* 520, A42, A42. DOI: 10.1051/0004-6361/200911831. arXiv: 0911.3740 [astro-ph.CO].

Cuciti, V. et al. (Mar. 2021). "Radio halos in a mass-selected sample of 75 galaxy clusters. I. Sample selection and data analysis". In: *A&A* 647, A50, A50. DOI: 10.1051/0004-6361/202039206. arXiv: 2101.01640 [astro-ph.CO].

Cui, Weiguang et al. (Nov. 2008). "An Ideal Mass Assignment Scheme for Measuring the Power Spectrum with Fast Fourier Transforms". In: *ApJ* 687.2, pp. 738–744. DOI: 10.1086/592079. arXiv: 0804.0070 [astro-ph].

Cui, Weiguang et al. (Nov. 2018). "The Three Hundred project: a large catalogue of theoretically modelled galaxy clusters for cosmological and astrophysical applications". In: *MNRAS* 480.3, pp. 2898–2915. DOI: 10.1093/mnras/sty2111. arXiv: 1809.04622 [astro-ph.GA].

Curtis, Heber D. (Oct. 1917). "Novae in the Spiral Nebulae and the Island Universe Theory". In: *PASP* 29.171, pp. 206–207. DOI: 10.1086/122632.

DESI Collaboration et al. (Mar. 2025). "DESI DR2 Results II: Measurements of Baryon Acoustic Oscillations and Cosmological Constraints". In: *arXiv e-prints*, arXiv:2503.14738, arXiv:2503.14738. DOI: 10.48550/arXiv.2503.14738. arXiv: 2503.14738 [astro-ph.CO].

Dai, Xinyu et al. (May 2015). "The SWIFT AGN and Cluster Survey. I. Number Counts of AGNs and Galaxy Clusters". In: *ApJS* 218.1, 8, p. 8. DOI: 10.1088/0067-0049/218/1/8. arXiv: 1503.03489 [astro-ph.CO].

Dalton, G. B. et al. (Aug. 1997). "The APM Galaxy Survey - V. Catalogues of galaxy clusters". In: *MNRAS* 289.2, pp. 263–284. DOI: 10.1093/mnras/289.2.263. arXiv: astro-ph/9701180 [astro-ph].

Day, Peter K. et al. (Oct. 2003). "A broadband superconducting detector suitable for use in large arrays". en. In: *Nature* 425.6960. Publisher: Nature Publishing Group, pp. 817–821. ISSN: 1476-4687. DOI: 10.1038/nature02037. URL: https://www.nature.com/articles/nature02037.

De Grandi, S. et al. (Mar. 1999). "A Flux-limited Sample of Bright Clusters of Galaxies from the Southern Part of the ROSAT All-Sky Survey: The Catalog and LOG N-LOG S". In: *ApJ* 514.1, pp. 148–163. DOI: 10.1086/306939. arXiv: astro-ph/9902067 [astro-ph].

Dekel, Avishai et al. (Mar. 1989). "Projection Contamination in Cluster Catalogs: Are the Abell Redshift Sample Correlations Significant?" In: *ApJ* 338, p. L5. DOI: 10.1086/185387.

Deng, Xin-Fa et al. (Nov. 2007). "The main galaxy groups from the SDSS data release 5". In: *A&A* 474.3, pp. 783–791. DOI: 10.1051/0004-6361:20066407.

Dey, Arjun et al. (May 2019). "Overview of the DESI Legacy Imaging Surveys". In: *AJ* 157.5, 168, p. 168. DOI: 10.3847/1538-3881/ab089d. arXiv: 1804.08657 [astro-ph.IM].

Díaz-Giménez, Eugenia et al. (Oct. 2012). "Compact groups of galaxies selected by stellar mass: the 2MASS compact group catalogue". In: *MNRAS* 426.1, pp. 296–316. DOI: 10.1111/j.1365-2966.2012.21705.x. arXiv: 1207.2196 [astro-ph.CO].

Díaz-Giménez, Eugenia et al. (Oct. 2018). "Improving Hickson-like compact group finders in redshift surveys: an implementation in the SDSS". In: *A&A* 618, A157, A157. DOI: 10.1051/0004-6361/201833329. arXiv: 1808.10051 [astro-ph.GA].

Dietrich, J. P. et al. (Aug. 2007). "BLOX: the Bonn lensing, optical, and X-ray selected galaxy clusters. I. Cluster catalog construction". In: *A&A* 470.3, pp. 821–834. DOI: 10.1051/0004-6361:20077281. arXiv: 0705.3455 [astro-ph].

Doeleman, Sheperd S et al. (Oct. 2019). *Mid-scale RI-1 (M1:DP): Next Generation Event Horizon Telescope Design*. NSF Award Number 1935980. Directorate for Mathematical and Physical Sciences, Division Of Astronomical Sciences. 2019.

Donahue, Megan et al. (Apr. 2002). "Distant Cluster Hunting. II. A Comparison of X-Ray and Optical Cluster Detection Techniques and Catalogs from the ROSAT Optical X-Ray Survey". In: *ApJ* 569.2, pp. 689–719. DOI: 10.1086/339401. arXiv: astro-ph/0112529 [astro-ph].

Doubrawa, L. et al. (May 2024). "The miniJPAS survey. Optical detection of galaxy clusters with PZWav". In: *A&A* 685, A98, A98. DOI: 10.1051/0004-6361/202349019. arXiv: 2312.12197 [astro-ph.CO].

Douspis, Marian et al. (Mar. 2022). "Retrieving cosmological information from small-scale CMB foregrounds. I. The thermal Sunyaev Zel'dovich effect". In: *A&A* 659, A99, A99. DOI: 10.1051/0004-6361/202142004. arXiv: 2109.03272 [astro-ph.CO].

Doyle, Simon (2008). "Lumped element Kinetic Inductance Detectors". en. ISBN: 9781303213311. phd. Cardiff University. URL: https://orca.cardiff.ac.uk/id/eprint/54728/.

Durret, F. et al. (Nov. 2011). "Galaxy cluster searches based on photometric redshifts in the four CFHTLS Wide fields". In: *A&A* 535, A65, A65. DOI: 10.1051/0004-6361/201116985. arXiv: 1109.0850 [astro-ph.CO].

Durret, F. et al. (June 2015). "Galaxy clusters in the SDSS Stripe 82 based on photometric redshifts". In: *A&A* 578, A79, A79. DOI: 10.1051/0004-6361/201425293. arXiv: 1504.00452 [astro-ph.CO].

Duus, A. and B. Newell (Oct. 1977). "A catalog of southern groups and clusters of galaxies." In: *ApJS* 35, pp. 209–219. DOI: 10.1086/190477.

Désert, F.X. et al. (in prep.). "NIKA2 LPSZ Results II: Point-source population across clusters of galaxies". In.

Eales, S. et al. (May 2010). "The Herschel ATLAS". In: *PASP* 122.891, pp. 499–515. DOI: 10.1086/653086. arXiv: 0910.4279 [astro-ph.CO].

Eales, Stephen et al. (Nov. 2000). "The Canada-UK Deep Submillimeter Survey. IV. The Survey of the 14 Hour Field". In: *AJ* 120.5, pp. 2244–2268. DOI: 10.1086/316823. arXiv: astro-ph/0009154 [astro-ph].

Ebeling, H. et al. (Dec. 1998). "The ROSAT Brightest Cluster Sample - I. The compilation of the sample and the cluster log N-log S distribution". In: *MNRAS* 301.4, pp. 881–914. DOI: 10.1046/j.1365-8711.1998.01949.x. arXiv: astro-ph/9812394 [astro-ph].

Ebeling, H. et al. (Oct. 2000). "The ROSAT Brightest Cluster Sample - IV. The extended sample". In: *MNRAS* 318.2, pp. 333–340. DOI: 10.1046/j.1365-8711.2000.03549.x. arXiv: astro-ph/0003191 [astro-ph].

Ebeling, H. et al. (June 2001). "MACS: A Quest for the Most Massive Galaxy Clusters in the Universe". In: *ApJ* 553.2, pp. 668–676. DOI: 10.1086/320958. arXiv: astro-ph/0009101 [astro-ph].

Ebeling, H. et al. (May 2007). "A Complete Sample of 12 Very X-Ray Luminous Galaxy Clusters at z ¿ 0.5". In: *ApJ* 661.1, pp. L33–L36. DOI: 10.1086/518603. arXiv: astro-ph/0703394 [astro-ph].

Ebeling, H. et al. (Sept. 2010). "The X-ray brightest clusters of galaxies from the Massive Cluster Survey". In: *MNRAS* 407.1, pp. 83–93. DOI: 10.1111/j.1365-2966.2010.16920.x. arXiv: 1004.4683 [astro-ph.CO].

Ebeling, Harald et al. (Dec. 2002). "A Systematic X-Ray Search for Clusters of Galaxies behind the Milky Way". In: *ApJ* 580.2, pp. 774–788. DOI: 10.1086/343790.

Echeverria, Miren Muñoz (Oct. 2023). "Multi-wavelength cosmology with clusters of galaxies". en. PhD thesis. Université Grenoble Alpes [2020-....] URL: https://theses.hal.science/tel-04497011 (visited on 05/20/2025).

Edge, A. C. et al. (July 1990). "An X-ray flux-limited sample of clusters of galaxies : evidence for evolution of the luminosity function." In: *MNRAS* 245, p. 559.

Ehlert, S. et al. (Feb. 2013). "X-ray bright active galactic nuclei in massive galaxy clusters - I. Number counts and spatial distribution". In: *MNRAS* 428.4, pp. 3509–3525. DOI: 10.1093/mnras/sts288. arXiv: 1209.2132 [astro-ph.CO].

Einasto, J. et al. (July 2003). "Clusters and superclusters in the Sloan Digital Sky Survey". In: *A&A* 405, pp. 425–443. DOI: 10.1051/0004-6361:20030419. arXiv: astro-ph/0212312 [astro-ph].

Einasto, M. et al. (Apr. 2012). "Multimodality in galaxy clusters from SDSS DR8: substructure and velocity distribution". In: *A&A* 540, A123, A123. DOI: 10.1051/0004-6361/201118697. arXiv: 1202.4927 [astro-ph.CO].

Einasto, Maret et al. (Dec. 2022). "Death at watersheds: Galaxy quenching in low-density environments". In: *A&A* 668, A69, A69. DOI: 10.1051/0004-6361/202244304. arXiv: 2210.10761 [astro-ph.GA].

Eisenhardt, Peter R. M. et al. (Sept. 2008). "Clusters of Galaxies in the First Half of the Universe from the IRAC Shallow Survey". In: *ApJ* 684.2, pp. 905–932. DOI: 10.1086/590105. arXiv: 0804.4798 [astro-ph].

Eke, V. R. et al. (Mar. 2004). "Galaxy groups in the 2dFGRS: the group-finding algorithm and the 2PIGG catalogue". In: *MNRAS* 348.3, pp. 866–878. DOI: 10.1111/j.1365-2966.2004.07408.x. arXiv: astro-ph/0402567 [astro-ph].

Elbaz, D. et al. (Sept. 2011). "GOODS-Herschel: an infrared main sequence for star-forming galaxies". In: *A&A* 533, A119, A119. DOI: 10.1051/0004-6361/201117239. arXiv: 1105.2537 [astro-ph.CO].

Epinat, B. et al. (Mar. 2024). "MAGIC: MUSE gAlaxy Groups In COSMOS - A survey to probe the impact of environment on galaxy evolution over the last 8 Gyr". In: *Astronomy and Astrophysics* 683. Publisher: EDP ADS Bibcode: 2024A&A...683A.205E, A205. ISSN: 0004-6361. DOI: 10.1051/0004-6361/202348038. URL: https://ui.adsabs.harvard.edu/abs/2024A&A...683A.205E.

Erfanianfar, G. et al. (Mar. 2013). "X-Ray Groups of Galaxies in the AEGIS Deep and Wide Fields". In: *ApJ* 765.2, 117, p. 117. DOI: 10.1088/0004-637X/765/2/117. arXiv: 1302.5114 [astro-ph.CO].

Erler, Jens et al. (Apr. 2019). "Introducing constrained matched filters for improved separation of point sources from galaxy clusters". In: *MNRAS* 484.2, pp. 1988–1999. DOI: 10.1093/mnras/stz101. arXiv: 1809.06446 [astro-ph.IM].

Euclid Collaboration et al. (July 2019). "Euclid preparation. III. Galaxy cluster detection in the wide photometric survey, performance and algorithm selection". In: *A&A* 627, A23, A23. DOI: 10.1051/0004-6361/201935088. arXiv: 1906.04707 [astro-ph.CO].

Euclid Collaboration et al. (Mar. 2023). "Euclid preparation. XXIV. Calibration of the halo mass function in $\Lambda(\nu)$CDM cosmologies". In: *A&A* 671, A100, A100. DOI: 10.1051/0004-6361/202244674. arXiv: 2208.02174 [astro-ph.CO].

Euclid Collaboration et al. (Mar. 2025a). "Euclid Quick Data Release (Q1) – Data release overview". In: *arXiv e-prints*, arXiv:2503.15302, arXiv:2503.15302. DOI: 10.48550/arXiv.2503.15302. arXiv: 2503.15302 [astro-ph.GA].

Euclid Collaboration et al. (Mar. 2025b). "Euclid Quick Data Release (Q1). First detections from the galaxy cluster workflow". In: *arXiv e-prints*, arXiv:2503.19196, arXiv:2503.19196. DOI: 10.48550/arXiv.2503.19196. arXiv: 2503.19196 [astro-ph.CO].

Everett, W. B. et al. (Sept. 2020). "Millimeter-wave Point Sources from the 2500 Square Degree SPT-SZ Survey: Catalog and Population Statistics". In: *ApJ* 900.1, 55, p. 55. DOI: 10.3847/1538-4357/ab9df7. arXiv: 2003.03431 [astro-ph.IM].

Farrens, S. et al. (Oct. 2011). "Friends-of-friends groups and clusters in the 2SLAQ catalogue". In: *MNRAS* 417.2, pp. 1402–1416. DOI: 10.1111/j.1365-2966.2011.19356.x. arXiv: 1106.5687 [astro-ph.CO].

Fasano, A. et al. (Dec. 2021). "Accurate sky signal reconstruction for ground-based spectroscopy with kinetic inductance detectors". In: *A&A* 656, A116, A116. DOI: 10.1051/0004-6361/202141419. arXiv: 2109.03145 [astro-ph.IM].

Fassbender, R. et al. (Dec. 2011). "The x-ray luminous galaxy cluster population at 0.9 ¡ z $\lesssim$ 1.6 as revealed by the XMM-Newton Distant Cluster Project". In: *New Journal of Physics* 13.12, 125014, p. 125014. DOI: 10.1088/1367-2630/13/12/125014. arXiv: 1111.0009 [astro-ph.CO].

Fernández-Torreiro, M. et al. (May 2025). "Scientific forecasts for cluster cosmology with a projected 4-band millimetre camera at the 30-m IRAM telescope". In: *Highlights of Spanish Astrophysics XII*. Ed. by M. Manteiga et al., p. 8.

Ferragamo, A. et al. (Nov. 2021). "Velocity dispersion and dynamical mass for 270 galaxy clusters in the Planck PSZ1 catalogue". In: *A&A* 655, A115, A115. DOI: 10.1051/0004-6361/202140382. arXiv: 2109.04967 [astro-ph.CO].

Ferragamo, A. et al. (May 2022). "Comparison of hydrostatic and lensing cluster mass estimates: A pilot study in MACS J0647.7+7015". In: *A&A* 661, A65, A65. DOI: 10.1051/0004-6361/202140276. arXiv: 2112.08298 [astro-ph.CO].

Finoguenov, A. et al. (Sept. 2007). "The XMM-Newton Wide-Field Survey in the COSMOS Field: Statistical Properties of Clusters of Galaxies". In: *ApJS* 172.1, pp. 182–195. DOI: 10.1086/516577. arXiv: astro-ph/0612360 [astro-ph].

Finoguenov, A. et al. (Apr. 2010). "X-ray groups and clusters of galaxies in the Subaru-XMM Deep Field". In: *MNRAS* 403.4, pp. 2063–2076. DOI: 10.1111/j.1365-2966.2010.16256.x. arXiv: 0912.0039 [astro-ph.CO].

Finoguenov, A. et al. (Apr. 2015). "Ultra-deep catalog of X-ray groups in the Extended Chandra Deep Field South". In: *A&A* 576, A130, A130. DOI: 10.1051/0004-6361/201323053. arXiv: 1501.03506 [astro-ph.HE].

Finoguenov, A. et al. (June 2020). "CODEX clusters. Survey, catalog, and cosmology of the X-ray luminosity function". In: *A&A* 638, A114, A114. DOI: 10.1051/0004-6361/201937283. arXiv: 1912.03262 [astro-ph.CO].

Fischler, Martin A. and Robert C. Bolles (June 1981). "Random sample consensus: a paradigm for model fitting with applications to image analysis and automated cartography". In: *Commun. ACM* 24.6, 381–395. ISSN: 0001-0782. DOI: 10.1145/358669.358692. URL: https://doi.org/10.1145/358669.358692.

Fixsen, D. J. et al. (Dec. 1996). "The Cosmic Microwave Background Spectrum from the Full COBE FIRAS Data Set". In: *ApJ* 473, p. 576. DOI: 10.1086/178173. arXiv: astro-ph/9605054 [astro-ph].

Foreman-Mackey, Daniel et al. (Mar. 2013). "emcee: The MCMC Hammer". In: *PASP* 125.925, p. 306. DOI: 10.1086/670067. arXiv: 1202.3665 [astro-ph.IM].

Forman, W. et al. (Dec. 1978). "The fourth Uhuru catalog of X-ray sources." In: *ApJS* 38, pp. 357–412. DOI: 10.1086/190561.

Fouque, P. et al. (May 1992). "Groups of galaxies within 80 Mpc. II. The catalogue of groups and group members." In: *A&AS* 93, pp. 211–233.

Franck, J. R. and S. S. McGaugh (Dec. 2016). "The Candidate Cluster and Protocluster Catalog (CCPC) II. Spectroscopically Identified Structures Spanning 2¡ z ¡ 6.6". In: *ApJ* 833.1, 15, p. 15. DOI: 10.3847/0004-637X/833/1/15. arXiv: 1610.00713 [astro-ph.GA].

Friedmann, A. (Dec. 1924). "Über die Möglichkeit einer Welt mit konstanter negativer Krümmung des Raumes". In: *Zeitschrift fur Physik* 21.1, pp. 326–332. DOI: 10.1007/BF01328280.

Gal, R. R. et al. (Jan. 2000). "The Northern Sky Optical Cluster Survey. I. Detection of Galaxy Clusters in DPOSS". In: *AJ* 119.1, pp. 12–20. DOI: 10.1086/301185. arXiv: astro-ph/9910173 [astro-ph].

Gal, R. R. et al. (Apr. 2003). "The Northern Sky Optical Cluster Survey. II. An Objective Cluster Catalog for 5800 Square Degrees". In: *AJ* 125.4, pp. 2064–2084. DOI: 10.1086/368240. arXiv: astro-ph/0301274 [astro-ph].

Gal, R. R. et al. (Feb. 2009). "The Northern Sky Optical Cluster Survey. III. A Cluster Catalog Covering PI Steradians". In: *AJ* 137.2, pp. 2981–2999. DOI: 10.1088/0004-6256/137/2/2981. arXiv: 0812.2962 [astro-ph].

Gao, Jinghua et al. (Feb. 2020). "A Catalog of Galaxy Clusters Identified from SCUSS, SDSS, and UNWISE". In: *PASP* 132.1008, 024101, p. 024101. DOI: 10.1088/1538-3873/ab6151. arXiv: 1912.10909 [astro-ph.GA].

Garcia, A. M. (July 1993). "General study of group membership. II. Determination of nearby groups." In: *A&AS* 100, pp. 47–90.

Gavazzi, R. and G. Soucail (Feb. 2007). "Weak lensing survey of galaxy clusters in the CFHTLS Deep". In: *A&A* 462.2, pp. 459–471. DOI: 10.1051/0004-6361:20065677. arXiv: astro-ph/0605591 [astro-ph].

Geach, J. E. et al. (Feb. 2017). "The SCUBA-2 Cosmology Legacy Survey: 850 μm maps, catalogues and number counts". In: *MNRAS* 465.2, pp. 1789–1806. DOI: 10.1093/mnras/stw2721. arXiv: 1607.03904 [astro-ph.GA].

Geach, James E. et al. (June 2011). "4098 galaxy clusters to z~ 0.6 in the Sloan Digital Sky Survey equatorial Stripe 82". In: *MNRAS* 413.4, pp. 3059–3067. DOI: 10.1111/j.1365-2966.2011.18380.x. arXiv: 1101.4585 [astro-ph.CO].

Geller, M. J. and J. P. Huchra (June 1983). "Groups of galaxies. III. THe CfA survey." In: *ApJS* 52, pp. 61–87. DOI: 10.1086/190859.

Gelman, Andrew and Donald B. Rubin (Jan. 1992). "Inference from Iterative Simulation Using Multiple Sequences". In: *Statistical Science* 7, pp. 457–472. DOI: 10.1214/ss/1177011136.

George, Matthew R. et al. (Dec. 2011). "Galaxies in X-Ray Groups. I. Robust Membership Assignment and the Impact of Group Environments on Quenching". In: *ApJ* 742.2, 125, p. 125. DOI: 10.1088/0004-637X/742/2/125. arXiv: 1109.6040 [astro-ph.CO].

Gerke, Brian F. et al. (May 2005). "The DEEP2 Galaxy Redshift Survey: First Results on Galaxy Groups". In: *ApJ* 625.1, pp. 6–22. DOI: 10.1086/429579. arXiv: astro-ph/0410721 [astro-ph].

Gerke, Brian F. et al. (May 2012). "The DEEP2 Galaxy Redshift Survey: The Voronoi-Delaunay Method Catalog of Galaxy Groups". In: *ApJ* 751.1, 50, p. 50. DOI: 10.1088/0004-637X/751/1/50. arXiv: 1203.3899 [astro-ph.CO].

Giacconi, R. et al. (June 1979). "The Einstein (HEAO 2) X-ray Observatory." In: *ApJ* 230, pp. 540–550. DOI: 10.1086/157110.

Gianfagna, Giulia et al. (Apr. 2021). "Exploring the hydrostatic mass bias in MUSIC clusters: application to the NIKA2 mock sample". In: *MNRAS* 502.4, pp. 5115–5133. DOI: 10.1093/mnras/stab308. arXiv: 2010.03634 [astro-ph.CO].

Giavalisco, M. et al. (Jan. 2004). "The Great Observatories Origins Deep Survey: Initial Results from Optical and Near-Infrared Imaging". In: *ApJ* 600.2, pp. L93–L98. DOI: 10.1086/379232. arXiv: astro-ph/0309105 [astro-ph].

Gioia, I. M. et al. (Aug. 1984). "The medium sensivity survey : a new sample of X-ray sources with optical identifications and the revised extragalactic log N-log S." In: *ApJ* 283, pp. 495–511. DOI: 10.1086/162332.

Gioia, I. M. et al. (Mar. 1990). "The Einstein Observatory Extended Medium-Sensitivity Survey. I. X-Ray Data and Analysis". In: *ApJS* 72, p. 567. DOI: 10.1086/191426.

Gioia, Isabella M. (Jan. 2000). "Cluster Surveys". In: *Constructing the Universe with Clusters of Galaxies*. Ed. by Florence Durret and Daniel Gerbal, 3.1, p. 3.1. DOI: 10.48550/arXiv.astro-ph/0010059. arXiv: astro-ph/0010059 [astro-ph].

Giuricin, Giuliano et al. (Nov. 2000). "Nearby Optical Galaxies: Selection of the Sample and Identification of Groups". In: *ApJ* 543.1, pp. 178–194. DOI: 10.1086/317070. arXiv: astro-ph/0001140 [astro-ph].

Gkogkou, A. et al. (Feb. 2023). "CONCERTO: Simulating the CO, [CII], and [CI] line emission of galaxies in a 117 deg^2 field and the impact of field-to-field variance". In: *A&A* 670, A16, A16. DOI: 10.1051/0004-6361/202245151. arXiv: 2212.02235 [astro-ph.CO].

Gladders, M. D. and H. K. C. Yee (Jan. 2001). "The Red-Sequence Cluster Survey." In: *The New Era of Wide Field Astronomy*. Ed. by Roger Clowes et al. Vol. 232. Astronomical Society of the Pacific Conference Series, p. 126. DOI: 10.48550/arXiv.astro-ph/0011073. arXiv: astro-ph/0011073 [astro-ph].

Gladders, Michael D. and H. K. C. Yee (Oct. 2000). "A New Method For Galaxy Cluster Detection. I. The Algorithm". In: *AJ* 120.4, pp. 2148–2162. DOI: 10.1086/301557. arXiv: astro-ph/0004092 [astro-ph].

— (Mar. 2005). "The Red-Sequence Cluster Survey. I. The Survey and Cluster Catalogs for Patches RCS 0926+37 and RCS 1327+29". In: *ApJS* 157.1, pp. 1–29. DOI: 10.1086/427327. arXiv: astro-ph/0411075 [astro-ph].

Gonzalez, A. (July 2014). "Cluster detection via wavelets". In: *Building the Euclid Cluster Survey - Scientific Program*, 7, p. 7.

Gonzalez, Anthony H. et al. (Nov. 2001). "The Las Campanas Distant Cluster Survey: The Catalog". In: *ApJS* 137.1, pp. 117–138. DOI: 10.1086/322541. arXiv: astro-ph/0106055 [astro-ph].

Gonzalez, Anthony H. et al. (Feb. 2019). "The Massive and Distant Clusters of WISE Survey. I. Survey Overview and a Catalog of ¿2000 Galaxy Clusters at z = 1". In: *ApJS* 240.2, 33, p. 33. DOI: 10.3847/1538-4365/aafad2. arXiv: 1809.06820 [astro-ph.CO].

Goto, Tomotsugu et al. (Apr. 2002). "The Cut-and-Enhance Method: Selecting Clusters of Galaxies from the Sloan Digital Sky Survey Commissioning Data". In: *AJ* 123.4, pp. 1807–1825. DOI: 10.1086/339303. arXiv: astro-ph/0112482 [astro-ph].

Goto, Tomotsugu et al. (Dec. 2008). "Galaxy Clusters at 0.9 ¡ z ¡ 1.7 in the AKARI NEP Deep Field". In: *PASJ* 60, S531. DOI: 10.1093/pasj/60.sp2.S531. arXiv: 0810.0529 [astro-ph].

Gozaliasl, G. et al. (June 2014). "Mining the gap: evolution of the magnitude gap in X-ray galaxy groups from the 3-square-degree XMM coverage of CFHTLS". In: *A&A* 566, A140, A140. DOI: 10.1051/0004-6361/201322459. arXiv: 1405.3412 [astro-ph.GA].

Gozaliasl, Ghassem et al. (Mar. 2019). "Chandra centres for COSMOS X-ray galaxy groups: differences in stellar properties between central dominant and offset brightest group galaxies". In: *Monthly Notices of the Royal Astronomical Society* 483.3, pp. 3545–3565. ISSN: 0035-8711. DOI: 10.1093/mnras/sty3203. URL: https://doi.org/10.1093/mnras/sty3203.

Gralla, Megan B. et al. (Apr. 2020). "Atacama Cosmology Telescope: Dusty Star-forming Galaxies and Active Galactic Nuclei in the Equatorial Survey". In: *ApJ* 893.2, 104, p. 104. DOI: 10.3847/1538-4357/ab7915. arXiv: 1905.04592 [astro-ph.GA].

Gregory, P. C. et al. (Apr. 1996). "The GB6 Catalog of Radio Sources". In: *ApJS* 103, p. 427. DOI: 10.1086/192282.

Grogin, Norman A. et al. (Dec. 2011). "CANDELS: The Cosmic Assembly Near-infrared Deep Extragalactic Legacy Survey". In: *ApJS* 197.2, 35, p. 35. DOI: 10.1088/0067-0049/197/2/35. arXiv: 1105.3753 [astro-ph.CO].

Grove, L. F. et al. (Feb. 2009). "Galaxy clusters in the CFHTLS. II. Matched-filter results in different pass-bands". In: *A&A* 494.3, pp. 845–855. DOI: 10.1051/0004-6361:200810384.

Guilloteau, S. (Jan. 1994). "The IRAM Interferometer on Plateau de Bure". In: *IAU Colloquium 140: Astronomy with Millimeter and Submillimeter Wave Interferometry*. Ed. by M. Ishiguro and J. Welch. Vol. 59. Astronomical Society of the Pacific Conference Series, pp. 27–34.

Gull, S. F. and K. J. E. Northover (Oct. 1976). "Detection of hot gas in clusters of galaxies by observation of the microwave background radiation". In: *Nature* 263.5578, pp. 572–573. DOI: 10.1038/263572a0.

Gunn, J. E. and J. B. Oke (Jan. 1975). "Spectrophotometry of faint cluster galaxies and the Hubble diagram: an approach to cosmology." In: *ApJ* 195, pp. 255–268. DOI: 10.1086/153325.

Gunn, J. E. et al. (July 1986). "A Systematic Survey for Distant Galaxy Clusters". In: *ApJ* 306, p. 30. DOI: 10.1086/164317.

Gursky, H. et al. (Aug. 1971). "A Strong X-Ray Source in the Coma Cluster Observed by UHURU". In: *ApJ* 167, p. L81. DOI: 10.1086/180765.

Guth, Alan H. (Jan. 1981). "Inflationary universe: A possible solution to the horizon and flatness problems". In: *Phys. Rev. D* 23.2, pp. 347–356. DOI: 10.1103/PhysRevD.23.347.

Guzzo, L. et al. (Mar. 1999). "The REFLEX cluster survey: observing strategy and first results on large-scale structure." In: *The Messenger* 95, pp. 27–32. DOI: 10.48550/arXiv.astro-ph/9903396. arXiv: astro-ph/9903396 [astro-ph].

Hand, Nick et al. (July 2012). "Evidence of Galaxy Cluster Motions with the Kinematic Sunyaev-Zel'dovich Effect". In: *Phys. Rev. Lett.* 109.4, 041101, p. 041101. DOI: 10.1103/PhysRevLett.109.041101. arXiv: 1203.4219 [astro-ph.CO].

Hanser, C. et al. (in prep.[a]). "NIKA2 LPSZ Results III. High-resolution SZ-X-ray synergy to obtain the thermodynamic profiles of a sample of high-redshift clusters". In.

Hanser, C. et al. (in prep.[b]). "NIKA2 LPSZ Results IV. Universal Pressure Profile". In.

Hanser, Corentin (Oct. 2025). "Cosmology with the galaxy clusters of the NIKA2 Sunyaev-Zeldovich Large Programme". en. PhD thesis. Université Grenoble Alpes [2020-....] URL: https://theses.hal.science/tel-05035347.

Hao, Jiangang et al. (Dec. 2010). "A GMBCG Galaxy Cluster Catalog of 55,424 Rich Clusters from SDSS DR7". In: *ApJS* 191.2, pp. 254–274. DOI: 10.1088/0067-0049/191/2/254. arXiv: 1010.5503 [astro-ph.CO].

Hasselfield, Matthew et al. (July 2013). "The Atacama Cosmology Telescope: Sunyaev-Zel'dovich selected galaxy clusters at 148 GHz from three seasons of data". In: *J. Cosmology Astropart. Phys.* 2013.7, 008, p. 008. DOI: 10.1088/1475-7516/2013/07/008. arXiv: 1301.0816 [astro-ph.CO].

Henry, J. P. et al. (Aug. 1995). "Groups of Galaxies in the ROSAT North Ecliptic Pole Survey". In: *ApJ* 449, p. 422. DOI: 10.1086/176067.

Henry, J. Patrick et al. (Feb. 2006). "The ROSAT North Ecliptic Pole Survey: The X-Ray Catalog". In: *ApJS* 162.2, pp. 304–328. DOI: 10.1086/498749. arXiv: astro-ph/0511195 [astro-ph].

Herard-Demanche, Thomas et al. (Feb. 2025). "Mapping dusty galaxy growth at z ¿ 5 with FRESCO: detection of Hα in submm galaxy HDF850.1 and the surrounding overdense structures". In: *MNRAS* 537.2, pp. 788–808. DOI: 10.1093/mnras/staf030. arXiv: 2309.04525 [astro-ph.GA].

Hernández-Lang, D. et al. (Oct. 2023). "The PSZ-MCMF catalogue of Planck clusters over the DES region". In: *MNRAS* 525.1, pp. 24–43. DOI: 10.1093/mnras/stad2319. arXiv: 2210.04666 [astro-ph.CO].

Herranz, D. et al. (Nov. 2002). "Filtering techniques for the detection of Sunyaev-Zel'dovich clusters ¡br/¿ in multifrequency maps". In: *MNRAS* 336.4, pp. 1057–1068. DOI: 10.1046/j.1365-8711.2002.05704.x. arXiv: astro-ph/0203486 [astro-ph].

Herschel, William (Jan. 1785). "On the Construction of the Heavens." In: *Philosophical Transactions of the Royal Society of London Series I* 75, pp. 213–266.

Hickson, P. (Apr. 1982). "Systematic properties of compact groups of galaxies." In: *ApJ* 255, pp. 382–391. DOI: 10.1086/159838.

Hilton, M. et al. (Mar. 2021). "The Atacama Cosmology Telescope: A Catalog of ¿4000 Sunyaev-Zel'dovich Galaxy Clusters". In: *ApJS* 253.1, 3, p. 3. DOI: 10.3847/1538-4365/abd023. arXiv: 2009.11043 [astro-ph.CO].

Hilton, Matt et al. (Mar. 2018). "The Atacama Cosmology Telescope: The Two-season ACTPol Sunyaev-Zel'dovich Effect Selected Cluster Catalog". In: *ApJS* 235.1, 20, p. 20. DOI: 10.3847/1538-4365/aaa6cb. arXiv: 1709.05600 [astro-ph.CO].

Hoekstra, Henk (July 2007). "A comparison of weak-lensing masses and X-ray properties of galaxy clusters". In: *MNRAS* 379.1, pp. 317–330. DOI: 10.1111/j.1365-2966.2007.11951.x. arXiv: 0705.0358 [astro-ph].

Hogan, M. T. et al. (Oct. 2015). "A comprehensive study of the radio properties of brightest cluster galaxies". In: *MNRAS* 453.2, pp. 1201–1222. DOI: 10.1093/mnras/stv1517. arXiv: 1507.03019 [astro-ph.GA].

Holland, W. S. et al. (Mar. 1999). "SCUBA: a common-user submillimetre camera operating on the James Clerk Maxwell Telescope". In: *MNRAS* 303.4, pp. 659–672. DOI: 10.1046/j.1365-8711.1999.02111.x. arXiv: astro-ph/9809122 [astro-ph].

Holmberg, E. B. et al. (Dec. 1975). "The ESO/Uppsala survey of the ESO (B) atlas of the southern sky. III." In: *A&AS* 22, p. 327.

Honda, S. et al. (Oct. 2023a). "Commissioning Observations in 2022 with 100-GHz MKID Camera at Nobeyama 45-m Telescope". In: ADS Bibcode: 2023ursi.confE.284H, p. 284. DOI: 10.23919/URSIGASS57860.2023.10265421. URL: https://ui.adsabs.harvard.edu/abs/2023ursi.confE.284H.

Honda, Shunsuke et al. (Jan. 2023b). "Development and Commissioning of 100 GHz Microwave Kinetic Inductance Detector (MKID) Camera at the Nobeyama 45 m Telescope". In: *URSI Radio Science Letters* 4. ADS Bibcode: 2023URSL....4...53H, p. 53. DOI: 10.46620/22-0053. URL: https://ui.adsabs.harvard.edu/abs/2023URSL....4...53H.

Honda, Shunsuke et al. (Jan. 2023). "Development and Commissioning of 100 GHz Microwave Kinetic Inductance Detector (MKID) Camera at the Nobeyama 45 m Telescope". In: *URSI Radio Science Letters* 4, 53, p. 53. DOI: 10.46620/22-0053.

Horner, Donald J. et al. (June 2008). "The WARPS Survey. VII. The WARPS-II Cluster Catalog". In: *ApJS* 176.2, pp. 374–413. DOI: 10.1086/529494.

Hu, W. et al. (Sept. 2024). "CONCERTO at APEX On-sky performance in continuum". In: *A&A* 689, A20, A20. DOI: 10.1051/0004-6361/202449260. arXiv: 2406.15572 [astro-ph.IM].

Huang, N. et al. (Mar. 2020). "Galaxy Clusters Selected via the Sunyaev-Zel'dovich Effect in the SPTpol 100-square-degree Survey". In: *aj* 159.3, 110, p. 110. DOI: 10.3847/1538-3881/ab6a96. arXiv: 1907.09621 [astro-ph.CO].

Hubble, Edwin (Mar. 1929). "A Relation between Distance and Radial Velocity among Extra-Galactic Nebulae". In: *Proceedings of the National Academy of Science* 15.3, pp. 168–173. DOI: 10.1073/pnas.15.3.168.

Huchra, J. P. and M. J. Geller (June 1982). "Groups of Galaxies. I. Nearby groups". In: *ApJ* 257, pp. 423–437. DOI: 10.1086/160000.

Huggins, William and W. A. Miller (Jan. 1864a). "On the Spectra of Some of the Fixed Stars". In: *Philosophical Transactions of the Royal Society of London Series I* 154, pp. 413–435.

— (Jan. 1864b). "On the Spectra of Some of the Nebulae. By William Huggins, F.R.A.S. A Supplement to the Paper "On the Spectra of Some of the Fixed Stars William Huggins F.R.A.S., and W. A. Miller, M.D., LL.D., Treas. and V.P.P.S."" In: *Philosophical Transactions of the Royal Society of London Series I* 154, pp. 437–444.

Hughes, David H. et al. (July 1998). "High-redshift star formation in the Hubble Deep Field revealed by a submillimetre-wavelength survey". In: *Nature* 394.6690, pp. 241–247. DOI: 10.1038/28328. arXiv: astro-ph/9806297 [astro-ph].

Humason, M. L. et al. (Jan. 1956). "Redshifts and magnitudes of extragalactic nebulae." In: *AJ* 61, pp. 97–162. DOI: 10.1086/107297.

Hurier, G. et al. (Sept. 2021). "MILCANN: A tSZ map for galaxy cluster detection assessed using a neural network". In: *A&A* 653, A106, A106. DOI: 10.1051/0004-6361/201730534. arXiv: 1702.00075 [astro-ph.CO].

Hurley-Walker, N. et al. (Jan. 2017). "GaLactic and Extragalactic All-sky Murchison Widefield Array (GLEAM) survey - I. A low-frequency extragalactic catalogue". In: *MNRAS* 464.1, pp. 1146–1167. DOI: 10.1093/mnras/stw2337. arXiv: 1610.08318 [astro-ph.GA].

Iovino, A. et al. (Apr. 2003). "A New Sample of Distant Compact Groups from the Digitized Second Palomar Observatory Sky Survey". In: *AJ* 125.4, pp. 1660–1681. DOI: 10.1086/373999.

Iovino, A. et al. (Aug. 2016). "A high definition view of the COSMOS Wall at z ~0.73". In: *A&A* 592, A78, A78. DOI: 10.1051/0004-6361/201527673. arXiv: 1606.06185 [astro-ph.GA].

Ishiyama, Tomoaki et al. (Sept. 2021). "The Uchuu simulations: Data Release 1 and dark matter halo concentrations". In: *MNRAS* 506.3, pp. 4210–4231. DOI: 10.1093/\mnras/stab1755. arXiv: 2007.14720 [astro-ph.CO].

Ishizaki, Yuji (Jan. 2025). "Performance evaluation of a 100 GHz band LEKID camera for deployment on the Nobeyama 45m radio telescope". Theses.

Itoh, Naoki et al. (July 1998). "Relativistic Corrections to the Sunyaev-Zeldovich Effect for Clusters of Galaxies". In: *ApJ* 502.1, pp. 7–15. DOI: 10.1086/305876. arXiv: astro-ph/9712289 [astro-ph].

Ivezić, Željko et al. (Mar. 2019). "LSST: From Science Drivers to Reference Design and Anticipated Data Products". In: *ApJ* 873.2, 111, p. 111. DOI: 10.3847/1538-4357/ab042c. arXiv: 0805.2366 [astro-ph].

Jõeveer, Mikhel et al. (Nov. 1978). "Spatial distribution of galaxies and of clusters of galaxies in the southern galactic hemisphere". In: *MNRAS* 185, pp. 357–370. DOI: 10.1093/mnras/185.2.357.

Jansen, F. et al. (Jan. 2001). "XMM-Newton observatory. I. The spacecraft and operations". In: *A&A* 365, pp. L1–L6. DOI: 10.1051/0004-6361:20000036.

Jedamzik, Karsten (July 1995). "The Cloud-in-Cloud Problem in the Press-Schechter Formalism of Hierarchical Structure Formation". In: *ApJ* 448, p. 1. DOI: 10.1086/175936. arXiv: astro-ph/9408080 [astro-ph].

Kaiser, N. (Sept. 1986). "Evolution and clustering of rich clusters." In: *MNRAS* 222, pp. 323–345. DOI: 10.1093/mnras/222.2.323.

Kawasaki, W. (Jan. 2000). "The APM/Matched-Filter Cluster Catalog". In: *Clustering at High Redshift*. Ed. by A. Mazure et al. Vol. 200. Astronomical Society of the Pacific Conference Series, p. 73. DOI: 10.48550/arXiv.astro-ph/9912305. arXiv: astro-ph/9912305 [astro-ph].

Kawasaki, W. et al. (June 1998). "An objective and automatic cluster finder: an improvement of the matched-filter method". In: *A&AS* 130, pp. 567–579. DOI: 10.1051/aas:1998245. arXiv: astro-ph/9705112 [astro-ph].

Kéruzoré, F. et al. (Dec. 2020). "Exploiting NIKA2/XMM-Newton imaging synergy for intermediate-mass high-z galaxy clusters within the NIKA2 SZ large program. Observations of ACT-CL J0215.4+0030 at z ∼ 0.9". In: *A&A* 644, A93, A93. DOI: 10.1051/0004-6361/202038933. arXiv: 2009.02563 [astro-ph.CO].

Kéruzoré, Florian (Sept. 2021). "Cosmologie à partir des observations Sunyaev-Zeldovich d'amas de galaxies avec NIKA2". Theses. Université Grenoble Alpes [2020-....] URL: https://theses.hal.science/tel-03555821.

Kéruzoré, Florian et al. (Mar. 2023). "panco2: a Python library to measure intracluster medium pressure profiles from Sunyaev-Zeldovich observations". In: *The Open Journal of Astrophysics* 6, 9, p. 9. DOI: 10.21105/astro.2212.01439. arXiv: 2212.01439 [astro-ph.IM].

Khostovan, Ali Ahmad et al. (Feb. 2025). "COSMOS Spectroscopic Redshift Compilation (First Data Release): 165k Redshifts Encompassing Two Decades of Spectroscopy". In: *arXiv e-prints*, arXiv:2503.00120, arXiv:2503.00120. DOI: 10.48550/arXiv.2503.00120. arXiv: 2503.00120 [astro-ph.GA].

Kim, Rita Seung Jung et al. (Jan. 2002). "Detecting Clusters of Galaxies in the Sloan Digital Sky Survey. I. Monte Carlo Comparison of Cluster Detection Algorithms". In: *AJ* 123.1, pp. 20–36. DOI: 10.1086/324727. arXiv: astro-ph/0110259 [astro-ph].

Kim, Suk et al. (Dec. 2014). "The Extended Virgo Cluster Catalog". In: *ApJS* 215.2, 22, p. 22. DOI: 10.1088/0067-0049/215/2/22. arXiv: 1409.3283 [astro-ph.GA].

Kitayama, Tetsu et al. (Feb. 2004). "Exploring Cluster Physics with High-Resolution Sunyaev–Zel'dovich Effect Images and X-Ray Data: The Case of the Most X-Ray-Luminous Galaxy Cluster RX J1347-1145". In: *PASJ* 56, pp. 17–28. DOI: 10.1093/pasj/56.1.17. arXiv: astro-ph/0311574 [astro-ph].

Kiuchi, Hitoshi et al. (May 2015). "A Frequency Sweeping Readout System for Kinetic Inductance Detectors Based on Submillimeter Radio Astronomy". In: *IEEE Transactions on Terahertz Science and Technology* 5.3, pp. 456–463. ISSN: 2156-3446. DOI: 10.1109/TTHZ.2015.2413751. URL: https://ieeexplore.ieee.org/document/7079501.

Klein, M. et al. (Sept. 2019). "A new RASS galaxy cluster catalogue with low contamination extending to z ∼ 1 in the DES overlap region". In: *MNRAS* 488.1, pp. 739–769. DOI: 10.1093/\mnras/stz1463. arXiv: 1812.09956 [astro-ph.CO].

Klein, M. et al. (July 2024a). "SPT-SZ MCMF: an extension of the SPT-SZ catalogue over the DES region". In: *MNRAS* 531.4, pp. 3973–3990. DOI: 10.1093/mnras/stae1359. arXiv: 2309.09908 [astro-ph.CO].

Klein, M. et al. (Oct. 2024b). "The ACT-DR5 MCMF galaxy cluster catalog". In: *A&A* 690, A322, A322. DOI: 10.1051/0004-6361/202451203. arXiv: 2406.14754 [astro-ph.CO].

Klein, Matthias et al. (Dec. 2023). "RASS-MCMF: a full-sky X-ray selected galaxy cluster catalogue". In: *MNRAS* 526.3, pp. 3757–3778. DOI: 10.1093/mnras/stad2729. arXiv: 2305.20066 [astro-ph.CO].

Klemola, A. R. (Aug. 1969). "Groups and clusters of southern galaxies." In: *AJ* 74, pp. 804–806. DOI: 10.1086/110861.

Knobel, C. et al. (June 2009). "An Optical Group Catalog to z = 1 from the zCOSMOS 10 k Sample". In: *ApJ* 697.2, pp. 1842–1860. DOI: 10.1088/0004-637X/697/2/1842. arXiv: 0903.3411 [astro-ph.CO].

Knobel, C. et al. (July 2012). "The zCOSMOS 20k Group Catalog". In: *The Astrophysical Journal* 753. Publisher: IOP ADS Bibcode: 2012ApJ...753..121K, p. 121. ISSN: 0004-637X. DOI: 10.1088/0004-637X/753/2/121. URL: https://ui.adsabs.harvard.edu/abs/2012ApJ...753..121K.

Kocevski, Dale D. et al. (June 2007). "A Systematic X-Ray Search for Clusters of Galaxies behind the Milky Way. II. The Second CIZA Subsample". In: *ApJ* 662.1, pp. 224–235. DOI: 10.1086/513303. arXiv: astro-ph/0512321 [astro-ph].

Kochanek, C. S. et al. (Mar. 2003). "Clusters of Galaxies in the Local Universe". In: *ApJ* 585.1, pp. 161–181. DOI: 10.1086/345896. arXiv: astro-ph/0208168 [astro-ph].

Koekemoer, A. M. et al. (Sept. 2007). "The COSMOS Survey: Hubble Space Telescope Advanced Camera for Surveys Observations and Data Processing". In: *ApJS* 172.1, pp. 196–202. DOI: 10.1086/520086. arXiv: astro-ph/0703095 [astro-ph].

Koester, B. P. et al. (May 2007). "A MaxBCG Catalog of 13,823 Galaxy Clusters from the Sloan Digital Sky Survey". In: *ApJ* 660.1, pp. 239–255. DOI: 10.1086/509599. arXiv: astro-ph/0701265 [astro-ph].

Kolokotronis, V. et al. (Feb. 2006). "The Serendipitous XMM-Newton Cluster Athens Survey (SEXCLAS): sample selection and the cluster logN-logS". In: *MNRAS* 366.1, pp. 163–170. DOI: 10.1111/j.1365-2966.2005.09827.x. arXiv: astro-ph/0503409 [astro-ph].

Komatsu, Eiichiro et al. (May 1999). "Submillimeter Detection of the Sunyaev-Zeldovich Effect toward the Most Luminous X-Ray Cluster at Z = 0.45". In: *ApJ* 516.1, pp. L1–L4. DOI: 10.1086/311983. arXiv: astro-ph/9902351 [astro-ph].

Komatsu, Eiichiro et al. (Feb. 2001). "Substructures Revealed by the Sunyaev-Zel'dovich Effect at 150 GHz in a High-Resolution Map of RX J1347-1145". In: *PASJ* 53.1, pp. 57–62. DOI: 10.1093/pasj/53.1.57. arXiv: astro-ph/0006293 [astro-ph].

Kompaneets, A. S. (May 1957). "The Establishment of Thermal Equilibrium between Quanta and Electrons". In: *Soviet Journal of Experimental and Theoretical Physics* 4.5, pp. 730–737.

Kornoelje, K. et al. (Mar. 2025). "The SPT-Deep Cluster Catalog: Sunyaev-Zel'dovich Selected Clusters from Combined SPT-3G and SPTpol Measurements over 100 Square Degrees". In: *arXiv e-prints*, arXiv:2503.17271, arXiv:2503.17271. DOI: 10.48550/arXiv.2503.17271. arXiv: 2503.17271 [astro-ph.CO].

Kosowsky, Arthur (Dec. 2003). "The Atacama Cosmology Telescope". In: *New A Rev.* 47.11-12, pp. 939–943. DOI: 10.1016/j.newar.2003.09.003. arXiv: astro-ph/0402234 [astro-ph].

Koulouridis, E. et al. (Aug. 2021). "The X-CLASS survey: A catalogue of 1646 X-ray-selected galaxy clusters up to z ∼ 1.5". In: *A&A* 652, A12, A12. DOI: 10.1051/0004-6361/202140566. arXiv: 2104.06617 [astro-ph.CO].

Kowalski, M. P. et al. (Dec. 1984). "An X-ray survey of clusters of galaxies. IV. A survey of southern clusters and a compilation of upper limits for both Abell and southern clusters." In: *ApJS* 56, pp. 403–506. DOI: 10.1086/190991.

Kuno, N. et al. (Apr. 1993). "Seven matched bolometers for millimeter wave observations". In: *International Journal of Infrared and Millimeter Waves* 14.4, pp. 749–762. DOI: 10.1007/BF02084285.

Kurtz, Michael J. et al. (May 2012). "Testing Weak-lensing Maps with Redshift Surveys: A Subaru Field". In: *ApJ* 750.2, 168, p. 168. DOI: 10.1088/0004-637X/750/2/168. arXiv: 1102.5743 [astro-ph.CO].

LSST Science Collaboration et al. (Dec. 2009). "LSST Science Book, Version 2.0". In: *arXiv e-prints*, arXiv:0912.0201, arXiv:0912.0201. DOI: 10.48550/arXiv.0912.0201. arXiv: 0912.0201 [astro-ph.IM].

Lacey, C. and S. Cole (Dec. 1994). "Merger Rates in Hierarchical Models of Galaxy Formation - Part Two - Comparison with N-Body Simulations". In: *MNRAS* 271, p. 676. DOI: 10.1093/mnras/271.3.676. arXiv: astro-ph/9402069 [astro-ph].

Lacy, M. et al. (Mar. 2020). "The Karl G. Jansky Very Large Array Sky Survey (VLASS). Science Case and Survey Design". In: *PASP* 132.1009, 035001, p. 035001. DOI: 10.1088/1538-3873/ab63eb. arXiv: 1907.01981 [astro-ph.IM].

Lagache, G. et al. (June 2025). "Overdense fireworks in GOODS-N: Unveiling a record number of massive dusty star forming galaxies at z∼5.2 with the N2CLS". In: *arXiv e-prints*, arXiv:2506.15322, arXiv:2506.15322. DOI: 10.48550/arXiv.2506.15322. arXiv: 2506.15322 [astro-ph.GA].

Lambert, Trystan S. et al. (Sept. 2020). "The 2MASS redshift survey galaxy group catalogue derived from a graph-theory based friends-of-friends algorithm". In: *MNRAS* 497.3, pp. 2954–2973. DOI: 10.1093/mnras/staa1946. arXiv: 2007.00581 [astro-ph.GA].

Laureijs, R. et al. (Oct. 2011). "Euclid Definition Study Report". In: *arXiv e-prints*, arXiv:1110.3193, arXiv:1110.3193. DOI: 10.48550/arXiv.1110.3193. arXiv: 1110.3193 [astro-ph.CO].

Leavitt, Henrietta S. and Edward C. Pickering (Mar. 1912). "Periods of 25 Variable Stars in the Small Magellanic Cloud." In: *Harvard College Observatory Circular* 173, pp. 1–3.

Lee, Brian C. et al. (Apr. 2004). "A Catalog of Compact Groups of Galaxies in the SDSS Commissioning Data". In: *AJ* 127.4, pp. 1811–1859. DOI: 10.1086/382236. arXiv: astro-ph/0312553 [astro-ph].

Lesci, G. F. et al. (Sept. 2022). "AMICO galaxy clusters in KiDS-DR3: Constraints on cosmological parameters and on the normalisation of the mass-richness relation from clustering". In: *A&A* 665, A100, A100. DOI: 10.1051/0004-6361/202243538. arXiv: 2203.07398 [astro-ph.CO].

Lesci, G. F. et al. (July 2025). "AMICO galaxy clusters in KiDS-1000: cosmological constraints and mass calibration from counts and weak lensing". In: *arXiv e-prints*, arXiv:2507.14285, arXiv:2507.14285. DOI: 10.48550/arXiv.2507.14285. arXiv: 2507.14285 [astro-ph.CO].

Lewis, Aaron D. et al. (Feb. 2002). "New X-Ray Clusters in the Einstein Extended Medium-Sensitivity Survey. I. Modifications to the X-Ray Luminosity Function". In: *ApJ* 566.2, pp. 744–770. DOI: 10.1086/324139. arXiv: astro-ph/0110156 [astro-ph].

Li, I. H. and H. K. C. Yee (Mar. 2008). "Finding Galaxy Groups in Photometric-Redshift Space: The Probability Friends-of-Friends Algorithm". In: *AJ* 135.3, pp. 809–822. DOI: 10.1088/0004-6256/135/3/809. arXiv: 0801.2410 [astro-ph].

Li, I. H. et al. (Apr. 2012). "Evolution of Group Galaxies from the First Red-Sequence Cluster Survey". In: *ApJ* 749.2, 150, p. 150. DOI: 10.1088/0004-637X/749/2/150. arXiv: 1202.4767 [astro-ph.CO].

Li, Qingyang et al. (July 2022). "Groups and Protocluster Candidates in the CLAUDS and HSC-SSP Joint Deep Surveys". In: *ApJ* 933.1, 9, p. 9. DOI: 10.3847/1538-4357/ac6e69. arXiv: 2205.05517 [astro-ph.CO].

Licitra, Rossella et al. (Sept. 2016a). "The Next Generation Virgo Cluster Survey. XX. RedGOLD Background Galaxy Cluster Detections". In: *ApJ* 829.1, 44, p. 44. DOI: 10.3847/0004-637X/829/1/44.

Licitra, Rossella et al. (Jan. 2016b). "The RedGOLD cluster detection algorithm and its cluster candidate catalogue for the CFHT-LS W1". In: *MNRAS* 455.3, pp. 3020–3041. DOI: 10.1093/mnras/stv2309.

Lidman, Christopher E. and Bruce A. Peterson (Dec. 1996). "An Optically Based Search for Distant Galaxy Clusters". In: *AJ* 112, p. 2454. DOI: 10.1086/118195.

Lim, S. H. et al. (Sept. 2017). "Galaxy groups in the low-redshift Universe". In: *MNRAS* 470.3, pp. 2982–3005. DOI: 10.1093/mnras/stx1462. arXiv: 1706.02307 [astro-ph.GA].

Linde, A. D. (Feb. 1982). "A new inflationary universe scenario: A possible solution of the horizon, flatness, homogeneity, isotropy and primordial monopole problems". In: *Physics Letters B* 108.6, pp. 389–393. DOI: 10.1016/0370-2693(82)91219-9.

Liu, A. et al. (May 2022). "The eROSITA Final Equatorial-Depth Survey (eFEDS). Catalog of galaxy clusters and groups". In: *A&A* 661, A2, A2. DOI: 10.1051/0004-6361/202141120. arXiv: 2106.14518 [astro-ph.CO].

Liu, Ang et al. (May 2020). "The chemical evolution of galaxy clusters: Dissecting the iron mass budget of the intracluster medium". In: *A&A* 637, A58, A58. DOI: 10.1051/0004-6361/202037506. arXiv: 2003.12426 [astro-ph.GA].

Liu, Teng et al. (Feb. 2015). "The Swift X-Ray Telescope Cluster Survey. III. Cluster Catalog from 2005-2012 Archival Data". In: *ApJS* 216.2, 28, p. 28. DOI: 10.1088/0067-0049/216/2/28. arXiv: 1503.04051 [astro-ph.CO].

Lloyd-Davies, E. J. et al. (Nov. 2011). "The XMM Cluster Survey: X-ray analysis methodology". In: *MNRAS* 418.1, pp. 14–53. DOI: 10.1111/j.1365-2966.2011.19117.x. arXiv: 1010.0677 [astro-ph.CO].

Lobo, C. et al. (Aug. 2000). "EISily looking for distant clusters of galaxies - a new algorithm and its application to the EIS-wide data". In: *A&A* 360, pp. 896–910. DOI: 10.48550/arXiv.astro-ph/0006431. arXiv: astro-ph/0006431 [astro-ph].

Lopes, P. A. A. et al. (Sept. 2004). "The Northern Sky Optical Cluster Survey. IV. An Intermediate-Redshift Galaxy Cluster Catalog and the Comparison of Two Detection Algorithms". In: *AJ* 128.3, pp. 1017–1045. DOI: 10.1086/423038.

Louis, Thibaut et al. (Mar. 2025). "The Atacama Cosmology Telescope: DR6 Power Spectra, Likelihoods and ΛCDM Parameters". In: *arXiv e-prints*, arXiv:2503.14452, arXiv:2503.14452. DOI: 10.48550/arXiv.2503.14452. arXiv: 2503.14452 [astro-ph.CO].

Lovisari, Lorenzo et al. (May 2021). "Scaling Properties of Galaxy Groups". In: *Universe* 7.5, 139, p. 139. DOI: 10.3390/universe7050139. arXiv: 2106.13256 [astro-ph.CO].

Lu, Yi et al. (Nov. 2016). "Galaxy Groups in the 2Mass Redshift Survey". In: *ApJ* 832.1, 39, p. 39. DOI: 10.3847/0004-637X/832/1/39. arXiv: 1607.03982 [astro-ph.GA].

Lugger, P. M. (May 1978). "High-galactic-latitude X-ray sources and southern clusters of galaxies." In: *ApJ* 221, pp. 745–755. DOI: 10.1086/156078.

Lumsden, S. L. et al. (Sept. 1992). "The Edinburgh-Durham southern galaxy catalogue. IV. Thecluster catalogue." In: *MNRAS* 258, pp. 1–22. DOI: 10.1093/mnras/258.1.1.

Lutz, D. et al. (Aug. 2011). "PACS Evolutionary Probe (PEP) - A Herschel key program". In: *A&A* 532, A90, A90. DOI: 10.1051/0004-6361/201117107. arXiv: 1106.3285 [astro-ph.CO].

Ma, Juntao et al. (May 2025). "A Widely Applicable Galaxy Group Finder Using Machine Learning: Application to SDSS DR13". In: *Research in Astronomy and Astrophysics* 25.5, 055020, p. 055020. DOI: 10.1088/1674-4527/adcf85.

MacGillivray, H. T. et al. (Sept. 1976). "Studies of clusters of galaxies using measurements by COSMOS-1. Properties of six rich southern clusters". In: *MNRAS* 176, pp. 649–666. DOI: 10.1093/mnras/176.3.649.

Macías-Pérez, J. F. et al. (Nov. 2024). "KISS: Instrument Description and Performance". In: *PASP* 136.11, 114505, p. 114505. DOI: 10.1088/1538-3873/ad8189. arXiv: 2409.20272 [astro-ph.IM].

Madhavacheril, Mathew S. et al. (Feb. 2024). "The Atacama Cosmology Telescope: DR6 Gravitational Lensing Map and Cosmological Parameters". In: *ApJ* 962.2, 113, p. 113. DOI: 10.3847/1538-4357/acff5f. arXiv: 2304.05203 [astro-ph.CO].

Magnelli, B. et al. (Mar. 2012). "A Herschel view of the far-infrared properties of submillimetre galaxies". In: *A&A* 539, A155, A155. DOI: 10.1051/0004-6361/201118312. arXiv: 1202.0761 [astro-ph.CO].

Magnelli, B. et al. (May 2019). "The IRAM/GISMO 2 mm Survey in the COSMOS Field". In: *ApJ* 877.1, 45, p. 45. DOI: 10.3847/1538-4357/ab1912. arXiv: 1904.10006 [astro-ph.GA].

Mahdavi, Andisheh et al. (May 2000). "The RASSCALS: An X-Ray and Optical Study of 260 Galaxy Groups". In: *ApJ* 534.1, pp. 114–132. DOI: 10.1086/308740. arXiv: astro-ph/9912121 [astro-ph].

Maia, M. A. G. et al. (Apr. 1989). "A Catalog of Southern Groups of Galaxies". In: *ApJS* 69, p. 809. DOI: 10.1086/191328.

Makarov, Dmitry and Igor Karachentsev (Apr. 2011). "Galaxy groups and clouds in the local (z~ 0.01) Universe". In: *MNRAS* 412.4, pp. 2498–2520. DOI: 10.1111/j.1365-2966.2010.18071.x. arXiv: 1011.6277 [astro-ph.CO].

Mann, Andrew W. and Harald Ebeling (Mar. 2012). "X-ray-optical classification of cluster mergers and the evolution of the cluster merger fraction". In: *MNRAS* 420.3, pp. 2120–2138. DOI: 10.1111/j.1365-2966.2011.20170.x. arXiv: 1111.2396 [astro-ph.CO].

Mantz, A. et al. (Aug. 2010). "The observed growth of massive galaxy clusters - II. X-ray scaling relations". In: *MNRAS* 406.3, pp. 1773–1795. DOI: 10.1111/j.1365-2966.2010.16993.x. arXiv: 0909.3099 [astro-ph.CO].

Marriage, Tobias A. et al. (Aug. 2011). "The Atacama Cosmology Telescope: Sunyaev-Zel'dovich-Selected Galaxy Clusters at 148 GHz in the 2008 Survey". In: *ApJ* 737.2, 61, p. 61. DOI: 10.1088/0004-637X/737/2/61. arXiv: 1010.1065 [astro-ph.CO].

Materne, J. (Feb. 1978). "The structure of nearby clusters of galaxies. Hierarchical clustering and an application to the Leo region." In: *A&A* 63, pp. 401–409.

Mather, J. C. (Aug. 1982). "The Cosmic Background Explorer (COBE)." In: *Optical Engineering* 21, pp. 769–774. DOI: 10.1117/12.7972975.

Mather, J. C. et al. (Feb. 1999). "Calibrator Design for the COBE Far-Infrared Absolute Spectrophotometer (FIRAS)". In: *ApJ* 512.2, pp. 511–520. DOI: 10.1086/306805. arXiv: astro-ph/9810373 [astro-ph].

Maturi, M. et al. (Oct. 2023). "The miniJPAS survey. Cluster and galaxy group detections with AMICO". In: *A&A* 678, A145, A145. DOI: 10.1051/0004-6361/202245323. arXiv: 2307.06412 [astro-ph.CO].

Maturi, Matteo et al. (May 2019). "AMICO galaxy clusters in KiDS-DR3: sample properties and selection function". In: *MNRAS* 485.1, pp. 498–512. DOI: 10.1093/mnras/stz294. arXiv: 1810.02811 [astro-ph.CO].

Mayet, F. et al. (June 2020). "Cluster cosmology with the NIKA2 SZ Large Program". In: *mm Universe NIKA2 - Observing the mm Universe with the NIKA2 Camera*. Vol. 228. European Physical Journal Web of Conferences, 00017, p. 00017. DOI: 10.1051/epjconf/202022800017. arXiv: 1911.03145 [astro-ph.CO].

McClintock, T. et al. (Jan. 2019). "Dark Energy Survey Year 1 results: weak lensing mass calibration of redMaPPer galaxy clusters". In: *MNRAS* 482.1, pp. 1352–1378. DOI: 10.1093/mnras/sty2711. arXiv: 1805.00039 [astro-ph.CO].

McConnachie, Alan W. et al. (May 2009). "Compact groups in theory and practice - III. Compact groups of galaxies in the Sixth Data Release of the Sloan Digital Sky Survey". In: *MNRAS* 395.1, pp. 255–268. DOI: 10.1111/j.1365-2966.2008.14340.x. arXiv: 0812.1580 [astro-ph].

McGee, Sean L. et al. (Dec. 2009). "The accretion of galaxies into groups and clusters". In: *MNRAS* 400.2, pp. 937–950. DOI: 10.1111/j.1365-2966.2009.15507.x. arXiv: 0908.0750 [astro-ph.CO].

McHardy, I. M. et al. (Dec. 1981). "The Ariel V (3A) catalogue of X-ray sources. II." In: *MNRAS* 197, pp. 893–919. DOI: 10.1093/mnras/197.4.893.

McHardy, I. (Sept. 1978). "X-ray sources in clusters of galaxies." In: *MNRAS* 184, pp. 783–799. DOI: 10.1093/mnras/184.4.783.

McIntosh, Avery (June 2016). "The Jackknife Estimation Method". In: *arXiv e-prints*, arXiv:1606.00497, arXiv:1606.00497. DOI: 10.48550/arXiv.1606.00497. arXiv: 1606.00497 [stat.ME].

Mehrtens, Nicola et al. (June 2012). "The XMM Cluster Survey: optical analysis methodology and the first data release". In: *MNRAS* 423.2, pp. 1024–1052. DOI: 10.1111/j.1365-2966.2012.20931.x. arXiv: 1106.3056 [astro-ph.CO].

Melin, J. B. et al. (Nov. 2006). "Catalog extraction in SZ cluster surveys: a matched filter approach". In: *A&A* 459.2, pp. 341–352. DOI: 10.1051/0004-6361:20065034. arXiv: astro-ph/0602424 [astro-ph].

Melin, J. B. et al. (Dec. 2012). "A comparison of algorithms for the construction of SZ cluster catalogues". In: *A&A* 548, A51, A51. DOI: 10.1051/0004-6361/201015689. arXiv: 1210.1416 [astro-ph.CO].

Melin, J. B. et al. (Mar. 2021). "PSZSPT: A joint Planck and SPT-SZ cluster catalog". In: *A&A* 647, A106, A106. DOI: 10.1051/0004-6361/202039471. arXiv: 2009.08822 [astro-ph.CO].

Menanteau, Felipe et al. (Dec. 2010a). "Southern Cosmology Survey. II. Massive Optically Selected Clusters from 70 Square Degrees of the Sunyaev-Zel'dovich Effect Common Survey Area". In: *ApJS* 191.2, pp. 340–351. DOI: 10.1088/0067-0049/191/2/340. arXiv: 1002.2226 [astro-ph.CO].

Menanteau, Felipe et al. (Nov. 2010b). "The Atacama Cosmology Telescope: Physical Properties and Purity of a Galaxy Cluster Sample Selected via the Sunyaev-Zel'dovich Effect". In: *ApJ* 723.2, pp. 1523–1541. DOI: 10.1088/0004-637X/723/2/1523. arXiv: 1006.5126 [astro-ph.CO].

Merchán, Manuel E. and Ariel Zandivarez (Sept. 2005). "Galaxy Groups in the Third Data Release of the Sloan Digital Sky Survey". In: *ApJ* 630.2, pp. 759–763. DOI: 10.1086/427989. arXiv: astro-ph/0412257 [astro-ph].

Merchán, Manuel and Ariel Zandivarez (Sept. 2002). "Galaxy groups in the 2dF Galaxy Redshift Survey: the catalogue". In: *MNRAS* 335.1, pp. 216–222. DOI: 10.1046/j.1365-8711.2002.05623.x. arXiv: astro-ph/0204493 [astro-ph].

Merloni, A. et al. (Sept. 2012). "eROSITA Science Book: Mapping the Structure of the Energetic Universe". In: *arXiv e-prints*, arXiv:1209.3114, arXiv:1209.3114. DOI: 10.48550/arXiv.1209.3114. arXiv: 1209.3114 [astro-ph.HE].

Merloni, A. et al. (Feb. 2024). "The SRG/eROSITA all-sky survey. First X-ray catalogues and data release of the western Galactic hemisphere". In: *A&A* 682, A34, A34. DOI: 10.1051/0004-6361/202347165. arXiv: 2401.17274 [astro-ph.HE].

Messier, Charles (Jan. 1781). *Catalogue des Nébuleuses et des Amas d'Étoiles (Catalog of Nebulae and Star Clusters)*. Connoissance des Temps ou des Mouvements Célestes, for 1784, p. 227-267.

Milkeraitis, M. et al. (July 2010). "3D-Matched-Filter galaxy cluster finder - I. Selection functions and CFHTLS Deep clusters". In: *MNRAS* 406.1, pp. 673–688. DOI: 10.1111/j.1365-2966.2010.16720.x. arXiv: 0912.0739 [astro-ph.CO].

Miller, Christopher J. et al. (Sept. 2005). "The C4 Clustering Algorithm: Clusters of Galaxies in the Sloan Digital Sky Survey". In: *AJ* 130.3, pp. 968–1001. DOI: 10.1086/431357. arXiv: astro-ph/0503713 [astro-ph].

Minamidani, Tetsuhiro et al. (July 2016). "Development of the new multi-beam 100 GHz band SIS receiver FOREST for the Nobeyama 45-m Telescope". In: *Millimeter, Submillimeter, and Far-Infrared Detectors and Instrumentation for Astronomy VIII*. Ed. by Wayne S. Holland and Jonas Zmuidzinas. Vol. 9914. Society of Photo-Optical Instrumentation Engineers (SPIE) Conference Series, 99141Z, 99141Z. DOI: 10.1117/12.2232137.

Miyatake, Hironao (May 2025). "Cosmology with Galaxy Clusters". In: *arXiv e-prints*, arXiv:2505.07697, arXiv:2505.07697. DOI: 10.48550/arXiv.2505.07697. arXiv: 2505.07697 [astro-ph.CO].

Miyazaki, Satoshi et al. (Nov. 2007). "A Subaru Weak-Lensing Survey. I. Cluster Candidates and Spectroscopic Verification". In: *ApJ* 669.2, pp. 714–728. DOI: 10.1086/521621. arXiv: 0707.2249 [astro-ph].

Moffett, Amanda J. et al. (Oct. 2015). "ECO and RESOLVE: Galaxy Disk Growth in Environmental Context". In: *ApJ* 812.2, 89, p. 89. DOI: 10.1088/0004-637X/812/2/89. arXiv: 1508.00948 [astro-ph.GA].

Monfardini, A. et al. (June 2011). "A Dual-band Millimeter-wave Kinetic Inductance Camera for the IRAM 30 m Telescope". In: *ApJS* 194.2, 24, p. 24. DOI: 10.1088/0067-0049/194/2/24. arXiv: 1102.0870 [astro-ph.IM].

Monfardini, A. et al. (Sept. 2014). "Latest NIKA Results and the NIKA-2 Project". In: *Journal of Low Temperature Physics* 176.5-6, pp. 787–795. DOI: 10.1007/s10909-013-0985-4. arXiv: 1310.1230 [astro-ph.IM].

Moretti, A. et al. (Dec. 2004). "The Brera Multi-scale Wavelet HRI Cluster Survey. I. Selection of the sample and number counts". In: *A&A* 428, pp. 21–37. DOI: 10.1051/0004-6361:20041326. arXiv: astro-ph/0408131 [astro-ph].

Morgan, W. W. et al. (Aug. 1975). "cD galaxies in poor clusters." In: *ApJ* 199, pp. 545–548. DOI: 10.1086/153721.

Morrison, Glenn E. et al. (May 2010). "Very Large Array 1.4 GHz Observations of the GOODS-North Field: Data Reduction and Analysis". In: *ApJS* 188.1, pp. 178–186. DOI: 10.1088/0067-0049/188/1/178. arXiv: 1004.1671 [astro-ph.CO].

Moyer-Anin, A. et al. (in prep.). "NIKA2 LPSZ Results V. The scaling relation between SZ observables and the hydrostatic equilibrium masses". In.

Mroczkowski, Tony et al. (Feb. 2019). "Astrophysics with the Spatially and Spectrally Resolved Sunyaev-Zeldovich Effects. A Millimetre/Submillimetre Probe of the Warm and Hot Universe". In: *Space Sci. Rev.* 215.1, 17, p. 17. DOI: 10.1007/s11214-019-0581-2. arXiv: 1811.02310 [astro-ph.CO].

Muñoz-Echeverría, M. et al. (Mar. 2023). "Multi-probe analysis of the galaxy cluster CL J1226.9+3332. Hydrostatic mass and hydrostatic-to-lensing bias". In: *A&A* 671, A28, A28. DOI: 10.1051/0004-6361/202244981. arXiv: 2209.07460 [astro-ph.CO].

Mullis, C. R. et al. (Sept. 2003). "The 160 Square Degree ROSAT Survey: The Revised Catalog of 201 Clusters with Spectroscopic Redshifts". In: *ApJ* 594.1, pp. 154–171. DOI: 10.1086/376866. arXiv: astro-ph/0305228 [astro-ph].

Murayama, Yosuke (Sept. 2022). "Development of 109-pixel MKID arrays for the 100-GHz band continuum camera". Theses.

Murphy, D. N. A. et al. (Mar. 2012). "ORCA: The Overdense Red-sequence Cluster Algorithm". In: *MNRAS* 420.3, pp. 1861–1881. DOI: 10.1111/j.1365-2966.2011.19782.x. arXiv: 1109.3182 [astro-ph.CO].

Muzzin, Adam et al. (Oct. 2008). "The Evolution of Dusty Star Formation and Stellar Mass Assembly in Clusters: Results from the IRAC 3.6, 4.5, 5.8, and 8.0 μm Cluster Luminosity Functions". In: *ApJ* 686.2, pp. 966–994. DOI: 10.1086/591542. arXiv: 0807.0227 [astro-ph].

Nagai, Daisuke et al. (Oct. 2007). "Effects of Galaxy Formation on Thermodynamics of the Intracluster Medium". In: *ApJ* 668.1, pp. 1–14. DOI: 10.1086/521328. arXiv: astro-ph/0703661 [astro-ph].

Nagai, M. et al. (Nov. 2022). "Configuration of Probe Tones for MKID Readout with Frequency Sweeping Scheme". In: *Journal of Low Temperature Physics* 209. Publisher: Springer ADS Bibcode: 2022JLTP..209..677N, pp. 677–685. ISSN: 1063-777X0022-2291. DOI: 10.1007/s10909-022-02865-y. URL: https://ui.adsabs.harvard.edu/abs/2022JLTP..209..677N.

Navarro, Julio F. et al. (May 1996). "The Structure of Cold Dark Matter Halos". In: *ApJ* 462, p. 563. DOI: 10.1086/177173. arXiv: astro-ph/9508025 [astro-ph].

Nolthenius, Richard (Mar. 1993). "A Revised Catalog of CfA1 Galaxy Groups in the Virgo/Great Attractor Flow Field". In: *ApJS* 85, p. 1. DOI: 10.1086/191753.

Oguri, Masamune (Oct. 2014). "A cluster finding algorithm based on the multiband identification of red sequence galaxies". In: *MNRAS* 444.1, pp. 147–161. DOI: 10.1093/mnras/stu1446. arXiv: 1407.4693 [astro-ph.CO].

Oguri, Masamune et al. (Jan. 2018). "An optically-selected cluster catalog at redshift 0.1 ¡ z ¡ 1.1 from the Hyper Suprime-Cam Subaru Strategic Program S16A data". In: *PASJ* 70, S20, S20. DOI: 10.1093/pasj/psx042. arXiv: 1701.00818 [astro-ph.CO].

Oliver, S. J. et al. (Aug. 2012). "The Herschel Multi-tiered Extragalactic Survey: HerMES". In: *MNRAS* 424.3, pp. 1614–1635. DOI: 10.1111/j.1365-2966.2012.20912.x. arXiv: 1203.2562 [astro-ph.CO].

Olsen, L. F. et al. (Jan. 2007). "Galaxy clusters in the CFHTLS: First matched filter candidate catalogue of the Deepfields". In: *Astronomy & Astrophysics* 461.1, pp. 81–93. ISSN: 0004-6361, 1432-0746. DOI: 10.1051/0004-6361:20066088. URL: http://www.aanda.org/10.1051/0004-6361:20066088.

Oppenheimer, B. R. et al. (June 1997). "A Survey of the Einstein IPC Database for Extended X-Ray Sources". In: *AJ* 113, pp. 2134–2146. DOI: 10.1086/118425.

Ostrander, E. J. et al. (Dec. 1998). "The Hubble Space Telescope Medium Deep Survey Cluster Sample: Methodology and Data". In: *AJ* 116.6, pp. 2644–2658. DOI: 10.1086/300627. arXiv: astro-ph/9808304 [astro-ph].

Pacaud, F. et al. (June 2016). "The XXL Survey. II. The bright cluster sample: catalogue and luminosity function". In: *A&A* 592, A2, A2. DOI: 10.1051/0004-6361/201526891. arXiv: 1512.04264 [astro-ph.CO].

Pacaud, F. et al. (Nov. 2018). "The XXL Survey. XXV. Cosmological analysis of the C1 cluster number counts". In: *A&A* 620, A10, A10. DOI: 10.1051/0004-6361/201834022. arXiv: 1810.01624 [astro-ph.CO].

Paliwal, A. et al. (June 2024). "3D scaling laws and projection effects in The300-NIKA2 Sunyaev-Zeldovich Large Program Twin Samples". In: *mm Universe 2023 - Observing the Universe at mm Wavelengths*. Vol. 293. European Physical Journal Web of Conferences, 00037, p. 00037. DOI: 10.1051/epjconf/202429300037. arXiv: 2404.03376 [astro-ph.CO].

Paliwal, A. et al. (June 2025). "Exploiting high-resolution NIKA2 data to study the intracluster medium and dynamical state of ACT-CL J0240.0+0116". In: *A&A* 698, A2, A2. DOI: 10.1051/0004-6361/202452597. arXiv: 2410.11668 [astro-ph.CO].

Panko, E. and P. Flin (Dec. 2006). "A Catalogue of Galaxy Clusters and Groups Based on the Muenster Red Sky Survey". In: *Journal of Astronomical Data* 12, p. 1.

Pardo, J.R. et al. (2001). "Atmospheric transmission at microwaves (ATM): an improved model for millimeter/submillimeter applications". In: *IEEE Transactions on Antennas and Propagation* 49.12, pp. 1683–1694. DOI: 10.1109/8.982447.

Pariiskii, Yu. N. (June 1973). "Detection of Hot Gas in the Coma Cluster of Galaxies." In: *Soviet Ast.* 16, p. 1048.

Paterno-Mahler, R. et al. (July 2017). "The High-redshift Clusters Occupied by Bent Radio AGN (COBRA) Survey: The Spitzer Catalog". In: *ApJ* 844.1, 78, p. 78. DOI: 10.3847/1538-4357/aa7b89. arXiv: 1611.00746 [astro-ph.GA].

Paul, S. et al. (Oct. 2017). "Understanding 'galaxy groups' as a unique structure in the universe". In: *MNRAS* 471.1, pp. 2–11. DOI: 10.1093/mnras/stx1488. arXiv: 1706.01916 [astro-ph.CO].

Penzias, A. A. and R. W. Wilson (July 1965). "A Measurement of Excess Antenna Temperature at 4080 Mc/s." In: *ApJ* 142, pp. 419–421. DOI: 10.1086/148307.

Perera, T. A. et al. (Dec. 2008). "An AzTEC 1.1mm survey of the GOODS-N field - I. Maps, catalogue and source statistics". In: *MNRAS* 391.3, pp. 1227–1238. DOI: 10.1111/j.1365-2966.2008.13902.x. arXiv: 0806.3791 [astro-ph].

Perlman, Eric S. et al. (June 2002). "The WARPS Survey. VI. Galaxy Cluster and Source Identifications from Phase I". In: *ApJS* 140.2, pp. 265–301. DOI: 10.1086/339685. arXiv: astro-ph/0112190 [astro-ph].

Perotto, L. et al. (May 2020). "Calibration and performance of the NIKA2 camera at the IRAM 30-m Telescope". In: *A&A* 637, A71, A71. DOI: 10.1051/0004-6361/201936220. arXiv: 1910.02038 [astro-ph.IM].

Pfeffermann, E. et al. (Jan. 1987). "The focal plane instrumentation of the ROSAT Telescope". In: *Soft X-ray optics and technology*. Ed. by E. Koch and Guenther A. Schmahl. Vol. 733. Society of Photo-Optical Instrumentation Engineers (SPIE) Conference Series, p. 519.

Piccinotti, G. et al. (Feb. 1982). "A complete X-ray sample of the high-latitude (b)-20 sky from HEAO 1 A-2 : log N-log S and luminosity functions." In: *ApJ* 253, pp. 485–503. DOI: 10.1086/159651.

Pierre, M. et al. (Oct. 1994a). "Optical observations of a ROSAT sample of clusters of galaxies. I. Techniques and X-ray/optical analysis". In: *A&A* 290, pp. 725–752.

— (Oct. 1994b). "Optical observations of a ROSAT sample of clusters of galaxies. I. Techniques and X-ray/optical analysis". In: *A&A* 290, pp. 725–752.

Piffaretti, R. et al. (Oct. 2011). "The MCXC: a meta-catalogue of x-ray detected clusters of galaxies". In: *A&A* 534, A109, A109. DOI: 10.1051/0004-6361/201015377. arXiv: 1007.1916 [astro-ph.CO].

Pilbratt, G. L. et al. (July 2010). "Herschel Space Observatory. An ESA facility for far-infrared and submillimetre astronomy". In: *A&A* 518, L1, p. L1. DOI: 10.1051/0004-6361/201014759. arXiv: 1005.5331 [astro-ph.IM].

Planck Collaboration et al. (Dec. 2011a). "Planck early results. VIII. The all-sky early Sunyaev-Zeldovich cluster sample". In: *A&A* 536, A8, A8. DOI: 10.1051/0004-6361/201116459. arXiv: 1101.2024 [astro-ph.CO].

Planck Collaboration et al. (Dec. 2011b). "Planck early results. XI. Calibration of the local galaxy cluster Sunyaev-Zeldovich scaling relations". In: *A&A* 536, A11, A11. DOI: 10.1051/0004-6361/201116458. arXiv: 1101.2026 [astro-ph.CO].

Planck Collaboration et al. (Feb. 2013). "Planck intermediate results. VII. Statistical properties of infrared and radio extragalactic sources from the Planck Early Release Compact Source Catalogue at frequencies between 100 and 857 GHz". In: *A&A* 550, A133, A133. DOI: 10.1051/0004-6361/201220053. arXiv: 1207.4706 [astro-ph.CO].

Planck Collaboration et al. (Nov. 2014a). "Planck 2013 results. XX. Cosmology from Sunyaev-Zeldovich cluster counts". In: *A&A* 571, A20, A20. DOI: 10.1051/0004-6361/201321521. arXiv: 1303.5080 [astro-ph.CO].

Planck Collaboration et al. (Nov. 2014b). "Planck 2013 results. XXIX. The Planck catalogue of Sunyaev-Zeldovich sources". In: *A&A* 571, A29, A29. DOI: 10.1051/0004-6361/201321523. arXiv: 1303.5089 [astro-ph.CO].

Planck Collaboration et al. (Sept. 2016a). "Planck 2015 results. XXII. A map of the thermal Sunyaev-Zeldovich effect". In: *A&A* 594, A22, A22. DOI: 10.1051/0004-6361/201525826. arXiv: 1502.01596 [astro-ph.CO].

Planck Collaboration et al. (Sept. 2016b). "Planck 2015 results. XXVI. The Second Planck Catalogue of Compact Sources". In: *A&A* 594, A26, A26. DOI: 10.1051/0004-6361/201526914. arXiv: 1507.02058 [astro-ph.CO].

Planck Collaboration et al. (Sept. 2016c). "Planck 2015 results. XXVII. The second Planck catalogue of Sunyaev-Zeldovich sources". In: *A&A* 594, A27, A27. DOI: 10.1051/0004-6361/201525823. arXiv: 1502.01598 [astro-ph.CO].

Planck Collaboration et al. (Nov. 2017). "Planck intermediate results. LII. Planet flux densities". In: *A&A* 607, A122, A122. DOI: 10.1051/0004-6361/201630311. arXiv: 1612.07151 [astro-ph.EP].

Planck Collaboration et al. (Sept. 2020a). "Planck 2018 results. I. Overview and the cosmological legacy of Planck". In: *A&A* 641, A1, A1. DOI: 10.1051/0004-6361/201833880. arXiv: 1807.06205 [astro-ph.CO].

Planck Collaboration et al. (Sept. 2020b). "Planck 2018 results. VI. Cosmological parameters". In: *A&A* 641, A6, A6. DOI: 10.1051/0004-6361/201833910. arXiv: 1807.06209 [astro-ph.CO].

Plionis, Manolis et al. (Apr. 1991). "Projected and intrinsic shapes of galaxy clusters." In: *MNRAS* 249, p. 662. DOI: 10.1093/mnras/249.4.662.

Poglitsch, A. et al. (July 2010). "The Photodetector Array Camera and Spectrometer (PACS) on the Herschel Space Observatory". In: *A&A* 518, L2, p. L2. DOI: 10.1051/0004-6361/201014535. arXiv: 1005.1487 [astro-ph.IM].

Pointecouteau, E. et al. (May 2002). "SZ and X-ray combined analysis of a distant galaxy cluster, RX J2228+2037." In: *A&A* 387, pp. 56–62. DOI: 10.1051/0004-6361:20020394. arXiv: astro-ph/0203268 [astro-ph].

Ponthieu, N. et al. (2025). "NIKA2 Cosmological Legacy Survey: First measure of the confusion noise at the IRAM 30 m telescope". In: *in prep.*

Popesso, P. et al. (Aug. 2004). "RASS-SDSS Galaxy clusters survey. I. The catalog and the correlation of X-ray and optical properties". In: *A&A* 423, pp. 449–467. DOI: 10.1051/0004-6361:20035818. arXiv: astro-ph/0403354 [astro-ph].

Popesso, P. et al. (Feb. 2023). "The main sequence of star-forming galaxies across cosmic times". In: *MNRAS* 519.1, pp. 1526–1544. DOI: 10.1093/mnras/stac3214. arXiv: 2203.10487 [astro-ph.GA].

Postman, Marc et al. (Feb. 1996). "The Palomar Distant Clusters Survey. I. The Cluster Catalog". In: *AJ* 111, p. 615. DOI: 10.1086/117811. arXiv: astro-ph/9511011 [astro-ph].

Postman, Marc et al. (Nov. 2002). "The KPNO/Deeprange Distant Cluster Survey. I. The Catalog and the Space Density of Intermediate-Redshift Clusters". In: *ApJ* 579.1, pp. 93–126. DOI: 10.1086/342725. arXiv: astro-ph/0205513 [astro-ph].

Postman, Marc et al. (Apr. 2012). "The Cluster Lensing and Supernova Survey with Hubble: An Overview". In: *ApJS* 199.2, 25, p. 25. DOI: 10.1088/0067-0049/199/2/25. arXiv: 1106.3328 [astro-ph.CO].

Poudel, A. et al. (May 2016). "Multifrequency studies of galaxies and groups. I. Environmental effect on galaxy stellar mass and morphology". In: *A&A* 590, A29, A29. DOI: 10.1051/0004-6361/201526851. arXiv: 1603.01773 [astro-ph.GA].

Prandoni, I. et al. (Apr. 1994). "Automated Search For Compact Groups of Galaxies in The Southern Sky". In: *AJ* 107, p. 1235. DOI: 10.1086/116936.

Pratt, G. W. et al. (May 2009). "Galaxy cluster X-ray luminosity scaling relations from a representative local sample (REXCESS)". In: *A&A* 498.2, pp. 361–378. DOI: 10.1051/0004-6361/200810994. arXiv: 0809.3784 [astro-ph].

Pratt, G. W. et al. (Feb. 2010). "Gas entropy in a representative sample of nearby X-ray galaxy clusters (REXCESS): relationship to gas mass fraction". In: *A&A* 511, A85, A85. DOI: 10.1051/0004-6361/200913309. arXiv: 0909.3776 [astro-ph.CO].

Pratt, N. M. et al. (Dec. 1975). "The Cosmos Facility at the Royal Observatory Edinburgh". In: *Image Processing Techniques in Astronomy*. Ed. by C. de Jager and H. Nieuwenhuijzen. Vol. 54. Astrophysics and Space Science Library, p. 217. DOI: 10.1007/978-94-010-1881-4_25.

Press, William H. and Paul Schechter (Feb. 1974). "Formation of Galaxies and Clusters of Galaxies by Self-Similar Gravitational Condensation". In: *ApJ* 187, pp. 425–438. DOI: 10.1086/152650.

Quintana, H. and R. A. White (Nov. 1990). "A Partial List of Southern Clusters of Galaxies". In: *Ap&SS* 173.2, pp. 265–292. DOI: 10.1007/BF00643936.

Rabitz, A. et al. (Nov. 2017). "Distant clusters of galaxies in the 2XMM/SDSS footprint: follow-up observations with the LBT". In: *A&A* 607, A56, A56. DOI: 10.1051/0004-6361/201731128. arXiv: 1709.02436 [astro-ph.CO].

Radovich, M. et al. (Feb. 2017). "Searching for galaxy clusters in the Kilo-Degree Survey". In: *A&A* 598, A107, A107. DOI: 10.1051/0004-6361/201629353. arXiv: 1701.02954 [astro-ph.CO].

Ramella, M. et al. (Feb. 1999). "The ESO slice project (ESP) galaxy redshift survey VI. Groups of galaxies". In: *A&A* 342, pp. 1–14. DOI: 10.48550/arXiv.astro-ph/9811150. arXiv: astro-ph/9811150 [astro-ph].

Ramella, M. et al. (Mar. 2001). "Finding galaxy clusters using Voronoi tessellations". In: *A&A* 368, pp. 776–786. DOI: 10.1051/0004-6361:20010071. arXiv: astro-ph/0101411 [astro-ph].

Ramella, Massimo et al. (Sept. 1989). "Groups of Galaxies in the Center for Astrophysics Redshift Survey". In: *ApJ* 344, p. 57. DOI: 10.1086/167777.

Ramella, Massimo et al. (Feb. 1997). "Groups of Galaxies in the Northern CfA Redshift Survey". In: *AJ* 113, p. 483. DOI: 10.1086/118270.

Ramella, Massimo et al. (June 2002). "The UZC-SSRS2 Group Catalog". In: *AJ* 123.6, pp. 2976–2984. DOI: 10.1086/340357. arXiv: astro-ph/0202326 [astro-ph].

Reese, Erik D. et al. (Dec. 2002). "Determining the Cosmic Distance Scale from Interferometric Measurements of the Sunyaev-Zeldovich Effect". In: *ApJ* 581.1, pp. 53–85. DOI: 10.1086/344137. arXiv: astro-ph/0205350 [astro-ph].

Reichardt, C. L. et al. (Feb. 2013). "Galaxy Clusters Discovered via the Sunyaev-Zel'dovich Effect in the First 720 Square Degrees of the South Pole Telescope Survey". In: *ApJ* 763.2, 127, p. 127. DOI: 10.1088/0004-637X/763/2/127. arXiv: 1203.5775 [astro-ph.CO].

Rengelink, R. B. et al. (Aug. 1997). "The Westerbork Northern Sky Survey (WENSS), I. A 570 square degree Mini-Survey around the North Ecliptic Pole". In: *A&AS* 124, pp. 259–280. DOI: 10.1051/aas:1997358.

Repp, A. and H. Ebeling (Sept. 2018). "Science from a glimpse: Hubble SNAPshot observations of massive galaxy clusters". In: *MNRAS* 479.1, pp. 844–864. DOI: 10.1093/mnras/sty1489. arXiv: 1706.01263 [astro-ph.GA].

Riess, Adam G. et al. (Sept. 1998). "Observational Evidence from Supernovae for an Accelerating Universe and a Cosmological Constant". In: *AJ* 116.3, pp. 1009–1038. DOI: 10.1086/300499. arXiv: astro-ph/9805201 [astro-ph].

Robotham, A. S. G. et al. (Oct. 2011). "Galaxy and Mass Assembly (GAMA): the GAMA galaxy group catalogue (G^3Cv1)". In: *MNRAS* 416.4, pp. 2640–2668. DOI: 10.1111/j.1365-2966.2011.19217.x. arXiv: 1106.1994 [astro-ph.CO].

Romer, A. K. et al. (Nov. 1994). "The large-scale distribution of X-ray clusters of galaxies". In: *Nature* 372.6501, pp. 75–77. DOI: 10.1038/372075a0.

Romer, A. K. et al. (Feb. 2000). "The Bright SHARC Survey: The Cluster Catalog". In: *ApJS* 126.2, pp. 209–269. DOI: 10.1086/313302. arXiv: astro-ph/9907401 [astro-ph].

Romero, C. et al. (Apr. 2018). "A multi-instrument non-parametric reconstruction of the electron pressure profile in the galaxy cluster CLJ1226.9+3332". In: *A&A* 612, A39, A39. DOI: 10.1051/0004-6361/201731599. arXiv: 1707.06113 [astro-ph.CO].

Rosati, Piero et al. (May 1995). "A First Determination of the Surface Density of Galaxy Clusters at Very Low X-Ray Fluxes". In: *ApJ* 445, p. L11. DOI: 10.1086/187877. arXiv: astro-ph/9503064 [astro-ph].

Rosati, Piero et al. (Jan. 1998). "The ROSAT Deep Cluster Survey: The X-Ray Luminosity Function out to z = 0.8". In: *ApJ* 492.1, pp. L21–L24. DOI: 10.1086/311085. arXiv: astro-ph/9710308 [astro-ph].

Rose, J. A. (Jan. 1976). "A catalogue of southern clusters of galaxies." In: *A&AS* 23, pp. 109–114.

— (Jan. 1977). "A survey of compact groups of galaxies." In: *ApJ* 211, pp. 311–318. DOI: 10.1086/154936.

Rossetti, M. et al. (June 2017). "The cool-core state of Planck SZ-selected clusters versus X-ray-selected samples: evidence for cool-core bias". In: *MNRAS* 468.2, pp. 1917–1930. DOI: 10.1093/mnras/stx493. arXiv: 1702.06961 [astro-ph.CO].

Rothschild, R. et al. (Apr. 1979). "The cosmic X-ray experiment aboard HEAO-1." In: *Space Science Instrumentation* 4, pp. 269–301.

Ruhl, John et al. (Oct. 2004). "The South Pole Telescope". In: *Z-Spec: a broadband millimeter-wave grating spectrometer: design, construction, and first cryogenic measurements*. Ed. by C. Matt Bradford et al. Vol. 5498. Society of Photo-Optical Instrumentation Engineers (SPIE) Conference Series, pp. 11–29. DOI: 10.1117/12.552473. arXiv: astro-ph/0411122 [astro-ph].

Ruppin, F. et al. (Jan. 2017). "Non-parametric deprojection of NIKA SZ observations: Pressure distribution in the Planck-discovered cluster PSZ1 G045.85+57.71". In: *A&A* 597, A110, A110. DOI: 10.1051/0004-6361/201629405. arXiv: 1607.07679 [astro-ph.CO].

Ruppin, F. et al. (July 2018). "First Sunyaev-Zel'dovich mapping with the NIKA2 camera: Implication of cluster substructures for the pressure profile and mass estimate". In: *A&A* 615, A112, A112. DOI: 10.1051/0004-6361/201732558. arXiv: 1712.09587 [astro-ph.CO].

Ruppin, F. et al. (Nov. 2019a). "Impact of ICM disturbances on the mean pressure profile of galaxy clusters: A prospective study of the NIKA2 SZ large program with MUSIC synthetic clusters". In: *A&A* 631, A21, A21. DOI: 10.1051/0004-6361/201935059. arXiv: 1901.04580 [astro-ph.CO].

Ruppin, F. et al. (Nov. 2019b). "Impact of the mean pressure profile of galaxy clusters on the cosmological constraints from the Planck tSZ power spectrum". In: *MNRAS* 490.1, pp. 784–796. DOI: 10.1093/mnras/stz2669. arXiv: 1905.05129 [astro-ph.CO].

Ruppin, Florian (Sept. 2018). "Cosmologie via les observations d'amas de galaxies par effet Sunyaev-Zel'dovich avec NIKA2". Theses. Université Grenoble Alpes. URL: https://theses.hal.science/tel-01978797.

Rykoff, E. S. et al. (Apr. 2014). "redMaPPer. I. Algorithm and SDSS DR8 Catalog". In: *ApJ* 785.2, 104, p. 104. DOI: 10.1088/0004-637X/785/2/104. arXiv: 1303.3562 [astro-ph.CO].

Rykoff, E. S. et al. (May 2016). "The RedMaPPer Galaxy Cluster Catalog From DES Science Verification Data". In: *ApJS* 224.1, 1, p. 1. DOI: 10.3847/0067-0049/224/1/1. arXiv: 1601.00621 [astro-ph.CO].

Sadibekova, T. et al. (Aug. 2024). "MCXC-II: Second release of the Meta-Catalogue of X-ray detected Clusters of galaxies". In: *A&A* 688, A187, A187. DOI: 10.1051/0004-6361/202449427. arXiv: 2402.01538 [astro-ph.CO].

Sandage, A. et al. (May 1976). "The extension of the Hubble diagram. I. New redshifts and BVR photometry of remote cluster galaxies, and an improved richness correction." In: *ApJ* 205, pp. 688–695. DOI: 10.1086/154324.

Sanders, D. B. et al. (Sept. 2007). "S-COSMOS: The Spitzer Legacy Survey of the Hubble Space Telescope ACS 2 deg^2 COSMOS Field I: Survey Strategy and First Analysis". In: *ApJS* 172.1, pp. 86–98. DOI: 10.1086/517885. arXiv: astro-ph/0701318 [astro-ph].

Sarron, F. et al. (May 2018). "Evolution of the cluster optical galaxy luminosity function in the CFHTLS: breaking the degeneracy between mass and redshift". In: *A&A* 613, A67, A67. DOI: 10.1051/0004-6361/201731981. arXiv: 1712.09481 [astro-ph.GA].

Sarron, Florian and Chrisopher J. Conselice (Sept. 2021). "DETECTIFz galaxy groups in the REFINE survey - I. Group detection and quenched fraction evolution at z ¡ 2.5". In: *MNRAS* 506.2, pp. 2136–2155. DOI: 10.1093/mnras/stab1844. arXiv: 2106.13101 [astro-ph.GA].

Sartoris, B. et al. (June 2016). "Next generation cosmology: constraints from the Euclid galaxy cluster survey". In: *MNRAS* 459.2, pp. 1764–1780. DOI: 10.1093/mnras/stw630. arXiv: 1505.02165 [astro-ph.CO].

Saulder, Christoph et al. (Nov. 2016). "The matter distribution in the local Universe as derived from galaxy groups in SDSS DR12 and 2MRS". In: *A&A* 596, A14, A14. DOI: 10.1051/0004-6361/201526711. arXiv: 1511.05856 [astro-ph.CO].

Scharf, C. A. et al. (Mar. 1997). "The Wide-Angle ROSAT Pointed X-Ray Survey of Galaxies, Groups, and Clusters. I. Method and First Results". In: *ApJ* 477.1, pp. 79–92. DOI: 10.1086/303698. arXiv: astro-ph/9608200 [astro-ph].

Schindler, S. et al. (Feb. 1997). "ROSAT/HRI and ASCA observations of the most luminous X-ray cluster RX J1347.5-1145". In: *A&A* 317, pp. 646–655. DOI: 10.48550/arXiv.astro-ph/9603037. arXiv: astro-ph/9603037 [astro-ph].

Schuecker, P. et al. (June 2004). "Detection of X-ray clusters of galaxies by matching RASS photons and SDSS galaxies within GAVO". In: *A&A* 420, pp. 61–74. DOI: 10.1051/0004-6361:20035597. arXiv: astro-ph/0403116 [astro-ph].

Scodeggio, M. et al. (May 1999). "ESO Imaging Survey. VII. Distant cluster candidates over 12 square degrees". In: *A&AS* 137, pp. 83–92. DOI: 10.1051/aas:1999477. arXiv: astro-ph/9807336 [astro-ph].

Scoville, N. et al. (Sept. 2007). "The Cosmic Evolution Survey (COSMOS): Overview". In: *ApJS* 172.1, pp. 1–8. DOI: 10.1086/516585. arXiv: astro-ph/0612305 [astro-ph].

Scudder, Jillian M. et al. (July 2012). "The dependence of galaxy group star formation rates and metallicities on large-scale environment". In: *MNRAS* 423.3, pp. 2690–2704. DOI: 10.1111/j.1365-2966.2012.21080.x. arXiv: 1204.2828 [astro-ph.CO].

Sembolini, Federico et al. (Feb. 2013). "The MUSIC of galaxy clusters - I. Baryon properties and scaling relations of the thermal Sunyaev-Zel'dovich effect". In: *MNRAS* 429.1, pp. 323–343. DOI: 10.1093/mnras/sts339. arXiv: 1207.4438 [astro-ph.CO].

Sereno, Mauro (July 2015). "CoMaLit - III. Literature catalogues of weak lensing clusters of galaxies (LC^2)". In: *MNRAS* 450.4, pp. 3665–3674. DOI: 10.1093/mnras/stu2505. arXiv: 1409.5435 [astro-ph.CO].

Sereno, Mauro and Giovanni Covone (Sept. 2013). "The mass-concentration relation in massive galaxy clusters at redshift ~1". In: *MNRAS* 434.1, pp. 878–887. DOI: 10.1093/mnras/stt1086. arXiv: 1306.6096 [astro-ph.CO].

Sereno, Mauro and Stefano Ettori (July 2017). "CoMaLit - V. Mass forecasting with proxies: method and application to weak lensing calibrated samples". In: *MNRAS* 468.3, pp. 3322–3341. DOI: 10.1093/mnras/stx576. arXiv: 1603.06581 [astro-ph.CO].

Sérsic, J. L. (June 1974). "A list of peculiar galaxies, interacting pairs, groups and clusters south of declination -43°". In: *Ap&SS* 28.2, pp. 365–373. DOI: 10.1007/BF00641933.

Shakhbazyan, R. K. and M. B. Petrosyan (Jan. 1974). "Compact groups of compact galaxies. II". In: *Astrophysics* 10.1, pp. 6–17. DOI: 10.1007/BF01005172.

Shapley, Harlow and Adelaide Ames (May 1932). "Photometric Survey of the Nearer Extragalactic Nebulae". In: *Harvard College Observatory Bulletin* 887, pp. 1–6.

Shectman, S. A. (Jan. 1985). "Clusters of galaxies from the Shane-Wirtanen counts." In: *ApJS* 57, pp. 77–90. DOI: 10.1086/190996.

Shimwell, T. W. et al. (Mar. 2022). "The LOFAR Two-metre Sky Survey. V. Second data release". In: *A&A* 659, A1, A1. DOI: 10.1051/0004-6361/202142484. arXiv: 2202.11733 [astro-ph.GA].

Sifón, Cristóbal et al. (Sept. 2016). "The Atacama Cosmology Telescope: dynamical masses for 44 SZ-selected galaxy clusters over 755 square degrees". In: *MNRAS* 461.1, pp. 248–270. DOI: 10.1093/mnras/stw1284. arXiv: 1512.00910 [astro-ph.CO].

Silk, J. and S. D. M. White (Dec. 1978). "The determination of q_0 using X-ray and microwave observation of galaxy clusters." In: *ApJ* 226, pp. L103–L106. DOI: 10.1086/182841.

Simpson, J. M. et al. (July 2019). "The East Asian Observatory SCUBA-2 Survey of the COSMOS Field: Unveiling 1147 Bright Sub-millimeter Sources across 2.6 Square Degrees". In: *ApJ* 880.1, 43, p. 43. DOI: 10.3847/1538-4357/ab23ff. arXiv: 1912.02229 [astro-ph.GA].

Skelton, Rosalind E. et al. (Oct. 2014). "3D-HST WFC3-selected Photometric Catalogs in the Five CANDELS/3D-HST Fields: Photometry, Photometric Redshifts, and Stellar Masses". In: *ApJS* 214.2, 24, p. 24. DOI: 10.1088/0067-0049/214/2/24. arXiv: 1403.3689 [astro-ph.GA].

Slipher, V. M. (Jan. 1913). "The radial velocity of the Andromeda Nebula". In: *Lowell Observatory Bulletin* 2.8, pp. 56–57.

Smail, Ian et al. (Nov. 1997). "A Deep Sub-millimeter Survey of Lensing Clusters: A New Window on Galaxy Formation and Evolution". In: *ApJ* 490.1, pp. L5–L8. DOI: 10.1086/311017. arXiv: astro-ph/9708135 [astro-ph].

Smith, Anthony G. et al. (May 2012). "Multiscale probability mapping: groups, clusters and an algorithmic search for filaments in SDSS". In: *MNRAS* 422.1, pp. 25–43. DOI: 10.1111/j.1365-2966.2012.20400.x. arXiv: 1201.0570 [astro-ph.CO].

Smoot, G. F. et al. (Sept. 1992). "Structure in the COBE Differential Microwave Radiometer First-Year Maps". In: *ApJ* 396, p. L1. DOI: 10.1086/186504.

Snow Jr., T. P. (Apr. 1970). "Groups and clusters of galaxies." In: *AJ* 75, pp. 237–238. DOI: 10.1086/110968.

Sobrin, J. A. et al. (Feb. 2022). "The Design and Integrated Performance of SPT-3G". In: *ApJS* 258.2, 42, p. 42. DOI: 10.3847/1538-4365/ac374f. arXiv: 2106.11202 [astro-ph.IM].

Söchting, Ilona K. et al. (July 2006). "The FSVS Cluster Catalogue: galaxy clusters and groups in the Faint Sky Variability Survey". In: *MNRAS* 369.3, pp. 1334–1350. DOI: 10.1111/j.1365-2966.2006.10380.x. arXiv: astro-ph/0604610 [astro-ph].

Söchting, Ilona K. et al. (July 2012). "Ultra Deep Catalogue of Galaxy Structures in the Cosmic Evolution Survey field". In: *MNRAS* 423.3, pp. 2436–2450. DOI: 10.1111/j.1365-2966.2012.21050.x.

Socolovsky, Miguel et al. (May 2018). "The enhancement of rapidly quenched galaxies in distant clusters at 0.5 ¡ z ¡ 1.0". In: *MNRAS* 476.1, pp. 1242–1257. DOI: 10.1093/mnras/sty312. arXiv: 1802.01593 [astro-ph.GA].

Sohn, Jubee et al. (Aug. 2016). "Catalogs of Compact Groups of Galaxies from the Enhanced SDSS DR12". In: *ApJS* 225.2, 23, p. 23. DOI: 10.3847/0067-0049/225/2/23. arXiv: 1603.06583 [astro-ph.GA].

Sohn, Jubee et al. (2020). "Velocity Dispersions of Brightest Cluster Galaxies and Their Host Clusters". In: *The Astrophysical Journal* 891.2, p. 129. DOI: 10.3847/1538-4357/ab6e6a. URL: https://dx.doi.org/10.3847/1538-4357/ab6e6a.

Sohn, Jubee et al. (Dec. 2021). "The HectoMAP Cluster Survey: Spectroscopically Identified Clusters and their Brightest Cluster Galaxies (BCGs)". In: *ApJ* 923.2, 143, p. 143. DOI: 10.3847/1538-4357/ac29c3. arXiv: 2106.11429 [astro-ph.CO].

Somboonpanyakul, Taweewat et al. (Mar. 2021). "The Clusters Hiding in Plain Sight (CHiPS) Survey: Complete Sample of Extreme BCG Clusters". In: *ApJ* 910.1, 60, p. 60. DOI: 10.3847/1538-4357/abe1bc. arXiv: 2101.01730 [astro-ph.CO].

Staguhn, Johannes G. et al. (July 2014). "The GISMO Two-millimeter Deep Field in GOODS-N". In: *ApJ* 790.1, 77, p. 77. DOI: 10.1088/0004-637X/790/1/77. arXiv: 1311.1485 [astro-ph.CO].

Staniszewski, Z. et al. (Aug. 2009). "Galaxy Clusters Discovered with a Sunyaev-Zel'dovich Effect Survey". In: *ApJ* 701.1, pp. 32–41. DOI: 10.1088/0004-637X/701/1/32. arXiv: 0810.1578 [astro-ph].

Starobinsky, A. A. (Nov. 1982). "Dynamics of phase transition in the new inflationary universe scenario and generation of perturbations". In: *Physics Letters B* 117.3-4, pp. 175–178. DOI: 10.1016/0370-2693(82)90541-X.

Stocke, John T. et al. (July 1991). "The Einstein Observatory Extended Medium-Sensitivity Survey. II. The Optical Identifications". In: *ApJS* 76, p. 813. DOI: 10.1086/191582.

Sun, Fengwu et al. (Jan. 2024). "JADES: Resolving the Stellar Component and Filamentary Overdense Environment of Hubble Space Telescope (HST)-dark Submillimeter Galaxy HDF850.1 at z = 5.18". In: *ApJ* 961.1, 69, p. 69. DOI: 10.3847/1538-4357/ad07e3. arXiv: 2309.04529 [astro-ph.GA].

Sunyaev, R. A. and Ya. B. Zeldovich (Apr. 1970a). "Small-Scale Fluctuations of Relic Radiation". In: *Ap&SS* 7.1, pp. 3–19. DOI: 10.1007/BF00653471.

— (Apr. 1970b). "The interaction of matter and radiation in the hot model of the Universe, II". In: *Ap&SS* 7.1, pp. 20–30. DOI: 10.1007/BF00653472.

— (Nov. 1972). "The Observations of Relic Radiation as a Test of the Nature of X-Ray Radiation from the Clusters of Galaxies". In: *Comments on Astrophysics and Space Physics* 4, p. 173.

— (Feb. 1980). "The velocity of clusters of galaxies relative to the microwave background - The possibility of its measurement." In: *MNRAS* 190, pp. 413–420. DOI: 10.1093/mnras/190.3.413.

Suzuki, Ryuji (Jan. 2020). "Performance evaluation of a 109-pixel mm-wave MKID camera with a multi-pixel readout system for the Nobeyama 45m telescope". Theses.

Szabo, T. et al. (July 2011). "An Optical Catalog of Galaxy Clusters Obtained from an Adaptive Matched Filter Finder Applied to Sloan Digital Sky Survey Data Release 6". In: *ApJ* 736.1, 21, p. 21. DOI: 10.1088/0004-637X/736/1/21. arXiv: 1011.0249 [astro-ph.CO].

Tago, E. et al. (May 2006). "Clusters and groups of galaxies in the 2dF galaxy redshift survey: A new catalogue". In: *Astronomische Nachrichten* 327.4, p. 365. DOI: 10.1002/asna.200510536. arXiv: astro-ph/0501099 [astro-ph].

Tago, E. et al. (Mar. 2008). "Groups of galaxies in the SDSS Data Release 5. A group-finder and a catalogue". In: *A&A* 479.3, pp. 927–937. DOI: 10.1051/0004-6361:20078036. arXiv: 0706.1593 [astro-ph].

Tago, E. et al. (May 2010). "Groups of galaxies in the SDSS Data Release 7 . Flux- and volume-limited samples". In: *A&A* 514, A102, A102. DOI: 10.1051/0004-6361/200913687.

Takey, A. et al. (Oct. 2011). "The 2XMMi/SDSS Galaxy Cluster Survey. I. The first cluster sample and X-ray luminosity-temperature relation". In: *A&A* 534, A120, A120. DOI: 10.1051/0004-6361/201117498. arXiv: 1109.1743 [astro-ph.CO].

— (Apr. 2014). "The 2XMMi/SDSS Galaxy Cluster Survey. III. Clusters associated with spectroscopically targeted luminous red galaxies in SDSS-DR10". In: *A&A* 564, A54, A54. DOI: 10.1051/0004-6361/201322973. arXiv: 1403.0758 [astro-ph.CO].

Takey, A. et al. (Oct. 2016). "The 3XMM/SDSS Stripe 82 Galaxy Cluster Survey. I. Cluster catalogue and discovery of two merging cluster candidates". In: *A&A* 594, A32, A32. DOI: 10.1051/0004-6361/201628105. arXiv: 1606.05536 [astro-ph.CO].

Tanimura, Hideki et al. (Jan. 2021). "Direct detection of the kinetic Sunyaev-Zel'dovich effect in galaxy clusters". In: *A&A* 645, A112, A112. DOI: 10.1051/0004-6361/202038846. arXiv: 2007.02952 [astro-ph.CO].

Tarrío, P. et al. (June 2019). "ComPRASS: a Combined Planck-RASS catalogue of X-ray-SZ clusters". In: *A&A* 626, A7, A7. DOI: 10.1051/0004-6361/201834979. arXiv: 1901.00873 [astro-ph.CO].

Tauber, J. A. et al. (Sept. 2010). "Planck pre-launch status: The Planck mission". In: *A&A* 520, A1, A1. DOI: 10.1051/0004-6361/200912983.

Tempel, E. et al. (Apr. 2012). "Groups and clusters of galaxies in the SDSS DR8. Value-added catalogues". In: *A&A* 540, A106, A106. DOI: 10.1051/0004-6361/201118687. arXiv: 1112.4648 [astro-ph.CO].

Tempel, E. et al. (June 2014). "Flux- and volume-limited groups/clusters for the SDSS galaxies: catalogues and mass estimation". In: *A&A* 566, A1, A1. DOI: 10.1051/0004-6361/201423585. arXiv: 1402.1350 [astro-ph.CO].

Tempel, E. et al. (Apr. 2016). "Friends-of-friends galaxy group finder with membership refinement. Application to the local Universe". In: *A&A* 588, A14, A14. DOI: 10.1051/0004-6361/201527755. arXiv: 1601.01117 [astro-ph.CO].

Tempel, Elmo et al. (Oct. 2018). "Bayesian group finder based on marked point processes. Method and feasibility study using the 2MRS data set". In: *A&A* 618, A81, A81. DOI: 10.1051/0004-6361/201833217. arXiv: 1806.04469 [astro-ph.CO].

Thanjavur, Karun et al. (Nov. 2009). "K2: A New Method for the Detection of Galaxy Clusters Based on Canada-France-Hawaii Telescope Legacy Survey Multicolor Images". In: *ApJ* 706.1, pp. 571–591. DOI: 10.1088/0004-637X/706/1/571. arXiv: 0910.4358 [astro-ph.CO].

The Dark Energy Survey Collaboration (Oct. 2005). "The Dark Energy Survey". In: *arXiv e-prints*, astro-ph/0510346, astro–ph/0510346. DOI: 10.48550/arXiv.astro-ph/0510346. arXiv: astro-ph/0510346 [astro-ph].

The Planck Collaboration (Apr. 2006). "The Scientific Programme of Planck". In: *arXiv e-prints*, astro-ph/0604069, astro–ph/0604069. DOI: 10.48550/arXiv.astro-ph/0604069. arXiv: astro-ph/0604069 [astro-ph].

Thongkham, Khunanon et al. (June 2024). "The Massive and Distant Clusters of WISE Survey 2: Equatorial First Data Release". In: *ApJ* 967.2, 123, p. 123. DOI: 10.3847/1538-4357/ad3c44. arXiv: 2403.16976 [astro-ph.CO].

Tinker, Jeremy et al. (Dec. 2008). "Toward a Halo Mass Function for Precision Cosmology: The Limits of Universality". In: *ApJ* 688.2, pp. 709–728. DOI: 10.1086/591439. arXiv: 0803.2706 [astro-ph].

Toni, G. et al. (July 2024). "AMICO-COSMOS galaxy cluster and group catalogue up to z = 2: Sample properties and X-ray counterparts". In: *Astronomy and Astrophysics* 687. Publisher: EDP ADS Bibcode: 2024A&A...687A..56T, A56. ISSN: 0004-6361. DOI: 10.1051/0004-6361/202348832. URL: https://ui.adsabs.harvard.edu/abs/2024A&A...687A..56T.

Toni, Greta et al. (May 2025). "The COSMOS-Web deep galaxy group catalog up to z = 3.7". In: *Astronomy and Astrophysics* 697. Publisher: EDP ADS Bibcode: 2025A&A...697A.197T, A197. ISSN: 0004-6361. DOI: 10.1051/0004-6361/202553759. URL: https://ui.adsabs.harvard.edu/abs/2025A&A...697A.197T.

Toshikawa, Jun et al. (Aug. 2016). "A Systematic Survey of Protoclusters at z ~3-6 in the CFHTLS Deep Fields". In: *ApJ* 826.2, 114, p. 114. DOI: 10.3847/0004-637X/826/2/114. arXiv: 1605.01439 [astro-ph.GA].

Trasarti-Battistoni, R. (June 1998). "Loose groups of galaxies in the Perseus-Pisces survey". In: *A&AS* 130, pp. 341–358. DOI: 10.1051/aas:1998229. arXiv: astro-ph/9711116 [astro-ph].

Truemper, J. (Jan. 1982). "The ROSAT mission". In: *Advances in Space Research* 2.4, pp. 241–249. DOI: 10.1016/0273-1177(82)90070-9.

Truemper, Joachim (June 1993). "ROSAT-A New Look at the X-ray Sky". In: *Science* 260.5115, pp. 1769–1771. DOI: 10.1126/science.260.5115.1769.

Tsuboi, M. et al. (Jan. 1998a). "Sunyaev-Zel'dovich Effect Observation Project with the Nobeyama 45-m Telescope". In: *The Hot Universe*. Ed. by Katsuji Koyama et al. Vol. 188. IAU Symposium, p. 330.

Tsuboi, Masato et al. (Feb. 1998b). "Measurement of the Sunyaev-Zel'dovich Effect toward Abell 2218 at 36GHz". In: *PASJ* 50, pp. 169–173. DOI: 10.1093/pasj/50.1.169.

Tsuboi, Masato et al. (July 2000). "New Q-band array SIS receiver with ultrawide band for the Nobeyama 45-m telescope". In: *Radio Telescopes*. Ed. by Harvey R. Butcher. Vol. 4015. Society of Photo-Optical Instrumentation Engineers (SPIE) Conference Series, pp. 278–286. DOI: 10.1117/12.390422.

Tsuboi, Masato et al. (Oct. 2004). "Sunyaev–Zel'dovich Effect toward Distant Galaxy Clusters at 43 GHz; Observation and Data". In: *PASJ* 56, pp. 711–721. DOI: 10.1093/pasj/56.5.711.

Tucker, Douglas L. et al. (Oct. 2000). "Loose Groups of Galaxies in the Las Campanas Redshift Survey". In: *ApJS* 130.2, pp. 237–265. DOI: 10.1086/317348. arXiv: astro-ph/0006153 [astro-ph].

Tully, R. Brent (Oct. 1987). "Nearby Groups of Galaxies. II. an All-Sky Survey within 3000 Kilometers per Second". In: *ApJ* 321, p. 280. DOI: 10.1086/165629.

— (May 2015). "Galaxy Groups: A 2MASS Catalog". In: *AJ* 149.5, 171, p. 171. DOI: 10.1088/0004-6256/149/5/171. arXiv: 1503.03134 [astro-ph.CO].

Turner, E. L. and J. R. Gott III (Nov. 1976). "Groups of galaxies. I. A catalog." In: *ApJS* 32, pp. 409–427. DOI: 10.1086/190403.

Vanderlinde, K. et al. (Oct. 2010). "Galaxy Clusters Selected with the Sunyaev-Zel'dovich Effect from 2008 South Pole Telescope Observations". In: *ApJ* 722.2, pp. 1180–1196. DOI: 10.1088/0004-637X/722/2/1180. arXiv: 1003.0003 [astro-ph.CO].

Vazquez, J. Alberto et al. (Oct. 2018). "Inflationary Cosmology: From Theory to Observations". In: *arXiv e-prints*, arXiv:1810.09934, arXiv:1810.09934. DOI: 10.48550/arXiv.1810.09934. arXiv: 1810.09934 [astro-ph.CO].

Vennik, J. (Jan. 1986). "Empirical properties of nearby groups of galaxies." In: *Astronomische Nachrichten* 307.3, pp. 157–169. DOI: 10.1002/asna.2113070302.

Vikhlinin, A. et al. (Aug. 1998). "A Catalog of 200 Galaxy Clusters Serendipitously Detected in the ROSAT PSPC Pointed Observations". In: *ApJ* 502.2, pp. 558–581. DOI: 10.1086/305951. arXiv: astro-ph/9803099 [astro-ph].

Vikhlinin, A. et al. (Apr. 2006). "Chandra Sample of Nearby Relaxed Galaxy Clusters: Mass, Gas Fraction, and Mass-Temperature Relation". In: *ApJ* 640.2, pp. 691–709. DOI: 10.1086/500288. arXiv: astro-ph/0507092 [astro-ph].

Voges, W. et al. (Sept. 1999). "The ROSAT all-sky survey bright source catalogue". In: *A&A* 349, pp. 389–405. DOI: 10.48550/arXiv.astro-ph/9909315. arXiv: astro-ph/9909315 [astro-ph].

Voit, G. M. (Apr. 2005). "Tracing cosmic evolution with clusters of galaxies". In: *Reviews of Modern Physics* 77, pp. 207–258. DOI: 10.1103/RevModPhys.77.207.

Voskresenskaia, S. et al. (June 2024). "ComPACT: combined Atacama Cosmology Telescope + Planck galaxy cluster catalogue". In: *MNRAS* 531.1, pp. 1998–2010. DOI: 10.1093/mnras/stae1269. arXiv: 2309.17077 [astro-ph.GA].

Wan, Jenny T. et al. (June 2021). "Measuring H_0 using X-ray and SZ effect observations of dynamically relaxed galaxy clusters". In: *MNRAS* 504.1, pp. 1062–1076. DOI: 10.1093/mnras/stab948. arXiv: 2101.09389 [astro-ph.CO].

Wang, Kai et al. (Nov. 2020). "Identifying galaxy groups at high redshift from incomplete spectroscopic data - I. The group finder and application to zCOSMOS". In: *MNRAS* 499.1, pp. 89–105. DOI: 10.1093/mnras/staa2816. arXiv: 2006.05426 [astro-ph.GA].

Watson, M. G. et al. (Jan. 2009). "The XMM-Newton serendipitous survey. V. The Second XMM-Newton serendipitous source catalogue". In: *A&A* 493.1, pp. 339–373. DOI: 10.1051/0004-6361:200810534. arXiv: 0807.1067 [astro-ph].

Weaver, J. R. et al. (Jan. 2022). "COSMOS2020: A Panchromatic View of the Universe to z~10 from Two Complementary Catalogs". In: *ApJS* 258.1, 11, p. 11. DOI: 10.3847/1538-4365/ac3078. arXiv: 2110.13923 [astro-ph.GA].

Weinmann, Simone M. et al. (Feb. 2006). "Properties of galaxy groups in the Sloan Digital Sky Survey - I. The dependence of colour, star formation and morphology on halo mass". In: *MNRAS* 366.1, pp. 2–28. DOI: 10.1111/j.1365-2966.2005.09865.x. arXiv: astro-ph/0509147 [astro-ph].

Weisskopf, Martin C. et al. (July 2000). "Chandra X-ray Observatory (CXO): overview". In: *X-Ray Optics, Instruments, and Missions III*. Ed. by Joachim E. Truemper and Bernd Aschenbach. Vol. 4012. Society of Photo-Optical Instrumentation Engineers (SPIE) Conference Series, pp. 2–16. DOI: 10.1117/12.391545. arXiv: astro-ph/0004127 [astro-ph].

Wen, Z. L. and J. L. Han (June 2011). "Galaxy Clusters at High Redshift and Evolution of Brightest Cluster Galaxies". In: *ApJ* 734.1, 68, p. 68. DOI: 10.1088/0004-637X/734/1/68. arXiv: 1104.1667 [astro-ph.CO].

— (July 2015). "Calibration of the Optical Mass Proxy for Clusters of Galaxies and an Update of the WHL12 Cluster Catalog". In: *ApJ* 807.2, 178, p. 178. DOI: 10.1088/0004-637X/807/2/178. arXiv: 1506.04503 [astro-ph.GA].

— (Jan. 2021). "Photometric redshifts for galaxies in the Subaru Hyper Suprime-Cam and unWISE and a catalogue of identified clusters of galaxies". In: *MNRAS* 500.1, pp. 1003–1017. DOI: 10.1093/mnras/staa3308. arXiv: 2010.11551 [astro-ph.CO].

— (July 2022). "Clusters of galaxies up to z = 1.5 identified from photometric data of the Dark Energy Survey and unWISE". In: *MNRAS* 513.3, pp. 3946–3959. DOI: 10.1093/mnras/stac1149. arXiv: 2204.11215 [astro-ph.CO].

— (June 2024). "A Catalog of 1.58 Million Clusters of Galaxies Identified from the DESI Legacy Imaging Surveys". In: *ApJS* 272.2, 39, p. 39. DOI: 10.3847/1538-4365/ad409d. arXiv: 2404.02002 [astro-ph.CO].

Wen, Z. L. et al. (Aug. 2009). "Galaxy Clusters Identified from the SDSS DR6 and Their Properties". In: *ApJS* 183.2, pp. 197–213. DOI: 10.1088/0067-0049/183/2/197. arXiv: 0906.0803 [astro-ph.CO].

— (Apr. 2012). "A Catalog of 132,684 Clusters of Galaxies Identified from Sloan Digital Sky Survey III". In: *ApJS* 199.2, 34, p. 34. DOI: 10.1088/0067-0049/199/2/34. arXiv: 1202.6424 [astro-ph.CO].

Wen, Z. L. et al. (Mar. 2018). "A catalogue of clusters of galaxies identified from all sky surveys of 2MASS, WISE, and SuperCOSMOS". In: *MNRAS* 475.1, pp. 343–352. DOI: 10.1093/mnras/stx3189. arXiv: 1712.02491 [astro-ph.GA].

Werner, S. V. et al. (Feb. 2023). "S-PLUS DR1 galaxy clusters and groups catalogue using PzWav". In: *MNRAS* 519.2, pp. 2630–2645. DOI: 10.1093/mnras/stac3273. arXiv: 2211.04243 [astro-ph.GA].

White, Richard A. et al. (Nov. 1999). "A Catalog of Nearby Poor Clusters of Galaxies". In: *AJ* 118.5, pp. 2014–2037. DOI: 10.1086/301103. arXiv: astro-ph/9907283 [astro-ph].

White, Simon D. M. et al. (Dec. 1993). "The baryon content of galaxy clusters: a challenge to cosmological orthodoxy". In: *Nature* 366.6454, pp. 429–433. DOI: 10.1038/366429a0.

Wicker, R. et al. (June 2023). "Constraining the mass and redshift evolution of the hydrostatic mass bias using the gas mass fraction in galaxy clusters". In: *A&A* 674, A48, A48. DOI: 10.1051/0004-6361/202243922. arXiv: 2204.12823 [astro-ph.CO].

Williams, Robert E. et al. (Oct. 1996). "The Hubble Deep Field: Observations, Data Reduction, and Galaxy Photometry". In: *AJ* 112, p. 1335. DOI: 10.1086/118105. arXiv: astro-ph/9607174 [astro-ph].

Williamson, R. et al. (Sept. 2011). "A Sunyaev-Zel'dovich-selected Sample of the Most Massive Galaxy Clusters in the 2500 deg^2 South Pole Telescope Survey". In: *ApJ* 738.2, 139, p. 139. DOI: 10.1088/0004-637X/738/2/139. arXiv: 1101.1290 [astro-ph.CO].

Willick, Jeffrey A. et al. (June 2001). "The Stanford Cluster Search: Scope, Method, and Preliminary Results". In: *PASP* 113.784, pp. 658–676. DOI: 10.1086/320814.

Wilson, Michelle L. et al. (Dec. 2016). "A Spectroscopic Survey of the Fields of 28 Strong Gravitational Lenses: the Group Catalog". In: *ApJ* 833.2, 194, p. 194. DOI: 10.3847/1538-4357/833/2/194. arXiv: 1710.09908 [astro-ph.GA].

Xiao, Mengyuan et al. (Nov. 2024). "Accelerated formation of ultra-massive galaxies in the first billion years". In: *Nature* 635.8038, pp. 311–315. DOI: 10.1038/s41586-024-08094-5. arXiv: 2309.02492 [astro-ph.GA].

Xu, Weiwei et al. (Nov. 2018). "A new X-ray-selected sample of very extended galaxy groups from the ROSAT All-Sky Survey". In: *A&A* 619, A162, A162. DOI: 10.1051/0004-6361/201833062. arXiv: 1809.02982 [astro-ph.CO].

— (Feb. 2022). "Catalog of X-ray-selected extended galaxy clusters from the ROSAT All-Sky Survey (RXGCC)". In: *A&A* 658, A59, A59. DOI: 10.1051/0004-6361/202140908. arXiv: 2110.14886 [astro-ph.CO].

Xu, Weiwei et al. (Nov. 2024). "XMM-SERVS X-ray extended Galaxy Cluster (XVXGC) catalog". In: *A&A* 691, A300, A300. DOI: 10.1051/0004-6361/202451064. arXiv: 2406.06701 [astro-ph.CO].

Yamada, Masako et al. (June 2010). "Search for the Sunyaev-Zel'dovich Effect in a Giant Radio Galaxy B1358+305". In: *AJ* 139.6, pp. 2494–2503. DOI: 10.1088/0004-6256/139/6/2494. arXiv: 1004.2335 [astro-ph.GA].

Yang, Xiaohu et al. (Feb. 2005). "A halo-based galaxy group finder: calibration and application to the 2dFGRS". In: *MNRAS* 356.4, pp. 1293–1307. DOI: 10.1111/j.1365-2966.2005.08560.x. arXiv: astro-ph/0405234 [astro-ph].

Yang, Xiaohu et al. (Dec. 2007). "Galaxy Groups in the SDSS DR4. I. The Catalog and Basic Properties". In: *ApJ* 671.1, pp. 153–170. DOI: 10.1086/522027. arXiv: 0707.4640 [astro-ph].

Yang, Xiaohu et al. (Mar. 2021). "An Extended Halo-based Group/Cluster Finder: Application to the DESI Legacy Imaging Surveys DR8". In: *ApJ* 909.2, 143, p. 143. DOI: 10.3847/1538-4357/abddb2. arXiv: 2012.14998 [astro-ph.GA].

Yantovski-Barth, M. J. et al. (June 2024). "The CluMPR galaxy cluster-finding algorithm and DESI legacy survey galaxy cluster catalogue". In: *MNRAS* 531.2, pp. 2285–2303. DOI: 10.1093/mnras/stae956. arXiv: 2307.10426 [astro-ph.CO].

Yee, H. K. C. and M. D. Gladders (Jan. 2002). "Optical Surveys for Galaxy Clusters". In: *AMiBA 2001: High-Z Clusters, Missing Baryons, and CMB Polarization*. Ed. by Lin-Wen Chen et al. Vol. 257. Astronomical Society of the Pacific Conference Series, p. 109. DOI: 10.48550/arXiv.astro-ph/0111431. arXiv: astro-ph/0111431 [astro-ph].

Yee, H. K. C. et al. (Feb. 1996). "The CNOC Cluster Redshift Survey Catalogs. I. Observational Strategy and Data Reduction Techniques". In: *ApJS* 102, p. 269. DOI: 10.1086/192259.

Yoon, Joo H. et al. (June 2008). "A Spectrophotometric Search for Galaxy Clusters in SDSS". In: *ApJS* 176.2, pp. 414–423. DOI: 10.1086/528958. arXiv: 0712.1054 [astro-ph].

York, Donald G. et al. (Sept. 2000). "The Sloan Digital Sky Survey: Technical Summary". In: *AJ* 120.3, pp. 1579–1587. DOI: 10.1086/301513. arXiv: astro-ph/0006396 [astro-ph].

Zamojski, M. A. et al. (Sept. 2007). "Deep GALEX Imaging of the COSMOS HST Field: A First Look at the Morphology of z ~0.7 Star-forming Galaxies". In: *ApJS* 172.1, pp. 468–493. DOI: 10.1086/516593. arXiv: astro-ph/0701478 [astro-ph].

Zandivarez, A. et al. (Nov. 2024). "Compact groups of galaxies in GAMA: Probing the densest minor systems at intermediate redshifts". In: *A&A* 691, A6, A6. DOI: 10.1051/0004-6361/202451471. arXiv: 2408.07031 [astro-ph.GA].

Zaritsky, Dennis et al. (May 1997). "Distant Galaxy Clusters Identified from Optical Background Fluctuations". In: *ApJ* 480.2, pp. L91–L94. DOI: 10.1086/310625. arXiv: astro-ph/9612021 [astro-ph].

Zatloukal, M. et al. (Oct. 2007). "Distant galaxy clusters in the COSMOS field found by HIROCS". In: *A&A* 474.1, pp. L5–L8. DOI: 10.1051/0004-6361:20078063. arXiv: 0709.0411 [astro-ph].

Zhang, Chaoli et al. (Oct. 2020). "High-redshift galaxy groups as seen by ATHENA/WFI". In: *A&A* 642, A17, A17. DOI: 10.1051/0004-6361/201937329. arXiv: 2008.09271 [astro-ph.CO].

Zheng, Yun-Liang and Shi-Yin Shen (Jan. 2020). "Compact Groups of Galaxies in Sloan Digital Sky Survey and LAMOST Spectral Survey. I. The Catalogs". In: *ApJS* 246.1, 12, p. 12. DOI: 10.3847/1538-4365/ab5c26. arXiv: 1911.11478 [astro-ph.GA].

Zmuidzinas, Jonas (Mar. 2012). "Superconducting Microresonators: Physics and Applications". en. In: *Annual Review of Condensed Matter Physics* 3.Volume 3, 2012. Publisher: Annual Reviews, pp. 169–214. ISSN: 1947-5454, 1947-5462. DOI: 10.1146/annurev-conmatphys-020911-125022. URL: https://www.annualreviews.org/content/journals/10.1146/annurev-conmatphys-020911-125022.

Zou, Hu et al. (Apr. 2021). "Galaxy Clusters from the DESI Legacy Imaging Surveys. I. Cluster Detection". In: *ApJS* 253.2, 56, p. 56. DOI: 10.3847/1538-4365/abe5b0. arXiv: 2101.12340 [astro-ph.GA].

Zou, Hu et al. (June 2022). "Photometric Redshifts and Galaxy Clusters for DES DR2, DESI DR9, and HSC-SSP PDR3 Data". In: *Research in Astronomy and Astrophysics* 22.6, 065001, p. 065001. DOI: 10.1088/1674-4527/ac6416. arXiv: 2203.17035 [astro-ph.GA].

Zubeldia, Íñigo et al. (May 2025). "The Planck SZiFi catalogues: a new set of Planck catalogues of Sunyaev-Zeldovich-detected galaxy clusters". In: *MNRAS* 539.1, pp. 185–213. DOI: 10.1093/mnras/staf463. arXiv: 2408.06189 [astro-ph.CO].

Zwicky, F. and C. T. Kowal (1968). *"Catalogue of Galaxies and of Clusters of Galaxies", Volume VI*.

Zwicky, F. et al. (1965). *"Catalogue of Galaxies and of Clusters of Galaxies", Vol. V*.

Zwicky, Fritz et al. (1963a). *Catalogue of galaxies and of clusters of galaxies, Vol. 2*.

— (1963b). *Catalogue of galaxies and of clusters of galaxies, Vol. 2*.

— (1966). *Catalogue of galaxies and of clusters of galaxies, Vol. 3*.

— (1968). *Catalogue of galaxies and of clusters of galaxies*.

Zylka, Robert (Mar. 2013). *MOPSIC: Extended Version of MOPSI*. Astrophysics Source Code Library, record ascl:1303.011.

d'Addabbo, Antonio (Oct. 2014). "Applications of Kinetic Inductance Detectors to Astronomy and Particle Physics". Theses. Université de Grenoble ; Università degli studi La Sapienza (Rome). URL: https://theses.hal.science/tel-01368000.

de Carvalho, R. R. et al. (Aug. 2005). "A Catalog of Distant Compact Groups Using the Digitized Second Palomar Observatory Sky Survey". In: *AJ* 130.2, pp. 425–444. DOI: 10.1086/430801. arXiv: astro-ph/0504217 [astro-ph].

de Hoon, A. et al. (Mar. 2013). "Distant galaxy clusters in a deep XMM-Newton field within the CFTHLS D4". In: *A&A* 551, A8, A8. DOI: 10.1051/0004-6361/201220389. arXiv: 1301.3506 [astro-ph.CO].

de Jong, Jelte T. A. et al. (Jan. 2013). "The Kilo-Degree Survey". In: *Experimental Astronomy* 35.1-2, pp. 25–44. DOI: 10.1007/s10686-012-9306-1. arXiv: 1206.1254 [astro-ph.CO].

de Vaucouleurs, G. (1975). "Nearby Groups of Galaxies". In: *Galaxies and the Universe*. Ed. by Allan Sandage et al., p. 557.

Šuhada, R. et al. (Jan. 2012). "The XMM-BCS galaxy cluster survey. I. The X-ray selected cluster catalog from the initial 6 deg^2". In: *A&A* 537, A39, A39. DOI: 10.1051/0004-6361/201117214. arXiv: 1111.0141 [astro-ph.CO].

van Breukelen, C. et al. (Nov. 2006). "Galaxy clusters at 0.6 ¡ z ¡ 1.4 in the UKIDSS Ultra Deep Survey Early Data Release". In: *MNRAS* 373.1, pp. L26–L30. DOI: 10.1111/j.1745-3933.2006.00236.x. arXiv: astro-ph/0608624 [astro-ph].

van Weeren, R. J. et al. (Feb. 2019). "Diffuse Radio Emission from Galaxy Clusters". In: *Space Sci. Rev.* 215.1, 16, p. 16. DOI: 10.1007/s11214-019-0584-z. arXiv: 1901.04496 [astro-ph.HE].

von der Linden, Anja et al. (Mar. 2014). "Weighing the Giants - I. Weak-lensing masses for 51 massive galaxy clusters: project overview, data analysis methods and cluster images". In: *MNRAS* 439.1, pp. 2–27. DOI: 10.1093/mnras/stt1945. arXiv: 1208.0597 [astro-ph.CO].